

REPORT DOCUMENTATION PAGE

AFRL-SR-AR-TR-04-

ining the
reducing
22202-
I currently

Public reporting burden for this collection of information is estimated to average 1 hour per response, including the time for review, data needed, and completing and reviewing this collection of information. Send comments regarding this burden estimate or any this burden to Department of Defense, Washington Headquarters Services, Directorate for Information Operations and Reports (4302. Respondents should be aware that notwithstanding any other provision of law, no person shall be subject to any penalty for failing to comply with a collection of information if it does not display a valid OMB control number. PLEASE DO NOT RETURN YOUR FORM TO THE ABOVE ADDRESS.

1. REPORT DATE (DD-MM-YYYY) January 26, 2004		2. REPORT TYPE Final Technical Report		0154
4. TITLE AND SUBTITLE DISTRIBUTED CONTROL OF NONLINEAR AIRCRAFT STRUCTURES INCLUDING AERODYNAMIC AND TEMPERATURE INTERACTIONS		5a. CONTRACT NUMBER 5b. GRANT NUMBER F49620-98-1-0467		05/01/1998- 05/14/2002
6. AUTHOR(S) H. S. Tzou, Department of Mechanical Engineering G. E. Blandford, Department of Civil Engineering University of Kentucky, Lexington, KY 40506-0503		5c. PROGRAM ELEMENT NUMBER 5d. PROJECT NUMBER		5e. TASK NUMBER 3484 /BS
7. PERFORMING ORGANIZATION NAME(S) AND ADDRESS(ES) University of Kentucky Research Foundation Office of Sponsored Project Admin Kinkead Hall Lexington, KY 40506-0420		8. PERFORMING ORGANIZATION REPORT NUMBER		5f. WORK UNIT NUMBER
9. SPONSORING / MONITORING AGENCY NAME(S) AND ADDRESS(ES) Major Brian P. Sanders (202) 767-6963 AFOSR, 4015 Wilson Blvd., Room 713, Arlington, VA 22203-1954		10. SPONSOR/MONITOR'S ACRONYM(S)		11. SPONSOR/MONITOR'S REPORT NUMBER(S)
12. DISTRIBUTION / AVAILABILITY STATEMENT Approved for public release, distribution unlimited				
13. SUPPLEMENTARY NOTES 20040315 027				
14. ABSTRACT Imposed shape changes and surface control of flexible structures can offer many aerodynamic advantages in flight maneuverability and precision control. Largely deformed shapes and surfaces often involve nonlinear deformations. Studies on the control of nonlinear behavior related to the deformed surfaces and shape changes would provide detailed information for future controlled surface design and implementation. This research is concerned with the controlling nonlinearly deformed structures, e.g., various shells and flexible wings, based on the smart structures technology. Distributed sensing/actuation, thermoelectromechanical/control equations and boundary conditions including elastic, temperature, and piezoelectric couplings are derived and applied to distributed sensing/actuation and control of various nonlinear and linear aerospace structures and components made of shells and plates. Analytical solutions are compared with experimental data and/or finite element solutions. A new finite element code, consisting of nonlinear/linear piezothermoelastic shell and hexahedral elements, is developed and applied to various nonlinear/linear aerospace structures with or without temperature excitations. Active control of imposed shape changes, nonlinear flexible deflections, thermal deformations, natural frequencies, and dynamic responses using distributed piezoelectric actuators are studied, and their nonlinear effects evaluated.				
15. SUBJECT TERMS				
16. SECURITY CLASSIFICATION OF: a. REPORT X b. ABSTRACT X c. THIS PAGE X		17. LIMITATION OF ABSTRACT	18. NUMBER OF PAGES 371	19a. NAME OF RESPONSIBLE PERSON Horn-sen Tzou 19b. TELEPHONE NUMBER (include area code) 859-257-6336 X80643

TABLE OF CONTENTS

EXECUTIVE SUMMARY	iii
CHAPTER 1 - DISTRIBUTED PRECISION CONTROL OF LINEAR AND NONLINEAR STRUCTRONIC SHELLS – THEORY	1
CHAPTER 2 - MODAL VOLTAGES OF LINEAR AND NONLINEAR STRUCTURES USING DISTRIBUTED ARTIFICIAL NEURONS	36
CHAPTER 3 - PRECISION ACTUATION OF NONLINEAR PLATES	50
CHAPTER 4 - A NEW X-ACTUATOR DESIGN FOR DUAL BENDING/TWISTING CONTROL OF WINGS	62
CHAPTER 5 - NEURAL POTENTIALS AND MICRO-SIGNALS OF NONLINEAR DEEP AND SHALLOW CONICAL SHELLS	75
CHAPTER 6 - MICRO-ACTUATION CHARACTERISTICS OF CONICAL SHELL SECTIONS	96
CHAPTER 7 - MICRO-SENSOR ELECTROMECHANICS AND DISTRIBUTED SIGNAL ANALYSIS OF PIEZO(ELECTRIC)-ELASTIC SPHERICAL SHELLS	111
CHAPTER 8 - MICRO-CONTROL ACTIONS OF ACTUATOR PATCHES LAMINATED ON HEMISPHERICAL SHELLS	130
CHAPTER 9 - MICRO-SENSING CHARACTERISTICS AND MODAL VOLTAGES OF LINEAR/NONLINEAR TOROIDAL SHELLS	154
CHAPTER 10 - MICRO-CONTROL ACTIONS AND LOCATION SENSITIVITY OF PATCHE ACTUATORS ON TOROIDAL SHELLS	176
CHAPTER 11 - MICRO-ELECTROMECHANICS OF SENSOR PATCHES ON FREE PARABOLOIDAL SHELL STRUCTRONIC SYSTEMS	199
CHAPTER 12 - DISTRIBUTED MODAL VOLTAGES OF NONLINEAR PARABOLOIDAL SHELLS WITH DISTRIBUTED NEURONS	216
CHAPTER 13 - ACTUATOR PLACEMENT AND MICRO-ACTUATION EFFICIENCY OF ADAPTIVE PARABOLOIDAL SHELLS	233

CHAPTER 14 - MICRO-CONTROL ACTIONS OF SEGMENTED ACTUATOR PATCHES LAMINATED ON DEEP PARABOLOIDAL SHELLS	254
CHAPTER 15 - OPTIMAL CONTROL OF PRECISION PARABOLOIDAL SHELL STRUCTRONIC SYSTEMS	270
CHAPTER 16 - DYNAMICS AND DISTRIBUTED CONTROL OF CONICAL SHELLS LAMINATED WITH FULL AND DIAGONAL ACTUATORS (Finite Element Development and Analysis)	292
CHAPTER 17 - VIBRATION CONTROL OF TOROIDAL SHELLS WITH PARALLEL AND DIAGONAL PIEZOELECTRIC ACTUATORS (Finite Formulation and Analysis)	310
CHAPTER 18 - CONTROL OF NONLINEAR ELECTRO/ELASTIC BEAM AND PLATE SYSTEMS (Finite Element Formulation and Analysis)	327
CHAPTER 19 - DYNAMICS AND CONTROL OF ADAPTIVE NONLINEAR PIEZOTHERMOELASTIC STRUCTURES WITH COUPLED ELECTRIC, THERMAL AND MECHANICAL FIELDS (A Finite Element Approach)	347
APPENDIX	367

EXECUTIVE SUMMARY

DISTRIBUTED CONTROL OF NONLINEAR AIRCRAFT STRUCTURES INCLUDING AERODYNAMIC AND TEMPERATURE INTERACTIONS

H. S. Tzou ¹, G. E. Blandford ², and V. B. Venkayya ³

¹ Department of Mechanical Engineering

² Department of Civil Engineering

University of Kentucky, Lexington, KY 40506-0108

³ Flight Dynamics Directorate, Wright Laboratory, WPAFB, Ohio 45433

Imposed shape changes and surface control of flexible structures can offer many aerodynamic advantages in flight maneuverability and precision control. Largely deformed shapes and surfaces often involve nonlinear deformations. Studies on the control of nonlinear behavior related to the deformed surfaces and shape changes would provide detailed information for future controlled surface design and implementation. This research is concerned with the controlling nonlinearly deformed structures, e.g., shells and flexible wings, based on the smart structures technology. Piezoelectric materials are widely used as sensors and actuators in sensing, actuation, and control of smart structures and structronic (structure-electronic) systems. Investigation of the control effectiveness of nonlinear flexible structures composed of piezoelectric laminates subjected to aerodynamic and temperature excitations are proposed. It is assumed that the flexible aerospace structures encounter the von Karman type geometric nonlinearity.

Distributed sensing/actuation, thermoelectromechanical equations and boundary conditions including elastic, temperature, and piezoelectric couplings are derived and applied to distributed sensing/actuation and control of various nonlinear and linear aerospace structures and components made of shells and plates. Analytical solutions are compared with experimental data and/or finite element solutions.

A new finite element code, consisting of nonlinear/linear piezothermoelastic shell and hexahedral elements, is developed and applied to various nonlinear/linear aerospace structures with or without temperature excitations. Active control of imposed shape changes, nonlinear flexible deflections, thermal deformations, natural frequencies, and dynamic responses using distributed piezoelectric actuators are studied, and their nonlinear effects evaluated.

DISTRIBUTION STATEMENT A

Significant advancements and findings on theories, finite element formulations and results are respectively detailed in various chapters presented next.

Chapter 1 discusses generic theories of piezo(electric)thermoelastic shells and distributed sensing and control of distributed parameter systems, such as typical shell/plate-type aerospace structures. A number of representative case studies of distributed sensing, micro-actuation, vibration control and optimal control, including beams, plates, conical shells, spherical shells, toroidal shells, and paraboloidal shells, etc., are respectively presented from Chapter 2 to Chapter 15. Chapter 16 to Chapter 19 outline new finite element formulation of piezothermoelastic shells, validation of codes and case studies of nonlinear/linear structures with or without temperature effects. Key publications are summarized in Appendix.

Personnel Involved:

1. Faculty or Research Scientist: H. S. Tzou (Department of Mechanical Engineering); G. E. Blandford (Department of Civil Engineering), and V. B. Venkayya (Flight Dynamics Directorate, Wright Laboratory, WPAFB); Y. Shimamura (Visiting Professor, Department of Mechano-Aerospace Engineering, Tokyo Institute of Technology)
2. Graduate Students: John W. Moore (Ph.D., Civil Engineering); Jianghong Ding (Ph.D., Mechanical Engineering; Dongwei Wang, Ph.D., Mechanical Engineering); Richard M. Howard (M.S., Mechanical Engineering); P. Smithmaitrie (Ph.D., Mechanical Engineering)
3. Undergraduate Students: Greg J. DeHaven (Mechanical Engineering) (Continue to Ph.D. in Mechanical Engineering); Jason Cullens; Brandon Crane; Chris Reeves; Shawn Stigall; Bryan Mueller; Scott Munich; Tara Conn; Brandon Delis

CHAPTER 1

DISTRIBUTED PRECISION CONTROL OF LINEAR AND NONLINEAR STRUCTRONIC SHELLS – THEORY

ABSTRACT

The complexity of multi-field photo-thermo-electromechanical/control couplings of distributed parameter systems (DPSs) always poses many challenging research issues. This multi-field coupling completely reflects the synergistic integration of multifunctional smart materials, sensors, actuators, control electronics with machines or structures, enabling new distributed strutronic (structure + electronic) systems capable of self-sensing, diagnosis, and control. Consequently, multi-field coupling and control of distributed strutronic systems further inspires many new research, development, and system integration issues. This article is to present a generic nonlinear piezo(electric)-thermoelectromechanical shell theory based on a nonlinear piezoelectric double-curvature strutronic shell continuum with permissible boundary conditions. Applications of the generic theory to distributed sensing and control of other standard linear and nonlinear strutronic DPSs (e.g., shell and non-shell continua or DPSs) based on four system parameters are also demonstrated. Fundamental background of the distributed parameter systems is introduced, followed by definitions of distributed sensors and actuators and their governing equations. Application examples and design principles are presented afterwards. Detailed sensing and control electromechanical characteristics of specific strutronic continua or DPSs are presented in later articles.

INTRODUCTION

Mass, stiffness, static and dynamic characteristics of elastic continua, machines, and structures (e.g., shells and plates) are generally "distributed" in nature, i.e., their properties or behaviors are functions of time and spatial coordinates. Accordingly, these systems are usually classified as *distributed parameter systems* (DPSs) and they are usually modeled by partial differential equations (PDEs). In practical applications, however, due to their complexity, discretization techniques are often employed and, for convenience, the derived simplified *lumped* (or *discrete*) *parameter systems* (LPSs) are analyzed and evaluated. Accordingly, simplified LPS only reveals partial system characteristics of the original DPS. Similarly, sensing and control of DPSs using conventional (discrete or point) sensors and actuators at spatially discrete locations also pose many technical deficiencies, especially they are placed at (or near) modal nodes or lines of DPSs. Eventually, these modes are neither observable nor controllable by these discrete transducers. To remedy the discrete sensor/actuator deficiencies and to observe and control the elastic DPSs, spatially distributed sensors and actuators are highly desirable.

The complexity of multi-field photo-thermo-electromechanical/control couplings of multifunctional distributed parameter systems (DPSs) always poses many challenging research issues over the years. Recent development of smart structures and structronic systems emphasizing synergistic integration of controllable smart materials, e.g., piezoelectrics, shape memory materials, electro- and magneto-strictive materials, electro- and magneto-rheological fluids, photostrictives, magneto-optical materials, etc., with high-performance structures, precision structronic and mechatronic systems represents a highlight of classical multi-field coupling and interactions. In general, these smart materials can respond to certain stimuli, e.g., strain, force, pressure, light, etc., and also be actively controlled via electrical field, magnetic field, currents, high-energy lights, etc. (Tzou, 1998). Accordingly, structures and structronic systems incorporating these smart materials are capable of responding to certain stimuli in a prescribed manner based on specified performance or control requirements (Tzou and Bergman, 1998). Furthermore, the multi-field photo-piezo(electric)-magneto-thermo-elastic-control coupling and interactions of smart structures and structronic systems, **Figure 1**, have been becoming much more complicated and they deserve in-depth studies to establish profound database and design guidelines for the next-generation high-performance smart structures and structronic systems.

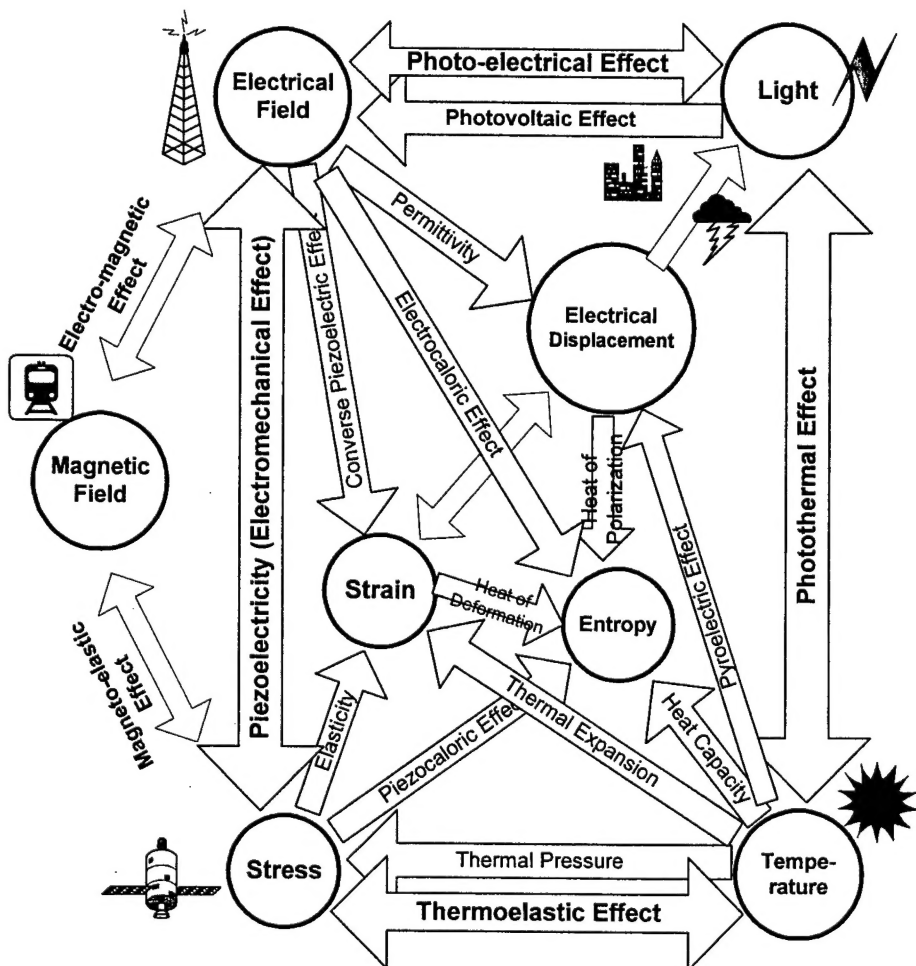


Fig.1 Multi-field coupling among elastic, electric, magnetic, temperature and light fields.

Piezoelectricity is an electromechanical phenomenon coupling the elastic (*dynamic coupling*) field and the electric (*static coupling*) field, which was first observed by the Curie brothers (Jacques and Pierre) in 1880. Piezoelectric materials exhibit two distinct electromechanical effects: the direct piezoelectric effect and the converse piezoelectric effect. The former is the fundamental for sensor applications, e.g., accelerometers, force/pressure transducers, etc; the latter is the basis for precision actuation and control applications. However, temperature fluctuation also influences the electromechanical behavior and thus, the two-field coupling extends to the three-field coupling – the piezo(electric)-thermoelastic coupling, as illustrated in **Figure 2**.

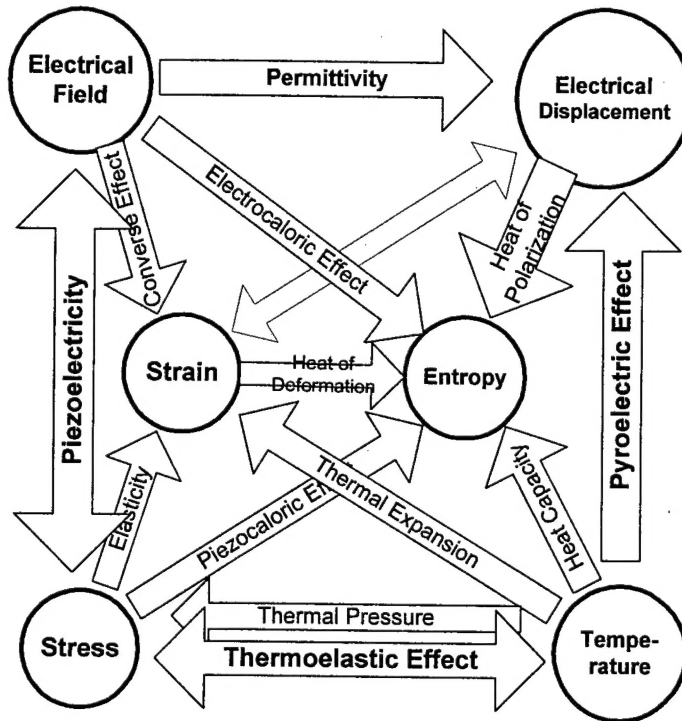


Fig.2 Piezo(electric)-thermoelasticity –
a piezothermoelectromechanical coupling.

Due to its versatility in both sensor and actuator applications (Mason, 1981; Sesseler, 1981; Dökmeci, 1983; Tzou, 1998), piezoelectric materials are also widely used in modern smart structures and strucronic systems. Over the years, sophisticated piezoelectricity theories were proposed and refined; new piezoelectric materials were discovered or synthesized (Mason, 1950; Cady, 1964; Mindlin, 1961&1972; Tiersten, 1969; Sesseler, 1981; Dökmeci, 1983; Tzou, 1993a&b; Rogacheva, 1994). Novel piezoelectric devices were invented and applied to a variety of engineering applications (Mason, 1981; Sessler, 1981; Dökmeci, 1983; Tzou and Anderson, 1992; Tzou and Fukuda, 1992; Tzou and Bergman, 1998; Gabbert and Tzou, 2001). Engineering application of the piezoelectric materials started with a depth-sounding device, based on Rochelle salt, invented by Langevin in 1917. Many other sensors (e.g., accelerometers, pressure transducer, force transducers, microphones, etc.), actuators (precision manipulator, robot manipulator, ultrasonic motors, driving mechanism for scanning tunneling microscopes, etc.), smart structures and strucronic systems (e.g., helicopter rotor blades, airplane wings, space

structures, precision trusses, etc.) have been documented. New devices are being invented and patented constantly.

In the recent development of active, adaptive (or smart) structures, micro-electromechanical and strucronic systems, active piezoelectric and elastic/piezoelectric structures (elastic or composite materials integrated with piezoelectric transducers, control electronics, etc.) are, again, very promising in both static and dynamic applications. Examples include aerospace/aircraft structures (Crawley and de Luis, 1987; Hanagud and Obal, 1988), robot manipulators (Tzou, 1989), vibration controls and isolations, high-precision devices, micro-sensors/actuators, thin-film micro-electromechanical systems (MEMS) (Polla, 1992), micro-displacement actuation and control (Tzou and Fukuda, 1991; 1992), etc. Additional applications in smart structures and strucronic systems encompass distributed structural control (Plumb, Hubbard, and Bailey, 1987; Baz and Poh, 1988; Tzou, 1987, 1993; Tzou and Zhou, 1997), rotor dynamics control (Palazzolo, et al., 1989), self-sensing actuators (Dosch, Inman, Garcia, 1992; Anderson, Hagood, Goodliffe, 1992; Tzou and Hollkamp, 1994), orthogonal modal sensors/actuators (Lee and Moon, 1988; Tzou, Zhong, and Natori, 1994; Tzou, Zhong, Hollkamp, 1994), space truss members (Fason and Gabra, 1988; Lih, et al, 2001), noise control (Banks and Smith, 1998), control of flexible robots, active constrained damping (Baz and Ro, 1994) etc. Recalled that commercial transducer applications were thoroughly reviewed by Mason (1981) and Sessler (1981). Other recent practical applications include piezoelectric damped skis, control of aeroelastic wing flutter, optical metering truss control, helicopter blade control, noise reduction, active constrained layer damping, biomedical applications, ultrasonic motors, etc. (Lynch, 1996; Ashley, 1995; Galletti, et al., 1988; Ueha, et al., 1993; Sashida and Kenjo, 1993; Uchino, 1997).

As the function requirement increases, the geometry of the piezoelectric devices also extends from the one-dimensional (1D) DPSs (i.e., rods and beams) to two-dimensional (2D) DPSs (e.g., flat rectangular and circular plates), and 2D curved DPSs (e.g., cylindrical shells, conical shells, spherical shells, etc.) (Tzou, 1993). Linear piezoelastic phenomena and theories have been studied for years (Chau, 1986; Dökmeci, 1983; Drumheller and Kalnins, 1970; Mindlin, 1972; Rogacheva, 1994; Senik and Kudriavtsev, 1980; Tzou and Gadre, 1989). An umbrella linear piezo-thermo-elastic shell theory based on a double-curvature generic shell was proposed and the derived governing equations can be easily simplified to account for many standard piezoelectric continua (Tzou and Howard, 1994). Linear thermo-electromechanical behavior and precision position control of distributed piezoelectric sensors and actuators were also investigated (Koppe, et al., 1998; Tzou and Ye, 1994). As the deformation goes beyond the linear elastic range, the large deformation geometric nonlinearity also comes into consideration. Geometrical nonlinearity of elastic shells was investigated over the years (Librescu, 1987; Palazotto and Dennis, 1992; Pietraszkiewicz, 1979; Chia, 1980). Pai, et al. (1993) proposed a nonlinear model for a piezoelectric plate. However, geometrical nonlinearity of anisotropic piezothermoelastic shells simultaneously exposed to mechanical, electric, and thermal fields have not been fully investigated (Tzou and Bao, 1997; Tzou and Zhou, 1995). This article is to present an advanced nonlinear piezo(electric)-thermoelastic shell theory (Tzou and Yang, 2000), distributed sensing and control of strucronic shells, and their applications to common or standard distributed strucronic structures and systems, e.g., isolators, reflectors, nozzles, mirrors, antennas, disks, wing boxes, rocket fairings, flexible robots, active struts, etc.

PIEZO(ELECTRIC)-THERMOELASTIC CONSTITUTIVE EQUATIONS AND NONLINEAR PIEZO-THERMOELASTIC FLEXIBLE SHELL CONTINUA

Mathematical model of the nonlinear piezo(electric)-thermoelastic shell continuum or DPS with the large-deformation geometric nonlinearity offers an umbrella approach that can be easily extended to nonlinear shells, (e.g., spherical, conical, cylindrical, etc.) and plates (e.g., rectangular, circular, etc.), linear shells and plates, and many other standard shapes (e.g., arches, rings, beams, etc.). **Figure 3** illustrates three fundamental double-curvature flexible shell continua, in which **Figure 3a** illustrates a generic double-curvature flexible piezo(electric)-thermoelastic shell subjected to mechanical, electric, and temperature excitations; **Figure 3b** shows a typical structronic shell with coupled distributed sensor and actuator layers; **Figure 3c** illustrates a composite piezothermoelastic shell with arbitrary sensor/actuator layers. All three shells are defined in a tri-orthogonal curvilinear coordinate system in which α_1 and α_2 define the in-plane axes and α_3 defines the transverse direction. Thus, fundamental theories, distributed control mechanisms, and solution procedures, etc. derived for the generic nonlinear flexible shell DPSs can be easily applied to a large number of flexible shell and non-shell structural DPSs. In this section, fundamental piezo(electric)-thermoelectromechanical properties of a piezoelectric continuum are briefly reviewed. A generic theory based on a nonlinear piezo(electric)-thermoelastic shell DPS with the von Karman geometric nonlinearity is proposed and its governing equations are derived.

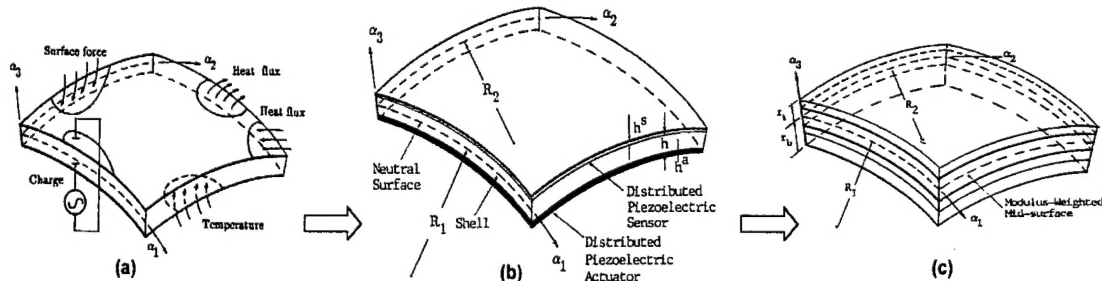


Fig.3 Three generic double-curvature shells: a) a piezothermoelastic shell, b) a structronic shell, and c) a structronic composite shell laminate.

Piezo(electric)-thermoelastic Constitutive Equations

Piezo-thermoelectromechanical constitutive relations, **Figure 2**, of a generic piezothermoelastic shell continuum DPS are governed by three fundamental equations (Tzou and Howard, 1994):

$$1) \text{ Stress equation: } \{T\} = [c]\{S\} - [e]^t\{E\} - \{\lambda\}\theta, \quad (1)$$

$$2) \text{ Electric displacement equation: } \{D\} = [e]\{S\} + [\varepsilon]\{E\} + \{p\}\theta, \quad (2)$$

$$3) \text{ Thermal entropy equation: } \Gamma = \{\lambda\}^t\{S\} + \{p\}^t\{E\} + \alpha_v\theta, \quad (3)$$

where $\{T\}$, $\{S\}$, $\{E\}$ and $\{D\}$ are respectively the stress, strain, electric field and electric displacement vectors; $[c]$, $[e]$, and $[\varepsilon]$ denote the elastic stiffness coefficient, the piezoelectric coefficient, and the dielectric permittivity matrices, respectively; Γ is the thermal entropy density; θ is the temperature rise ($\theta = \Theta - \Theta_0$ where Θ is the absolute

temperature and Θ_0 the temperature of natural state in which stresses and strains are zero); $\{\lambda\}$ is the stress-temperature coefficient vector; $\{p\}$ is the pyroelectric coefficient vector; and α_v is a material constant ($\alpha_v = \rho c_v / \Theta_0$ where ρ is the material density and c_v is the specific heat at a constant volume). $[\cdot]^t$ and $\{\cdot\}^t$ denote the matrix and vector transpose, respectively. The electric fields E_1, E_2, E_3 and the electric potential ϕ in the shell curvilinear shell coordinate system are defined by $[E_i] = -[f_{ii}] \cdot \{\partial\phi / \partial\alpha_i\}$, $i = 1, 2, 3$, where $f_{ii}(\alpha_1, \alpha_2, \alpha_3) = A_i(1 + \alpha_3/R_i)$ ($i = 1, 2$), $f_{33}(\alpha_1, \alpha_2, \alpha_3) = 1$; α_3 is a finite distance measured from the reference surface; A_1 and A_2 are the Lamé parameters; R_1 and R_2 are the radii of curvature of the α_1 and α_2 axes on the neutral surface defined by $\alpha_3 = 0$. The Lamé parameters (A_1 and A_2) and two radii (R_1 and R_2) are the four essential parameters used in simplification and application of the generic shell theory to other geometries and shell/non-shell continua and DPSs (Tzou, 1993). Nonlinear piezo-thermoelastic shells are evaluated and generic thermo-electromechanical equations are defined next.

Large-deformation Geometric Nonlinearity

Shape transformation and imposed shape control often involves large deformations – the geometric nonlinearity. A generic nonlinear deflection U_i in the i -th direction of the shell can be expressed as a summation of an (in-plane) membrane displacement $u_i(\alpha_1, \alpha_2, t)$ and a higher order nonlinear shear deformation effect represented by the summation of angular rotations $\beta_{ij}(\alpha_1, \alpha_2, t)$:

$$U_i(\alpha_1, \alpha_2, \alpha_3, t) = u_i(\alpha_1, \alpha_2, t) + \sum_{j=1}^m \alpha_3^j \beta_{ij}(\alpha_1, \alpha_2, t), \quad i=1, 2, 3. \quad (4)$$

Note that β_{11} and β_{21} represent the rotational angles in the positive sense of the α_1 and α_2 axes, respectively; and $\beta_{3j} = 0$. This expression includes the higher order nonlinear shear deformation effects. However, according to the Love-Kirchhoff thin shell assumptions and a linear displacement approximation (first order shear deformation theory), only the first term is kept in the equation, i.e., $m = 1$. The displacements and rotational angles are independent variables in thick shells. However, the rotational angles are dependent variables in thin shells, and they can be derived from the thin shell assumptions in which the transverse normal strain S_3 is negligible and the shear strains S_4 and S_5 are zeros. Based on the thin shell assumptions, the rotational angles $\beta_1 = \beta_{11}$ and $\beta_2 = \beta_{21}$ are derived from the transverse shear strain equations, i.e., $S_4 = 0$ and $S_5 = 0$. Thus, the rotational angles are defined as

$$\beta_i = \frac{u_i}{R_i} - \frac{1}{A_i} \frac{\partial u_3}{\partial \alpha_i}, \quad i = 1, 2. \quad (5)$$

In general, since $\alpha_3/R_1 \ll 1$ $\alpha_3/R_2 \ll 1$, thus, the ratios of the finite distance to the radius of curvature are usually negligible, i.e., $f_{11} \approx A_1$ and $f_{22} \approx A_2$.

Although it is assumed that the piezoelectric shell experiences large deformations in three axial directions, however, in reality, the in-plane deflections are still much smaller than the transverse deflection. Thus, the nonlinear effects due to the in-plane large deflections are usually neglected, i.e., the von Karman-type assumptions (Palazotto and Dennis, 1992; Chia, 1980; Tzou and Yang, 2000). The nonlinear strain-displacement

relations of a thin shell with a large transverse deflection u_3 include a linear effect, denoted by a superscript ℓ , and a nonlinear effect, denoted by a superscript n , induced by the large deformation:

$$\{S_i\} = [\{s_i^0\}^\ell + \{s_i^0\}^n] + \alpha_3 \{k_i\}, \quad i = 1, 2, 6, \quad (6)$$

where the subscripts 1 and 2 respectively denote two normal strains and 6 is the in-plane shear strain. Detailed membrane and bending strains (s_i^0 and k_i) are expressed as functions of displacements - u_i 's, the Lamé parameters (A_1 and A_2), and two radii (R_1 and R_2).

Membrane strains:

$$s_1^0 = \frac{1}{A_1} \frac{\partial u_1}{\partial \alpha_1} + \frac{u_2}{A_1 A_2} \frac{\partial A_1}{\partial \alpha_2} + \frac{u_3}{R_1} + \frac{1}{2} \left(\frac{\partial u_3 / \partial \alpha_1}{A_1} \right)^2, \quad (7)$$

$$s_2^0 = \frac{1}{A_2} \frac{\partial u_2}{\partial \alpha_2} + \frac{u_1}{A_1 A_2} \frac{\partial A_2}{\partial \alpha_1} + \frac{u_3}{R_2} + \frac{1}{2} \left(\frac{\partial u_3 / \partial \alpha_2}{A_2} \right)^2, \quad (8)$$

$$s_6^0 = \frac{1}{A_2} \frac{\partial u_1}{\partial \alpha_2} + \frac{1}{A_1} \frac{\partial u_2}{\partial \alpha_1} - \frac{u_1}{A_1 A_2} \frac{\partial A_1}{\partial \alpha_2} - \frac{u_2}{A_1 A_2} \frac{\partial A_2}{\partial \alpha_1} + \left(\frac{1}{A_1 A_2} \frac{\partial u_3}{\partial \alpha_1} \frac{\partial u_3}{\partial \alpha_2} \right); \quad (9)$$

Bending strains:

$$k_1 = \frac{1}{A_1} \frac{\partial}{\partial \alpha_1} \left(\frac{u_1}{R_1} - \frac{1}{A_1} \frac{\partial u_3}{\partial \alpha_1} \right) + \frac{1}{A_1 A_2} \left(\frac{u_2}{R_2} - \frac{1}{A_2} \frac{\partial u_3}{\partial \alpha_2} \right) \frac{\partial A_1}{\partial \alpha_2}, \quad (10)$$

$$k_2 = \frac{1}{A_2} \frac{\partial}{\partial \alpha_2} \left(\frac{u_2}{R_2} - \frac{1}{A_2} \frac{\partial u_3}{\partial \alpha_2} \right) + \frac{1}{A_1 A_2} \left(\frac{u_1}{R_1} - \frac{1}{A_1} \frac{\partial u_3}{\partial \alpha_1} \right) \frac{\partial A_2}{\partial \alpha_1}, \quad (11)$$

$$k_6 = \frac{1}{A_2} \frac{\partial}{\partial \alpha_2} \left(\frac{u_1}{R_1} - \frac{1}{A_1} \frac{\partial u_3}{\partial \alpha_1} \right) + \frac{1}{A_1} \frac{\partial}{\partial \alpha_1} \left(\frac{u_2}{R_2} - \frac{1}{A_2} \frac{\partial u_3}{\partial \alpha_2} \right) - \frac{1}{A_1 A_2} \left(\frac{u_1}{R_1} - \frac{1}{A_1} \frac{\partial u_3}{\partial \alpha_1} \right) \frac{\partial A_1}{\partial \alpha_2} - \frac{1}{A_1 A_2} \left(\frac{u_2}{R_2} - \frac{1}{A_2} \frac{\partial u_3}{\partial \alpha_2} \right) \frac{\partial A_2}{\partial \alpha_1}. \quad (12)$$

Note that the quadratic terms (nonlinear terms) inside the brackets are contributed by the large deflection. The membrane force resultants N_{ij} and the bending moments M_{ij} of the piezothermoelastic shell, **Figure 3a**, are defined by the elastic, electric, and the temperature components.

$$\begin{bmatrix} N_{11} \\ N_{22} \\ N_{12} \\ M_{11} \\ M_{22} \\ M_{12} \end{bmatrix} = \begin{bmatrix} A_{11} & A_{12} & A_{16} & 0 & 0 & 0 \\ A_{12} & A_{22} & A_{26} & 0 & 0 & 0 \\ A_{16} & A_{26} & A_{66} & 0 & 0 & 0 \\ 0 & 0 & 0 & D_{11} & D_{12} & D_{16} \\ 0 & 0 & 0 & D_{12} & D_{22} & D_{26} \\ 0 & 0 & 0 & D_{16} & D_{26} & D_{66} \end{bmatrix} \begin{bmatrix} s_1^0 \\ s_2^0 \\ s_6^0 \\ k_1 \\ k_2 \\ k_6 \end{bmatrix} - \begin{bmatrix} N_{11}^e \\ N_{22}^e \\ N_{12}^e \\ M_{11}^e \\ M_{22}^e \\ M_{12}^e \end{bmatrix} - \begin{bmatrix} N_{11}^\theta \\ N_{22}^\theta \\ N_{12}^\theta \\ M_{11}^\theta \\ M_{22}^\theta \\ M_{12}^\theta \end{bmatrix}. \quad (13)$$

Furthermore, membrane force resultants N_{ij} and bending moments M_{ij} of the piezothermoelastic laminated composite shell, **Figure 3c**, can be defined as follows (Tzou and Bao, 1997):

$$\begin{bmatrix} N_{11} \\ N_{22} \\ N_{12} \\ M_{11} \\ M_{22} \\ M_{12} \end{bmatrix} = \begin{bmatrix} A_{11} & A_{12} & A_{16} & B_{11} & B_{12} & B_{16} \\ A_{12} & A_{22} & A_{26} & B_{12} & B_{22} & B_{26} \\ A_{16} & A_{26} & A_{66} & B_{16} & B_{26} & B_{66} \\ B_{11} & B_{12} & B_{16} & D_{11} & D_{12} & D_{16} \\ B_{12} & B_{22} & B_{26} & D_{12} & D_{22} & D_{26} \\ B_{16} & B_{26} & B_{66} & D_{16} & D_{26} & D_{66} \end{bmatrix} \begin{bmatrix} s_1^0 \\ s_2^0 \\ s_6^0 \\ k_1 \\ k_2 \\ k_6 \end{bmatrix} - \begin{bmatrix} N_{11}^e \\ N_{22}^e \\ N_{12}^e \\ M_{11}^e \\ M_{22}^e \\ M_{12}^e \end{bmatrix} - \begin{bmatrix} N_{11}^\theta \\ N_{22}^\theta \\ N_{12}^\theta \\ M_{11}^\theta \\ M_{22}^\theta \\ M_{12}^\theta \end{bmatrix}, \quad (14)$$

where A_{ij} , B_{ij} and D_{ij} are the extensional, coupling, and bending stiffness constants. Superscripts e and θ respectively denote the electric and temperature components. The membrane strains and the bending strains are coupled by the coupling stiffness coefficients B_{ij} in the elastic force/moment resultants. N_{ij}^e and N_{ij}^θ are the electric and temperature induced forces; M_{ij}^e and M_{ij}^θ are the electric and temperature induced moments, respectively. In actuator applications, these electric forces and moments are used to control shell's static and dynamic characteristics. These strain/displacement relations, membrane force resultants, bending moment resultants, etc. are used in Hamilton's equation to derive thermo-electromechanical equations and boundary conditions of the nonlinear piezothermoelastic shells. Although it is assumed that the transverse shear deflections can be neglected, the integrated effect of the transverse shear stress resultants Q_{13} and Q_{23} are not neglected. Note that the effects of rotary inertias can be neglected in thin shells without large rotational effects.

Hamilton's Principle and Nonlinear System Equations

Hamilton's principle is used to derive the thermo-electromechanical shell equations and boundary conditions of the piezothermoelastic shell continuum. Hamilton's principle assumes that the energy variations over an arbitrary period of time are zero. Considering all energies, one can write Hamilton's equation as (Tzou and Bao, 1998; Tzou and Yang, 2000)

$$\delta \int_{\alpha} \left\{ \left(\int_V \frac{1}{2} \rho \dot{U}_j \dot{U}_j dV - \left[\int_V (H(S_i, E_i, \Theta) + \Im \Theta) dV - \int_S (t_j U_j - Q_j \phi) dS \right] dt \right) \right\} dt = 0. \quad (15)$$

where ρ is the mass density; H is the electric enthalpy; t_j is the surface traction in the α_j direction; Q_j is the surface electric charge; ϕ is the electrical potential; V and S are the volume and surface of the piezothermoelastic shell continuum, respectively; and U_j and \dot{U}_j are the displacement and velocity vectors. It is assumed that only the transverse electric field E_3 is considered in the analysis. Substituting all energy expressions into Hamilton's equation and carrying out all variations, one can derive the nonlinear piezothermoelastic shell equations and boundary conditions of the nonlinear piezothermoelastic shell continuum.

$$-\frac{\partial(N_{11}A_2)}{\partial\alpha_1} + N_{22}\frac{\partial A_2}{\partial\alpha_1} - \frac{\partial(N_{21}A_1)}{\partial\alpha_2} - N_{12}\frac{\partial A_1}{\partial\alpha_2} - \frac{1}{R_1}\left[\frac{\partial(M_{11}A_2)}{\partial\alpha_1}\right. \\ \left.- M_{22}\frac{\partial A_2}{\partial\alpha_1} + \frac{\partial(M_{21}A_1)}{\partial\alpha_2} + M_{12}\frac{\partial A_1}{\partial\alpha_2}\right] + A_1A_2\rho\dot{u}_1 = A_1A_2F_1, \quad (16)$$

$$-\frac{\partial(N_{22}A_1)}{\partial\alpha_2} + N_{11}\frac{\partial A_1}{\partial\alpha_2} - \frac{\partial(N_{12}A_2)}{\partial\alpha_1} - N_{21}\frac{\partial A_2}{\partial\alpha_1} - \frac{1}{R_2}\left[\frac{\partial(M_{22}A_1)}{\partial\alpha_2}\right. \\ \left.- M_{11}\frac{\partial A_1}{\partial\alpha_2} + \frac{\partial(M_{12}A_2)}{\partial\alpha_1} + M_{21}\frac{\partial A_2}{\partial\alpha_1}\right] + A_1A_2\rho\dot{u}_2 = A_1A_2F_2, \quad (17)$$

$$-\frac{\partial}{\partial\alpha_1}\left[\frac{1}{A_1}\left(\frac{\partial(M_{11}A_2)}{\partial\alpha_1} - M_{22}\frac{\partial A_2}{\partial\alpha_1} + \frac{\partial(M_{21}A_1)}{\partial\alpha_2} + M_{12}\frac{\partial A_1}{\partial\alpha_2}\right)\right] - \frac{\partial}{\partial\alpha_2}\left[\frac{1}{A_2}\left(\frac{\partial(M_{22}A_1)}{\partial\alpha_2}\right.\right. \\ \left.\left.- M_{11}\frac{\partial A_1}{\partial\alpha_2} + \frac{\partial(M_{12}A_2)}{\partial\alpha_1} + M_{21}\frac{\partial A_2}{\partial\alpha_1}\right)\right] + A_1A_2\left(\frac{N_{11}}{R_1} + \frac{N_{22}}{R_2}\right) + A_1A_2\rho\dot{u}_3 \\ - \left\{\left[\frac{\partial(N_{11}A_2/A_1)}{\partial\alpha_1} + \frac{\partial N_{12}}{\partial\alpha_2}\right]\frac{\partial u_3}{\partial\alpha_1} + \left[\frac{\partial(N_{22}A_1/A_2)}{\partial\alpha_2} + \frac{\partial N_{12}}{\partial\alpha_1}\right]\frac{\partial u_3}{\partial\alpha_2} + 2N_{12}\frac{\partial^2 u_3}{\partial\alpha_1\partial\alpha_2}\right. \\ \left.+ N_{11}\frac{A_2}{A_1}\frac{\partial^2 u_3}{\partial\alpha_1^2} + N_{22}\frac{A_1}{A_2}\frac{\partial^2 u_3}{\partial\alpha_2^2}\right\} = A_1A_2F_3. \quad (18)$$

Note that all terms inside the braces are contributed by the nonlinear effects and the **nonlinear influence** on the transverse equation u_3 is significant. The thermo-electromechanical shell equations look similar to the standard shell equations. However, the force and moment expressions defined by the mechanical, thermal, and electric effects are much more complicated than the conventional elastic expressions, Eqs.(13) and (14). Substituting the expressions of N_{11} , N_{22} , N_{12} , M_{11} , M_{22} , M_{12} into the above equations yields the thermo-electromechanical equations defined in the reference displacements u_1 , u_2 , u_3 . Recall that the transverse shear deformation and the rotatory inertia effects are not considered. The electric terms, forces and moments, can be used in controlling the mechanical and/or temperature induced excitations (Tzou and Ye, 1994; Ye and Tzou, 2000).

Using Hamilton's equation, one can also derive all admissible mechanical and electric boundary conditions. Admissible mechanical boundary conditions on the boundary surfaces defined by a distance α_2 and α_1 are respectively summarized in Table 1 and Table 2.

Table 1 Boundary conditions (α_1 axis).

	Force/Moment	Displacement
1	$N_{11} = N_{11}^*$	$u_1 = u_1^*$
2	$M_{11} = M_{11}^*$	$\beta_1 = \beta_1^*$
3	$N_{12} + M_{12}/R_2 = V_{12}^*$	$u_2 = u_2^*$

4	$Q_{13} + \frac{\partial}{\partial \alpha_2} \left(\frac{M_{12}}{A_2} \right)$ $+ \left(N_{11} \left(\frac{1}{A_1} \cdot \frac{\partial u_3}{\partial \alpha_1} \right) + N_{12} \left(\frac{1}{A_2} \cdot \frac{\partial u_3}{\partial \alpha_2} \right) \right) = V_{13}^*$	$u_3 = u_3^*$
---	---	---------------

Table 2 Boundary conditions (α_2 axis).

	Force/Moment	Displacement
1	$N_{22} = N_{22}^*$	$u_2 = u_2^*$
2	$M_{22} = M_{22}^*$	$\beta_2 = \beta_2^*$
3	$N_{21} + \frac{M_{21}}{R_1} = V_{21}^*$	$u_1 = u_1^*$
4	$Q_{23} + \frac{\partial}{\partial \alpha_1} \left(\frac{M_{21}}{A_1} \right)$ $+ \left(N_{22} \left(\frac{1}{A_2} \cdot \frac{\partial u_3}{\partial \alpha_2} \right) + N_{21} \left(\frac{1}{A_1} \cdot \frac{\partial u_3}{\partial \alpha_1} \right) \right) = V_{23}^*$	$u_3 = u_3^*$

The superscript * denotes the boundary forces, moments, displacements, and slopes. Usually, only either the force/moment boundary conditions or the displacement/slope boundary conditions are selected for a given physical boundary condition (Tzou, 1993; Soedel, 1993). In addition, additional transverse shear force terms Q_{ij} are nonlinear components induced by large deformations. These force terms do not appear in the linear case. The shear stress resultants are defined as

$$V_{12} = N_{12} + \left(\frac{M_{12}}{R_1} \right), \quad (19)$$

$$V_{21} = N_{21} + \left(\frac{M_{21}}{R_1} \right), \quad (20)$$

$$V_{13} = Q_{13} + \frac{\partial}{\partial \alpha_2} \left(\frac{M_{12}}{A_2} \right), \quad (21)$$

$$V_{23} = Q_{23} + \frac{\partial}{\partial \alpha_1} \left(\frac{M_{21}}{A_1} \right), \quad (22)$$

where V_{13} and V_{23} are the Kirchhoff effective shear stress resultants of the first kind; V_{12} and V_{21} are the Kirchhoff effective shear stress resultants of the second kind (Soedel, 1993). Note that all elastic, electric, and thermal related terms are included in the force and moment expressions. These electric terms can be used, in conjunction with control algorithms, as control forces/moments counteracting mechanical and temperature induced vibrations in distributed structural control of shells (Tzou, Johnson, and Liu, 1999). Applications and simplifications of the nonlinear piezothermoelastic shell equations can be demonstrated in two ways: 1) material simplifications and 2) geometry simplifications

(Tzou, 1993; Tzou and Bao, 1996). In the next section, detailed distributed sensing and control mechanisms of distributed shell sensor/actuator layers are investigated. Generic sensing and actuation theories based on the double-curvature shells are defined next, follow by applications to other geometries using four system parameters, two Lamé parameters (A_1 and A_2) and two radii of curvature (R_1 and R_2).

DISTRIBUTED SENSING OF NONLINEAR STRUCTRONIC SHELLS

Distributed piezoelectric layers laminated on the generic nonlinear structronic shell respond to shell strain variations and consequently generate electric signals based on the direct piezoelectric effect, **Figure 4** – an enlarged version of **Figure 3b**. Assume the distributed sensor layer is made of hexagonal piezoelectric materials.

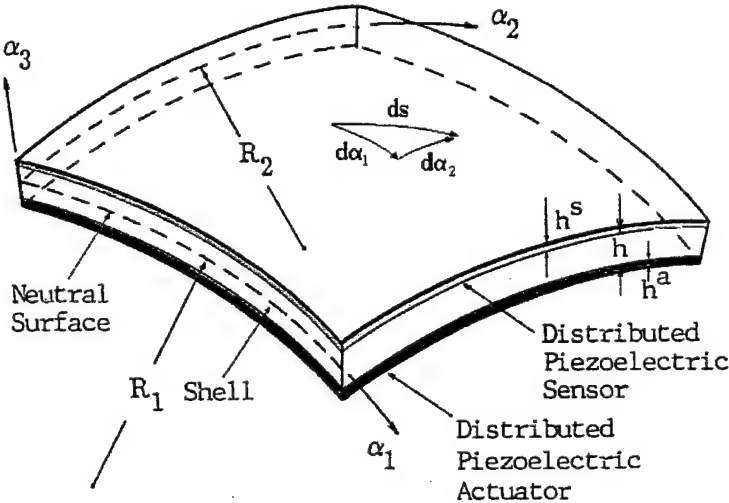


Fig.4 An elastic shell laminated with distributed piezoelectric sensor and actuator – a structronic shell DPS.

Based on the Gauss theory $\nabla \{D_i\} = 0$, the Maxwell equation $\{E_j\} = -\nabla \{\phi\}$, and the direct piezoelectric effect, one can define an open-circuit voltage ϕ^s in the transverse direction. The open-circuit signal ϕ^s is a function of induced local strains S_{ij} and the piezoelectric constants h_{ij} .

$$\phi^s = (h^s/S^e) \int_{\alpha_1} \int_{\alpha_2} [h_{31}S_{11}^s + h_{32}S_{22}^s + h_{36}S_{12}^s] \bullet A_1 A_2 d\alpha_1 d\alpha_2 \quad (23)$$

where h^s is the sensor thickness; S^e is the effective sensor electrode area; h_{3i} is the piezoelectric (displacement) constant indicating a signal generation in the transverse direction due to the strain in the i^{th} direction; S_{ij}^s is the strain on the i^{th} surface in the j^{th} direction; and A_1 and A_2 are the Lamé parameters. The surface integration denotes the total charge generated over the effective electrode area defined by the α_1 and α_2 axes. Note that since the sensor is spatially distributed, the signal is averaged over the total effective electrode area (Tzou, Zhong, Natori, 1993). The strain can be divided into the membrane strain and the bending strain. Thus, the sensor signal resulting from a nonlinear shell DPS can be further expressed as (Tzou and Yang, 2000)

$$\begin{aligned}
\phi^s = & (h^s/S^s) \int_{\alpha_1} \int_{\alpha_2} \left[h_{31} \left\{ \frac{1}{A_1} \frac{\partial u_1}{\partial \alpha_1} + \frac{u_2}{A_1 A_2} \frac{\partial A_1}{\partial \alpha_2} + \frac{u_3}{R_1} + \left[\frac{1}{2} \left(\frac{\partial u_3 / \partial \alpha_1}{A_1} \right)^2 \right] \right. \right. \\
& + r^s \left(\frac{1}{A_1} \frac{\partial}{\partial \alpha_1} \left(\frac{u_1}{R_1} - \frac{1}{A_1} \frac{\partial u_3}{\partial \alpha_1} \right) + \frac{1}{A_1 A_2} \left(\frac{u_2}{R_2} - \frac{1}{A_2} \frac{\partial u_3}{\partial \alpha_2} \right) \frac{\partial A_1}{\partial \alpha_2} \right\} \\
& + h_{32} \left\{ \frac{1}{A_2} \frac{\partial u_2}{\partial \alpha_2} + \frac{u_1}{A_1 A_2} \frac{\partial A_2}{\partial \alpha_1} + \frac{u_3}{R_2} + \left[\frac{1}{2} \left(\frac{\partial u_3 / \partial \alpha_2}{A_2} \right)^2 \right] \right. \\
& \left. \left. + r^s \left(\frac{1}{A_2} \frac{\partial}{\partial \alpha_2} \left(\frac{u_2}{R_2} - \frac{1}{A_2} \frac{\partial u_3}{\partial \alpha_2} \right) + \frac{1}{A_1 A_2} \left(\frac{u_1}{R_1} - \frac{1}{A_1} \frac{\partial u_3}{\partial \alpha_1} \right) \frac{\partial A_2}{\partial \alpha_1} \right\} \right. \\
& + h_{36} \left\{ \frac{1}{A_2} \frac{\partial u_1}{\partial \alpha_2} + \frac{1}{A_1} \frac{\partial u_2}{\partial \alpha_1} - \frac{u_1}{A_1 A_2} \frac{\partial A_1}{\partial \alpha_2} - \frac{u_2}{A_1 A_2} \frac{\partial A_2}{\partial \alpha_1} + \left[\frac{1}{A_1 A_2} \frac{\partial u_3}{\partial \alpha_1} \frac{\partial u_3}{\partial \alpha_2} \right] \right. \\
& + r^s \left[\frac{A_1}{A_2} \frac{\partial}{\partial \alpha_2} \left[\left(\frac{u_1}{R_1} - \frac{1}{A_1} \frac{\partial u_3}{\partial \alpha_1} \right) / A_1 \right] + \frac{A_2}{A_1} \frac{\partial}{\partial \alpha_1} \left[\left(\frac{u_2}{R_2} - \frac{1}{A_2} \frac{\partial u_3}{\partial \alpha_2} \right) / A_2 \right] \right. \\
& \left. \left. - \frac{1}{A_1 A_2} \left(\frac{u_1}{R_1} - \frac{1}{A_1} \frac{\partial u_3}{\partial \alpha_1} \right) \frac{\partial A_1}{\partial \alpha_2} - \frac{1}{A_1 A_2} \left(\frac{u_2}{R_2} - \frac{1}{A_2} \frac{\partial u_3}{\partial \alpha_2} \right) \frac{\partial A_2}{\partial \alpha_1} \right] \right\} \bullet A_1 A_2 d\alpha_1 d\alpha_2
\end{aligned} \quad (24)$$

where u_i 's are the (neutral-surface) displacements; R_i is the radius of curvature of the i th axis; and r^s is the sensor location away from the shell neutral surface. The terms following r^s represent the bending strain component; others are the membrane strain component. The membrane strain component is related to in-plane oscillations and the bending component is related to bending oscillation of the generic shell. Note that the large deformation effect is included with the membrane strains, the quadratic terms, based on the von Karman geometric nonlinearity theory. To demonstrate the distributed sensing concept, distributed sensing behavior of various shells is investigated later.

DISTRIBUTED CONTROL OF STRUCTRONIC SHELLS

Distributed control of linear/nonlinear strucronic shell continua or DPSs requires different approaches, as compared with that of the discrete parameter systems. Distributed control effectiveness of shells suggests that the overall control effect can be divided into two major control actions: 1) the membrane control action and 2) the bending control action. Usually, the membrane control action dominates the lower-mode control of deep shells, e.g., cylindrical shell, and the bending control action dominates the control of higher deep-shell modes and all modes of zero-curvature continua, e.g., plates and beams (Tzou, Bao, and Venkayya, 1998). (These detailed electromechanical or piezothermoelastic coupling phenomena will be demonstrated in Case Studies presented later.)

Distributed actuation and control of elastic DPSs using distributed piezoelectric layer is based on the converse piezoelectric effect. Strains induced by a control potential ϕ^a (the converse piezoelectric effect) leads to stresses (i.e., strain multiplied by Young's modulus Y_p), and then the membrane control forces N_{ii}^a , **Figure 5**.

$$N_{ii}^a = d_{ii} Y_p \phi^a . \quad (25)$$

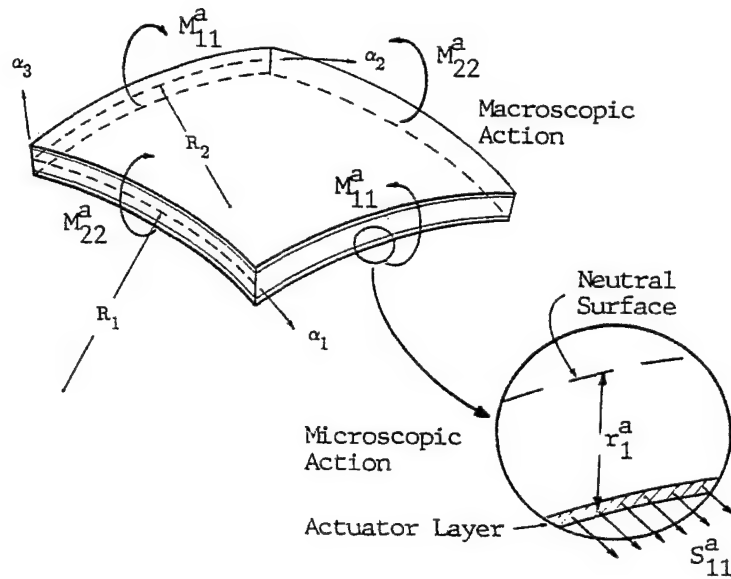


Fig.5 Distributed control induced by the distributed actuator layer.

Since the distributed actuator is surface laminated, thus, the control forces also induce counteracting control moments (M_{ii}^a) to the strucronic shell continuum. (See enlarged microscopic actions in **Figure 5.**)

$$M_{ii}^a = r_i^a d_{ii} Y_p \phi^a , \quad (26)$$

where r_i^a is the moment arm measured from the shell neutral surface to the mid-plane of the distributed actuator. If both sensor/actuator layers and the elastic shell are uniform thickness, the moment arms are equal in both directions, i.e., $r_1^a = r_2^a = r^a$. Accordingly, distributed actuation and control can be achieved. Previous studies have revealed that the membrane control force is important to control of curved structures (e.g., shells and rings) and the control moment is effective to control of zero-curvature structures (e.g., plates and beams) Tzou, 1993). Furthermore, control deficiencies can also occur on anti-symmetrical modes of symmetrical structures, due to cancellation of input control potential on the distributed actuator layer. Utilizing the segmentation and shaping (thickness or surface) techniques can alleviate the signal cancellation problem and maximize sensing/control effectiveness. (These two design approaches will be discussed next.)

Following Hamilton's principle and integrating all control forces/moments into thin shell equations yields the (open or closed-loop) strucronic shell system equations in three axial directions:

$$-\frac{\partial(N_{11}^* A_2)}{\partial \alpha_1} + N_{22}^* \frac{\partial A_2}{\partial \alpha_1} - \frac{\partial(N_{21} A_1)}{\partial \alpha_2} - N_{12} \frac{\partial A_1}{\partial \alpha_2} - \frac{1}{R_1} \left[\frac{\partial(M_{11}^* A_2)}{\partial \alpha_1} \right] \quad (27)$$

$$-M_{22}^* \frac{\partial A_2}{\partial \alpha_1} + \frac{\partial(M_{21} A_1)}{\partial \alpha_2} + M_{12} \frac{\partial A_1}{\partial \alpha_2}] + A_1 A_2 \rho h \ddot{u}_1 = A_1 A_2 F_1 ,$$

$$-\frac{\partial(N_{22}^* A_1)}{\partial \alpha_2} + N_{11}^* \frac{\partial A_1}{\partial \alpha_2} - \frac{\partial(N_{12} A_2)}{\partial \alpha_1} - N_{21} \frac{\partial A_2}{\partial \alpha_1} - \frac{1}{R_2} \left[\frac{\partial(M_{22}^* A_1)}{\partial \alpha_2} \right] \quad (28)$$

$$-M_{11}^* \frac{\partial A_1}{\partial \alpha_2} + \frac{\partial(M_{12} A_2)}{\partial \alpha_1} + M_{21} \frac{\partial A_2}{\partial \alpha_1}] + A_1 A_2 \rho h \ddot{u}_2 = A_1 A_2 F_2 ,$$

$$-\frac{\partial}{\partial \alpha_1} \left[\frac{1}{A_1} \left(\frac{\partial(M_{11}^* A_2)}{\partial \alpha_1} - M_{22}^* \frac{\partial A_2}{\partial \alpha_1} + \frac{\partial(M_{21} A_1)}{\partial \alpha_2} + M_{12} \frac{\partial A_1}{\partial \alpha_2} \right) \right] \quad (29)$$

$$-\frac{\partial}{\partial \alpha_2} \left[\frac{1}{A_2} \left(\frac{\partial(M_{22}^* A_1)}{\partial \alpha_2} - M_{11}^* \frac{\partial A_1}{\partial \alpha_2} + \frac{\partial(M_{12} A_2)}{\partial \alpha_1} + M_{21} \frac{\partial A_2}{\partial \alpha_1} \right) \right]$$

$$+ A_1 A_2 \left(\frac{N_{11}^*}{R_1} + \frac{N_{22}^*}{R_2} \right) + A_1 A_2 \rho h \ddot{u}_3 = A_1 A_2 F_3 ,$$

where, again, u_i is the displacement in the α_i direction; ρ is the mass density; F_i is the external input; A_1 and A_2 are the Lamé parameters; and R_1 and R_2 are the radii of curvature. Note that the force and moment components consist of the original elastic component and the control component, i.e., $N_{ii}^* = N_{ii} + N_{ii}^a$ and $M_{ii}^* = M_{ii} + M_{ii}^a$, governed by control algorithms, either open-loop or closed-loop. This set generic control shell equations can be simplified to account for other geometries or DPSs such that distributed sensing and control of other standard geometries and DPSs can be investigated. (Note that this set of control equations is similar to that of the piezothermoelastic shell equations. However, their physical significances are totally different. The former represents inherent internal effects, although the electrical component can still be used to manipulate the physical properties of the nonlinear piezothermoelastic shells. The latter denotes the open- or closed-loop control equations of linear/nonlinear strucronic shells or DPSs. Furthermore, N_{ii}^* or M_{ii}^* can also accommodate the temperature induced effect N_{ii}^θ or M_{ii}^θ , i.e., $N_{ii}^* = N_{ii} + N_{ii}^a + N_{ii}^\theta$ or $M_{ii}^* = M_{ii} + M_{ii}^a + M_{ii}^\theta$. There is only temperature induced membrane force and no moment when the temperature is uniformly distributed.

Modal Separation and Independent Modal Control

Assume the control components N_{ij}^a in the flexible shell equation can be generally represented by a control function: $N_{ij}^a = L_i^a(\phi_1, \phi_2, \phi_3) = L_i^a(\phi_i)$, $i = 1, 2, 3$ where ϕ_i is the control signal. Define a distributed feedback function: $L_i^a(\phi_i) = \{ \Lambda_i(\alpha_1, \alpha_2, t) \}$, $i = 1, 2, 3$ where Λ_i can be displacement, velocity, acceleration or combination of several reference factors (Tzou, 1993). Expanding the distributed feedback function in the modal domain:

$L_i^a(\phi_i) = \sum_{k=1}^{\infty} G_{ik}^*(\alpha_1, \alpha_2) \cdot \eta_k^*(t)$, $i = 1, 2, 3$, one can express the distributed control force as

$$\hat{F}_k = \frac{1}{\rho h N_k} \int_{\alpha_1} \int_{\alpha_2} \sum_{j=1}^3 \sum_{k=1}^{\infty} G_{jk}^*(\alpha_1, \alpha_2) \eta_k^*(t) \cdot U_{jk}(\alpha_1, \alpha_2)] A_1 A_2 d\alpha_1 d\alpha_2, \quad (30)$$

where $N_k = \int_{\alpha_1} \int_{\alpha_2} \sum_{j=1}^3 U_{jk}^2(\alpha_1, \alpha_2)] A_1 A_2 d\alpha_1 d\alpha_2$; U_{jk} is the mode shape function; $G_{jk}^*(\alpha_1, \alpha_2)$ is a spatial gain function; and η_k^* is a modal coordinate of the k -th mode. Assuming the distributed control force is velocity dependent and the gain factor G_{jk}^* is a constant, one can derive the modal domain control equation as

$$\ddot{\eta}_k + \frac{1}{\rho h} \left[c - \frac{G_k^v}{N_k} \int_{\alpha_1} \int_{\alpha_2} U_{jk}^2 \cdot A_1 A_2 d\alpha_1 d\alpha_2 \right] \dot{\eta}_k + \omega_k^2 \eta_k = 0. \quad (31)$$

Accordingly, modal responses of nonlinear flexible shell continua can be independently controlled. Spatial shapes of required actuators can also be represented by the spatial gain function such that single mode or combination of natural modes can be optimally controlled with limited distributed actuators (Tzou, Zhong, and Natori, 1993; Tzou, Zhong, and Hollkamp, 1994).

DESIGN PRINCIPLES OF DISTRIBUTED SENSORS/ACTUATORS

Figure 3 illustrates a typical strucronic shell system – an elastic shell coupled with distributed sensor and actuator layers. However, in reality, the distributed layers often only cover critical regions or areas of the DPSs in order to address the control efficiency and cost issues, i.e., to control the maximal or critical mode(s) with the minimal area(s) or number of distributed sensors and actuators. Accordingly, placements and shapes of these sensor/actuator layers become critical design issues. There are, in general, two design principles: 1) *the segmentation technique* and 2) *the shaping technique* in the distributed transducer design. These two design principles are discussed in this section.

The Segmentation Technique

Figure 6 illustrates *the segmentation technique*, in which a distributed sensor/actuator layer is segmented into a number of regular-shape patches that can be equal or unequal sizes (Tzou, Bao, Venkayya, 1996; Tzou and Fu, 1994). Each segmented patch or a group of patches can be individually monitored or controlled. When the size of patches approaches to infinitesimal, these elements become distributed *neurons* or “*muscle*” elements, either monitoring microscopic behaviors or leading to microscopic control actions. **Figure 6b** shows four-segmented patches on a cylindrical shell panel (Tzou, Bao, Venkayya, 1996); **Figure 6c** shows four-segmented patches on a zero-curvature shell – a plate (Tzou and Fu, 1994).

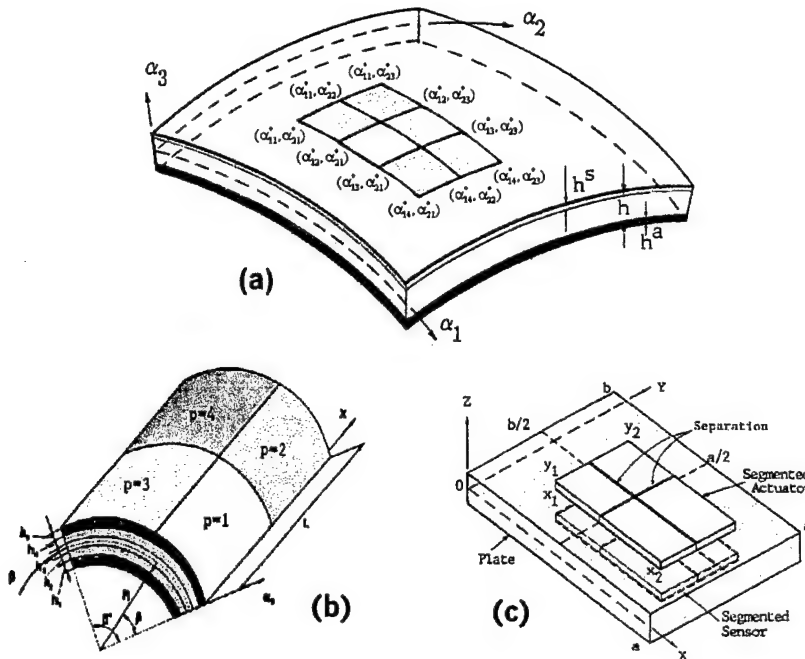


Fig.6 The segmentation technique of distributed sensor/actuator.

The Shaping Technique

On the other hand, *the shaping technique* involves either *the planner shape variation*, Figure 7a, or *the thickness variation*, Figure 7b. These shapes usually are modal sensitive and they are designed based on specific mode shape functions or modal strain functions (Tzou, Hollkamp, and Venkayya, 1998; Tzou, Zhong, and Natori, 1993; Tzou and Hollkamp, 1994). Accordingly, these shaped sensors/actuators are only effective to selected modal oscillations of the DPS. For example, Figure 7c illustrates designs of the first and second orthogonal modal sensors/actuators for a cantilever beam (Tzou, Hollkamp, and Venkayya, 1998); Figure 7d illustrates those of the second to fourth modes of a free-floating ring (Tzou, Zhong, and Natori, 1993).

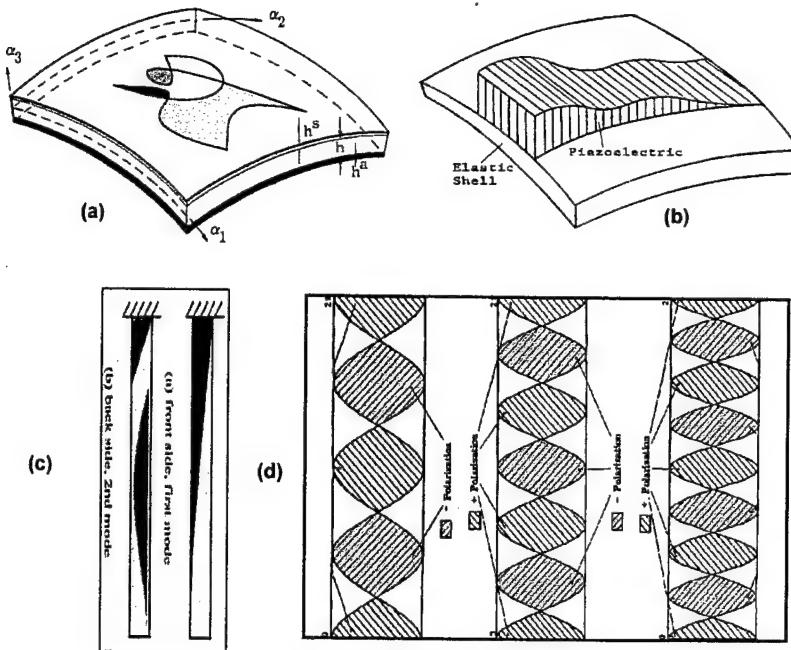


Fig.7 The shaping technique of distributed sensor/actuator.

Applications of the generic strucronic shell equations and sensor/actuator equations to other standard DPSs or standard shapes (i.e., common geometries) are demonstrated next.

APPLICATIONS

As discussed previously, the thermoelectromechanical/control governing PDEs and distributed sensor/actuator equations were respectively derived based on generic double-curvature piezo(electric)thermoelastic and strucronic shell DPSs, **Figure 3**, and these equations can be directly simplified to account for many shell and non-shell standard DPSs widely used in many aerospace, mechanical and structural systems. Examples of various simplified geometries and their relations are shown in **Figure 8**. Simplification procedures and demonstration cases are presented in this section.

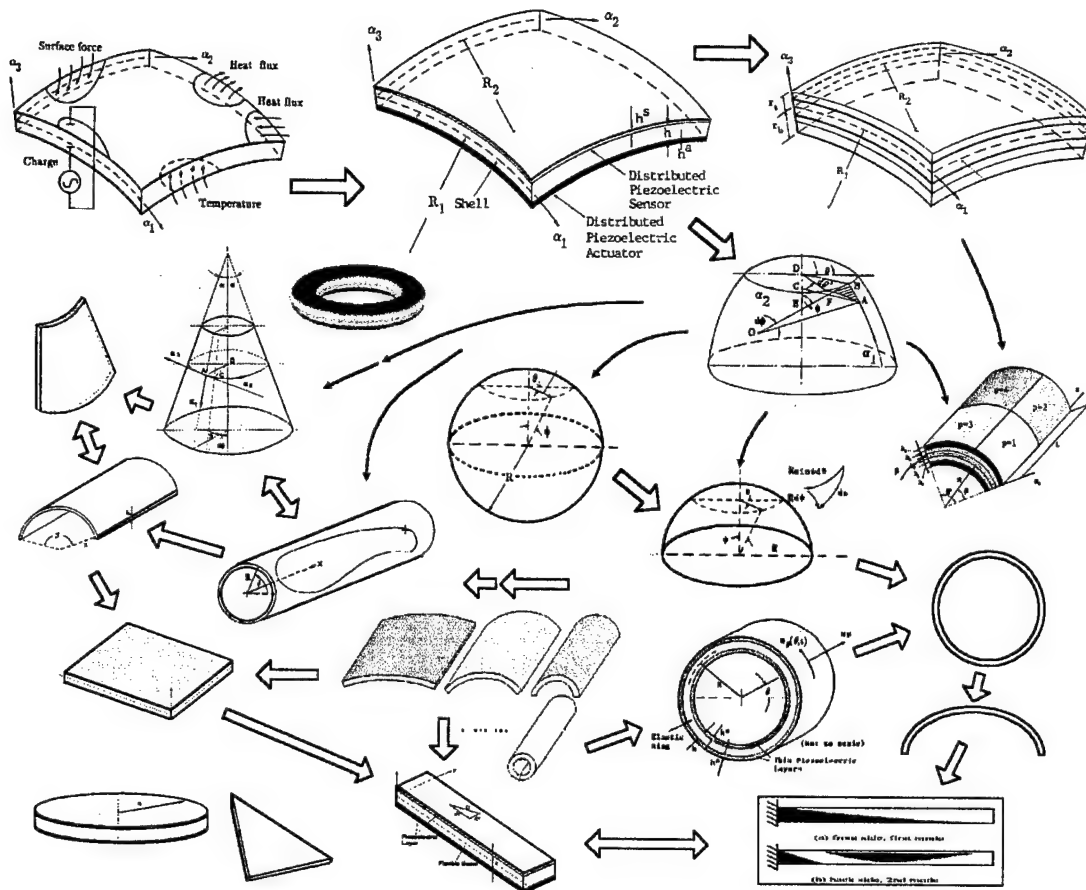


Fig.8 Applications of the shell theories.

Procedures

There are four geometric parameters, i.e., two Lamé parameters (A_1 and A_2) and two radii (R_1 and R_2) of curvature, required to carry out the simplification and reduction of generic piezothermoelastic/control equations and shell sensing/control governing equations. Simplification procedures are briefly discussed below.

1) Select a Coordinate System

The original generic shell continuum or DPS was defined in a tri-orthogonal curvilinear coordinate system (α_1 , α_2 , α_3). Depending on the given geometry (the host elastic structure) and/or sensor/actuator shapes, these coordinates can be redefined to best represent the DPS, e.g., $\alpha_1 = x$ and $\alpha_2 = y$ for a rectangular plate; $\alpha_1 = x$ and $\alpha_2 = \beta$ for a cylindrical shell and thin cylindrical tube shell; $\alpha_1 = \phi$ and $\alpha_2 = \psi$ for a spherical shell, etc.

2) Determine the Radii of Curvature

The radii of curvatures R_1 and R_2 of the two in-plane coordinate axes α_1 and α_2 can be easily observed from the coordinate system defined in Step 1. For example, the radii of x and y axes in a rectangular plate are $R_1 = \infty$ and $R_2 = \infty$. In a cylindrical shell, $R_1 = \infty$ and $R_2 = R$. In a spherical shell, radii are $R_1 = R_2 = R$.

3) Derive a Fundamental Form

A *fundamental form* represents an infinitesimal distance ds on the neutral surface of the shell continuum; the distance is the hypotenuse of a (or an approximate) right-angle triangle defined by the projected infinitesimal distances ($d\alpha_1$ and $d\alpha_2$) of the two in-plane coordinates, see **Figure 8**. From the *fundamental form*, two Lamé parameters A_1 and A_2 and the two selected coordinates α_1 and α_2 can be defined, i.e.,

$$(ds)^2 = (A_1)^2(d\alpha_1)^2 + (A_2)^2(d\alpha_2)^2. \quad (32)$$

For example, the fundamental form for a rectangular plate (defined in a Cartesian coordinate system x and y) is $(ds)^2 = (1)^2(dx)^2 + (1)^2(dy)^2$, thus, the Lamé parameters are $A_1 = 1$ and $A_2 = 1$. For a cylindrical shell defined by the x and β axes, the fundamental form is $(ds)^2 = (1)^2(dx)^2 + (R)^2(d\beta)^2$, thus, $A_1 = 1$ and $A_2 = R$ (radius of the cylinder). The fundamental form defining the spherical shell is $(ds)^2 = (R)^2(d\phi)^2 + (R\sin\phi)^2(d\psi)^2$ where R is the radius of the spherical shell. Thus, the Lamé parameters are $A_1 = R$ and $A_2 = R \sin\phi$. Other geometries can be defined accordingly.

4) Simplify the Shell Sensor/Actuator Equations

By substituting the four parameters A_1 , A_2 , R_1 , and R_2 into the generic shell sensor/actuator and/or piezotermoelastic/control system equations, one can *easily* derive the governing equations for that DPS or sensor/actuator, e.g., shell (cylindrical shells, conical shells, spherical shells, shells of revolution, etc.) or non-shell DPSs (rings, arches, beams, etc.), **Figure 8**.

Detailed sensing/actuation and shell equations of a number of DPS cases are presented next. Studies and evaluations of microscopic sensing and control characteristics are presented in later chapters.

Case 1: Control of Spherical Shell

There are three equations of motion describing the electromechanical and control behaviors of spherical shells of revolution respectively defined in the $\alpha_1 = \phi$, $\alpha_2 = \psi$, and α_3 directions, **Figure 9**, and they can be directly derived by simplifying the electromechanical equations of motion of a generic double-curvature shell using two Lamé parameters (A_1 and A_2) and two radii of curvature (R_1 and R_2) defined for the spherical shell coordinate system where $\alpha_1 = \phi$ and $\alpha_2 = \psi$. The fundamental form defining the Lamé parameters is derived based on an infinitesimal distance (ds) on the neutral surface of a thin spherical shell.

$$(ds)^2 = (R)^2(d\phi)^2 + (R\sin\phi)^2(d\psi)^2. \quad (33)$$

Thus, the Lamé parameters $A_1 = R$ and $A_2 = R \sin\phi$; the radii of curvature of a spherical shell are $R_1 = R_2 = R$.

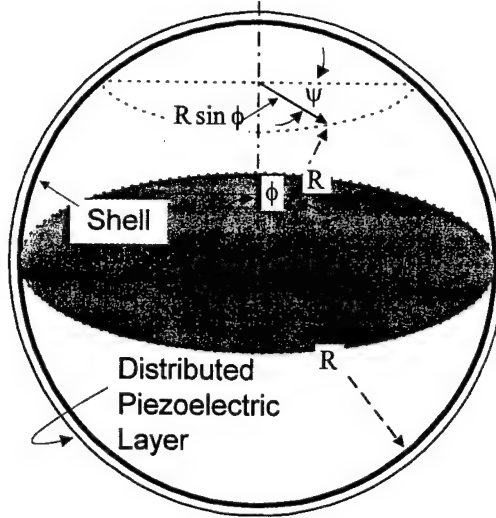


Fig.9 A spherical shell laminated with a distributed piezoelectric layer.

Substituting Lamé parameters and radii of curvatures of spherical shells into the shell equations and simplifying yields three equations of motion respectively defined in the α_1 , α_2 , and α_3 directions (Tzou, and Smithmaitrie, 2001).

$$\frac{\partial}{\partial \phi} (N_{\phi\phi} \sin \phi) + \frac{\partial}{\partial \psi} (N_{\psi\phi}) - N_{\psi\psi} \cos \phi + Q_{\phi 3} \sin \phi + R q_{\phi} \sin \phi = R \sin \phi \rho h \frac{\partial^2 u_{\phi}}{\partial t^2}, \quad (34)$$

$$\frac{\partial}{\partial \phi} (N_{\phi\psi} \sin \phi) + \frac{\partial}{\partial \psi} (N_{\psi\psi}) + N_{\psi\phi} \cos \phi + Q_{\psi 3} \sin \phi + R q_{\psi} \sin \phi = R \sin \phi \rho h \frac{\partial^2 u_{\psi}}{\partial t^2}, \quad (35)$$

$$\frac{\partial}{\partial \phi} (Q_{\phi 3} \sin \phi) + \frac{\partial}{\partial \psi} (Q_{\psi 3}) - (N_{\phi\phi} + N_{\psi\psi}) \sin \phi + R q_3 \sin \phi = R \sin \phi \rho h \frac{\partial^2 u_3}{\partial t^2}; \quad (36)$$

The transverse shear effects Q_{ij3} are defined by moments:

$$Q_{\phi 3} = \frac{1}{R \sin \phi} \left[\frac{\partial}{\partial \phi} (M_{\phi\phi} \sin \phi) + \frac{\partial}{\partial \psi} (M_{\psi\phi}) - M_{\psi\psi} \cos \phi \right], \quad (37)$$

$$Q_{\psi 3} = \frac{1}{R \sin \phi} \left[\frac{\partial}{\partial \phi} (M_{\phi\psi} \sin \phi) + \frac{\partial}{\partial \psi} (M_{\psi\psi}) + M_{\psi\phi} \cos \phi \right]. \quad (38)$$

N_{ij} are the membrane forces; M_{ij} are the bending moments; q_i is the external excitation; ρ is the mass density; h is the shell thickness, and u_i is the displacement. Membrane forces N_{ij} and bending moments M_{ij} are functions of membrane strains s_{ij}^o and bending strains k_{ij} .

$$N_{\phi\phi} = K(s_{\phi\phi}^o + \mu s_{\psi\psi}^o), \quad N_{\psi\psi} = K(s_{\psi\psi}^o + \mu s_{\phi\phi}^o), \quad N_{\phi\psi} = N_{\psi\phi} = \frac{K(1-\mu)}{2} s_{\phi\psi}^o; \quad (39-41)$$

$$M_{\phi\phi} = D(k_{\phi\phi} + \mu k_{\psi\psi}), \quad M_{\psi\psi} = D(k_{\psi\psi} + \mu k_{\phi\phi}), \quad M_{\phi\psi} = M_{\psi\phi} = \frac{D(1-\mu)}{2} k_{\phi\psi}; \quad (42-44)$$

where $K = (Yh)/(1-\mu^2)$ is the membrane stiffness; $D = (Yh^3)/[12(1-\mu^2)]$ is the bending stiffness; Y is the modulus of elasticity (Young's modulus); and μ is Poisson's ratio. The strain-displacement relations of thin spherical shells are

$$s_{\phi\phi}^{\circ} = \frac{1}{R} \left(\frac{\partial}{\partial \phi} (u_{\phi}) + u_3 \right), \quad s_{\psi\psi}^{\circ} = \frac{1}{R \sin \phi} \left(\frac{\partial}{\partial \psi} (u_{\psi}) + u_{\phi} \cos \phi + u_3 \sin \phi \right), \quad (45,46)$$

$$s_{\phi\psi}^{\circ} = \frac{1}{R} \left(\frac{\partial}{\partial \phi} (u_{\psi}) - u_{\psi} \cot \phi + \frac{1}{\sin \phi} \frac{\partial}{\partial \psi} (u_{\phi}) \right); \quad (47)$$

$$k_{\phi\phi} = \frac{1}{R} \left(\frac{\partial}{\partial \phi} (\beta_{\phi}) \right), \quad k_{\psi\psi} = \frac{1}{R} \left(\frac{1}{\sin \phi} \frac{\partial}{\partial \psi} (\beta_{\psi}) + \beta_{\phi} \cot \phi \right), \quad (48,49)$$

$$k_{\phi\psi} = \frac{1}{R} \left(\frac{\partial}{\partial \phi} (\beta_{\psi}) - \beta_{\psi} \cot \phi + \frac{1}{\sin \phi} \frac{\partial}{\partial \psi} (\beta_{\phi}) \right); \quad (50)$$

and the rotation angles are $\beta_{\phi} = \frac{1}{R} \left(u_{\phi} - \frac{\partial u_3}{\partial \phi} \right)$ and $\beta_{\psi} = \frac{1}{R} \left(u_{\psi} - \frac{1}{\sin \phi} \frac{\partial u_3}{\partial \psi} \right)$, respectively.

Case 2: Distributed Sensing of Conical Shells

In this case, distributed sensing characteristic of conical shell DPS is presented. The Lamé parameters, radii of curvature, and principle directions of conical shells are respectively defined by $A_1 = 1$, $A_2 = x \sin \beta^*$, $R_1 = R_x = \infty$, $R_2 = R_{\psi} = x \tan \beta^*$, $\alpha_1 = x$, and $\alpha_2 = \psi$. **Figure 10** illustrates a conical shell, the coordinate system, and its parameters.

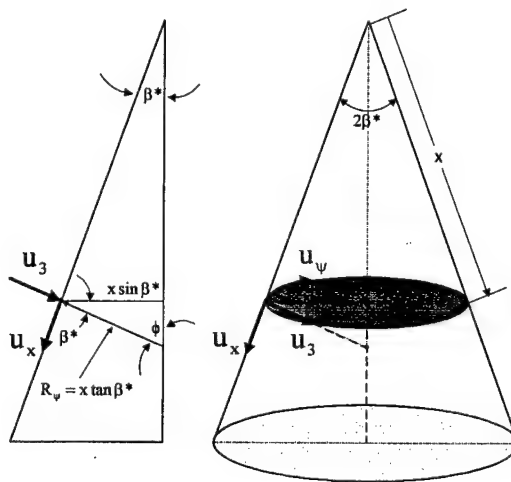


Fig.10 A conical shell of revolution.

Assume there is a distributed piezoelectric sensor layer laminated on the conical shell and the sensor layer is insensitive to the in-plane twisting S_{12}^s . The signal-strain relation of the distributed conical shell sensor layer becomes (Tzou and Chai, 2001)

$$\phi^s = \left(\frac{h^s}{S^e} \right) \int_x \int_{\psi} (h_{31} S_{xx}^s + h_{32} S_{\psi\psi}^s) \bullet x \sin \beta^* dx d\psi , \quad (51)$$

where the strain terms are $S_{xx}^s = s_{xx}^o + r_x^s k_{xx}$ and $S_{\psi\psi}^s = s_{\psi\psi}^o + r_{\psi}^s k_{\psi\psi}$. The membrane strain-displacement relations of the linear conical shell are

$$s_{xx}^o = \frac{\partial u_x}{\partial x} \quad \text{and} \quad s_{\psi\psi}^o = \frac{1}{x \sin \beta^*} \frac{\partial u_{\psi}}{\partial \psi} + \frac{u_x}{x} - \frac{u_3}{x \tan \beta^*} . \quad (52,53)$$

According to the **Donnel-Mushtari-Vlasov theory**, the in-plane displacements u_x and u_{ψ} are usually neglected in the bending strains. Thus, the bending strains of the conical shell with the Donnel-Mushtari-Vlasov assumptions are

$$k_{xx} = -\frac{\partial^2 u_3}{\partial x^2} \quad \text{and} \quad k_{\psi\psi} = -\frac{1}{x^2 \sin^2 \beta^*} \frac{\partial^2 u_3}{\partial \psi^2} - \frac{1}{x} \frac{\partial u_3}{\partial x} . \quad (54,55)$$

Substituting all strain-displacement relations into the sensing signal equation gives the signal-displacement expression of the generic distributed conical shell sensor.

$$\begin{aligned} \phi^s = & \left(\frac{h^s}{S^e} \right) \int_x \int_{\psi} h_{31} \left\{ \frac{\partial u_x}{\partial x} - r_x^s \frac{\partial^2 u_3}{\partial x^2} \right\} + h_{32} \left\{ \frac{1}{x \sin \beta^*} \frac{\partial u_{\psi}}{\partial \psi} + \frac{u_x}{x} - \frac{u_3}{x \tan \beta^*} \right. \\ & \left. + r_{\psi}^s \left[-\frac{1}{x^2 \sin^2 \beta^*} \frac{\partial^2 u_3}{\partial \psi^2} - \frac{1}{x} \frac{\partial u_3}{\partial x} \right] \right\} \bullet x \sin \beta^* dx d\psi \end{aligned} , \quad (56)$$

Note that this signal-displacement equation is only valid for linear conical shell sensors, since it does not involve any large deformation effect (Tzou and Chai, 2001). Detailed modal contributions to the signal outputs of the distributed conical shell sensor are discussed later.

Case 3: Sensing and Control of Adaptive Cylindrical Shells

One of the important applications of distributed sensors and actuators is to evaluate detailed electromechanical behaviors of distributed adaptive structronic systems. Adaptive structures and structronic systems usually involve shape transformation changing from one geometry to the other, in order to achieve specific functional advantages in practical applications. A zero-curvature plate can transform to a shallow shell, a deep shell, and to a closed cylindrical shell (i.e., tube shell) when its curvature continuously changes from 0° to 360° , **Figure 11**. Usually, the bending effect dominates the plate or shallow shell dynamics; however, the membrane effect dominates the deep shell dynamics, especially for lower natural modes. (Recall that plates are defined as zero-curvature shells, i.e., radii R_1 and R_2 are infinity and Lamé parameters A_1 and A_2 are 1's.) This cylindrical shell case is to demonstrate the utilities of distributed sensors and actuators and to reveal detailed electromechanics and functionalities of these devices as applied to various shell structures with different curvatures (Tzou, 1993; Tzou and Zhong, 1996; Tzou, Bao, Venkayya, 1996; Tzou and Yang, 2001).

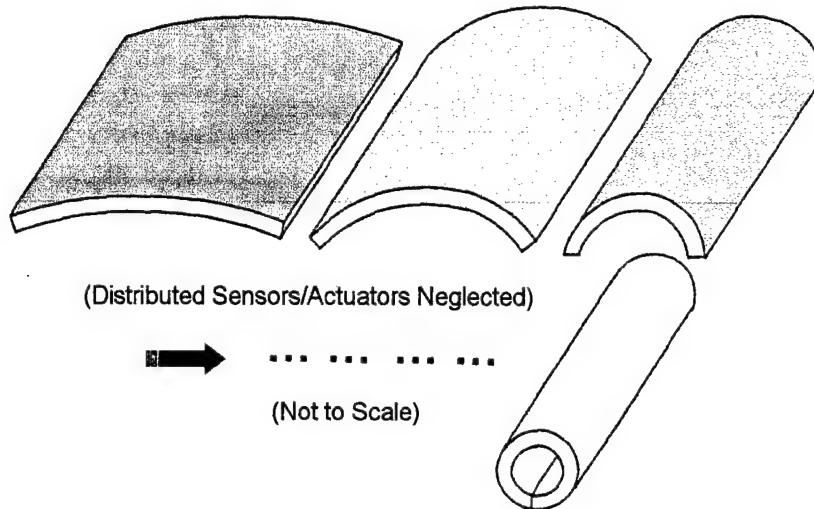


Fig.11 Shell transformation, from a shallow shell to a cylindrical.

A composite cylindrical shell strucronic system consists of elastic shell layers and distributed piezoelectric layers serving as distributed sensors and/or actuators, **Figure 12**. It is assumed perfect bonding between the layers. Recall that the cylindrical shell is defined by the x and β axes, the fundamental form is $(ds)^2 = (1)^2(dx)^2 + (R)^2(d\beta)^2$. Thus, the Lamé parameters are $A_1 = 1$ and $A_2 = R$ (radius of the cylinder). (Note that the segmented sensor/actuator patches laminated on the cylindrical shell can be defined by their corresponding x and β coordinates generically. When $x=L$ and $\beta=\beta^*$, it becomes a fully distributed sensor/actuator case.

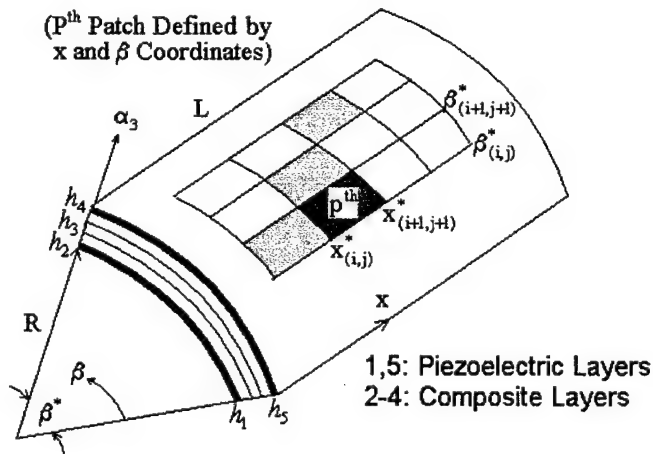


Fig.12 A cylindrical shell laminated with distributed piezoelectric layers.

Following the procedures described previously and substituting the four parameters into the generic shell system equations yields the governing equations of cylindrical shells.

$$-\frac{\partial N_{xx}}{\partial x} - \frac{1}{R} \frac{\partial N_{x\beta}}{\partial \beta} + \rho h \ddot{u}_1 = F_1 + \frac{\partial N_{xx}^c}{\partial x} , \quad (57)$$

$$-\frac{\partial N_{x\beta}}{\partial x} - \frac{1}{R} \frac{\partial N_{\beta\beta}}{\partial \beta} - \frac{1}{R} \left[\frac{\partial M_{x\beta}}{\partial x} + \frac{1}{R} \frac{\partial M_{\beta\beta}}{\partial \beta} \right] + \rho h \ddot{u}_2 = F_2 + \frac{1}{R} \frac{\partial N^c_{\beta\beta}}{\partial \beta} + \frac{1}{R^2} \frac{\partial M^c_{\beta\beta}}{\partial \beta}, \quad (58)$$

$$\begin{aligned} & -\frac{\partial^2 M_{xx}}{\partial x^2} - \frac{2}{R} \frac{\partial^2 M_{x\beta}}{\partial x^2} - \frac{1}{R^2} \frac{\partial^2 M_{\beta\beta}}{\partial \beta^2} + \frac{N_{\beta\beta}}{R} + \rho h \ddot{u}_3 \\ & = F_3 + \frac{\partial^2 M^c_{xx}}{\partial x^2} + \frac{1}{R^2} \frac{\partial^2 M^c_{\beta\beta}}{\partial \beta^2} - \frac{N^c_{\beta\beta}}{R}, \end{aligned} \quad (59)$$

and forces and moments are defined by $N_{ii}/M_{ii} = N_{ii}^m/M_{ii}^m + N_{ii}^a/M_{ii}^a$ and $N_{ij}^c \equiv N_{ij}^a$. As discussed previously, injecting high voltages into the distributed piezoelectric actuators induces two major control actions. One is the in-plane membrane control force(s) and the other is the out-of-plane control (bending) moment(s). In general, the control moments are essential in planar structures, e.g., plates and beams; the membrane control forces are effective to deep shells.

Case 4: Control of Plates

A rectangular plate is usually defined in a Cartesian coordinate system, in which x and y define the two in-plane directions and z defines the transverse direction, **Figure 13**. The strucronic plate system consists of an elastic plate (with thickness h and Young's modulus Y , mass density ρ) sandwiched between two piezoelectric layers (with negligible mass and stiffness). Following the procedures described previously, one can define the Lamé parameters (A_1 and A_2), radii of curvature (R_1 and R_2), and then system equations sensing/control equations, as well as related strain -displacement equations, force/moment - displacement equations, etc. (Tzou and Fu, 1994; Shih and Tzou, 2000).

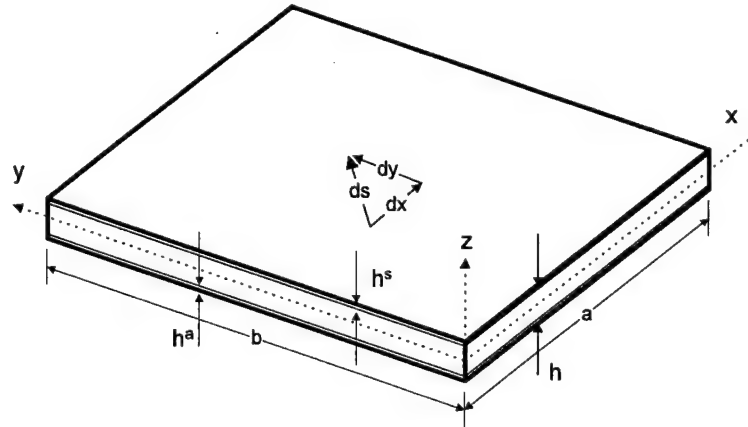


Fig.13 Distributed strucronic plate/sensor/actuator system.

Substituting the four parameters into the generic shell thermo-electromechanical equations yields the nonlinear plate equations.

$$-\frac{\partial(N_{xx})}{\partial x} + \frac{\partial(N_{yx})}{\partial y} + F_x = \rho h \ddot{u}_x, \quad (60)$$

$$-\frac{\partial(N_{yy})}{\partial y} + \frac{\partial(N_{xy})}{\partial x} + F_y = \rho h \ddot{u}_y, \quad (61)$$

$$\begin{aligned} & \left[\frac{\partial^2(M_{xx})}{\partial x^2} + 2 \frac{\partial^2(M_{xy})}{\partial x \partial y} + \frac{\partial^2(M_{yy})}{\partial y^2} \right] \\ & + \left[N_{xx} \frac{\partial^2 u_z}{\partial x^2} + 2N_{xy} \frac{\partial^2 u_z}{\partial x \partial y} + N_{yy} \frac{\partial^2 u_z}{\partial y^2} \right] + F_z = \rho h \ddot{u}_z \end{aligned} \quad (62)$$

and forces and moments are defined by

$$N_{ij}/M_{ij} = N_{ij}^m/M_{ij}^m + N_{ij}^e/M_{ij}^e + N_{ij}^\theta/M_{ij}^\theta. \quad (63)$$

Circular plates are common models for computer disks, optical mirrors, etc. Precision control of circular plates can be evaluated using the same procedures, **Figure 14**, (Tzou and Zhou, 1995, 1997).

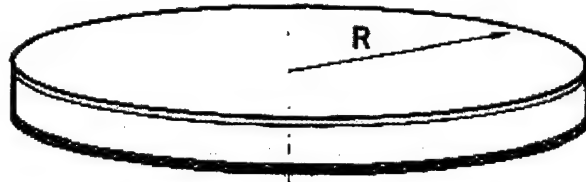


Fig.14 Distributed strucronic circular plate/sensor/actuator system.

Case 5: Control of Strucronic Rings

Rings laminated with distributed sensors and actuators establish strucronic ring systems and their sensing/control characteristics can be evaluated accordingly (Tzou, Zhong, and Natori, 1993; Tzou, Zhong, and Hollkamp, 1994; Tzou, 1993). One can also design orthogonal sensors and actuators based on its modal characteristics, such that modal dynamic sensitivities and controllabilities can be investigated. **Figure 15** illustrates a ring and **Figure 16** illustrates a ring system subjected to impacts. Control of impact-induced vibration can also be studied.

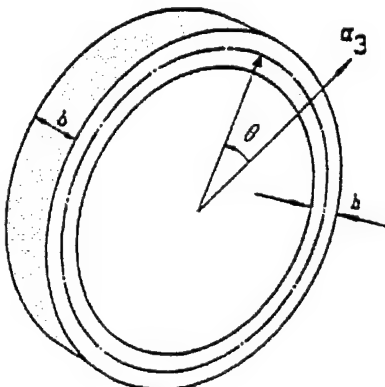


Fig.15 Distributed strucronic ring system.

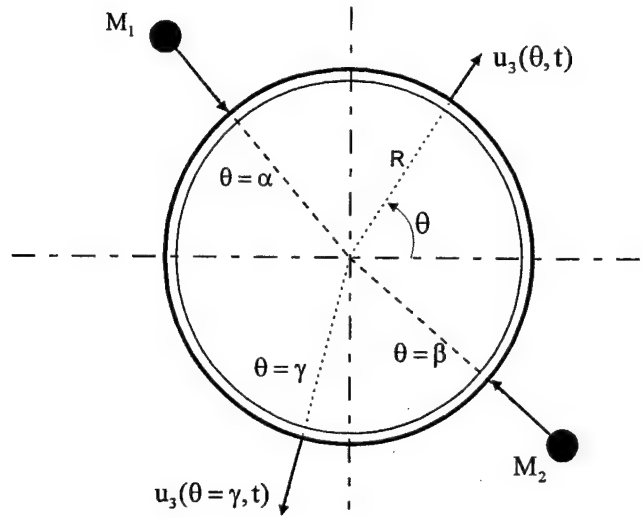


Fig.16 Distributed structronic ring system subjected to impacts.

Case 6: Control of Beams

An elastic Euler-Bernoulli beam is among the simplest distributed systems typically modeled by a fourth-order PDE:

$$YI \frac{\partial^4 u_3}{\partial x^4} + \rho A \ddot{u}_3 = b F_3, \quad (60)$$

where Y is Young's modulus; $I = bh^3/12$ is the area moment of inertia; b is the beam width; h is the beam thickness; u_3 denotes the transverse displacement; ρ is the mass density; $A = bh$ is the cross-section area; and F_3 is the transverse excitation. Consider a generic cantilever Euler-Bernoulli beam sandwiched between two thin piezoelectric layers serving as distributed sensor and actuator, respectively, **Figure 17**, i.e., a distributed structronic cantilever beam system. Sensing signal acquired from the distributed sensor is amplified and fed back to the distributed actuator counteracting the beam oscillation. System equation of a structronic beam system can be derived accordingly (Tzou, Johnson, and Liu, 1999).

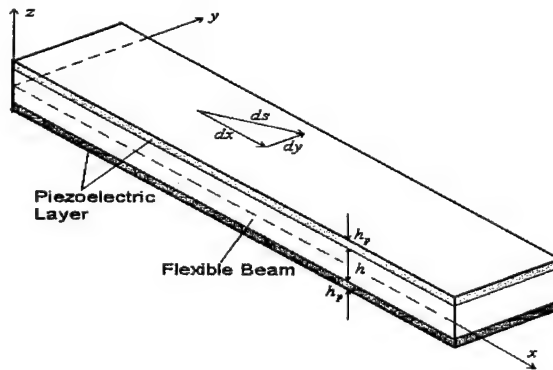


Fig.17 Distributed structronic beam/sensor/actuator system.

As discussed previously, there are two design principles applied to the distributed sensor/actuator design in practice. **Figure 18** illustrates an orthogonal self-sensing actuation design based on the shaping technique (Tzou and Hollkamp, 1994); **Figure 19** illustrates the segmented sensors and actuators laminated on a beam based on the segmentation technique.



Fig.18 Distributed orthogonal self-sensing actuation system (Tzou and Hollkamp, 1994).

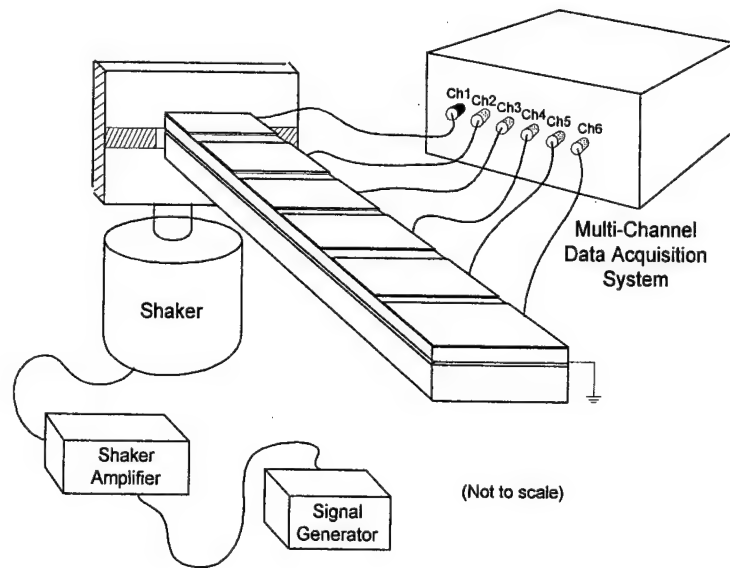


Fig.19 Distributed segmented sensor and actuator system.

Distributed sensors and actuators can be surface or thickness shaped using orthogonal functions, e.g., modal strain functions. In this case, the shaped sensor or actuator is sensitive only to the designated natural mode (i.e., the orthogonal modal sensor or actuator) and insensitive to other natural modes, based on the modal orthogonality of natural modes (Tzou and Hollkamp, 1994).

REMARKS

The synergistic integration of smart materials, sensors, actuators, control electronics with machines or structures enabling new distributed structronic (structure + electronic) systems capable of self-sensing, diagnosis, and control reveals the classic complexity of multi-field opto-thermo-electromechanical/control couplings of distributed parameter systems (DPSs). Consequently, multi-field coupling and control of distributed structronic systems further raises many new research, development, and system integration issues in recent years. This paper presented a generic nonlinear piezo(electric)-thermoelectromechanical shell theory and a distributed sensor/actuator theory based on piezoelectric double-curvature structronic shell DPSs with permissible mechanical, electrical, and temperature boundary conditions. Fundamental background of the distributed parameter systems was introduced, followed by definitions of distributed sensors and actuators and their governing equations. Application examples and design principles were presented afterwards. Applications of the generic theory to distributed sensing and control and other structronic 1D, 2D (flat and shell) DPSs (e.g., a spherical shell, a conical shell, an adaptive cylindrical shell DPSs) based on four system parameters were also demonstrated. Other DPSs (e.g., rectangular and circular plates, rings, beams, etc.) were also discussed.

Detailed micro-thermo-electromechanics and sensing/control effectiveness of various 1D (**Figure 20**), 2D plate DPSs (**Figure 21**), and advanced shell DPSs (**Figure 22**) are presented later. Again, note that the purpose to study shell and plate DPSs is to investigate multi-field piezothermoelastic/control characteristics and sensing/control of practical systems represented by standard geometries as illustrated in **Figures 20-22**.

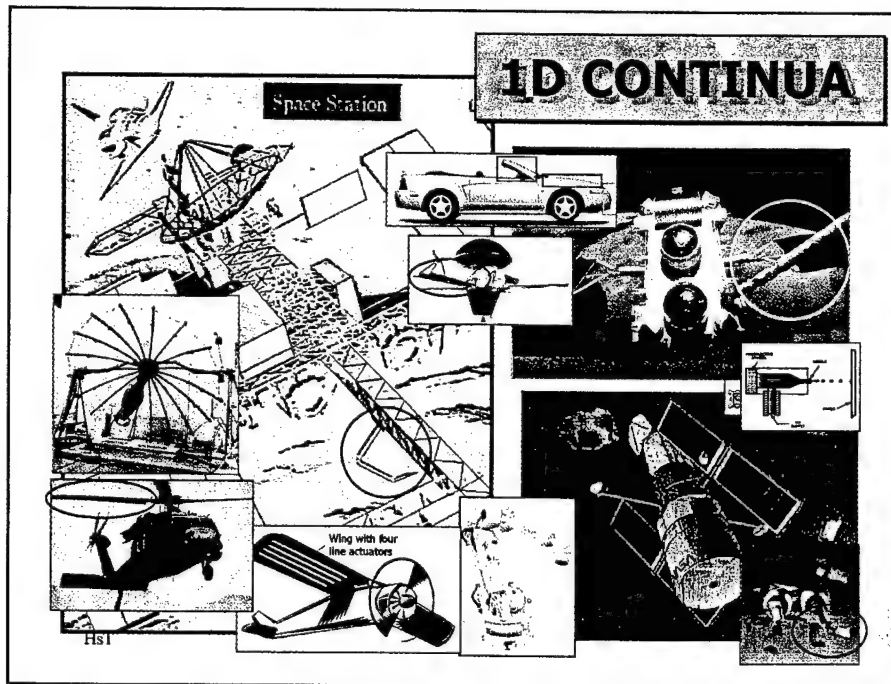
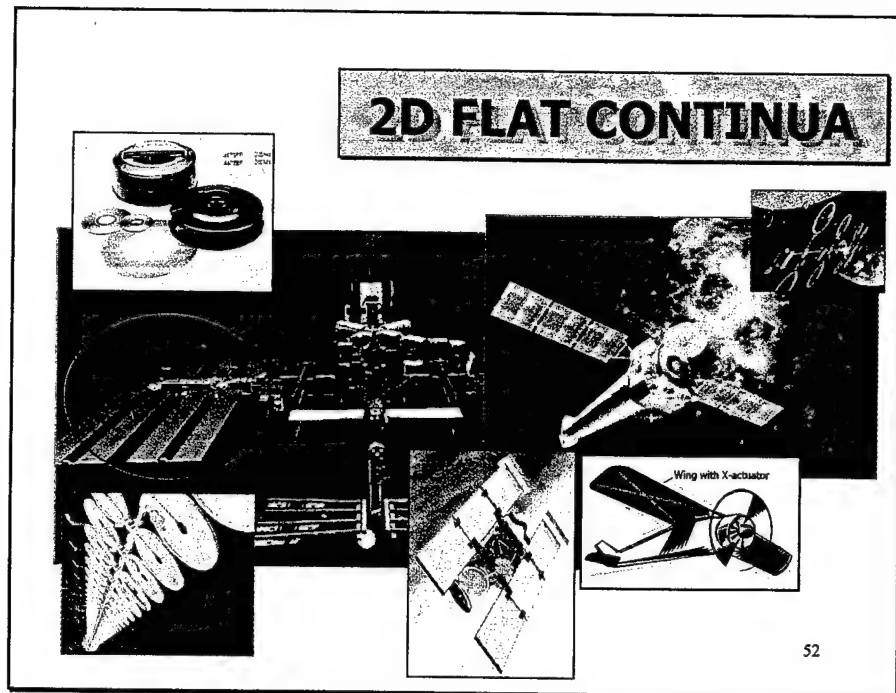


Fig.20 Examples of 1D DPSs.



52

Fig.21 Examples of 2D flat (plate) DPSs.

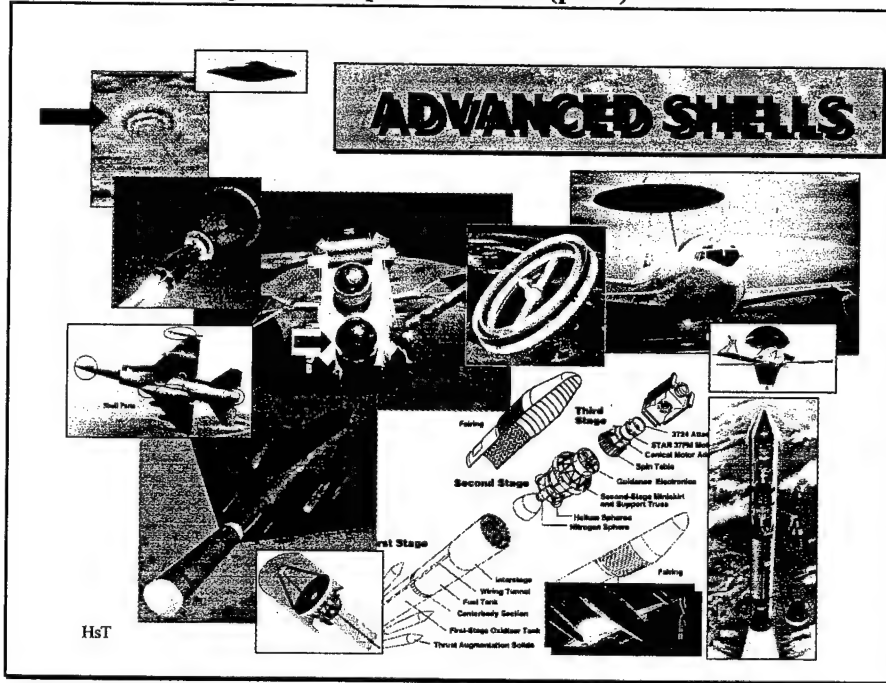


Fig.22 Examples of 2D shell DPSs.

ACKNOWLEDGEMENT

Arts, pictures, photos, figures, patents, designs, etc. acquired from various sources are gratefully acknowledged.

Bibliography

Adelman, N.T. and Stavsky, Y., 1975a, "Axisymmetric Vibrations of Radially Polarized Piezoelectric Ceramic Cylinders," *J. Sound and Vibration*, 38(2), pp.245-254.

Adelman, N.T. and Stavsky, Y., 1975b, "Vibrations of Radially Polarized Composite Piezoelectric Cylinders and Disks," *J. Sound and Vibration*, 43(1), pp.37-44.

Allik, H. and Hughes, T.J.R., "Finite Element Method for Piezoelectric Vibration," *Int. J. of Numerical Methods Eng.*, Vol. 2, 1979, pp.151-168.

Anderson, E.H., Hagood, N.W., and Goodliffe, J.M., 1992, "Self-sensing Piezoelectric Actuation: Analysis and Application to Controlled Structures," AIAA Paper: AIAA-92-2465-CP at 33 SDM Conference.

Ashley, S., 1995, "Smart Skis and Other Adaptive Structures, *Mechanical Engineering*, Vol.117, No.11, pp.76-81.

Bahrami, H. and Tzou, H.S., 1997, "Precision Placement Analysis with Lagrangian Finite Element," Paper No. DETC'97/Vib3945, *Symposium on Smart Materials and Mechatronics*, 1997 Biannual Conference on Mechanical Vibration and Noise and Design Technical Conference, Sacramento, CA, September 14-17, 1997.

Banks, H.T. and Smith, R.C., 1998, "Numerical Techniques for Simulation, Parameter Estimation, and Noise Control in Structural Acoustic Systems," in *Dynamics and Control of Distributed Systems*, Tzou, H.S. and Bergman, L.A., (Ed), Cambridge University Press, New York, pp.202-263.

Baz A. and Poh S., 1988, "Performance of an Active Control System with Piezoelectric Actuators," *Journal of Sound and Vibration*, Vol.126, No.2, pp.327-343.

Baz A. and Ro, J., 1994, "The Concept and Performance of Active Constrained Layer Damping Treatments," *Sound and Vibration*, Vol.28, No.3, pp.18-21.

Cady, W.G., *Piezoelectricity*, Dover Pub., New York, 1964.

Chau, L.K., 1986, "The Theory of Piezoelectric Shells," *PMM U.S.S.R.*, 50(1), pp.98-105.

Crawley, E.F. and de Luis, J., 1987, "Use of Piezoelectric Actuator as Elements of Intelligent Structures," *AIAA Journal*, 25(10), pp.1373-1385.

Dökmeci, M.C., 1978, "Theory of Vibrations of Coated, Thermopiezoelectric Lamine," *J. Math. Phys.*, 19(1), January.

Dökmeci, M.C., 1980, "Vibrations of Piezoelectric Crystals," *J. Eng. Soc.*, 18, pp.431-448.

Dökmeci, M.C., 1983, "Dynamic Applications of Piezoelectric Crystals," *The Shock and Vibration Digest*, 15(3), pp.9-22.

Dosch, J.J., Inman, D.J., and Garcia, E., 1992, "A Self-sensing Piezoelectric Actuator for Collocated Control," *J. of Intell. Materl. Systems and Structures*, Vol.3, pp.166-185.

Drumheller, D.S. and Kalnins, A., 1970, "Dynamic Shell Theory for Ferroelectric Ceramics," *J. Acoust. Soc. Am.*, 47(5), pp.1343-1349.

Ealey, M. A., and Davis, P. A., 1990, "Standard SELECT electrostrictive lead magnesium niobate actuators for active and adaptive optical components," *Optical Engineering*, Vol. 29, pp.1373-1382.

Fason J.L. and Gabra, J.A., 1988, "Experimental Studies of Active Members in Control of Large Space Structures," AIAA Paper 88-2207.

Galletti, P.M., De Rossi, D.E. and De Raggi, A.S., 1988, *Medical Applications of Piezoelectric Polymers*, Gordon and Breach Sc. Pub, New York.

Galvagni, J., 1990, "Electrostrictive Actuators and Their Use in Optical Engineering," *Optical Engineering*, Vol.29, pp.1389-1391.

Hanagud S. and Obal, M.W., 1988, "Identification of Dynamic Coupling Coefficients in a Structure with Piezoelectric Sensors and Actuators," AIAA paper No.88-2418.

Haskins, J.F. and Walsh, X., 1957, "Vibration of Ferroelectric Cylindrical Shells with Transverse Isotropy," *J. Acoust. Soc. Am.*, 29, pp.729-734.

Inman, D.J., Mayne, R.W., Dorsch, J.J., 1994, Dual Function System Having a Piezoelectric Element (Self Sensing Actuator), U.S. Patent No.5347870.

Jian, X.H., Tzou, H.S., Lissenden, C.J., and Penn, L.S. 1997, "Damage Detection Using Piezoelectric Patches - Free Vibration Approach," *Journal of Composite Engineering*, Vol.31, No.4, pp.345-359.

Koppe, H., Gabbert, U., and Tzou, H.S., 1998, "On Three-Dimensional Layered Piezoelectric Shell Elements for Design Simulation of Adaptive Structures, *Fortschritt-Berichte VDI, Smart Mechanical Systems – Adaptronics*, 1998. (To appear)

Lee, C.K. and Moon, F., 1988, "Modal Sensors/Actuators," IBM Report, RJ 6306 (61975), Research Division, IBM.

Lee K.M. and Arjunan, S., 1989, "A Three Degree of Freedom Micro-motion in Parallel Actuated Manipulator," *Proceedings of 1989 IEEE Intl. Conf. on Robotics and Automation*, Vol. (3), pp.1698-1703.

Liu, B. and Tzou, H.S., 1998, "Distributed Photostrictive Actuation and Opto-piezothermoelasticity Applied to Vibration Control of Plates," *ASME Transactions, Journal of Vibration & Acoustics*, Vol.120, pp.937-943, October 1998.

Lynch, T., 1996, Piezoelectric Damper Hones Ski Performance," Reprint from *Design News*, February 5.

Mason, W. P., 1950, *Piezoelectric Crystals and Their Application to Ultrasonics*, Nostrand, NY.

Mason, W.P., 1981, "Piezoelectricity, its History and Applications," *J. Acoust. Soc. Am.*, 70(6), Dec. 1981, pp.1561-1566.

Mindlin, R.D., 1961, "On the Equations of Motion of Piezoelectric Crystals, *Problems on Continuum Mechanics*," Radok, J., Editor, Soc. Ind. Appl. Math., Philadelphia, pp.282-290.

Mindlin, R.D., 1972, "High Frequency Vibrations of Piezoelectric Crystal Plates," *Inl. J. Solid Struc.*, Vol. (8), pp.895-906.

Nailon, M., Coursant, R.H., and Besnier, F., 1983, "Analysis of Piezoelectric Structures by a Finite Element Method," *ACTA Electronica*, Vol. 25, No.4, pp.341-362.

Palazzolo, A.B., Lin, R.R., Kascak, R.R., and Alexander, R.M., 1989, "Active Control of Transient Rotordynamic Vibration by Optimal Control methods," *ASME Journal of Engineering for Gas Turbines and Power*, Vol. (111), p.265.

Paul, H.S., 1978, "Vibrations of a Hollow Circular Cylinder of Piezoelectric Ceramics," *J. Acoust. Soc. Am.*, 82(3), pp.952-956.

Paul, H.S., 1982, "Asymptotic Analysis of the Modes of Wave Propagation in a Piezoelectric Solid Cylinder," *J. Acoust. Soc. Am.*, 71(2), pp.255-263.

Paul, H.S., 1986, "Axisymmetric Vibration of a Piezoelectric Solid Cylinder Guided by a Thin Film," *J. Acoust. Soc. Am.*, 80(4), pp.1091-1096.

Paul, H.S., 1987, "Wave Propagation in a Piezoelectric Solid Cylinder of Arbitrary Cross Section," *J. Acoust. Soc. Am.* 82(6), pp.2013-2020.

Plumb, J.M., Hubbard, J.E., and Bailey, T., 1987, "Nonlinear Control of a Distributed System: Simulation and Experimental Results," *ASME Journal of Dynamic Systems, Measurements, and Control*, 109(2), pp.133-139.

Polla, D.L., 1992, "Micromachining of Piezoelectric Microsensors and Microactuators for Robotics applications," *Precision Sensors, Actuators and Systems*, Tzou and Fukuda (Ed.), Kluwer Pub., pp.139-174.

Robinson, A.C., 1971, "A Survey of Optimal Control of Distributed Parameter Systems," *Automatica* 7, pp.371-388.

Rogacheva, N.N., 1982, "Equations of State of Piezoceramic Shells," *PMM U.S.S.R.*, 45(5), pp.677-684.

Rogacheva, N.N., 1984a, "On Stain?Venant Type Conditions in the Theory of Piezoelectric Shells," *PMM U.S.S.R.*, 48(2), pp.213-216.

Rogacheva, N.N., 1984b, "On Boundary conditions in the Theory of Piezoceramic Shells Polarized Along Coordinate Lines," *PMM U.S.S.R.*, 47(2), pp.220-226.

Rogacheva, N.N., 1986, "Classification of Free Piezoceramic Shell Vibrations," *PMM U.S.S.R.*, 50(1), pp.106-111.

Sashida, T. and Kenjo, T., 1993, *An Introduction to Ultrasonic Motors*, Clarendon Press, Oxford.

Senik, N.A. and Kudriavtsev, B.A., 1980, "Equations on the Theory of Piezoceramic Shells," In: *Mechanics of a solid deformable body and related analytical problems*. Moscow, Izd. mosk. Inst. Chim. Mashinostroeniia, U.S.S.R.

Sessler, G.M., 1981, "Piezoelectricity in Polyvinylidene Fluoride," *J. Acoust. Soc. Am.*, 70(6), pp.1596-1608.

Shih, H.R. and Tzou, H.S., 2000, "Opto-Piezothermoelastic Constitutive Modeling Of A New 2-D Photostrictive Composite Plate Actuator, the Adaptive Structures and Materials Symposium (Aero), AD-Vol.61, pp.1-8, 2000 ASME International Mechanical Engineering Congress, Orlando, FL, Nov.5-10, 2000.

Sirlin, S.W., 1987, "Vibration Isolation for Spacecraft Using the Piezoelectric Polymer PVF₂," *Proceedings*, the 114th Meeting of the Acoustic Soc. Am., Nov. 1987.

Stavroulakis, P., 1983, *Distributed Parameter System Theory, Part 1 & 2*, Hutchinson Ross Pub. Co., Stroudsburg, PA.

Tiersten, H.F., 1969, *Linear Piezoelectric Plate Vibrations*, Plenum, New York.

Toupin, R.A., 1959, "Piezoelectric Relation and the Rachial Deformation of Polarized Spherical Shell," *J. Acoust. Soc. Am.*, 31(3), pp.315-318.

Tzou, H.S., 1987, "Active Vibration Control of Flexible Structures via Converse Piezoelectricity," *Development in Mechanics*, Vol.14(b), Proceedings of the 20th Midwest Mechanical Conference, pp.1201-1206.

Tzou, H.S., 1988, "Integrated Sensing and Adaptive Vibration Suppression of Distributed Systems," *Recent Development in Control of Nonlinear and Distributed Parameter Systems*, ASME-DSC-Vol.10, December 1988, pp.51-58.

Tzou, H.S., 1989a, "Development of a Light-weight Robot End-effector using Polymeric Piezoelectric Bimorph," *Proceedings of 1989 IEEE Intl. Conf. on Robotics and Automation*, Vol. (3), pp.1704-1709.

Tzou, H.S., 1989b, "Integrated Distributed Sensing and Active Vibration Suppression of Flexible Manipulators using Distributed Piezoelectrics," *Journal of Robotic Systems*, Vol. (6.6), pp.745-767. December 1989.

Tzou, H.S., 1990, *Intelligent Piezoelectric Systems*, Industrial Technology Research Institute, Mechanical Industry Research Laboratories, Hsinchu, Taiwan, ROC.

Tzou, H.S., 1991a, "Distributed Modal Identification and Vibration Control of Continua: Theory and Applications," *ASME Journal of Dynamic Systems, Measurements, and Control*, 113(3), pp.494-499.

Tzou, H.S., 1991b, "Distributed Piezoelectric Neurons and Muscles for Shell Continua," *Structural Vibration and Acoustics*, Ed. Huang, Tzou, et al., ASME-DE-Vol. 34, pp.1-6, 1991 ASME 13th Biennial Conference on Mechanical Vibration and Noise, Symposium on Intelligent Structures and Systems, Miami, FL, Sep. 22-25, 1991.

Tzou, H.S., 1992a, "A New Distributed Sensation and Control Theory for "Intelligent Shells," *Journal of Sound & Vibration*, Vol.152, No.3, pp.335-350, March 1992.

Tzou, H.S., 1992b, *Distributed Sensors and Actuators*, Tutorial Notes (300 pages), 1992 IEEE International Conference on Intelligent Robots and Systems (IROS'92), Raleigh, NC, July 7-10, 1992.

Tzou, H.S., 1993, *Piezoelectric Shells (Distributed Sensing and Control of Continua)*, Kluwer Academic Publishers.

Tzou, H.S. and Anderson, G.L. (Editors), 1992, *Intelligent Structural Systems*, ISBN No.0-7923-1920-6, 488 pages, Book, Kluwer Academic Publishers, Dordrecht/Boston/London, August 1992.

Tzou, H.S., and Bao, Y., 1997, "Nonlinear Piezothermoelasticity and Multi-field Actuations, Part-1: Nonlinear Anisotropic Piezothermoelastic Shell Laminates," *ASME Transactions, Journal of Vibration & Acoustics*, Vol.119, pp.374-381.

Tzou, H.S. and Bao, Y., 1995, "A Theory on Anisotropic Piezothermoelastic Shell Laminates with Sensor/Actuator Applications," *Journal of Sound & Vibration*, Vol.184, No.3, pp.453-473.

Tzou, H.S. and Bao, Y., 1995, "Dynamics and Control of Adaptive Shells with Curvature Transformations," *Shock and Vibration Journal*, Vol.2, No.2, pp.143-154.

Tzou, H.S. and Bao, Y., 1996, "Spatially Filtered Multi-field Responses of Piezothermoelastic Cylindrical Shell Composites," *Structural Engineering and Mechanics*, Vol.4, No.2.

Tzou, H.S., and Bao, Y., 1998, "Analysis of Nonlinear Piezothermoelastic Laminated Beams with Electric and Temperature Effects," *Journal of Sound & Vibration*, Vol.209, No.3, pp.505-518.

Tzou, H.S., Bao, Y., Venkayya, V.B., 1996, "Study of Segmented Transducers Laminated on Cylindrical Shells, Part-1: Sensor Patches," *Journal of Sound & Vibration*, Vol.197, No.2, pp.207-224.

Tzou, H.S., Bao, Y., Venkayya, V.B., 1996, "Study of Segmented Transducers Laminated on Cylindrical Shells, Part-2: Actuator Patches," *Journal of Sound & Vibration*, Vol.197, No.2, pp.225-249, October 1996.

Tzou, H.S., Baz, A.M., Duclos, T.E., Inman, D.J., 1994, *Intelligent Structural Systems*, Lecture Notes, SC-5, 1994 North American Conference on Smart Structures and Materials, Orlando, FL, February 17-18, 1994.

Tzou, H.S. and Bergman, L.A., (Ed), 1998, *Dynamics and Control of Distributed Systems*, Cambridge University Press, 1998.

Tzou, H.S., Chai, W.K., and Wang, D.W., 2001, "Modal Voltages and Distributed Signal Analysis of Conical Shells of Revolution," Paper No.Vib21544, 2001 Design Technical Conference, Pittsburgh, PA, Spt.9-12, 2001.

Tzou, H. S. and Ding, J. H., 2001, "Spatially Distributed Signals of Nonlinear Paraboloidal Shells with Distributed Neurons," Paper No.Vib21545, 2001 Design Technical Conference, Pittsburgh, PA, Spt.9-12, 2001.

Tzou, H.S. and Ding, J.H., 2001, "Precision Actuation Effectiveness of Segmented Actuators Laminated on Paraboloidal Reflectors," Symposium on Active Control of Vibration and Noise, 2001 ASME International Mechanical Engineering Congress, New York, NY, Nov.12-17, 2001.

Tzou, H.S. and Fu, H., 1994, "A Study of Segmentation of Distributed Sensors and Actuators, Part-1, Theoretical Analysis," *Journal of Sound & Vibration*, Vol.172, No.2, pp.247-260, April 1994.

Tzou, H.S. and Fu, H., 1994, "A Study of Segmentation of Distributed Sensors and Actuators, Part-2, Parametric Study and Vibration Controls," *Journal of Sound & Vibration*, Vol.172, No.2, pp.261-276, April 1994.

Tzou, H.S. and Fukuda, T., 1991, *Piezoelectric Smart Systems Applied to Robotics, Micro-Systems, Identification, and Control*, Workshop Notes, IEEE Robotics and Automation Society, 1991 IEEE International Conference on Robotics and Automation, Sacramento, CA, April 7-12, 1991.

Tzou, H.S. and Fukuda, T. (Editors), 1992, *Precision Sensors, Actuators, and Systems*, Book (470 pages), Kluwer Academic Publishers, December 1992.

Tzou, H.S. and Gabbert, U., 1997, "STRUCTRONICS- A New Discipline and Its Challenging Issues," *Fortschritt-Berichte VDI, Smart Mechanical Systems – Adaptronics*, Reihe 11: Schwingungstechnik Nr.244, pp.245-250, Düsseldorf, Germany.

Tzou H.S. and Gadre, M., 1988, "Active Vibration Isolation by Piezoelectric Polymer with Variable Feedback Gain," *AIAA Journal*, Vol.26, No.8, 1014-1017.

Tzou, H.S., and Gadre, M, 1989, "Theoretical Analysis of a Multi-Layered Thin Shell Coupled with Piezoelectric Shell Actuators for Distributed Vibration Control," *Journal of Sound and Vibration*, Vol.132, No.3, pp.433-450.

Tzou H.S., and Gadre, M., 1990, "Active Vibration Isolation and Excitation by a Piezoelectric Slab with Constant Feedback Gains," *Journal of Sound and Vibration*, Vol.136, No.3, pp.477-490.

Tzou, H.S., Guran A. (Editors), Gabbert, U., Tani, J. and Breitbach, A. (Associate Editors), 1998, *Structronic Systems - Smart Structures, Devices, and Systems*, Volume-2: *Systems and Control*, World Scientific Publishing Co., New Jersey/Singapore.

Tzou, H.S. and Hollkamp, J.J., 1994, "Collocated Independent Modal Control with Self-Sensing Orthogonal Piezoelectric Actuators (Theory and Experiment)," *Journal of Smart Materials and Structures*, Vol.3, pp.277-284.

Tzou, H.S., Johnson, D., and Liu, J., 1995, "Nonlinear Control and Boundary Transition of Cantilever Distributed Systems," in *Wave Motion, Intelligent Structures and Nonlinear Mechanics*, Guran a. and Inman D.J. (Editors), World Scientific Publishing, Singapore, pp.163-193.

Tzou, H.S., Johnson, D., and Liu, Jack, 1999, "Damping Behavior of Cantilever Structronic Systems with Boundary Control," H.S. Tzou, D. Johnson, and K.J. Liu, *ASME Transactions, Journal of Vibration & Acoustics*, pp.402-407, July 1999.

Tzou, H.S. and Smithmaitrie, P., 2001, "Sensor Electromechanics and Distributed Signal Analysis of Piezo(Electptc)-Elastic Spherical Shells Based on the Bending Approximation," Paper No.Vib21494, 2001 Design Technical Conference, Pittsburgh, PA, Spt.9-12, 2001.

Tzou, H.S. and Wang,D.W., 2001, "Distributed Signals of Piezoelectric Laminated Toroidal Shell Structures," the Adaptive Structures and Materials Symposium (Aero), 2001 ASME International Mechanical Engineering Congress, New York, NY, Nov.12-17, 2001.

Tzou, H.S., Wang, D.W., and Chai, W.K., 2001, "Control of Conical Shells Laminated with Full and Diagonal Actuators," Paper No.CIE21272, 2001 Design Technical Conference, Pittsburgh, PA, Spt.9-12, 2001.

Tzou, H.S. and Ye, R., 1996, "Analysis of Piezoelastic Systems with Laminated Piezoelectric Triangle Shell Elements," *AIAA Journal*, Vol.34, No.1, pp.110-115.

Tzou, H.S. and Ye, R., 1996, "Pyroelectric and Thermal Strain Effects in Piezoelectric (PVDF and PZT) Devices," *Mechanical Systems and Signal Processing (Journal of)*, Vol.10, No.4, pp.459-479.

Tzou, H.S., Ye, R., and J. H. Ding 2001, "A New X-Actuator Design For Controlling Wing Bending And Twisting Modes," H. S. Tzou, R. Ye, , *Journal of Sound & Vibration*, 241(2), pp.271-281.

Tzou H.S. and Tseng, C.I., 1990, "Distributed piezoelectric sensor/actuator design for dynamic measurement/control of distributed parameter systems: a finite element approach," *Journal of Sound and Vibration*, Vol.138, No.1, pp.17-34.

Tzou H.S. and Yang, R.J., 2000, "Nonlinear Piezo-thermoelastic Shell Theory applied to Control of Variable-geometry Shells," *Journal of Theoretical and Applied Mechanics*, No.3, Vol.38, pp.623-644.

Tzou, H. S., R. Ye, R., and Ding, J. H., 2001, "A New X-Actuator Design For Controlling Wing Bending And Twisting Modes," *Journal of Sound & Vibration*, 241(2), pp.271-281.

Tzou, H.S. and Zhong, J., 1996, "Spatially Filtered Vibration Control of Cylindrical Shells," *Shock and Vibration Journal*, Vol.3, No.4, pp.269-278.

Tzou, H.S., Zhong, J.P., and Natori, M.C., 1993, "Sensor Mechanics of Distributed Shell Convolving Sensors Applied to Flexible Rings," *ASME Transactions, Journal of Vibration & Acoustics*, Vol.115, No.1, pp.40-46.

Tzou, H.S., Zhong, J.P., and Hollkamp, J.J., 1994, "Spatially Distributed Orthogonal Piezoelectric Shell Actuators: Theory and Applications," *Journal of Sound & Vibration*, Vol.177, No.3, pp.363-378.

Tzou, H.S. and Zhou, Y., 1995, "Dynamics and Control of Nonlinear Circular Plates with Piezoelectric Actuators," *Journal of Sound & Vibration*, Vol.188, No.2, pp.189-207.

Tzou, H.S., and Zhou, Y., 1997, "Nonlinear Piezothermoelasticity and Multi-field Actuations, Part-2: Control of Nonlinear Buckling and Dynamics," *ASME Transactions, Journal of Vibration & Acoustics*, Vol.119, pp.382-389.

Uchino, K., 1997, *Piezoelectric Actuators and Ultrasonic Motors*, Kluwer Academic Pub., Dordrecht/Boston/London.

Ueha, S., Tomikawa, Y., Kurosawa, M., and Nakamura, N., 1993, *Ultrasonic Motors*, Clarendon Press, Oxford.

Ye, R., Tzou, H.S., and Tani, J., 1996, "Distributed Control of Semicircular Shells Subjected to Thermal Shock and Mechanical Excitations," *Active Control of Vibration and Noise*, DE-Vol.93, pp.329-338, ASME 1996 International Mechanical Engineering Congress, Atlanta, GA, November 17-22, 1996.

Ye, R. and Tzou, H.S., 2000, "Control of Adaptive Shells with Thermal and Mechanical Excitations," *Journal of Sound & Vibration*, Vol.231(5), pp.1321-1338.

Zhong, J., Tzou, H.S., and Tani, J., 1996, "Sensing and Control of Shell Symmetrical Modes using Diagonal Line Sensors and Actuators," *Active Control of Vibration and Noise*, DE-Vol.93, pp.263-269, ASME 1996 International Mechanical Engineering Congress, Atlanta, GA, November 17-22, 1996.

Zhou Y.H. and Tzou, H.S., 2000, "Control of Nonlinear Piezoelectric Circular Shallow Spherical Shells," *Journal of Solids and Structures*, Vol.37, pp.1663-1677.

(Lec2ShlDPS.TIT01.Wd00.Document8)

CHAPTER 2

MODAL VOLTAGES OF LINEAR AND NONLINEAR STRUCTURES USING DISTRIBUTED ARTIFICIAL NEURONS

ABSTRACT

Laminated or embedded distributed neurons on structural components serve as in-situ sensors monitoring structure's dynamic state and health status. Thin film piezoelectric patches are perfect candidates for this purpose. A generic piezoelectric neuron concept is introduced first, followed by definitions of neural signals generated by an arbitrary neuron laminated on a generic nonlinear double-curvature elastic shell. This generic neuron theory can be applied to a large class of linear and nonlinear common geometries, e.g., spheres, cylindrical shells, plates, etc. To demonstrate the neuron concept, an Euler-Bernoulli beam laminated with segmented neurons is studied. Neural signals and modal voltages are presented. Theoretical results are compared with experimental data favorably.

INTRODUCTION

Structural health monitoring, diagnosis, and failure prevention are essential to structural integrity, reliability, performance, safety, etc. of high-performance structures and machines. Conventional sensing technologies usually utilize strain gages, eddy current proximeters, linear variable differential transformers (LVDT), accelerometers, potentiometers, etc. These sensing systems are, of course, capable of carrying out the sensing functions and fulfilling design and control requirements. However, these transducers are all add-on devices, i.e., devices are installed on the structures using off-the-shelf sensors. These add-on transducers can add additional weights to the structures, which often is not desirable in many applications.

In the recent development of smart structures and strucronic systems (Plubm, et al., 1987; Crawley and de Luis, 1987; Baz and Poh, 1988; Hanagud and Obal, 1988; Tzou, 1987), distributed piezoelectric layers laminated on flexible structures can serve as in-situ neurons monitoring local strain variations of structures, Figure 1. Since the distributed piezoelectric layers are spatially distributed, the induced sensing signal is surface averaged over the effective sensor area. Accordingly, the sensitivity of piezoelectric neurons depends on not only the piezoelectric material properties, but also structural dynamic characteristics, such as natural

frequencies, mode shapes, locations, etc. (Tzou, 1992). Significant sensing deficiency can occur when the segmented sensors are symmetrically laminated on symmetrical structures with symmetrical boundary conditions (Tzou, 1993). In this paper, detailed electromechanical characteristics (sensor electromechanics) of spatially distributed piezoelectric neurons are discussed and the governing equations are derived. Demonstration examples are presented. Experimental results are compared with theoretical solutions.

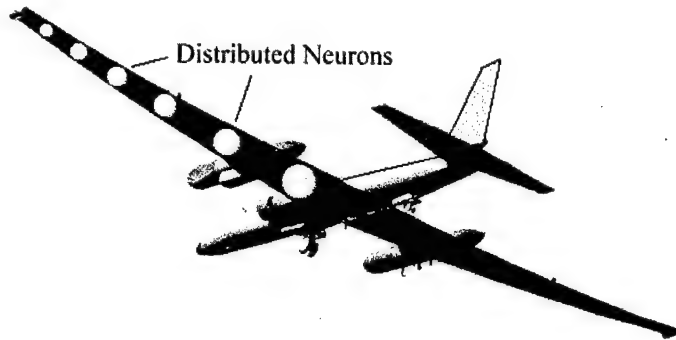


Fig.1 Distributed structural neurons.

DISTRIBUTED STRUCTURAL NEURONS

It is assumed that distributed piezoelectric layers serving as distributed neurons are arbitrarily located on a generic nonlinear elastic shell continuum defined in a tri-orthogonal curvilinear coordinate system, Figure 2. A generic distributed neuron theory of segmented sensors is derived based on the direct piezoelectric effect and the generic double-curvature shell theory. Application of the generic neuron theory to other geometries (e.g., spheres, cylinders, plates, etc.) depends on four geometric parameters: two Lamé parameters and two radii of curvature (Tzou, 1993). A generic piezoelectric neuron theory is derived in this section. A case study based on an Euler-Bernoulli elastic beam is presented in the next section.

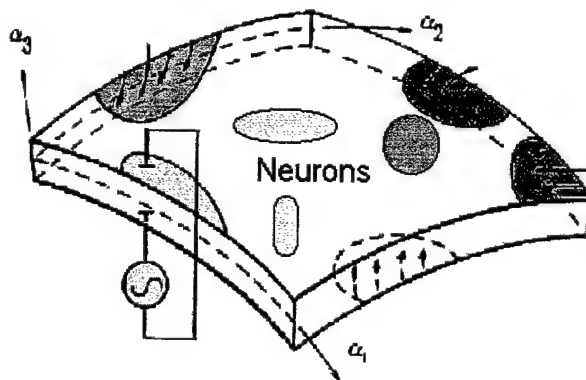


Fig.2 A generic nonlinear shell laminated with distributed neurons.

Distributed piezoelectric neurons laminated on the generic nonlinear shell respond to shell strain variations and consequently generate electric signals based on the direct piezoelectric effect. The open-circuit neural signal ϕ^s from an arbitrary neuron is a function of induced local linear or nonlinear strains S_{ij} and the piezoelectric constants d_{ij} .

$$\phi^s = (h^s/S^e) \int_{\alpha_1} \int_{\alpha_2} [d_{31}S_{11}^s + d_{32}S_{22}^s + d_{36}S_{12}^s] \bullet A_1 A_2 d\alpha_1 d\alpha_2, \quad (1)$$

where h^s is the sensor thickness; S^e is the effective electrode area; A_1 and A_2 are Lamé parameters. The surface integration denotes the total charge generated over the effective electrode area defined by the α_1 and α_2 axes. Note that since the neuron is spatially distributed, the signal is averaged over the total effective electrode area (Tzou, Zhong, Natori, 1993).

Since the strain, in general, can be divided into the membrane strain and the bending strain. The signal equation can be further expressed as

$$\begin{aligned} \phi^s = & (h^s/S^e) \int_{\alpha_1} \int_{\alpha_2} \left[d_{31} \left\{ \frac{1}{A_1} \frac{\partial u_1}{\partial \alpha_1} + \frac{u_2}{A_1 A_2} \frac{\partial A_1}{\partial \alpha_2} + \frac{u_3}{R_1} + \left[\frac{1}{2} \left(\frac{\partial u_3 / \partial \alpha_1}{A_1} \right)^2 \right] \right. \right. \\ & \left. \left. + r^s \left(\frac{1}{A_1} \frac{\partial}{\partial \alpha_1} \left(\frac{u_1}{R_1} - \frac{1}{A_1} \frac{\partial u_3}{\partial \alpha_1} \right) + \frac{1}{A_1 A_2} \left(\frac{u_2}{R_2} - \frac{1}{A_2} \frac{\partial u_3}{\partial \alpha_2} \right) \frac{\partial A_1}{\partial \alpha_2} \right) \right\} \right. \\ & \left. + d_{32} \left\{ \frac{1}{A_1} \frac{\partial u_2}{\partial \alpha_2} + \frac{u_1}{A_1 A_2} \frac{\partial A_2}{\partial \alpha_1} + \frac{u_3}{R_2} + \left[\frac{1}{2} \left(\frac{\partial u_3 / \partial \alpha_2}{A_2} \right)^2 \right] \right. \right. \\ & \left. \left. + r^s \left(\frac{1}{A_2} \frac{\partial}{\partial \alpha_2} \left(\frac{u_2}{R_2} - \frac{1}{A_2} \frac{\partial u_3}{\partial \alpha_2} \right) + \frac{1}{A_1 A_2} \left(\frac{u_1}{R_1} - \frac{1}{A_1} \frac{\partial u_3}{\partial \alpha_1} \right) \frac{\partial A_2}{\partial \alpha_1} \right) \right\} \right. \\ & \left. + d_{36} \left\{ \frac{1}{A_2} \frac{\partial u_1}{\partial \alpha_2} + \frac{1}{A_1} \frac{\partial u_2}{\partial \alpha_1} - \frac{u_1}{A_1 A_2} \frac{\partial A_1}{\partial \alpha_2} - \frac{u_2}{A_1 A_2} \frac{\partial A_2}{\partial \alpha_1} + \left[\frac{1}{A_1 A_2} \frac{\partial u_3}{\partial \alpha_1} \frac{\partial u_3}{\partial \alpha_2} \right] \right. \right. \\ & \left. \left. + r^s \left[\frac{A_1}{A_2} \frac{\partial}{\partial \alpha_2} \left[\left(\frac{u_1}{R_1} - \frac{1}{A_1} \frac{\partial u_3}{\partial \alpha_1} \right) / A_1 \right] + \frac{A_2}{A_1} \frac{\partial}{\partial \alpha_1} \left[\left(\frac{u_2}{R_2} - \frac{1}{A_2} \frac{\partial u_3}{\partial \alpha_2} \right) / A_2 \right] \right. \right. \\ & \left. \left. - \frac{1}{A_1 A_2} \left(\frac{u_1}{R_1} - \frac{1}{A_1} \frac{\partial u_3}{\partial \alpha_1} \right) \frac{\partial A_1}{\partial \alpha_2} - \frac{1}{A_1 A_2} \left(\frac{u_2}{R_2} - \frac{1}{A_2} \frac{\partial u_3}{\partial \alpha_2} \right) \frac{\partial A_2}{\partial \alpha_1} \right] \right\} \bullet A_1 A_2 d\alpha_1 d\alpha_2 \right] \quad (2) \end{aligned}$$

where u_i 's are the displacements; R_i is the radius of curvature of the i th axis; and r^s is the neuron location away from the shell neutral surface. The terms following r^s represent the bending strain component; others are the membrane strain component. The membrane strain component is related to in-plane oscillations and the bending component is related to bending oscillation of the generic shell. Note that the large deformation effect is included with the membrane strains, the quadratic terms, based on the von Karman geometric nonlinearity theory (Tzou, Bao, and Zhou, 1997). Accordingly, each piezoelectric neuron responds to local strain

variations induced by all possible oscillations of the elastic shell continuum. This implies that the neuron can actively monitor the structural condition and provides the linear or nonlinear state information for further diagnosis and/or control applications. To demonstrate the concept and technology, an elastic beam laminated with piezoelectric neuron patches is investigated analytically and experimentally in the following sections. However, for simplicity and better comparison, only the linear theory is considered in the case study.

CASE STUDY: EULER-BERNOULLI BEAM

An Euler-Bernoulli beam is the simplest elastic continuum that can be used to demonstrate the distributed neuron concept. A cantilever Euler-Bernoulli beam laminated with a number of distributed piezoelectric neurons is investigated theoretically and experimentally in this study. It is assumed that the piezoelectric neurons are much thinner than that of the elastic beam and they are perfectly bonded on the beam. The effects of bonding material and the piezoelectric layers are not considered in the electromechanical analysis. In this section, theoretical derivation of the laminated beam model is presented.

For an elastic beam, Lamé parameters are $A_1 = 1$ and $A_2 = 1$; radii of curvature are $R_1 = \infty$ and $R_2 = \infty$. Also, the transverse oscillation dominates the structural dynamics and the in-plane oscillations, i.e., x and y , are usually neglected within the linear theory. Figure 3 illustrates the Euler-Bernoulli beam laminated with six thin piezoelectric neurons.

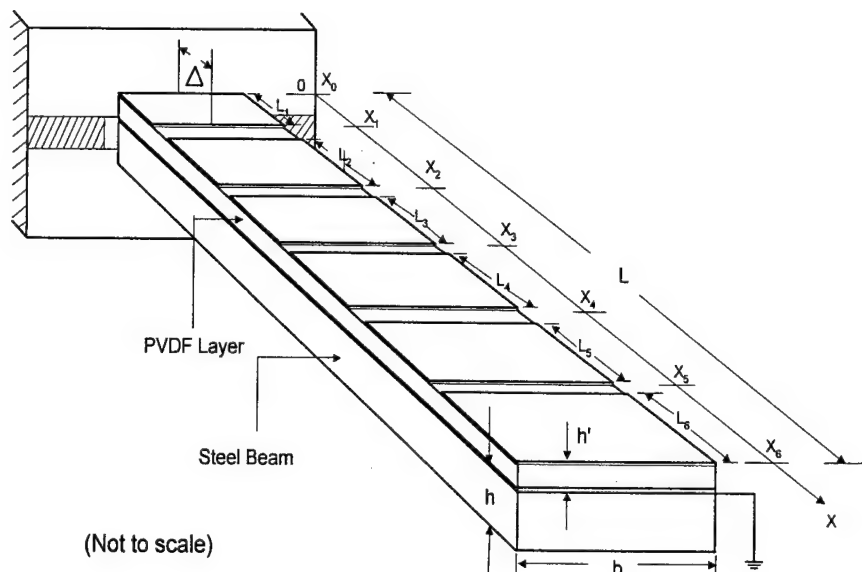


Fig.3 Euler-Bernoulli beam laminated with thin piezoelectric neurons.

Theoretical Modeling and Analysis

The equation of motion of the Euler-Bernoulli beam model is

$$-\frac{\partial^2 M_{xx}}{\partial x^2} + \rho h \ddot{u}_3 = 0 \quad (3)$$

where $M_{xx} = -YI \frac{\partial^2 u_3}{\partial x^2}$ (4)

where ρ is the mass density; H is the beam thickness; Y is Young's modulus and; $I = h^3/12$ is the area moment of per unit width. Substituting Eq.(4) into Eq.(3) yields the classic beam equation

$$YI \frac{\partial^4 u_3}{\partial x^4} + \rho h \ddot{u}_3 = 0 \quad (5)$$

For harmonical free vibration $u_3(x, t) = U_3(x)e^{j\omega t}$ at natural frequencies, Eq.(5) becomes

$$\frac{\partial^4 U_3}{\partial x^4} - \lambda^4 U_3 = 0 \quad (6)$$

where $U_3(x)$ is the mode shape function; ω is the frequency; and λ is the eigenvalue, i.e.,

$$\lambda^4 = \frac{\omega^2 \rho'}{YI} \quad (7)$$

where ρ' is a mass density per unit length. The solution (mode shape function $U_3(x)$) of Eq.(6) is

$$U_3(x) = U_3(0)A(\lambda x) + \frac{1}{\lambda} \frac{dU_3(0)}{dx} B(\lambda x) + \frac{1}{\lambda^2} \frac{d^2U_3(0)}{dx^2} C(\lambda x) + \frac{1}{\lambda^3} \frac{d^3U_3(0)}{dx^3} D(\lambda x), \quad (8)$$

where

$$A(\lambda x) = \frac{1}{2}(\cosh \lambda x + \cos \lambda x) \quad (9a)$$

$$B(\lambda x) = \frac{1}{2}(\sinh \lambda x + \sin \lambda x) \quad (9b)$$

$$C(\lambda x) = \frac{1}{2}(\cosh \lambda x - \cos \lambda x) \quad (9c)$$

$$D(\lambda x) = \frac{1}{2}(\sinh \lambda x - \sin \lambda x) \quad (9d)$$

The derivatives of mode shape function $U_3(x)$ are given as follows.

$$\frac{dU_3}{dx}(x) = \lambda U_3(0) D(\lambda x) + \frac{dU_3(0)}{dx} A(\lambda x) + \frac{1}{\lambda} \frac{d^2 U_3(0)}{dx^2} B(\lambda x) + \frac{1}{\lambda^2} \frac{d^3 U_3(0)}{dx^3} C(\lambda x) \quad (10a)$$

$$\frac{d^2 U_3}{dx^2}(x) = \lambda^2 U_3(0) C(\lambda x) + \lambda \frac{dU_3(0)}{dx} D(\lambda x) + \frac{d^2 U_3(0)}{dx^2} A(\lambda x) + \frac{1}{\lambda} \frac{d^3 U_3(0)}{dx^3} B(\lambda x) \quad (10b)$$

$$\frac{d^3 U_3}{dx^3}(x) = \lambda^3 U_3(0) B(\lambda x) + \lambda^2 \frac{dU_3(0)}{dx} C(\lambda x) + \lambda \frac{d^2 U_3(0)}{dx^2} D(\lambda x) + \frac{d^3 U_3(0)}{dx^3} A(\lambda x) \quad (10c)$$

These derivatives are used to define the exact mode shape function, frequency of beams with specific boundary conditions., In this case, the boundary conditions at the clamped end (at $x = 0$) are

$$u_3(x = 0, t) = 0 \quad \text{or} \quad U_3(x = 0, t) = 0 \quad (11)$$

$$\frac{\partial u_3}{\partial x}(x = 0, t) = 0 \quad \text{or} \quad \frac{\partial U_3}{\partial x}(x = 0, t) = 0 \quad (12)$$

and at the free end ($x = L$)

$$M_{xx}(x = L, t) = 0 \quad \text{and} \quad Q_{x3}(x = L, t) = 0 \quad (13,14)$$

Using the moment and shear force definitions, one can derive

$$\frac{\partial^2 u_3}{\partial x^2}(x = L, t) = 0 \quad \text{or} \quad \frac{\partial^2 U_3}{\partial x^2}(x = L, t) = 0 \quad (15)$$

$$\frac{\partial^3 u_3}{\partial x^3}(x = L, t) = 0 \quad \text{or} \quad \frac{\partial^3 U_3}{\partial x^3}(x = L, t) = 0 \quad (16)$$

Also, using the boundary conditions, one can calculate the natural frequencies.

$$\omega_n = \frac{(\lambda_n L)^2}{L_n^2} \sqrt{\frac{EI}{\rho'}} \quad (17)$$

The natural modes (mode shapes) $U_3(x)$ are

$$\begin{aligned} U_{3n}(x) &= \frac{1}{\lambda_n^2} \frac{d^2 U_{3n}(0)}{dx^2} \left(C(\lambda_n x) - \frac{A(\lambda_n L)}{B(\lambda_n L)} D(\lambda_n x) \right) \\ &= P \left\{ \cosh(\lambda_n x) - \cos(\lambda_n x) - \frac{\cosh(\lambda_n L) + \cos(\lambda_n L)}{\sinh(\lambda_n L) + \sin(\lambda_n L)} \cdot (\sinh(\lambda_n x) - \sin(\lambda_n x)) \right\}. \end{aligned} \quad (18)$$

where P is an amplitude constant and

$$P = \frac{1}{\lambda_n^2} \frac{d^2 U_{3n}(0)}{dx^2} \quad (19)$$

Distributed Neuron Signal

Neural signal of the distributed piezoelectric neurons can be directly simplified from the generic neural signal equation using four geometric parameters: two Lamé parameters (i.e., $A_1 = 1$ and $A_2 = 1$) and two radii of curvature (i.e., $R_1 = \infty$ and $R_2 = \infty$). On the other hand, the neural signal can be directly derived based on induced strains and the converse piezoelectric effect. The charge equation of electrostatics is

$$\frac{\partial(e_{31}S_{xx} + \epsilon_{33}E_3)}{\partial \alpha_3} = 0 \quad (20)$$

Eq.(20) implies that the electric displacement $D_3 = e_{31}S_{xx} + \epsilon_{33}E_3$ which is independent of α_3 and it is a function of location x and time t .

$$e_{31}S_{xx} + \epsilon_{33}E_3 = f(x, t) \quad (21)$$

Substituting strain-displacement relations yields the electric field E_3

$$E_3 = \frac{1}{\epsilon_{33}} (f(x, t) - e_{31}S_{xx}) = \frac{1}{\epsilon_{33}} \left(f(x, t) + \alpha_3 e_{31} \frac{\partial^2 u_3}{\partial x^2} \right) \quad (22)$$

where function $f(x, t)$ can be calculated based on the electric boundary conditions which are determined by external voltages. For free vibration, the external voltage is equal to zero so that the function $f(x, t)$ is equal to zero and Eq.(22) can be rewritten as :

$$E_3 = \frac{e_{31}}{\epsilon_{33}} \frac{\partial^2 u_3}{\partial x^2} \alpha_3 \quad (23)$$

The signal output ϕ_{3i} of the i' th piezoelectric neuron is

$$\begin{aligned} \phi_{3i} &= \frac{e_{31}b}{\epsilon_{33}S_i} \int_{x_{i-1}}^{x_i} \frac{\partial^2 u_3}{\partial x^2} dx \int_{h/2}^{h/2+h'} \alpha_3 d\alpha_3 = \frac{e_{31}}{\epsilon_{33}\Delta} \frac{h'(h+h')}{2} \int_{x_{i-1}}^{x_i} \frac{\partial^2 u_3}{\partial x^2} dx \\ &= \frac{e_{31}}{\epsilon_{33}\Delta} \frac{h'(h+h')}{2} \left(\frac{\partial u_3}{\partial x}(X_i) - \frac{\partial u_3}{\partial x}(X_{i-1}) \right) \end{aligned} \quad (24)$$

where Δ is the neuron segment length shown in Figure 3. Substituting mode shape function Eq.(18) into Eq.(24) yields the generic modal neural signal equation

$$\begin{aligned}
 \phi_{3i} = & \frac{e_{31}}{\varepsilon_{33}\Delta} \frac{h'(h+h')}{2} P \lambda_n \{ [\sinh(\lambda_n x_i) - \sinh(\lambda_n x_{i-1}) + \sin(\lambda_n x_i) - \sin(\lambda_n x_{i-1}) \\
 & - \frac{\sinh(\lambda_n L) - \sin(\lambda_n L)}{\cosh(\lambda_n L) + \cos(\lambda_n L)} \cdot [\cosh(\lambda_n x_i) - \cosh(\lambda_n x_{i-1}) - \cos(\lambda_n x_i) + \cos(\lambda_n x_{i-1})] \}
 \end{aligned} \quad (25)$$

Plotting the neural signals of the distributed neurons yields the **modal voltages** of the *i*th natural mode.

PHYSICAL MODEL AND LABORATORY SETUP

In order to demonstrate the distributed neuron concept and the neural sensing phenomena of segmented piezoelectric neurons, an Euler-Bernoulli beam (90x12x0.7mm) laminated with segmented piezoelectric neurons (15x12x0.04mm) is fabricated, Figure 3. The cantilever steel beam bonded with segmented polyvinylidene fluoride (PVDF) film (40 μ m) is fully tested in the Dynamics and Structronics Laboratory. Experimental data are compared with analytical solutions.

To test its frequency response and the modal sensitivities of the distributed neurons, sinusoidal waves generated from a signal generator (Wavetek) is input to a shaker amplifier and then to an electromagnetic shaker where the beam is mounted on. Figure 4 illustrates the experimental setup and apparatus. Signal voltages from the six PVDF neurons are simultaneously inputted to a Multi-Channel Signal Sampling/Analysis System. The six-channel data are recorded to identify the location of nodes and also for further analysis and comparison of beam's dynamic characteristics.

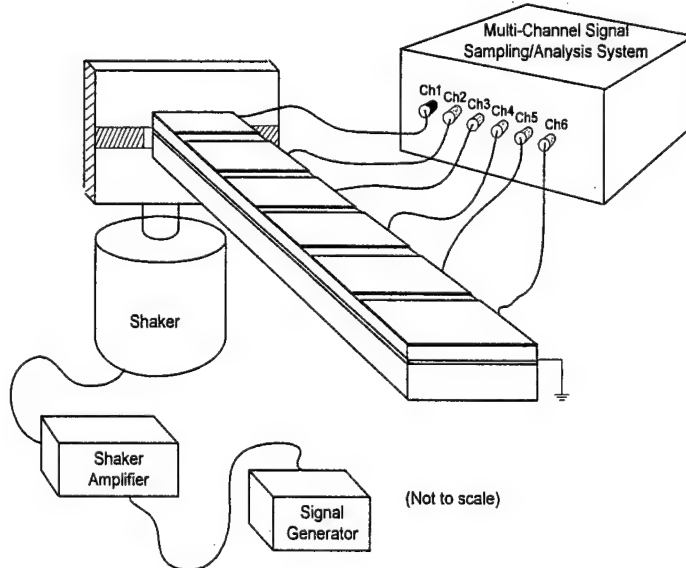


Fig.4 Laboratory setup and apparatus.

RESULTS AND DISCUSSION

Neural signals of the six piezoelectric neurons laminated on the cantilever beam are acquired. Modal information and modal voltages are then investigated. Experimental data are also compared with analytical solutions in this section.

Neural Signals

Time responses of individual piezoelectric neurons at five natural modes are presented in Figures 5-9. All neural signals have the same sign indicating that all these neurons experiencing either compression or tension simultaneously and there is no nodes along the beam in Figure 5. This implies that the mode shape is indeed the first bending mode.

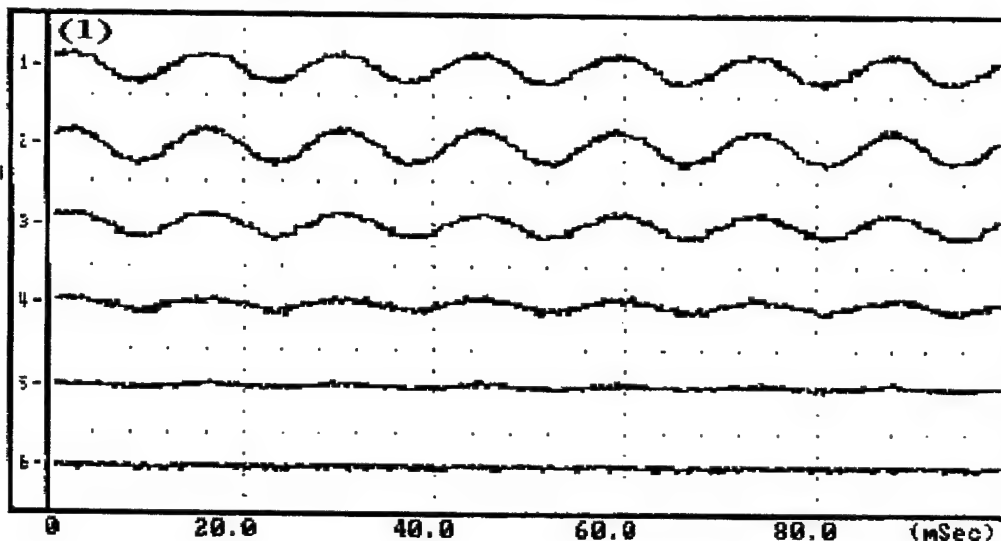


Fig.5 Neural signals of the first mode.

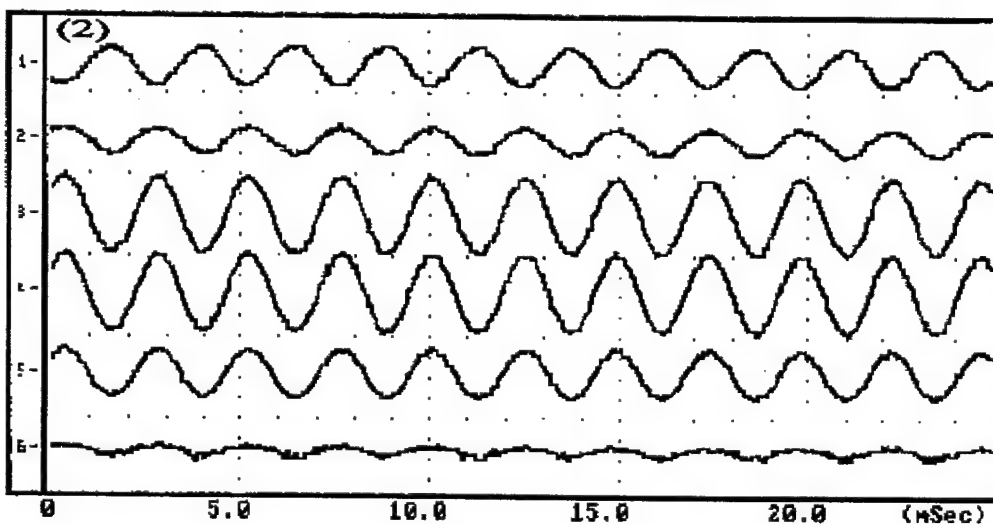


Fig.6 Neural signals of the second mode.

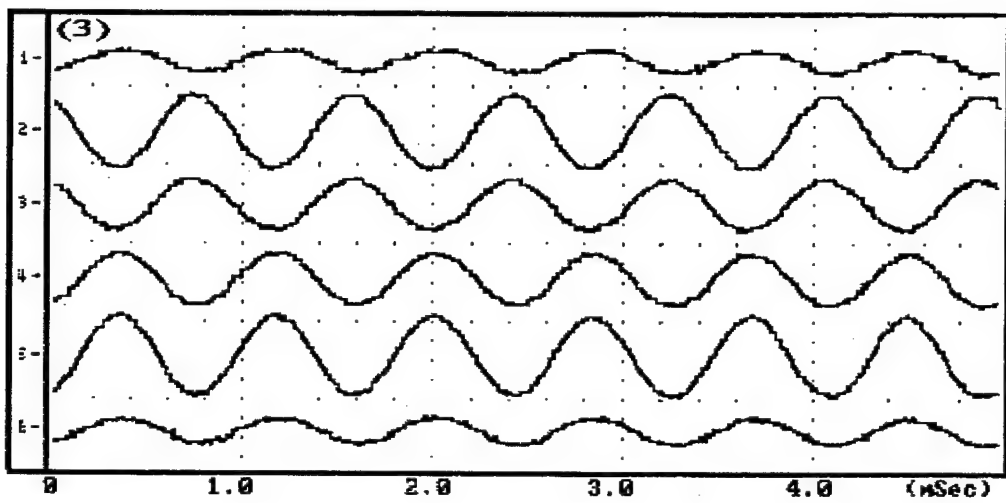


Fig.7 Neural signals of the third mode.

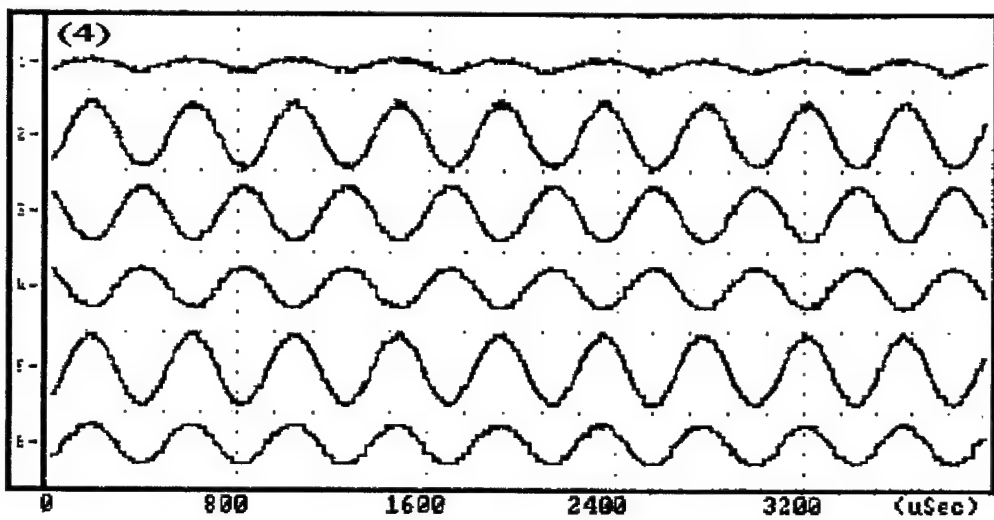


Fig.8 Neural signals of the fourth mode.

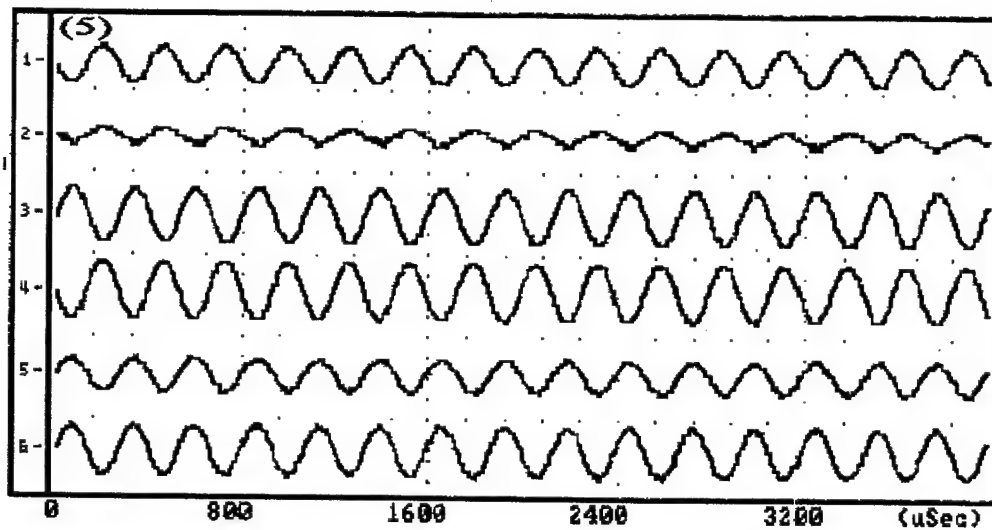


Fig.9 Neural signals of the fifth mode.

In Figure 6, however, the first channel time history has the opposite sign as compared with the other five neural signals. This indicates that there is a node between the 1st and second neurons. Accordingly, the beam oscillates at the second natural mode. Furthermore, sign changes can be observed in other neural signals obtained from various piezoelectric neurons laminated on the beam. (Note that certain engineering judgement was employed to verify the natural modes, since there could be even nodes existing between two neurons when the signals exhibit the same signs.) Also, because there are only 6 neuron segments laminated along the beam, higher modes can not be identified by these neuron segments.

Modal Voltages and Modal Identification

Recall that the piezoelectric neurons respond to local strains and generate voltage signal accordingly. As discussed previously, the mode shape functions and neural sensing signals are respectively represented by

$$U_{3n}(x) = P \left\{ \cosh(\lambda_n x) - \cos(\lambda_n x) - \frac{\cosh(\lambda_n L) + \cos(\lambda_n L)}{\sinh(\lambda_n L) + \sin(\lambda_n L)} \cdot (\sinh(\lambda_n x) - \sin(\lambda_n x)) \right\}$$

$$\phi_{3i} = \frac{e_{31}}{\epsilon_{33} \Delta} \frac{h'(h+h')}{2} P \lambda_n \left\{ [\sinh(\lambda_n x_i) - \sinh(\lambda_n x_{i-1}) + \sin(\lambda_n x_i) - \sin(\lambda_n x_{i-1})] \right. \\ \left. - \frac{\sinh(\lambda_n L) - \sin(\lambda_n L)}{\cosh(\lambda_n L) + \cos(\lambda_n L)} \cdot [\cosh(\lambda_n x_i) - \cosh(\lambda_n x_{i-1}) - \cos(\lambda_n x_i) + \cos(\lambda_n x_{i-1})] \right\}$$

where P is constant and Δ is the neuron segment length. The sensor equation indicates that the highest signal occurs at the highest strain location. Positive strains yield positive signals; negative strains yield negative signals. Plotting magnitudes of neural signals yields the modal voltage pattern or **modal voltage**. Thus, modal voltages are distinct to natural modes of the

structure. Accordingly, one can reconstruct natural mode shapes based on the modal voltages measured at various piezoelectric neurons along the beam. Experimental results are compared with analytical solutions. Reference eddy current proximity sensors are also used to calibrate the experimental results. Figures 10-12 show the theoretical and experimental comparisons of the modal voltages for the first three natural modes.

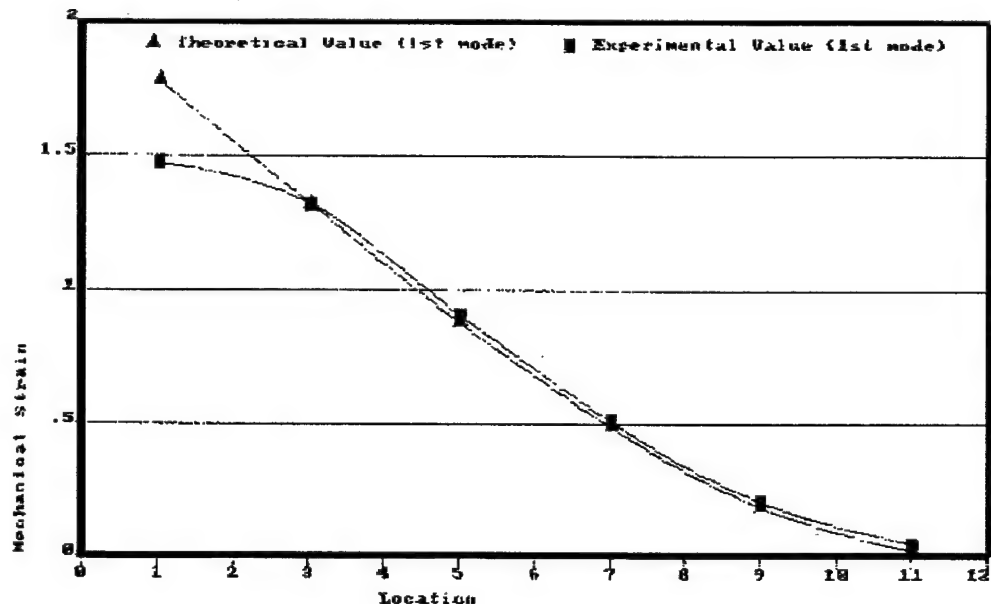


Fig.10 Neural signals (modal voltage) of the first mode.

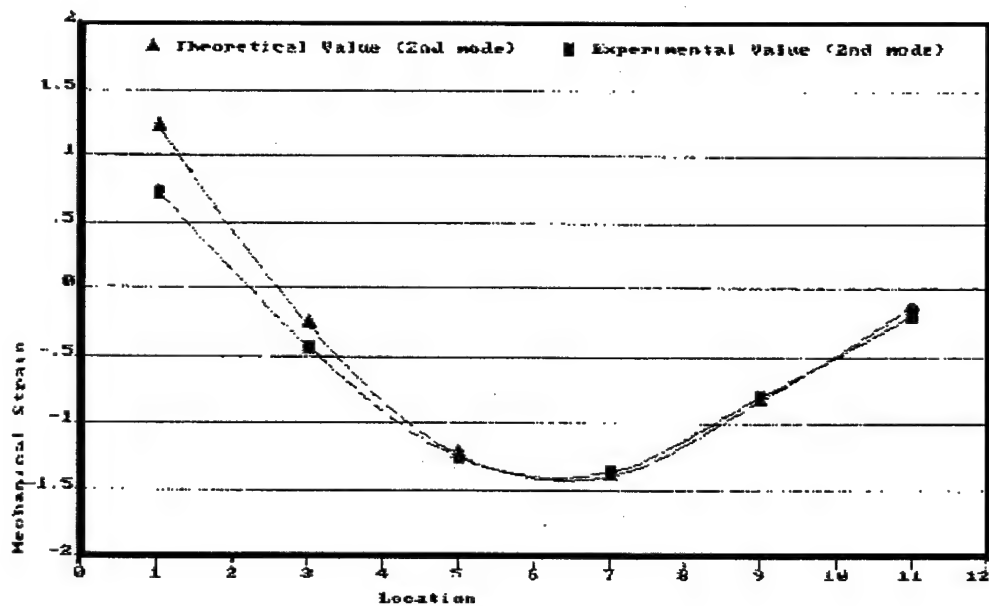


Fig.11 Neural signals (modal voltage) of the second mode.

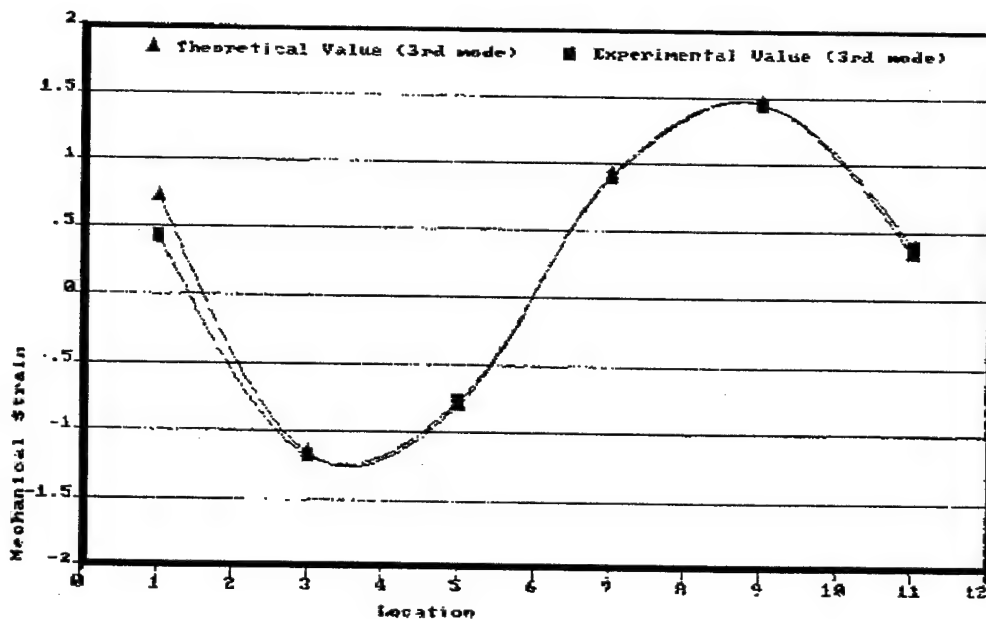


Fig.12 Neural signals (modal voltage) of the third mode.

These figures suggest that the experimental results are compared closely with the analytical solutions. However, errors are observed at the fixed end – the highest strain location. This could be caused by imperfect fabrication or bonding of the experimental model.

CONCLUSIONS

Artificial structural neurons can provide essential sensing information regarding structure's dynamic state, health condition, etc. Unlike conventional add-on transducers, these thin-film piezoelectric neurons can be surface laminated or embedded in structures and/or components, which are sensitive to local strain variations and consequently provide vital information of structures.

A generic neural sensing equation was defined for a double-curvature nonlinear shell continuum subject to large deformation – the von Karman geometric nonlinearity. This generic neural signal equation can be easily simplified and applied to a broad class of linear and nonlinear structures and components, e.g., spheres, cylinders, rings, arches, plates, beams, etc. Furthermore, for demonstration purpose, an Euler-Bernoulli beam model laminated with six segmented thin-film piezoelectric neurons was fabricated and fully tested in laboratory. Neural sensing signals from the six neurons were presented and analyzed. Modal voltages of various natural modes were identified and experimental results were compared closely with the analytical solutions.

ACKNOWLEDGEMENT

This research is supported, in part, by a grant (F49620-98-1-0467) from the Air Force Office of Scientific Research (Project manager: Brian Sanders). This support is gratefully acknowledged.

REFERENCES

Baz A. and Poh S., 1988, "Performance of an Active Control System with Piezoelectric Actuators," *Journal of Sound and Vibration*, Vol.126, No.2, pp.327-343.

Crawley, E.F. and de Luis, J., 1987, "Use of Piezoelectric Actuator as Elements of Intelligent Structures," *AIAA Journal*, 25(10), pp.1373-1385.

Hanagud S. and Obal, M.W., 1988, "Identification of Dynamic Coupling Coefficients in a Structure with Piezoelectric Sensors and Actuators," AIAA paper No.88-2418.

Plumb, J.M., Hubbard, J.E., and Bailey, T., 1987, "Nonlinear Control of a Distributed System: Simulation and Experimental Results," *ASME Journal of Dynamic Systems, Measurements, and Control*, 109(2), pp.133-139.

Tzou, H.S., 1987, "Active Vibration Control of Flexible Structures via Converse Piezoelectricity," *Development in Mechanics*, 14(b), 20th Midwest Mechanical Conference, pp.1201-1206.

Tzou, H.S., 1993, *Piezoelectric Shells (Distributed Sensing and Control of Continua)*, Kluwer Academic Publishers, Boston /Dordrecht.

Tzou, H.S., Zhong, J.P., and Natori, M.C., 1993, "Sensor Mechanics of Distributed Shell Convolving Sensors Applied to Flexible Rings," *ASME Journal of Vibration & Acoustics*, Vol.(115), No.1, pp.40-46.

Tzou, H.S., 1992, "Thin-Layer Distributed Piezoelectric Neurons and Muscles: Electromechanics and Applications," *Precision Sensors, Actuators, and Systems*, H.S. Tzou and T. Fukuda, (Editors), pp.175-218, Kluwer Academic Publishers, Dordrecht /Boston /London.

Tzou, H.S., Bao, Y., and Zhou, Y., 1997, "Nonlinear Piezothermoelasticity and Multi-field Actuations, Part-1: Nonlinear Anisotropic Piezothermoelastic Shell Laminates; Part-2: Control of Nonlinear Buckling and Dynamics," *ASME Transactions, Journal of Vibration & Acoustics*, Vol.119, pp.374-389. (Neuron99.Wam99.Conf1.D4) (NeuS&V99.B5.Doc5)

CHAPTER 3

PRECISION ACTUATION OF NONLINEAR PLATES

ABSTRACT

Adaptive shape control is essential in many high-performance engineering systems, such as nozzles, airplane wings, helicopter blades, etc. Recent development of smart structures and strucronic systems offers new alternatives to shape control with inherent and embedded actuator components. Imposed shape control often involves large deformations implying that the conventional linear theory is no longer applicable. This study is to explore a new structural control concept based on nonlinear theories. Nonlinear piezoelectric shell equations are derived based on von Karman geometric nonlinearity. Physical significance and application are discussed. As to compare the linear and nonlinear theories, a zero-curvature shell – plate is investigated. Analytical results suggest that the linear theory is indeed invalid when large deformation shape control is considered. Differences between the two theories are presented. Control effects of the plate with polymeric and ceramic piezoelectric actuators are compared.

INTRODUCTION

Adaptive shapes and surface control of structural and mechanical systems can revolutionize many engineering systems, such as flow control, precision manipulation and positioning, etc. Imposed shape change of shells and flat panels of aerospace structures offers several aerodynamic advantages, such as lift control, flutter control, improved maneuverability, vibration and noise control, etc. Active shape control often involves large deformations and thus control of large deformation becomes an important issue in adaptive structures and strucronic systems

Geometrical nonlinearity of elastic shells were studied over the years (Librescu, 1987; Palazotto and Dennis, 1992; Pietraszkiewicz, 1979; Chia, 1980). A nonlinear model for a piezoelectric plate was recently proposed by Pai, et al (1993). Yu (1993) reviewed recent advances on modeling of linear and nonlinear elastic and piezoelectric plates. Linear thermo-electromechanical behavior and precision position control of distributed piezoelectric sensors and actuators were investigated (Tzou and Ye, 1994). Tzou and Howard (1993) also studied the thermo-electromechanical couplings of a single layer mm2 piezothermoelastic shell. However, geometrical nonlinearity of anisotropic piezothermoelastic shells simultaneously exposed to mechanical, electric, and thermal fields has not been fully investigated (Tzou and Bao, 1997; Tzou and Zhou, 1995).

This paper is concerned with a study of static and dynamic control of nonlinear flexible shells and plates subjected to mechanical, electric, and temperature excitations. A generic nonlinear thermo-piezoelectric shell is evaluated and its nonlinear thermo-electromechanical equations are derived based on the Hamilton's principle. Thermo-electromechanical couplings among the elastic, electric, and temperature fields are discussed, and nonlinear components identified. Application of the theory to control of wing box panels (plates) is demonstrated. Boundary control induced by the distributed piezoelectric actuator is investigated. Active control effects on nonlinear static deflections and natural frequencies imposed by the piezoelectric actuators are investigated.

NONLINEAR THERMO-PIEZOELECTRIC SHELL

Fundamental thermo-electromechanical properties of a piezoelectric continuum are briefly reviewed. Since shape control naturally involves large deformation geometric nonlinearity, a generic nonlinear thermo-piezoelectric shell based on the von Karman nonlinear theory is investigated and its governing equations are derived in this section. Thermo-electromechanical couplings are evaluated and its structural control applications are discussed. Figure 1 illustrates a generic double curvature piezoelectric shell continuum.

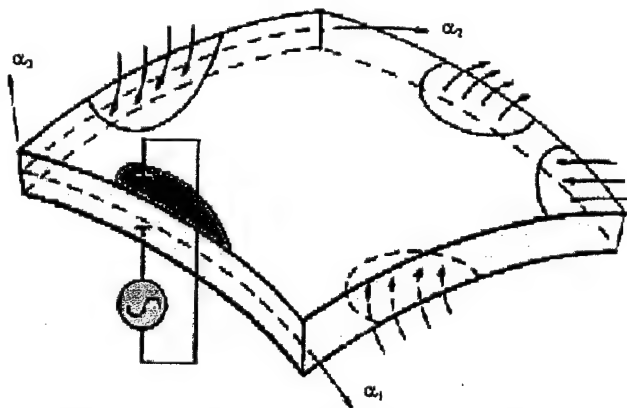


Fig.1 A double-curvature piezoelectric shell.

Thermopiezoelectric Constitutive Equations

Electric fields E_1, E_2, E_3 and electric potential ϕ in a shell curvilinear shell coordinate system, Figure 1, are defined by (Tzou and Zhong, 1993)

$$\begin{pmatrix} E_1 \\ E_2 \\ E_3 \end{pmatrix} = - \begin{bmatrix} f_{11} & 0 & 0 \\ 0 & f_{22} & 0 \\ 0 & 0 & f_{33} \end{bmatrix} \begin{pmatrix} \partial/\partial\alpha_1 \\ \partial/\partial\alpha_2 \\ \partial/\partial\alpha_3 \end{pmatrix} \phi, \quad (1)$$

where $f_{ii}(\alpha_1, \alpha_2, \alpha_3) = A_i(1 + \alpha_3/R_i)$ ($i = 1, 2$), $f_{33}(\alpha_1, \alpha_2, \alpha_3) = 1$; α_3 is a finite distance measured from the reference surface; A_1 and A_2 are Lamé parameters; R_1 and R_2 are the radii of curvature of the

α_1 and α_2 axes on the neutral surface defined by $\alpha_3 = 0$. Thermo-electromechanical constitutive relations of a generic piezoelectric shell continuum are governed by three equations: 1) the stress equation, 2) the electric displacement equation, and 3) the thermal entropy equation (Tzou and Bao, 1997).

$$\{T\} = [c]\{S\} - [e]^t\{E\} - \{\lambda\}\theta, \quad (2)$$

$$\{D\} = [e]\{S\} + [\varepsilon]\{E\} + \{p\}\theta, \quad (3)$$

$$\mathfrak{I} = \{\lambda\}^t\{S\} + \{p\}^t\{E\} + \alpha_v\theta, \quad (4)$$

where $\{T\}$, $\{S\}$, $\{E\}$ and $\{D\}$ are respectively the stress, strain, electric field and electric displacement vectors; $[c]$, $[e]$, and $[\varepsilon]$ denote the elastic stiffness coefficient, piezoelectric coefficient, and dielectric permittivity matrices, respectively; \mathfrak{I} is the thermal entropy density; θ is the temperature rise ($\theta = \Theta - \Theta_0$ where Θ is the absolute temperature and Θ_0 the temperature of natural state in which stresses and strains are zero); $\{\lambda\}$ is the stress-temperature coefficient vector; $\{p\}$ is the pyroelectric coefficient vector; and α_v is a material constant ($\alpha_v = \rho c_v / \Theta_0$ where ρ is the material density and c_v is the specific heat at a constant volume). $[\cdot]^t$ and $\{\cdot\}^t$ are matrix and vector transpose, respectively. Nonlinear piezoelectric shells are evaluated and generic thermo-electromechanical equations and boundary conditions defined next.

Large Deformation Geometric Nonlinearity

As discussed previously, imposed shape control often involves large deformations – the geometric nonlinearity. A generic nonlinear deflection U_i in the i -th direction of the shell can be expressed as a summation of a (in-plane) membrane displacement $u_i(\alpha_1, \alpha_2, t)$ and a higher order nonlinear shear deformation effect represented by the summation of angular rotations $\beta_{ij}(\alpha_1, \alpha_2, t)$:

$$U_i(\alpha_1, \alpha_2, \alpha_3, t) = u_i(\alpha_1, \alpha_2, t) + \sum_{j=1}^m \alpha_3^j \beta_{ij}(\alpha_1, \alpha_2, t), \quad i=1,2,3, \quad (5)$$

where β_{11} and β_{21} represent the rotational angles in the positive sense of the α_1 and α_2 axes, respectively; and $\beta_{3j} = 0$. This expression includes higher order nonlinear shear deformation effects. However, according to the Love-Kirchhoff thin shell assumptions and a linear displacement approximation (first order shear deformation theory), only the first term is kept in the equation, i.e., $m = 1$ (Tzou, 1993). The displacements and rotational angles are independent variables in thick shells. However, the rotational angles are dependent variables in thin shells, and they can be derived from the thin shell assumptions in which the transverse normal strain S_3 is negligible and shear strains S_4 and S_5 are zeros (Soedel, 1993). Based on the thin shell assumptions, the rotational angles $\beta_1 = \beta_{11}$ and $\beta_2 = \beta_{21}$ are derived from the transverse shear strain equations, i.e., $S_4 = 0$ and $S_5 = 0$.

$$\beta_i = \frac{u_i}{R_i} - \frac{1}{A_i} \frac{\partial u_i}{\partial \alpha_i}, \quad i = 1,2. \quad (6)$$

In general, $\alpha_3/R_1 \ll 1$ $\alpha_3/R_2 \ll 1$, thus, the ratios of the finite distance to the radius of curvature are

negligible, i.e., $f_{11} \approx A_1$ and $f_{22} \approx A_2$. Although, it is assumed that the piezoelectric shell experiences large deformations in three axial directions, however, in reality, the in-plane deflections are still much smaller than the transverse deflections. Thus, the nonlinear effects due to the in-plane large deflections are usually neglected, i.e., the von Karman-type assumptions (Palazotto and Dennis, 1992; Chia, 1980). The nonlinear strain-displacement relations of a thin shell with a large transverse deflection u_3 include a linear effect, denoted by a superscript ℓ , and a nonlinear effect, denoted by a superscript n , induced by the large deformation:

$$\begin{bmatrix} S_1 \\ S_2 \\ S_6 \end{bmatrix} = \left[\begin{bmatrix} S_1^\ell \\ S_2^\ell \\ S_6^\ell \end{bmatrix} + \begin{bmatrix} S_1^n \\ S_2^n \\ S_6^n \end{bmatrix} \right] + \alpha_3 \begin{bmatrix} k_1 \\ k_2 \\ k_6 \end{bmatrix}, \quad (7)$$

where the subscripts 1 and 2 respectively denote two normal strains and 6 is the in-plane shear strain. Detailed membrane and bending strains are functions of displacements - u_i 's.

1) Membrane strains:

$$S_1^\ell = \frac{1}{A_1} \frac{\partial u_1}{\partial \alpha_1} + \frac{u_2}{A_1 A_2} \frac{\partial A_1}{\partial \alpha_2} + \frac{u_3}{R_1} + \frac{1}{2} \left(\frac{\partial u_3 / \partial \alpha_1}{A_1} \right)^2, \quad (8)$$

$$S_2^\ell = \frac{1}{A_2} \frac{\partial u_2}{\partial \alpha_2} + \frac{u_1}{A_1 A_2} \frac{\partial A_2}{\partial \alpha_1} + \frac{u_3}{R_2} + \frac{1}{2} \left(\frac{\partial u_3 / \partial \alpha_2}{A_2} \right)^2, \quad (9)$$

$$S_6^\ell = \frac{1}{A_2} \frac{\partial u_1}{\partial \alpha_2} + \frac{1}{A_1} \frac{\partial u_2}{\partial \alpha_1} - \frac{u_1}{A_1 A_2} \frac{\partial A_1}{\partial \alpha_2} - \frac{u_2}{A_1 A_2} \frac{\partial A_2}{\partial \alpha_1} + \left(\frac{1}{A_1 A_2} \frac{\partial u_3}{\partial \alpha_1} \frac{\partial u_3}{\partial \alpha_2} \right); \quad (10)$$

2) Bending strains:

$$k_1 = \frac{1}{A_1} \frac{\partial}{\partial \alpha_1} \left(\frac{u_1}{R_1} - \frac{1}{A_1} \frac{\partial u_3}{\partial \alpha_1} \right) + \frac{1}{A_1 A_2} \left(\frac{u_2}{R_2} - \frac{1}{A_2} \frac{\partial u_3}{\partial \alpha_2} \right) \frac{\partial A_1}{\partial \alpha_2}, \quad (11)$$

$$k_2 = \frac{1}{A_2} \frac{\partial}{\partial \alpha_2} \left(\frac{u_2}{R_2} - \frac{1}{A_2} \frac{\partial u_3}{\partial \alpha_2} \right) + \frac{1}{A_1 A_2} \left(\frac{u_1}{R_1} - \frac{1}{A_1} \frac{\partial u_3}{\partial \alpha_1} \right) \frac{\partial A_2}{\partial \alpha_1}, \quad (12)$$

$$\begin{aligned} k_6 = & \frac{1}{A_2} \frac{\partial}{\partial \alpha_2} \left(\frac{u_1}{R_1} - \frac{1}{A_1} \frac{\partial u_3}{\partial \alpha_1} \right) + \frac{1}{A_1} \frac{\partial}{\partial \alpha_1} \left(\frac{u_2}{R_2} - \frac{1}{A_2} \frac{\partial u_3}{\partial \alpha_2} \right) \\ & - \frac{1}{A_1 A_2} \left(\frac{u_1}{R_1} - \frac{1}{A_1} \frac{\partial u_3}{\partial \alpha_1} \right) \frac{\partial A_1}{\partial \alpha_2} - \frac{1}{A_1 A_2} \left(\frac{u_2}{R_2} - \frac{1}{A_2} \frac{\partial u_3}{\partial \alpha_2} \right) \frac{\partial A_2}{\partial \alpha_1} \end{aligned} \quad (13)$$

Note that the quadratic terms (nonlinear terms) inside the brackets are contributed by the large deflection. Membrane force resultants N_{ij} and bending moments M_{ij} of the thermo-piezoelectric shell laminate can be derived based on the induced strains (Tzou and Bao, 1997):

$$\begin{bmatrix} N_{11} \\ N_{22} \\ N_{12} \\ M_{11} \\ M_{22} \\ M_{12} \end{bmatrix} = \begin{bmatrix} A_{11} & A_{12} & A_{16} & B_{11} & B_{12} & B_{16} \\ A_{12} & A_{22} & A_{26} & B_{12} & B_{22} & B_{26} \\ A_{16} & A_{26} & A_{66} & B_{16} & B_{26} & B_{66} \\ B_{11} & B_{12} & B_{16} & D_{11} & D_{12} & D_{16} \\ B_{12} & B_{22} & B_{26} & D_{12} & D_{22} & D_{26} \\ B_{16} & B_{26} & B_{66} & D_{16} & D_{26} & D_{66} \end{bmatrix} \begin{bmatrix} s_1^0 \\ s_2^0 \\ s_6^0 \\ k_1 \\ k_2 \\ k_6 \end{bmatrix} - \begin{bmatrix} N_{11}^e \\ N_{22}^e \\ N_{12}^e \\ M_{11}^e \\ M_{22}^e \\ M_{12}^e \end{bmatrix} - \begin{bmatrix} N_{11}^\theta \\ N_{22}^\theta \\ N_{12}^\theta \\ M_{11}^\theta \\ M_{22}^\theta \\ M_{12}^\theta \end{bmatrix}. \quad (14)$$

It is observed that there are three components, i.e., mechanical, electric, and temperature, in the force/moment expressions. Superscripts e and θ respectively denote the electric and temperature components. The membrane strains and bending strains are coupled by the coupling stiffness coefficients B_{ij} in elastic force/moment resultants. N_{ije} and N_{ij}^θ are the electric and temperature induced forces; M_{ije} and M_{ij}^θ are the electric and temperature induced moments, respectively. In actuator applications, these electric forces and moments are used to control shell's static and dynamic characteristics. A_{ij} , B_{ij} and D_{ij} are the extensional, coupling, and bending stiffness constants. These strain/displacement relations, membrane force resultants, bending moment resultants, etc. are used in Hamilton's equation to derive thermo-electromechanical equations and boundary conditions of the nonlinear thermo-piezoelectric shells. Although it is assumed that the transverse shear deflections can be neglected, the integrated effect of the transverse shear stress resultants Q_{13} and Q_{23} are not neglected. Note that the effects of rotatory inertias can be neglected in thin shells without large rotational effects.

Hamilton's Principle and Nonlinear System Equations

Hamilton's principle is used in deriving the shell thermo-electromechanical equations and boundary conditions of the piezothermoelastic shell continuum. Hamilton's principle assumes that the energy variations over an arbitrary period of time are zero. Considering all energies, one can write Hamilton's equation:

$$\delta \int_{\text{V}} \left\{ \left(\int \frac{1}{2} \rho \dot{U}_j \dot{U}_j dV - \left[\int (H(S_i, E_i, \Theta) + \mathfrak{I} \Theta) dV - \int (t_j U_j - Q_j \phi) dS \right] dt \right) \right\} = 0. \quad (15)$$

where ρ is the mass density; H is the electric enthalpy; t_j is the surface traction in the α_j direction; Q_j is the surface electric charge; ϕ is the electrical potential; V and S are the volume and surface of the piezothermoelastic shell continuum, respectively; and U_j and \dot{U}_j are the displacement and velocity vectors. It is assumed that only the transverse electric field E_3 is considered in the analysis. Substituting all energy expressions into Hamilton's equation and carrying out all variations, one can derive the nonlinear piezothermoelastic shell equations and boundary conditions of the piezothermoelastic shell continuum.

$$\begin{aligned} & - \frac{\partial(N_{11}A_2)}{\partial\alpha_1} + N_{22} \frac{\partial A_2}{\partial\alpha_1} - \frac{\partial(N_{21}A_1)}{\partial\alpha_2} - N_{12} \frac{\partial A_1}{\partial\alpha_2} - \frac{1}{R_1} \left[\frac{\partial(M_{11}A_2)}{\partial\alpha_1} \right. \\ & \left. - M_{22} \frac{\partial A_2}{\partial\alpha_1} + \frac{\partial(M_{21}A_1)}{\partial\alpha_2} + M_{12} \frac{\partial A_1}{\partial\alpha_2} \right] + A_1 A_2 \rho \dot{h} \ddot{U}_1 = A_1 A_2 F_1 \end{aligned} \quad (16)$$

$$\begin{aligned}
& -\frac{\partial(N_{22}A_1)}{\partial\alpha_2} + N_{11}\frac{\partial A_1}{\partial\alpha_2} - \frac{\partial(N_{12}A_2)}{\partial\alpha_1} - N_{21}\frac{\partial A_2}{\partial\alpha_1} - \frac{1}{R_2}\left[\frac{\partial(M_{22}A_1)}{\partial\alpha_2}\right] \\
& - M_{11}\frac{\partial A_1}{\partial\alpha_2} + \frac{\partial(M_{12}A_2)}{\partial\alpha_1} + M_{21}\frac{\partial A_2}{\partial\alpha_1} + A_1A_2\rho\ddot{u}_2 = A_1A_2F_2
\end{aligned} \quad , \quad (17)$$

$$\begin{aligned}
& -\frac{\partial}{\partial\alpha_1}\left[\frac{1}{A_1}\left(\frac{\partial(M_{11}A_2)}{\partial\alpha_1}\right) - M_{22}\frac{\partial A_2}{\partial\alpha_1} + \frac{\partial(M_{21}A_1)}{\partial\alpha_2} + M_{12}\frac{\partial A_1}{\partial\alpha_2}\right] \\
& -\frac{\partial}{\partial\alpha_2}\left[\frac{1}{A_2}\left(\frac{\partial(M_{22}A_1)}{\partial\alpha_2}\right) - M_{11}\frac{\partial A_1}{\partial\alpha_2} + \frac{\partial(M_{12}A_2)}{\partial\alpha_1} + M_{21}\frac{\partial A_2}{\partial\alpha_1}\right] + A_1A_2\left(\frac{N_{11}}{R_1} + \frac{N_{22}}{R_2}\right) + A_1A_2\rho\ddot{u}_3 \\
& -\left\{\left[\frac{\partial(N_{11}A_2/A_1)}{\partial\alpha_1} + \frac{\partial N_{12}}{\partial\alpha_2}\right]\frac{\partial u_3}{\partial\alpha_1} + \left[\frac{\partial(N_{22}A_1/A_2)}{\partial\alpha_2} + \frac{\partial N_{12}}{\partial\alpha_1}\right]\frac{\partial u_3}{\partial\alpha_2}\right. \\
& \left. + 2N_{12}\frac{\partial^2 u_3}{\partial\alpha_1\partial\alpha_2} + N_{11}\frac{A_2}{A_1}\frac{\partial^2 u_3}{\partial\alpha_1^2} + N_{22}\frac{A_1}{A_2}\frac{\partial^2 u_3}{\partial\alpha_2^2}\right\} = A_1A_2F_3
\end{aligned} \quad (18)$$

Note that all terms inside the braces are contributed by the nonlinear effects. The **nonlinear influence** on the transverse equation u_3 is significant. Also, the thermo-electromechanical equations are similar to standard shell equations. However, the force and moment expressions defined by mechanical, thermal, and electric effects are much more complicated than the conventional elastic expressions. Substituting the expressions of N_{11} , N_{22} , N_{12} , M_{11} , M_{22} , M_{12} into the above equations leads to the thermo-electromechanical equations defined in the reference displacements u_1 , u_2 , u_3 . The transverse shear deformation and rotatory inertia effects are not considered. The electric terms, forces and moments, can be used in controlling the mechanical and/or temperature induced excitations (Tzou and Ye, 1994).

Using Hamilton's equation, one can also derive all admissible mechanical and electric boundary conditions. Admissible mechanical boundary conditions on the boundary surfaces defined by a distance α_2 and α_1 are respectively summarized in Table 1 and Table 2.

Table 1 Boundary conditions (α_1 axis).

	Force/Moment	Displacement
1	$N_{11} = N_{11}^*$	$u_1 = u_1^*$
2	$M_{11} = M_{11}^*$	$\beta_1 = \beta_1^*$
3	$N_{12} + \frac{M_{12}}{R_2} = V_{12}^*$	$u_2 = u_2^*$
4	$Q_{13} + \frac{\partial}{\partial\alpha_2}\left(\frac{M_{12}}{A_2}\right)$ $+ \left(N_{11}\left(\frac{1}{A_1}\frac{\partial u_3}{\partial\alpha_1}\right) + N_{12}\left(\frac{1}{A_2}\frac{\partial u_3}{\partial\alpha_2}\right)\right) = V_{13}^*$	$u_3 = u_3^*$

Table 2 Boundary conditions (α_2 axis).

	Force/Moment	Displacement
1	$N_{22} = N_{22}^*$	$u_2 = u_2^*$
2	$M_{22} = M_{22}^*$	$\beta_2 = \beta_2^*$
3	$N_{21} + M_{21}/R_1 = V_{21}^*$	$u_1 = u_1^*$
4	$Q_{23} + \frac{\partial}{\partial \alpha_1} \left(M_{21}/A_1 \right)$ $+ \left(N_{22} \left(\frac{1}{A_2} \cdot \frac{\partial u_3}{\partial \alpha_2} \right) + N_{21} \left(\frac{1}{A_1} \cdot \frac{\partial u_3}{\partial \alpha_1} \right) \right) = V_{23}^*$	$u_3 = u_3^*$

The superscript * denotes the boundary forces, moments, displacements, and slopes. Usually, only either the force/moment boundary conditions or the displacement/slope boundary conditions are selected for a given physical boundary condition (Tzou, 1993; Soedel, 1993). In addition, additional transverse shear force terms Q_{i3} are nonlinear components induced by large deformations. These force terms do not appear in the linear case. The shear stress resultants are defined as

$$V_{12} = N_{12} + \left(M_{12}/R_1 \right), \quad (19)$$

$$V_{21} = N_{21} + \left(M_{21}/R_1 \right), \quad (20)$$

$$V_{13} = Q_{13} + \frac{\partial}{\partial \alpha_2} \left(M_{12}/A_2 \right), \quad (21)$$

$$V_{23} = Q_{23} + \frac{\partial}{\partial \alpha_1} \left(M_{21}/A_1 \right), \quad (22)$$

where V_{13} and V_{23} are the Kirchhoff effective shear stress resultants of the first kind; V_{12} and V_{21} are the Kirchhoff effective shear stress resultants of the second kind (Soedel, 1993). Note that all elastic, electric, and thermal related terms are included in the force and moment expressions. These electric terms can be used, in conjunction with control algorithms, as control forces/moments counteracting mechanical and temperature induced vibrations in distributed structural control of shells. Applications and simplifications of the nonlinear piezothermoelastic shell equations can be demonstrated in two ways: 1) material simplifications and 2) geometry simplifications. In the next section, the generic thermo-electromechanical equations are simplified to a zero-curvature shell – plate. Detailed comparisons of the linear and nonlinear theories are compared and numerical simulations are presented.

CONTROL OF NONLINEAR PLATES

Plates are defined as zero-curvature shells, i.e., radii R_1 and R_2 are infinity and Lamé parameters A_1 and A_2 are 1's. Distributed piezoelectric layers laminated (coupled or embedded) on elastic continua can be used as distributed sensors and/or actuators, Figure 2.

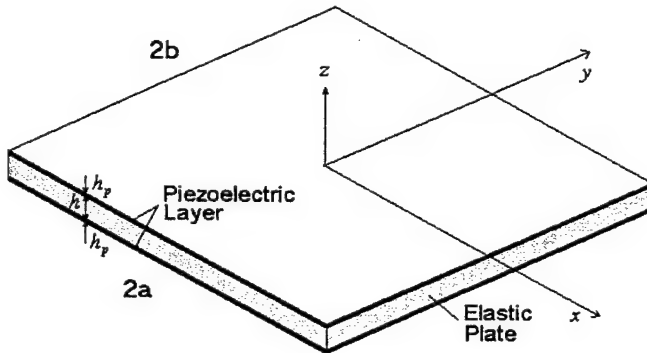


Fig.2 A nonlinear zero-curvature shell – plate with laminated distributed piezoelectric layers.

Substituting the four parameters into the generic shell thermo-electromechanical equations yields the nonlinear plate equations

$$-\frac{\partial(N_{xx})}{\partial x} + \frac{\partial(N_{yx})}{\partial y} + F_x = \rho h \ddot{u}_x, \quad (23)$$

$$-\frac{\partial(N_{yy})}{\partial y} + \frac{\partial(N_{xy})}{\partial x} + F_y = \rho h \ddot{u}_y, \quad (24)$$

$$[\frac{\partial^2(M_{xx})}{\partial x^2} + 2\frac{\partial^2(M_{xy})}{\partial x \partial y} + \frac{\partial^2(M_{yy})}{\partial y^2}] + [N_{xx} \frac{\partial^2 u_z}{\partial x^2} + 2N_{xy} \frac{\partial^2 u_z}{\partial x \partial y} + N_{yy} \frac{\partial^2 u_z}{\partial y^2}] + F_z = \rho h \ddot{u}_z, \quad (25)$$

and forces and moments are defined by

$$N_{ij} / M_{ij} = N_{ij}^m / M_{ij}^m + N_{ij}^e / M_{ij}^e + N_{ij}^\theta / M_{ij}^\theta. \quad (26)$$

Injecting high voltages into the distributed piezoelectric actuators induces two major control actions. One is the in-plane membrane control force(s) and the other is the out-of-plane bending control moment(s). In general, the control moments are essential in planar structures, e.g., plates and beams; the membrane control forces are effective in shells. In this study, the piezoelectric actuators are used to control the nonlinear large deformation of flexible plates, and their control effectiveness is evaluated. Numerical solutions are derived to evaluate the control effectiveness of nonlinear plates in the case studies presented next.

CASE STUDY: PRECISION PLATE CONTROL

A simply supported nonlinear square plate (dimensions: $2ax2bxh$) is considered in the case study. The piezoelectric laminated plate is subjected to both thermal and electric bending loads: $\phi_3^3 = -\phi_3^1 = \phi$ and $\theta(z) = \Delta\theta(z/h)$ where $\Delta\theta = \theta_t - \theta_b$ and θ_t, θ_b are the temperatures on the top and the bottom of the plate, respectively. A nondimensional loading parameter δ is defined by the piezoelectric constant, the moment arm, Young's modulus, the thermal stress coefficient, the plate thickness and width, and, of course, the temperature and the control voltage. The central deflections due to the nondimensional loading δ calculated based on the linear and nonlinear theories are plotted in Figure 3. Center deflections of the simply supported nonlinear composite plate with control voltages and temperature loadings are analyzed and results are plotted in Figures 4-5. Note that the elastic plate is made of steels and the piezoelectric material layers are PZT materials. The plate dimensions are: steel thickness $h = 1.0 \times 10^{-3}$ m, piezoelectric layer thickness $h_p = 6.0 \times 10^{-5}$ m, plate length/width $2a = 0.5$ m.

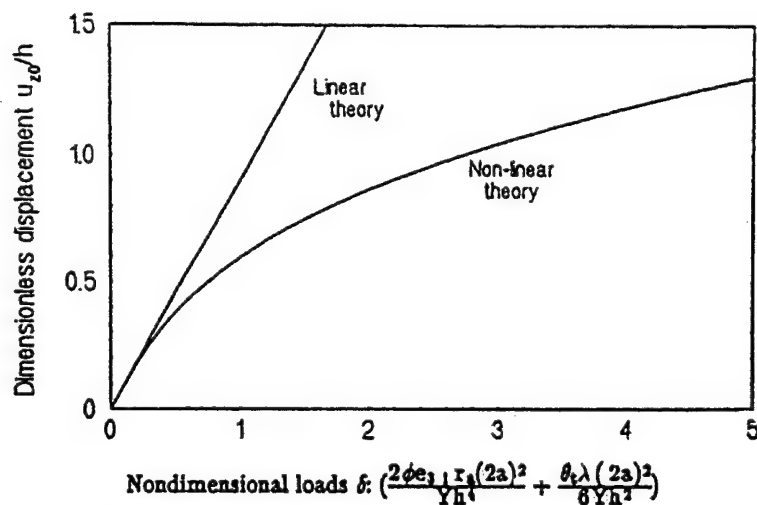


Fig.3 Center deflection of a simply supported piezoelectric laminated plate.

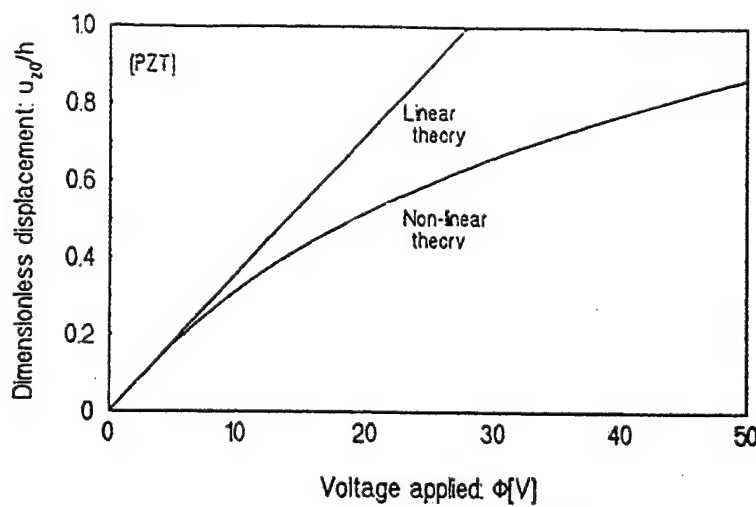


Fig.4 Center deflection of plate versus voltage (PZT).

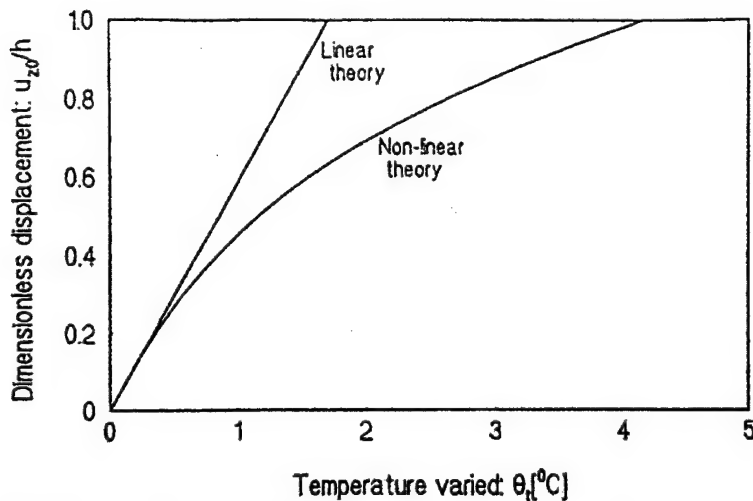


Fig.5 Center deflection of plate versus temperature.

Figure 2 shows the linear and nonlinear relationships between the plate deflection and the control voltage. This voltage induced action can be used to counteract the deflections induced by the mechanical or temperature loadings, e.g., Figure 3. (Note that the PZT induced control action is superior to the polyvinylidene fluoride (PVDF) induced control action. (This can be easily inferred from the inherent piezoelectric constants: $e_{31} = 10.43 \text{ C/m}^2$ for PZT while $e_{31} = 9.6 \times 10^{-3} \text{ C/m}^2$ for PVDF.) For comparison of control authorities between the PZT actuator and the PVDF actuator, analysis between deflection and control voltage of piezoelectric polymeric PVDF actuator is also conducted and plotted in Figure 6. Comparing Figures 4 and 6, one can clearly observe the superior control authority of the PZT actuator.

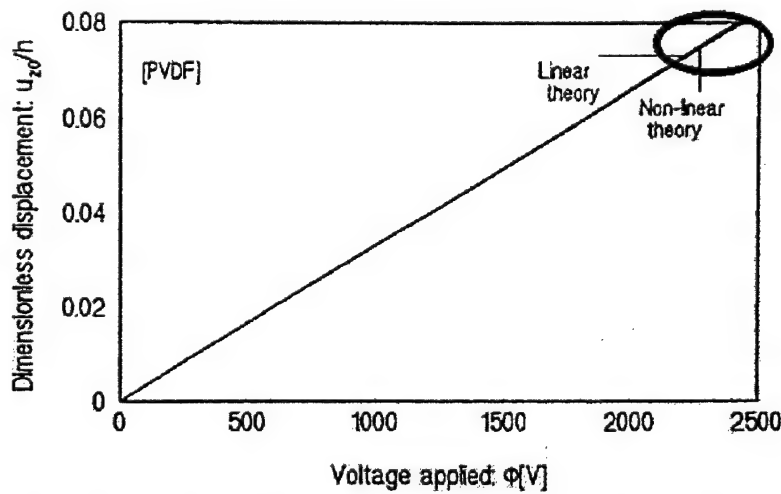


Fig.6 Center deflection versus control voltage (PVDF).

CONCLUSION

In the recent development of smart structures and structronic systems, piezoelectric materials are widely used as sensors and actuators in sensing, actuation, and control applications. This research is to investigate the control effectiveness of piezoelectric nonlinear flexible shells and plates (rectangular and square plates) subjected to mechanical and temperature excitations. It is assumed that the flexible shells and plates encounter the von Karman type geometrical nonlinearity. Nonlinear thermo-piezoelectric shell equations and generic boundary conditions were derived based on the von Karman geometric nonlinearity. Physical significance and application were discussed. As to compare the linear and nonlinear theories, a zero-curvature shell – plate was investigated.

Active control of nonlinear flexible deflections and thermal deformations using distributed piezoelectric actuators were studied, and their nonlinear effects were evaluated. Nonlinear static deflections with the influence of temperature and control voltage were studied. Voltage-temperature and displacement relations were investigated. The voltage imposed actuation can be used to compensate the nonlinear deformation and the temperature induced deformation. Simulation results also suggested that the voltage induced control displacement/force can be used to compensate the nonlinear static deflection, temperature effects, and natural frequencies of the piezoelectric laminated plate.

This study clearly revealed that the geometric nonlinearity theory has to be considered in the active structural and shape control of smart structures and structronic systems. Neglecting the nonlinear effect in the design and simulation studies can lead to catastrophic errors in reliability, safety, performance, etc.

ACKNOWLEDGEMENT

This research is supported, in part, by a grant (F49620-98-1-0467) from the Air Force Office of Scientific Research (Project manager: Brian Sanders and Dan Segalman).

REFERENCES

Chia, C.Y., 1980, *Nonlinear Analysis of Plates*, McGraw-Hill International Book Co., New York
Lalande, F., Chaudhry, Z., and Rogers, C.A., 1993, "A Simplified Geometrically Nonlinear Approach to the Analysis of the Moonie Actuator," *Adaptive Structures and Material Systems*, AD-Vol.35, pp.149-155, 1993 ASME WAM, New Orleans, LA, Nov.28-Dec.3, 1993.

Librescu, L., 1987, "Refined Geometrically Nonlinear Theories of Anisotropic Laminated Shells," *Quarterly of Applied Mathematics*, Vol.XLV, No.1, pp.1-22.

Pai, P.F., Nafeh, A.H., Oh, K., and Mook, D.T., 1993, "A Refined Nonlinear Model of Piezoelectric Plate," *J. Solids and Structures*, Vol.30, pp.1603-1630.

Palazotto, A.N. and Dennis, S.T., 1992, *Nonlinear Analysis of Shell Structures*, AIAA Pub., Washington, D.C.

Pietraszkiewicz, W., 1979, *Finite Rotations and Lagrangean Description in the Non-linear Theory of Shells*, Polish Academy of Science, Polish Scientific Publishers.

Soedel, W., 1981, *Vibrations of Shells and Plates*, Dekker, New York.

Tzou, H.S., 1993, *Piezoelectric Shells, Distributed Sensing and Control of Continua*, Kluwer Academic Pub. Dordrecht/Boston

Tzou, H.S. and Bao, Y., 1997, "Nonlinear Piezothermoelasticity and Multi-field Actuations, Part-1: Nonlinear Anisotropic Piezothermoelastic Shell Laminates," *Journal of Vibration & Acoustics*, Vol.119, pp.374-381.

Tzou, H.S. and Zhou, Y-H., 1995, "Dynamics and Control of Nonlinear Circular Plates with Piezoelectric Actuators," *J of Sound & Vibration*, Vol.188, No.2, pp.189-207.

Tzou, H.S. and Howard, R.V., 1994, "A Piezothermoelastic Thin Shell Theory Applied to Active Structures," *ASME Transactions, Journal of Vibration & Acoustics*, Vol.116, No.3, pp.295-302.

Tzou, H.S. and Ye, R., 1994, "Piezothermoelasticity and Precision Control of Piezoelectric Systems: Theory and Finite Element Analysis," *ASME Transactions, Journal of Vibration & Acoustics*, Vol.116, No.4, pp.489-495.

Tzou, H.S. and Zhong, J.P., 1993, "Electromechanics and Vibrations of Piezoelectric Shell Distributed Systems: Theory and Applications," *ASME Journal of Dynamic Systems, Measurements, and Control*, Vol.115, No.3, pp.506-517.

Yu, Y.Y., 1993, "Some Recent Advances in Linear and Nonlinear Dynamical Modeling of Elastic and Piezoelectric Plates," *Adaptive Structures and Material Systems*, AD-Vol.35, pp.185-195, 1993 ASME WAM, New Orleans, LA, Nov.28-Dec.3, 1993.(NonStr99x.Vib99/B5.Conf1.Document4)

CHAPTER 4

A NEW X-ACTUATOR DESIGN FOR DUAL BENDING/TWISTING CONTROL OF WINGS

ABSTRACT

Recent development of smart structures and strucronic systems has demonstrated the technology in many engineering applications. Active structural control of aircraft wings or helicopter blades (e.g., shapes, flaps, leading and/or trailing edges) can significantly enhance the aerodynamic efficiency and flight maneuverability of high-performance airplanes and helicopters. This paper is to evaluate the dual bending and torsion vibration control effects of an X-actuator configuration reconfigured from a parallel configuration. Finite element (FE) formation of a new FE using the layerwise constant shear angle theory is reviewed and the derived governing equations are discussed. Bending and torsion control effects of plates are studied using the FE method and also demonstrated via laboratory experiments. FE and experimental results both suggest the X-actuator is effective to both bending and torsion control of plates.

INTRODUCTION

Smart structures and strucronics technology has been increasingly explored and gradually applied to engineering systems in recent years [1]. This technology emphasizes a true synergistic integration of structures and mechatronic/strucronic systems with smart materials serving as in-situ sensors, actuators, and/or elastic components in the design process. This synergistic integration can significantly simplify the system complexity and also improve the performance of next-generation precision machines, structures, mechatronic and strucronic systems [2, 3].

Counteracting and controlling transverse bending vibration of wing or blade structures can reduce structural fatigue and thus enhance the reliability and service-life. Twisting airplane wings can effectively enhance its turning capability and flight maneuverability. (Flying birds inherently adopt this capability in natural environment.) Conventional actuator configuration applies parallel layouts of distributed actuators which are effective to control of bending oscillations and ineffective to control of twisting or torsion oscillations. Thus, a new design configuration with diagonally arranged piezoelectric actuator patches, the X-actuator configuration, is proposed, Figure 1. Vibration control effectiveness of the X-actuator

configuration is studied using a newly developed finite element code and also demonstrated in laboratory experiments in this study.

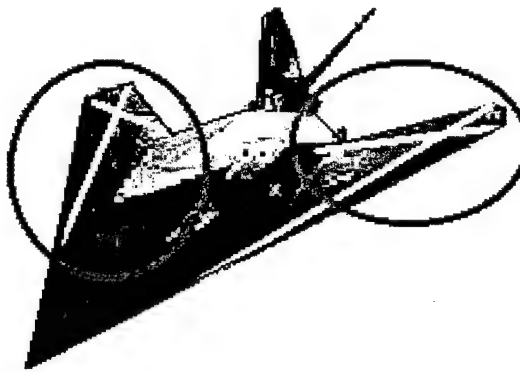


Figure 1. Wings with new X-actuators.

Modern finite element (FE) technique provides the utilities and versatility in modeling, simulation, and analysis of various engineering designs. Thus, the finite element method is used in analyzing and evaluating the two different actuator configurations. Isoparametric piezoelectric hexahedron and tetrahedron FE's were developed for piezoceramic transducer designs [4, 5]. Obal [6] used a piezoelectric beam FE in distributed vibration control of PZT-steel laminated beams. Tzou and Tseng [7] developed a non-conforming thin piezoelectric hexahedron FE with three internal degree-of-freedom and applied it to distributed sensing and vibration control of layered plates. Ha, et al. [8] derived an eight-node composite brick element. Hwang and Park [9] developed a piezoelectric plate element and compared their results with published data. Rao and Sunar [10] proposed a thermopiezoelectric element. Tzou and Ye also derived a 3-D thin piezothermoelastic element [11] and a triangle shell element [12], and examined the piezothermoelasticity and control effects of piezoelectric systems [13]. This paper is concerned with an application of a newly developed laminated quadratic C° piezoelectric triangular shell FE. FE formulation of a laminated piezoelectric shell FE based on the layerwise constant shear angle theory is briefly discussed. Finite element analysis of the new X-actuator configuration is presented. Furthermore, an experimental model is fabricated and its bending/torsion control effectiveness is evaluated in this study.

FINITE ELEMENT FORMULATION

Fundamental piezoelectric constitutive equations are reviewed and introduction of finite element formulation is presented in this section. The constitutive strain (S_{ij}) and electric field (E_i) equations of a piezoelectric continuum can be defined in generic tensor expressions [13]:

$$T_{ij} = c_{ijkl} S_{kl} - e_{mij} E_m, \quad D_n = e_{nkl} S_{kl} + \epsilon_{nm} E_m, \quad (1,2)$$

$$S_{ij} = (u_{i,j} + u_{j,i})/2, \quad E_i = -\phi_{,i}, \quad (3,4)$$

where T_{ij} are the stresses, c_{ijkl} are the elastic moduli; e_{nlk} are the piezoelectric coefficients; D_n is the electric displacement; ϵ_{nm} are the dielectric constants or permittivities, u_i are the displacements; and ϕ is electric potential [11-14]. The first equation denotes the induced stress as a function of electric field in control applications; the second equation indicates the electric charge as a function of induced strain in sensor applications.

Finite element formulation is based on the electromechanical coupling of piezoelectricity, emphasizing distributed sensing and control of structures. The layerwise constant shear angle theory is used in the shell finite element formulation. A quadratic C° piezoelastic triangular shell finite element with twelve nodes, four degrees of freedom ($u_\alpha, u_\beta, w, \phi$) per node, is derived, Figure 2. The element is quadratic in the two in-plane axes and linear in the transverse direction. The i -th layer triangular element is bounded by the i -th and $(i+1)$ -th interfaces; the interface triangle is characterized by six nodes, one at each triangular corner, and one at the center of each side in the interface plane parallel to the α_1 - α_2 plane.

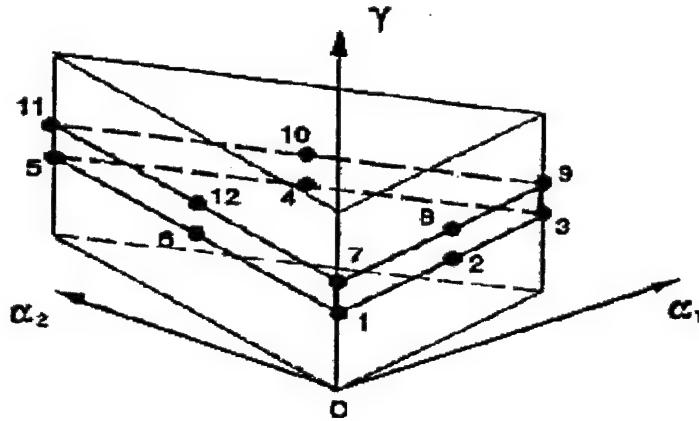


Figure 2. A triangle piezoelectric shell finite element.

Thus, the displacement and electric fields $u_{(i)}(\zeta)$, $u_{(j)}(\zeta)$, $w_{(i)}(\zeta)$, and $\phi_{(i)}(\zeta)$ for the arbitrary i -th layer can be expressed as

$$u_{\alpha_1}^{(i)}(\zeta) = \bar{u}_{\alpha_1}^{(i)}(1 - \zeta/h_i) + \bar{u}_{\alpha_1}^{(i+1)}(\zeta/h_i), \quad (5)$$

$$u_{\alpha_2}^{(i)}(\zeta) = \bar{u}_{\alpha_2}^{(i)}(1 - \zeta/h_i) + \bar{u}_{\alpha_2}^{(i+1)}(\zeta/h_i), \quad (6)$$

$$w^{(i)}(\zeta) = \bar{w}^{(i)}(1 - \zeta/h_i) + \bar{w}^{(i+1)}(\zeta/h_i), \quad (7)$$

$$\phi^{(i)}(\zeta) = \bar{\phi}^{(i)}(1 - \zeta/h_i) + \bar{\phi}^{(i+1)}(\zeta/h_i), \quad (8)$$

or simply written as

$$\{u^{(i)}(\zeta)\} = [N_u^{(i)}(\zeta)] \cdot \{\bar{u}^{(i)}\}, \quad (9)$$

$$\{\phi^{(i)}(\zeta)\} = [N_{\phi}^{(i)}(\zeta)] \bullet \{\bar{\phi}^{(i)}\}, \quad (10)$$

where $\{\bar{u}^{(i)}\} = \{\bar{u}_{a_1}^{(i)}, \bar{u}_{a_2}^{(i)}, \bar{w}^{(i)}, \bar{u}_{a_1}^{(i+1)}, \bar{u}_{a_2}^{(i+1)}, \bar{w}^{(i+1)}\}$ is the displacement vector and $\{\bar{\phi}^{(i)}\} = \{\bar{\phi}^{(i)}, \bar{\phi}^{(i+1)}\}$ is the electric potential vector of the i -th and $(i+1)$ -th interfaces along the curvilinear coordinate axes; $[N_u^{(i)}(\zeta)]$ and $[N_{\phi}^{(i)}(\zeta)]$ are the shape functions in terms of the coordinate ζ ; and h_i is the thickness of the i -th layer. Note that the coordinate ζ is local to each layer. Furthermore, one can derive the nodal governing equations of the j -th (planar) layer element located in the i -th (thickness) layer in a matrix representation:

$$\begin{bmatrix} [M_{uu}^{(i)}] & 0 \\ 0 & 0 \end{bmatrix} \begin{Bmatrix} \{\ddot{u}_j^{(i)}\} \\ \{\ddot{\phi}_j^{(i)}\} \end{Bmatrix} + \begin{bmatrix} [C_{uu}^{(i)}] & 0 \\ 0 & 0 \end{bmatrix} \begin{Bmatrix} \{\dot{u}_j^{(i)}\} \\ \{\dot{\phi}_j^{(i)}\} \end{Bmatrix} + \begin{bmatrix} [K_{uu}^{(i)}] & [K_{u\phi}^{(i)}] \\ [K_{\phi u}^{(i)}] & [K_{\phi\phi}^{(i)}] \end{bmatrix} \begin{Bmatrix} \{u_j^{(i)}\} \\ \{\phi_j^{(i)}\} \end{Bmatrix} = \begin{Bmatrix} \{F_u^{(i)}\} \\ \{F_{\phi}^{(i)}\} \end{Bmatrix}, \quad (11)$$

where $[M_{uu}]$ is the mass matrix; $[C_{uu}]$ is the damping matrix; $[K_{uu}]$, $[K_{u\phi}]$, $[K_{\phi u}]$, and $[K_{\phi\phi}]$ are the stiffness matrices defined for the displacement and electric potential fields; and $\{F_u\}$ and $\{F_{\phi}\}$ are the mechanical and electric excitations, respectively. Based on the nodal equation, one can assemble the element matrices to yield the global system matrices.

$$\begin{bmatrix} [M_{uu}] & 0 \\ 0 & 0 \end{bmatrix} \begin{Bmatrix} \{\ddot{u}_j\} \\ \{\ddot{\phi}_j\} \end{Bmatrix} + \begin{bmatrix} [C_{uu}] & 0 \\ 0 & 0 \end{bmatrix} \begin{Bmatrix} \{\dot{u}_j\} \\ \{\dot{\phi}_j\} \end{Bmatrix} + \begin{bmatrix} [K_{uu}] & [K_{u\phi}] \\ [K_{\phi u}] & [K_{\phi\phi}] \end{bmatrix} \begin{Bmatrix} \{u_j\} \\ \{\phi_j\} \end{Bmatrix} = \begin{Bmatrix} \{F_u\} \\ \{F_{\phi}\} \end{Bmatrix}. \quad (12)$$

In general, the control force is introduced in the force vector $\{F_{\phi}\}$ which can be setup based on various control algorithms, such as the proportional feedback, the Lyapunov feedback, etc. [15]. Distributed control and sensing of distributed systems can be formulated afterwards.

A NEW X-ACTUATOR DESIGN FOR DUAL BENDING/TWISTING CONTROL OF WINGS

In this study, the negative velocity, proportional feedback is used to evaluate the two actuator configurations: 1) the parallel-actuator and 2) the X-actuator laminated on wing structures.

As to investigate the bending and torsion control effectiveness of wing panels, a finite element plate model consisting of an elastic plate and piezoelectric control patches is studied. Note that the plate dimensions are specifically selected such that the first mode is the bending mode and the second mode is the torsion mode, although the first few natural modes of most aircraft wings are usually bending modes. **Figures 3a&b** illustrate the FE models laminated with a number of diagonally or parallelly aligned piezoelectric patches serving as distributed sensors and actuators. Note that the diagonally aligned actuator configuration has the identical

total actuator area as that of the parallel configuration. **Figures 4a&b** show the first plate bending mode and the first torsion mode (the second plate mode).

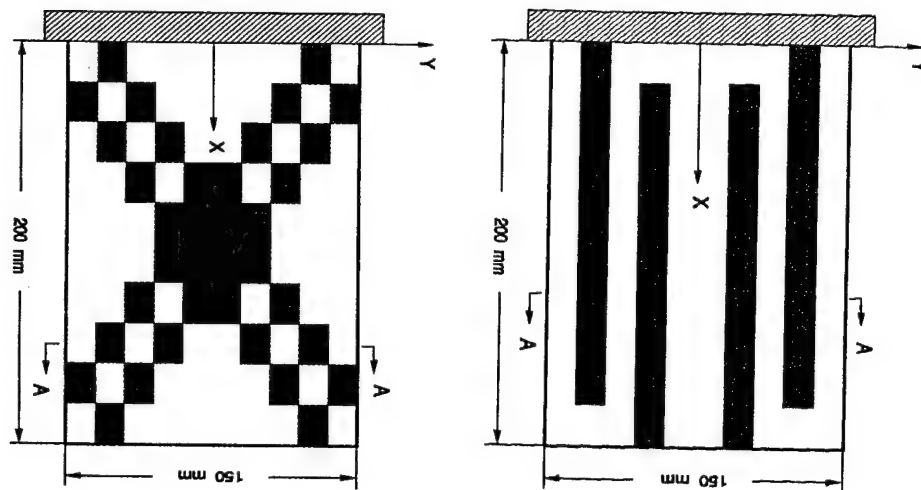
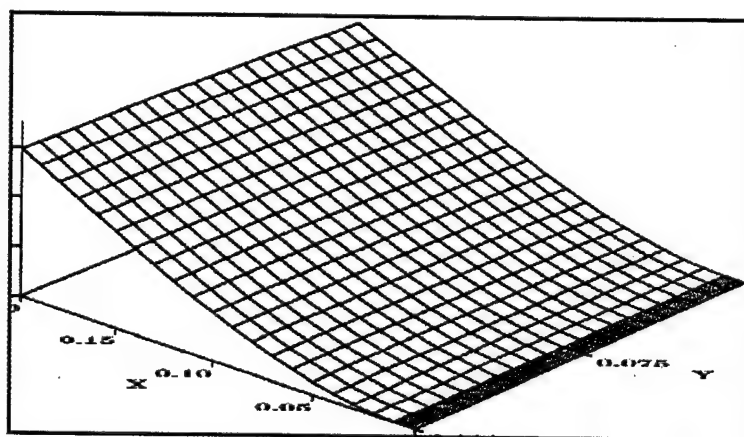
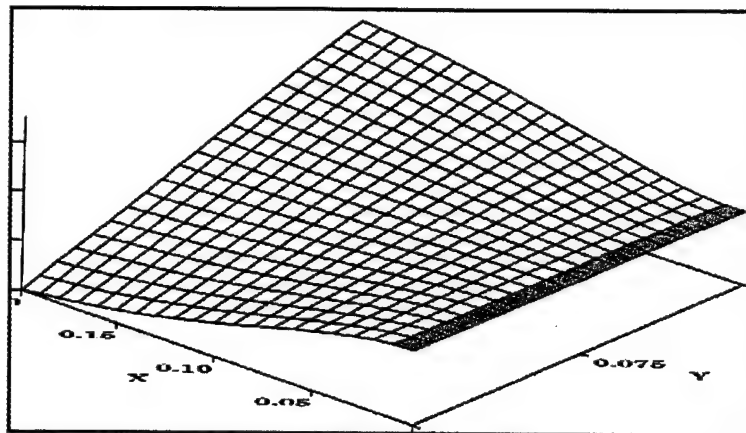


Figure 3a&b. Diagonal and parallel configurations of the distributed actuators.



(a) Plate bending (1st plate mode).



(b) Torsion (2nd plate mode) modes

Figure 4a&b. Plate bending (1st plate mode) and torsion (2nd plate mode) modes.

Control of Bending Mode

Snap-back free and controlled responses of the plate bending mode are presented in **Figures 5-7**. Note that both parallel and diagonal configurations provide identical bending control effects. These time histories clearly show the effectiveness of the negative proportional feedback control at various gains. Besides, comparing the above three snap-back responses suggests that both configurations are effective to bending mode control.

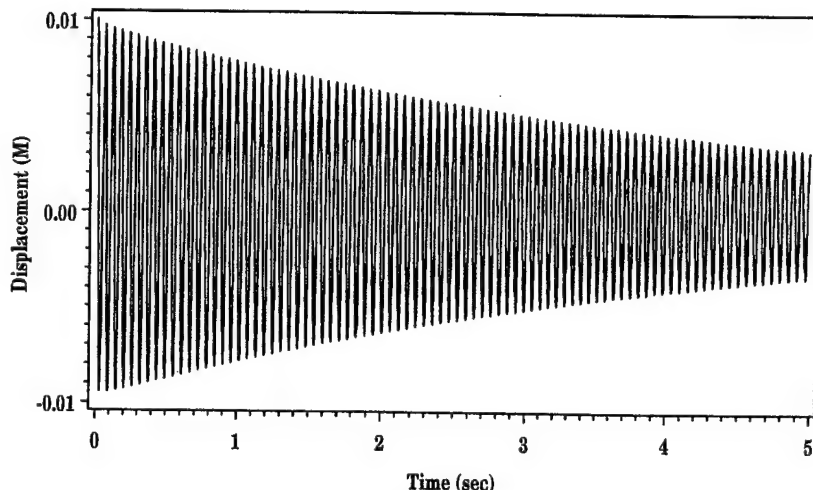


Figure 5. Free snap-back response of the plate bending mode.

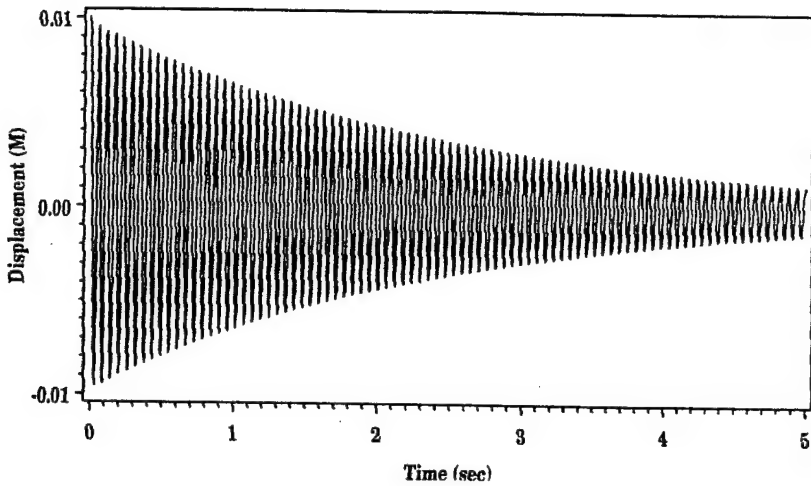


Figure 6. Controlled snap-back response.

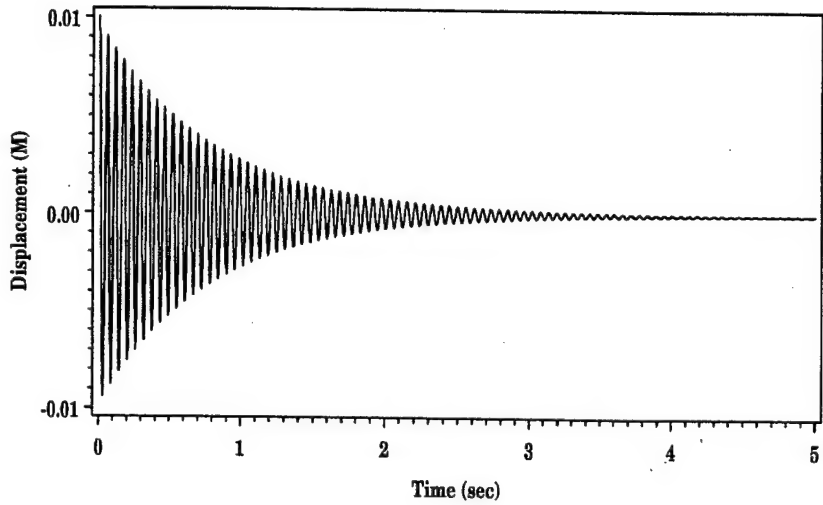


Figure 7. Controlled snap-back response (high gain).

Control of Torsion Mode

Furthermore, snap-back free and controlled torsion vibrations are also presented in **Figures 8-10**. Recall that the parallel actuator configuration is only effective to control of bending oscillations (**Figures 6 and 7**) and ineffective to any torsion oscillations. However, the new X-configuration is effective to both bending and torsion vibrations, as shown in Figures 5-10. Finite element simulation results prove that the parallel and diagonal configurations both have identical bending control effectiveness. However, only the X-actuator configuration has the torsion control capability. Thus, redesigning the actuator layouts to the diagonal X-configuration based on the identical actuator area does enhance the torsion controllability, without loosing the bending controllability. Note that there is a gap between the last actuator patch and the fixed end in both models. Adding an extra actuator patch filling into the gap would enhance the control effectiveness, especially for bending modes. Furthermore, spatially

shaping the distributed sensors and actuators can make them sensitive to only a single mode or a group of natural modes [15-17]. Accordingly, a single critical mode or a group of modes can be independently controlled.

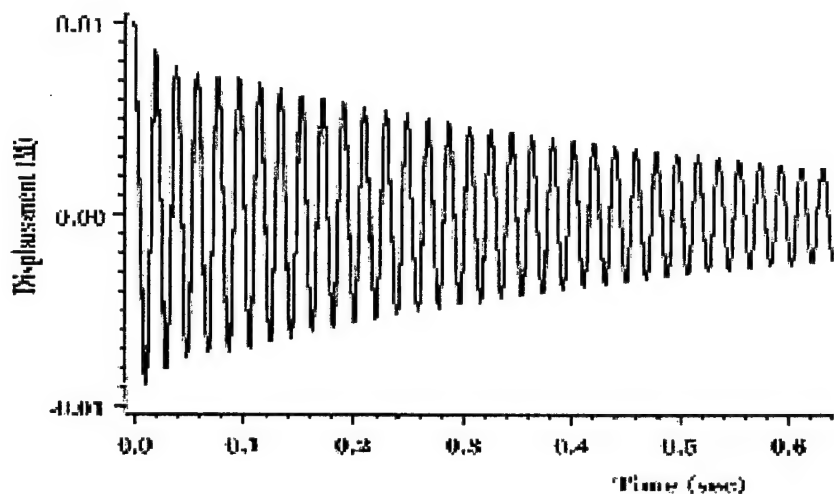


Figure 8. Free torsion vibration.

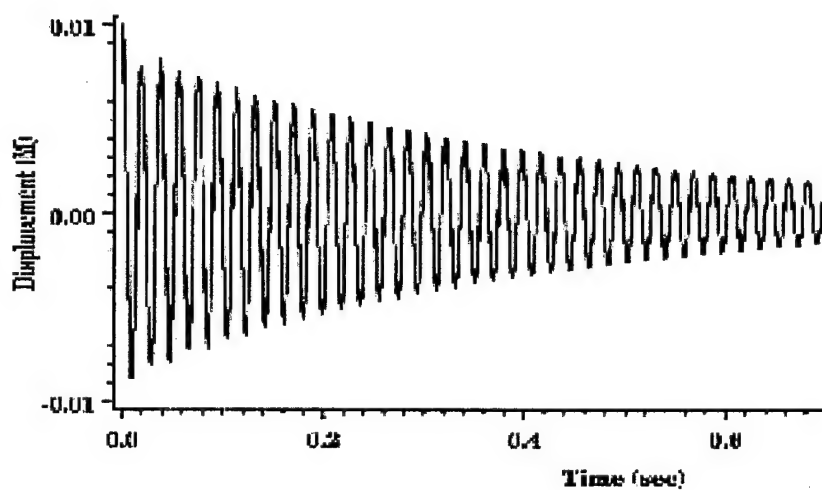


Figure 9. Controlled torsion vibration (gain=1 ω).

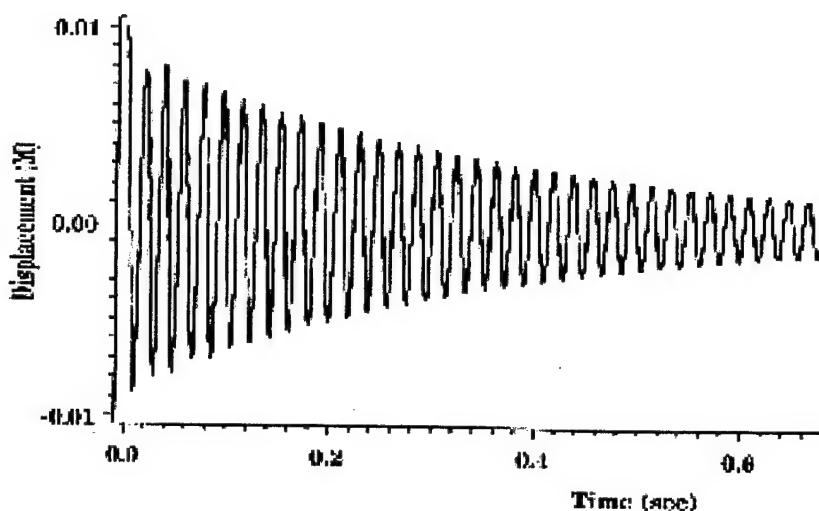


Figure 10. Controlled torsion vibration (gain=2 ω).

LABORATORY EXPERIMENTS

A scaled-model (10cm×7.5cm×0.5mm) of a Plexiglas plate sandwiched between two layers of piezoelectric polyvinylidene fluoride (PVDF) films (40 μ m) is fabricated and its bending/torsion control characteristics are investigated. Note that one PVDF layer serves as a distributed sensor and the other PVDF layer serves as the distributed actuator. Signal from the sensor layer is amplified and fed back to the distributed actuator layer inducing counteracting control moments. **Figure 11** shows the physical model mounted on a shaker and **Figure 12** illustrates the experimental setup and apparatus. As discussed previously, the physical model exhibits a bending mode and a torsion mode as its first two natural modes. Besides, to demonstrate the dual-mode controllability of the X-actuator, the original and controlled bending and torsion vibrations are evaluated. (Since the X-configuration has the same bending control effect as that of the parallel actuator, the parallel configuration model is neither fabricated nor tested.)

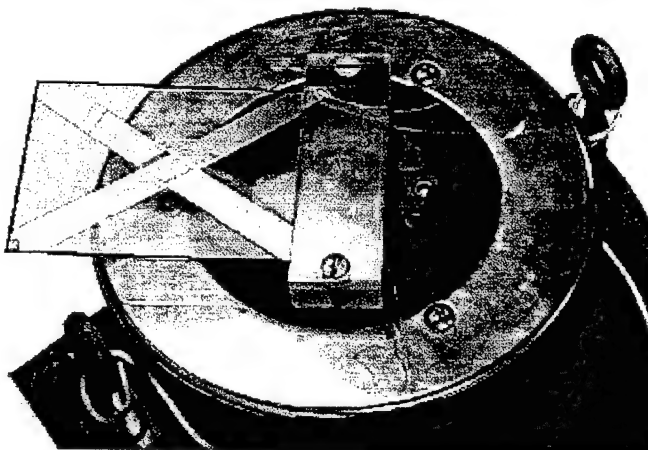


Figure 11. A physical model mounted on a shaker.

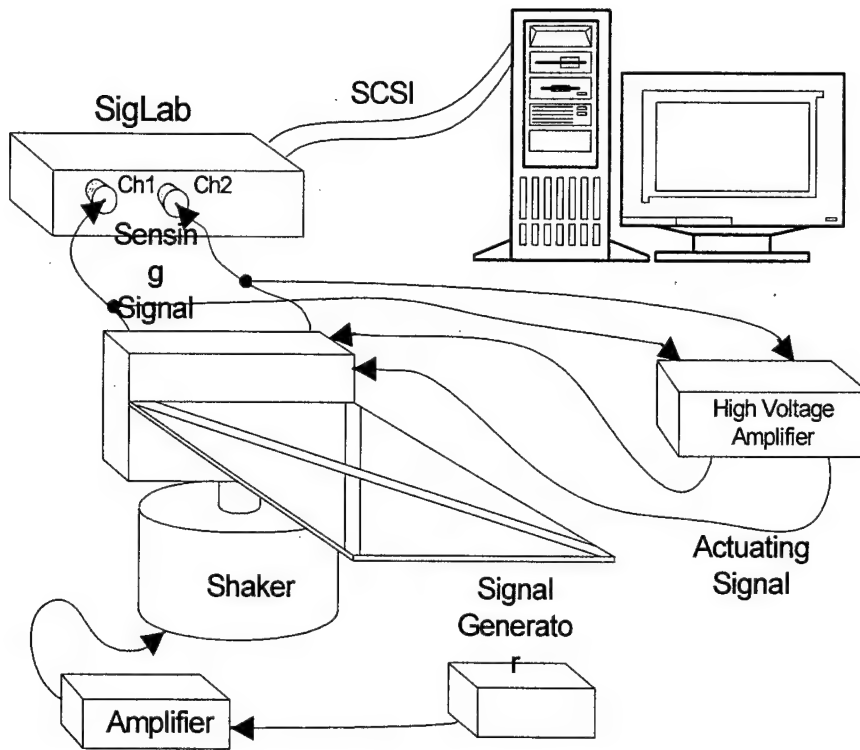
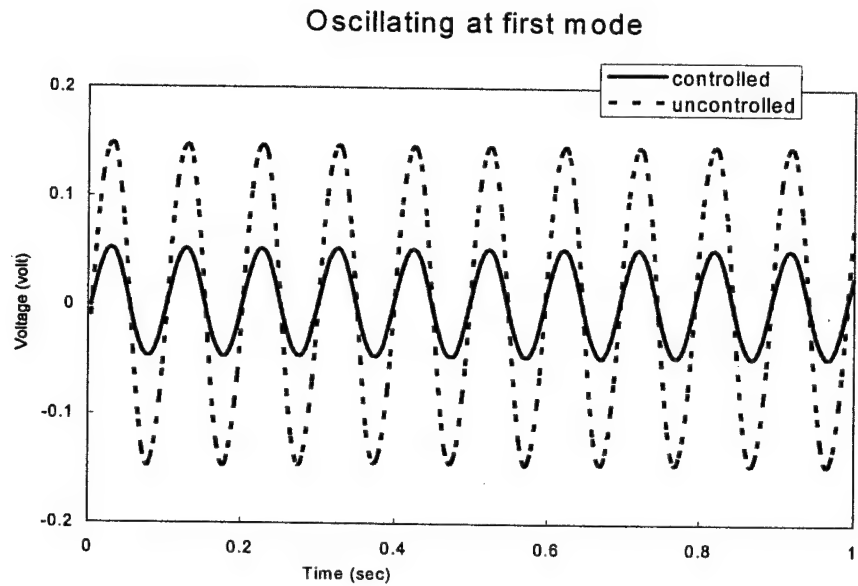
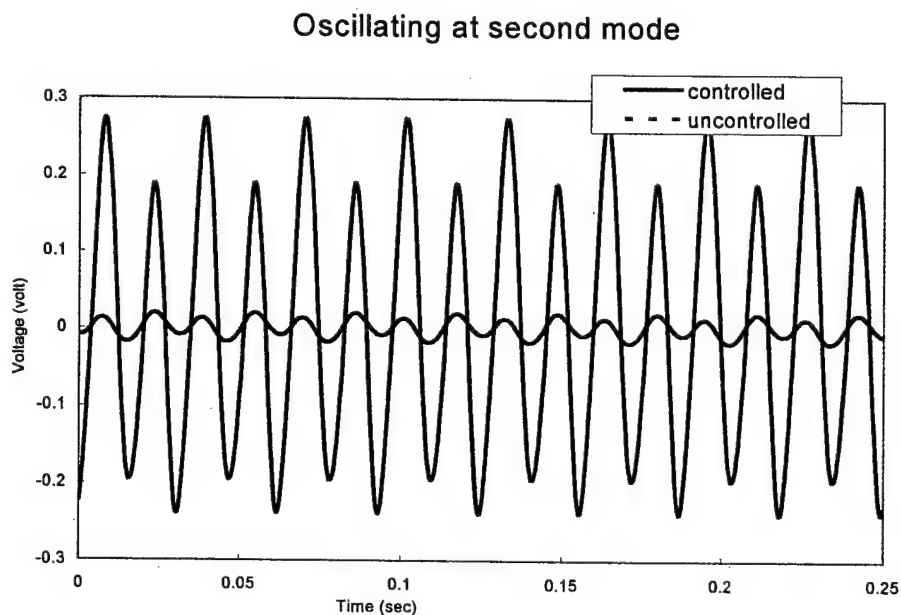


Figure 12. Laboratory setup and apparatus. (Not to scale)

The first plate bending mode can be easily excited using either the initial displacement (the snap-back response), the laminated PVDF actuator layer, or the shaker (the sinusoidal steady state response). However, due to technical difficulty in exciting the torsion mode via the electromagnetic shaker, the diagonally laminated PVDF is used to excite the torsion mode. An excitation signal at the torsion frequency is amplified using a high-voltage amplifier and then input to the diagonal PVDF actuator. Steady state responses of the controlled and uncontrolled plate time histories obtained from the PVDF sensor are presented in **Figure 13** (the bending mode) and **Figure 14** (the torsion mode). (Note that the initial displacement applied to the first mode was 10mm and these vibration amplitudes were in the mm range.) These figures clearly demonstrate the diagonally laminated actuators are capable of controlling the bending and torsion modes of the plate. Also, due to imperfect fabrication techniques, the time histories also exhibit repeated waveforms of uneven torsion oscillations.



**Figure 13. Steady state responses of the bending mode.
(Original and controlled responses)**



**Figure 14. Steady state responses of the torsion mode.
(Original and controlled responses)**

CONCLUSIONS

Distributed structural control based on the strucronics technology has demonstrated its effectiveness in many engineering applications, i.e., airplane wings, helicopter blades, nozzles, satellites, aerospace systems, etc. Early studies of vibration control of airplane wings and

helicopter blades revealed that the parallel-actuator configuration is effective to control of bending modes and ineffective to control of torsion modes. Thus, reconfiguring the actuator layout, based on the same effective actuator area, capable of controlling both bending and torsion modes is highly desirable. Accordingly, the actuator patches were reconfigured into an X-actuator configuration and its bending and torsion controllability was evaluated using a newly developed finite element code and was also demonstrated in laboratory experiments.

Fundamental piezoelectric constitutive relations were briefly reviewed. Development of a laminated quadratic piezoelastic triangular shell FE using the layerwise constant shear angle theory was also presented. Governing piezoelectric matrix equation was derived and its distributed control applications were discussed. Finite element models of the new X-actuator configuration and the original parallel-actuator configuration were analyzed. Bending and torsion control effects of the finite element models were studied. Analysis results suggested that the X-actuator configuration does provide the torsion mode controllability, while maintaining the bending mode controllability. Laboratory experiments also demonstrated the bending and torsion control effects of the X-actuator configuration. Thus, effective and innovative design layouts of available distributed actuators can maximize the control effectiveness encompassing multiple vibration modes.

ACKNOWLEDGEMENT

This research is supported, in part, by a grant (F49620-98-1-0467) from the Air Force Office of Scientific Research (Project managers: Dan Segalman and Brian Sanders). This support is gratefully acknowledged.

REFERENCES

1. H.S. Tzou and G.L. Anderson (Ed.) 1992 *Intelligent Structural Systems*. Dordrecht/Boston: Kluwer Aca Pub.
2. H.S. Tzou and A. Gurur (Editors) G.L. Anderson; M.C. Natori, U. Gabbert, J. Tani and E. Breitbach (Associate Editors) 1998 *Structronic Systems - Smart Structures, Devices and Systems*, Volume-1: *Materials and Structures*, and Volume-2: *Systems and Control*. Singapore/New Jersey: World Science Publishing Co.
3. H.S. Tzou and L.A. Bergman (Editors) 1998 *Dynamics and Control of Distributed Systems*. NY: Cambridge University Press.
4. H. Allik and T.J.R. Hughes 1979 *Int. J. of Numerical Methods Engng* 2, 151-168. Finite Element Method for Piezoelectric Vibration.
5. M. Nailon, R.H. Coursant and F. Besnier 1983 *ACTA Electronica* 25(4), 341-362. Analysis of piezoelectric structures by a finite element method.
6. M.W. Obal 1986 *Vibration Control of Flexible Structures Using Piezoelectric Devices as Sensors and Actuators*. Ph.D. Thesis, Georgia Institute of Technology.
7. H.S. Tzou and C.I. Tseng 1990 *Journal of Sound and Vibration* 138(1), 17-34. Distributed piezoelectric sensor/actuator design for dynamic measurement/control of distributed parameter systems: a finite element approach.

8. S.K. Ha, C. Keilers and F.-K. Chang 1992 *AIAA Journal* **30**(3), 772-780. Finite element analysis of composite structures containing distributed piezoceramics sensors and actuators.
9. W.-S. Hwang and H.C. Park 1993 *AIAA Journal* **31**(5), 930-937. Finite element modeling of piezoelectric sensors and actuators.
10. S.S. Rao and M. Sunar 1993 *AIAA Journal* **31**(7), 1280-1286. Analysis of distributed thermopiezoelectric sensors and actuators in advanced intelligent structures.
11. H.S. Tzou and R. Ye 1994 *ASME Journal of Vibration and Acoustics* **116**(4), 489-495. Piezothermoelasticity and control of piezoelectric systems.
12. H.S. Tzou and R. Ye 1996 *AIAA Journal* **34**(1), 110-115. Analysis of piezoelastic systems with laminated piezoelectric triangle shell elements.
13. R. Ye and H.S. Tzou 2000 *Journal of Sound & Vibration* **231**(5), 1321-1338. Control of adaptive shells with thermal and mechanical excitations.
14. R.D. Mindlin 1974 *Intl. J. Solids and Structures* **10**, 625-637. Equations of high frequency vibrations of thermopiezoelectric crystal plates.
15. H.S. Tzou 1993 *Piezoelectric Shells (Distributed Sensing and Control of Continua)*. Boston/Dordrecht : Kluwer Academic Publishers.
16. H.S. Tzou, J.P. Zhong and M.C. Natori 1993 *ASME Journal of Vibration & Acoustics* **115**(1), 40-46. Sensor mechanics of distributed shell convolving sensors applied to flexible rings. (PltBdTwsY.b600)
17. H.S. Tzou, J.P. Zhong and J.J. Hollkamp 1994 *Journal of Sound & Vibration* **177**(3), 363-378. Spatially distributed orthogonal piezoelectric shell actuators: theory and applications.

CHAPTER 5

NEURAL POTENTIALS AND MICRO-SIGNALS OF NONLINEAR DEEP AND SHALLOW CONICAL SHELLS

ABSTRACT

Conventional sensors, such as proximeters and accelerometers, are add-on devices usually adding additional weights to structures and machines. Health monitoring of flexible structures by electroactive smart materials has been investigated over the years. Thin-film piezoelectric material, e.g., polyvinylidene fluoride (PVDF) polymeric material, is a lightweight and dynamic sensitive material appearing to be a perfect candidate in monitoring structure's dynamic state and health status of flexible shell structures with complex geometries. The complexity of shell structures has thwarted the progress in studying the distributed sensing of shell structures. Linear distributed sensing of various structures have been studied, e.g., beams, plates, cylindrical shells, conical shells, spherical shells, paraboloidal shells and toroidal shells. However, distributed microscopic neural signals of nonlinear shell structures has not been carried out rigorously. This study is to evaluate microscopic signals, modal voltages and distributed micro-neural signal components of truncated nonlinear conical shells laminated with distributed infinitesimal piezoelectric neurons. Signal generation of distributed neuron sensors laminated on conical shells is defined first. The dynamic neural signal of truncated nonlinear conical shells consists of microscopic linear and nonlinear membrane components and linear bending component based on the von Karman geometric nonlinearity. Micro-signals, modal voltages and distributed neural signal components of two different truncated nonlinear conical shells are investigated and their sensitivities discussed.

INTRODUCTION

Health monitoring and diagnosis is an important issue in modern high-performance precision structures and systems. Conventional "discrete" add-on sensors, such as proximeters, LVDT, and accelerometers, usually add additional weights and often influence dynamic responses of precision structures and machines. Thin-film piezoelectric material, e.g., polyvinylidene fluoride (PVDF) polymeric material, is a lightweight and dynamic sensitive material and it can be easily segmented and shaped to account for various in-situ distributed monitoring applications of flexible structures [1,2]. Unlike conventional discrete add-on sensors, thin piezoelectric layers can be spatially spread and distributed over the surfaces of precision structures. Accordingly, these distributed piezoelectric layers can serve as distributed neurons and actuators in sensing and control of advanced structures and machines [3-5].

Dynamics and vibrations of conical shell structures have been investigated over the years [6-15]. Distributed sensing characteristics of rings, cylindrical shells, toroidal shells, paraboloidal shells, etc. have been evaluated [16-20]. However, distributed sensing and control of conical shells have not been thoroughly investigated. Dynamic sensing characteristics, micro-signal generations, and distributed modal voltages of truncated linear conical shell sections have been evaluated recently [21]. This study is to investigate microscopic signal generations and neural spatial distributed modal signals of nonlinear conical shells based on infinitesimal piezoelectric neurons.

Signal generation of distributed neuron sensors laminated on nonlinear conical shells is defined first. Closed-form sensing signal generation of distributed conical shell sensors is then defined based on given boundary conditions and mode shape functions following the Donnel-Mushtari-Valsov theory. Micro-signals, modal voltages and distributed sensing components of two free-free truncated nonlinear conical shells are investigated and their sensitivities discussed in case studies.

DISTRIBUTED SENSING OF NONLINEAR SHELLS

The generic shell sensing signal equation is derived based on the direct piezoelectric effect and also the generic double curvature shell theory. In general, in-plane strains S_{ij}^s in the neural sensor layer contribute to the signal generation ϕ^s :

$$\phi^s = \frac{h^s}{S^e} \int \int_{\alpha_1 \alpha_2} (h_{31} S_{11}^s + h_{32} S_{22}^s + h_{36} S_{12}^s) A_1 A_2 d\alpha_1 d\alpha_2, \quad (1)$$

where h^s is the thickness of the sensor layer; the superscript 's' denotes the distributed sensor layer; S^e is the effective electrode area of the sensor layer. α_1 and α_2 are the two principle directions in generic shell continuum; A_1 and A_2 are the Lamé parameters; and h_{31} , h_{32} and h_{36} are the piezoelectric constants. The effect of transverse strains S_{13} , S_{23} and S_{33} are neglected, since the variation is small in the α_3 direction, provided the shell and the sensor are thin. The generic sensing equation can also account for both the linear and nonlinear effects. Moreover, the strain terms in the sensing signal equation can be divided into the membrane strains and the bending strains. Thus, the signal generation of a generic shell sensor layer laminated on an elastic thin shell with the von-Karman geometric nonlinearity becomes

$$\begin{aligned}
\phi^s = & \left(\frac{h^s}{S^e} \right) \int_{\alpha_1} \int_{\alpha_2} \left\{ h_{31} \left\{ \left(\frac{1}{A_1} \frac{\partial u_1}{\partial \alpha_1} + \frac{u_2}{A_1 A_2} \frac{\partial A_1}{\partial \alpha_2} + \frac{u_3}{R_1} + \left[\frac{1}{2} \left(\frac{\partial u_3 / \partial \alpha_1}{A_1} \right)^2 \right] \right) \right. \right. \\
& + r_i^s \left[\frac{1}{A_1} \frac{\partial}{\partial \alpha_1} \left(\frac{u_1}{R_1} - \frac{1}{A_1} \frac{\partial u_3}{\partial \alpha_1} \right) + \frac{1}{A_1 A_2} \left(\frac{u_2}{R_2} - \frac{1}{A_2} \frac{\partial u_3}{\partial \alpha_2} \right) \frac{\partial A_1}{\partial \alpha_2} \right] \} \\
& + h_{32} \left\{ \left(\frac{1}{A_2} \frac{\partial u_2}{\partial \alpha_2} + \frac{u_1}{A_1 A_2} \frac{\partial A_2}{\partial \alpha_1} + \frac{u_3}{R_2} + \left[\frac{1}{2} \left(\frac{\partial u_3 / \partial \alpha_2}{A_2} \right)^2 \right] \right) \right. \\
& + r_2^s \left[\frac{1}{A_2} \frac{\partial}{\partial \alpha_2} \left(\frac{u_2}{R_2} - \frac{1}{A_2} \frac{\partial u_3}{\partial \alpha_2} \right) + \frac{1}{A_1 A_2} \left(\frac{u_1}{R_1} - \frac{1}{A_1} \frac{\partial u_3}{\partial \alpha_1} \right) \frac{\partial A_2}{\partial \alpha_1} \right] \} \\
& + h_{36} \left\{ \left(\frac{1}{A_2} \frac{\partial u_1}{\partial \alpha_2} + \frac{1}{A_1} \frac{\partial u_2}{\partial \alpha_1} - \frac{u_1}{A_1 A_2} \frac{\partial A_1}{\partial \alpha_2} - \frac{u_2}{A_1 A_2} \frac{\partial A_2}{\partial \alpha_1} + \left[\frac{1}{A_1 A_2} \frac{\partial u_3}{\partial \alpha_1} \frac{\partial u_3}{\partial \alpha_2} \right] \right) \right. \\
& + r_{12}^s \left[\frac{A_1}{A_2} \frac{\partial}{\partial \alpha_2} \left(\frac{u_1}{R_1} - \frac{1}{A_1} \frac{\partial u_3}{\partial \alpha_1} \right) \frac{1}{A_1} + \frac{A_2}{A_1} \frac{\partial}{\partial \alpha_1} \left(\frac{u_2}{R_2} - \frac{1}{A_2} \frac{\partial u_3}{\partial \alpha_2} \right) \frac{1}{A_2} \right. \\
& \left. \left. - \frac{1}{A_1 A_2} \left(\frac{u_1}{R_1} - \frac{1}{A_1} \frac{\partial u_3}{\partial \alpha_1} \right) \frac{\partial A_1}{\partial \alpha_2} - \frac{1}{A_1 A_2} \left(\frac{u_2}{R_2} - \frac{1}{A_2} \frac{\partial u_3}{\partial \alpha_2} \right) \frac{\partial A_2}{\partial \alpha_1} \right] \right\} \bullet A_1 A_2 d\alpha_1 d\alpha_2
\end{aligned} \tag{2}$$

where A_i is the Lamé parameter; R_i is the radius of curvature of the α_i axis; u_i is the displacement in the α_i direction; r_i^s denotes the sensor location away from the shell neutral surface; the terms inside the parentheses following the piezoelectric constant denote the membrane strain; the terms with r_i^s are the bending strains; and the quadratic terms in the membrane strains are the large deformation effect based on the von Karman geometric nonlinearity [22]. Application of the generic sensing equation depends on two Lamé parameters and two radii of curvatures of a given geometry.

NONLINEAR CONICAL SHELL SENSING EQUATION

Two Lamé parameters and two radii of curvature are needed in deriving the conical shell's sensing equation. **Figure 1** illustrates a conical shell and its parameters. The Lamé parameters, radii of curvature, and principle directions of conical shells are respectively defined by $A_1 = 1$, $A_2 = x \sin \beta^*$, $R_1 = R_x = \infty$, $R_2 = R_\psi = x \tan \beta^*$, $\alpha_1 = x$, and $\alpha_2 = \psi$. β^* is the half-apex angle; x is the distance measured from the apex. Note that the Donnel-Mushtari-Vlasov theory is used and micro-signal generations of a free-free truncated nonlinear conical shell are investigated in this study.

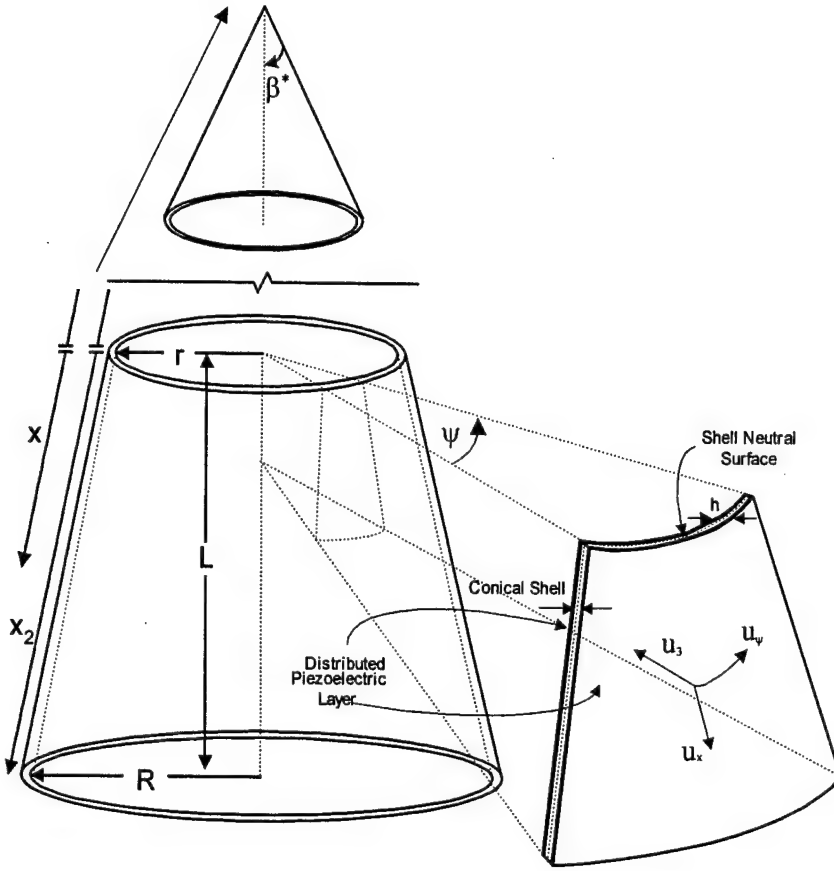


Fig.1 A conical shell of revolution and its section.

Assume the sensor material is insensitive to the in-plane twisting S_{12}^s . Eq.(1) becomes

$$\phi^s = \frac{h^s}{S_{x\psi}^s} \iint (h_{31}S_{xx}^s + h_{32}S_{\psi\psi}^s) \bullet x \sin \beta^* dx d\psi. \quad (3)$$

The strain terms can be written as the summation of the membrane strain s_{ij}^o and the bending strain k_{ij} : $S_{xx}^s = s_{xx}^o + r_x^s k_{xx}$ and $S_{\psi\psi}^s = s_{\psi\psi}^o + r_\psi^s k_{\psi\psi}$. Since the large deformation effect takes place in the membrane strains only, the membrane strains of the nonlinear conical shell are redefined as

$$s_{xx}^o = \frac{\partial u_x}{\partial x} + \frac{1}{2} \left(\frac{\partial u_3}{\partial x} \right)^2, \quad (4a)$$

$$s_{\psi\psi}^o = \frac{1}{x \sin \beta^*} \frac{\partial u_\psi}{\partial \psi} + \frac{u_x}{x} - \frac{u_3}{x \tan \beta^*} + \frac{1}{2} \frac{1}{x \sin \beta^*} \left(\frac{\partial u_3}{\partial \psi} \right)^2. \quad (4b)$$

Furthermore, in-plane displacements u_x and u_ψ are neglected in bending strains based on the Donnel-Mushtari-Vlasov theory. Thus, the bending strains of the conical shell are

$$k_{xx} = -\frac{\partial^2 u_3}{\partial x^2} \text{ and } k_{\psi\psi} = -\frac{1}{x^2 \sin^2 \beta^*} \frac{\partial^2 u_3}{\partial \psi^2} - \frac{1}{x} \frac{\partial u_3}{\partial x} . \quad (5a,b)$$

Accordingly, the sensing signal equation of a distributed neural sensor laminated on a nonlinear conical shell becomes

$$\begin{aligned} \phi^s = & \left(\frac{h^s}{S^e} \right) \int_x \int_\psi \left\{ h_{31} \left\{ \frac{\partial u_x}{\partial x} + \frac{1}{2} \left(\frac{\partial u_3}{\partial x} \right)^2 - r_x^s \frac{\partial^2 u_3}{\partial x^2} \right\} \right. \\ & + h_{32} \left\{ \frac{1}{x \sin \beta^*} \frac{\partial u_\psi}{\partial \psi} + \frac{u_x}{x} - \frac{u_3}{x \tan \beta^*} + \frac{1}{2} \frac{1}{x \sin \beta^*} \left(\frac{\partial u_3}{\partial \psi} \right)^2 \right. \\ & \left. \left. + r_\psi^s \left[-\frac{1}{x^2 \sin^2 \beta^*} \frac{\partial^2 u_3}{\partial \psi^2} - \frac{1}{x} \frac{\partial u_3}{\partial x} \right] \right\} \right\} \bullet x \sin \beta^* dx d\psi \end{aligned} \quad (6)$$

Boundary shear forces and moments are zero for free-free boundaries conditions, i.e., $N_{xx} = N_{xx}^* = 0$ at $x = x_1$ and x_2 and $N_{x\psi} = N_{x\psi}^* = 0$ at $x = x_1$ and x_2 . Thus,

$$\begin{aligned} \frac{1}{x} \left[\frac{\partial}{\partial x} (x M_{xx}) - M_{\psi\psi} - 2 \frac{\partial M_{x\psi}}{\partial \psi} \csc \beta^* \right] &= \frac{1}{x} [x Q_{xx}^* - \csc \beta^* \frac{\partial M_{x\psi}^*}{\partial \psi}] \\ &= 0 \quad \text{at } x = x_1 \text{ and } x = x_2 \end{aligned} \quad (7)$$

$$M_{xx} = M_{xx}^* = 0 \quad \text{at } x = x_1 \text{ and } x_2 \quad (8)$$

Accordingly, the assumed displacement solutions for a free-free truncated conical shell are

$$u_x = U_{xm}(x) \cos m\psi \sin \omega t, \quad u_\psi = U_{\psi m}(x) \sin m\psi \sin \omega t, \quad u_3 = U_{3m}(x) \cos m\psi \sin \omega t, \quad (9a,b,c)$$

where $U_{xm}(x)$, $U_{\psi m}(x)$ and $U_{3m}(x)$ are the longitudinal displacement functions defined as functions of x and they can be specified depending on accuracy requirement [10]; m is the (circumferential) wave number. Combining the longitudinal and circumferential functions, $U_{xm}(x) \cos m\psi$ denotes the longitudinal mode shape function; $U_{\psi m}(x) \sin m\psi$ denotes the circumferential mode shape function; and $U_{3m}(x) \cos m\psi$ denotes the transverse mode shape function. In free vibration analysis, the longitudinal displacement function is chosen to be $\left(\frac{x}{x_2} \right)^p$ where p is the power of the polynomial function that can be regarded as the wave number in the longitudinal direction; x_2 is the (longitudinal) length from the apex to the bottom perimeter. Higher-order polynomial function of $U_{xm}(x)$, $U_{\psi m}(x)$ and $U_{3m}(x)$, i.e., more flexible,

can improve the accuracy of the free vibration analysis, especially for higher natural modes at higher natural frequencies. The power p of the longitudinal mode shape polynomial function selected in this analysis is based on a free vibration analysis evaluated previously [10]. Note that the microscopic signal analysis is to reveal the modal signals corresponding to spatially distributed microscopic directional strains generated by free vibrations. Accordingly, one can infer that precise free-vibration analysis leads to better strain prediction resulting in accurate modal signal prediction and vibration diagnosis. Based on this analysis, one can easily utilize piezoelectric neurons placed at optimal locations and directions to diagnose shell dynamic states. Substituting mode shape functions and taking derivatives with respect to ψ , one can derive the sensing signal generation of a free-free truncated nonlinear conical shell.

$$\phi^s = \left(\frac{h^s}{S^e} \right) \int_x \int_\psi \left\{ h_{31} \left[\frac{\partial U_{xm}(x) \cos m\psi}{\partial x} \right. \right. \\ \left. \left. + \frac{1}{2} \left(\frac{\partial U_{3m}(x)}{\partial x} \right)^2 (\cos m\psi)^2 + r_x^s \left(- \frac{\partial^2 U_{3m}(x) \cos m\psi}{\partial x^2} \right) \right] \right. \\ \left. + h_{32} \left[\frac{m \cdot U \psi m(x) \cos m\psi}{x \sin \beta^*} + \frac{U_{xm}(x) \cos m\psi}{x} \right. \right. \\ \left. \left. - \frac{U_{3m}(x) \cos m\psi}{x \tan \beta^*} + \frac{1}{2} \frac{1}{x^2 \sin \beta^*} \left(\frac{\partial U_{3m}(x)}{\partial x} \right)^2 (\cos m\psi)^2 \right. \right. \\ \left. \left. + r_\psi^s \left(\frac{m^2 U_{3m}(x) \cos m\psi}{x^2 \sin^2 \beta^*} - \frac{1}{x} \frac{\partial U_{3m}(x) \cos m\psi}{\partial x} \right) \right] \right\} \cdot x \sin \beta^* dx d\psi. \quad (10)$$

Furthermore, using the generic displacement function $\left(\frac{x}{x_2} \right)^p$ with $p = 1$ and taking derivatives with respect to x yields the signal generation of the first mode group (1,m) of truncated nonlinear conical shells.

$$\phi^s = \left(\frac{h^s}{S^e} \right) \int_x \int_\psi h_{31} \left\{ \left[\frac{\cos m\psi}{x_2} + \frac{1}{2} \frac{(\cos m\psi)^2}{x_2^2} \right] \right. \\ \left. + h_{32} \left[\frac{m \cdot \cos m\psi}{x_2 \sin \beta^*} + \frac{\cos m\psi}{x_2} - \frac{\cos m\psi}{x_2 \tan \beta^*} \right. \right. \\ \left. \left. + \frac{1}{2} \frac{1}{(x \sin \beta^*)^2} \frac{(\cos m\psi)^2}{x_2^2} + r_\psi^s \left(\frac{m^2 \cos m\psi}{x x_2 \sin^2 \beta^*} - \frac{1}{x} \frac{\cos m\psi}{x_2} \right) \right] \right\} \cdot x \sin \beta^* dx d\psi. \quad (11)$$

Following the same procedures and using $p=2$ yields the signal generation of the second mode group (2,m) of truncated nonlinear conical shells..

$$\begin{aligned}
\phi^s = & \left(\frac{h^s}{S^e} \right) \int_x \int_\psi \left\{ h_{31} \left[2 \cos m\psi \frac{x}{x_2^2} [1 + \frac{x}{x_2^2} \cos m\psi] \right. \right. \\
& \left. \left. + r_x^s \left(-2 \cos m\psi \frac{1}{x_2^2} \right) \right] + h_{32} \left[\frac{x}{x_2^2} \left(1 + \frac{m}{\sin \beta^*} - \frac{1}{\tan \beta^*} \right. \right. \\
& \left. \left. + \frac{1}{x \sin \beta^*} \frac{2}{x_2^2} \cos m\psi \right) \cos m\psi + r_\psi^s \left(\frac{1}{x_2^2} \cos m\psi \left(\frac{m^2}{\sin^2 \beta^*} - 2 \right) \right) \right] \cdot x \sin \beta^* dx d\psi . \right\}
\end{aligned} \tag{12}$$

Note that the above sensing signal is defined for a distributed sensor neuron with an effective electrode area S^e . Removing the surface integration and dropping the surface average yields a microscopic signal component of an infinitesimal sensor neuron. Detailed spatial distribution of local micro-signals (i.e., the distributed **modal voltages**) can be established and spatially distributed modal sensing characteristics can be evaluated. For higher mode groups of nonlinear truncated conical shells, one can assign $p=n$ and follow the same procedures to define explicit signal generations.

EVALUATION OF MICRO-SIGNAL GENERATION AND DISTRIBUTION

Micro-signal generations and spatially distributed neural signals of two nonlinear truncated conical shells of revolution are investigated in this section. Dimensions of these two conical shells are summarized in **Table 1** and these two shells are referred as Model-1 and Model-2 in later analyses, **Figure 2**. Note that Model-2 is wider and shorter than Model-1. Spatial signal distributions of two mode groups ($p=1,2$) and four natural modes ($m=2,3,4,5$) of each model are evaluated and detailed micro-signal contributions are compared and analyzed. (Note that the $m=1$ mode is a rigid-body mode. Hence, there is no signal generation.)

Table 1 Definitions of the two conical shell models.

	Model 1	Model 2
Conical Shell Half-Apex Angle β^*	14.24°	30.24°
Major Radius, R	6.07 in	7.95 in
Minor Radius, r	2.72 in	3.49 in
Length, L	13.2 in	7.65 in
Thickness, h	0.01 in	0.01 in.

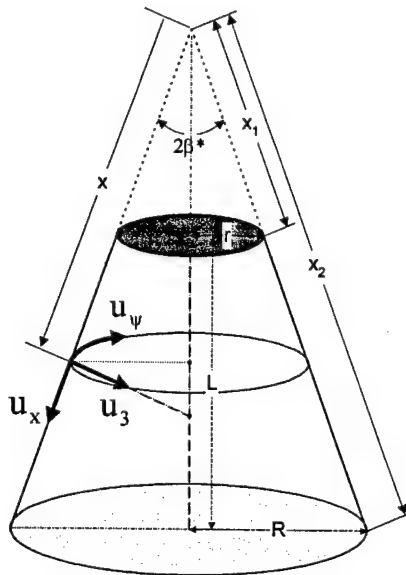


Fig.2 A truncated conical shell section.

Model-1, the First Mode Group (1,m=2-5)

Distributed micro-signal components and modal neural voltages of the first mode group (1,m=2-5) of Model-1 are presented in **Figures 3-6**. The top-left signal distribution denotes the signal component resulting from the longitudinal membrane strain; the top-right signal denotes the signal component resulting from the circumferential membrane strain; the bottom-left signal denotes the signal component resulting from the circumferential bending strain; and the bottom-right denotes the overall signal distribution – ***the (k,m)-th modal voltage***, including all contributing micro-signal components. Note that the longitudinal bending strain (k_{xx}) signal vanishes due to the selected displacement function with $p=1$. The shaded spatial distribution (with patches) illustrates the spatially distributed signals superimposed on the wire-frame conical shell model.

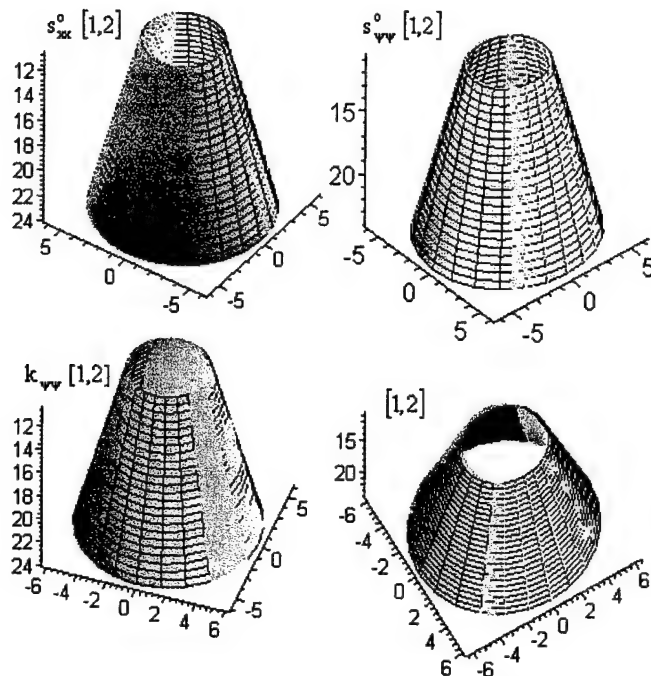


Fig.3 Signal components and modal voltage of (1,2) mode, Model-1.

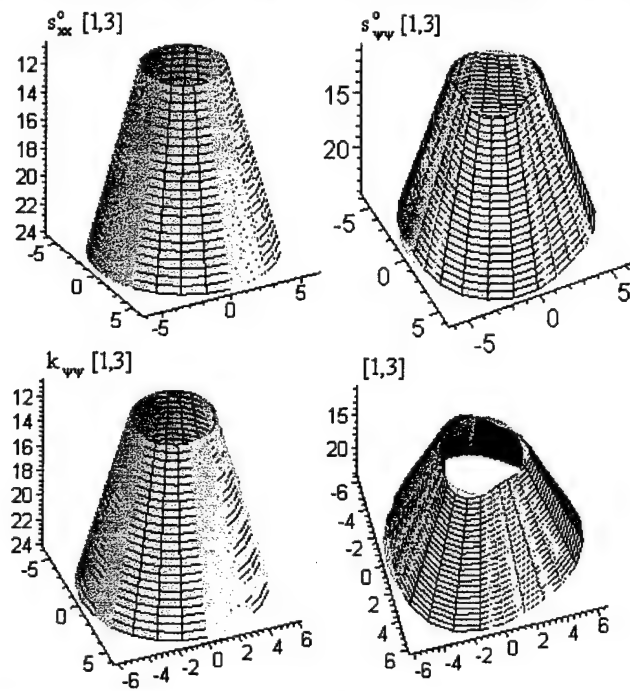


Fig.4 Signal components and modal voltage of (1,3) mode, Model-1.

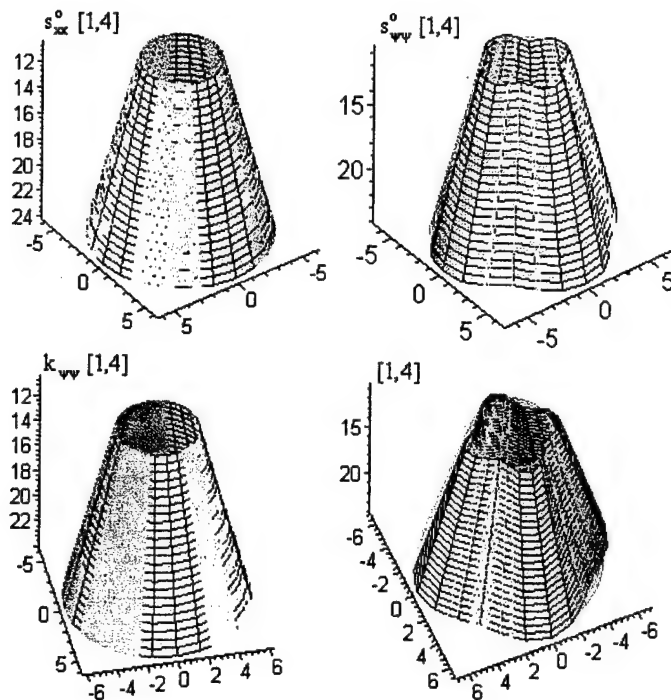


Fig.5 Signal components and modal voltage of (1,4) mode, Model-1.

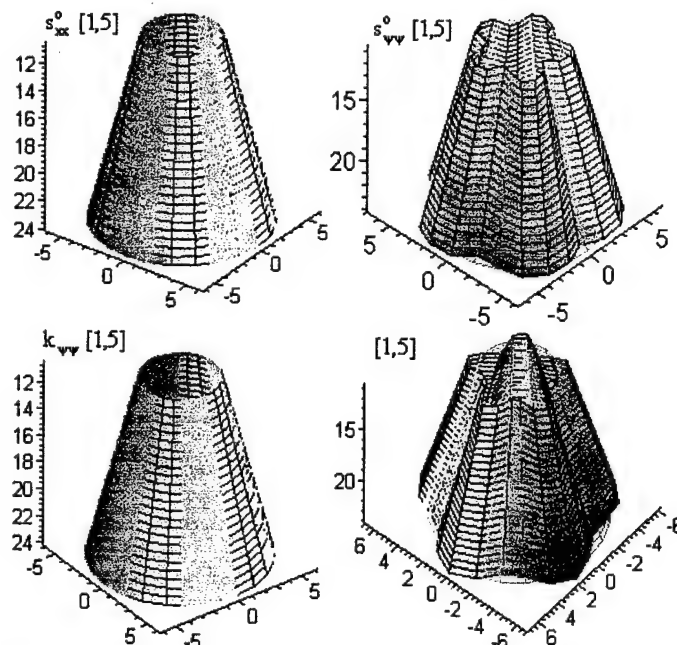


Fig.6 Signal components and modal voltage of (1,5) mode, Model-1.

Model-1, the Second Mode Group (2,m=2-5)

Distributed micro-signal components and modal voltages of the second mode group (2,m=2-5) of Model-1 are presented in **Figures 7-10**. The top-left signal distribution denotes the signal component resulting from the longitudinal membrane strain; the top-right signal

denotes the signal component resulting from the circumferential membrane strain; the middle-left signal denotes the signal component resulting from the longitudinal bending strain; the middle-right signal denotes the signal component resulting from the circumferential bending strain; and the bottom-left denotes the overall signal distribution – ***the (k,m)-th modal voltage***, including all contributing signal components. Note that the longitudinal bending strain exists in this case, with the displacement function $p=2$.

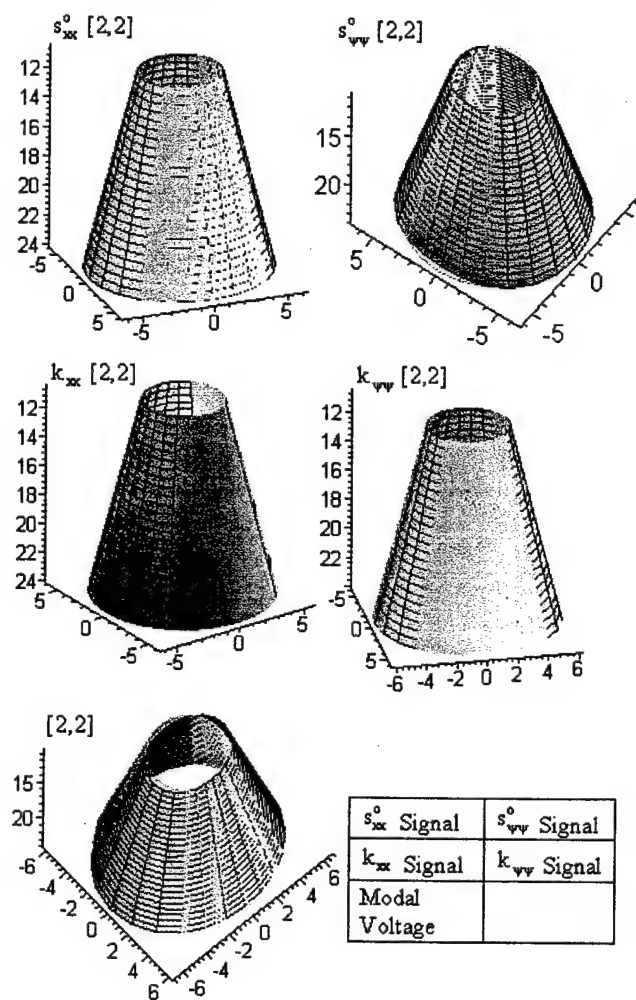


Fig.7 Signal components and modal voltage of (2,2) mode, Model-1.

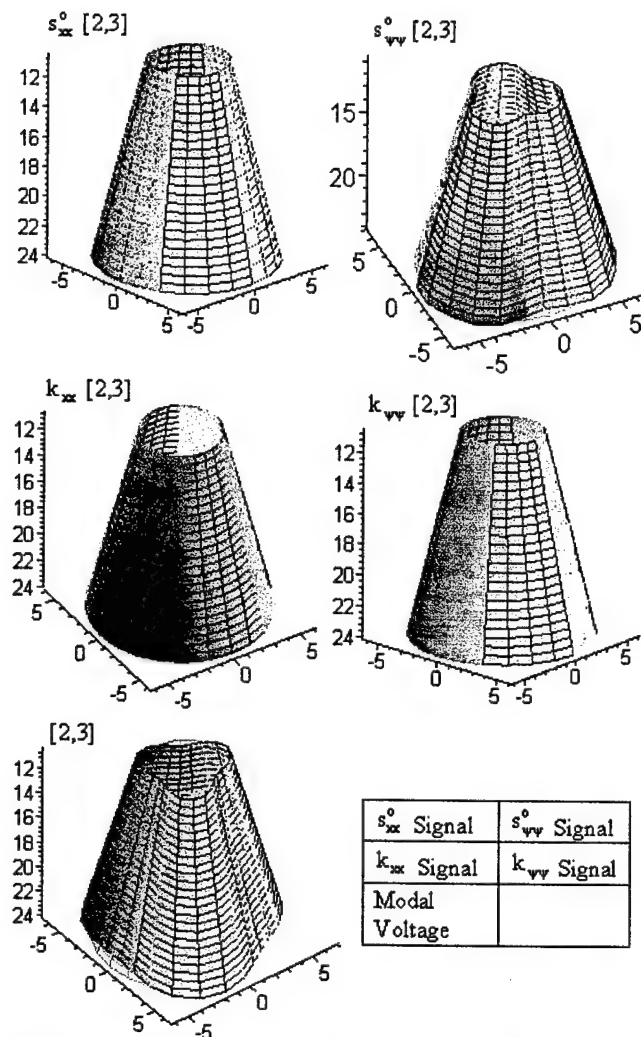


Fig.8 Signal components and modal voltage of (2,3) mode, Model-1.

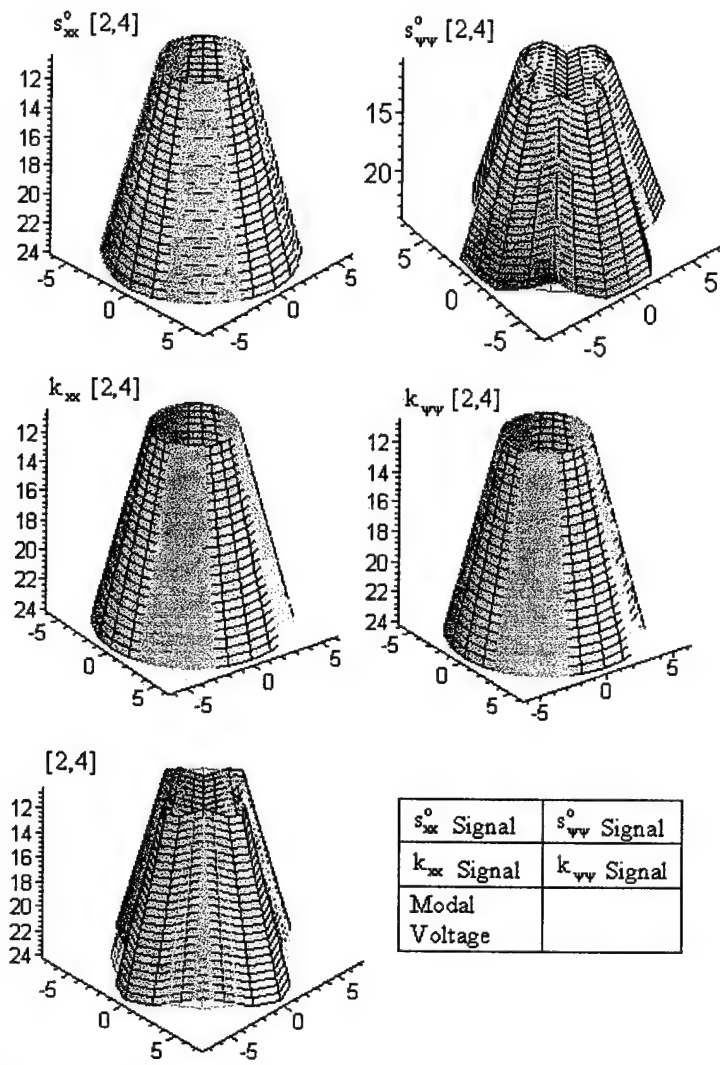


Fig.9 Signal components and modal voltage of (2,4) mode, Model-1.

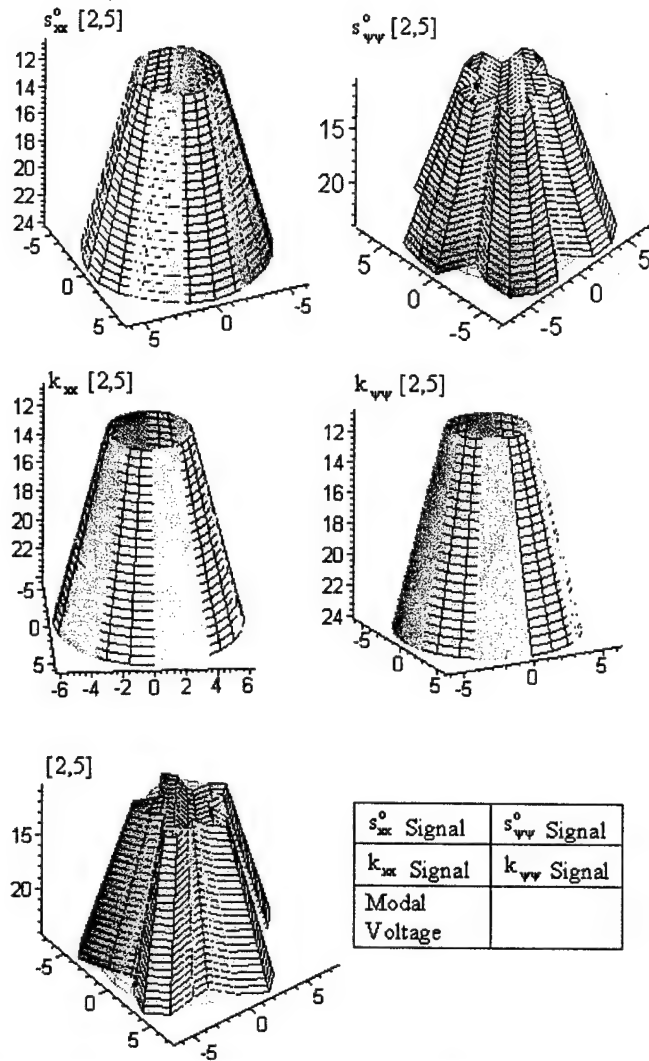


Fig.10 Signal components and modal voltage of (2,5) mode, Model-1.

Model-2, the First Mode Group (1,m=2-5)

Distributed micro-signal components and modal voltages of the first mode group (1,m=2-5) of Model-2 are presented in **Figures 11-14**. Layouts of the signal components are the same as those of the 1st mode group of Model-1. The final signal distribution – ***the (k,m)-th modal voltage***, including all contributing signal components, is the bottom-right plot. Again, the longitudinal bending strain vanishes due to the selected displacement function with p=1.

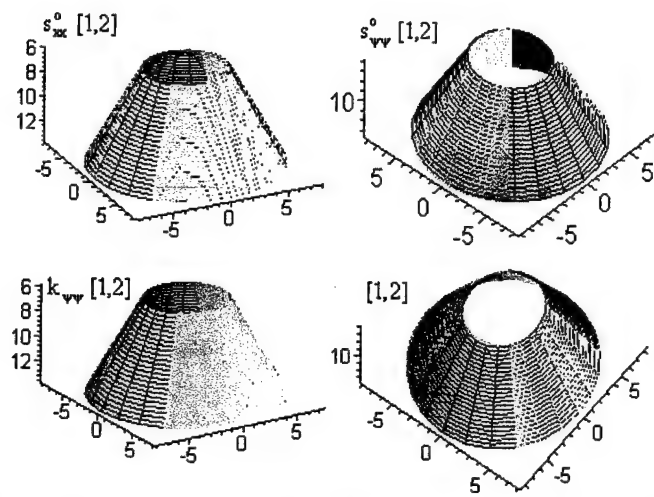


Fig.11 Signal components and modal voltage of (1,2) mode, Model-2.

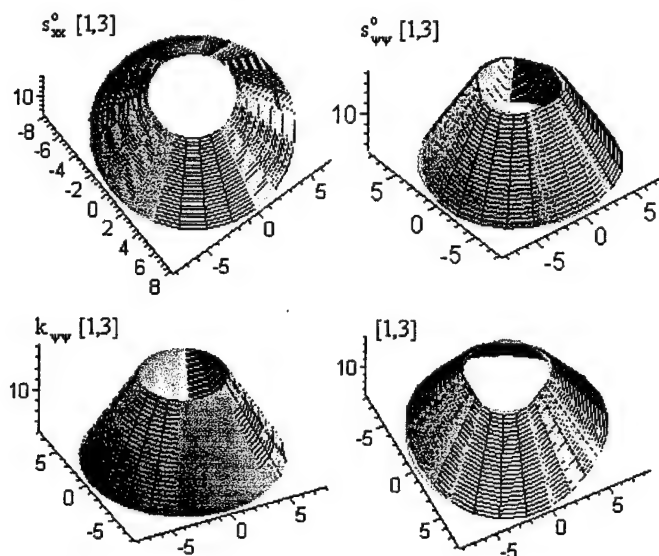


Fig.12 Signal components and modal voltage of (1,3) mode, Model-2.

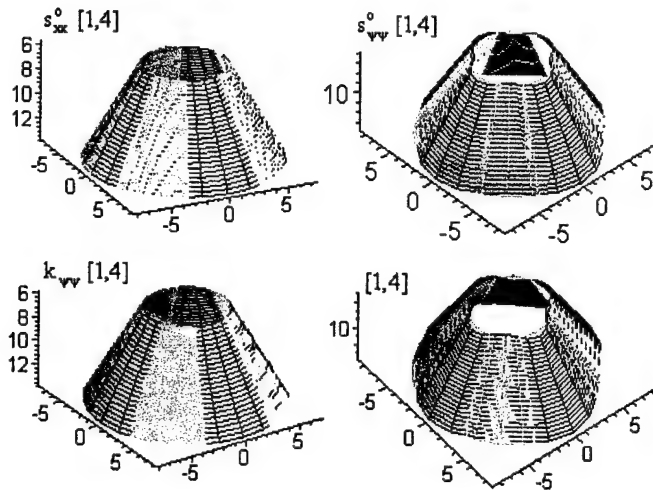


Fig.13 Signal components and modal voltage of (1,4) mode, Model-2.

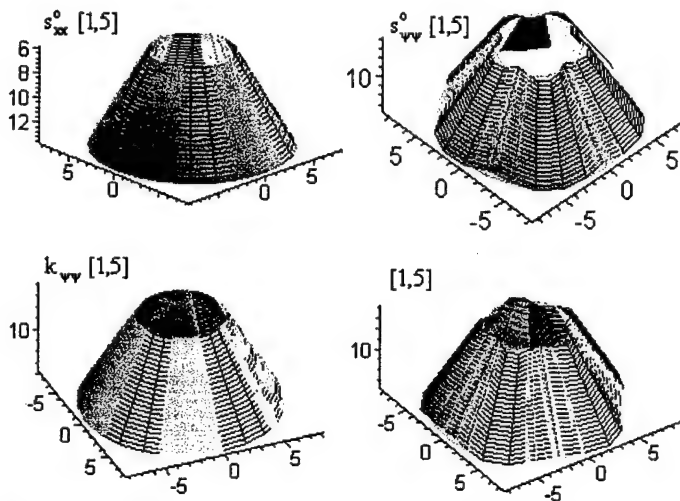


Fig.14 Signal components and modal voltage of (1,5) mode, Model-2.

Model-2, the Second Mode Group (2,m=2-5)

Distributed micro-signal components and modal voltages of the second mode group (2,m=2-5) of Model-2 are presented in **Figures 15-18**. Arrangements of component plots are similar to the second mode group of Model-1. The bottom-left signal distribution denotes ***the (k,m)-th modal voltage***, including all contributing signal components. Note that the longitudinal bending strain exists due to the selected displacement function with $p=2$. Note that the spatially distributed signal generations basically exhibit distinct modal characteristics and the spatially distributed signal patterns – ***the modal voltages*** – clearly reveal the distinct modal dynamic and micro-strain characteristics of conical shells. (Usually, high strain regions result in high signal magnitudes.) Observing these micro-neural signal components (i.e., the longitudinal/circumferential membrane components and the longitudinal/circumferential bending components) and comparing these two conical shell models suggests that 1) the dominating micro-signal component among the four signal components is the circumferential membrane component, 2) the micro-signals resulting from the nonlinear membrane strain is

insignificant, and 3) the circumferential component dominates the signal generation for lower shell modes and deep shells.

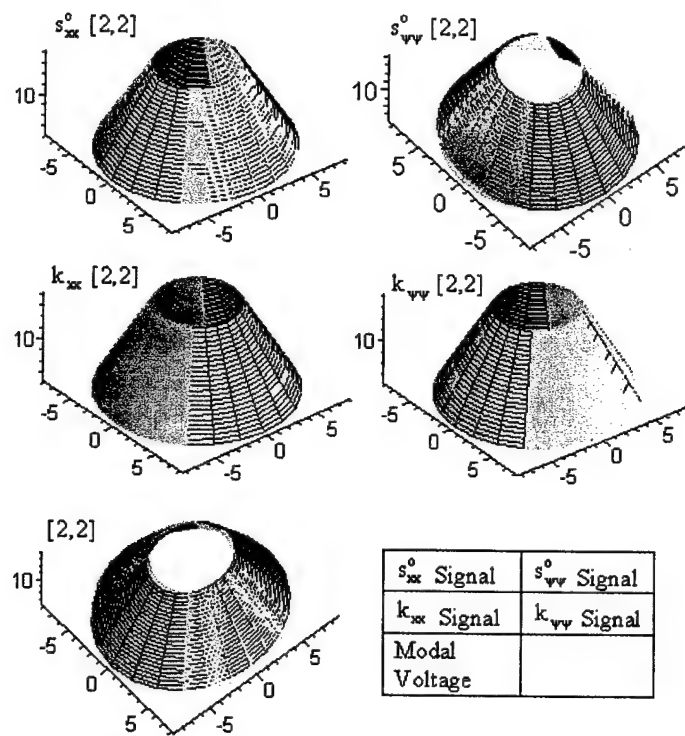


Fig.15 Signal components and modal voltage of (2,2) mode, Model-2.

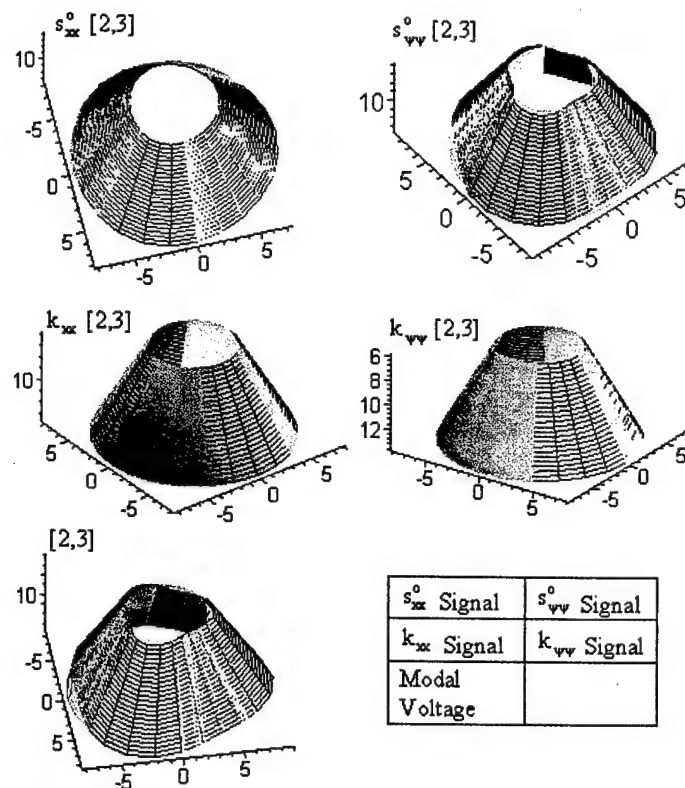


Fig.16 Signal components and modal voltage of (2,3) mode, Model-2.

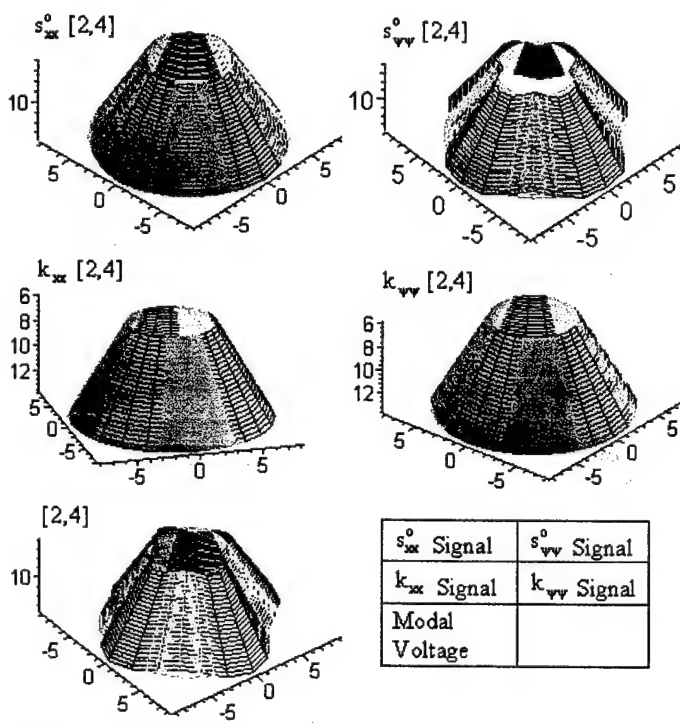


Fig.17 Signal components and modal voltage of (2,4) mode, Model-2.

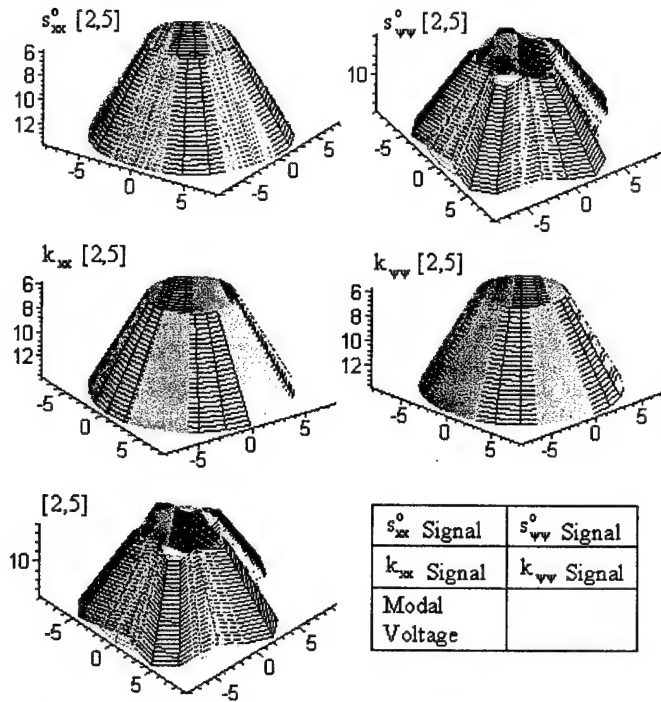


Fig.18 Signal components and modal voltage of (2,5) mode, Model-2.

CONCLUSIONS

Health monitoring and diagnosis is an important issue in modern high-performance precision structures and systems. Although dynamics and vibration of conical shell structures have been investigated over the years, distributed sensing and control of precision conical shells have not been thoroughly investigated. Conventional “discrete” add-on sensors, such as proximeters, LVDT, and accelerometers, usually add additional weights and often influence dynamic responses of precision structures and machines. However, unlike conventional discrete add-on sensors, thin-film piezoelectric layers are lightweight and they can be spatially spread and distributed over the surfaces of precision structures. Accordingly, these distributed piezoelectric layers can serve as distributed neurons and actuators in sensing and control of advanced structures and machines. Dynamic sensing characteristics, micro-signal generations, and distributed modal voltages of truncated nonlinear conical shell sections with infinitesimal piezoelectric neurons are investigated in this study. Signal generation of distributed neuron sensors laminated on nonlinear conical shells was defined first. Microscopic sensing signal generations for free-free truncated nonlinear conical were defined based on the Donnel-Mushtari-Valsov theory and assumed mode shape functions with a polynomial expression $(x/x_2)^p$ for the longitudinal waves and trigonometric (sine or cosine) expression for the circumferential waves.

Micro-neural signals, modal voltages and distributed sensing components of two free-free truncated nonlinear conical shells were investigated and their sensitivities discussed in case studies. Two mode groups ($p=1,2$) and four modal signals ($m=2-5$) of the two conical shell models were calculated and plotted. Directional micro-signal components (i.e., the longitudinal membrane component, the circumferential membrane component, the longitudinal bending

component, and the circumferential bending component) and spatially distributed modal voltages of the two conical shell models were investigated. These microscopic signal generations reveal that the dominating signal component among the four contributing micro-signal components is the circumferential membrane component and this circumferential component becomes even more significant in deep shells. Both geometry and boundary conditions influence modal characteristics, strain distributions, as well as signal generations. The free-free deep truncated conical shell has smaller openings at two ends and higher strains occur at these ends, resulting in increased modal signals. Modal signals induced by the geometrical nonlinearity of the nonlinear conical shell are minimal as compared with those generated by the linear components of the conical shell [21]. The modal signals of the nonlinear component are only 2~5% of the total modal signal in these analyses. The spatially distributed neural signal patterns – ***the modal voltages*** – clearly represent the distinct modal dynamic characteristics and micro-strain variations of conical shells.

ACKNOWLEDGEMENT

This research is supported, in part, by a grant (F49620-98-1-0467) from the Air Force Office of Scientific Research (Project Manager: Brian Sanders). This support is gratefully acknowledged.

REFERENCES

1. U. Gabbert and H.S. Tzou Editors 2001 *Smart Structures and Structronic Systems* IUTAM Symposium on Smart Structures and Structronic Systems, Kluwer Academic Publishers, Dordrecht/Boston/London.
2. H.S. Tzou and G.L. Anderson Editors 1992 *Intelligent Structural Systems* Kluwer Aca. Pub., Dordrecht/Boston.
3. R. Howard, W.K. Chai and H.S. Tzou 2001 *Mechanical Systems and Signal Processing* 15, 629-640. Modal Voltages of linear and non linear Structures Using Distributed Artificial Neurons.
4. R. Howard 1991 *Piezothermoelasticity Applied to Distributed Sensing and Control* M.S. thesis, The University of Kentucky.
5. H.S. Tzou 1993 *Piezoelectric Shells-Distributed Sensing and Control of Continua* Kluwer Academic Publishers, Boston/Dordrecht.
6. W.C.L. Hu 1964 NASA Report TN D-2666. Free Vibration of Conical Shells.
7. D.H. Platus 1965 NASA Report TN D-2767. Conical Shell Vibrations.
8. R.A. Newton 1966 *AIAA J.* 4, 1303-1305. Free Vibrations of Rocket Nozzles.
9. W.C.L. Hu, J.F. Gormley and U.S. Lindholm 1966 NASA Report CR 384. Flexural Vibrations of Conical Shells with Free Edges.
10. F.A. Krause 1968 *Natural Frequencies and Mode Shapes of the Truncated Conical Shell with Free Edges* Ph.D. dissertation, The University of Arizona.
11. V.G. Bazhenov and V. Igonicheva 1987 *Prikladnaya Mekhanika* 23, 10-17. Nonlinear Analysis of Nonaxisymmetric Buckling of Cylindrical and Conical Shells in Axial Impact.
12. B. Wang and C.W.S. To 1991 *J. of Sound and Vibration* 150, 509-516. Vibration Analysis of Truncated Conical Thin Shell Structures.

13. C.W. Lim and K.M. Liew 1996 *Int. J. Solids Structures* 33, 451-468. Vibration of Shallow Conical Shells with Shear Flexibility: A First Order Theory.
14. L. Tong 1996 *Transaction of the ASME, Journal of Vibration & Acoustics* 118, 164-168. Effect of Axial Load on Free Vibration of Orthotropic Truncated Conical Shells
15. C.S. Xu, Z.Q. Xia and C.Y. Chia 1996 *Int. J. Non-Linear Mechanics* 31, 139-154. Nonlinear Theory and Vibration Analysis of Laminated Truncated, Thick, Conical Shells
16. H.S. Tzou, J.P. Zhong and M.C. Natori 1993 *ASME Journal of Vibration & Acoustics* 115, 40-46. Sensor Mechanics of Distributed Shell Convolving Sensors Applied to Flexible Rings
17. H.S. Tzou, Y. Bao and V.B. Venkayya 1996 *Journal of Sound & Vibration* 197, 207-224. Study of Segmented Transducers Laminated On Cylindrical Shells, Part-1: Sensor Patches
18. H.S. Tzou and D.W. Wang 2002 *Journal of Sound and Vibration* 254, 203-218. Micro-sensing Characteristics and Modal Voltages of Linear/nonlinear Toroidal Shell
19. H.S. Tzou and J.H. Ding 2001 *Proceedings of DETC'01, ASME 2001 Design Engineering Technical Conferences and Computers and Information in Engineering Conference*, Pittsburgh, Pennsylvania, (Paper No. DETC2001/VIB-21545). Distributed Modal Signals of Nonlinear Paraboloidal Shells with Distributed Neurons
20. H.S. Tzou 1992 *Precision Sensors, Actuators, and Systems*, H.S. Tzou and T. Fukuda, (Editors), Kluwer Academic Publishers, Dordrecht /Boston /London, 175-218. Thin-Layer Distributed Piezoelectric Neurons and Muscles: Electromechanics and Applications
21. H.S. Tzou, W.K. Chai and D.W. Wang 2003 *Journal of Sound & Vibration* 260, 589-609. Modal Voltages and Micro-Signal Analysis of Conical Shells of Revolution
22. H.S. Tzou and R.J. Yang 2000 *Journal of Theoretical and Applied Mechanics* 38, 623-644. Nonlinear Piezo-thermoelastic Shell Theory applied to Control of Variable-geometry Shells (xConeNonSen3F.ShlConeNon)

CHAPTER 6

MICRO-ACTUATION CHARACTERISTICS OF CONICAL SHELL SECTIONS

ABSTRACT

Conical shell has a large load carrying capacity per unit weight due to its high-strength, high-rigidity and light-weight properties. Rocket fairings, load carrying structures of solid rocket motor case, e.g., inter-stage joint, satellite-rocket joint, etc., usually take the shape of conical shell sections. This paper is to evaluate spatially distributed microscopic control characteristics of distributed actuator patches bonded on conical shell surfaces. The converse effect of piezoelectric materials has been recognized as one of the best electromechanical effects for precision distributed control applications. The resultant control forces and micro-control actions induced by the distributed actuators depend on applied voltages, geometrical (e.g., spatial segmentation and shape) and material (i.e., various actuator materials) properties. Mathematical models and modal domain governing equations of the conical shell section laminated with distributed actuator patches are presented first, followed by formulations of distributed control forces and micro-control actions which can be divided into longitudinal/circumferential membrane and bending control components. Spatially distributed electromechanical microscopic actuation characteristics and control effects resulting from various longitudinal/circumferential actions of actuator patches are evaluated.

INTRODUCTION

Conical shells and components are commonly found in structures of many vehicular/machine applications, such as nozzles, injectors, rocket fairings, and turbine engines. Effective distributed control of the conical shell section can enhance its performance accuracy, precision and reliability. Free vibration analysis and flexural vibrations of conical shells with free edges were studied by Hu, et al. [1,2]. Krause investigated natural frequencies and vibration characteristics of truncated conical shells with free edges [3]. Tong examined the effect of axial load on free vibration of orthotropic truncated conical shells [4]. Recent development of smart materials further advances distributed actuation technologies that can be spatially laminated over structures [5]. Distributed control of conical shell laminated with full and diagonal actuators was investigated [6]. In addition, distributed control of paraboloidal shells was also studied [7]. Moreover, distributed sensing of linear structures using distributed artificial neurons [8], and distributed sensing of linear [9] and nonlinear conical shells [10] or conical shell section has been investigated recently. This study focuses on dynamic distributed control and microscopic control actions of conical shell sections laminated with segmented piezoelectric

actuator patches. Mathematical models and modal domain governing equations of the conical shell section laminated with distributed actuator patches are presented first, followed by formulations of distributed control forces and micro-control actions which can be divided into longitudinal/circumferential membrane and bending control components. Spatially distributed electromechanical microscopic actuation characteristics and control effects resulting from various longitudinal/circumferential actions are evaluated.

CONTROL OF CONICAL SHELLS WITH DISTRIBUTED ACTUATORS

A conical shell structure laminated with piezoelectric actuator layers is illustrated in Figure 1 where x denotes the longitudinal direction, ψ the circumferential direction, and z the transverse direction. The geometric parameters of a conical shell are: the Lamé parameters $A_1 = 1$ and $A_2 = x \sin \beta^*$, the radii of curvature $R_1 = \infty$ and $R_2 = x \tan \beta^*$. Independent modal control of conical shells with distributed piezoelectric actuators is discussed in this section. Micro-control actions and their directional control characteristics induced by actuator patches are discussed in the next section.

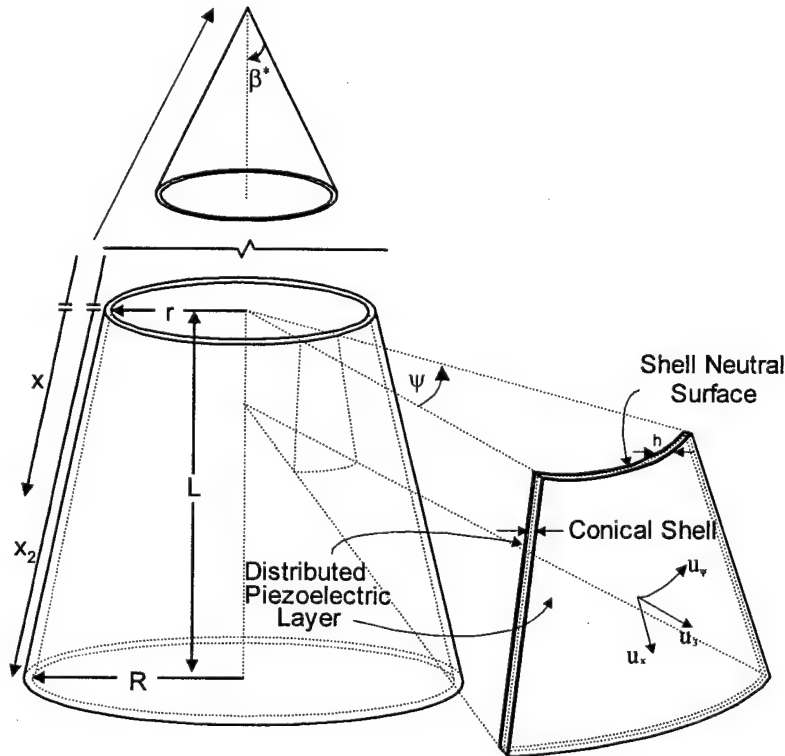


Fig.1 A Conical shell section and its coordinate system.

The modal expansion concept implies that the total response of the conical shell is composed of all participating modes. Thus, independent modal control characteristic of conical shells can be independently defined for each natural mode, considered there is no spillover and modal coupling.

$$\ddot{\eta}_m + 2\zeta_m \omega_m \dot{\eta}_m + \omega_m^2 \eta_m = F_m \quad (1)$$

where $\eta_m(t)$ is the modal participation factor; ζ_m is the modal damping ratio; ω_m is the natural frequency; F_m is the modal force; and the subscript m denotes the m -th mode. The generic modal force F_m of the conical shell structure consists of two primary components: 1) the mechanical force induced by an external loads F_i and 2) the control force induced by the distributed actuators $L_i^c(\phi_3)$ with a transversely applied electric control signal ϕ_3 (in *italic*).

$$F_m = \frac{1}{\rho h N_m} \int_{\alpha_1} \int_{\alpha_2} \left\{ \sum_{i=1}^3 [F_i + L_i^c(\phi_3)] U_{i_m} \right\} A_1 A_2 d\alpha_1 d\alpha_2 = \hat{F}_m + \hat{F}_m^c \quad (2)$$

where ρ is the shell mass density; h is the shell thickness; A_1 and A_2 are the Lamé parameters; α_1 and α_2 respectively denote the x and ψ directions; $\hat{F}_m = \frac{1}{\rho h N_m} \int_{\alpha_1} \int_{\alpha_2} \left\{ \sum_{i=1}^3 F_i U_{i_m} \right\} A_1 A_2 d\alpha_1 d\alpha_2$, $\hat{F}_m^c = \frac{1}{\rho h N_m} \int_{\alpha_1} \int_{\alpha_2} \left\{ \sum_{i=1}^3 L_i^c(\phi_3) U_{i_m} \right\} A_1 A_2 d\alpha_1 d\alpha_2$ and $N_m = \int_{\alpha_1} \int_{\alpha_2} \left(\sum_{i=1}^3 U_{i_m}^2 \right) A_1 A_2 d\alpha_1 d\alpha_2$.

(Note that *italic* ϕ_3 denotes the control signal used in control action analysis presented later). $L_i^c(\phi_3)$ is Love's control operator induced by the converse piezoelectric effects and only a transverse applied voltage ϕ_3 is considered. The subscript i denote the coordinate directions, i.e., x , ψ and 3. The generic control operators imposed to a generic double-curvature shell in three directions are contributed by membrane control forces N_{ij}^c and counteracting control moments M_{ij}^c [11].

$$L_1^c \{ \phi_3 \} = -\frac{1}{A_1 A_2} \left\{ \frac{\partial}{\partial \alpha_1} (N_{11}^c A_2) - N_{22}^c \frac{\partial}{\partial \alpha_1} A_2 + \frac{1}{R_1} \left[\frac{\partial}{\partial \alpha_1} (M_{11}^c A_2) - M_{22}^c \frac{\partial}{\partial \alpha_1} A_2 \right] \right\} \quad (3)$$

$$L_2^c \{ \phi_3 \} = -\frac{1}{A_1 A_2} \left\{ \frac{\partial}{\partial \alpha_2} (N_{22}^c A_1) - N_{11}^c \frac{\partial}{\partial \alpha_2} A_1 + \frac{1}{R_2} \left[\frac{\partial}{\partial \alpha_2} (M_{22}^c A_1) - M_{11}^c \frac{\partial}{\partial \alpha_2} A_1 \right] \right\} \quad (4)$$

$$L_3^c \{ \phi_3 \} = -\frac{1}{A_1 A_2} \left\{ \frac{\partial}{\partial \alpha_1} \left(\frac{1}{A_1} \frac{\partial (M_{11}^c A_2)}{\partial \alpha_1} - \frac{M_{22}^c}{A_1} \frac{\partial A_2}{\partial \alpha_1} \right) + \frac{\partial}{\partial \alpha_2} \left(\frac{1}{A_2} \frac{\partial (M_{22}^c A_1)}{\partial \alpha_2} - \frac{M_{11}^c}{A_2} \frac{\partial A_1}{\partial \alpha_2} \right) - A_1 A_2 \left(\frac{N_{11}^c}{R_1} + \frac{N_{22}^c}{R_2} \right) \right\}. \quad (5)$$

Substituting the Lamé parameters (i.e., $A_1 = 1$ and $A_2 = x \sin \beta^*$), radii of curvature (i.e., $R_1 = \infty$ and $R_2 = x \tan \beta^*$) and two principle directions $\alpha_1 = x$, $\alpha_2 = \psi$ of the conical shell into the generic control forces yields Love's control operators of conical shells.

$$L_x^c \{ \phi_3 \} = - \left\{ \frac{\partial N_{xx}^c}{\partial x} + \frac{1}{x} (N_{xx}^c - N_{\psi\psi}^c) \right\} \quad (6)$$

$$L_\psi^c \{ \phi_3 \} = - \frac{1}{x \sin \beta^*} \left\{ \frac{\partial N_{\psi\psi}^c}{\partial \psi} + \frac{1}{x \tan \beta^*} \frac{\partial M_{\psi\psi}^c}{\partial \psi} \right\} \quad (7)$$

$$L_3^c \{ \phi_3 \} = - \left\{ \frac{2}{x} \frac{\partial M_{xx}^c}{\partial x} + \frac{\partial^2 M_{xx}^c}{\partial x^2} - \frac{1}{x} \frac{\partial M_{\psi\psi}^c}{\partial x} + \frac{1}{x^2 \sin^2 \beta^*} \frac{\partial^2 M_{\psi\psi}^c}{\partial \psi^2} - \frac{N_{\psi\psi}^c}{x \tan \beta^*} \right\} \quad (8)$$

The mode shape functions of the conical shell section with free boundary condition at both major and minor ends are based on the Donnell-Mushtari-Vlasov theory [3,9]. Thus, these mode shape functions are expressed as

$$U_{xm} = U_{xm}(x) \cos(m\psi) \sin \omega_m t \quad (9)$$

$$U_{\psi m} = U_{\psi m}(x) \sin(m\psi) \sin \omega_m t \quad (10)$$

$$U_{3m} = U_{3m}(x) \cos(m\psi) \sin \omega_m t \quad (11)$$

where m is the wave number and $m=2\dots\infty$; ω_m is the natural frequency. $U_{xm}(x)$, $U_{\psi m}(x)$ and $U_{3m}(x)$ are arbitrary displacement functions of x , satisfying the free-free displacement boundary conditions and it selected as $(x/x_2)^p$ where p denotes the longitudinal mode. $U_{xm}(x) \cos m\psi$ is the longitudinal mode shape function; $U_{\psi m}(x) \sin m\psi$ is the circumferential mode shape function; and $U_{3m}(x) \cos m\psi$ is the transverse mode shape function. Thus, the modal forces induced by distributed mechanical loading (i.e., external forces) and the distributed actuator (i.e., control forces) become

$$\begin{aligned} \hat{F}_m &= \frac{1}{\rho h N_m} \int_x \int_\psi \{ F_x [U_{xm}(x) \cos(m\psi)] + F_\psi [U_{\psi m}(x) \sin(m\psi)] \\ &\quad + F_3 [U_{3m}(x) \cos(m\psi)] \} x \sin \beta^* d\phi d\psi \end{aligned} \quad (12)$$

$$\begin{aligned} \hat{F}_m^c &= \frac{1}{\rho h N_m} \int_x \int_\psi \left\{ - \left\{ \frac{\partial N_{xx}^c}{\partial x} + \frac{1}{x} (N_{xx}^c - N_{\psi\psi}^c) \right\} \cdot U_{xm}(x) \cos(m\psi) - \frac{1}{x \sin \beta^*} \right. \\ &\quad \cdot \left\{ \frac{\partial N_{\psi\psi}^c}{\partial \psi} + \frac{1}{x \tan \beta^*} \frac{\partial M_{\psi\psi}^c}{\partial \psi} \right\} U_{\psi m}(x) \sin(m\psi) - \left\{ \frac{2}{x} \frac{\partial M_{xx}^c}{\partial x} + \frac{\partial^2 M_{xx}^c}{\partial x^2} - \frac{1}{x} \frac{\partial M_{\psi\psi}^c}{\partial x} \right. \\ &\quad \left. + \frac{1}{x^2 \sin^2 \beta^*} \frac{\partial^2 M_{\psi\psi}^c}{\partial \psi^2} - \frac{N_{\psi\psi}^c}{x \tan \beta^*} \right\} \cdot U_{3m}(x) \cos(m\psi) \} \cdot x \sin \beta^* dx d\psi \end{aligned} \quad (13)$$

and

$$N_m = \int_x \int_\psi \left\{ \left[\left(\frac{x}{x_2} \right)^p \cos m\psi \right]^2 + \left[\left(\frac{x}{x_2} \right)^p \sin m\psi \right]^2 + \left[\left(\frac{x}{x_2} \right)^p \cos m\psi \right]^2 \right\} x \sin \beta^* dx d\psi. \quad (14)$$

Detailed distributed control forces and moments induced by distributed actuators are further defined next.

DISTRIBUTED MICRO-CONTROL CHARACTERISTICS

The control forces and moments induced by the piezoelectric actuator with an applied voltage ϕ^a are given as [11]

$$N_{xx}^c = d_{31} Y_p \phi^a \quad (15)$$

$$N_{\psi\psi}^c = d_{32} Y_p \phi^a \quad (16)$$

$$M_{xx}^c = r_x^a d_{31} Y_p \phi^a \quad (17)$$

$$M_{\psi\psi}^c = r_\psi^a d_{32} Y_p \phi^a \quad (18)$$

Substituting actuator induced forces and moments into the generic modal control force expression \hat{F}_m^c and separating them into individual contributing microscopic membrane/bending control actions gives

$$(\hat{T}_m)_{x,mem} = \frac{d_{31} Y_p}{\rho h N_m} \int_x \int_\psi \left\{ \left(-\frac{\partial \phi^a}{\partial x} - \frac{\phi^a}{x} \right) U_{xm}(x) \cos(m\psi) \right\} x \sin \beta^* dx d\psi \quad (19)$$

$$(\hat{T}_m)_{\psi,mem} = \frac{d_{32} Y_p}{\rho h N_m} \int_x \int_\psi \left\{ \frac{1}{x} \phi^a \cdot U_{xm}(x) \cos(m\psi) - \frac{1}{x \sin \beta^*} \left(\frac{\partial \phi^a}{\partial \psi} \right) \right. \\ \left. \cdot U_{\psi m}(x) \sin(m\psi) + \frac{\phi^a}{x \tan \beta^*} U_{3m}(x) \cos(m\psi) \right\} x \sin \beta^* dx d\psi \quad (20)$$

$$(\hat{T}_m)_{x,bend} = \frac{r_x^a d_{31} Y_p}{\rho h N_m} \int_x \int_\psi \left\{ \left[-\frac{2}{x} \frac{\partial \phi^a}{\partial x} - \frac{\partial^2 \phi^a}{\partial x^2} \right] U_{3m}(x) \cos(m\psi) \right\} x \sin \beta^* dx d\psi \quad (21)$$

$$(\hat{T}_m)_{\psi,bend} = \frac{r_\psi^a d_{32} Y_p}{\rho h N_m} \int_x \int_\psi \left\{ \left[-\frac{\cos \beta^*}{x^2 \sin^2 \beta^*} \frac{\partial \phi^a}{\partial \psi} \right] U_{\psi m}(x) \sin(m\psi) \right. \\ \left. + \left[\frac{1}{x} \frac{\partial \phi^a}{\partial x} - \frac{1}{x^2 \sin^2 \beta^*} \frac{\partial^2 \phi^a}{\partial \psi^2} \right] U_{3m}(x) \cos(m\psi) \right\} x \sin \beta^* dx d\psi \quad (22)$$

Note that $(\hat{T}_m)_{x,mem}$ is the membrane force component in the x direction, $(\hat{T}_m)_{\psi,mem}$ is the membrane force component in the ψ direction, $(\hat{T}_m)_{x,bend}$ is the bending force component in the x direction, and $(\hat{T}_m)_{\psi,bend}$ is the bending force component in the ψ direction. Assume the piezoelectric actuator is hexagonal structure ($C_{6v} = 6\text{mm}$) i.e., $d_{32} = d_{31}$, with uniform thickness and recall that the conical shell is also constant thickness. Thus, the distances measured from the shell neutral surface to the actuator mid-surface are $r_x^a = r_\psi^a = r^a$. The micro-control actions defined in Eqs.(19)-(22) now become

$$(\hat{T}_m)_{x,mem} = \frac{d_{31} Y_p}{\rho h N_m} \int_x \int_{\psi} \left\{ \left(-\frac{\partial \phi^a}{\partial x} - \frac{\phi^a}{x} \right) U_{xm}(x) \cos(m\psi) \right\} x \sin \beta^* dx d\psi \quad (23)$$

$$(\hat{T}_m)_{\psi,mem} = \frac{d_{31} Y_p}{\rho h N_m} \int_x \int_{\psi} \left\{ \frac{1}{x} \phi^a \cdot U_{xm}(x) \cos(m\psi) - \frac{1}{x \sin \beta^*} \left(\frac{\partial \phi^a}{\partial \psi} \right) \right. \\ \left. \cdot U_{\psi m}(x) \sin(m\psi) + \frac{\phi^a}{x \tan \beta^*} U_{3m}(x) \cos(m\psi) \right\} x \sin \beta^* dx d\psi \quad (24)$$

$$(\hat{T}_m)_{x,bend} = \frac{r^a d_{31} Y_p}{\rho h N_m} \int_x \int_{\psi} \left\{ \left[-\frac{2}{x} \frac{\partial \phi^a}{\partial x} - \frac{\partial^2 \phi^a}{\partial x^2} \right] U_{3m}(x) \cos(m\psi) \right\} x \sin \beta^* dx d\psi \quad (25)$$

$$(\hat{T}_m)_{\psi,bend} = \frac{r^a d_{31} Y_p}{\rho h N_m} \int_x \int_{\psi} \left\{ \left[-\frac{\cos \beta^*}{x^2 \sin^2 \beta^*} \frac{\partial \phi^a}{\partial \psi} \right] U_{\psi m}(x) \sin(m\psi) + \left[\frac{1}{x} \frac{\partial \phi^a}{\partial x} \right. \right. \\ \left. \left. - \frac{1}{x^2 \sin^2 \beta^*} \frac{\partial^2 \phi^a}{\partial \psi^2} \right] U_{3m}(x) \cos(m\psi) \right\} x \sin \beta^* dx d\psi \quad (26)$$

Thus, the generic control force \hat{F}_m^c can be explicitly defined by its four contributing micro-control actions, i.e.,

$$\hat{F}_m^c = (\hat{T}_m)_{x,mem} + (\hat{T}_m)_{\psi,mem} + (\hat{T}_m)_{x,bend} + (\hat{T}_m)_{\psi,bend}. \quad (27)$$

MICRO-CONTROL ACTIONS OF PATCH ACTUATORS

Note that $F_m = \hat{F}_m + \hat{F}_m^c$ and the mechanical input \hat{F}_m is neglected in the control action analysis. The transverse actuating voltages $\phi^a(x, \psi, t)$ applied to an actuator patch defined from x_1^* to x_2^* in the longitudinal direction and ψ_1^* to ψ_2^* in the circumferential direction can be expressed by a time dependent part and a spatial distribution part,

$$\phi^a(x, \psi, t) = \phi^a(t) [u_s(x - x_1^*) - u_s(x - x_2^*)] [u_s(\psi - \psi_1^*) - u_s(\psi - \psi_2^*)] \quad (28)$$

where $u_s(\cdot)$ is the unit step function: $u_s(\psi - \psi_i^*) = 1$ when $\psi > \psi_i^*$, and = 0 when $\psi < \psi_i^*$. Thus, the spatial derivatives of the transverse actuating signals in Eqs.(23)-(26) are

$$\frac{\partial}{\partial x} \phi^a(x, \psi, t) = \phi^a(t) [\delta(x - x_1^*) - \delta(x - x_2^*)] [u_s(\psi - \psi_1^*) - u_s(\psi - \psi_2^*)] \quad (29)$$

$$\frac{\partial}{\partial \psi} \phi^a(x, \psi, t) = \phi^a(t) [u_s(x - x_1^*) - u_s(x - x_2^*)] [\delta(\psi - \psi_1^*) - \delta(\psi - \psi_2^*)] \quad (30)$$

where $\delta(\cdot)$ is a Dirac delta function: $\delta(\psi - \psi_i^*) = 1$ when $\psi = \psi_i^*$, and = 0 when $\psi \neq \psi_i^*$. Thus, the micro-control actions restricted by the segmented electrode on the segmented actuator can

be further explicitly defined accordingly. Substituting the patch definition and further manipulating the four micro-control actions yields

$$(\hat{T}_m)_{x,mem} = -\frac{d_{31} Y_p \phi^a(t) \sin \beta^*}{\rho h N_m} \int_x \{ [x[\delta(x - x_1^*) - \delta(x - x_2^*)] + 1] \cdot U_{xm}(x) \} dx \cdot \int_{\psi} \cos(m\psi) d\psi \quad (31)$$

$$(\hat{T}_m)_{\psi,mem} = \frac{d_{31} Y_p \phi^a(t)}{\rho h N_m} \{ \sin \beta^* \int_x U_{xm}(x) dx \cdot \int_{\psi} \cos(m\psi) d\psi - \int_{\psi} [\delta(\psi - \psi_1^*) - \delta(\psi - \psi_2^*)] \sin(m\psi) d\psi \cdot \int_x U_{\psi m}(x) dx + \cos \beta^* \int_x U_{3m}(x) dx \cdot \int_{\psi} \cos(m\psi) d\psi \} \quad (32)$$

$$(\hat{T}_m)_{x,bend} = \frac{r^a d_{31} Y_p \phi^a(t) \sin \beta^*}{\rho h N_m} \{ \int_x [-2[\delta(x - x_1^*) - \delta(x - x_2^*)] - x \frac{\partial}{\partial x} [\delta(x - x_1^*) - \delta(x - x_2^*)]] U_{3m}(x) dx \cdot \int_{\psi} \cos(m\psi) d\psi \} \quad (33)$$

$$(\hat{T}_m)_{\psi,bend} = \frac{r^a d_{31} Y_p \phi^a(t)}{\rho h N_m} \{ -\frac{1}{\tan \beta^*} \int_x \frac{U_{\psi m}(x)}{x} dx \int_{\psi} [\delta(\psi - \psi_1^*) - \delta(\psi - \psi_2^*)] \cdot \sin(m\psi) d\psi + \sin \beta^* \int_x U_{3m}(x) [\delta(x - x_1^*) - \delta(x - x_2^*)] dx \int_{\psi} \cos(m\psi) d\psi - \frac{1}{\sin \beta^*} \int_x \frac{U_{3m}(x)}{x} dx \cdot \int_{\psi} \frac{\partial}{\partial \psi} [\delta(\psi - \psi_1^*) - \delta(\psi - \psi_2^*)] \cdot \cos(m\psi) d\psi \} \quad (34)$$

These four equations represent directional modal micro-control characteristics of distributed patch actuators laminated on a conical shell. Detailed micro-control characteristics are presented in case studies next.

PARAMETRIC STUDIES OF MICRO-CONTROL ACTIONS

To keep the generality, material parameters, e.g., d_{31} , d_{32} , Y_p and ρ , are assumed unity when evaluating the micro-control actions of conical shell sections. Thus, manipulating these parameters (e.g., $(r^a d_{31} Y_p)/\rho$), one can further extrapolate analysis data and evaluate control characteristics of specific actuator materials and natural modes. Note that the control signal $\phi^a(t)$ is assumed unity for all cases also. Thus, the segmented actuator patches would reveal the true inherent actuator characteristics and micro-control actions. Dimensions of the truncated conical shell model are: major edge radius $R=0.154m$ (6.07in), minor edge radius $r=0.069m$ (2.72in), semi-vertex angle=14.24° (0.248535 rad), shell thickness $h=0.000254m$ (0.01in), actuator placement at $r^a=0.000127m$ (0.005in), and length $L=0.33528m$ (13.2in). The conical shell has free boundary conditions at the top and bottom end edges, Figure 2. Note that the actuator patch is assumed thin, such that its elastic effect is neglected. Piezoelectric actuator patches with an area of 15° in the circumferential direction (i.e., the first patch is from 0-15°, the

next patch is from 15° - 30° and so on in the ψ direction), and 0.02894m in the longitudinal direction are laminated throughout the conical shell section, **Figure 2**. Note that although all actuation characteristics of a full-revolution truncated conical shell are calculated, control actions related to a half of the revolution (i.e., $\psi = \pi$) are presented later.

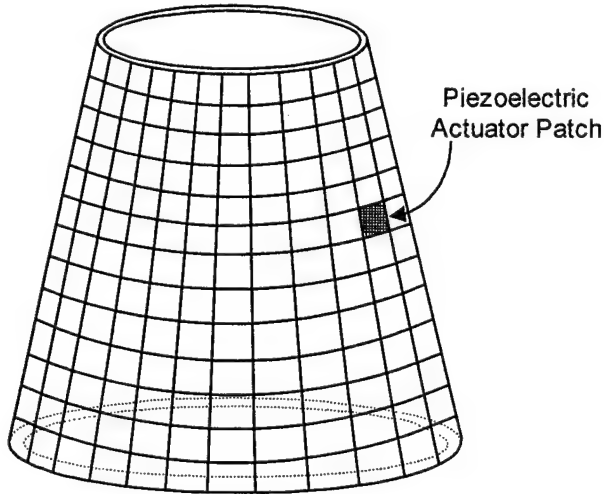


Fig.2 A conical shell laminated with piezoelectric actuator patches.

Recall that $(\hat{T}_m)_{x,mem}$ is the longitudinal micro-membrane control force component, $(\hat{T}_m)_{\psi,mem}$ is the circumferential membrane control force component, $(\hat{T}_m)_{x,bend}$ is the longitudinal bending control component, and $(\hat{T}_m)_{\psi,bend}$ is the circumferential bending control component. These actuator induced micro-control actions of the conical shell modes, i.e., 1st and 2nd x-mode group with $m=2..5$ are analyzed and grouped. Recall that m denotes the circumferential wave number. Each data point on the graph represents the micro-control action of a segmented actuator patch at the corresponding location of the conical shell section.

Mode Group 1: (p=1; m=2-5) Modes

For the first mode group (i.e., $(x/x_2)^p$ with $p=1$) of the conical shell section, longitudinal $U_{xm}(x)$, $U_{\psi m}(x)$ and $U_{3m}(x)$ is (x/x_2) [9]. Detailed longitudinal and circumferential membrane/bending micro-control actions of actuator patches laminated at various locations are plotted in **Figures 3-6** where $m=2-5$ of the 1st mode group, i.e., (1, $m=2-5$). To illustrate the prospective view of the conical shell in micro-actuation characteristics, the half conical shell section remains in the original aspect ratio and both longitudinal and circumferential dimensions (in meter) are used in these figures.

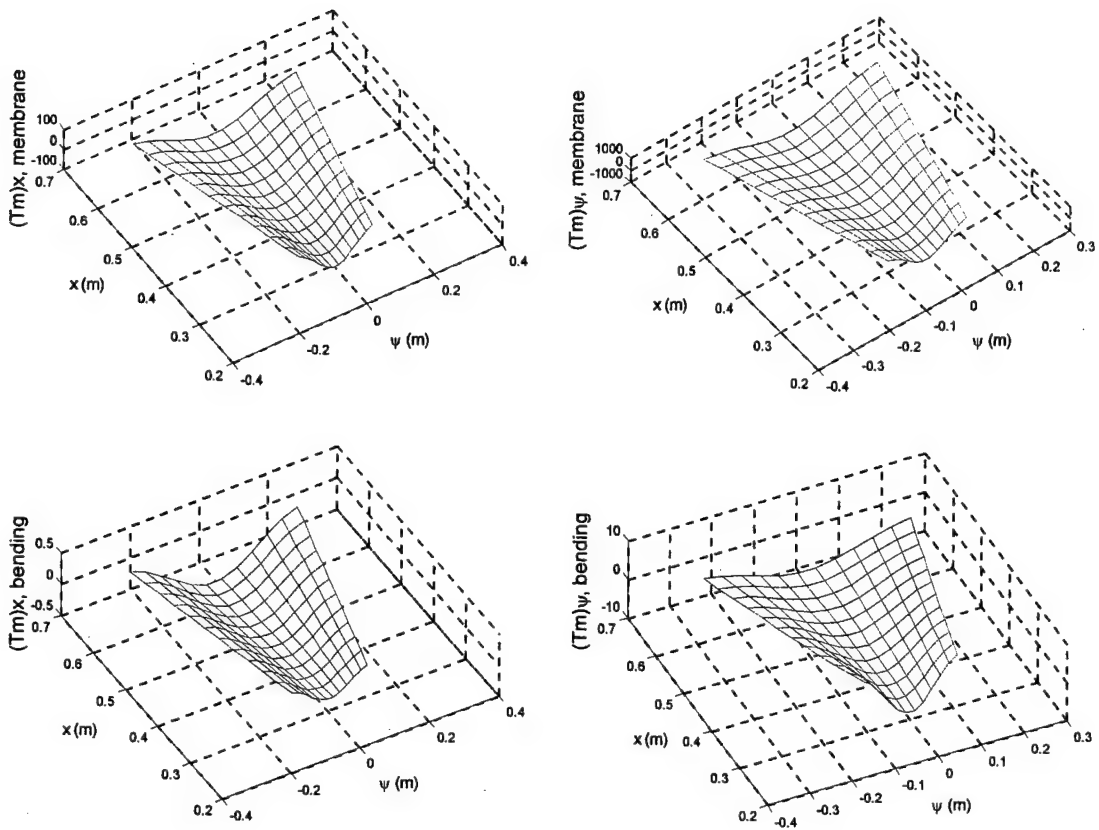
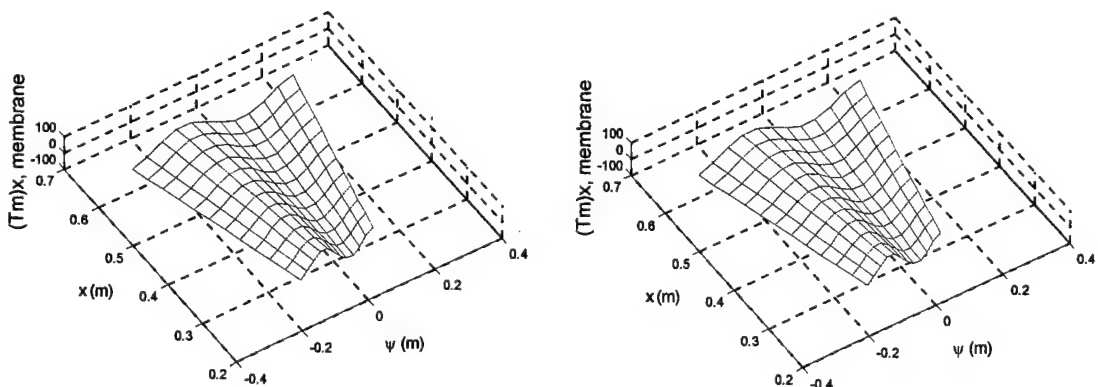


Fig.3 Micro-control actions of the (1,2) conical shell mode.

Top-left: $(\hat{T}_m)_x,_{mem}$; top-right: $(\hat{T}_m)_{y,mem}$; bottom-left: $(\hat{T}_m)_x,_{bend}$; bottom-right: $(\hat{T}_m)_{y,_{bend}}$.



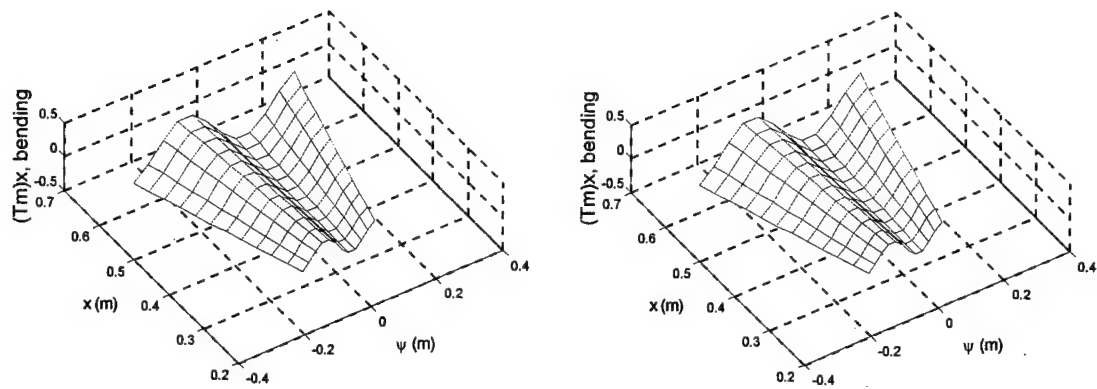


Fig.4 Micro-control actions of the (1,3) conical shell mode.

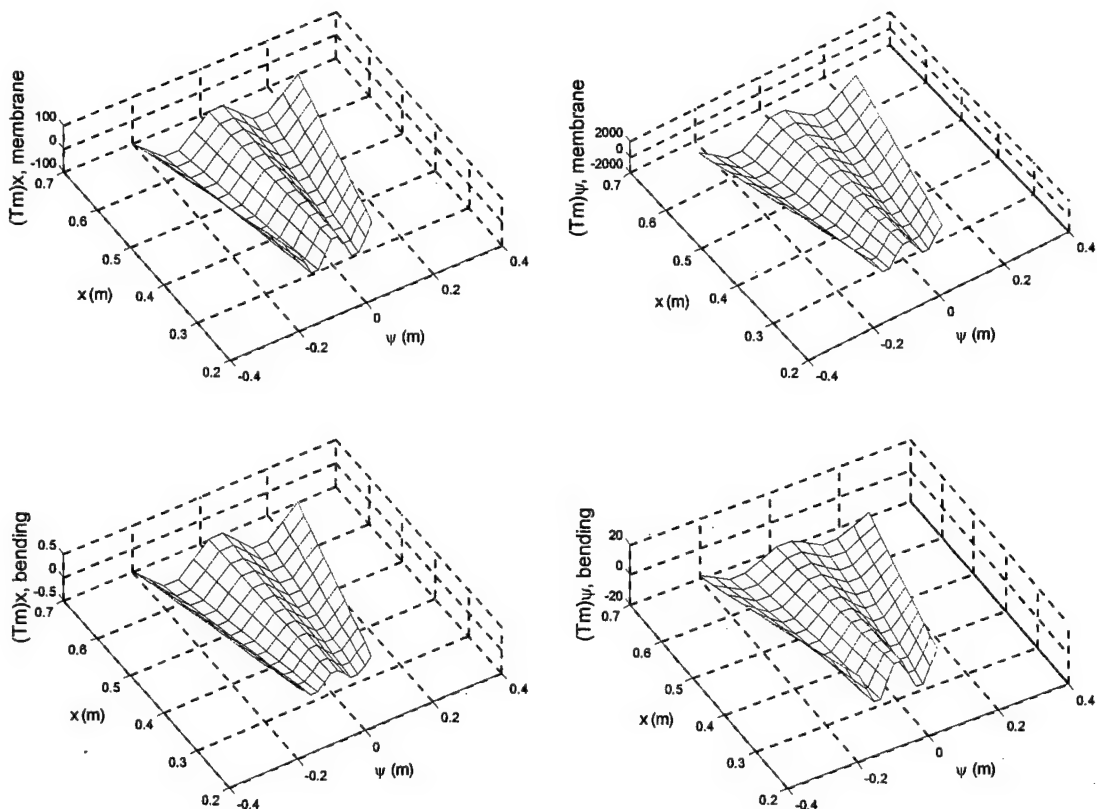


Fig.5 Micro-control actions of the (1,4) conical shell mode.

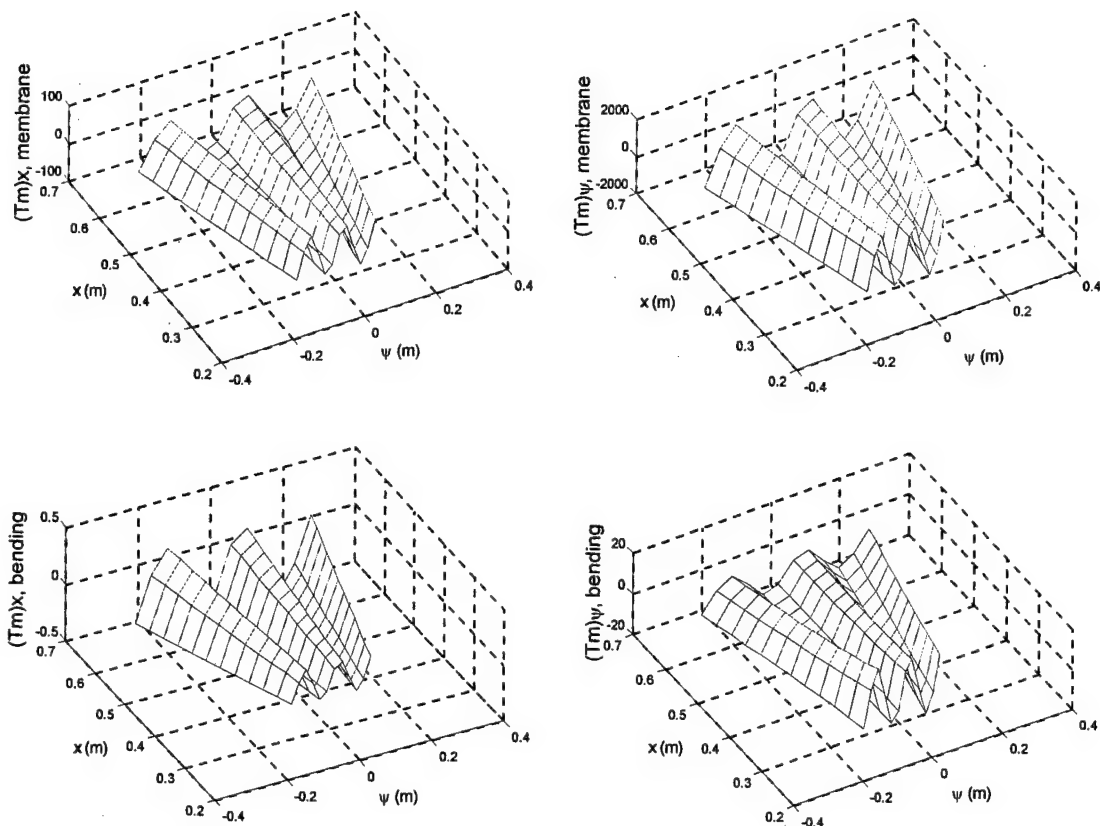
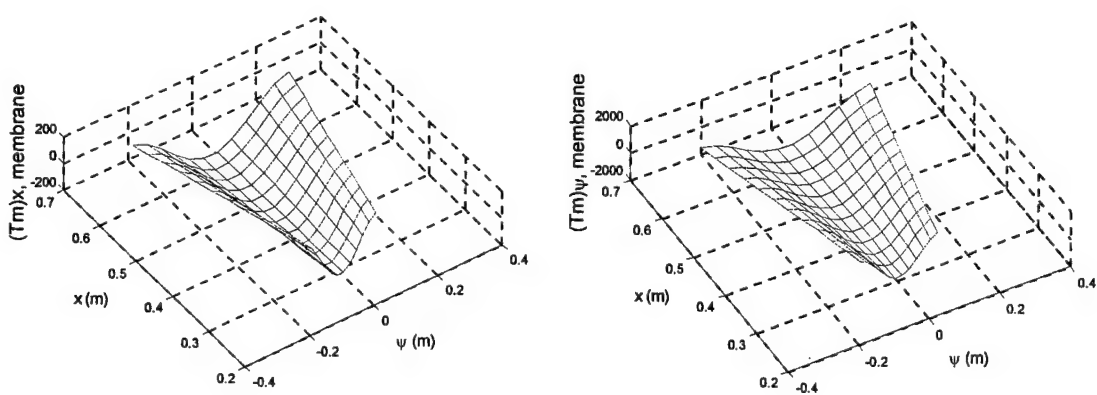


Fig.6 Micro-control actions of the (1,5) conical shell mode.

Mode Group 2: (p=2;m=2-5) Modes

For the second mode group (i.e., $(x/x_2)^p$ with $p=2$) of the conical shell section, the $U_{xm}(x)$, $U_{\psi m}(x)$ and $U_{3m}(x)$ is $(x/x_2)^2$ [9]. Detailed longitudinal and circumferential membrane/bending micro-control actions are plotted in **Figures 7-10** where $m=2-5$ of the 2nd mode group, i.e., (2,m=2-5).



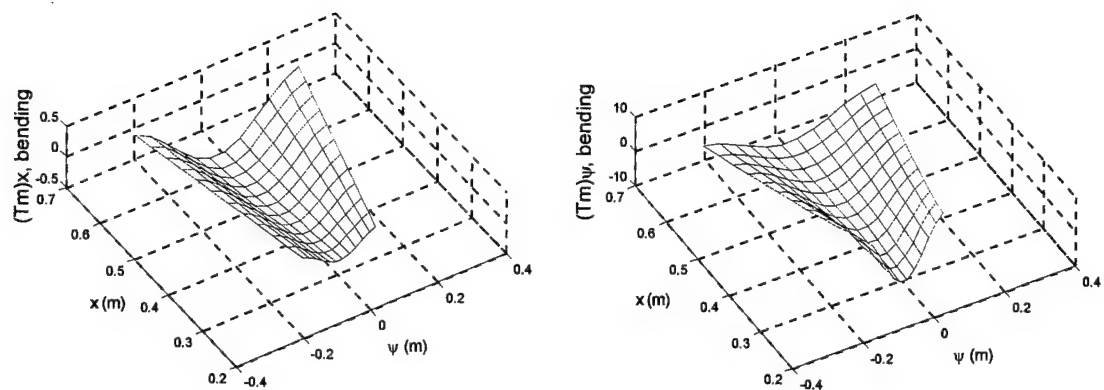


Fig.7 Micro-control actions of the (2,2) conical shell mode.

Top-left: $(\hat{T}_m)_x,mem$; top-right: $(\hat{T}_m)_y,mem$; bottom-left: $(\hat{T}_m)_x,bend$; bottom-right: $(\hat{T}_m)_y,bend$.

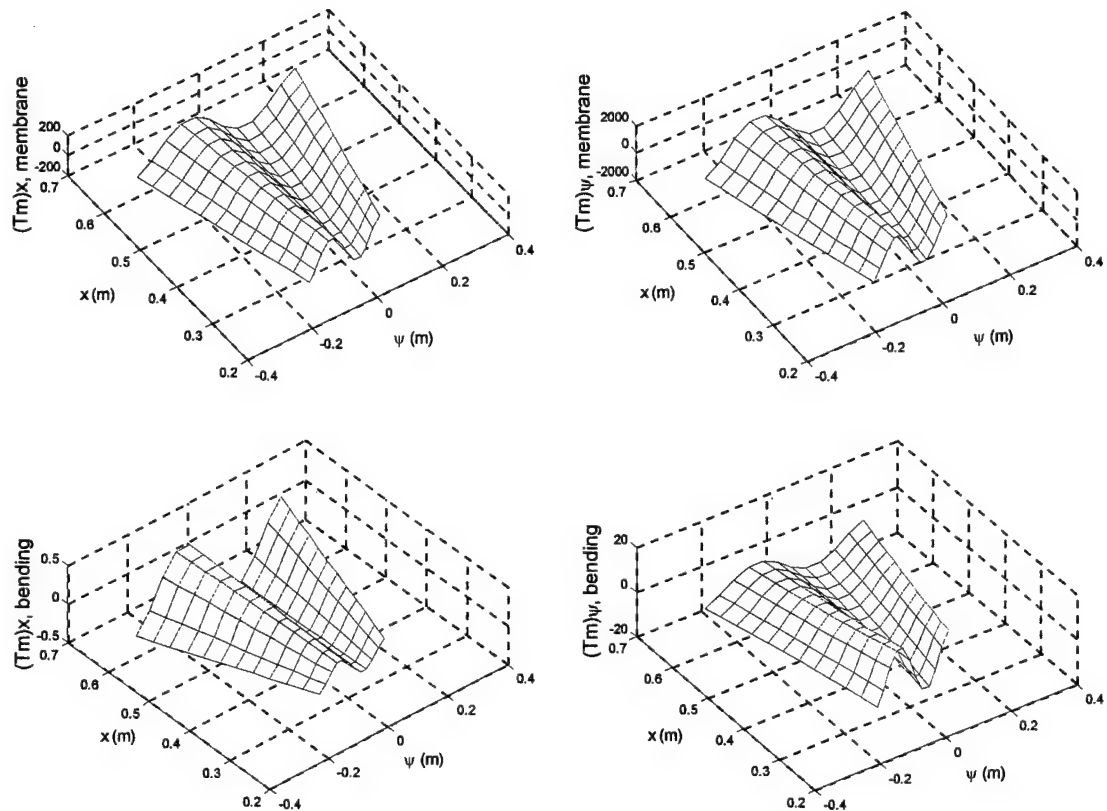


Fig.8 Micro-control actions of the (2,3) conical shell mode.

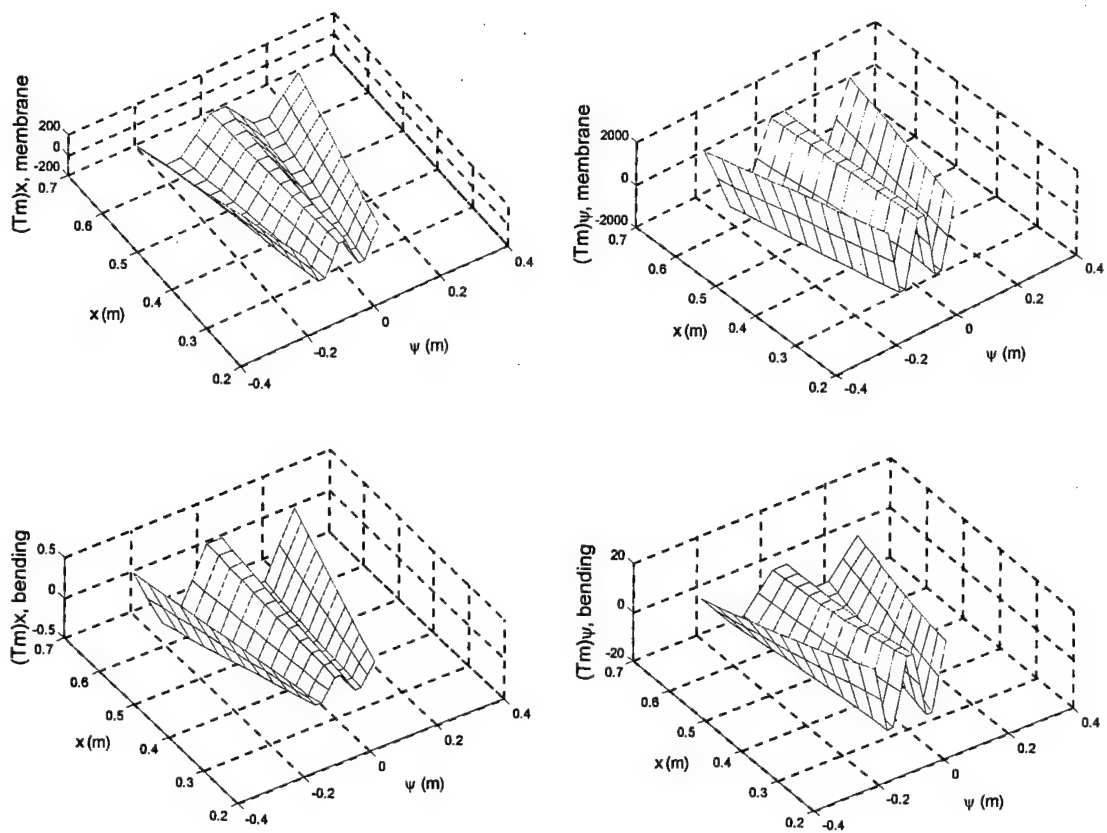
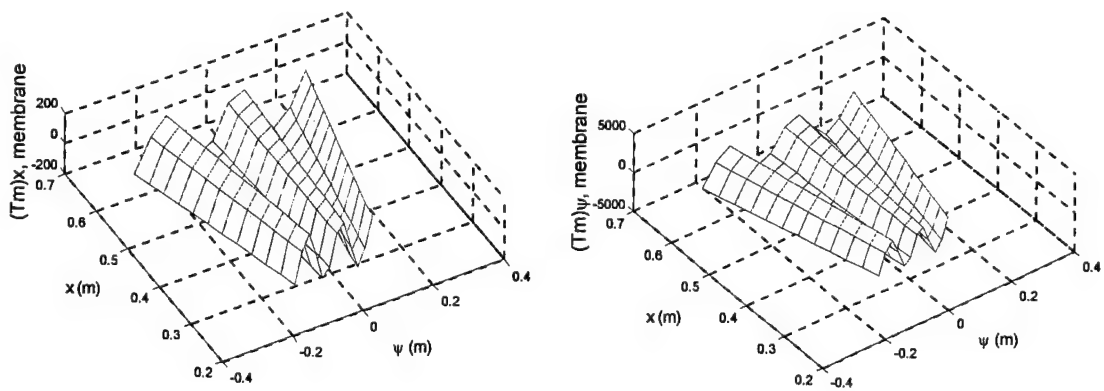


Fig.9 Micro-control actions of the (2,4) conical shell mode.



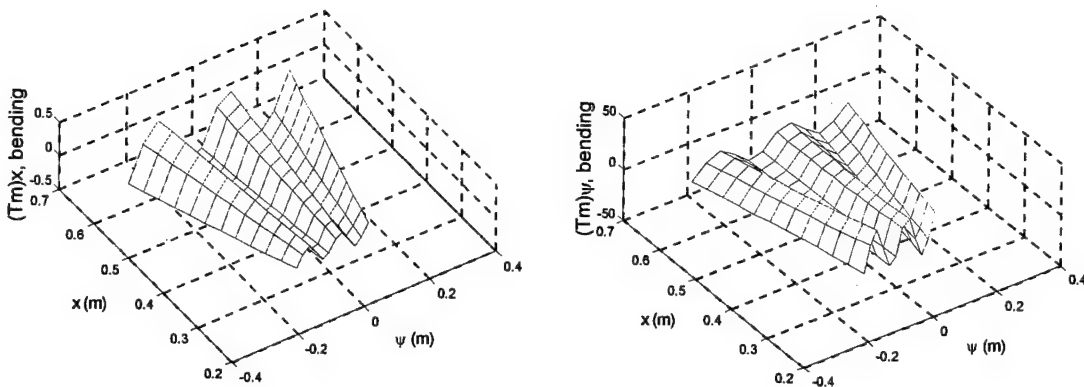


Fig.10 Micro-control actions of the (2,5) conical shell mode.

The micro-control actions of the $(1,m=2-5)$ and $(2,m=2-5)$ conical shell modes reveal that the magnitudes of micro-control actions are $(\hat{T}_m)_{\psi, \text{mem}} \gg (\hat{T}_m)_{x, \text{mem}} \gg (\hat{T}_m)_{\psi, \text{bend}} \gg (\hat{T}_m)_{x, \text{bend}}$. $(\hat{T}_m)_{\psi, \text{mem}}$ dominates and $(\hat{T}_m)_{x, \text{bend}}$ is almost negligible in the total control force. Moreover, the analyses show that $(\hat{T}_m)_{x, \text{mem}}$ and $(\hat{T}_m)_{x, \text{bend}}$ remain about the same order of magnitude when mode m changes from 2 to 5. $(\hat{T}_m)_{\psi, \text{mem}}$ and $(\hat{T}_m)_{\psi, \text{bend}}$ actions increase at higher circumferential wave number. $(\hat{T}_m)_{\psi, \text{mem}}$ is larger than $(\hat{T}_m)_{x, \text{mem}}$, ranging from two to twenty times depending on modes. Detailed data also reveal that the micro-control action at the minor-end of the conical shell is relatively high as compared with that at the major-end of the shell section, see Eq.(34).

CONCLUSION

Distributed precision control of conical shell sections is a critical issue in high-performance structural systems, e.g., rocket fairings, turbines, load carrying structures of solid rocket motor cases, etc. This study is to evaluate microscopic actuation characteristics and control actions of segmented actuator patches laminated on flexible conical shells. Mathematical models and modal domain governing equations of the conical shell section laminated with distributed actuator patches were presented first, followed by formulation of distributed control forces and micro-control actions including longitudinal/circumferential membrane and bending control components. The mode shape functions of the conical shell section with free-free boundary conditions are based on the Donnell-Mushtari-Vlasov theory. These mode shape functions were used in the modal control force expression and the micro-control action analyses. Spatially distributed electromechanical actuation characteristics contributed by various longitudinal/circumferential membrane and bending control actions were investigated. Distributed control forces and micro actions of actuator patches at various locations were analyzed and its modal-dependent spatial control effectives evaluated.

Analysis data shown that, for conical shell mode $(1,m=2-5)$ and $(2,m=2-5)$, the circumferential micro-control action $(\hat{T}_m)_{\psi, \text{mem}}$ dominants as compared with the other modal

control actions and it is followed by $(\hat{T}_m)_{x,mem}$, $(\hat{T}_m)_{\psi,bend}$ and $(\hat{T}_m)_{x,bend}$ control actions in both cases. Note that the controls signal $\phi^a(t)$ and other material parameters $(r^a d_{3i} Y_p)/\rho$ were assumed unity for all cases, thus the segmented actuator patches would reveal the true inherent actuator characteristics and micro-control actions. Specific spatial control behavior can be explicitly defined once these parameters are identified. Furthermore, the magnitudes of control forces and micro-control actions are modal dependent. Referring to these data, one can effectively configure actuator placements to achieve the maximal control effectiveness at minimal actuator power or size requirements.

ACKNOWLEDGEMENT

This research is supported, in part, by a grant (F49620-98-1-0467) from the Air Force Office of Scientific Research (Project Manager: Brian Sanders). This support is gratefully acknowledged.

REFERENCES

1. Hu, W.C.L., 1964, *Free Vibration of Conical Shells*, NASA Report TN D-2666.
2. Hu, W.C.L., Gormley, J.F., and Lindholm, U.S., 1966, "Flexural Vibrations of Conical Shells with Free Edges," NASA Report CR 384.
3. Krause, F.A., 1968, Natural Frequencies and Mode Shapes of the Truncated Conical Shell with Edges, Ph.D. Dissertation, The University of Arizona.
4. Tong, L., 1996, "Effect of Axial Load on Free Vibration of Orthotropic Truncated Conical Shells," ASME Transaction, Journal of Vibration & Acoustics Vol.118, pp.164-168.
5. Gabbert, U., and Tzou, H.S. (Ed.) 2001 Smart Structures and Structronic Systems, Kluwer Academic Publishers, Boston/Dordrecht.
6. Tzou, H.S., Wang, D.W. and Chai, W.K., 2001, "Dynamics and Distributed Control of Conical Shell Laminated with Full and Diagonal Actuators," Journal of Sound & Vibration Volume 256(1), Sept. 2002, pp.65-79.
7. Tzou, H.S., Ding, J.H., and Hagiwara, I., 2002, "Micro-control Actions of Distributed Actuators Laminated on Precision Paraboloidal Structronics Shells," JSME International Journal. Series C, Vol.45, No 1, pp.8-15.
8. Howard, R., Chai., W.K., and Tzou., H.S., 2001, "Modal Voltages of Linear and Non linear Structures Using Distributed Artificial Neurons," *Mechanical Systems and Signal Processing*, Vol. 15, No. 3, pp. 629-640.
9. Tzou, H.S., Chai, W.K. and Wang, D.W., 2003, "Modal Voltages and Distributed Signal Analysis of Conical Shells of Revolution," Journal of Sound and Vibration, Vol. 260, No. 4, pp. 589-609.
10. Chai., W.K., Smithmaitrie, P. and Tzou., H.S., 2003, "Neural Potentials and Micro Signals of Nonlinear Deep and Shallow Conical Shells," *Mechanical Systems and Signal Processing*. (To appear)
11. Tzou, H.S., 1993 *Piezoelectric Shells - Distributed Sensing and Control of Continua*. Kluwer Academic Publishers, Boston/Dordrecht. (ConeAct_J3.ShlConeAct)

CHAPTER 7

MICRO-SENSOR ELECTROMECHANICS AND DISTRIBUTED SIGNAL ANALYSIS OF PIEZO(ELECTRIC)-ELASTIC SPHERICAL SHELLS

ABSTRACT

Spatially distributed modal voltages and sensing signal generations of a distributed piezoelectric sensor layer bonded on spherical shells of revolution are investigated in this study. The generic sensing signal equation is derived based on the direct piezoelectric effect, the Gauss theory, the open-circuit assumption, the Maxwell equation, and also the generic double-curvature thin shell theory. Due to difficulties in analytical solution procedures, assumed mode shape functions based on the bending approximation theory are used in the modal signal expressions and analyses. Spatially distributed micro-electromechanical characteristics resulting from various meridional and circumferential membrane/bending strain components of infinitesimal sensor neurons are evaluated and major signal sources are identified. Analytical results suggest that the spatially distributed modal voltages clearly illustrate the distinct modal behavior, similar to mode shapes. The major signal source of a free-edge hemispherical shell is the circumferential bending component. Accordingly, circumferential layout of distributed sensor strips would provide effective monitoring and diagnosis of free hemispheric shells.

INTRODUCTION

Recent research and development of smart structures and stractronic systems has broadened the measurement and control techniques from conventional “discrete” off-the-shelf devices to “distributed” fully integrated devices or systems using smart materials, e.g., piezoelectrics, shape memory materials, electro- and magneto-strictive materials, electro- and magneto-rheological fluids, photostrictive materials, etc. [1-2]. Among these smart materials, piezoelectric materials provide both sensing and control capability. Thus, piezoelectric layers can serve as distributed sensors/neurons for structural health monitoring and diagnosis, and distributed actuators/controllers for precision actuation and control of shells and plates [3-6].

Spherical shell structures and components appear in many engineering systems, such as radar domes, pressure vessels, storage tanks, etc. Dynamics of spherical shells have been

investigated over the years [7-15]. Natural frequencies of a shallow spherical shell and a thin hemisphere shell with free boundary condition have been experimentally verified [16-17]. Distributed sensing and control of shallow spherical shells have been investigated over the past few years [18-22]. However, distributed sensing and control of hemispherical shells have not been thoroughly investigated. This study is to investigate the distributed dynamic modal sensing characteristics, distributed modal voltages, and detailed micro-signal sources of spherical shells of revolution covered with distributed piezoelectric sensor layers and infinitesimal sensor neurons. Mathematical modeling, strain-displacement relations, force/moment-displacement relations of spherical shells are presented first. In order to define modal dependent distributed signals, assumed mode shape functions based on the bending approximation theory are used in the signal-displacement equations. Detailed signal sources and distributed modal voltages of hemispheric shell are evaluated in case studies.

MATHEMATICAL MODELING

Assume there is a transversely polarized hexagonal distributed thin sensor layer bonded on a thin spherical shell of revolution, and this sensor layer reveals the distributed modal sensing signal characteristics of spherical shells, Figure 1. Since the sensor layer is much thinner and more flexible than the elastic shell, its influence to the overall shell dynamics is negligible [5]. There are three equations of motion describing the dynamics of spherical shells of revolution respectively defined in the $\alpha_1 = \phi$, $\alpha_2 = \psi$, and α_3 directions and they can be directly derived by simplifying the equations of motion of a generic double-curvature thin shell using two Lamé parameters (A_1 and A_2) and two radii of curvature (R_1 and R_2) defined for the spherical shell coordinate system where $\alpha_1 = \phi$ and $\alpha_2 = \psi$.

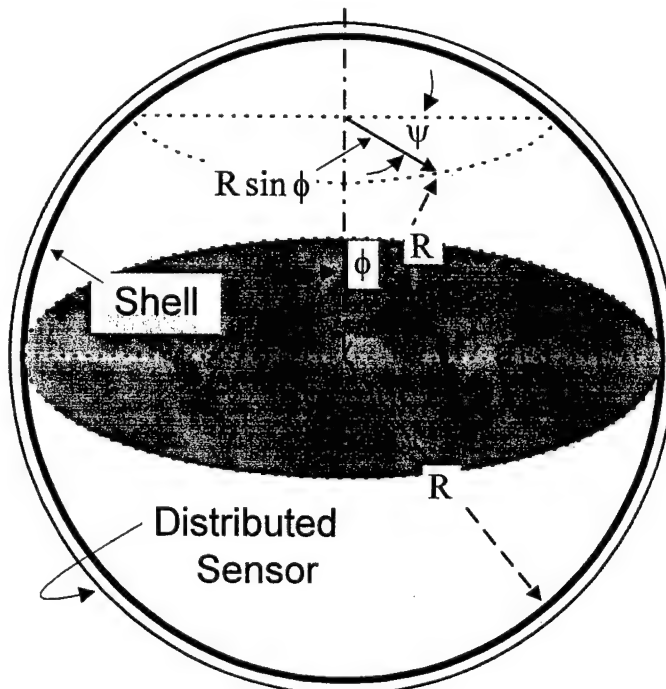


Fig.1 A spherical shell laminated with a distributed sensor layer.

The fundamental form defining the Lamé parameters is derived based on an infinitesimal distance (ds) on the neutral surface of a thin spherical shell.

$$(ds)^2 = (R)^2(d\phi)^2 + (R\sin\phi)^2(d\psi)^2. \quad (1)$$

Thus, the Lamé parameters $A_1 = R$ and $A_2 = R \sin\phi$; the radii of curvature of a spherical shell are $R_1 = R_2 = R$. Substituting Lamé parameters and radii of curvatures of spherical shells into the system equations of a generic double-curvature thin shell yields three equations of motion of a thin spherical shell respectively defined in the ϕ , ψ , and α_3 directions.

$$\frac{\partial}{\partial\phi}(N_{\phi\phi}\sin\phi) + \frac{\partial}{\partial\psi}(N_{\psi\phi}) - N_{\psi\psi}\cos\phi + Q_{\phi 3}\sin\phi + Rq_{\phi}\sin\phi = R\sin\phi\rho h \frac{\partial^2 u_{\phi}}{\partial t^2}, \quad (2)$$

$$\frac{\partial}{\partial\psi}(N_{\phi\psi}\sin\phi) + \frac{\partial}{\partial\psi}(N_{\psi\psi}) + N_{\psi\phi}\cos\phi + Q_{\psi 3}\sin\phi + Rq_{\psi}\sin\phi = R\sin\phi\rho h \frac{\partial^2 u_{\psi}}{\partial t^2}, \quad (3)$$

$$\frac{\partial}{\partial\phi}(Q_{\phi 3}\sin\phi) + \frac{\partial}{\partial\psi}(Q_{\psi 3}) - (N_{\phi\phi} + N_{\psi\psi})\sin\phi + Rq_3\sin\phi = R\sin\phi\rho h \frac{\partial^2 u_3}{\partial t^2}; \quad (4)$$

and $Q_{\phi 3} = \frac{1}{R\sin\phi} \left[\frac{\partial}{\partial\phi}(M_{\phi\phi}\sin\phi) + \frac{\partial}{\partial\psi}(M_{\psi\phi}) - M_{\psi\psi}\cos\phi \right], \quad (5)$

$$Q_{\psi 3} = \frac{1}{R\sin\phi} \left[\frac{\partial}{\partial\phi}(M_{\phi\psi}\sin\phi) + \frac{\partial}{\partial\psi}(M_{\psi\psi}) + M_{\psi\phi}\cos\phi \right]. \quad (6)$$

N_{ij} are the membrane forces; M_{ij} are the bending moments; Q_{i3} denote the traverse shear stress resultants; q_i is the external excitation; ρ is the mass density; h is the shell thickness; and u_i is the displacement in the i -th direction. Note that q_i can also be discrete or distributed control forces. Membrane forces N_{ij} and bending moments M_{ij} are functions of membrane strains s_{ij}^o and bending strains k_{ij} .

$$N_{\phi\phi} = K(s_{\phi\phi}^o + \mu s_{\psi\psi}^o), \quad N_{\psi\psi} = K(s_{\psi\psi}^o + \mu s_{\phi\phi}^o), \quad N_{\phi\psi} = N_{\psi\phi} = \frac{K(1-\mu)}{2} s_{\phi\psi}^o; \quad (7-9)$$

$$M_{\phi\phi} = D(k_{\phi\phi} + \mu k_{\psi\psi}), \quad M_{\psi\psi} = D(k_{\psi\psi} + \mu k_{\phi\phi}), \quad M_{\phi\psi} = M_{\psi\phi} = \frac{D(1-\mu)}{2} k_{\phi\psi}; \quad (10-12)$$

where $K = (Yh)/(1-\mu^2)$ is the membrane stiffness; $D = (Yh^3)/[12(1-\mu^2)]$ is the bending stiffness; Y is the modulus of elasticity (Young's modulus); and μ is Poisson's ratio. The strain-displacement relations of thin spherical shells are

$$s_{\phi\phi}^o = \frac{1}{R} \left(\frac{\partial}{\partial\phi}(u_{\phi}) + u_3 \right), \quad s_{\psi\psi}^o = \frac{1}{R\sin\phi} \left(\frac{\partial}{\partial\psi}(u_{\psi}) + u_{\phi}\cos\phi + u_3\sin\phi \right), \quad (13,14)$$

$$s_{\phi\psi}^{\circ} = \frac{1}{R} \left(\frac{\partial}{\partial \phi} (u_{\psi}) - u_{\psi} \cot \phi + \frac{1}{\sin \phi} \frac{\partial}{\partial \psi} (u_{\phi}) \right); \quad (15)$$

$$k_{\phi\phi} = \frac{1}{R} \left(\frac{\partial}{\partial \phi} (\beta_{\phi}) \right), \quad k_{\psi\psi} = \frac{1}{R} \left(\frac{1}{\sin \phi} \frac{\partial}{\partial \psi} (\beta_{\psi}) + \beta_{\phi} \cot \phi \right), \quad (16,17)$$

$$k_{\phi\psi} = \frac{1}{R} \left(\frac{\partial}{\partial \phi} (\beta_{\psi}) - \beta_{\psi} \cot \phi + \frac{1}{\sin \phi} \frac{\partial}{\partial \psi} (\beta_{\phi}) \right); \quad (18)$$

and the rotation angles are $\beta_{\phi} = \frac{1}{R} \left(u_{\phi} - \frac{\partial u_3}{\partial \phi} \right)$ and $\beta_{\psi} = \frac{1}{R} \left(u_{\psi} - \frac{1}{\sin \phi} \frac{\partial u_3}{\partial \psi} \right)$.

THE BENDING APPROXIMATION

Due to the complexity of the spherical-shell governing equations, assumptions and simplifications are often employed. There are three approximation theories, namely, 1) the bending approximation (or the inextensional approximation), 2) the membrane approximation (or the extensional approximation), and 3) the Donnell-Mushtari-Vlasov approximation [13]. All membrane forces are neglected in the bending approximation, i.e., $N_{11} = N_{22} = N_{12} = 0$, and all bending moments are neglected in the membrane approximation, i.e., $M_{11} = M_{22} = M_{12} = Q_{13} = Q_{23} = 0$. There are three assumptions in the Donnell-Mushtari-Vlasov approximation: 1) in-plane displacements can be neglected in the bending strain expressions, but not in the membrane strain expressions; 2) in-plane inertia forces can be neglected, i.e., $\rho h \ddot{u}_k \approx 0$, $k = \phi, \psi$; and 3) the transverse shear effects, i.e., Q_{31}/R_1 and Q_{32}/R_2 , in the in-plane equations can be neglected. Employing the bending approximation to the spherical shells, neglecting the membrane strains, i.e., $s_{\phi\phi}^{\circ} = s_{\psi\psi}^{\circ} = s_{\phi\psi}^{\circ} = 0$, and using equations (7)-(9) yields zero membrane force resultants, i.e., $N_{\phi\phi} = N_{\psi\psi} = N_{\phi\psi} = 0$. The bending strain-displacement relations are the same as equations (16)-(18). Accordingly, a set of spherical governing equations based on the bending approximation can be derived.

$$Q_{\phi 3} \sin \phi + R q_{\phi} \sin \phi = R \sin \phi \rho h \frac{\partial^2}{\partial t^2} (u_{\phi}), \quad (19)$$

$$Q_{\psi 3} \sin \phi + R q_{\psi} \sin \phi = R \sin \phi \rho h \frac{\partial^2}{\partial t^2} (u_{\psi}), \quad (20)$$

$$\frac{\partial}{\partial \phi} (Q_{\phi 3} \sin \phi) + \frac{\partial}{\partial \psi} (Q_{\psi 3}) + R q_3 \sin \phi = R \sin \phi \rho h \frac{\partial^2}{\partial t^2} (u_3); \quad (21)$$

The bending moment and strain relations are the same as the original spherical shell definitions in equations (10)-(12). Distributed micro-sensing characteristics of spherical shells are analyzed based on the bending approximation theory presented later.

NATURAL FREQUENCY AND MODE SHAPE

Since modal voltages and spatially distributed micro-sensing signals are modal dependent, natural modes of spherical shells are discussed in this section. Bending (inextensional) mode shape functions of an open spherical shell ($0 < \phi < \phi_0$) with free boundary condition at $\phi = \phi_0$ (Figure 2) are [7,14]:

$$U_\phi = -A_k \left(\tan \frac{\phi}{2}\right)^k \sin k\psi, \quad (22)$$

$$U_\psi = -B_k \sin \phi \left(\tan \frac{\phi}{2}\right)^k \cos k\psi, \quad (23)$$

$$U_3 = C_k R (k + \cos \phi) \left(\tan \frac{\phi}{2}\right)^k \cos k\psi, \quad (24)$$

where U_ϕ is the meridional mode shape; U_ψ is the circumferential mode shape; U_3 is the radial (transverse) mode shape; k is the number of circumferential waves; and A_k , B_k , and C_k are the k -th modal amplitudes. For simplicity, $A_k = A$, $B_k = B$, and $C_k = C$ in later derivations.

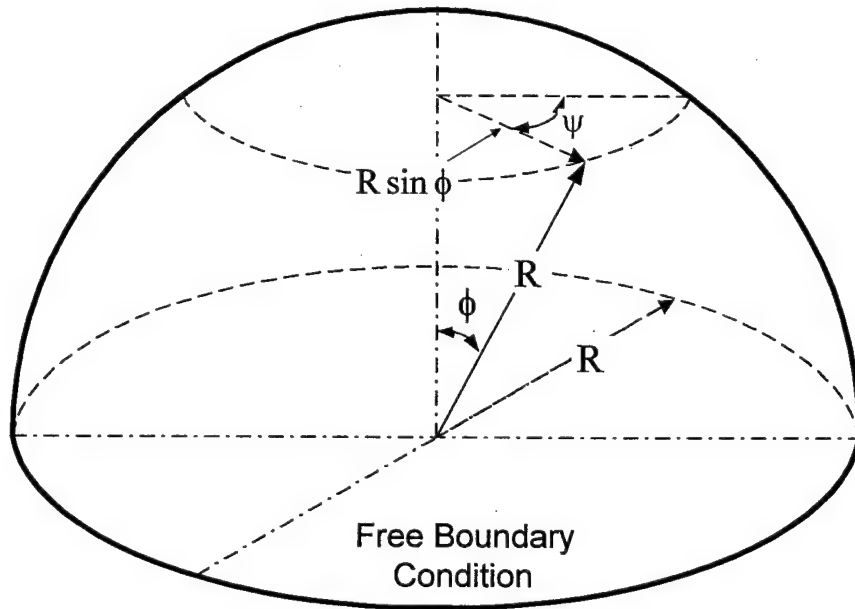


Fig.2 An open spherical shell with free boundary condition.

Natural frequencies associated with the bending mode shapes are

$$f_k = \frac{\lambda_k}{2\pi R} \left(\frac{Y}{\rho} \right)^{1/2}, \quad k = 2, 3, 4, \dots \quad (25)$$

$$\lambda_k^2 = \frac{(k^2 - 1)^2 k^2}{3(1 + \mu)} \left(\frac{h}{R} \right)^2 \frac{g_1(k, \phi_0)}{g_2(k, \phi_0)} \quad (26)$$

where f_k is the k -th natural frequency in Hertz. The dimensionless parameter λ_k is a function of the meridional angle subtended by the shell segment [14].

And

$$g_1(k, \phi_0) = \frac{1}{8} \left(\frac{(\tan \frac{\phi_0}{2})^{2k-2}}{k-1} + \frac{2(\tan \frac{\phi_0}{2})^{2k}}{k} + \frac{(\tan \frac{\phi_0}{2})^{2k+2}}{k+1} \right), \quad (27)$$

$$g_2(k, \phi_0) = \int_0^{\phi_0} (\tan \frac{\phi}{2})^{2k} [(k + \cos \phi)^2 + 2(\sin \phi)^2] \sin \phi \, d\phi. \quad (28)$$

For a hemisphere thin shell, $\phi_0 = \pi/2$ and $\tan(\phi_0/2) = 1$. The dimensionless parameter λ_k^2 becomes

$$\lambda_k^2 = \frac{1}{12(1 + \mu)} \left(\frac{h}{R} \right)^2 \frac{(k^3 - k)(2k^2 - 1)}{g_2(k, \phi_0 = \pi/2)}, \quad k = 2, 3, 4, \dots \quad (29)$$

where $g_2(k, \phi_0 = \pi/2) = 1.52961$ when $k=2$, 1.88156 when $k=3$, 2.29609 when $k=4$, ... [14]. Natural frequencies of a shallow shell (i.e., small ϕ_0) and a thin hemisphere shell with a free boundary condition have been experimentally verified, respectively [16-17].

DISTRIBUTED SENSING SIGNALS

Assume there is a distributed thin hexagonal piezoelectric sensor layer, with thickness h^s , bonded on the spherical shell, Figure 3. The sensor layer is much thinner than the spherical shell ($h^s \ll h$) and its effect to shell dynamics is negligible. Based on the direct piezoelectric effect, the Gauss theory and the Maxwell equation, a transverse open-circuit signal voltage ϕ^s is contributed by the strain variations (S_{ij}^s) in the sensor layer. Accordingly, the signal over the sensor surface is defined by [23-24]

$$\phi^s = \frac{h^s}{S^e} \int (h_{31} S_{11}^s + h_{32} S_{22}^s + h_{36} S_{12}^s) A_1 A_2 d\alpha_1 d\alpha_2, \quad (30)$$

where h^s is the sensor thickness; h_{ij} are the piezoelectric (displacement) constant; S^e is the effective sensor area.

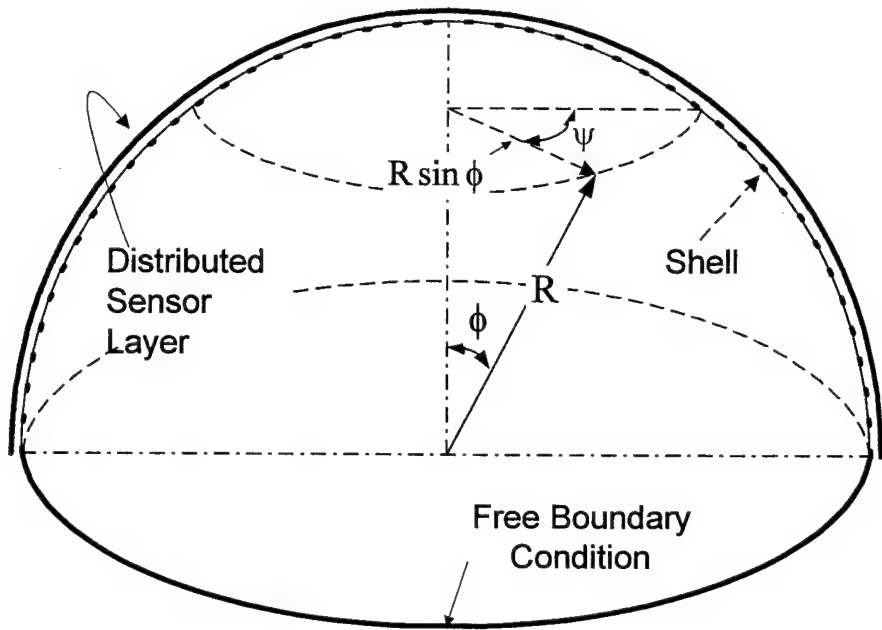


Fig.3 A hemispherical shell with a distributed piezoelectric sensor layer.

Neglecting the in-plane twisting effect h_{36} , the sensing signal equation becomes

$$\phi^s = \frac{h^s}{S^e} \int (h_{31}S_{11}^s + h_{32}S_{22}^s) A_1 A_2 d\alpha_1 d\alpha_2. \quad (31)$$

Recall that the strain consists of two components: the membrane strain and the bending strain:

$$S_{11}^s = s_{11}^0 + r_1^s k_{11} \quad \text{and} \quad S_{22}^s = s_{22}^0 + r_2^s k_{22}, \quad (32,33)$$

where r_i^s is the distance from the middle of the sensor layer to the shell neutral surface, i.e., $r_i^s = (h + h^s)/2 \cong h/2$, if $h \gg h^s$. That is, the shell piezoelectric sensor strains are assumed to be constant and equal to the outer surface strains of the shell.

Modal Signals

Since the mode shape functions were defined based on the bending approximation, the membrane strains are zero and the bending strains remain unchanged. Substituting the mode shape functions into the strain-displacement relationships yields modal dependent strain equations. With the mode shape functions of the hemispherical shell, the rotational angles are explicitly redefined as

$$\begin{aligned}\beta_\phi &= \frac{1}{R} \left[-A \left(\tan \frac{\phi}{2} \right)^k \sin k\psi - C \frac{k}{2} R (k + \cos \phi) \left(\tan \frac{\phi}{2} \right)^{k-1} \left(\sec \frac{\phi}{2} \right)^2 \cos k\psi \right. \\ &\quad \left. + CR \sin \phi \left(\tan \frac{\phi}{2} \right)^k \cos k\psi \right],\end{aligned}\quad (34)$$

$$\beta_\psi = \frac{1}{R} \left(-B \sin \phi \left(\tan \frac{\phi}{2} \right)^k \cos k\psi + \frac{1}{\sin \phi} C k R (k + \cos \phi) \left(\tan \frac{\phi}{2} \right)^k \sin k\psi \right). \quad (35)$$

And note that

$$\frac{\partial \beta_\psi}{\partial \psi} = \frac{1}{R} \left[kB \sin \phi \left(\tan \frac{\phi}{2} \right)^k \sin k\psi + \frac{Ck^2 R}{2} (k + \cos \phi) \left(\sin \frac{\phi}{2} \right)^{k-1} \left(\sec \frac{\phi}{2} \right)^{k+1} \cos k\psi \right]. \quad (36)$$

Thus, the bending strains are defined with respect to mode shape functions.

$$\begin{aligned}k_{11} &= \frac{1}{R^2} \left[-A \frac{k}{2} \left(\tan \frac{\phi}{2} \right)^{k-1} \left(\sec \frac{\phi}{2} \right)^2 \sin k\psi + CR \cos \phi \left(\tan \frac{\phi}{2} \right)^k \cos k\psi \right. \\ &\quad \left. + CR \sin \phi \left(\tan \frac{\phi}{2} \right)^{k-1} \left(\sec \frac{\phi}{2} \right)^2 \cos k\psi \right. \\ &\quad \left. - C \frac{k}{2} R (k + \cos \phi) \left(\tan \frac{\phi}{2} \right)^k \left(\sec \frac{\phi}{2} \right)^2 \cos k\psi \right. \\ &\quad \left. - C \frac{k}{4} R (k + \cos \phi) (k - 1) \left(\tan \frac{\phi}{2} \right)^{k-2} \left(\sec \frac{\phi}{2} \right)^4 \cos k\psi \right];\end{aligned}\quad (37)$$

and

$$\begin{aligned}k_{22} &= \frac{1}{R^2} \left\{ kB \left(\tan \frac{\phi}{2} \right)^k \sin k\psi + \frac{Ck^2 R}{4} (k + \cos \phi) \left(\sin \frac{\phi}{2} \right)^{k-2} \left(\sec \frac{\phi}{2} \right)^{k+2} \cos k\psi \right. \\ &\quad \left. + \cos \phi \left[-\frac{A}{2} \left(\sin \frac{\phi}{2} \right)^{k-1} \left(\sec \frac{\phi}{2} \right)^{k+1} \sin k\psi - C \frac{k}{4} R (k + \cos \phi) \left(\sin \frac{\phi}{2} \right)^{k-2} \right. \right. \\ &\quad \left. \cdot \left(\sec \frac{\phi}{2} \right)^{k+2} \cos k\psi + CR \left(\tan \frac{\phi}{2} \right)^k \cos k\psi \right] \right\}.\end{aligned}\quad (38)$$

Accordingly, the sensing signal can be rewritten as a function of induced strains in the sensor layer:

$$\phi^s = \frac{h^s}{S^e} \int (h_{31}(r_1^s k_{11}) + h_{32}(r_2^s k_{22})) A_1 A_2 d\alpha_1 d\alpha_2 \quad (39)$$

In practical applications, the piezoelectric constants $h_{31}=h_{32}$ in hexagonal piezoelectric materials without being mechanically stretched during the manufacturing process and $r_1^s = r_2^s = h/2$ for uniform thickness of sensor and shell layers. Separating the membrane and bending contributed signals as

$$\begin{aligned}
\phi^s &= \phi_{\text{mem}}^s + \phi_{\text{bend}}^s = \frac{h^s h_{31}}{S^e} \int [r_1^s k_{11} + r_2^s k_{22}] \cdot R^2 \sin \phi d\phi d\psi \\
&= \frac{h^s h_{31}}{S^e} \int \left\{ r_1^s \left[-A \frac{k}{R^2} \left(\tan \frac{\phi}{2} \right)^{k-1} \left(\sec \frac{\phi}{2} \right)^2 \sin k\psi + CR \cos \phi \left(\tan \frac{\phi}{2} \right)^k \cos k\psi \right. \right. \\
&\quad + CkR \sin \phi \left(\tan \frac{\phi}{2} \right)^{k-1} \left(\sec \frac{\phi}{2} \right)^2 \cos k\psi - C \frac{k}{2} R (k + \cos \phi) \left(\tan \frac{\phi}{2} \right)^k \left(\sec \frac{\phi}{2} \right)^2 \cos k\psi \\
&\quad \left. \left. - C \frac{k}{4} R (k + \cos \phi) (k-1) \left(\tan \frac{\phi}{2} \right)^{k-2} \left(\sec \frac{\phi}{2} \right)^4 \cos k\psi \right] \right. \\
&\quad \left. + r_2^s \left[\frac{1}{R^2} \left\{ kB \left(\tan \frac{\phi}{2} \right)^k \sin k\psi + \frac{Ck^2 R}{4} (k + \cos \phi) \left(\sin \frac{\phi}{2} \right)^{k-2} \left(\sec \frac{\phi}{2} \right)^{k+2} \cos k\psi \right. \right. \right. \\
&\quad \left. \left. + \cos \phi \left[-\frac{A}{2} \left(\sin \frac{\phi}{2} \right)^{k-1} \left(\sec \frac{\phi}{2} \right)^{k+1} \sin k\psi - C \frac{k}{4} R (k + \cos \phi) \left(\sin \frac{\phi}{2} \right)^{k-2} \left(\sec \frac{\phi}{2} \right)^{k+2} \cos k\psi \right. \right. \\
&\quad \left. \left. \left. + CR \left(\tan \frac{\phi}{2} \right)^k \cos k\psi \right] \right\} \right] \right\} \cdot R^2 \sin \phi d\phi d\psi . \tag{40}
\end{aligned}$$

Thus, the spatially distributed k -th modal signal of the hemispherical shell can be represented by the summation of the distributed modal membrane and bending signal components, i.e., $(\Phi_k)_{\text{mem}}$ and $(\Phi_k)_{\text{bend}}$, as

$$\phi_k^s = h^s h_{31} (\Phi_k) = h^s h_{31} [(\Phi_k)_{\text{mem}} + (\Phi_k)_{\text{bend}}], \tag{41}$$

where each component consists of the meridional and the circumferential components: $(\Phi_k)_{\text{mem}} = (\Phi_{\phi\phi})_{\text{mem}} + (\Phi_{\psi\psi})_{\text{mem}}$; $(\Phi_k)_{\text{bend}} = r_1^s [(\Phi_{\phi\phi})_{\text{bend}} + (\Phi_{\psi\psi})_{\text{bend}}]$. Furthermore, the signal generated by the membrane strain is zero, i.e., $\phi_{\text{mem}}^s = 0$, since the membrane strains are neglected in the bending approximation theory. Thus, the primary signal generation depends on the bending strains in the sensor layer, i.e.,

$$\phi_{\text{bend}}^s = \frac{h^s h_{31} r_1^s}{S^e} \int (k_{11} + k_{22}) \cdot R^2 \sin \phi d\phi d\psi, \tag{42}$$

where the subscripts “mem” and “bend” respectively denote the membrane and bending components. In order to illustrate spatially distributed electromechanical characteristics, the sensor electrode shrinks to infinitesimally small - neurons, so that local sensing phenomena of distributed sensing neurons can be fully illustrated. Assembling all local neural signals contributed by the local micro-strains constitutes spatially distributed modal voltages. The micro-signal component contributed by the infinitesimal sensor neurons is

$$\begin{aligned}
\phi_k^s = h^s h_{31} \cdot \left\{ r_1^s \left[\frac{1}{R^2} \left[-A \frac{k}{2} \left(\tan \frac{\phi}{2} \right)^{k-1} \left(\sec \frac{\phi}{2} \right)^2 \sin k\psi + CR \cos \phi \left(\tan \frac{\phi}{2} \right)^k \cos k\psi \right. \right. \right. \\
+ CkR \sin \phi \left(\tan \frac{\phi}{2} \right)^{k-1} \left(\sec \frac{\phi}{2} \right)^2 \cos k\psi - C \frac{k}{2} R (k + \cos \phi) \left(\tan \frac{\phi}{2} \right)^k \left(\sec \frac{\phi}{2} \right)^2 \cos k\psi \\
\left. - C \frac{k}{4} R (k + \cos \phi) (k - 1) \left(\tan \frac{\phi}{2} \right)^{k-2} \left(\sec \frac{\phi}{2} \right)^4 \cos k\psi \right] \\
\left. + r_2^s \left[\frac{1}{R^2} \left\{ kB \left(\tan \frac{\phi}{2} \right)^k \sin k\psi + \frac{Ck^2 R}{4} (k + \cos \phi) \left(\sin \frac{\phi}{2} \right)^{k-2} \left(\sec \frac{\phi}{2} \right)^{k+2} \cos k\psi \right. \right. \right. \\
+ \cos \phi \left[-\frac{A}{2} \left(\sin \frac{\phi}{2} \right)^{k-1} \left(\sec \frac{\phi}{2} \right)^{k+1} \sin k\psi - C \frac{k}{4} R (k + \cos \phi) \left(\sin \frac{\phi}{2} \right)^{k-2} \left(\sec \frac{\phi}{2} \right)^{k+2} \cos k\psi \right. \\
\left. \left. \left. + CR \left(\tan \frac{\phi}{2} \right)^k \cos k\psi \right] \right\} \right] \right\}.
\end{aligned} \tag{43}$$

Detailed micro-meridional and circumferential contributing signal components $(\Phi_{\phi\phi})_{\text{mem}}$, $(\Phi_{\psi\psi})_{\text{mem}}$, $(\Phi_{\phi\phi})_{\text{bend}}$, and $(\Phi_{\psi\psi})_{\text{bend}}$ and the global spatially distributed modal voltages are evaluated next.

DISTRIBUTED MODAL VOLTAGES AND SIGNAL COMPONENTS

A hemispheric shell with a meridional angle ϕ from 0 to 90 degrees and a full revolution in the circumferential direction (i.e., angle ψ from 0 to 360 degrees) laminated with a distributed sensor layer is studied. Distributed modal voltages and micro-signal components generated from various components are investigated in this section. Recall that the bottom open perimeter of the hemispheric shell is free, Figure 3. The modal amplitudes A, B, and C and the radius R are assumed unity in these distributed signal calculations. The distributed modal signal components $(\Phi_{\phi\phi})_{\text{mem}}$, $(\Phi_{\psi\psi})_{\text{mem}}$, $(\Phi_{\phi\phi})_{\text{bend}}$, and $(\Phi_{\psi\psi})_{\text{bend}}$ for $k=2,3,4,5,6$ modes are calculated. Figure 4 respectively illustrate $(\Phi_k)_{\text{mem}}$ and $(\Phi_{\phi\phi})_{\text{bend}} + (\Phi_{\psi\psi})_{\text{bend}}$ signal distributions in which modal signal components and mode numbers are respectively labeled. Since the membrane strains are neglected for the shell with the bending approximation, sensing signals resulting from the membrane strain are all zero. Figure 4 shows the zero signals (or the original hemispheric shell surface) of the $k=2-6$ modes. On the other hand, the bending strains are essential in the bending approximation. This figure also illustrates the distributed modal signals ($k=2-6$) contributed by of the bending strains. Similar to mode shapes, these modal voltages clearly illustrate the distinct modal characteristics of a free-edge hemispheric shell.

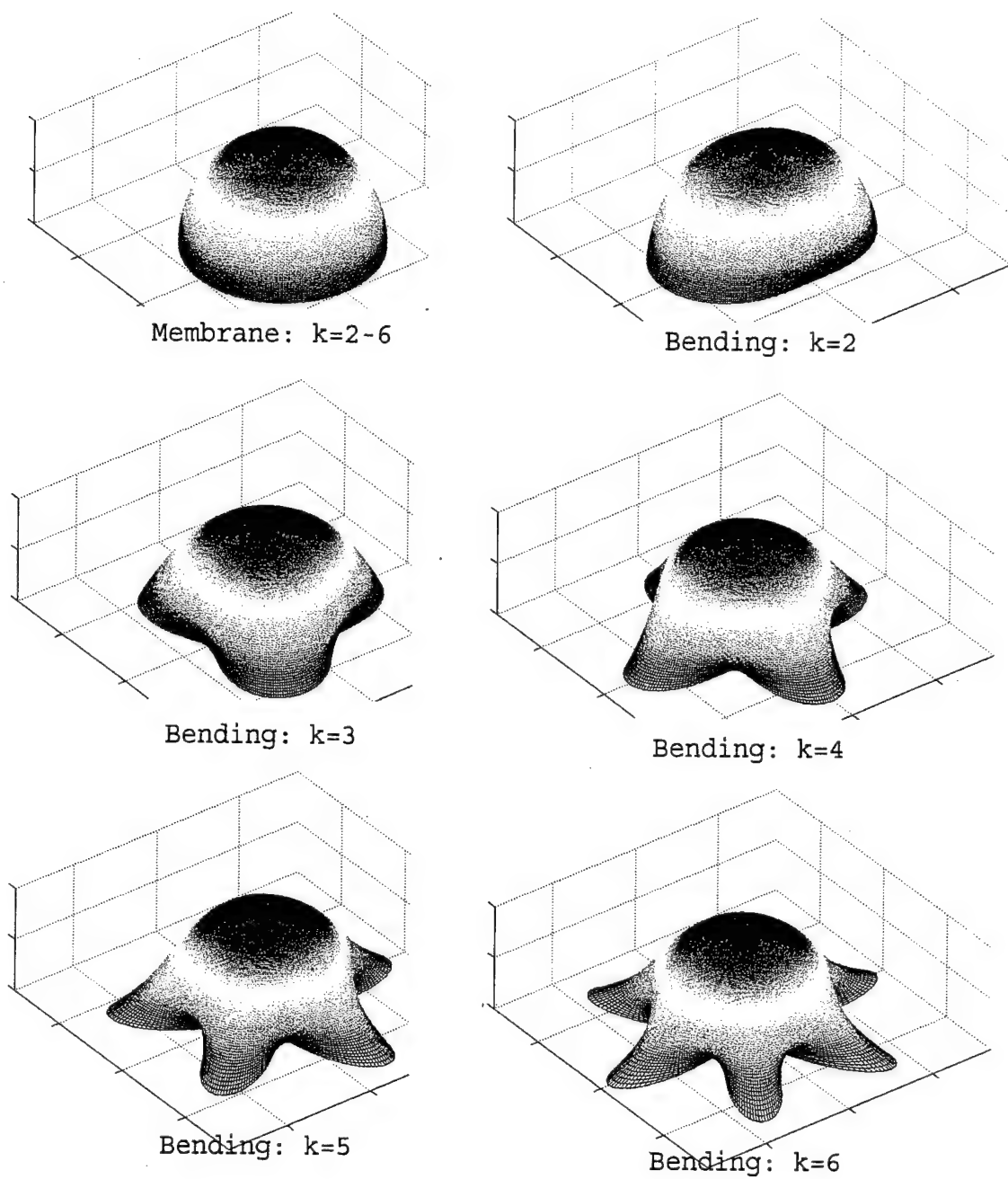


Fig.4 Distributed membrane signal ($k=2-6$) and distributed bending signals ($k=2-6$).

Furthermore, evaluating the distributed bending strain signals reveals that there are actually two bending strain components respectively in the meridional and circumferential directions contributing to the overall signal generation. Accordingly, micro-signal contributions of these individual components warrant further detailed investigation. Figures 5-9 illustrate these modal component (bending) signals. There are three signal plots in a set. The top one (a) is the meridional signal component, the second one (b) is the circumferential signal component, and the bottom one (c) is the total bending signal. Note that the meridional angle varies from 0 to $\pi/2$ radians; the circumferential angle varies from 0 to 2π radians in these plots. The signal at

the center pole is zero, and the signal at the free edge varies with respect to different natural modes. The number of full cycles corresponds to the mode (wave) number of the hemispheric shell. Observing these component bending modal signals suggest that the circumferential bending signal dominates the overall modal signal distribution of hemispheric shells.

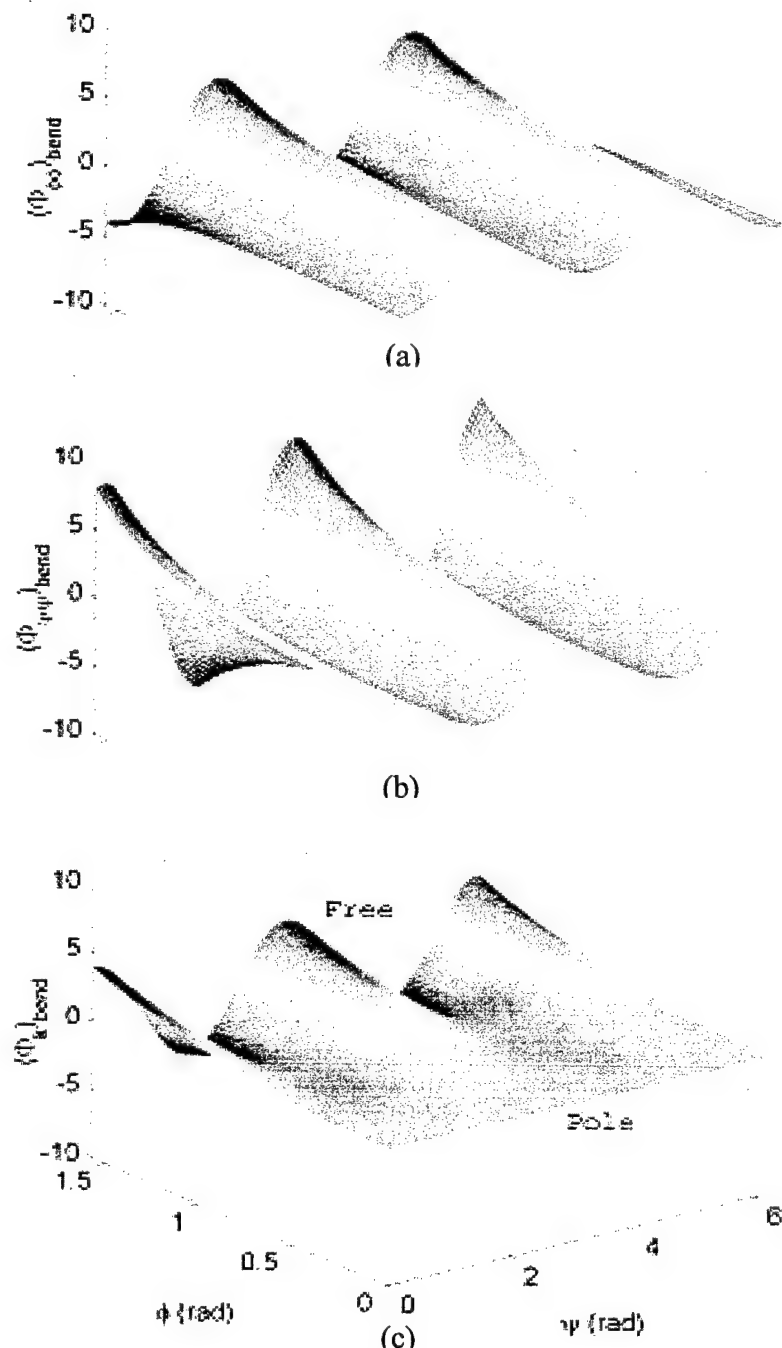


Fig.5 (a) The meridional signal component; (b) The circumferential signal component; (c) Total distributed modal bending signal ($k=2$ mode).

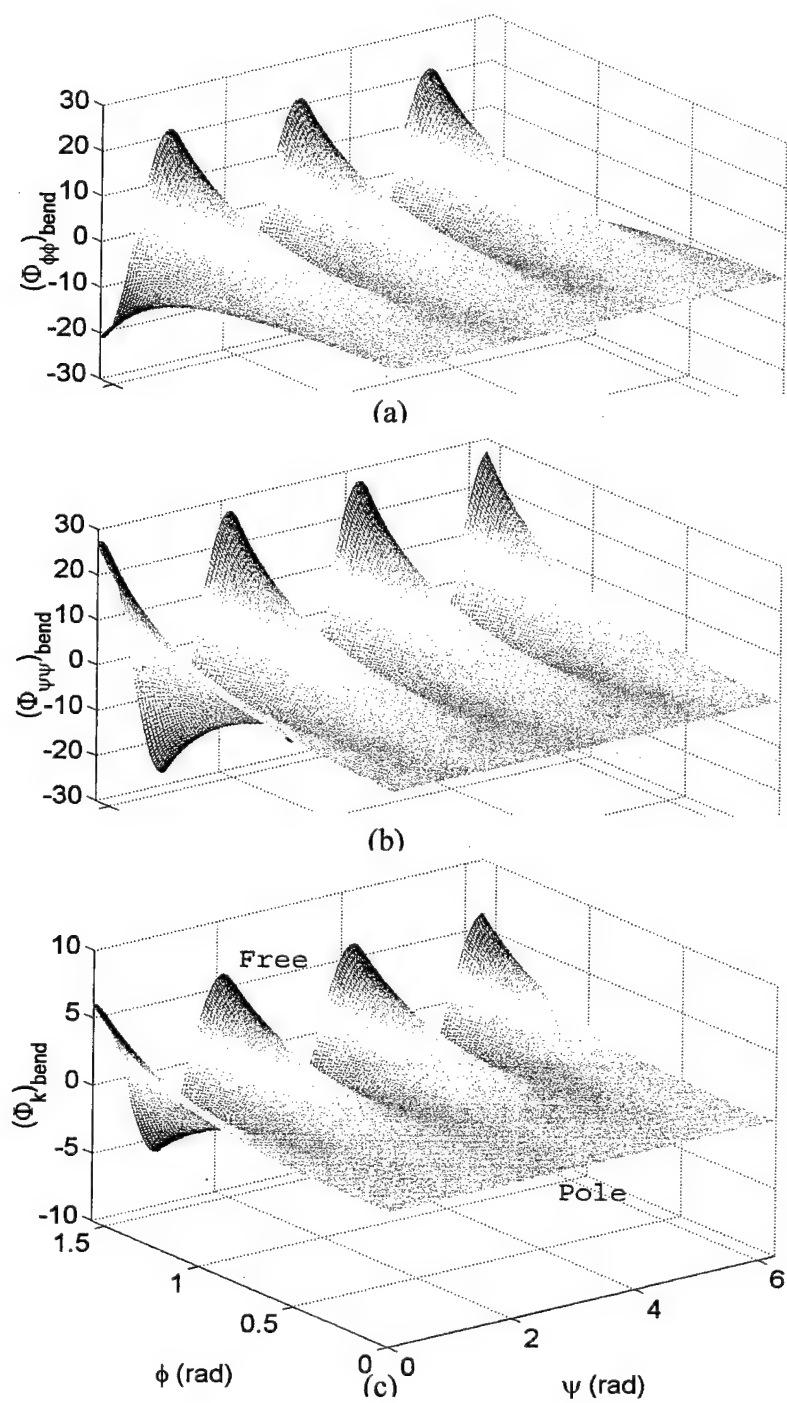


Fig.6 (a) The meridional signal component; (b) The circumferential signal component; (c) Total distributed modal bending signal ($k=3$ mode).

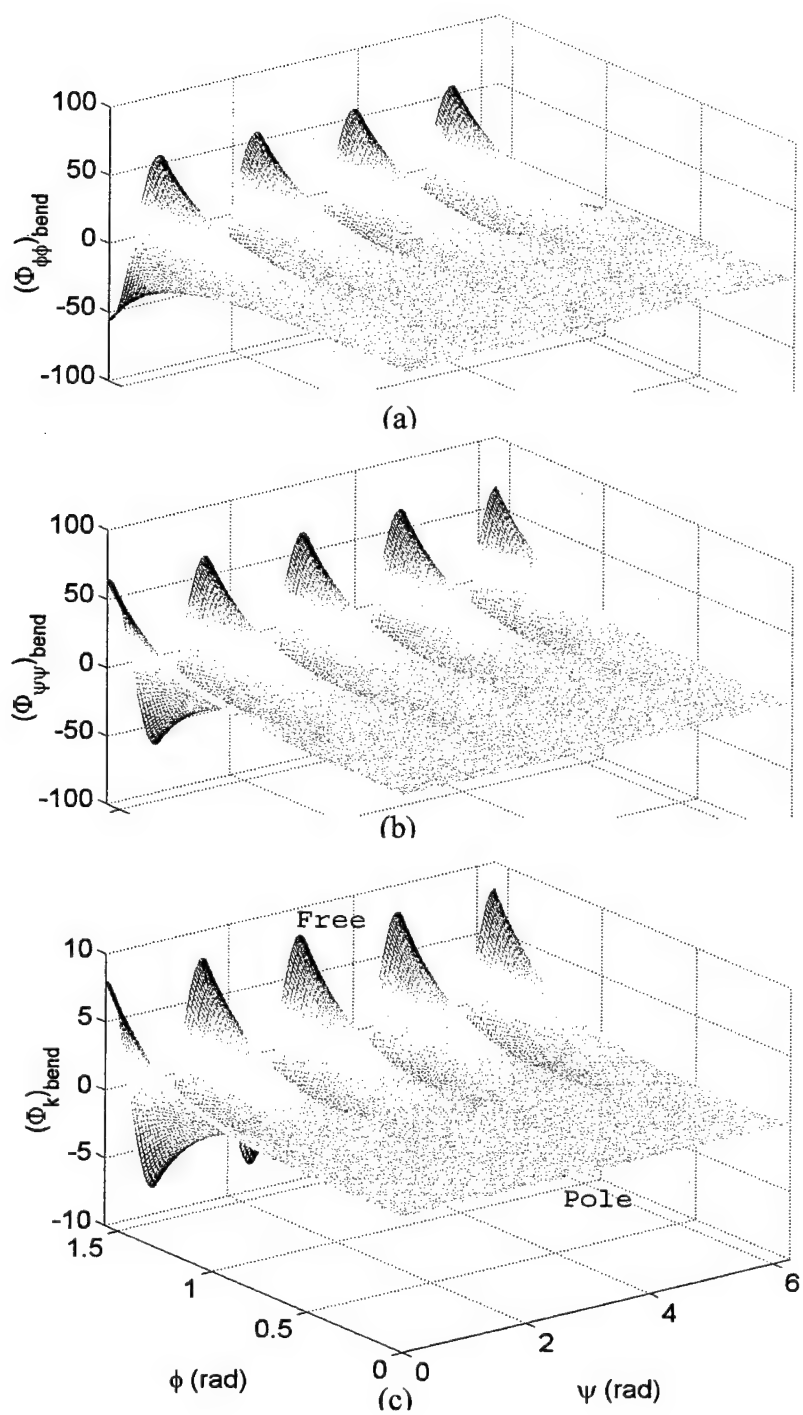


Fig.7 (a) The meridional signal component; (b) The circumferential signal component; (c) Total distributed modal bending signal ($k=4$ mode).

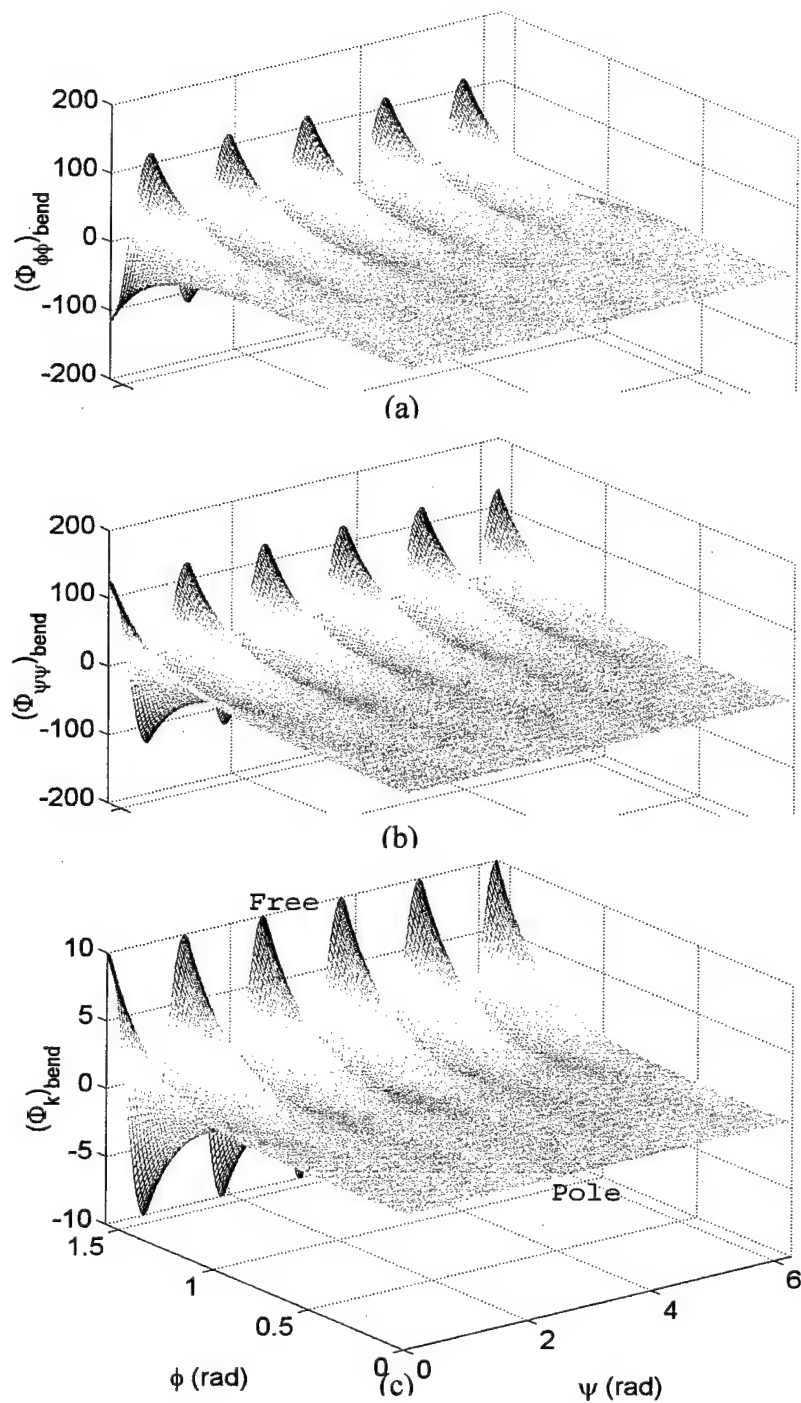


Fig.8 (a) The meridional signal component; (b) The circumferential signal component; (c) Total distributed modal bending signal (k=5 mode).

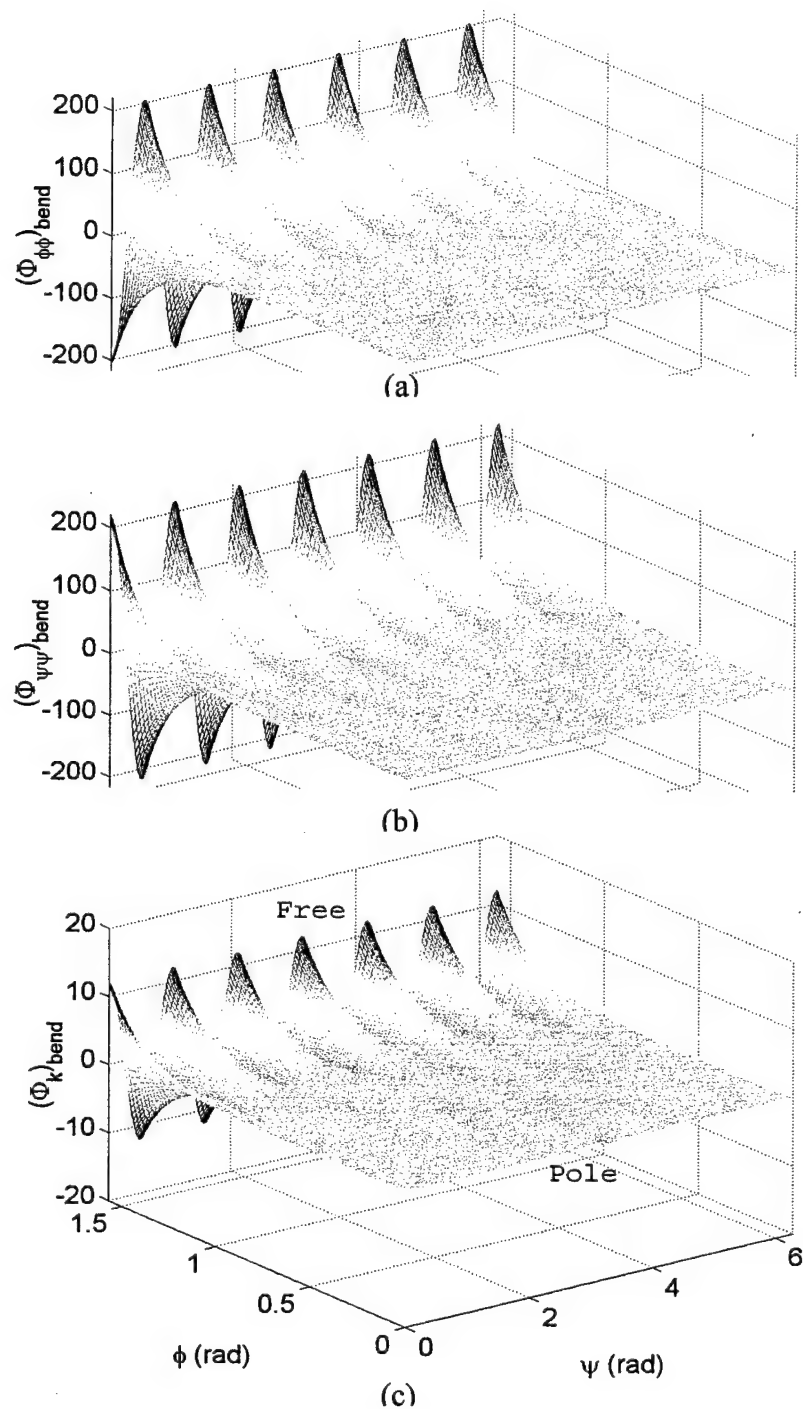


Fig.9 (a) The meridional signal component; (b) The circumferential signal component; (c) Total distributed modal bending signal ($k=6$ mode).

Based on the distributed signal component analyses, a general design guideline can be established. The detailed parametric study of signal components suggests that the

circumferential layout of sensor strips would provide the most significant and cost-effective measurement of free hemispheric shell structures, Figure 10.

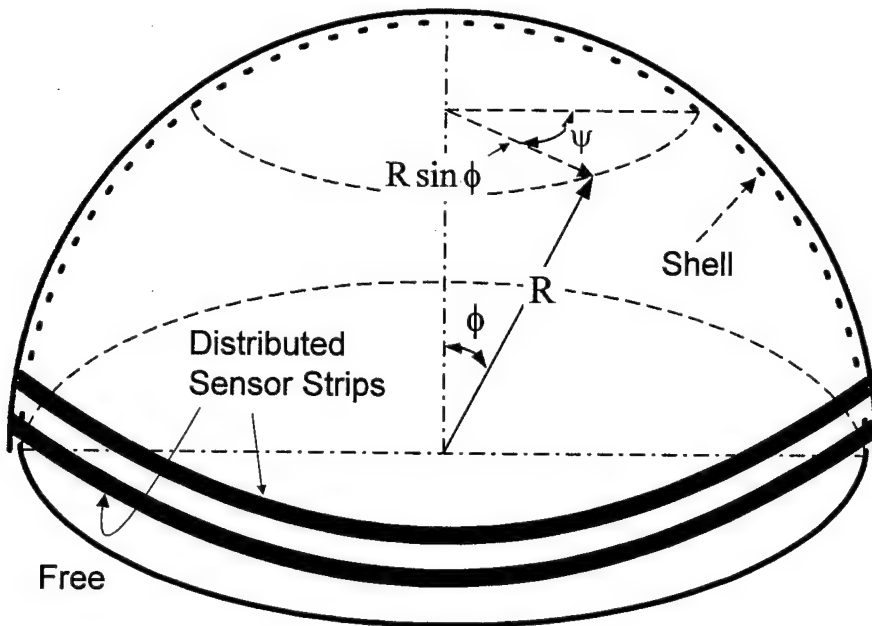


Fig.1. Circumferential layout of distributed sensor strips on a hemispheric shell.

SUMMARY AND CONCLUSION

Spherical shell structures and components appear in many engineering structures, e.g., radar domes, storage tanks, pressure vessels, etc. This paper is to evaluate spatially distributed dynamic micro-sensing characteristics of piezoelectric laminated spherical shells. Modeling of spherical shells of revolution laminated with a distributed sensor layer was presented first. Detailed strain-displacement equations, force/moment-displacement relations and system equations of spherical shells were defined. Spatially distributed sensing signals of a distributed piezoelectric sensor layer bonded on the spherical shell were defined. The generic sensing signal equation was derived based on the direct piezoelectric effect, the Gauss theory, the open-circuit assumption, the Maxwell equation, and also the generic double-curvature thin shell theory. Due to difficulties in analytical solutions, the bending approximation theory was applied to the spherical shell and simplified system equations, strain-displacement equations, force/moment-displacement equations, and distributed sensing signal-displacement equation were then redefined.

Bending mode shape functions and modal micro-signal components contributed from various meridional and circumferential membrane/bending strain components of a free-edge hemispheric shell were evaluated and the final signal-displacement equation was defined. Distributed membrane signals were all zero, due to the bending assumption. Distributed bending signals reveal the distinct modal characteristics of the free-edge hemispherical shell.

The signal amplitudes at the pole are all zero and those at the free edge clearly illustrate the modal dependent behavior. High strain regions result in high signal magnitudes. Accordingly, the spatially distributed modal signal patterns – *the modal voltages* – clearly represent the micro modal dynamic and strain characteristics of hemispheric shells. Spatially distributed signals also reveal critical regions showing maximal or minimal signal magnitudes. Further studies on the bending signals suggest the dominating signal component is the circumferential bending component and the meridional signal component is less crucial in the overall modal voltage distribution. Appropriate selection of regional signal components and designs can further enhance the distributed control effectiveness of hemispheric shells. Note that this study is an analytical work based on electromechanics and dynamics of spherical shells. The design principle is evolved from detailed parametric studies. Practical implementation of the technique would require mono- or bi-axially oriented piezoelectric materials and multiple-channel data acquisition to display spatially distributed modal signal patterns.

REFERENCES

1. U. Gabbert and H.S. Tzou (Ed.) 2001 *Smart Structures and Structronic Systems*. Kluwer Academic Publishers, Boston/Dordrecht.
2. H.S. Tzou and G.L. Anderson (Ed.) 1992 *Intelligent Structural Systems*, Kluwer Academic Publishers, Dordrecht/Boston/London.
3. J. Callahan and H. Baruh 1999 *Smart Materials and Structures* **8**, 125-135. Modal Sensing of Circular Cylinder Shells Using Segmented Piezoelectric Elements.
4. C.K. Sung, T.F. Chen, and S.G. Chen 1996 *Journal of Vibration and Acoustics* **118**(1), 48-55. Piezoelectric Modal Sensor/Actuator Design for Monitoring/Generating Flexural and Torsional Vibrations of Cylindrical Shells.
5. H.S. Tzou 1993 *Piezoelectric Shells (Distributed Sensing and Control of Continua)*, Kluwer Academic Publishers, Boston/Dordrecht.
6. H.S. Tzou and R.J. Yang 2000 *Journal of Theoretical and Applied Mechanics* **38**(3), 623-644. Nonlinear Piezo-thermoelastic Shell Theory Applied to Control of Variable-geometry Shells.
7. J.W. S. Rayleigh 1945 *Theory of Sound*, 2nd Ed. 1, Dover Publications, New York. 418-432.
8. W.E. Baker 1961 *The Journal of The Acoustical Society of America* **33**(12), 1749-1758. Axisymmetric Modes of Vibration of Thin Spherical Shells.
9. A. Kalnins 1961 *The Journal of The Acoustical Society of America* **33**(8), 1102-1107. On Vibrations of Shallow Spherical Shells.
10. A. Kalnins 1964 *The Journal of The Acoustical Society of America* **36**(1), 74-81. Effect of Bending on Vibrations of Spherical Shells.
11. A. Kalnins 1964 *The Journal of The Acoustical Society of America* **36**(7), 1355-1365. Free Vibration of Rotationally Symmetric Shells.
12. A.K. Eikrem and A.G. Doige 1972 *Experimental Mechanics* **12**, 575-579. Natural Frequencies of a Hemispherical Shell.
13. W. Soedel 1981 *Vibrations of Shells and Plates*, Marcel Dekker Inc., New York.
14. R.D. Blevins 1987 *Formulas for Natural Frequency And Mode Shape*, Reprint Ed., Krieger Publisher Company, Florida. 330-336.
15. Z.E. Mazurkiewicz and R.T. Nagorski 1991 *Shells of Revolution*, PWN-Polish Scientific Publishers, Warsaw, 7-9, 333-341.

16. M.W. Johnson and E. Reissner 1956 *Journal of Mathematics and Physics* **34**, 335-346. On Inextensional Deformations of Shallow Elastic Shells.
17. C. Hwang 1966 *Journal of Applied Mechanics* **33**, 817-824. Some Experiments on the Vibration of a Hemispherical Shell.
18. V. Birman, G.J. Knowles and J.J. Murray 1999 *Smart Materials and Structures* **8**, 128-222. Application of Piezoelectric Actuators to Active Control of Composite Spherical Caps.
19. K. Chandrashekara and C.P. Smyser 1998 *Journal of Intelligent Material Systems and Structures* **9**, 29-43. Dynamic Modeling and Neural Control of Composite Shells Using Piezoelectric Devices.
20. V. Jayachandran and J.Q. Sun 1998 *Smart Materials and Structures* **7**, 72-84. Modeling Shallow-Spherical-Shell Piezoceramic Actuators as Acoustic Boundary Control Elements.
21. V. Jayachandran, M.A. Westervelt, N.E. Meyer and J.Q. Sun 1998 *Smart Materials and Structures* **7**, 467-471. Experimental Studies of Shallow Spherical Shell Piezoceramic Actuators as Acoustic Boundary Control Elements.
22. Y.H. Zhou, and H.S. Tzou, 2000 *International Journal of Solids and Structures* **37**, 1663-1977. Active Control of Nonlinear Piezoelectric Circular Shallow Spherical Shells.
23. H.S. Tzou, 1992 *Precision Sensors, Actuators, and Systems*, H.S. Tzou and T. Fukuda, (Editors), Kluwer Academic Publishers, Dordrecht /Boston /London. 175-218. Thin-Layer Distributed Piezoelectric Neurons and Muscles: Electromechanics and Applications.
24. R.V. Howard, W.K. Chai and H.S. Tzou 2001 *Mechanical Systems and Signal Processing* Vol.15, No.3, pp.629-640. Modal Voltages of Linear and Nonlinear Structures Using Distributed Artificial Neurons (A Theoretical and Experimental Study).
(MsspSensor.ShlSphere.2001)

CHAPTER 8

MICRO-CONTROL ACTIONS OF ACTUATOR PATCHES LAMINATED ON HEMISPHERICAL SHELLS

ABSTRACT

Spherical shell-type structures and components appear in many engineering systems, such as radar domes, pressure vessels, storage tanks, etc. This study is to evaluate the micro-control actions and distributed control effectiveness of segmented actuator patches laminated on hemispheric shells. Mathematical models and governing equations of the hemispheric shells laminated with distributed actuator patches are presented first, followed by formulations of distributed control forces and micro-control actions including meridional/circumferential membrane and bending control components. Due to difficulties in analytical solution procedures, assumed mode shape functions based on the bending approximation theory are used in the modal control force expressions and analyses. Spatially distributed electromechanical actuation characteristics resulting from various meridional and circumferential actions of segmented actuator patches are evaluated. Distributed control forces, patch sizes, actuator locations, micro-control actions, and normalized control authorities of a free-floating hemispheric shell are analyzed in case studies. Parametric analysis indicates that 1) the control forces and membrane/bending components are mode and location dependent, 2) actuators placed near the free boundary contributes the most significant control actions, and 3) the meridional/circumferential membrane control actions dominate the overall control effect.

INTRODUCTION

Radar domes, pressure vessels, storage tanks, etc. often take the form of spherical shells. Dynamic characteristics and vibrations of spherical shells and structures have been investigated over the years [1-5]. Natural frequencies of a shallow spherical shell and a thin hemisphere shell with free boundary condition have been investigated and experimentally verified [6-7]. Dynamic modal sensing characteristics, distributed modal voltages, and micro-signal components of spherical shells of revolution laminated with distributed piezoelectric sensor layers were recently investigated [8]. Actuations of spherical shells with piezoceramic actuators were also studied [9-11], so the conical shells and deep paraboloidal shells [12-13]. This study is to evaluate microscopic electromechanical actuation and control effectiveness of segmented patch actuators laminated on hemispherical shells.

Mathematical modeling of spherical shells coupled with distributed actuators is presented first, followed by analysis of actuator induced forces and micro-control actions respectively in the meridional, circumferential, and transverse directions. In order to evaluate modal dependent distributed micro-control actions, assumed mode shape functions based on the bending approximation theory are used in formulation of control forces and their contributing microscopic actions in the modal domain. Detailed control forces, contributing meridional and circumferential membrane/bending micro-control actions, and normalized control effects of free-hemispheric shells with various design parameters (e.g., actuator patch locations, shell thickness, and shell radius of curvature, etc.) are evaluated in case studies.

SEGMENTED DISTRIBUTED ACTUATOR PATCHES ON SPHERICAL SHELL

It is assumed that an arbitrary segmented piezoelectric actuator patch defined from ϕ_1 to ϕ_2 in the meridional direction and from ψ_1 to ψ_2 in the circumferential direction is laminated on the hemispherical shell, **Figure 1**. By the thin shell approximation, the radius of curvature of the actuator patch is $(R + h/2 + h^a/2) \approx R$, and the effective actuator area is approximately $R^2(\psi_2 - \psi_1)(\cos\phi_1 - \cos\phi_2)$.

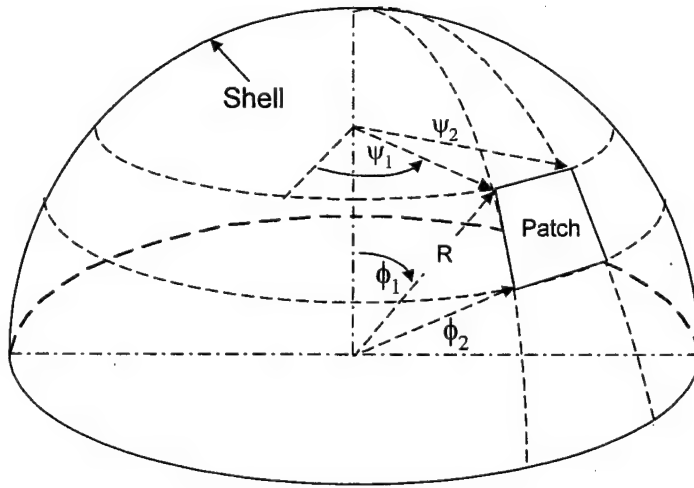


Fig.1 An arbitrary actuator patch laminated on a hemispheric shell.

If the electrode resistance is neglected, the control voltage on the segmented patch is constant. Thus, an actuator control voltage $\phi^a(\phi, \psi, t)$ (in *italic*) applied to the distributed actuator patch can be defined by

$$\phi^a(\phi, \psi, t) = \phi^a(t)[u_s(\phi - \phi_1) - u_s(\phi - \phi_2)][u_s(\psi - \psi_1) - u_s(\psi - \psi_2)], \quad (1)$$

where the superscript “a” denotes the induced actuator voltage; $u_s(\cdot)$ is a unit step function, $u_s(\phi - \phi^*) = 1$ when $\phi \geq \phi^*$, and = 0 when $\phi < \phi^*$. Accordingly, control actions induced by the actuator patch include a control force $N_{\phi\phi}^c$ in the ϕ -direction, a control force $N_{\psi\psi}^c$ in the ψ -

direction, a control moment $M_{\phi\phi}^c$ in the ϕ -direction, and a control moment $M_{\psi\psi}^c$ in the ψ -direction respectively and they are defined by

$$N_{\phi\phi}^c = Y_p d_{31} \phi^a [u_s(\phi - \phi_1) - u_s(\phi - \phi_2)][u_s(\psi - \psi_1) - u_s(\psi - \psi_2)], \quad (2)$$

$$N_{\psi\psi}^c = Y_p d_{32} \phi^a [u_s(\phi - \phi_1) - u_s(\phi - \phi_2)][u_s(\psi - \psi_1) - u_s(\psi - \psi_2)], \quad (3)$$

$$M_{\phi\phi}^c = r_i^a Y_p d_{31} \phi^a [u_s(\phi - \phi_1) - u_s(\phi - \phi_2)][u_s(\psi - \psi_1) - u_s(\psi - \psi_2)], \quad (4)$$

$$M_{\psi\psi}^c = r_i^a Y_p d_{32} \phi^a [u_s(\phi - \phi_1) - u_s(\phi - \phi_2)][u_s(\psi - \psi_1) - u_s(\psi - \psi_2)], \quad (5)$$

where Y_p is the actuator elastic modulus; d_{3i} is the piezoelectric strain constant; r_i^a defines the distance measured from the neutral surface to the mid-plane of the actuator patch (i.e., the moment arm); ϕ^a (in *italic*) is the imposed control voltage determined by control algorithms (e.g., open-loop or closed-loop control) [14-15]. Substituting the control forces and moments into the system equations of the spherical shell/actuator system and imposing the bending approximation theory [8], i.e., $N_{\phi\phi} = N_{\psi\psi} = N_{\phi\psi} = 0$, yields the simplified governing equations.

$$\frac{\partial}{\partial \phi} (-N_{\phi\phi}^c \sin \phi) - (-N_{\psi\psi}^c) \cos \phi + Q_{\phi 3} \sin \phi + R q_\phi \sin \phi = R \sin \phi \rho h \frac{\partial^2 u_\phi}{\partial t^2}, \quad (6)$$

$$\frac{\partial}{\partial \psi} (-N_{\psi\psi}^c) + Q_{\psi 3} \sin \phi + R q_\psi \sin \phi = R \sin \phi \rho h \frac{\partial^2 u_\psi}{\partial t^2}, \quad (7)$$

$$\frac{\partial}{\partial \phi} (Q_{\phi 3} \sin \phi) + \frac{\partial}{\partial \psi} (Q_{\psi 3}) - (-N_{\phi\phi}^c - N_{\psi\psi}^c) \sin \phi + R q_3 \sin \phi = R \sin \phi \rho h \frac{\partial^2 u_3}{\partial t^2}; \quad (8)$$

and
$$Q_{\phi 3} = \frac{1}{R \sin \phi} \left[\frac{\partial}{\partial \phi} ((M_{\phi\phi} - M_{\phi\phi}^c) \sin \phi) + \frac{\partial}{\partial \psi} (M_{\psi\phi}) - (M_{\psi\psi} - M_{\psi\psi}^c) \cos \phi \right], \quad (9)$$

$$Q_{\psi 3} = \frac{1}{R \sin \phi} \left[\frac{\partial}{\partial \phi} (M_{\phi\psi} \sin \phi) + \frac{\partial}{\partial \psi} (M_{\psi\psi} - M_{\psi\psi}^c) + M_{\psi\phi} \cos \phi \right]. \quad (10)$$

The first two equations are respectively the meridional and the circumferential dynamic/control equations; the third one is the transverse dynamic/control equation; and the last two define the transverse shear effects contributed by elastic and control moments. Distributed control components appear in all three equations and thus, open- or closed-loop distributed control of spherical shells can be achieved. These three equations are fully coupled spherical shell/actuator system equations and the membrane control effects are still preserved in the system equations, although the elastic membrane forces of the spherical shell are neglected in the bending approximation. Note that the objective of this study is to evaluate spatially distributed micro-control actions of strategically placed actuator patches at various locations, not the hemispherical shell dynamics. To focus on the micro-membrane and bending control characteristics, assumed mode shape functions and natural frequencies resulting from the bending approximation theory are used in the parametric study of modal control forces

contributed by distributed actuator segments. Although the elastic membrane effects are essential to the fully-coupled shell dynamics, they are neglected in the classical bending approximation theory.

ANALYSIS OF CONTROL ACTIONS IN MODAL DOMAIN

The modal expansion assumption states that the displacement response $u_i(\phi, \psi, t)$ in the i -th direction of the hemispherical shell is composed of all participating modes, i.e., $u_i(\phi, \psi, t) = \sum_{k=2}^{\infty} \eta_{ik}(t) U_{ik}(\phi, \psi)$, $i=\phi, \psi, 3$. Imposing the modal expansion and the modal orthogonality and including a viscous damping, one can derive the modal equation of the hemispherical shell as

$$\ddot{\eta}_k + 2\zeta_k \omega_k \dot{\eta}_k + \omega_k^2 \eta_k = F_k^m(t) + F_k^c(t) \equiv \hat{F}_k(t), \quad (11)$$

where η_k is the modal participation factor; ζ_k is the damping ratio $\zeta_k = \frac{c}{2\rho h \omega_k}$; c is the damping constant; ω_k is the k -th natural frequency; ρ is the mass density of the shell; $F_k^m(t)$ is the mechanical excitation; $F_k^c(t)$ is the electrical control excitation; k denotes the circumferential wave number; and $\hat{F}_k(t)$ is the total modal force. **Figure 2** shows the open-loop control of the hemispherical shell system.

Recall that the modal electric control force F_k^c induced by the piezoelectric actuator patch includes four control actions: a control force $N_{\phi\phi}^c$ in the ϕ -direction, a control force $N_{\psi\psi}^c$ in the ψ -direction, a control moment $M_{\phi\phi}^c$ in the ϕ -direction, and a control moment $M_{\psi\psi}^c$ in the ψ -direction defined previously. Although the elastic membrane forces are neglected in the bending approximation, the membrane control forces are still preserved in the system equations, such that their spatially distributed micro-control actions can still be evaluated. The assumed mode shape functions based on the bending approximation theory are used to evaluate modal control forces and microscopic control actions. The micro-control actions of actuator patches depend on actuator characteristics, spatial locations, and modal behavior. Although the elastic membrane effect of the shell will affect the modal behavior, it doesn't explicitly appear in micro-control actions of actuator patches. Detailed modal control forces and micro-control actions of spherical actuator patches are analyzed next.

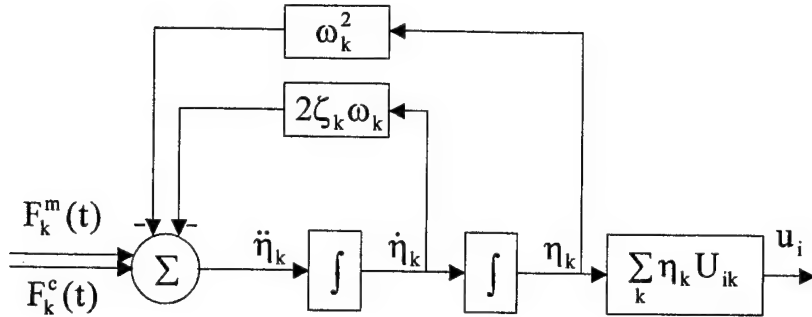


Fig.2 Open-loop control of a hemispherical shell/actuator system.

Modal Characteristics and Modal Control Forces

Evaluation of modal micro-sensing and actuation characteristics of distributed and segmented sensors/actuators depends on fundamental structural dynamics and free-vibration behavior. For a free-edge boundary hemispherical shell with the bending approximation, the free-vibration mode shape functions $U_{ik}(\phi, \psi)$ are [1,8,16]

$$U_{\phi k} = -A(\tan \frac{\phi}{2})^k \sin k\psi, \quad (12)$$

$$U_{\psi k} = -B \sin \phi (\tan \frac{\phi}{2})^k \cos k\psi, \quad (13)$$

$$U_{3k} = CR(k + \cos \phi) (\tan \frac{\phi}{2})^k \cos k\psi, \quad (14)$$

where $U_{\phi k}$ is the meridional mode shape function; $U_{\psi k}$ is the circumferential mode shape function; U_{3k} is the radial (transverse) mode shape function; k is the circumferential wave number; ϕ is the meridional angle measured from the pole; ψ is the circumferential angle; and A , B , and C are the modal amplitudes. Natural frequencies of a shallow shell and a thin hemispherical shell with free boundary condition have been studied and experimentally verified, respectively [6-7]. To evaluate the control actions, the mechanical excitation is neglected and hence the modal control force $\hat{F}_k(t)$ is defined by actuator induced forces.

$$\hat{F}_k(t) = \frac{1}{\rho h N_k} \int \int \left\{ \sum_i L_i^c(\phi_3) U_{ik} \right\} R^2 \sin \phi d\phi d\psi, \quad i = \phi, \psi, 3, \quad (15)$$

where $N_k = \int \int \left\{ \sum_i U_{ik}^2 \right\} R^2 \sin \phi d\phi d\psi$; $L_i^c(\phi_3)$ denotes a control operator derived from the converse piezoelectric effect with a transverse control signal ϕ_3 [17]. Detailed microscopic membrane and bending control actions induced by actuator patches are analyzed next.

MICRO-CONTROL ACTIONS OF ACTUATOR PATCHES

Micro-control actions of an arbitrary segmented actuator patch defined from ϕ_1 to ϕ_2 in the meridional direction and from ψ_1 to ψ_2 in the circumferential direction, **Figure 1**, are evaluated in this section. It is assumed that the actuator is made of a hexagonal piezoelectric material, i.e., $d_{31}=d_{32}$ and both the actuator and the shell are of uniform thickness. Rewriting the modal control force $\hat{F}_k(t)$ in its meridional, circumferential, and transverse components respectively yields

$$\hat{F}_k(t) = \frac{1}{\rho h N_k} \int \int \{L_\phi^c(\phi_3) U_{\phi k} + L_\psi^c(\phi_3) U_{\psi k} + L_3^c(\phi_3) U_{3k}\} R^2 \sin \phi d\phi d\psi , \quad (16)$$

$$\text{or } \hat{F}_k(t) = \frac{Y_p d_{31} \phi^a(t)}{\rho} [(\hat{T}_k)_{\text{Total}}] = \frac{Y_p d_{31} \phi^a(t)}{\rho} [(\hat{T}_{k_merd}) + (\hat{T}_{k_cir}) + (\hat{T}_{k_trans})], \quad i = 1, 2 , \quad (17)$$

where $(\hat{T}_k)_{\text{Total}}$ denotes the overall actuation action determined by actuator location and modal characteristics, but excluding material constants and modal amplitudes (assumed unity); (\hat{T}_{k_merd}) , (\hat{T}_{k_cir}) and (\hat{T}_{k_trans}) respectively denote the actuation magnitudes in the meridional, circumferential and transverse directions defined next. Note that design parameters $h N_k$ are included in control action expressions and d_{3i} is the piezoelectric constant which will be specifically defined with respect to these control actions later, although $d_{31}=d_{32}$ in commonly used piezoelectric materials. Since the piezoelectric strain constants $d_{31}=d_{32}$ and the effective distance (i.e., moment arm) $r_1^a = r_2^a = r^a$, both the control membrane forces and the control moments are equal, i.e., $N_{\phi\phi}^c = N_{\psi\psi}^c$ and $M_{\phi\phi}^c = M_{\psi\psi}^c$. Using the control force and moment definitions of the actuator patch bounded by ϕ_1 to ϕ_2 and ψ_1 to ψ_2 , substituting the mode shape functions and keeping two design parameters $h N_k$ in control actions, one can rewrite the meridional and the circumferential control forces of spherical actuator patches as

$$\begin{aligned} \frac{1}{\rho h N_k} \int \int L_\phi^c(\phi_3) U_{\phi k} R^2 \sin \phi d\phi d\psi &= \frac{1}{\rho h N_k} \int \int_{\psi_1 \phi_1}^{\psi_2 \phi_2} A \left(\tan \frac{\phi}{2} \right)^k \sin k\psi \cdot \sin \phi \cdot (R + r^a) \\ &\quad \cdot Y_a d_{31} \phi^a \cdot [\delta(\phi - \phi_1) - \delta(\phi - \phi_2)] [u_s(\psi - \psi_1) - u_s(\psi - \psi_2)] d\phi d\psi \\ &= \frac{Y_p d_{31} \phi^a}{\rho h N_k} \frac{A}{k} \cdot (R + r^a) \cdot \left[\left(\tan \frac{\phi_1}{2} \right)^k \cdot \sin \phi_1 - \left(\tan \frac{\phi_2}{2} \right)^k \cdot \sin \phi_2 \right] (\cos k\psi_1 - \cos k\psi_2) \\ &= \frac{Y_p d_{31} \phi^a(t)}{\rho} [(\hat{T}_{k_merd})]; \end{aligned} \quad (18)$$

$$\begin{aligned} \frac{1}{\rho h N_k} \int \int L_\psi^c(\phi_3) U_{\psi k} R^2 \sin \phi d\phi d\psi &= \frac{1}{\rho h N_k} \int \int_{\psi_1 \phi_1}^{\psi_2 \phi_2} B \sin \phi \left(\tan \frac{\phi}{2} \right)^k \cos k\psi \cdot (R + r^a) \\ &\quad \cdot Y_p d_{32} \phi^a \cdot [u_s(\phi - \phi_1) - u_s(\phi - \phi_2)] [\delta(\psi - \psi_1) - \delta(\psi - \psi_2)] d\phi d\psi \end{aligned}$$

$$\begin{aligned}
&= \frac{Y_p d_{32} \phi^a}{\rho h N_k} B \cdot (R + r^a) \cdot (\cos k\psi_1 - \cos k\psi_2) \int_{\phi_1}^{\phi_2} \sin \phi (\tan \frac{\phi}{2})^k d\phi \\
&= \frac{Y_p d_{32} \phi^a(t)}{\rho} [(\hat{T}_{k_cir})], \tag{19}
\end{aligned}$$

where $\delta(\cdot)$ is a Dirac delta function: $\delta(\phi - \phi^*) = 1$ when $\phi = \phi^*$, and = 0 when $\phi \neq \phi^*$. And, the transverse modal control force can be rewritten as

$$\begin{aligned}
\frac{1}{\rho h N_k} \int_{\psi} \int_{\phi} L_3^c(\phi_3) U_{3k} R^2 \sin \phi d\phi d\psi &= \frac{1}{\rho h N_k} \int_{\psi} \int_{\phi} \left\{ \frac{\partial}{\partial \phi} \left[\frac{\partial (M_{\phi\phi}^c \sin \phi)}{\partial \phi} \right] - \frac{\partial}{\partial \phi} (M_{\psi\psi}^c \cos \phi) \right. \\
&\quad \left. + \frac{1}{\sin \phi} \frac{\partial}{\partial \psi} \left[\frac{\partial (M_{\psi\psi}^c)}{\partial \psi} \right] - R \sin \phi [N_{\phi\phi}^c + N_{\psi\psi}^c] \right\} \cdot \left[-CR(k + \cos \phi) (\tan \frac{\phi}{2})^k \cos k\psi \right] d\phi d\psi. \tag{20}
\end{aligned}$$

Note that $\frac{\partial}{\partial \phi} \left[\frac{\partial (M_{\phi\phi}^c \sin \phi)}{\partial \phi} \right] = \frac{\partial}{\partial \phi} [M_{\phi\phi}^c \cos \phi + \sin \phi \frac{\partial (M_{\phi\phi}^c)}{\partial \phi}] = \frac{\partial}{\partial \phi} [M_{\phi\phi}^c \cos \phi] + \frac{\partial}{\partial \phi} [\sin \phi \frac{\partial (M_{\phi\phi}^c)}{\partial \phi}]$
 $= \frac{\partial}{\partial \phi} [M_{\phi\phi}^c \cos \phi] + \sin \phi \frac{\partial}{\partial \phi} \left[\frac{\partial (M_{\phi\phi}^c)}{\partial \phi} \right] + \cos \phi \frac{\partial (M_{\phi\phi}^c)}{\partial \phi}$ and $N_{\phi\phi}^c = N_{\psi\psi}^c$, $M_{\phi\phi}^c = M_{\psi\psi}^c$. Then, the transverse control force is reduced to

$$\begin{aligned}
\frac{1}{\rho h N_k} \int_{\psi} \int_{\phi} L_3^c(\phi_3) U_{3k} R^2 \sin \phi d\phi d\psi &= \frac{1}{\rho h N_k} \int_{\psi} \int_{\phi} \left\{ \sin \phi \frac{\partial}{\partial \phi} \left[\frac{\partial (M_{\phi\phi}^c)}{\partial \phi} \right] + \cos \phi \frac{\partial (M_{\phi\phi}^c)}{\partial \phi} \right. \\
&\quad \left. + \frac{1}{\sin \phi} \frac{\partial}{\partial \psi} \left[\frac{\partial (M_{\psi\psi}^c)}{\partial \psi} \right] - R \sin \phi [N_{\phi\phi}^c + N_{\psi\psi}^c] \right\} \cdot \left[-CR(k + \cos \phi) (\tan \frac{\phi}{2})^k \cos k\psi \right] d\phi d\psi \tag{21} \\
&= \frac{Y_p d_{31} \phi^a(t)}{\rho} [(\hat{T}_{k_trans})],
\end{aligned}$$

where the transverse control action (\hat{T}_{k_trans}) and its contributing meridional and circumferential membrane/bending components, i.e., $(\hat{T}_{k_trans}) = (\hat{T}_{k_trans})_{\phi,bend} + (\hat{T}_{k_trans})_{\psi,bend} + (\hat{T}_{k_trans})_{\phi,mem} + (\hat{T}_{k_trans})_{\psi,mem}$, will be explicitly defined next. Unlike the meridional and the circumferential control actions, the transverse action requires integration by parts to reveal detailed micro-control characteristics. Analyze the transverse control action in Eq.(21) term by term, beginning with the first term related to the meridional control moment.

$$\begin{aligned}
& \frac{1}{\rho h N_k} \iint_{\psi \phi} \sin \phi \frac{\partial}{\partial \phi} \left[\frac{\partial (M_{\phi \phi}^c)}{\partial \phi} \right] \cdot [-U_{3k}] d\phi d\psi = \frac{1}{\rho h N_k} \iint_{\psi_1 \phi_1}^{\psi_2 \phi_2} -CR(k + \cos \phi) (\tan \frac{\phi}{2})^k \cos k\psi \cdot \sin \phi \\
& \quad \cdot r^a Y_p d_{31} \phi^a \cdot \frac{\partial}{\partial \phi} [\delta(\phi - \phi_1) - \delta(\phi - \phi_2)] [u_s(\psi - \psi_1) - u_s(\psi - \psi_2)] d\phi d\psi \\
& = \frac{Y_p d_{31} \phi^a}{\rho h N_k} \left(-\frac{C}{k} R \cdot r^a \right) \cdot (\sin k\psi_2 - \sin k\psi_1) \{ [-(k + \cos \phi_2) (\tan \frac{\phi_2}{2})^k \sin \phi_2 \right. \\
& \quad \left. - (k + \cos \phi_1) (\tan \frac{\phi_1}{2})^k \sin \phi_1] - [(k^2 + 2k \cos \phi_1 + \cos 2\phi_1) (\tan \frac{\phi_1}{2})^k \right. \\
& \quad \left. - (k^2 + 2k \cos \phi_2 + \cos 2\phi_2) (\tan \frac{\phi_2}{2})^k] \} . \tag{22a}
\end{aligned}$$

And the second term due to the meridional control moment becomes

$$\begin{aligned}
& \frac{1}{\rho h N_k} \iint_{\psi \phi} \cos \phi \frac{\partial (M_{\phi \phi}^c)}{\partial \phi} \cdot [-U_{3k}] d\phi d\psi = \frac{1}{\rho h N_k} \iint_{\psi_1 \phi_1}^{\psi_2 \phi_2} -CR(k + \cos \phi) (\tan \frac{\phi}{2})^k \cos k\psi \cdot \cos \phi \\
& \quad \cdot r^a Y_p d_{31} \phi^a \cdot [\delta(\phi - \phi_1) - \delta(\phi - \phi_2)] [u_s(\psi - \psi_1) - u_s(\psi - \psi_2)] d\phi d\psi \\
& = \frac{Y_p d_{31} \phi^a}{\rho h N_k} \left(-\frac{CR}{k} \cdot r^a \right) \cdot (\sin k\psi_2 - \sin k\psi_1) \\
& \quad \cdot [(k + \cos \phi_1) (\tan \frac{\phi_1}{2})^k \cos \phi_1 - (k + \cos \phi_2) (\tan \frac{\phi_2}{2})^k \cos \phi_2] . \tag{22b}
\end{aligned}$$

Combining Eq.(22a) and Eq.(22b) yields the control action from the meridional control moment: $\frac{Y_p d_{31} \phi^a(t)}{\rho} [(\hat{T}_{k_trans})_{\phi, bend}]$. Then, the third term of the circumferential control moment in the transverse control action becomes

$$\begin{aligned}
& \frac{1}{\rho h N_k} \iint_{\psi \phi} \frac{1}{\sin \phi} \frac{\partial}{\partial \psi} \left[\frac{\partial (M_{\psi \psi}^c)}{\partial \psi} \right] \cdot [-U_{3k}] d\phi d\psi = \frac{1}{\rho h N_k} \iint_{\psi_1 \phi_1}^{\psi_2 \phi_2} -CR(k + \cos \phi) (\tan \frac{\phi}{2})^k \cos k\psi \cdot \frac{1}{\sin \phi} \\
& \quad \cdot r^a Y_p d_{32} \phi^a \cdot [u_s(\phi - \phi_1) - u_s(\phi - \phi_2)] \frac{\partial}{\partial \psi} [\delta(\psi - \psi_1) - \delta(\psi - \psi_2)] d\phi d\psi \\
& = \frac{Y_p d_{32} \phi^a}{\rho h N_k} (-CR \cdot r^a) \{ (-\cos k\psi_2 - \cos k\psi_1) + k(\sin k\psi_1 - \sin k\psi_2) \} \int_{\phi_1}^{\phi_2} (k + \cos \phi) (\tan \frac{\phi}{2})^k \frac{1}{\sin \phi} d\phi \\
& = \frac{Y_p d_{32} \phi^a(t)}{\rho} [(\hat{T}_{k_trans})_{\psi, bend}] . \tag{22c}
\end{aligned}$$

Finally, the fourth term of the transverse action related to the meridional and circumferential membrane control forces becomes

$$\begin{aligned}
 & \frac{1}{\rho h N_k} \iint_{\psi \phi} -R \sin \phi [N_{\phi \phi}^c + N_{\psi \psi}^c] \cdot [-U_{3k}] d\phi d\psi = \frac{1}{\rho h N_k} \iint_{\psi_1 \phi_1}^{\psi_2 \phi_2} 2CR^2 (k + \cos \phi) (\tan \frac{\phi}{2})^k \cos k\psi \cdot \sin \phi \\
 & \cdot Y_p d_{31} \phi^a \cdot [u_s(\phi - \phi_1) - u_s(\phi - \phi_2)][u_s(\psi - \psi_1) - u_s(\psi - \psi_2)] d\phi d\psi \\
 & = \frac{Y_p d_{31} \phi^a}{\rho h N_k} \left(2 \frac{C}{k} R^2 \right) \cdot (\sin k\psi_2 - \sin k\psi_1) \int_{\phi_1}^{\phi_2} (k + \cos \phi) (\tan \frac{\phi}{2})^k \sin \phi d\phi \\
 & = \frac{Y_p d_{31} \phi^a (t)}{\rho} [(\hat{T}_{k_trans})_{\phi,mem} + (\hat{T}_{k_trans})_{\psi,mem}].
 \end{aligned} \tag{22d}$$

Note that the meridional and the circumferential membrane control forces (i.e., $N_{\phi \phi}^c$ and $N_{\psi \psi}^c$) appear equal, due to the two piezoelectric constants $d_{31}=d_{32}$ in hexagonal piezoelectric materials and each contributes one half the total membrane control action in the above equation. Accordingly, all three control forces and their detailed micro-control actions in the total control force $\hat{F}_k(t) = \frac{1}{\rho h N_k} \iint_{\psi \phi} \{L_\phi^c(\phi_3)U_{\phi k} + L_\psi^c(\phi_3)U_{\psi k} + L_3^c(\phi_3)U_{3k} \cdot R^2 \sin \phi\} d\phi d\psi$ are defined and its simplified microscopic contributing meridional/circumferential bending and membrane control components: $\hat{F}_k(t) = \frac{Y_p d_{31} \phi^a (t)}{\rho} [(\hat{T}_k)_{Total}]$ are respectively derived in Eqs.(18), (19), and (22a,b,c,d). And their detailed microscopic control actions can be rewritten as

$$(\hat{T}_{k_merd}) = (\hat{T}_{k_mer})_{\phi,bend} + (\hat{T}_{k_mer})_{\psi,bend} + (\hat{T}_{k_mer})_{\phi,mem} + (\hat{T}_{k_mer})_{\psi,mem}, \tag{23}$$

$$(\hat{T}_{k_cir}) = (\hat{T}_{k_cir})_{\phi,bend} + (\hat{T}_{k_cir})_{\psi,bend} + (\hat{T}_{k_cir})_{\phi,mem} + (\hat{T}_{k_cir})_{\psi,mem}, \tag{24}$$

$$(\hat{T}_{k_trans}) = (\hat{T}_{k_trans})_{\phi,bend} + (\hat{T}_{k_trans})_{\psi,bend} + (\hat{T}_{k_trans})_{\phi,mem} + (\hat{T}_{k_trans})_{\psi,mem}, \tag{25}$$

where $(\hat{T}_k)_{\phi,bend}$ and $(\hat{T}_k)_{\psi,bend}$ denote the bending control moment actions resulting from $M_{\phi \phi}^c$ and $M_{\psi \psi}^c$; $(\hat{T}_k)_{\phi,mem}$ and $(\hat{T}_k)_{\psi,mem}$ denote the membrane control force actions resulting from $N_{\phi \phi}^c$ and $N_{\psi \psi}^c$ respectively. Note that the transverse meridional bending control action $(\hat{T}_{k_trans})_{\phi,bend}$ is the summation of Eqs.(22a) and (22b) and the transverse circumferential bending control action $(\hat{T}_{k_trans})_{\psi,bend}$ is equal to Eq.(22c). The total membrane control action, Eq.(22d), consists of a transverse meridional membrane control action $(\hat{T}_{k_trans})_{\phi,mem}$ and a transverse circumferential membrane control action $(\hat{T}_{k_trans})_{\psi,mem}$. Since the effective moment

arm $r_1^a = r_2^a = r^a$ and the piezoelectric constants $d_{31}=d_{32}$, magnitudes of these two membrane actions are equal, i.e., $(\hat{T}_{k_trans})_{\phi,mem} = (\hat{T}_{k_trans})_{\psi,mem}$. These detailed microscopic modal control actions and components corresponding to various design and geometric parameters are analyzed in case studies presented next.

PARAMETRIC STUDY OF ACTIVE VIBRATION CONTROL

A systematic study of actuator characteristics, micro-control actions, and control effectiveness of segmented actuator patches on free-edge hemispheric shells is presented in this section. Parametric analyses of design parameters, such as actuator position, shell thickness, shell curvature, etc., are conducted to evaluate actuator characteristics and microscopic control actions. Standard dimensions of the hemispherical shell are as follows. Shell curvature radius $R = 1\text{m}$, shell thickness $h = 0.01\text{m}$, and piezoelectric actuator thickness $h^a = 40\text{ }\mu\text{m}$. Effects of dimensional changes are compared with those derived from these standard dimensions. Other

actuator material constants and control signal, e.g., $\frac{Y_p d_{31} \phi^a(t)}{\rho}$, are assumed constant, such that control forces can be calculated when actuator materials and signals are specified. Note that although the current piezoelectric materials may not be strong enough to achieve effective control, these parametric analyses still reveal actuator's spatial control actions and desirable locations for various natural mode controls.

Control characteristics of natural modes ($k=2,3,4$) are evaluated in case studies. Since the in-plane meridional and circumferential vibrations are usually small as compared with the transverse vibration, this study primarily focuses on control effects and micro-control actions that are essential to the transverse vibration, i.e., (\hat{T}_{k_trans}) . The transverse modal control force $(\hat{T}_k)_{Total}$ and its micro-contributing components, i.e., $(\hat{T}_k)_{\phi,bend}$, $(\hat{T}_k)_{\psi,bend}$, $(\hat{T}_k)_{\phi,mem}$ and $(\hat{T}_k)_{\psi,mem}$, related to actuator positions, shell thickness, shell curvature, etc. are evaluated next.

Actuator Patch Positions

The segmented actuator patches are laminated on the shell at 0-10, 10-20, 20-30, ..., 80-90 meridian degrees and the patch is circumferentially divided at every $(2n-1)\pi/(2k)$ radians where n is the number of divisions, $n=1, 2, 3, \dots, 2k$, and k is the circumferential wave number. Note that the circumferential division, i.e., $(2n-1)\pi/(2k)$, assures that the patches are divided based on nodal lines without any phase shift, such that the maximal control effect can be achieved. **Figure 3** illustrates the actuator patch segmentation designed for the 4-th hemispheric shell mode.

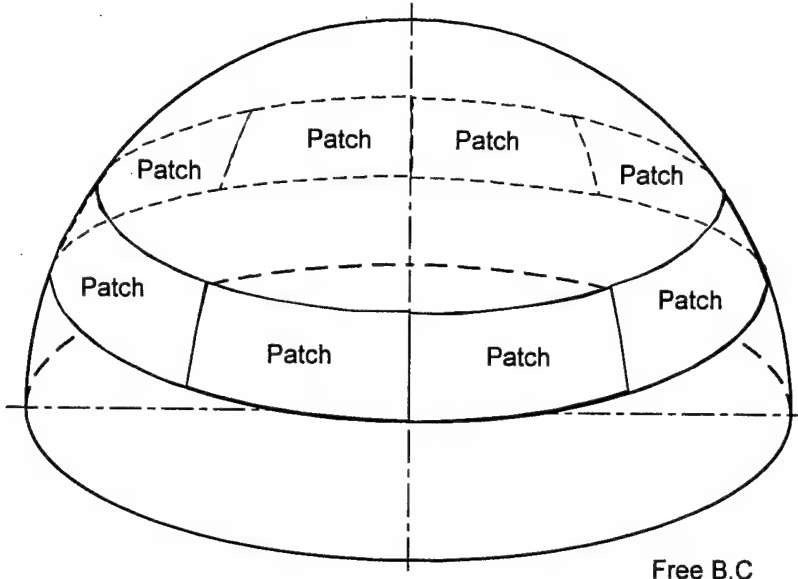


Fig.3 Piezoelectric actuator patch positions for the $k=4$ mode.

The overall modal control force of patch actuators (i.e., including the surface integration over the patch) is calculated for the $k=2,3,4$ natural modes. With the segmented actuator patches designed as discussed previously, i.e., $(2n-1)\pi/(2k)$, the in-plane control actions (\hat{T}_{k_mer}) and (\hat{T}_{k_cir}) are zero, due to the spatial effect that $\cos k\psi_1$ and $\cos k\psi_2$ become zero when specific circumferential angles are considered in Eqs.(18) and (19). Thus, only the transverse control action (\hat{T}_{k_trans}) contributes to the overall control action (\hat{T}_k), which includes 1) micro-control actions induced by control moments, i.e., $(\hat{T}_{k_trans})_{\phi,bend}$ and $(\hat{T}_{k_trans})_{\psi,bend}$, and 2) those induced by membrane control forces, i.e., $(\hat{T}_{k_trans})_{\phi,mem}$ and $(\hat{T}_{k_trans})_{\psi,mem}$. The total transverse control actions (\hat{T}_{k_trans}) for the $k=2,3,4$ modes at various patch locations (from $0-90^\circ$) are calculated and plotted in **Figure 4**. Detailed microscopic meridional and circumferential control actions including the membrane control components and the bending moment control components for the $k=2,3,4$ modes are respectively calculated and summarized in **Figures 5-7**, and so N_k plotted in **Figure 8**.

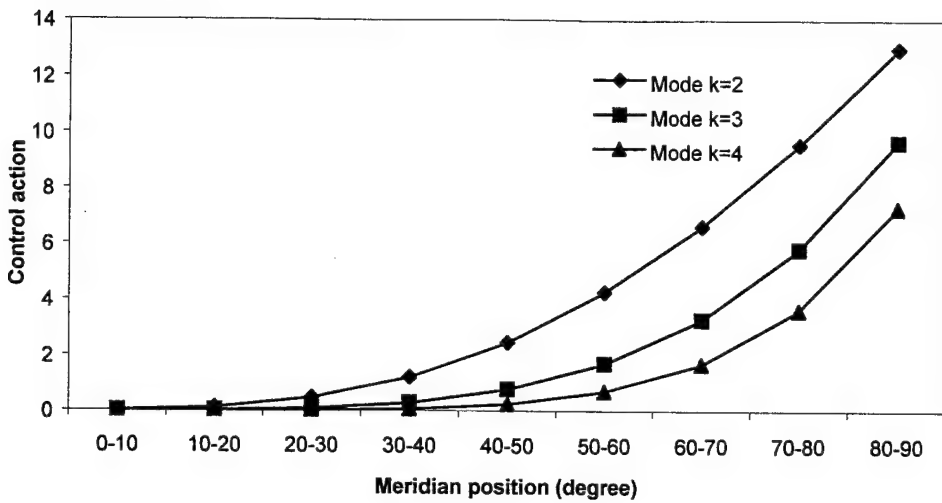


Fig.4 Total modal control action (\hat{T}_{k_trans}) at various locations ($k=2,3,4$)
 (♦: $k=2$ mode; ■: $k=3$ mode; ▲: $k=4$ mode.)

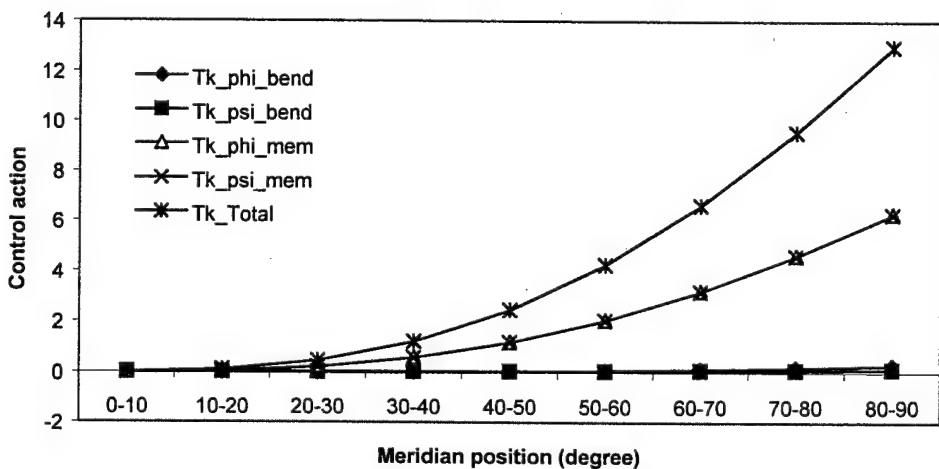


Fig.5 Micro-modal control actions at various actuator locations ($k=2$).
 (♦: $(\hat{T}_{k_trans})_{\phi,bend}$; ■: $(\hat{T}_{k_trans})_{\psi,bend}$; △: $(\hat{T}_{k_trans})_{\phi,mem}$; and ×: $(\hat{T}_{k_trans})_{\psi,mem}$; *: (\hat{T}_k) .)

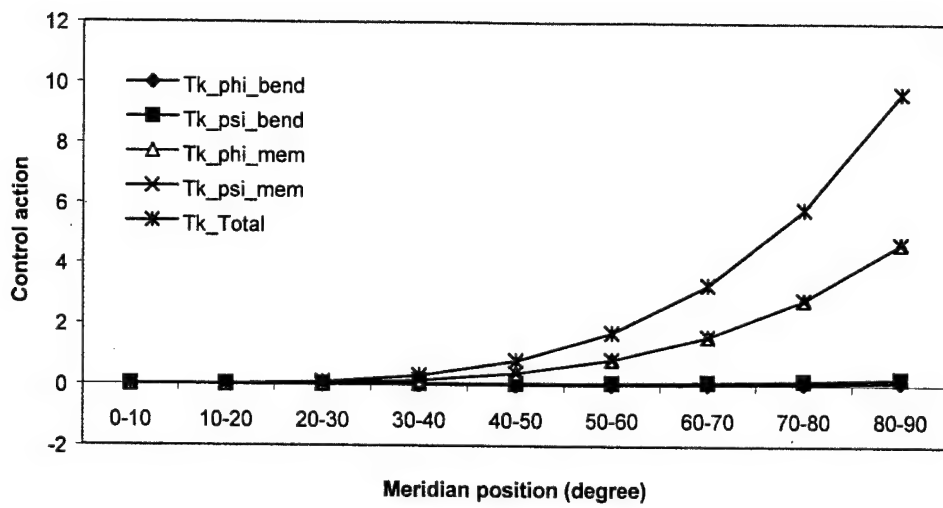


Fig.6 Modal control actions at various actuator locations (k=3).
 (♦: $(\hat{T}_k \text{trans})_{\phi, \text{bend}}$; ■: $(\hat{T}_k \text{trans})_{\psi, \text{bend}}$; Δ: $(\hat{T}_k \text{trans})_{\phi, \text{mem}}$; and ×: $(\hat{T}_k \text{trans})_{\psi, \text{mem}}$; *: (\hat{T}_k) .)

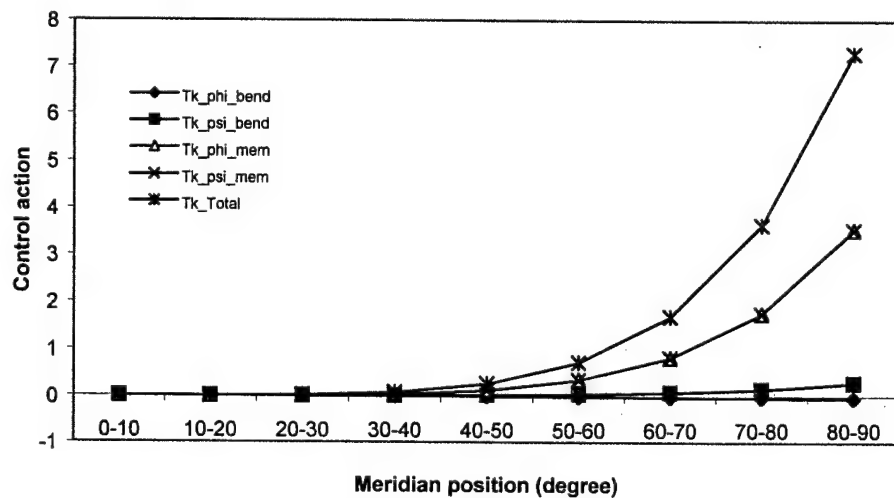


Fig.7 Modal control actions at various actuator locations (k=4).
 (♦: $(\hat{T}_k \text{trans})_{\phi, \text{bend}}$; ■: $(\hat{T}_k \text{trans})_{\psi, \text{bend}}$; Δ: $(\hat{T}_k \text{trans})_{\phi, \text{mem}}$; and ×: $(\hat{T}_k \text{trans})_{\psi, \text{mem}}$; *: (\hat{T}_k) .)

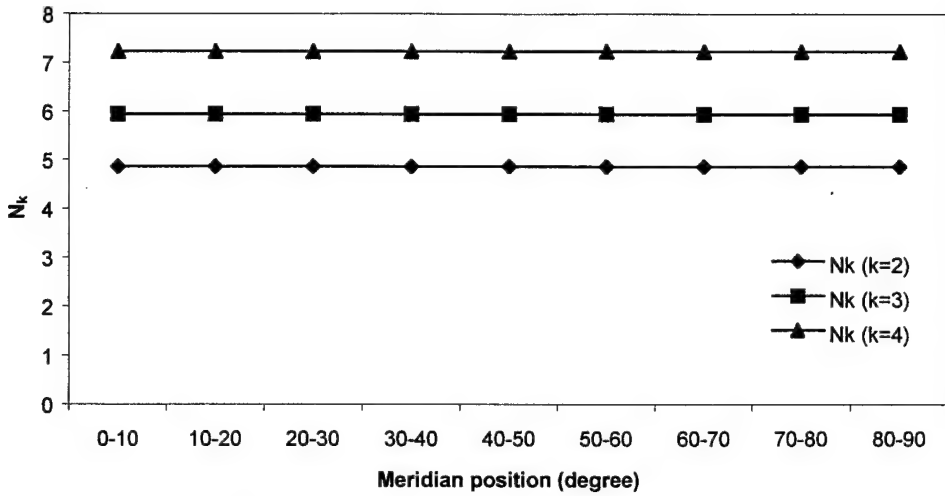


Fig.8 N_k at various actuator locations ($k=2,3,4$).

(♦: $k=2$ mode; ■: $k=3$ mode; ▲: $k=4$ mode.)

Figure 4 illustrates that the control action increases when the actuator patch moves from the pole to the free edge and it decreases at higher natural modes. Observing **Figures 5-7** suggests that 1) the total control action decreases when the circumferential wave number (or the mode) increases and 2) the membrane components, $(\hat{T}_k)_{\phi,\text{mem}}$ and $(\hat{T}_k)_{\psi,\text{mem}}$, dominate the overall control action. **Figure 8** shows that N_k increases when the mode increases, which results in a reduced control action at higher modes, since $h \times N_k$ is on the denominator of the control force definition.

Shell Thickness

The bending behavior becomes relatively significant in a thicker shell. Variation of shell thickness is to evaluate the thickness effect to actuation characteristics. The hemispherical shell thickness is assumed changing from 1cm to 6cm, while the standard shell radius R remains at 1m or diameter of 2 meters. The piezoelectric actuator thickness h^a is 40 μm , located at 80-90 degree meridian, and the actuators are circumferentially segmented at every $(2n-1)\pi/(2k)$ radians where $n=1, 2, 3, \dots, 2k$. The patch control forces of the $k=2-4$ modes are analyzed and plotted in **Figure 9**. It shows that the control action decreases when the shell thickens, due to increased flexible rigidity, and it also decreases at higher natural modes. Detailed $k=2-4$ modal micro-control actions of various shell thickness are also calculated and plotted in **Figures 10-12**.

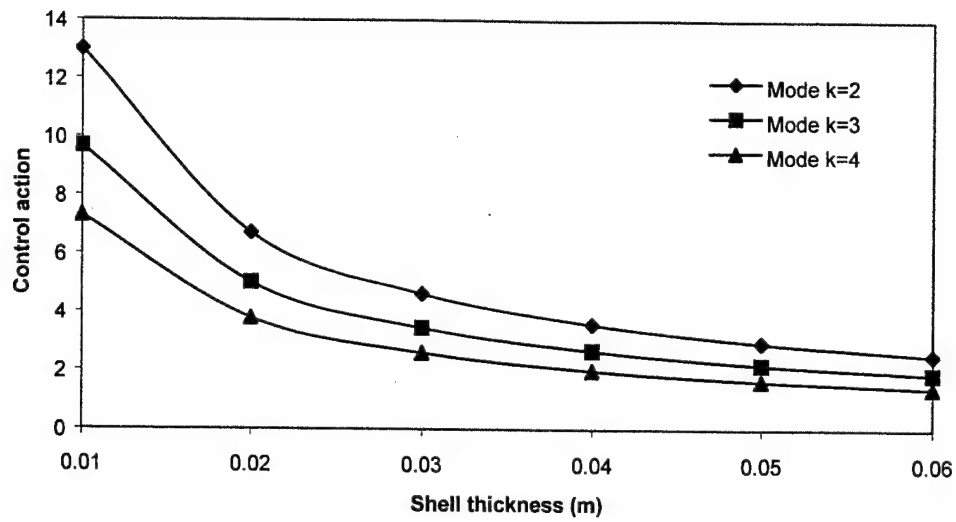


Fig.9 Total modal patch control action (\hat{T}_{k_trans}) at various shell thickness (Position 80-90°, R=1m, k=2,3,4). (♦: k=2 mode; ■: k=3 mode; ▲: k=4 mode.)

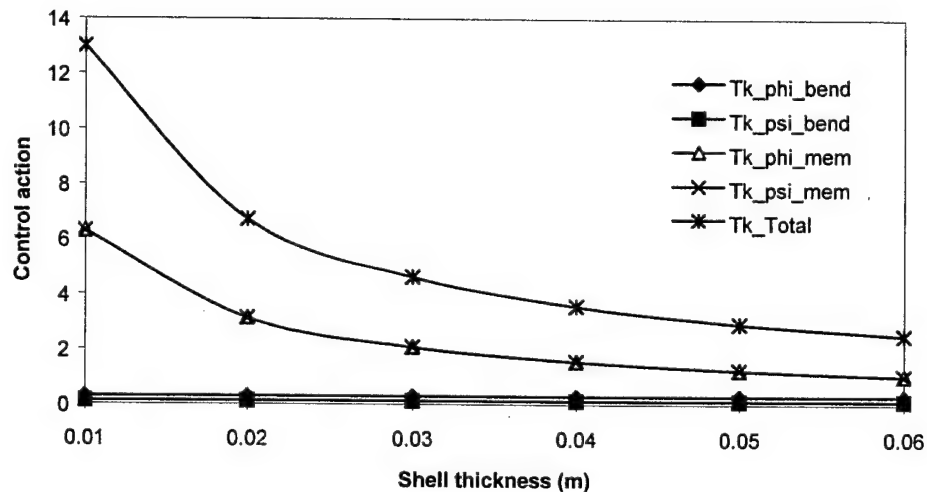


Fig.10 Modal control actions at various shell thickness (Position 80-90°, R=1m, k=2). (♦: $(\hat{T}_{k_trans})_{\phi,bend}$; ■: $(\hat{T}_{k_trans})_{\psi,bend}$; ▲: $(\hat{T}_{k_trans})_{\phi,mem}$; and ×: $(\hat{T}_{k_trans})_{\psi,mem}$; *: (\hat{T}_k) .)

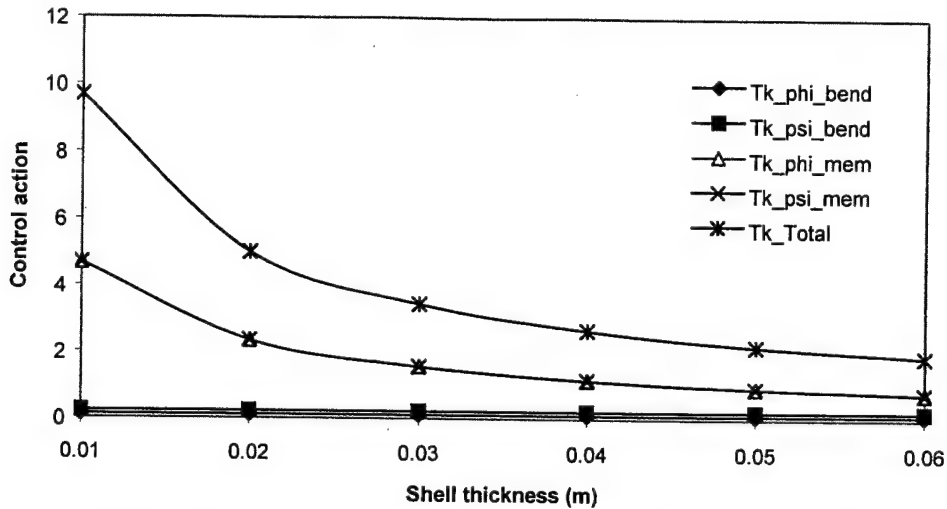


Fig.11 Modal control actions at various shell thickness (Position 80-90°, R=1m, k=3).

(♦: $(\hat{T}_{k_trans})_{\phi,bend}$; ■: $(\hat{T}_{k_trans})_{\psi,bend}$; Δ: $(\hat{T}_{k_trans})_{\phi,mem}$; and ×: $(\hat{T}_{k_trans})_{\psi,mem}$; *: (\hat{T}_k) .)

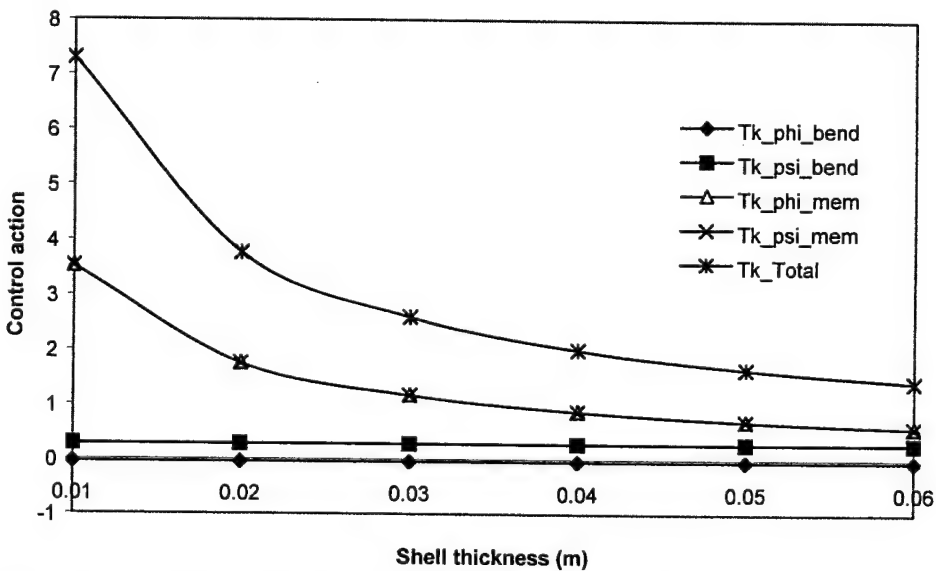


Fig.12 Modal control actions at various shell thickness (Position 80-90°, R=1m, k=4).

(♦: $(\hat{T}_{k_trans})_{\phi,bend}$; ■: $(\hat{T}_{k_trans})_{\psi,bend}$; Δ: $(\hat{T}_{k_trans})_{\phi,mem}$; and ×: $(\hat{T}_{k_trans})_{\psi,mem}$; *: (\hat{T}_k) .)

These data suggest, again, the micro-membrane control actions dominate the overall control action and the control action decreases when the shell thickens or at higher natural modes. The membrane control force is usually independent of shell thickness, i.e., Eqs.(2-3). However, the micro-control actions $(\hat{T}_k)_{\phi,mem}$ and $(\hat{T}_k)_{\psi,mem}$ are defined in Eq.(22d), resulting in reduction of $(\hat{T}_k)_{\phi,mem}$ and $(\hat{T}_k)_{\psi,mem}$ when the shell thickness h increases. On the other hand,

the bending control actions $(\hat{T}_k)_{\phi,\text{bend}}$ and $(\hat{T}_k)_{\psi,\text{bend}}$ usually influenced by the transverse location $r^a = (h/2 + h^a/2)$, i.e., Eqs.(4-5), show little variation, since the actions are defined in Eqs.(22a,b) and $h^a/(h \times N_k)$ is very small.

Radius of Curvature

Next, the hemispherical shell radius changes from 1m to 2m, with a standard shell thickness $h = 0.01\text{m}$. The piezoelectric actuator thickness h^a remains at $40\text{ }\mu\text{m}$, located at 80-90 degree meridian, and the actuators are circumferentially segmented at every $(2n-1)\pi/(2k)$ radians. The patch actuator induced control actions of modes $k=2,3,4$ are presented in **Figure 13**, in which the modal control action decreases as the radius of curvature increases or at higher natural modes. Detailed micro-control actions resulting from the meridional/circumferential membrane/bending components of modes $k=2,3,4$ are respectively calculated and plotted in **Figures 14-16**. Again, these data indicate that the primary contributing components are the two micro-membrane control actions which decrease due to increased radius of curvature.

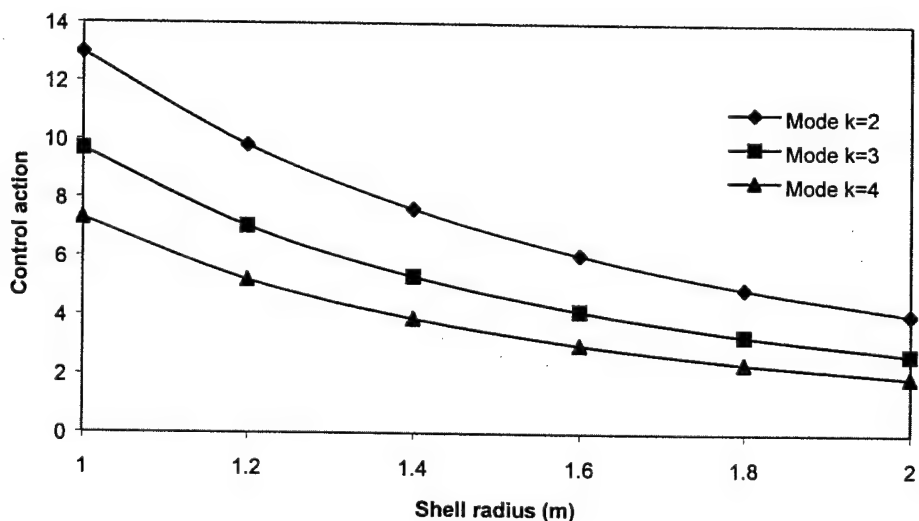


**Fig.13 Total modal patch control actions (\hat{T}_{k_trans}) at various shell radius (Position 80-90, $h=0.01$, $k=2,3,4$).
(\diamond : $k=2$ mode; \blacksquare : $k=3$ mode; \blacktriangle : $k=4$ mode.)**

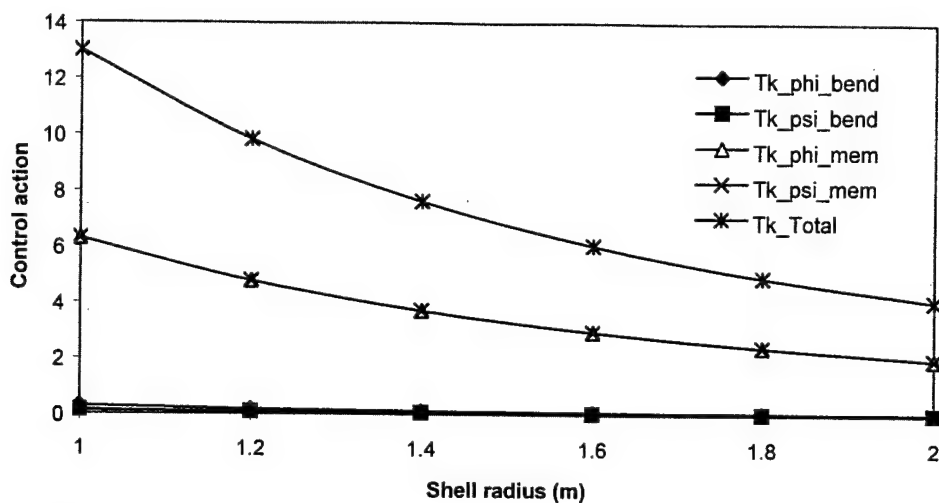


Fig.14 Modal control actions at various shell radius (Position 80-90, $h=0.01$, $k=2$).
 (♦: $(\hat{T}_{k_trans})_{\phi,bend}$; ■: $(\hat{T}_{k_trans})_{\psi,bend}$; Δ: $(\hat{T}_{k_trans})_{\phi,mem}$; and ×: $(\hat{T}_{k_trans})_{\psi,mem}$; *: (\hat{T}_k) .)

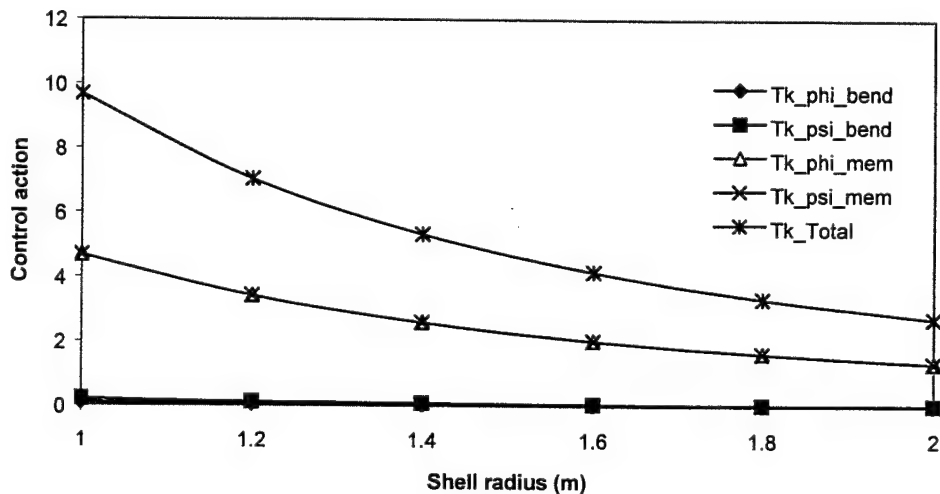


Fig.15 Modal control actions at various shell radius (Position 80-90, $h=0.01$, $k=3$).
 (♦: $(\hat{T}_{k_trans})_{\phi,bend}$; ■: $(\hat{T}_{k_trans})_{\psi,bend}$; Δ: $(\hat{T}_{k_trans})_{\phi,mem}$; and ×: $(\hat{T}_{k_trans})_{\psi,mem}$; *: (\hat{T}_k) .)

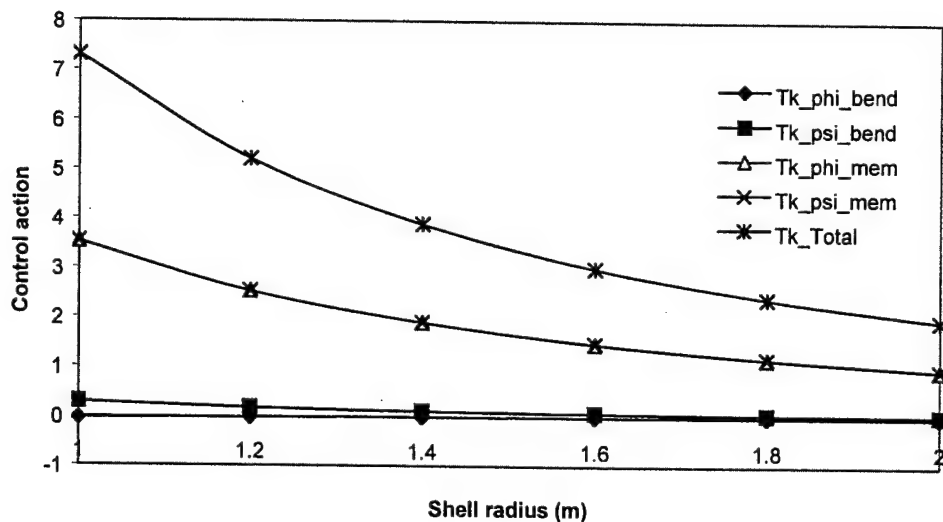


Fig.16 Modal control actions at various shell radius (Position 80-90, $h=0.01$, $k=4$).

(\diamond : $(\hat{T}_k \text{ trans})_{\phi, \text{bend}}$; \blacksquare : $(\hat{T}_k \text{ trans})_{\psi, \text{bend}}$; Δ : $(\hat{T}_k \text{ trans})_{\phi, \text{mem}}$; and \times : $(\hat{T}_k \text{ trans})_{\psi, \text{mem}}$; $*$: (\hat{T}_k) .)

Figure 17 shows that N_k significantly increases as the radius increases, resulting in reduction of control actions as the radius increases. And similar to the first two cases, N_k increases at higher modes and it causes reduction of control actions at higher natural modes.

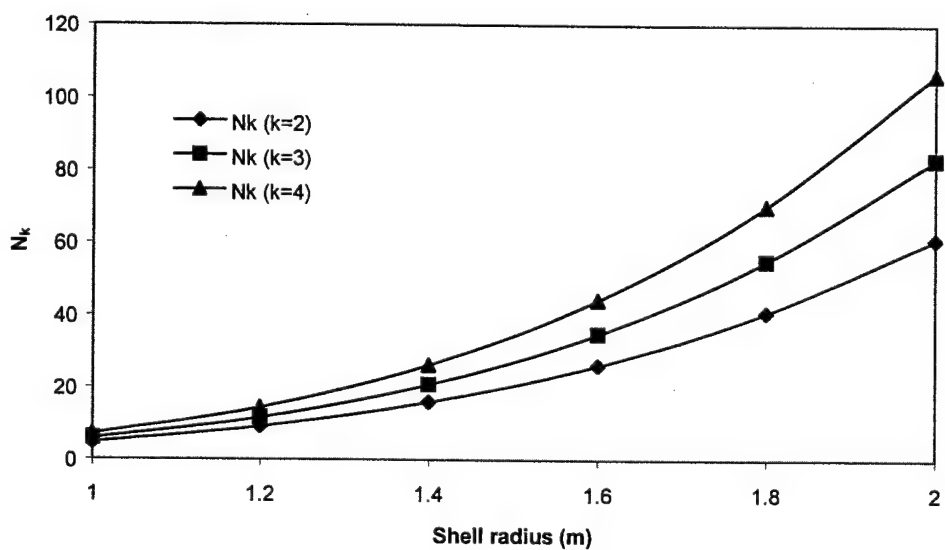


Fig.17 N_k at various shell radius ($k=2,3,4$).
(\diamond : $k=2$ mode; \blacksquare : $k=3$ mode; Δ : $k=4$ mode.)

Control Effectiveness

With the segmentation technique described previously, i.e., segmented at every $(2n-1)\pi/(2k)$, the effective actuator area actually increases as the actuator patch moving from the

pole down to the boundary rim and it decreases as the natural mode k increases. **Figure 18** illustrates three types ($k=2,3,4$) of actuator layouts and their actuator size variations. **Figure 19** shows the effective actuator area of three types of layouts increases as the shell radius increases.

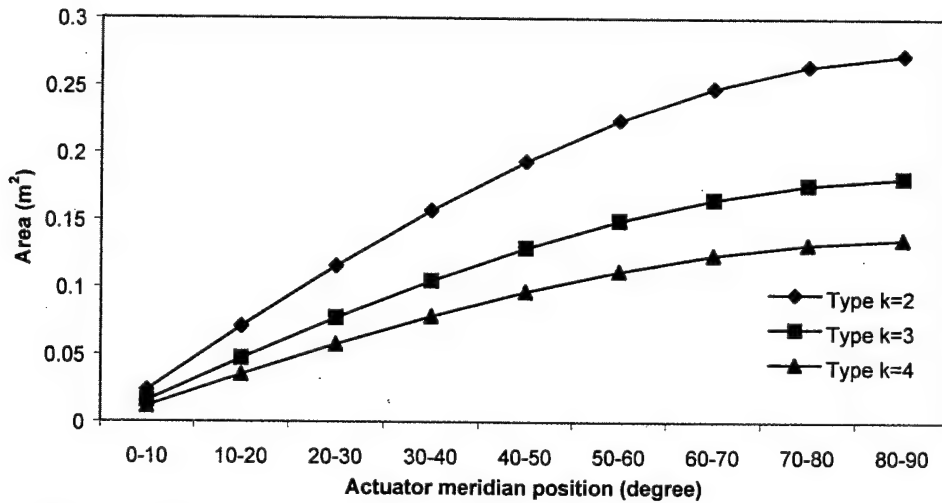


Fig.18 Effective actuator sizes at various patch locations ($R=1m$).
(♦: Type $k=2$; ■: Type $k=3$; ▲: Type $k=4$.)

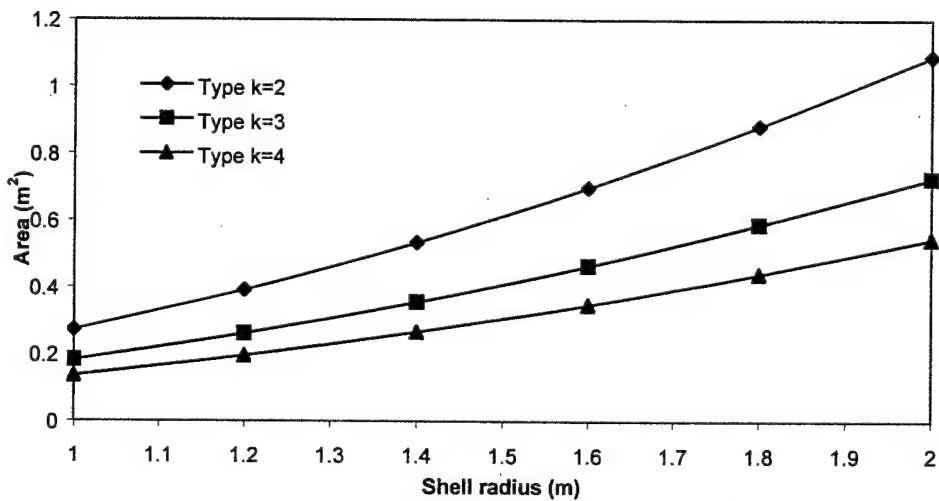


Fig.19 Effective actuator sizes versus shell radiiuses (Position 80-90°).
(♦: Type $k=2$; ■: Type $k=3$; ▲: Type $k=4$.)

Since the actuator sizes are not constant, consequently the control actions need to be normalized such that the true control authority per actuator area can be inferred. These effective (normalized) control actions of three actuator layouts are presented in **Figures 20-22**. These data suggest that 1) the effective control effect reaches maximal at the free edge, positioned at 80-90 degree meridian, **Figure 20**, 2) the effective control action decreases as the shell

thickness increases, **Figure 21**, and 3) the effective (normalized) control action decreases when the shell radius increases, **Figure 22**.

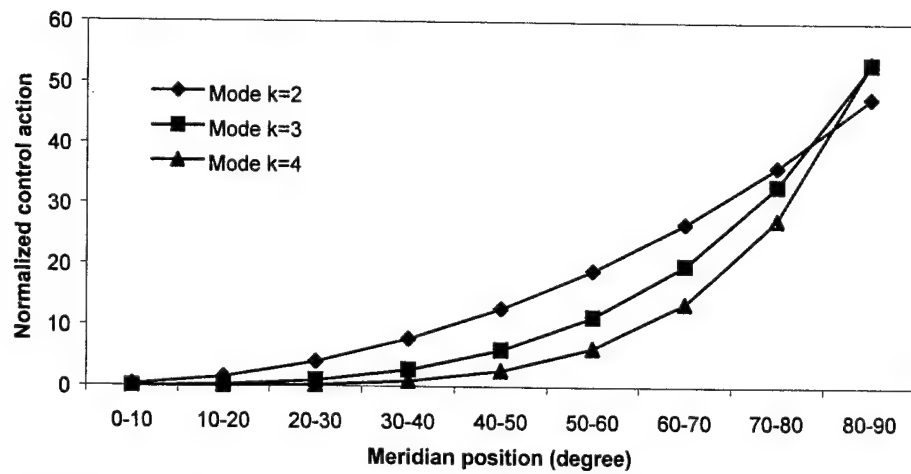


Fig.20 Normalized control actions at various locations ($R=1$, $h=0.01$).
(♦: $k=2$ mode; ■: $k=3$ mode; ▲: $k=4$ mode.)

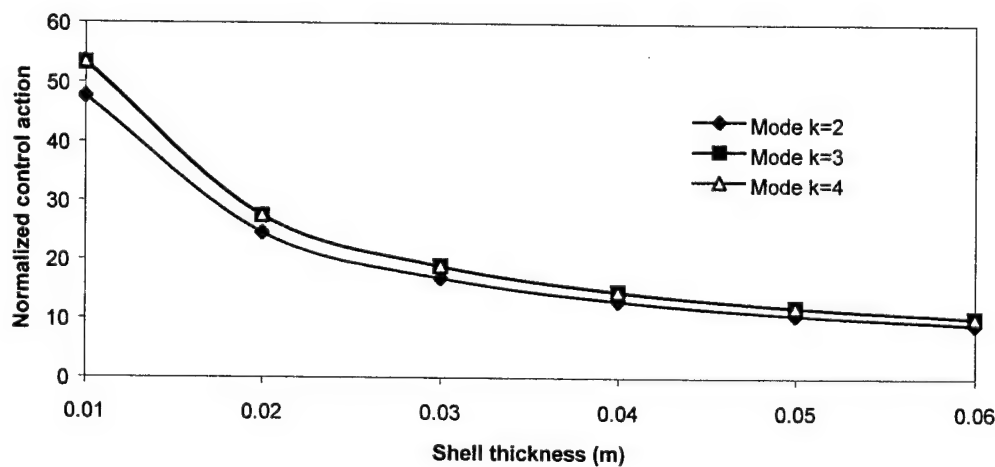


Fig.21 Normalized control actions at various shell thickness (Position 80-90, $R=1$).
(♦: $k=2$ mode; ■: $k=3$ mode; ▲: $k=4$ mode.)

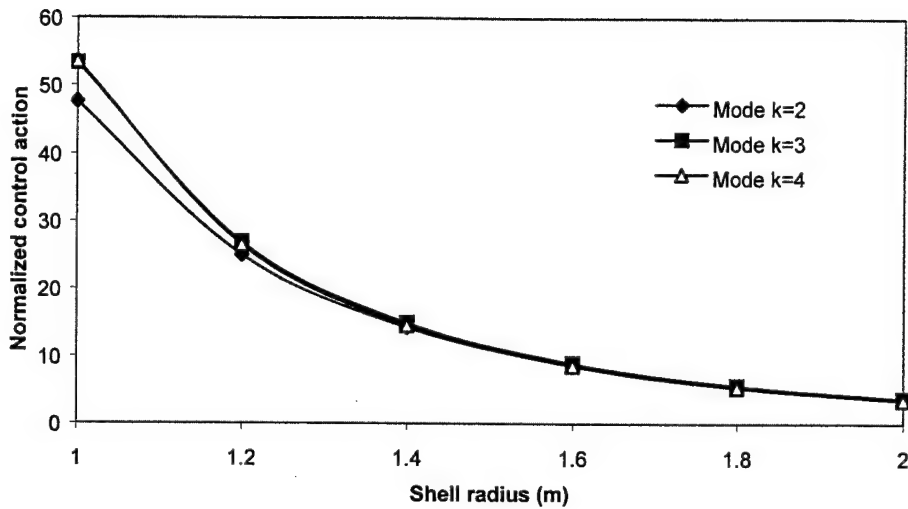


Fig.22 Normalized control actions at various shell radius (Position 80-90, $h=0.01$).
 (♦: $k=2$ mode; ■: $k=3$ mode; ▲: $k=4$ mode.)

CONCLUSIONS

Actuation and control of hemispherical shells using segmented distributed piezoelectric actuators are investigated in this study. Mathematical models for spherical/hemispherical shells laminated with distributed actuator layers were defined first, followed by formulations of distributed control forces and their contributing microscopic meridional/circumferential membrane and bending control actions based on a simplified bending approximation theory. Detailed modal control forces, directional micro-control actions, and normalized control effects of free-edge hemispheric shells with various geometric parameters (or design parameters) were evaluated. With a delicate modal-dependent segmentation mechanism, i.e., $(2n-1)\pi/(2k)$, effects of the in-plane meridional and circumferential control forces are eliminated from the overall control actions and that of the transverse control action is retained. The total control action $(\hat{T}_k)_{\text{Total}}$ depends on actuator locations and modal characteristics, excluding actuator material properties and control signals. The modal control force $\hat{F}_k(t)$ can be inferred from the control action by multiplying actuator parameters, i.e., $\frac{Y_p d_{31} \phi^a(t)}{\rho}$, when specific piezoelectric actuator and control signals are selected. Qualitative parametric analyses of hemispheric shells with segmented patch actuators suggest that

- 1) The micro-meridional/circumferential membrane control actions dominate the overall modal control force;
- 2) The modal patch control force increases as the actuator patch moves toward the free edge;
- 3) The actuation magnitude decreases at higher natural modes;
- 4) The modal control force decreases as the shell thickens, due to increased shell rigidity;

- 5) The modal control force decreases as the radius of curvature increases and the shell radius significantly influences the nominal value of N_k ;
- 6) The effective actuator size enlarges as the patch location moving from the pole to the free boundary rim for a specified k ; and
- 7) The effective (or normalized) actuator induced control action reaches maximal at the free edge and it decreases as the shell thickness or the shell radius increases.

These generic guidelines can be applied to design of segmented actuator patches, their spatial layouts, and control effectiveness of precision hemispheric shells.

ACKNOWLEDGEMENT

This research is supported, in part, by a grant (F49620-98-1-0467) from the Air Force Office of Scientific Research (Project Manager: Brian Sanders). This support is gratefully acknowledged.

REFERENCES

- [1] J.W. Strutt and B. Rayleigh, *Theory of Sound (Vol. I)*, 2nd Ed., Dover Publications, New York, 1945, pp.418-432.
- [2] A. Kalnins, Effect of Bending on Vibrations of Spherical Shells. *The Journal of The Acoustical Society of America* **36**(1) 1964 74-81.
- [3] W.E. Baker, Axisymmetric Modes of Vibration of Thin Spherical Shells. *The Journal of The Acoustical Society of America* **33**(12) 1961 1749-1758.
- [4] A.K. Eikrem and A.G. Doige, Natural Frequencies of a Hemispherical Shell. *Experimental Mechanics* **12** 1972 575-579.
- [5] Z.E. Mazurkiewicz and R.T. Nagorski, *Shells of Revolution*, PWN-Polish Scientific Publishers, Warsaw, 1991, pp.7-9, pp.333-341.
- [6] M.W. Johnson and E. Reissner, On Inextensional Deformations of Shallow Elastic Shells. *Journal of Mathematics and Physics* **34** 1956 335-346.
- [7] C. Hwang, Some Experiments on the Vibration of a Hemispherical Shell. *Journal of Applied Mechanics* **33** 1966 817-824.
- [8] H.S. Tzou, P. Smithmaitrie and J.H. Ding, Micro-Sensor Electromechanics and Distributed Signal Analysis of Piezo(Electric)-Elastic Spherical Shells. *Mechanical Systems and Signal Processing (Journal of)* **16**(2-3) 2002 185-199.
- [9] V. Jayachandran and J.Q. Sun, Modeling Shallow-spherical-shell Piezoceramic Actuators as Acoustic Boundary Control Elements. *Smart Materials and Structures* **7**(1) 1998 72-84.
- [10] V. Birman, S. Griffin and G. Knowles, Axisymmetric Dynamics of Composite Spherical Shells with Active Piezoelectric/Composite Stiffeners. *Acta Mechanica*, **141**(1) 2000 71-83.
- [11] S.K. Ghaedi and A.K. Misra, Active Control of Shallow Spherical Shells Using Piezoceramic Sheets, *Proceedings of SPIE – The International Society for Optical Engineering*, v 3668 n II, Mar 1999, pp.890-912.
- [12] H.S. Tzou, D.W. Wang and W.K. Chai, Dynamics and Distributed Control of Conical Shells Laminated with Full and Diagonal Actuators. *Journal of Sound and Vibration*, **256**(1) 2002 65-79.

- [13] H.S. Tzou, J.H. Ding and I. Hagiwara, Micro-control Actions of Segmented Actuator Patches Laminated on Deep Paraboloidal Shells. *JSME International Journal Series C* **45**(1) 2002 8-15.
- [14] H.S. Tzou, Thin-Layer Distributed Piezoelectric Neurons and Muscles: Electromechanics and Applications. *Precision Sensors, Actuators, and Systems*, H.S. Tzou and T. Fukuda, (Editors), Kluwer Academic Publishers, Dordrecht /Boston /London, 1992, pp.175-218.
- [15] R.V. Howard, W.K. Chai and H.S. Tzou, Modal Voltages of Linear and Nonlinear Structures using Distributed Artificial Neurons (A Theoretical and Experimental Study). *Mechanical Systems and Signal Processing (Journal of)* **15**(3) 2001 629-640.
- [16] R.D. Blevins, *Formulas for Natural Frequency And Mode Shape*, Reprint Ed., Krieger Publisher Company, Florida, 1987, pp.330-336.
- [17] H.S. Tzou, *Piezoelectric Shells (Distributed Sensing and Control of Continua)*, Kluwer Academic Publishers, Boston/Dordrecht, 1993.

CHAPTER 9

MICRO-SENSING CHARACTERISTICS AND MODAL VOLTAGES OF LINEAR/NONLINEAR TOROIDAL SHELLS

ABSTRACT

Toroidal shells belong to the shells of revolution family. Dynamic sensing signals and their distributed characteristics of spatially distributed sensors or neurons laminated on thin toroidal shell structures are investigated in this study. Spatially distributed modal voltages and signal patterns are related to the meridional and circumferential membrane/bending strains, based on the direct piezoelectricity, the Gauss theorem, the Maxwell principle and the open-circuit assumption; linear and nonlinear toroidal shells are defined based on the thin shell theory and the von Karman geometric nonlinearity. With the simplified mode shape functions defined by the Donnell-Mushtari-Vlasov theory, modal dependent distributed signals and detailed signal components of spatially distributed sensors or neurons are defined and these signals are quantitatively illustrated. Signal distributions basically reveal distinct modal characteristics of toroidal shells. Parametric studies suggest that the dominating signal component results from the meridional membrane strains. Shell dimensions, materials, boundary conditions, natural modes, sensor locations/distributions/sizes, modal strain components, etc. all influence the spatially distributed modal voltages and signal generations.

INTRODUCTION

Toroidal shell structures and components are often proposed for space telescopes, inflatable space structures, neutron accelerators, space colonies, cooling tubes, etc. over the years. Effective distributed control of these toroidal shell structures can enhance their operation precision, accuracy, and reliability. Static, dynamic, vibration, and buckling characteristics of toroidal shells have been studied [1-5]. Stress and free-vibration analyses of pipe-type toroidal shells have also been investigated recently [6-8].

Precision maneuver and control of shells requires thorough understanding not only the dynamic behavior, but also distributed sensing characteristics serving as performance indices or feedback signals [9]. Distributed sensing characteristics of distributed segmented sensors and spatially shaped orthogonal sensors of cylindrical shells and rings have been evaluated recently [10-12]. This study is to evaluate distributed sensing characteristics of linear and nonlinear toroidal shells of revolution laminated with spatially distributed piezoelectric sensors or

neurons. Mathematical modeling of a generic toroidal shell of revolution is presented first, followed by distributed sensing of toroidal shells with spatially distributed sensors. Due to the complexity of the original toroidal shells, exact solutions are difficult to derive. Thus, the Donnell-Mushtari-Vlasov theory is employed and thus a set of mode shape functions can be assumed and distributed sensor signals can be defined. Detailed spatially distributed sensing signals and modal voltages are presented in case studies.

MATHEMATICAL MODELING

A thin toroidal shell of revolution and its cross-section are shown in **Figure 1** where $\alpha_1 = \phi$ denotes the meridional coordinate and $\alpha_2 = \psi$ denotes the circumferential coordinate, respectively. For convenience, a secondary circumferential coordinate χ is adopted as $\chi = R\psi/r$ where R is the toroidal shell (major) radius R and r is the shell cross-sectional radius. Assume the toroidal shell is thin (with thickness h), and thus it follows the Love-Kirchhoff thin shell theory and assumptions. Mathematical models of the linear and nonlinear toroidal shells are defined first, followed by the Donnell-Mushtari-Vlasov simplifications.

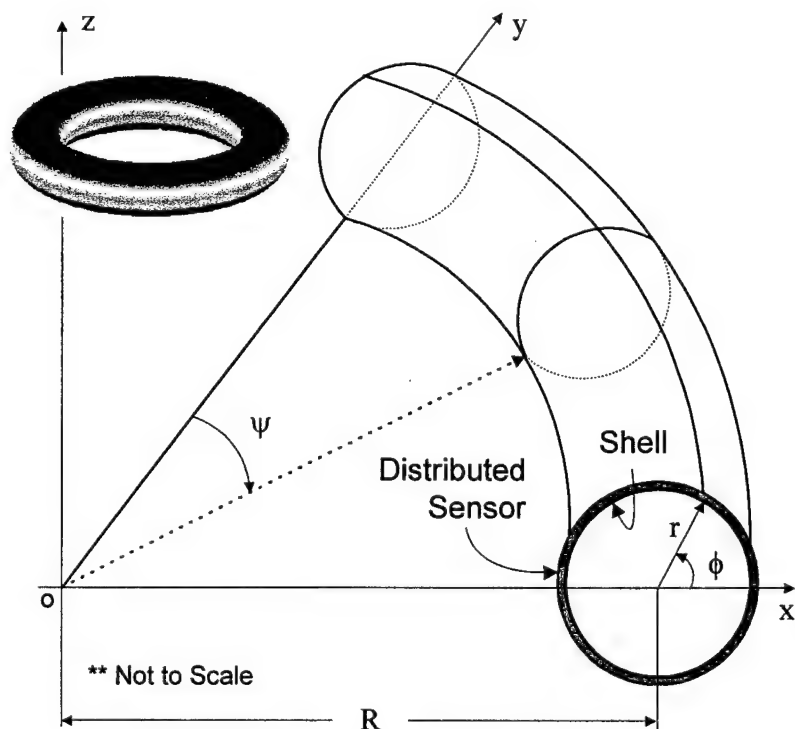


Fig.1 A toroidal shell of revolution with a distributed sensor layer.

Furthermore, a spatially distributed sensor layer (with thickness h^s) is laminated on the shell surface and it is much thinner than the elastic shell, i.e., $h \gg h^s$. Thus, the influence of sensor elastic properties to the elastic toroidal shell dynamics is neglected. The distributed sensor layer responds to the dynamic oscillations and generates signals. The sensor layer can be further discretized into spatially distributed infinitesimal “neurons” revealing microscopic

distributed local signals of the toroidal shells. These spatially distributed signals and modal voltages are investigated in this study.

The Lamé parameters and curvature radii of toroidal shells of revolution are

$$A_1 = r, \quad A_2 = r\xi, \quad R_1 = r, \quad R_2 = r\xi/(\gamma \cos \phi). \quad (1)$$

where $\xi = 1 + \gamma \cos \phi$ and $\gamma = r/R$. The membrane and bending strains (s_{ij}^o and k_{ij}) of the toroidal shells are functions of displacements u_i .

$$s_{\phi\phi}^o = \frac{1}{r} \left(\frac{\partial u_\phi}{\partial \phi} + u_3 \right), \quad (2)$$

$$s_{xx}^o = \frac{1}{r\xi} \left(-u_\phi \gamma \sin \phi + \frac{\partial u_x}{\partial \chi} + u_3 \gamma \cos \phi \right), \quad (3)$$

$$s_{\phi x}^o = \frac{1}{r\xi} \left(\frac{\partial u_\phi}{\partial \chi} + u_x \gamma \sin \phi \right) + \frac{1}{r} \frac{\partial u_x}{\partial \phi}, \quad (4)$$

$$k_{\phi\phi} = \frac{1}{r^2} \left(\frac{\partial u_\phi}{\partial \phi} - \frac{\partial^2 u_3}{\partial \phi^2} \right), \quad (5)$$

$$k_{xx} = -\frac{\sin \phi}{rR\xi} \left(u_\phi - \frac{\partial u_3}{\partial \phi} \right) + \frac{\cos \phi}{rR\xi^2} \frac{\partial u_x}{\partial \chi} - \frac{1}{(r\xi)^2} \frac{\partial^2 u_3}{\partial \chi^2}, \quad (6)$$

$$k_{\phi x} = \frac{1}{r^2 \xi} \frac{\partial u_\phi}{\partial \chi} + \frac{\cos \phi}{rR\xi} \frac{\partial u_x}{\partial \phi} + \frac{u_x}{(R\xi)^2} \sin \phi \cos \phi - \frac{1}{r^2 \xi} \frac{\partial^2 u_3}{\partial \phi \partial \chi} - \frac{\sin \phi}{rR\xi^2} \frac{\partial u_3}{\partial \chi}. \quad (7)$$

The total strains S_{ij} are the summation of the membrane strain and the bending strain.

$$S_{\phi\phi} = s_{\phi\phi}^o + \alpha_3 k_{\phi\phi}, \quad S_{xx} = s_{xx}^o + \alpha_3 k_{xx}, \quad S_{\phi x} = s_{\phi x}^o + \alpha_3 k_{\phi x}. \quad (8-10)$$

where α_3 denotes the location measured from the shell neutral surface. These strain-displacement relations will be used in the signal-displacement equation of spatially distributed sensors and neurons later. Following the thin shell assumptions, the rotation angles are defined

as $\beta_\phi = \frac{1}{r} (u_\phi - \frac{\partial u_3}{\partial \phi})$ and $\beta_x = \frac{1}{r\xi} (u_x \gamma \cos \phi - \frac{\partial u_3}{\partial \chi})$. For nonlinear toroidal shells with geometric

nonlinearity defined by the von Karman geometric nonlinearity, the membrane strains need to include the quadratic effect of the transverse displacement [13].

$$s_{\phi\phi}^o = \frac{1}{r} \left(\frac{\partial u_\phi}{\partial \phi} + u_3 \right) + \frac{1}{2} \left(\frac{\partial u_3}{\partial \phi} \right)^2, \quad (11)$$

$$s_{xx}^o = \frac{1}{r\xi} \left(-u_\phi \gamma \sin \phi + \frac{\partial u_x}{\partial \chi} + u_3 \gamma \cos \phi \right) + \frac{1}{2} \left(\frac{\partial u_3}{\partial \chi} \right)^2. \quad (12)$$

The resulting membrane forces N_{ij} and moments M_{ij} are defined as functions of membrane strains s_{ij}^o and bending strains k_{ij} .

$$N_{\phi\phi} = K(s_{\phi\phi}^o + \mu s_{xx}^o), \quad N_{xx} = K(s_{xx}^o + \mu k_{\phi\phi}), \quad N_{\phi x} = N_{x\phi} = \frac{K(1-\mu)}{2} s_{\phi x}^o, \quad (13-15)$$

$$M_{\phi\phi} = D(k_{\phi\phi} + \mu k_{xx}), \quad M_{xx} = D(k_{xx} + \mu k_{\phi\phi}), \quad M_{\phi x} = M_{x\phi} = \frac{D(1-\mu)}{2} k_{\phi x}. \quad (16-18)$$

where the membrane stiffness K and the bending stiffness D are respectively defined as $K = Yh/(1-\mu^2)$ and $D = Yh^3/[12(1-\mu^2)]$ and Y is the modulus of elasticity, μ is Poisson's ratio. Accordingly, the system equations of the thin toroidal shells in three axial directions are respectively defined as follows.

$$-r\xi \frac{\partial N_{\phi\phi}}{\partial \phi} + r\gamma(N_{\phi\phi} - N_{xx}) \sin \phi - r \frac{\partial N_{x\phi}}{\partial \chi} - r\xi Q_{\phi 3} + r^2 \xi \rho h \ddot{u}_\phi = r^2 \xi q_\phi, \quad (19)$$

$$-r\xi \frac{\partial N_{\phi x}}{\partial \phi} + 2r\gamma N_{\phi x} \sin \phi - r \frac{\partial N_{xx}}{\partial \chi} - r\gamma Q_{x 3} \cos \phi + r^2 \xi \rho h \ddot{u}_x = r^2 \xi q_x, \quad (20)$$

$$-r\xi \frac{\partial Q_{\phi 3}}{\partial \phi} + r\gamma Q_{\phi 3} \sin \phi - r \frac{\partial Q_{x 3}}{\partial \chi} + r\xi N_{\phi\phi} + r\gamma N_{xx} \cos \phi + r^2 \xi \rho h \ddot{u}_3 = r^2 \xi q_3. \quad (21)$$

where ρ is the mass density; \ddot{u}_i is the acceleration; q_i is the external excitation; and the transverse shear effects Q_{ij} are defined as functions of moments.

$$Q_{\phi 3} = \frac{1}{r \xi} \left[\xi \frac{\partial M_{\phi x}}{\partial \phi} + \gamma(M_{xx} - M_{\phi\phi}) \sin \phi + \frac{\partial M_{x\phi}}{\partial \chi} \right], \quad (22)$$

$$Q_{x 3} = \frac{1}{r \xi} \left[\xi \frac{\partial M_{\phi x}}{\partial \phi} - 2\gamma M_{\phi x} \sin \phi + \frac{\partial M_{xx}}{\partial \chi} \right]. \quad (23)$$

As discussed previously, exact analytical solutions of thin toroidal shells of revolutions are difficult to obtain. Thus, simplification theories are often employed and simplified analytical solutions are derived. In this study, the Donnell-Mushtari-Vlasov simplification theory is used. There are three fundamental assumptions in the Donnell-Mushtari-Vlasov approximation: 1) in-plane displacements can be neglected in the bending strain expressions, but not in the membrane strain expressions; 2) in-plane inertia forces can be neglected, i.e., $\rho h \ddot{u}_k \approx 0$, $k = \phi, \psi$; and 3) the transverse shear effects, i.e., Q_{31}/R_1 and Q_{32}/R_2 , in the transverse equations can be neglected. Based on the first assumption, one can simplify the bending strain-displacement equations.

$$k_{\phi\phi} = -\frac{1}{r^2} \frac{\partial^2 u_3}{\partial \phi^2}, \quad k_{xx} = \frac{\sin \phi}{rR\xi} \frac{\partial u_3}{\partial \phi} - \frac{1}{(r\xi)^2} \frac{\partial^2 u_3}{\partial \chi^2}, \quad k_{\phi x} = -\frac{1}{r^2 \xi} \frac{\partial^2 u_3}{\partial \phi \partial \chi} - \frac{\sin \phi}{rR\xi^2} \frac{\partial u_3}{\partial \chi}. \quad (24-26)$$

Based on the second and third assumptions, the influence of in-plane inertia forces is neglected and the transverse shear terms are also neglected. Thus, the simplified system equations based on the Donnell-Mushtari-Vlasov theory become

$$-r\xi \frac{\partial N_{\phi\phi}}{\partial \phi} + r\gamma(N_{\phi\phi} - N_{xx}) \sin \phi - r \frac{\partial N_{x\phi}}{\partial \chi} = 0, \quad (27)$$

$$-r\xi \frac{\partial N_{\phi x}}{\partial \phi} + 2r\gamma N_{\phi x} \sin \phi - r \frac{\partial N_{xx}}{\partial \chi} = 0, \quad (28)$$

$$r\xi D \nabla^4 u_3 + \xi N_{\phi\phi} + N_{xx} \gamma \cos \phi + r\xi \rho h \ddot{u}_3 = r\xi q_3. \quad (29)$$

where $\nabla^2(\bullet) = \frac{1}{r^2 \xi} \left[\frac{\partial}{\partial \phi} \left(\xi \frac{\partial(\bullet)}{\partial \phi} \right) + \frac{\partial}{\partial \chi} \left(\frac{1}{\xi} \frac{\partial(\bullet)}{\partial \chi} \right) \right]$. A set of assumed mode shape functions based on the simplified theory are then defined and used in the modal signal-displacement expressions next.

DISTRIBUTED SENSING AND MODAL VOLTAGES

The spatially distributed piezoelectric sensor layer responds to dynamic strains and generates electrical signals, due to the direct piezoelectric effect. Based on the modal expansion concept, the displacement is composed of all participating modes. Thus, the sensor signals are also functions of modal dependent strains. In this section, mode shape functions are defined first, followed by modal dependent signals – modal voltages. Based on the Gauss theory, Maxwell's principle and the open-voltage assumption, the sensor signal ϕ^s of a generic shell sensor can be expressed as [9,14]

$$\phi^s = \frac{h^s}{S^e} \int_{S^e} (h_{31} S_{11} + h_{32} S_{22} + h_{36} S_{12}) dS^e. \quad (30)$$

where S^e is the effective sensor area; h^s is the sensor thickness; S_{11} and S_{22} are the normal strains; S_{12} is the in-plane shear strain; and h_{31} , h_{32} and h_{36} are the piezoelectric (displacement) constants. Note that $h_{31} = h_{32}$ and $h_{36} = 0$ for most commercial piezoelectric materials. (Note that since the in-plane electric fields are negligible for most widely used piezoelectric materials, e.g., polyvinylidene fluoride (PVDF), the sensing signals resulting from the in-plane electric fields are not considered here. However, it has been reported that, for some specific piezoelectric structures, the in-plane electric field could be more significant than the through-the-thickness electric field and the through-thickness electric potential is not linear even in the case of a thin-walled structure [15,16].) Expanding the surface integration and using the toroidal shell parameters yields

$$\phi^s = \frac{h^s}{S^e} \int_e (h_{31}S_{11}^s + h_{32}S_{22}^s) A_1 A_2 d\alpha_1 d\alpha_2, \quad (31a)$$

$$\phi^s(\phi, \psi) = \frac{h^s}{S^e} \int_{\phi} \int_{\psi} (h_{31}S_{\phi\phi}^s + h_{32}S_{\psi\psi}^s) r^2 (1 + \gamma \cos \phi) d\phi d\psi \quad (31b)$$

where the superscript "s" denotes the sensor related properties. A_1 and A_2 are the Lamé parameters; α_1 and α_2 are the two curvilinear coordinates. The mode shape functions (or the displacement fields) U_i ($i=\phi, \psi, 3$) defined in the modal domain of the shear-diaphragm supported toroidal shells following the Donnell-Mushtari-Vlasov approximation are [8]

$$U_{\phi} = \sum_{m=1}^{\infty} \sum_{n=1}^{\infty} A_{mn} \sin(m\phi) \sin\left(\frac{n\pi\psi}{\psi^*}\right), \quad (32a)$$

$$U_{\psi} = \sum_{m=1}^{\infty} \sum_{n=1}^{\infty} B_{mn} \cos(m\phi) \cos\left(\frac{n\pi\psi}{\psi^*}\right), \quad (32b)$$

$$U_3 = \sum_{m=1}^{\infty} \sum_{n=1}^{\infty} C_{mn} \cos(m\phi) \sin\left(\frac{n\pi\psi}{\psi^*}\right) \quad (32c)$$

where A_{mn} , B_{mn} , and C_{mn} are the modal oscillation amplitudes; ψ^* defines the circumferential angle ($2\pi \geq \psi^* > 0$); and m (meridional), n (circumferential) are the mode (or half-wave) numbers, $m, n = 1, 2, \dots$ (Note that the rigid body mode has no strain variations and thus there is no signal generation associated with the rigid body mode, although there exists a rigid mode for a totally free toroidal shell.) Thus, the mn -th mode shape functions of the shear-diaphragm supported toroidal shells are $U_{\phi}(m, n) = A_{mn} \sin(m\phi) \sin\left(\frac{n\pi\psi}{\psi^*}\right)$,

$U_{\psi}(m, n) = B_{mn} \cos(m\phi) \cos\left(\frac{n\pi\psi}{\psi^*}\right)$, and $U_3(m, n) = C_{mn} \cos(m\phi) \sin\left(\frac{n\pi\psi}{\psi^*}\right)$, respectively. For convenience, the subscripts m and n associated with the modal amplitudes are neglected in the following derivations. Note that the mode shape functions satisfy the so-called shear diaphragm boundary condition analogous to the simply supported boundary condition of a simple beam [8,17].

Recall that the distributed sensor layer is surface laminated and its mid-plane distance measured from the shell neutral surface is $r_1^s = r_2^s = (h + h^s)/2$. Accordingly, toroidal shell strains $S_{\phi\phi}(m, n) = s_{\phi\phi}^0 + \alpha_3 k_{\phi\phi}$ and $S_{\psi\psi}(m, n) = s_{\psi\psi}^0 + \alpha_3 k_{\psi\psi}$ defined by the modal amplitudes are respectively written as

$$s_{\phi\phi}^0(m, n) = \frac{(mA + C)}{r} \sin\left(\frac{n\pi\psi}{\psi^*}\right) \cos(m\phi), \quad k_{\phi\phi}(m, n) = \frac{(m^2 C)}{r^2} \sin\left(\frac{n\pi\psi}{\psi^*}\right) \cos(m\phi), \quad (33-34)$$

$$s_{\psi\psi}^0(m, n) = \frac{1}{r\xi} \left[-A\gamma \sin(m\phi) \sin\phi - B\left(\frac{n\pi\psi}{\psi^*}\right) \cos(m\phi) + C\gamma \cos(m\phi) \cos\phi \right] \sin\left(\frac{n\pi\psi}{\psi^*}\right), \quad (35)$$

$$k_{\psi\psi}(m, n) = \left\{ -\frac{mC}{rR\xi} \sin(m\phi) \sin\phi + \frac{C}{(r\xi)^2} \left(\frac{n\pi\gamma}{\psi^*} \right)^2 \cos(m\phi) \right\} \sin\left(\frac{n\pi\psi}{\psi^*}\right) \quad (36)$$

Since the sensor layer is thin and surface laminated, the strains in the sensor layer is equal to the outmost surface strains of the toroidal shell. Imposing the Donell-Mushtari-Vlssov assumption and including the sensor location effect yields the strain-mode shape function relations and the sensor signal equation of the distributed sensor layer laminated on the toroidal thin shell.

$$S_{\phi\phi}^s(m, n) = \left[\frac{(mA + C)}{r} + \frac{(h + h^s)(m^2C)}{2r^2} \right] \sin\left(\frac{n\pi\psi}{\psi^*}\right) \cos(m\phi), \quad (37)$$

$$S_{\psi\psi}^s(m, n) = \left\{ \left[-\frac{A\gamma}{r\xi} - \frac{(h + h^s)(mC)}{2rR\xi} \right] \sin(m\phi) \sin\phi \right. \\ \left. + \left[-B\left(\frac{n\pi\gamma}{\psi^*}\right) + \frac{C(h + h^s)}{2(r\xi)^2} \left(\frac{n\pi\gamma}{\psi^*}\right)^2 \right] \cos(m\phi) \right. \\ \left. + C\gamma \cos(m\phi) \cos\phi \right\} \sin\left(\frac{n\pi\psi}{\psi^*}\right) \quad (38)$$

$$\phi_{mn}^s(\phi, \psi) = \frac{h^s}{S^e} \int \int \left\{ h_{31} \left[\frac{(mA + C)}{r} + \frac{(h + h^s)(m^2C)}{2r^2} \right] \sin\left(\frac{n\pi\psi}{\psi^*}\right) \cos(m\phi) \right] \\ + h_{32} \left[\left\{ \left[-\frac{A\gamma}{r\xi} - \frac{(h + h^s)(mC)}{2rR\xi} \right] \sin(m\phi) \sin\phi \right. \right. \\ \left. \left. + \left[-B\left(\frac{n\pi\gamma}{\psi^*}\right) + \frac{C(h + h^s)}{2(r\xi)^2} \left(\frac{n\pi\gamma}{\psi^*}\right)^2 \right] \cos(m\phi) \right. \right. \\ \left. \left. + C\gamma \cos(m\phi) \cos\phi \right\} \sin\left(\frac{n\pi\psi}{\psi^*}\right) \right] \cdot r^2 (1 + \gamma \cos\phi) d\phi d\psi \quad (39) \right.$$

ANALYSIS OF DISTRIBUTED SIGNAL COMPONENTS

Note that the sensing signals defined previously are the distributed signals integrated over the whole sensor area S^e and averaged over the sensor area, due to instantaneous charge distribution and averaging on the sensor surface. Accordingly, only the "averaged" spatial effect is displayed. In order to study microscopic signal-strain relations, the sensor electrodes are assumed infinitesimally small - "sensor neurons" and thus local signal distributions can be revealed. Spatial modal voltage distributions can be established by plotting all local neuron signals $\phi_{mn}^s(\phi_a^*, \psi_a^*)$, where "*" denotes a specified neuron location "a".

$$\begin{aligned}
\phi_{mn}^s(\phi_a^*, \psi_a^*) = & h^s \left\{ h_{31} \left[\frac{(mA + C)}{r} + \frac{(h + h^s)(m^2C)}{2r^2} \right] \sin\left(\frac{n\pi\psi}{\psi^*}\right) \cos(m\phi) \right. \\
& + h_{32} \left[\left(-\frac{A\gamma}{r\xi} - \frac{(h + h^s)(mC)}{2rR\xi} \right) \sin(m\phi) \sin\phi + \left[-B\left(\frac{n\pi\gamma}{\psi^*}\right) + \frac{C(h + h^s)}{2(r\xi)^2} \left(\frac{n\pi\gamma}{\psi^*}\right)^2 \right] \right. \\
& \left. \cdot \cos(m\phi) + (C\gamma) \cos(m\phi) \cos\phi \right) \sin\left(\frac{n\pi\psi}{\psi^*}\right) \} \quad (40)
\end{aligned}$$

Thus, the total signal is $[\phi_{mn}^s(\phi_a^*, \psi_a^*)] = [\phi_{mn}^s(\phi_a^*, \psi_a^*)]_{mem} + [\phi_{mn}^s(\phi_a^*, \psi_a^*)]_{bend}$ where the subscripts "mem" and "bend" denote the membrane and the bending effects, respectively. The modal sensing signal $[\phi_{mn}^s(\phi_a^*, \psi_a^*)]_{mem}$ induced by the membrane strains and that $[\phi_{mn}^s(\phi_a^*, \psi_a^*)]_{bend}$ induced by the bending strains are respectively defined as

$$\begin{aligned}
[\phi_{mn}^s(\phi_a^*, \psi_a^*)]_{mem} = & h^s (h_{31} s_{\phi\phi}^0 + h_{32} s_{\psi\psi}^0) = h^s \left\{ h_{31} \cdot \frac{(mA + C)}{r} \sin\left(\frac{n\pi\psi}{\psi^*}\right) \cos(m\phi) \right. \\
& \left. + h_{32} \cdot \frac{1}{r\xi} \left[-A\gamma \sin(m\phi) \sin\phi - B\left(\frac{n\pi\gamma}{\psi^*}\right) \cos(m\phi) + C\gamma \cos(m\phi) \cos\phi \right] \sin\left(\frac{n\pi\psi}{\psi^*}\right) \right\}, \quad (41)
\end{aligned}$$

$$[\phi_{mn}^s(\phi_a^*, \psi_a^*)]_{bend} = h^s (h_{31} r_1^s k_{\phi\phi} + h_{32} r_2^s k_{\psi\psi}) \text{ with } r_1^s = r_2^s = \frac{1}{2}(h + h^s) \quad (42)$$

$$\begin{aligned}
[\phi_{mn}^s(\phi_a^*, \psi_a^*)]_{bend} = & \frac{h^s(h + h^s)}{2} \left\{ h_{31} \frac{(m^2C)}{r^2} \sin\left(\frac{n\pi\psi}{\psi^*}\right) \cos(m\phi) \right. \\
& \left. + h_{32} \left[-\frac{(mC)}{rR\xi} \sin(m\phi) \sin\phi + \frac{C}{(r\xi)^2} \left(\frac{n\pi\gamma}{\psi^*}\right)^2 \cos(m\phi) \right] \sin\left(\frac{n\pi\psi}{\psi^*}\right) \right\}. \quad (43)
\end{aligned}$$

Accordingly, detailed signal contributions from various strain components and their modal voltages can be evaluated and significant components identified.

SENSOR SIGNALS OF NONLINEAR TOROIDAL SHELLS

Distributed signals and their strain contributions of a distributed sensor layer laminated on a thin linear toroidal shell of revolution are defined previously. Distributed signals and modal voltages of a sensor layer and neurons laminated on a nonlinear toroidal shell are defined in this section. As discussed previously, based on the von Karman geometrical nonlinearity, the bending strains of the nonlinear toroidal shell remain identical to the linear case. However, a quadratic effect of the nonlinear transverse displacement is added to the membrane strains [18].

$$s_{\phi\phi}^o = \frac{1}{r} \left(\frac{\partial u_\phi}{\partial \phi} + u_3 \right) + \frac{1}{2} \left(\frac{\partial u_3}{\partial \phi} \right)^2, \quad (44)$$

$$s_{xx}^o = \frac{1}{r\xi} \left(-u_\phi \gamma \sin \phi + \frac{\partial u_x}{\partial \chi} + u_3 \gamma \cos \phi \right) + \frac{1}{2} \left(\frac{\partial u_3}{\partial \chi} \right)^2. \quad (45)$$

Assume that the geometric nonlinearity is small and its influence to natural modes is insignificant. Substituting the mode shape functions defined for the toroidal shell with the Denell-Mushtari-Vlssov assumption and simplifying gives the strain-mode shape function relations.

$$\frac{1}{2} \left(\frac{\partial u_3}{\partial \phi} \right)^2 = \frac{1}{2} (mC)^2 \sin^2 \left(\frac{n\pi\psi}{\psi} \right) \sin^2 (m\phi), \quad (46)$$

$$\frac{1}{2} \left(\frac{\partial u_3}{\partial \chi} \right)^2 = \frac{1}{2} C^2 \left(\frac{n\pi\gamma}{\psi} \right)^2 \cos^2 \left(\frac{n\pi\psi}{\psi} \right) \cos^2 (m\phi), \quad (47)$$

$$s_{\phi\phi}^o (m, n) = \frac{(mA + C)}{r} \sin \left(\frac{n\pi\psi}{\psi} \right) \cos (m\phi) + \frac{1}{2} (mC)^2 \sin^2 \left(\frac{n\pi\psi}{\psi} \right) \sin^2 (m\phi), \quad (48)$$

$$s_{\psi\psi}^o (m, n) = \frac{1}{r\xi} \left[-A\gamma \sin (m\phi) \sin \phi - B \left(\frac{n\pi\gamma}{\psi} \right) \cos (m\phi) + C\gamma \cos (m\phi) \cos \phi \right] \sin \left(\frac{n\pi\psi}{\psi} \right) + \frac{1}{2} C^2 \left(\frac{n\pi\gamma}{\psi} \right)^2 \cos^2 \left(\frac{n\pi\psi}{\psi} \right) \cos^2 (m\phi). \quad (49)$$

The mn -th modal sensing signals $[\phi_{mn}^s(\phi_a^*, \psi_a^*)]_{men}$ induced by the membrane strains, that $[\phi_{mn}^s(\phi_a^*, \psi_a^*)]_{bend}$ contributed by the bending strains, the total signals $[\phi_{mn}^s(\phi_a^*, \psi_a^*)] = [\phi_{mn}^s(\phi_a^*, \psi_a^*)]_{men} + [\phi_{mn}^s(\phi_a^*, \psi_a^*)]_{bend}$, and the spatially distributed signals $[\phi_{mn}^s(\phi, \psi)]$ including the geometric nonlinearity effect can be respectively defined as follows. Note that $[\phi_{mn}^s(\phi_a^*, \psi_a^*)]_{bend}$ is identical to the linear case.

$$\begin{aligned} [\phi_{mn}^s(\phi_a^*, \psi_a^*)]_{men} &= h^s (h_{31} s_{\phi\phi}^o + h_{32} s_{\psi\psi}^o) \\ &= h^s \left(h_{31} \left[\frac{(mA + C)}{r} \sin \left(\frac{n\pi\psi}{\psi} \right) \cos (m\phi) + \frac{1}{2} (mC)^2 \sin^2 \left(\frac{n\pi\psi}{\psi} \right) \sin^2 (m\phi) \right] \right. \\ &\quad \left. + h_{32} \left\{ \frac{1}{r\xi} \left[-A\gamma \sin (m\phi) \sin \phi - B \left(\frac{n\pi\gamma}{\psi} \right) \cos (m\phi) + C\gamma \cos (m\phi) \cos \phi \right] \sin \left(\frac{n\pi\psi}{\psi} \right) \right. \right. \\ &\quad \left. \left. + \frac{1}{2} C^2 \left(\frac{n\pi\gamma}{\psi} \right)^2 \cos^2 \left(\frac{n\pi\psi}{\psi} \right) \cos^2 (m\phi) \right\} \right), \quad (50) \end{aligned}$$

$$[\phi_{mn}^s(\phi_a^*, \psi_a^*)]_{bend} = \frac{h^s(h + h^s)}{2} \left\{ h_{31} \frac{(m^2 C)}{r^2} \sin\left(\frac{n\pi\psi}{\psi^*}\right) \cos(m\phi) \right. \\ \left. + h_{32} \left[-\frac{(mC)}{rR\xi} \sin(m\phi) \sin\phi + \frac{C}{(r\xi)^2} \left(\frac{n\pi\psi}{\psi^*}\right)^2 \cos(m\phi) \right] \right\} \sin\left(\frac{n\pi\psi}{\psi^*}\right) , \quad (51)$$

$$\phi_{mn}^s(\phi_a^*, \psi_a^*) = h^s \left\{ h_{31} \left[\frac{(mA + C)}{r} + \frac{(h + h^s)(m^2 C)}{2r^2} \right] \sin\left(\frac{n\pi\psi}{\psi^*}\right) \cos(m\phi) \right. \\ \left. + \frac{1}{2} (mC)^2 \sin^2\left(\frac{n\pi\psi}{\psi^*}\right) \sin^2(m\phi) \right] + h_{32} \left[\left(-\frac{A\gamma}{r\xi} - \frac{(h + h^s)(mC)}{2rR\xi} \right) \sin(m\phi) \sin\phi \right. \\ \left. + \left[-B\left(\frac{n\pi\psi}{\psi^*}\right) + \frac{C(h + h^s)}{2(r\xi)^2} \left(\frac{n\pi\psi}{\psi^*}\right)^2 \right] \cdot \cos(m\phi) + (C\gamma) \cos(m\phi) \cos\phi \right] \sin\left(\frac{n\pi\psi}{\psi^*}\right) \\ \left. + \frac{1}{2} C^2 \left(\frac{n\pi\psi}{\psi^*}\right)^2 \cos^2\left(\frac{n\pi\psi}{\psi^*}\right) \cos^2(m\phi) \right\} , \quad (52)$$

$$\phi_{mn}^s(\phi, \psi) = \frac{h^s}{S^s} \int_{\phi} \int_{\psi} \left\{ h_{31} \left[\frac{(mA + C)}{r} + \frac{(h + h^s)(m^2 C)}{2r^2} \right] \sin\left(\frac{n\pi\psi}{\psi^*}\right) \cos(m\phi) \right. \\ \left. + \frac{1}{2} (mC)^2 \sin^2\left(\frac{n\pi\psi}{\psi^*}\right) \sin^2(m\phi) \right] + h_{32} \left[\left(-\frac{A\gamma}{r\xi} - \frac{(h + h^s)(mC)}{2rR\xi} \right) \sin(m\phi) \sin\phi \right. \\ \left. + \left[-B\left(\frac{n\pi\psi}{\psi^*}\right) + \frac{C(h + h^s)}{2(r\xi)^2} \left(\frac{n\pi\psi}{\psi^*}\right)^2 \right] \cdot \cos(m\phi) + (C\gamma) \cos(m\phi) \cos\phi \right] \sin\left(\frac{n\pi\psi}{\psi^*}\right) \\ \left. + \frac{1}{2} C^2 \left(\frac{n\pi\psi}{\psi^*}\right)^2 \cos^2\left(\frac{n\pi\psi}{\psi^*}\right) \cos^2(m\phi) \right\} \cdot r^2 (1 + \gamma \cos\phi) d\phi d\psi \quad (53)$$

Thus, distributed modal voltages and signal contributions of nonlinear toroidal shells can be evaluated accordingly. Again, the sensing signals are calculated based on "small" geometric nonlinearity of toroidal shells, such that the mode shape functions remain uninfluenced.

MODAL VOLTAGES AND SIGNAL ANALYSIS

Recall that the signal generation is a function of strains induced in the sensor layer at various modal oscillations of the toroidal shells. Modal voltages and signal components associated with various strain components are analyzed in this section. It is assumed that the piezoelectric constants h_{31} and h_{32} are the same, the radius ratio $R/r = 4$, and the modal amplitudes A_{mn} , B_{mn} , and C_{mn} are assumed unity. Thus, the modal signals are normalized with respect to the modal amplitudes, per se. Note that the modal amplitudes A_{mn} , B_{mn} , and C_{mn} fluctuate at different modes and their relative amplitudes vary with respect to the shell geometries and/or sizes in reality. Accordingly, the following modal voltage plots and various signal components only provide qualitative information. Quantitative modal voltages can be inferred only if the "true" modal amplitudes of the toroidal shell are well defined. This modal amplitude influence to the nonlinear component is significant, since there is a quadratic term involved in

the expression, due to the von Karman geometric nonlinearity. The true signals of the nonlinear component are usually small when the true modal amplitudes are considered.

Figures 2-5 illustrate the distributed modal signal components of the toroidal shell respectively induced by the meridional membrane strains, the circumferential membrane strains, the meridional bending strains, and the circumferential bending strains. In order to illustrate the individual modal effect in a specific direction, only one wave number is allowed to change from 1 to 4, while the other wave number is fixed. For example, m varies from 1 to 4, while n is fixed at 1, i.e., $(m=1-4, n=1)$. **Figures 2 and 4** illustrate the signal variations ($m=1-4, n=1$) in the meridional direction ϕ on the open cross-sections; **Figures 3 and 5** show the circumferential signal variations ($m=1, n=1-4$) of the toroidal shell. Note that the top left is “1”, the top right is “2”, the bottom left is “3”, and the bottom right is “4” in the following modal signals. Furthermore, modal voltages ($m=1-4, n=1-4$) contributed by the total membrane strain components and those contributed by the total bending components are presented in **Figures 6 and 7**. There are a total of sixteen modal voltage components to illustrate the signal variations at various natural modes in each plot. Again, the modes are arranged from the top left to the top right, and then from the bottom left to the bottom right in these distributed modal signals. These modal voltages and their signal components clearly illustrate distinct modal characteristics. Again, these signal distributions are calculated based on the infinite number of infinitesimally small sensor electrodes - neurons, such that the microscopic distributed signal behaviors can be observed clearly.

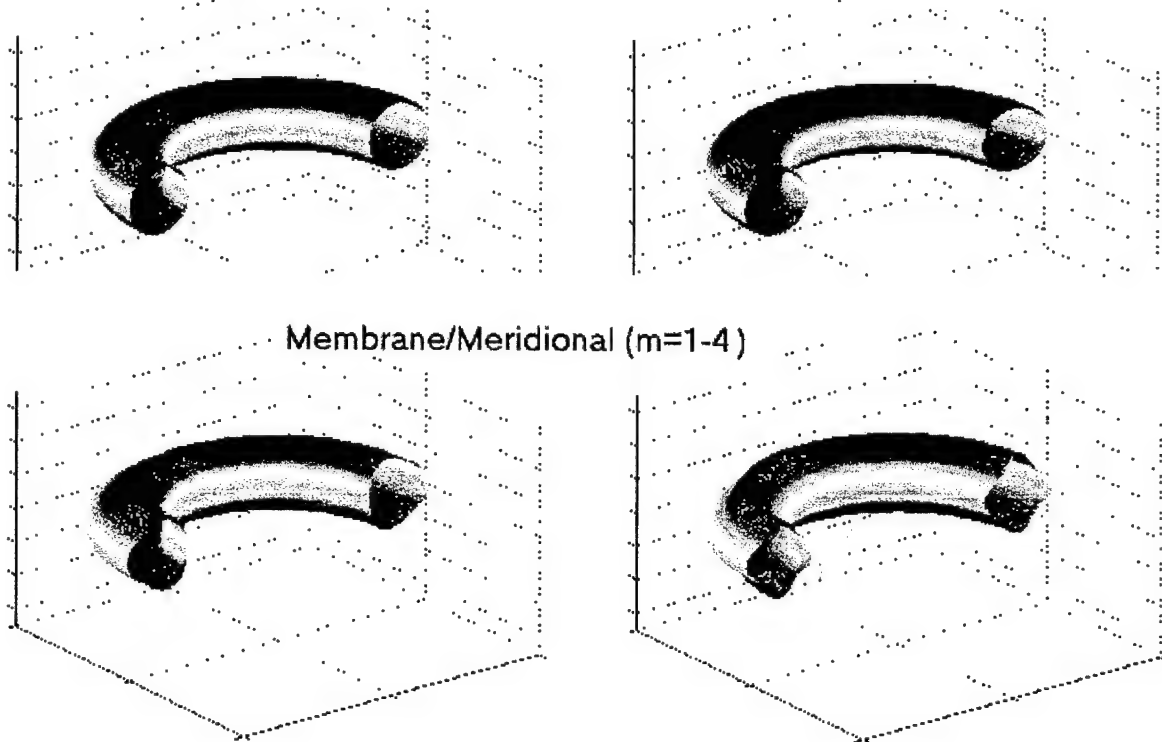


Fig.2 Signal distributions induced by the meridional membrane strains.

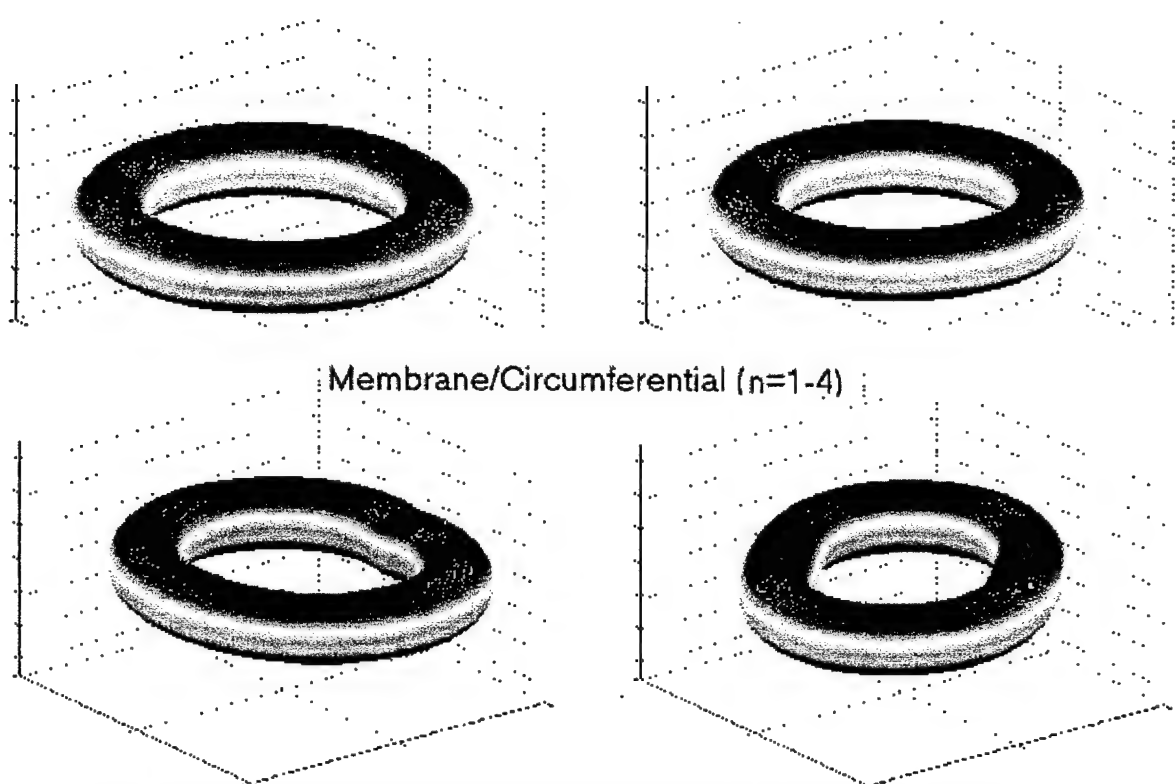


Fig.3 Signal distributions induced by the circumferential membrane strains.

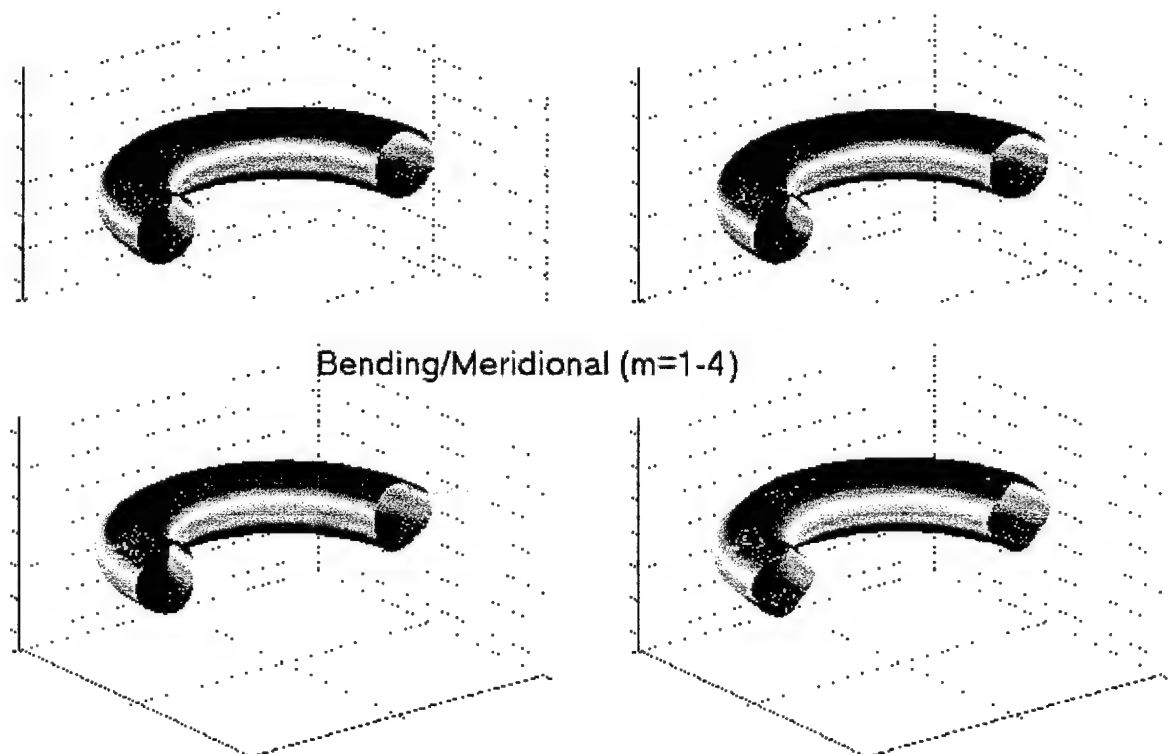


Fig.4 Signal distributions induced by the meridional bending strains.

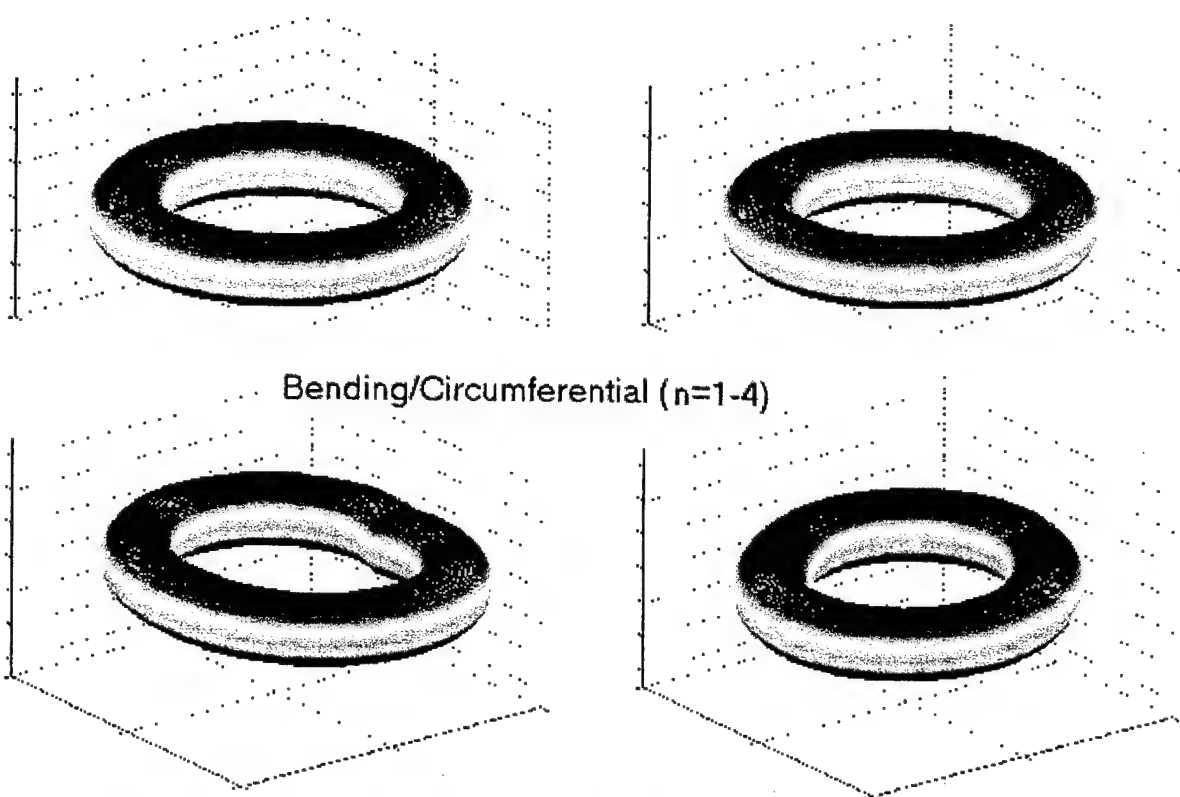
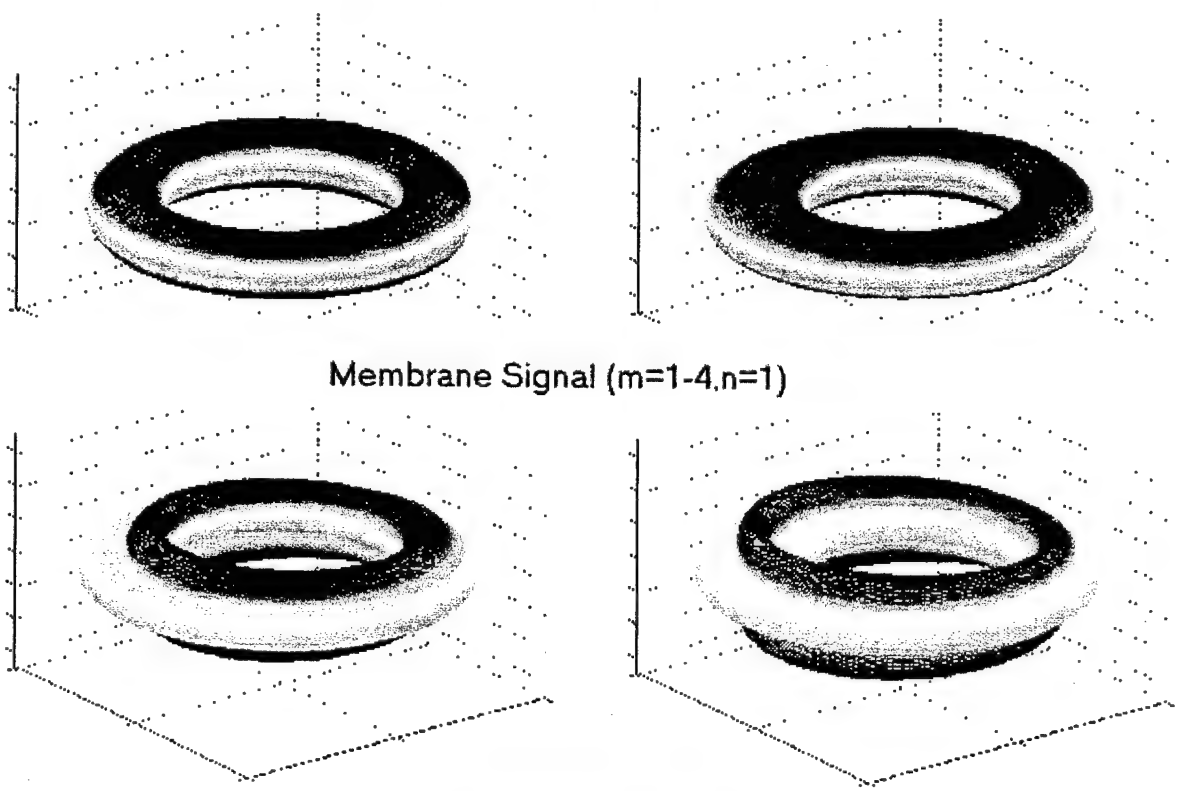
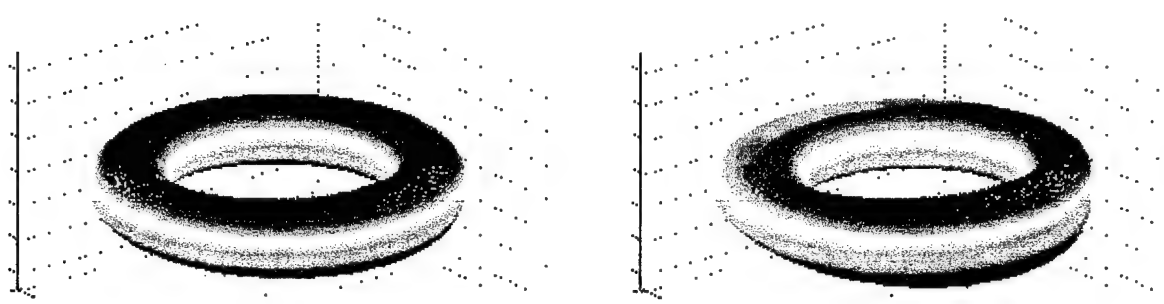


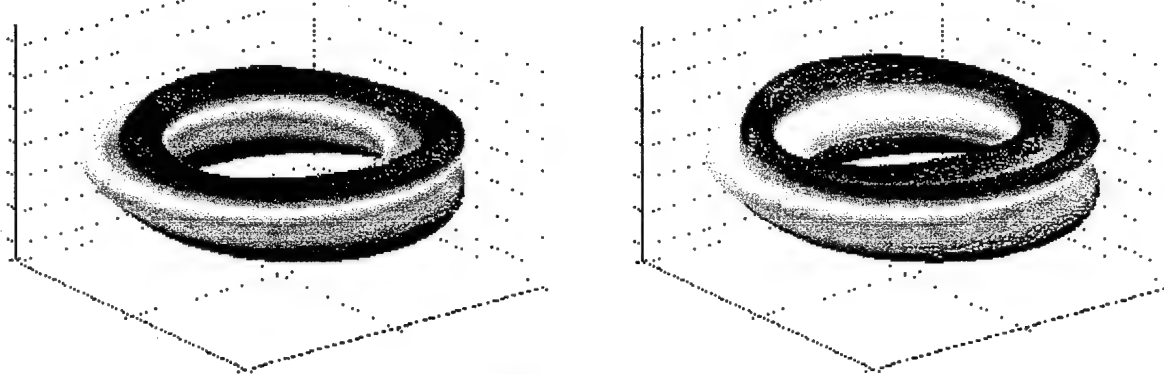
Fig.5 Signal distributions induced by the circumferential bending strains.



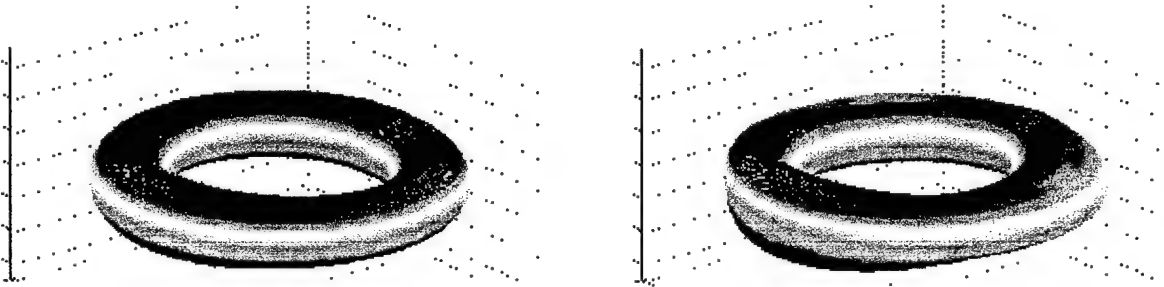
(a) Modes (m=1-4,n=1)



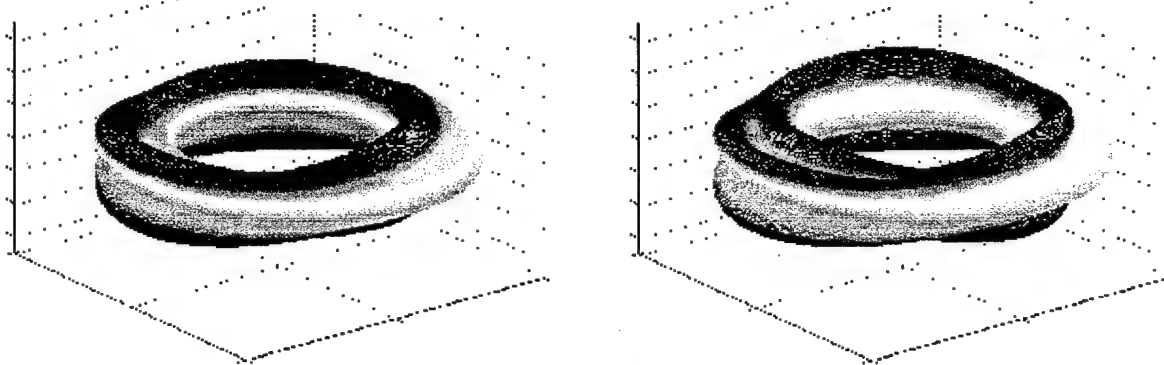
Membrane Signal ($m=1-4, n=2$)



(b) Modes ($m=1-4, n=2$)



Membrane Signal ($m=1-4, n=3$)



(c) Modes ($m=1-4, n=3$)

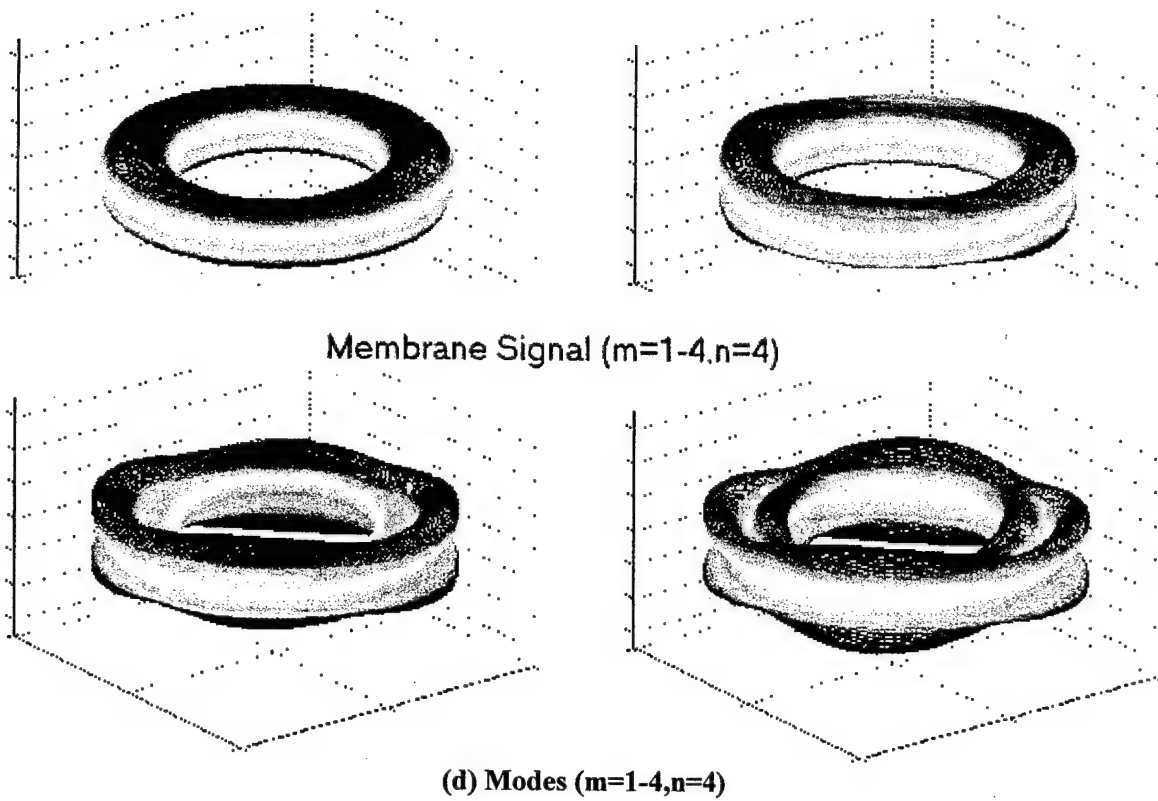
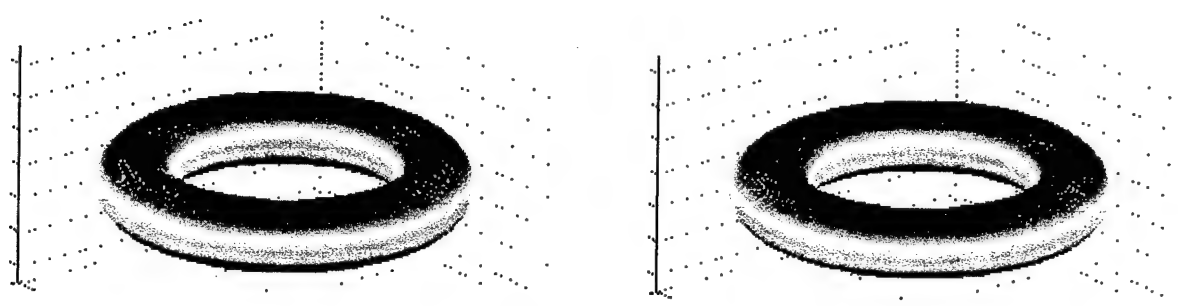
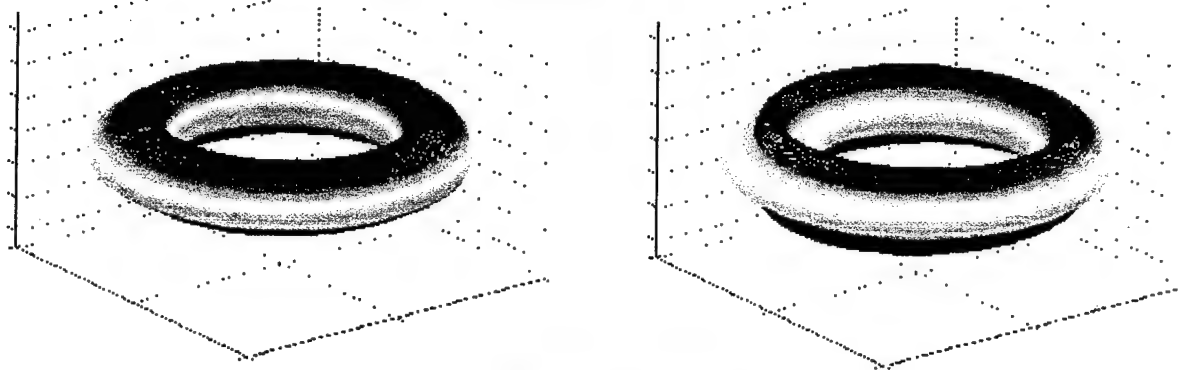


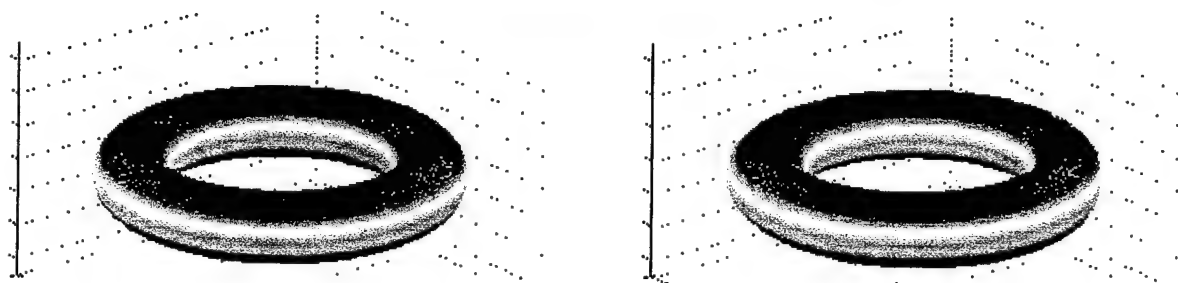
Fig.6 Modal voltage distributions contributed by the membrane strains
($m=1-4; n=1-4$). (a) Modes ($m=1-4, n=1$); (b) Modes ($m=1-4, n=2$); (c) Modes ($m=1-4, n=3$);
(d) Modes ($m=1-4, n=4$).



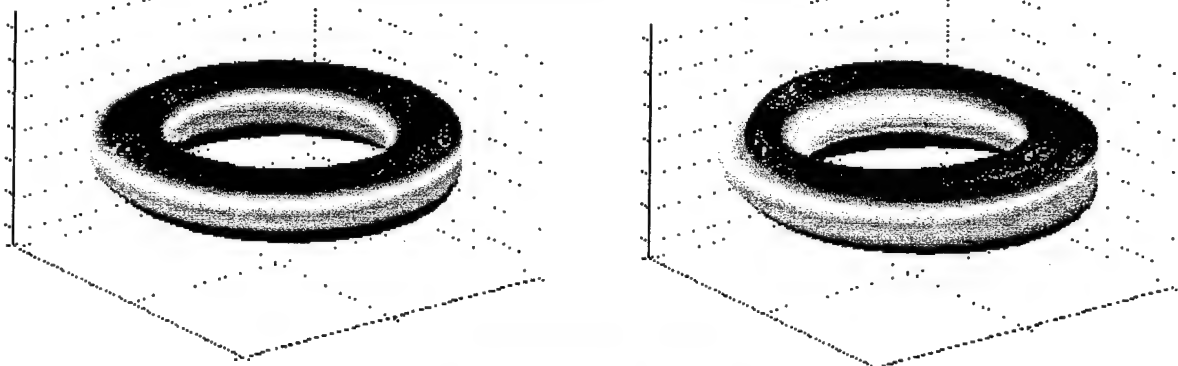
Bending Signal ($m=1-4, n=1$)



(a) Modes ($m=1-4, n=1$)



Bending Signal ($m=1-4, n=2$)



(b) Modes ($m=1-4, n=2$)

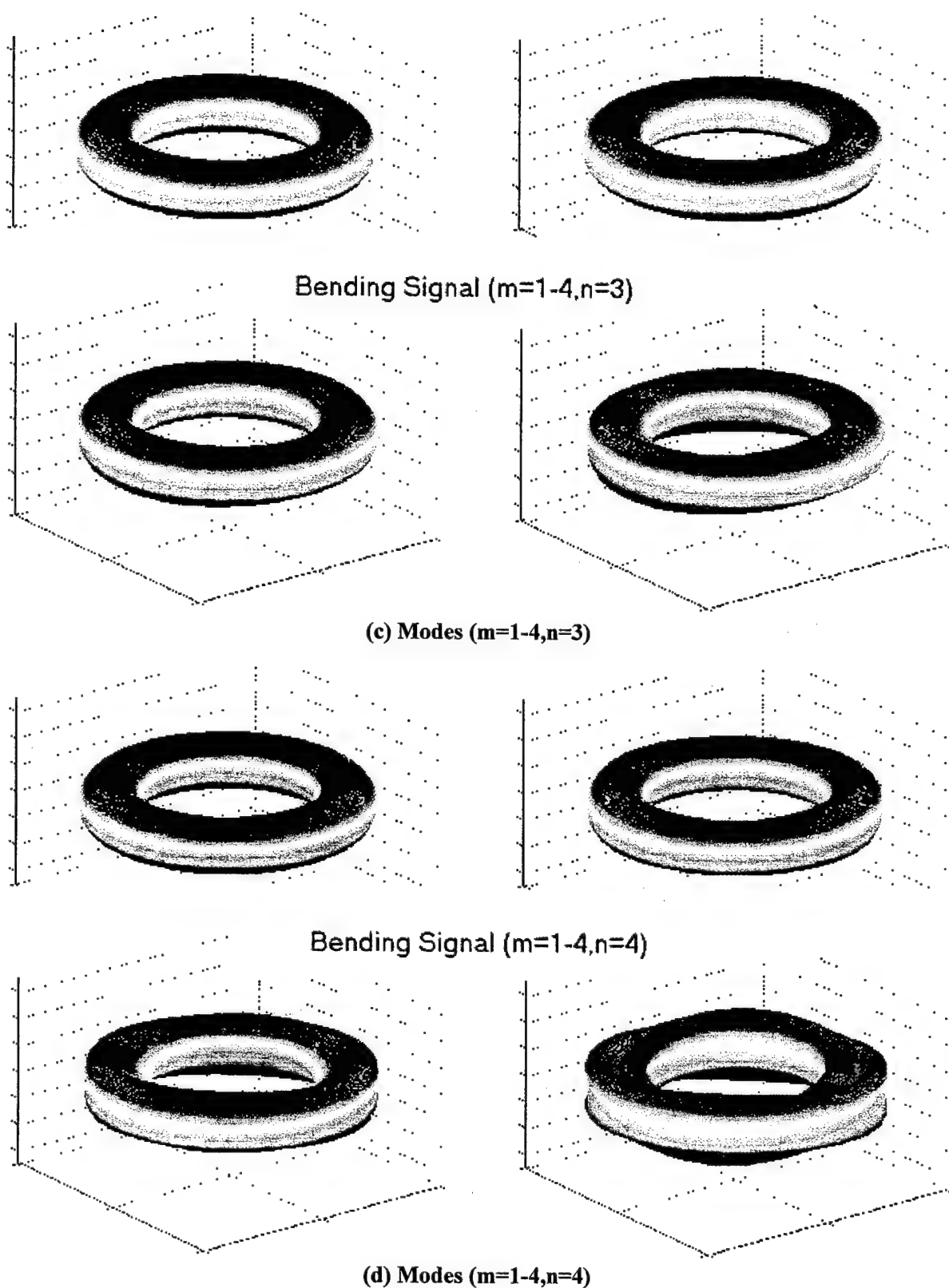


Fig.7 Modal voltage distributions contributed by the bending strains (m=1-4; n=1-4).
 (a) Modes (m=1-4, n=1); (b) Modes (m=1-4, n=2); (c) Modes (m=1-4, n=3); (d) Modes (m=1-4, n=4)

Again, these modal voltage plots and various signal components only provide qualitative spatial distribution of sensing signals. Quantitative modal voltages can be inferred only if the “true” modal amplitudes and geometries of the toroidal shell are well defined. Analytical solutions also suggest that the membrane induced signal component is much larger than the bending induced signal component. The meridional membrane component is larger than the circumferential component.

Detailed two-dimensional distributed signals in the meridional and circumferential directions are also calculated and plotted. **Figure 8** illustrates the signals ($m=1-4, n=1$) and ($m=1, n=1-4$) respectively induced by the meridional and circumferential membrane strains of a linear toroidal shell; **Figure 9** illustrates the signals ($m=1-4, n=1$) and ($m=1, n=1-4$) induced by the meridional and circumferential bending strains of the linear toroidal shell. **Figures 10 and 11** respectively illustrate the distributed signals induced by the meridional and circumferential membrane strains of a nonlinear toroidal shell. For convenience, a reference point is used in the circumferential plots. Note that the signals induced by the meridional component are more significant than those induced by the circumferential component, because the strain levels are higher in the meridional direction. The signal distribution patterns, **Figures 10 and 11**, of the nonlinear toroidal shell are different from those, Figure 8, of the linear toroidal shell, due to the quadratic nonlinear term in the membrane strains. The signal distributions, **Figure 9**, induced by the bending strains remains identical for both linear and nonlinear toroidal shells.

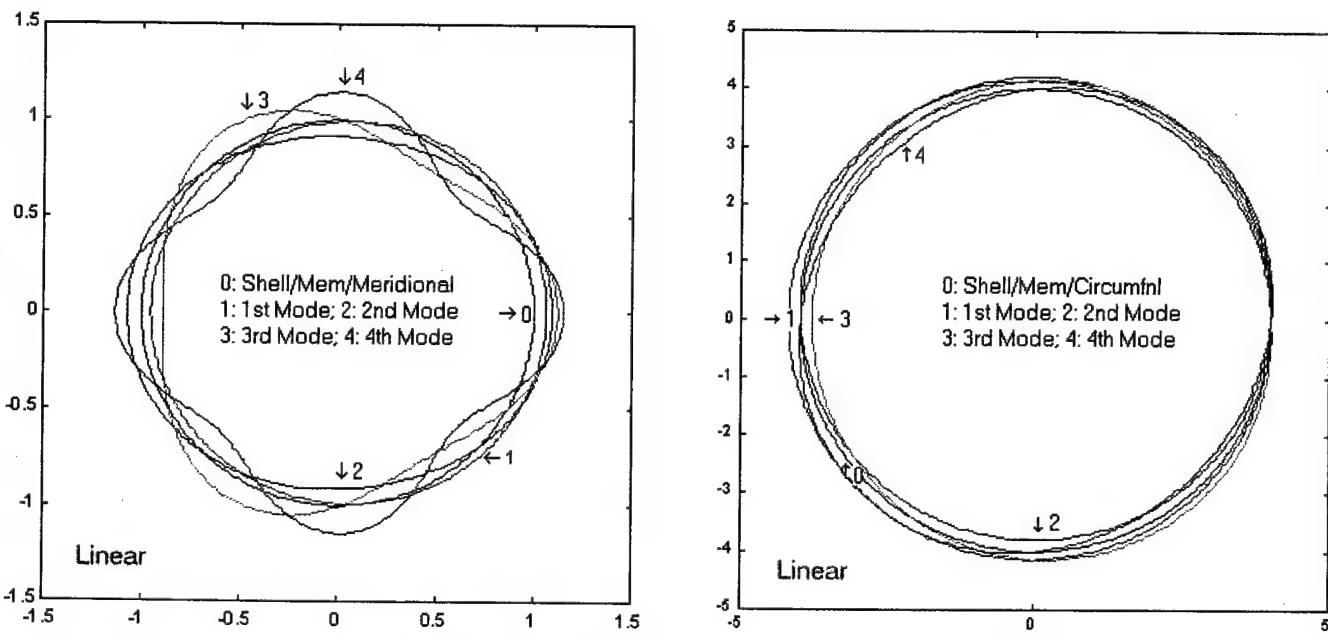


Fig.8 Signal distributions ($m=1-4, n=1$) and ($m=1, n=1-4$) respectively induced by the meridional and circumferential membrane strains. (0: Toroidal shell; 1-4: 1st-4th modes)

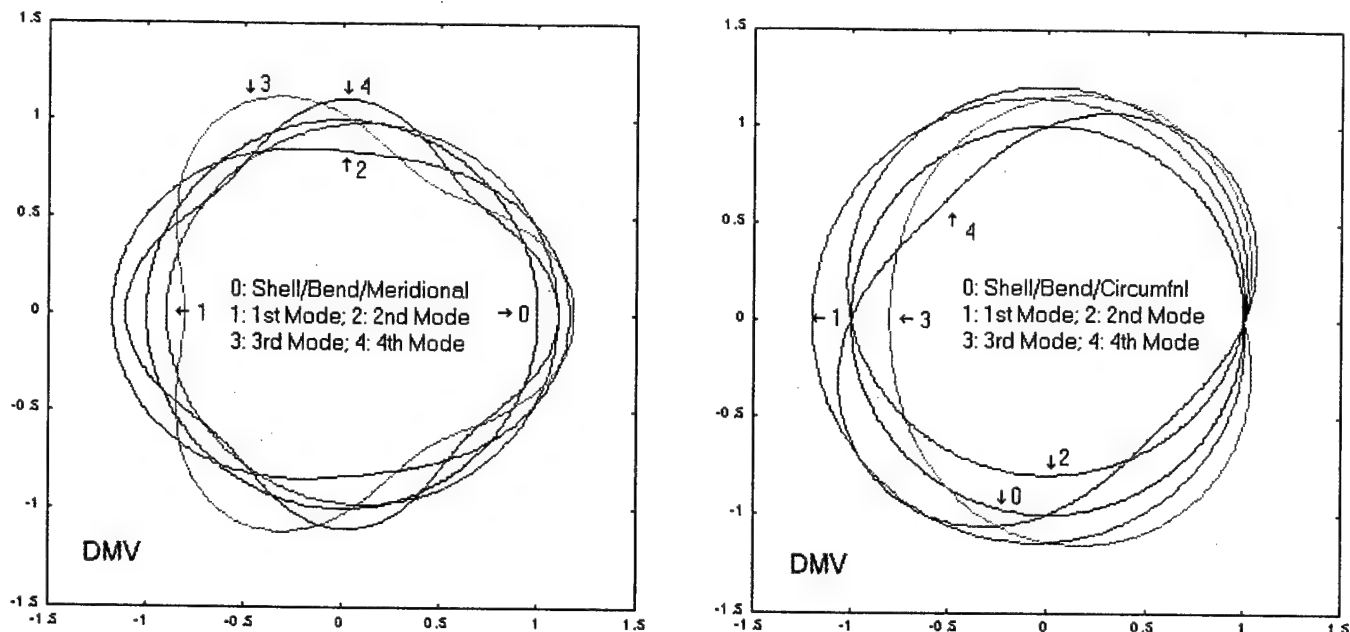


Fig.9 Signal distributions ($m=1-4, n=1$) and ($m=1, n=1-4$) respectively induced by the meridional and circumferential bending strains. (0: Toroidal shell; 1-4: 1st-4th modes)

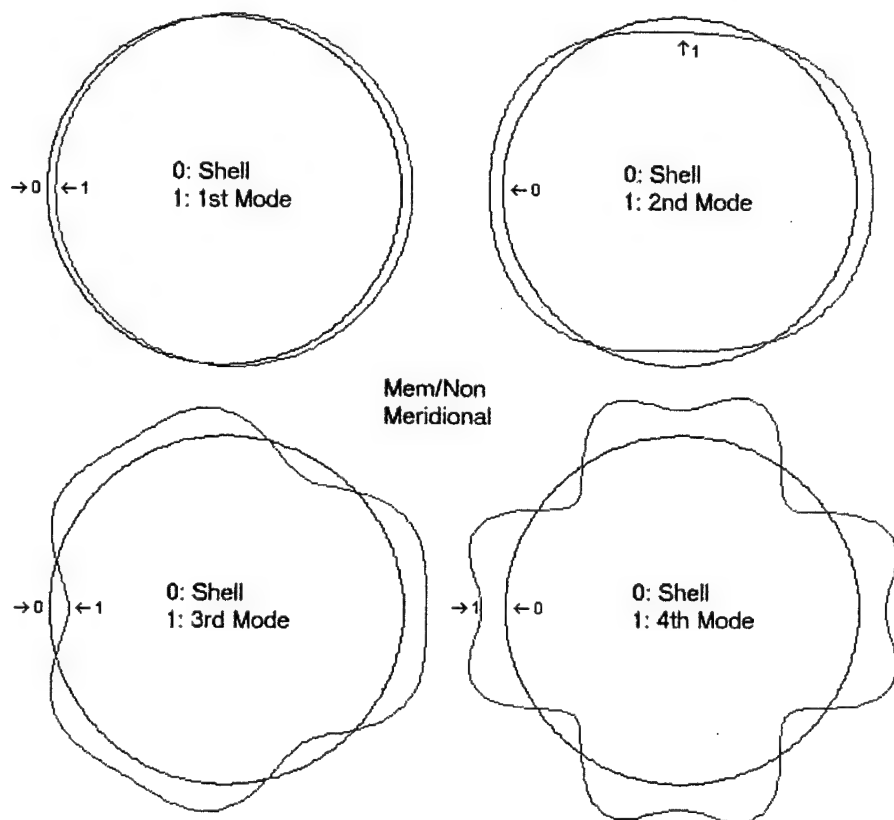


Fig.10 Signal distributions ($m=1-4, n=1$) induced by the meridional membrane strains of a nonlinear toroidal shell. (0: Toroidal shell; 1-4: 1st-4th modes)

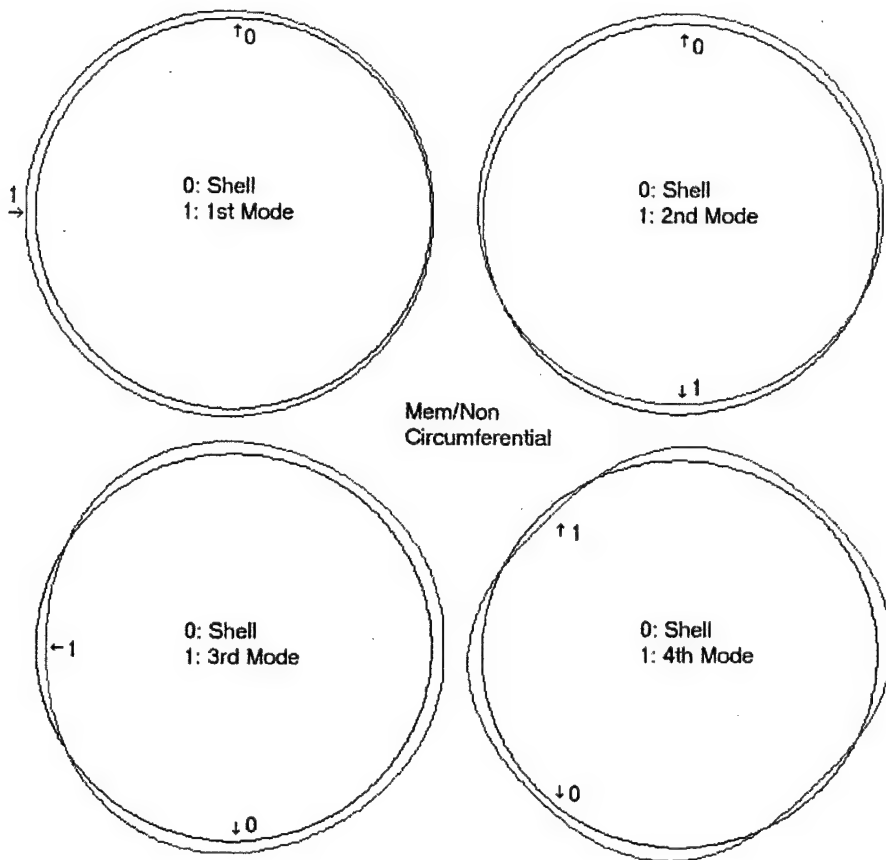


Fig.11 Signal distributions ($m=1, n=1-4$) induced by the circumferential membrane strains of a nonlinear toroidal shell. (0: Toroidal shell; 1-4: 1st-4th modes)

CONCLUSIONS

Toroidal shells belong to the shells of revolution family, in which the shell surfaces are formed based on full or partial rotations of specified lines or curves. Dynamics, measurement, and control are critical issues to advanced precision toroidal shell structures and components. Dynamic sensing signals and their distributed characteristics of spatially distributed sensors or neurons laminated on toroidal shell structures are investigated in this study. Mathematical models of linear and nonlinear toroidal shells were established based on the thin shell theory and the von Karman geometric nonlinearity assumptions. Modal dependent distributed signals and detailed signal components of spatially distributed sensors or neurons were defined based on the simplified mode shape functions defined by the Donnell-Mushtari-Vlasov theory. Detailed modal signal distributions depend on variations of the meridional and circumferential membrane/bending strains, defined by the direct piezoelectricity, the Gauss theorem, the Maxwell principle and the open-circuit assumption. Accordingly, with the analytical solutions, various distributed signals, modal voltages, and contributing signal components of distributed thin-film sensors and neurons laminated on linear and nonlinear toroidal shells were evaluated quantitatively. Parametric studies of distributed modal voltages and signal distributions suggest that the dominating signal component results from the meridional membrane strains, then the

circumferential membrane strains. The signals contributed by the bending components are relatively insignificant, as compared with the membrane counterparts. Signal distributions basically reveal distinct modal characteristics of toroidal shells. Analysis data also infer that the distributed sensor layout of this toroidal shell is meridionally laminated strips that would provide the best measurement effect at the least material cost. This analysis also suggests that distributed signals and dominating signal components of toroidal shells depends on not only materials and dimensions, but also boundary conditions, natural modes, sensor locations, modal strain components, etc. As these design parameters change, the effective distributed sensor layouts or signal patterns would also change.

ACKNOWLEDGEMENT

This research is supported, in part, by a grant (F49620-98-1-0467) from the Air Force Office of Scientific Research (Project Manager: Brian Sanders). This support is gratefully acknowledged.

REFERENCES

1. F. Zhang and F. Redekop 1992 *Computers and Structures* **43**, 1019-1028. Surface loading of a thin-walled toroidal shell.
2. S.K. Naboulsi A.N. Palazotto and J.M. Jr. Greer 2000 *Journal of Aerospace Engineering* **13**, 110-121. Static-dynamic analyses of toroidal shells.
3. A.Y.T. Leung and T.C. Kwok 1995 *Thin-Walled Structures* **21**, 43-64. Dynamic stiffness analysis of toroidal shells.
4. G.D. Galletly and D.A. Galletly 1996 *Thin-Walled Structures* **26**, 195-212. Buckling of complex toroidal shell structures.
5. D. Redekop B. Xu and Y.M. Zhang 1999 *International Journal of Pressure Vessels and Piping* **76**, 575-581. Stability of a toroidal fluid-containing shell.
6. F.J.M.Q. Melo and P.M.S.T. de Castro 1997 *Journal of Strain Analysis for Engineering Design* **32**, 47-59. Linear elastic stress analysis of curved pipes under generalized loads using a reduced integration finite ring element.
7. D.W. Huang, D. Redekop and B. Xu 1997 *Compsite Structures* **63**, 465-473. Natural frequencies and mode shapes of curved pipes.
8. A.Y.T. Leung and T.C. Kwok 1994 *Thin-Walled Structures* **19**, 317-332. Free Vibration analysis of a toroidal shell.
9. H.S. Tzou 1993 *Piezoelectric Shells (Distributed Sensing and Control of Continua)*, Kluwer Academic Publishers, Boston /Dordrecht.
10. H.S. Tzou J.P. Zhong and M.C. Natori 1993 *ASME Journal of Vibration & Acoustics* **115**, 40-46. Sensor mechanics of distributed shell convolving sensors applied to flexible rings.
11. H.S. Tzou Y. Bao and V.B. Venkayya 1996 *Journal of Sound & Vibration* **197**, 207-224. Study of segmented transducers laminated on cylindrical shells, Part-1: Sensor patches.
12. H.S. Tzou V.B. Venkayya and J.J. Hollkamp 1998 *Dynamics and Control of Distributed Systems* H.S. Tzou and L.A. Bergman, (Editors), Cambridge University Press 304-370. Orthogonal sensing and control of continua with distributed transducers.
13. H.S. Tzou Y. Bao and Y. Zhou 1997 *ASME Transactions, Journal of Vibration & Acoustics* **119**, 374-389. Nonlinear piezothermoelasticity and multi-field actuators, Part-1: Nonlinear

anisotropic piezothermoelastic shell laminates; Part-2: Control of nonlinear buckling and dynamics.

14. H.S. Tzou 1992 *Precision Sensors, Actuators, and Systems* H.S. Tzou and T. Fukuda, (Editors), Kluwer Academic Publishers, Dordrecht /Boston /London 175-218. Thin-layer distributed piezoelectric neurons and muscles: electromechanics and applications.
15. L.H. He, C.W. Lim and A.K. Soh 2000 *Acta Mechanica* **145**, 189-204. Three-dimensional analysis of an antiparallel piezoelectric bimorph.
16. Z. Cheng C.W. Lim and S. Kitipornchai 2000 *International Journal of Solids and Structures* **37**, 3153-3175. Three-dimensional asymptotic approach to inhomogeneous and laminated piezoelectric plates.
17. A.W. Leissa 1973 *Vibration of Shells*, NASA Report SP-288.
18. H.S. Tzou and R.J. Yang 2000 *Journal of Theoretical and Applied Mechanics* **38**, 623-644. Nonlinear piezothermoelastic shell theory applied to control of variable-geometry shells.

(TorShl_MVD3F_1.Sh1Tord1.Doc700)

CHAPTER 10

MICRO-CONTROL ACTIONS AND LOCATION SENSITIVITY OF PATCH ACTUATORS ON TOROIDAL SHELLS

ABSTRACT

Toroidal shell structures have been proposed for components of inflatable telescopes and space structures, etc. over the years. Thus, distributed control of toroidal shells becomes a critical issue in precision maneuver, operation, and reliability. The converse effect of piezoelectric materials has made it one of the best candidates for distributed actuators. The resultant control forces and micro-control actions induced by the distributed actuators depend on applied voltages, geometrical (e.g., spatial segmentation and shape) and material (i.e., various actuator materials) properties of the actuators. The purpose of this analysis is to study the spatial location effects of actuator placement and to evaluate the micro-control actions imposed upon toroidal shell structures. Mathematical models and governing equations of the toroidal shells laminated with distributed actuator patches are presented first, followed by formulations of distributed control forces and micro-control actions including meridional/circumferential membrane and bending control components. Spatially distributed electromechanical microscopic actuation characteristics and control effects resulting from various meridional and circumferential actions of actuator patches at various shell locations are evaluated.

INTRODUCTION

Over the years, toroidal shells have been used or proposed for structures and/or components of tubular cooling systems, neutron accelerators, space telescopes, inflatable space structures, space colonies, etc. Effective control of these toroidal shell structures or components can enhance operational accuracy, precision, and reliability of these high-performance structural systems. Static, dynamic, vibration, and buckling characteristics of toroidal shells have been studied (Naboulsi, Palazotto and Greer, 2000; Redekop, Xu and Zhang, 1999; Galletly and Galletly, 1996; Leung and Kwok, 1995). Stress and free-vibration analyses of pipe-type toroidal shells have also been investigated (Gavelya and Kononenko, 1975; Melo and de Castro, 1997; Huang, Redekop and Xu, 1997; Leung and Kwok, 1994). Recent development of smart structures and strucronics technology has demonstrated a number of new distributed actuators that can be spatially distributed over shell structures (Gabbert and Tzou, 2000; Tzou and Bergman, 1998). Distributed control characteristics and effectiveness of plates, rings, cylindrical shells, paraboloidal shells using distributed segmented or shaped actuators have been investigated (Liu and Tzou, 1998; Tzou, Zhong, and Hollkamp,

1994; Tzou, Bao, and Venkayya, 1996; Tzou, Ding, and Hagiwara, 2002), as have the nonlinear structures (Zhou and Tzou, 2000; Tzou and Bao, 1997). Micro-sensing characteristics and modal voltages of linear and nonlinear toroidal shells have been recently studied (Tzou and Wang, 2002). This study focuses on detailed evaluation of dynamic distributed control and microscopic control actions of toroidal shells laminated with segmented piezoelectric actuator patches. Modal domain governing equations incorporating global actuator-induced distributed control forces of toroidal shells laminated with distributed actuator patches are defined first. Distributed control forces and micro-control actions resulting from a constant-size actuator patch at various shell locations are analyzed and its modal-dependent spatial control effectiveness is evaluated. Spatially distributed electromechanical actuation characteristics contributed by various meridional/circumferential membrane and bending control actions are investigated in case studies.

MODELING OF TOROIDAL SHELL WITH SPATIALLY DISTRIBUTED ACTUATORS

A toroidal shell structure laminated with piezoelectric actuator layers is illustrated in **Figure 1** where ϕ denotes the meridional direction, ψ the circumferential direction, and α_3 the transverse direction. (Note that *italic* ϕ_3 denotes the control signal used in control action analysis presented later.) Key geometric parameters of a toroidal shell are: “R” the circumferential radius, “r” the meridional radius, the Lamé parameters $A_1 = r$ and $A_2 = r\xi$, and the radii of curvature $R_1 = r$ and $R_2 = \frac{r\xi}{\gamma \cos \phi}$ where $\xi = 1 + \gamma \cos \phi$ and $\gamma = r/R$ (Tzou and Wang, 2002). Independent modal control of toroidal shells with distributed piezoelectric actuators is discussed in this section. Micro-control actions and their directional behavior induced by actuator patches are discussed in the next section.

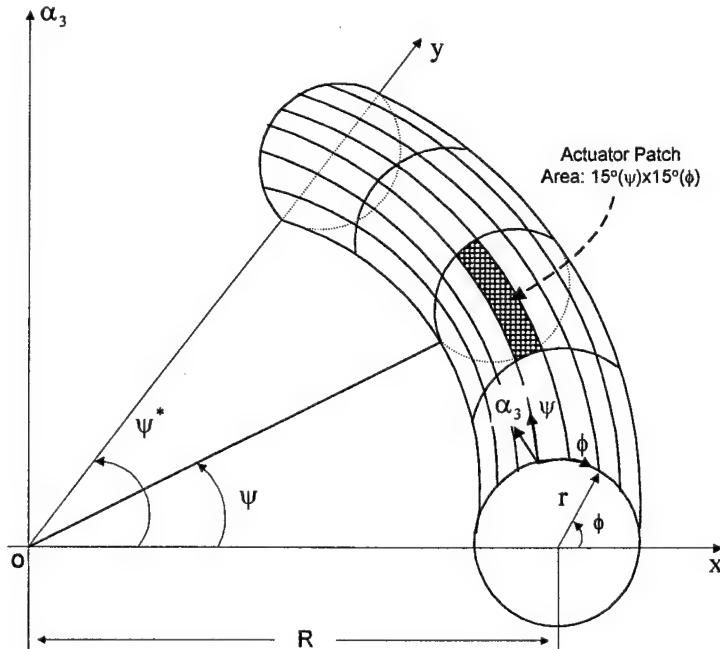


Fig.1 Toroidal shell section laminated with piezoelectric actuators.

Assume that the total response of the toroidal shell is composed of all participating modes based on the modal expansion concept. Accordingly, independent modal control characteristics, without spillover and modal coupling, of toroidal shells derived from the modal expansion method can be written as

$$\ddot{\eta}_{mn} + 2\zeta_{mn}\omega_{mn}\dot{\eta}_{mn} + \omega_{mn}^2\eta_{mn} = F_{mn}, \quad (1)$$

where $\eta_{mn}(t)$ is the modal participation factor; ζ_{mn} is the modal damping ratio; ω_{mn} is the m - n -th natural frequency; F_{mn} is the modal force; and m denotes the meridional wave number and n denotes the circumferential wave number. The generic modal force F_{mn} of the toroidal shell structure consists of two primary components: 1) the mechanical force induced by external loads F_i and 2) the control force induced by the distributed actuators $L_i^c(\phi_3)$ with a transversely applied electric control signal ϕ_3 (in *italic*).

$$F_{mn} = \frac{1}{\rho h N_{mn}} \int_{\alpha_1} \int_{\alpha_2} \left\{ \sum_{i=1}^3 [F_i + L_i^c(\phi_3)] U_{i,mn} \right\} A_1 A_2 d\alpha_1 d\alpha_2 = \hat{F}_{mn} + \hat{F}_{mn}^c; \quad (2)$$

where ρ is the shell mass density; h is the shell thickness; A_1 and A_2 are the Lamé parameters; α_1 and α_2 respectively denote the ϕ and ψ directions;

$$\hat{F}_{mn} = \frac{1}{\rho h N_{mn}} \int_{\alpha_1} \int_{\alpha_2} \left\{ \sum_{i=1}^3 F_i U_{i,mn} \right\} A_1 A_2 d\alpha_1 d\alpha_2; \quad (3a)$$

$$\hat{F}_{mn}^c = \frac{1}{\rho h N_{mn}} \int_{\alpha_1} \int_{\alpha_2} \left\{ \sum_{i=1}^3 L_i^c(\phi_3) \cdot U_{i,mn} \right\} \cdot A_1 A_2 d\alpha_1 d\alpha_2; \quad (3b)$$

$N_{mn} = \int_{\alpha_1} \int_{\alpha_2} \left(\sum_{i=1}^3 U_{i,mn}^2 \right) A_1 A_2 d\alpha_1 d\alpha_2$; and $U_{i,mn}$ is the mn -th mode shape function of the toroidal shell. Again, $L_i^c(\phi_3)$ is defined as a control action induced by the converse piezoelectric effects with a transversely applied control signal ϕ_3 (Tzou, 1993). The subscript i denotes the coordinate directions, which are $1=\phi$, $2=\psi$ and 3 , i.e., the meridional, circumferential, and transverse directions, respectively. The control actions imposed to the toroidal shell in three directions can be respectively written as

$$L_1^c \{ \phi_3 \} = -\frac{1}{A_1 A_2} \left\{ \frac{\partial}{\partial \phi} (N_{\phi\phi}^c A_2) - N_{\phi\phi}^c \frac{\partial}{\partial \phi} A_2 + \frac{1}{R_1} \left[\frac{\partial}{\partial \phi} (M_{\phi\phi}^c A_2) - M_{\phi\phi}^c \frac{\partial}{\partial \phi} A_2 \right] \right\}, \quad (4)$$

$$L_2^c \{ \phi_3 \} = -\frac{1}{A_1 A_2} \left\{ \frac{\partial}{\partial \psi} (N_{\psi\psi}^c A_1) - N_{\psi\psi}^c \frac{\partial}{\partial \psi} A_1 + \frac{1}{R_1} \left[\frac{\partial}{\partial \psi} (M_{\psi\psi}^c A_1) - M_{\psi\psi}^c \frac{\partial}{\partial \psi} A_1 \right] \right\}, \quad (5)$$

$$L_3^c \{\phi_3\} = -\frac{1}{r^2} \frac{\partial^2 M_{\phi\phi}^c}{\partial \phi^2} + \frac{\cos \vartheta}{R\xi} N_{xx}^c - \frac{1}{(r\xi)^2} \frac{\partial^2 M_{xx}^c}{\partial \chi^2} + \frac{1}{r} N_{\phi\phi}^c + \frac{1}{rR\xi} (-2 \sin \vartheta \frac{\partial M_{\phi\phi}^c}{\partial \phi} + \cos \vartheta M_{\phi\phi}^c + \sin \vartheta \frac{\partial M_{xx}^c}{\partial \phi} - \cos \vartheta M_{xx}^c). \quad (6)$$

Where N_{ij}^c denotes the membrane control force, M_{ij}^c denotes the control moment induced by the distributed actuators and $\vartheta = \pi - \phi$. Substituting the Lamé parameters ($A_1 = r$ and $A_2 = r\xi$), the radii of curvature ($R_1 = r$ and $R_2 = r\xi/\gamma \cos \phi$ where $\xi = 1 + \gamma \cos \phi$ and $\gamma = r/R$) and two principle directions $\alpha_1 = \phi$, $\alpha_2 = \chi$ (where $\chi = (R/r)\psi = \gamma\psi$) of the toroidal shell into the generic control forces yields

$$L_\phi^c \{\phi_3\} = -\frac{1}{r} \frac{\partial N_{\phi\phi}^c}{\partial \phi} + \frac{1}{R\xi} \sin \vartheta (N_{xx}^c - N_{\phi\phi}^c) + \frac{1}{rR\xi} \sin \vartheta (M_{xx}^c - M_{\phi\phi}^c) - \frac{1}{r^2} \frac{\partial M_{\phi\phi}^c}{\partial \phi}, \quad (7)$$

$$L_\psi^c \{\phi_3\} = -\frac{1}{r\xi} \frac{\partial N_{xx}^c}{\partial \chi} - \frac{\gamma \cos \vartheta}{(r\xi)^2} \frac{\partial M_{xx}^c}{\partial \chi}, \quad (8)$$

$$L_3^c \{\phi_3\} = -\frac{1}{r^2} \frac{\partial^2 M_{\phi\phi}^c}{\partial \phi^2} + \frac{\cos \vartheta}{R\xi} N_{xx}^c - \frac{1}{(r\xi)^2} \frac{\partial^2 M_{xx}^c}{\partial \chi^2} + \frac{1}{r} N_{\phi\phi}^c + \frac{1}{rR\xi} (-2 \sin \vartheta \frac{\partial M_{\phi\phi}^c}{\partial \phi} + \cos \vartheta M_{\phi\phi}^c + \sin \vartheta \frac{\partial M_{xx}^c}{\partial \phi} - \cos \vartheta M_{xx}^c). \quad (9)$$

Recall that mode shape functions are required to explicitly define all modal forces. The shear-diaphragm boundary conditions are considered in this analysis. Following the shear-diaphragm boundary conditions and the Donnell-Mushtari-Vlasov approximation, one can define the mode shape functions of toroidal shells as (Huang, Redekop and Xu, 1997)

$$U_{\phi_{mn}} = \sum_{m=1}^3 \sum_{n=1}^3 A_{mn} \sin(m\vartheta) \sin\left(\frac{n\pi\psi^*}{\psi}\right), \quad (11)$$

$$U_{\psi_{mn}} = \sum_{m=1}^3 \sum_{n=1}^3 B_{mn} \cos(m\vartheta) \cos\left(\frac{n\pi\psi^*}{\psi}\right), \quad (12)$$

$$U_{3_{mn}} = \sum_{m=1}^3 \sum_{n=1}^3 C_{mn} \cos(m\vartheta) \sin\left(\frac{n\pi\psi^*}{\psi}\right), \quad (13)$$

where A_{mn} , B_{mn} and C_{mn} , are the modal oscillation amplitudes; ψ^* defines the circumferential angle ($2\pi \geq \psi^* \geq 0$); m (meridional), n (circumferential) are the mode or wave numbers. (Note that although the elasticity of toroidal shells follows the Donnell-Mushtari-Vlasov approximation, the control forces and micro-control actions are generic without any simplification.) Thus, the modal force induced by distributed mechanical loadings (external forces) and the distributed actuator respectively become

$$\hat{F}_{mn} = \frac{1}{\rho h N_{mn}} \int_{\phi} \int_{\psi} \{ F_{\phi} [A_{mn} \sin(m\theta) \sin(\frac{n\pi\psi}{\psi})] + F_{\psi} [B_{mn} \cos(m\theta) \cos(\frac{n\pi\psi}{\psi})] \\ + F_3 [C_{mn} \cos(m\theta) \sin(\frac{n\pi\psi}{\psi})] \} r^2 \xi d\phi d\psi ; \quad (14)$$

$$\hat{F}_{mn}^c = \frac{1}{\rho h N_{mn}} \int_{\phi} \int_{\psi} \{ [-\frac{1}{r} \frac{\partial N_{\phi\phi}^c}{\partial \phi} + \frac{1}{R\xi} \sin \theta (N_{xx}^c - N_{\phi\phi}^c) + \frac{1}{rR\xi} \sin \theta (M_{xx}^c - M_{\phi\phi}^c) \\ - \frac{1}{r^2} \frac{\partial M_{\phi\phi}^c}{\partial \phi}] A_{mn} \sin(m\theta) \sin(\frac{n\pi\psi}{\psi}) \\ - [\frac{1}{r\xi} \frac{\partial N_{xx}^c}{\partial \chi} + \frac{\gamma \cos \theta}{(r\xi)^2} \frac{\partial M_{xx}^c}{\partial \chi}] B_{mn} \cos(m\theta) \cos(\frac{n\pi\psi}{\psi}) \\ + [\frac{\cos \theta}{R\xi} N_{xx}^c - \frac{1}{r^2} \frac{\partial^2 M_{\phi\phi}^c}{\partial \phi^2} - \frac{1}{(r\xi)^2} \frac{\partial^2 M_{xx}^c}{\partial \chi^2} + \frac{1}{r} N_{\phi\phi}^c \\ + \frac{1}{rR\xi} (\cos \theta M_{\phi\phi}^c - 2 \sin \theta \frac{\partial M_{\phi\phi}^c}{\partial \phi} + \sin \theta \frac{\partial M_{xx}^c}{\partial \phi} \\ - \cos \theta M_{xx}^c)] C_{mn} \cos(m\theta) \sin(\frac{n\pi\psi}{\psi}) \} r^2 \xi d\phi d\psi ; \quad (15)$$

$$N_{mn} = \int_{\phi} \int_{\psi} \{ [A_{mn} \sin(m\theta) \sin(\frac{n\pi\psi}{\psi})]^2 + [B_{mn} \cos(m\theta) \cos(\frac{n\pi\psi}{\psi})]^2 \}$$

and

$$+ [C_{mn} \cos(m\theta) \sin(\frac{n\pi\psi}{\psi})]^2 \} r^2 \xi d\phi d\psi .$$

Distributed Piezoelectric Actuators and Micro-control Actions

The distributed control forces and moments induced by the piezoelectric actuator with a transversely applied control signal ϕ^a (i.e., $\phi^a \equiv \phi_3$) are respectively defined as

$$N_{\phi\phi}^c = d_{31} Y_p \phi^a \quad \text{and} \quad N_{\psi\psi}^c = d_{32} Y_p \phi^a ; \quad (16,17)$$

$$M_{\phi\phi}^c = r_{\phi}^a d_{31} Y_p \phi^a \quad \text{and} \quad M_{\psi\psi}^c = r_{\chi}^a d_{32} Y_p \phi^a . \quad (18,19)$$

Substituting $\chi = (R/r)\psi$ into \hat{F}_{mn}^c to convert from χ to the conventional circumferential ψ coordinate yields

$$\begin{aligned}
\hat{F}_{mn}^c = & \frac{1}{\rho h N_{mn}} \int_{\phi} \int_{\psi} \left\{ \left[-\frac{1}{r} \frac{\partial N_{\phi\phi}^c}{\partial \phi} + \frac{1}{R\xi} \sin \theta (N_{\psi\psi}^c - N_{\phi\phi}^c) + \frac{1}{rR\xi} \sin \theta (M_{\psi\psi}^c - M_{\phi\phi}^c) \right. \right. \\
& - \frac{1}{r^2} \frac{\partial M_{\phi\phi}^c}{\partial \phi} \left. \right] A_{mn} \sin(m\theta) \sin\left(\frac{n\pi\psi}{\psi^*}\right) \\
& - \left[\frac{1}{R\xi} \frac{\partial N_{\psi\psi}^c}{\partial \psi} + \frac{\cos \theta}{(R\xi)^2} \frac{\partial M_{\psi\psi}^c}{\partial \psi} \right] B_{mn} \cos(m\theta) \cos\left(\frac{n\pi\psi}{\psi^*}\right) \\
& \left. \left. + \left[\frac{\cos \theta}{R\xi} N_{\psi\psi}^c - \frac{1}{r^2} \frac{\partial^2 M_{\phi\phi}^c}{\partial \phi^2} - \frac{1}{(R\xi)^2} \frac{\partial^2 M_{\psi\psi}^c}{\partial \psi^2} + \frac{1}{r} N_{\phi\phi}^c \right. \right. \right. \\
& + \frac{1}{rR\xi} \left(\cos \theta M_{\phi\phi}^c - 2 \sin \theta \frac{\partial M_{\phi\phi}^c}{\partial \phi} + \sin \theta \frac{\partial M_{\psi\psi}^c}{\partial \phi} \right. \\
& \left. \left. \left. - \cos \theta M_{\psi\psi}^c \right] C_{mn} \cos(m\theta) \sin\left(\frac{n\pi\psi}{\psi^*}\right) \right\} r^2 \xi d\phi d\psi. \right. \tag{20}
\end{aligned}$$

Assume the piezoelectric actuator is uniform thickness (i.e., $r_{\phi}^a = r_{\psi}^a = r^a$) and two piezoelectric constants are equal (i.e., $d_{31} = d_{32}$). Substituting definitions of actuator induced forces and moments into the above generic control force expression \hat{F}_{mn}^c , and separating them into individual contributing micro-membrane/bending control actions gives

$$\hat{F}_{mn}^c = (\hat{T}_{mn})_{\phi,mem} + (\hat{T}_{mn})_{\phi,bend} + (\hat{T}_{mn})_{\psi,mem} + (\hat{T}_{mn})_{\psi,bend}. \tag{21}$$

Note that $(\hat{T}_{mn})_{\phi,mem}$ is the meridional membrane control force component, $(\hat{T}_{mn})_{\psi,mem}$ is the ψ membrane control force component, $(\hat{T}_{mn})_{\phi,bend}$ is the meridional bending control component, and $(\hat{T}_{mn})_{\psi,bend}$ is the ψ -bending control component. These micro-control actions are

$$\begin{aligned}
(\hat{T}_{mn})_{\phi,mem} = & \frac{d_{31} Y_p}{\rho h N_{mn}} \int_{\phi} \int_{\psi} \left\{ \frac{\phi^a}{r} C_{mn} \cos(m\theta) \sin\left(\frac{n\pi\psi}{\psi^*}\right) \right. \\
& \left. - \left[\frac{1}{r} \frac{\partial \phi^a}{\partial \phi} + \frac{\phi^a \sin \theta}{R\xi} \right] A_{mn} \sin(m\theta) \sin\left(\frac{n\pi\psi}{\psi^*}\right) \right\} r^2 \xi d\phi d\psi, \tag{22}
\end{aligned}$$

$$\begin{aligned}
(\hat{T}_{mn})_{\psi,mem} = & \frac{d_{31} Y_p}{\rho h N_{mn}} \int_{\phi} \int_{\psi} \left\{ \left[\frac{\phi^a \sin \theta}{R\xi} \right] A_{mn} \sin(m\theta) \sin\left(\frac{n\pi\psi}{\psi^*}\right) \right. \\
& - \left[\frac{1}{R\xi} \frac{\partial \phi^a}{\partial \psi} \right] B_{mn} \cos(m\theta) \cos\left(\frac{n\pi\psi}{\psi^*}\right) + \left[\frac{\cos \theta \phi^a}{R\xi} \right] C_{mn} \cos(m\theta) \\
& \left. \cdot \sin\left(\frac{n\pi\psi}{\psi^*}\right) \right\} r^2 \xi d\phi d\psi, \tag{23}
\end{aligned}$$

$$\begin{aligned}
(\hat{T}_{mn})_{\phi, \text{bend}} = & \frac{r^a d_{31} Y_p}{\rho h N_{mn}} \int_{\phi} \int_{\psi} \left\{ -\left[\frac{\phi^a \sin \theta}{r R \xi} + \frac{1}{r^2} \frac{\partial \phi^a}{\partial \phi} \right] A_{mn} \sin(m\theta) \sin\left(\frac{n\pi\psi}{\psi^*}\right) \right. \\
& \left. + \left[\frac{1}{r R \xi} \left(\cos \theta \phi^a - 2 \sin \theta \frac{\partial \phi^a}{\partial \phi} \right) - \frac{1}{r^2} \frac{\partial^2 \phi^a}{\partial \phi^2} \right] C_{mn} \cos(m\theta) \sin\left(\frac{n\pi\psi}{\psi^*}\right) \right\} (24) \\
& \cdot r^2 \xi d\phi d\psi,
\end{aligned}$$

$$\begin{aligned}
(\hat{T}_{mn})_{\psi, \text{bend}} = & \frac{r^a d_{31} Y_p}{\rho h N_{mn}} \int_{\phi} \int_{\psi} \left\{ \left[\frac{1}{r R \xi} \sin \theta \phi^a \right] A_{mn} \sin(m\theta) \sin\left(\frac{n\pi\psi}{\psi^*}\right) \right. \\
& - \left[\frac{\cos \theta}{(R\xi)^2} \frac{\partial \phi^a}{\partial \psi} \right] B_{mn} \cos(m\theta) \cos\left(\frac{n\pi\psi}{\psi^*}\right) + \left[\frac{1}{r R \xi} \left(\sin \theta \frac{\partial \phi^a}{\partial \phi} \right. \right. \\
& \left. \left. - \cos \theta \phi^a \right) - \frac{1}{(R\xi)^2} \frac{\partial^2 \phi^a}{\partial \psi^2} \right] C_{mn} \cos(m\theta) \sin\left(\frac{n\pi\psi}{\psi^*}\right) \right\} r^2 \xi d\phi d\psi. \quad (25)
\end{aligned}$$

PATCH ACTUATOR INDUCED MICRO-CONTROL ACTIONS

Note that $F_{mn} = \hat{F}_{mn} + \hat{F}_{mn}^c$ where the mechanical force \hat{F}_{mn} is neglected in the analysis of micro-control actions. The transversely applied control signal $\phi^a(\phi, \psi, t)$ (in *italic*) can be expressed by a temporal part and a spatial part where the spatial part defines the patch boundary:

$$\phi^a(\phi, \psi, t) = \phi^a(t) [u_s(\phi - \phi_1) - u_s(\phi - \phi_2)][u_s(\psi - \psi_1) - u_s(\psi - \psi_2)], \quad (26)$$

where $u_s(\cdot)$ is the unit step function: $u_s(\phi - \phi_i) = 1$ when $\phi > \phi_i$, and = 0 when $\phi < \phi_i$. Its spatial derivatives are

$$\frac{\partial}{\partial \phi} \phi^a(\phi, \psi, t) = \phi^a(t) [\delta(\phi - \phi_1) - \delta(\phi - \phi_2)][u_s(\psi - \psi_1) - u_s(\psi - \psi_2)], \quad (27)$$

$$\frac{\partial}{\partial \psi} \phi^a(\phi, \psi, t) = \phi^a(t) [u_s(\phi - \phi_1) - u_s(\phi - \phi_2)][\delta(\psi - \psi_1) - \delta(\psi - \psi_2)]. \quad (28)$$

where $\delta(\cdot)$ is a Dirac delta function: $\delta(\phi - \phi^*) = 1$ when $\phi = \phi^*$, and = 0 when $\phi \neq \phi^*$. These two expressions will be used in micro-control actions of segmented actuator patches later. Thus, the micro-control actions restricted by the segmented electrode on the segmented actuator can be further defined. Substituting the patch definition, further manipulating the four micro-control actions, and eliminating the $r^2 \xi$ terms yields the final forms which are used to evaluate their modal control characteristics of distributed patch actuators laminated on a toroidal shell in case studies.

$$\begin{aligned}
(\hat{T}_{mn})_{\phi,mem} = & \frac{d_{31} Y_p \phi^a(t)}{\rho h N_{mn}} \left\{ \left\{ \int_{\phi_1}^{\phi_2} \left[C_{mn} r \xi \cos(m\theta) - A_{mn} \frac{r^2}{R} \sin \theta \sin(m\theta) \right] d\phi \right. \right. \\
& \left. \left. \cdot \int_{\psi_1}^{\psi_2} \sin\left(\frac{n\pi\psi}{\psi^*}\right) d\psi \right\} - A_{mn} r \left\{ \left[1 + \frac{r}{R} \cos(\pi - \phi_1) \right] \sin[m(\pi - \phi_1)] \right. \\
& \left. \left. - \left[1 + \frac{r}{R} \cos(\pi - \phi_2) \right] \cdot \sin[m(\pi - \phi_2)] \right] \cdot \int_{\psi_1}^{\psi_2} \sin\left(\frac{n\pi\psi}{\psi^*}\right) d\psi \right\} \right\}, \quad (29)
\end{aligned}$$

$$\begin{aligned}
(\hat{T}_{mn})_{\psi,mem} = & \frac{d_{31} Y_p \phi^a(t)}{\rho h N_{mn}} \frac{r^2}{R} \left\{ \left\{ \int_{\phi_1}^{\phi_2} \left[A_{mn} \sin \theta \sin(m\theta) + C_{mn} \cos \theta \right. \right. \right. \\
& \left. \left. \cdot \cos(m\theta) \right] d\phi \cdot \int_{\psi_1}^{\psi_2} \sin\left(\frac{n\pi\psi}{\psi^*}\right) d\psi \right\} - B_{mn} \left\{ \left[\cos\left(\frac{n\pi\psi_1}{\psi^*}\right) \right. \right. \\
& \left. \left. - \cos\left(\frac{n\pi\psi_2}{\psi^*}\right) \right] \int_{\phi_1}^{\phi_2} \cos(m\theta) d\theta \right\} \right\}, \quad (30)
\end{aligned}$$

$$\begin{aligned}
(\hat{T}_{mn})_{\phi,bend} = & \frac{r^a d_{31} Y_p \phi^a(t)}{\rho h N_{mn}} \left\{ \frac{r}{R} \left\{ \int_{\phi_1}^{\phi_2} \left[C_{mn} \cos \theta \cos(m\theta) - A_{mn} \sin \theta \right. \right. \right. \\
& \left. \cdot \sin(m\theta) \right] d\phi \int_{\psi_1}^{\psi_2} \sin\left(\frac{n\pi\psi}{\psi^*}\right) d\psi \right\} - A_{mn} \left\{ \left[1 + \frac{r}{R} \cos(\pi - \phi_1) \right] \right. \\
& \left. \cdot \sin[m(\pi - \phi_1)] - \left[1 + \frac{r}{R} \cos(\pi - \phi_2) \right] \cdot \sin[m(\pi - \phi_2)] \right] \\
& \int_{\psi_1}^{\psi_2} \sin\left(\frac{n\pi\psi}{\psi^*}\right) d\psi \right\} - C_{mn} \frac{2r}{R} \left\{ \left[\sin(\pi - \phi_1) \cos[m(\pi - \phi_1)] \right. \right. \\
& \left. \left. - \sin(\pi - \phi_2) \cos[m(\pi - \phi_2)] \right] \int_{\psi_1}^{\psi_2} \sin\left(\frac{n\pi\psi}{\psi^*}\right) d\psi \right\} - C_{mn} \\
& \left\{ \int_{\phi_1}^{\phi_2} \left[\frac{\partial}{\partial \phi} [\delta(\phi - \phi_1) - \delta(\phi - \phi_2)] \right] \cdot \xi \cos(m\theta) d\phi \right. \\
& \left. \cdot \int_{\psi_1}^{\psi_2} \sin\left(\frac{n\pi\psi}{\psi^*}\right) d\psi \right\}, \quad (31)
\end{aligned}$$

$$\begin{aligned}
(\hat{T}_{mn})_{\psi, \text{bend}} = & \frac{r^a d_{31} Y_p \phi^a(t)}{\rho h N_{mn}} \left\{ \frac{r}{R} \left\{ \int_{\psi_1}^{\psi_2} \left[A_{mn} \sin \theta \sin(m\theta) - C_{mn} \cos \theta \right. \right. \right. \\
& \cdot \cos(m\theta) \left. \right] d\theta \int_{\psi_1}^{\psi_2} \sin\left(\frac{n\pi\psi}{\psi^*}\right) d\psi \} + C_{mn} \frac{r}{R} \left\{ \left[\sin(\pi - \phi_1) \right. \right. \\
& \cdot \cos[m(\pi - \phi_1)] - \sin(\pi - \phi_2) \cos[m(\pi - \phi_2)] \left. \right] \int_{\psi_1}^{\psi_2} \sin\left(\frac{n\pi\psi}{\psi^*}\right) d\psi \} \\
& - B_{mn} \left(\frac{r}{R} \right)^2 \left\{ \left[\cos\left(\frac{n\pi\psi_1}{\psi^*}\right) - \cos\left(\frac{n\pi\psi_2}{\psi^*}\right) \right] \int_{\psi_1}^{\psi_2} \frac{1}{\xi} \cos \theta \cos(m\theta) d\theta \} \\
& - C_{mn} \left(\frac{r}{R} \right)^2 \left\{ \int_{\psi_1}^{\psi_2} \left[\frac{\partial}{\partial \psi} [\delta(\psi - \psi_1) - \delta(\psi - \psi_2)] \sin\left(\frac{n\pi\psi}{\psi^*}\right) \right] d\psi \right. \\
& \cdot \int_{\psi_1}^{\psi_2} \frac{1}{\xi} \cos(m\theta) d\theta \} .
\end{aligned} \tag{32}$$

CONTROL FORCES OF ACTUATORS PATCHES

To examine the microscopic control actions induced by the segmented toroidal actuator patch, non-essential parameters, e.g., d_{31} , d_{32} , Y_p , ρ , A_{mn} , B_{mn} , and C_{mn} , are assumed unity. Thus, manipulating these parameters (e.g., $(r^a d_{31} Y_p)/\rho$ and modal amplitudes), one can further extrapolate analysis data and evaluate control characteristics of specific actuator materials and natural modes. A toroidal shell with circumferential radius $R=3.2\text{m}$, meridional radius $r=0.56\text{m}$, one full revolution $\psi^* = 2\pi$, shell thickness $h = 0.01\text{m}$ is used in the case study; actuator segments are perfectly bonded on the shell surface (i.e., $r^a \approx \frac{1}{2}h = 0.005\text{m}$ where the actuator thickness is neglected). Note that the actuator patch is assumed thin, such that its elastic effect is neglected. The toroidal shell has shear-diaphragm boundary conditions at $(\phi = 0^\circ, \psi = 0^\circ)$ and $(\phi = 180^\circ, \psi = 360^\circ)$. Piezoelectric actuator patches with an area of 15° in the circumferential direction and 15° in the meridional direction are laminated throughout the toroidal shell, **Figure 1**. (That is if a piezoelectric actuator patch has an area starting from 0° - 15° in the ψ or ϕ directions, the next patch then starts from 15° - 30° in the ψ or ϕ directions.)

The actuator-patch induced individual modal actuation characteristics, i.e., the meridional/circumferential membrane and bending actions, are calculated based on their specific locations, and their microscopic actuation magnitudes at various locations are then connected to illustrate the global spatial actuation phenomenon on the toroidal shell. Accordingly, each data point on the surface contour represents the actuation sensitivity (or authority) at that specific location – the location effect that is also modal sensitive, i.e., control actions of an actuator patch at one location contribute differently to various modal oscillations. A positive magnitude combined with a positive control voltage implies an attenuation or control effect; a negative magnitude, however, needs a negative control voltage to achieve the attenuation effect. Recall that $(\hat{T}_{mn})_{\phi, \text{mem}}$ is the meridional micro-membrane control force component, $(\hat{T}_{mn})_{\psi, \text{mem}}$ is the ψ membrane control force component, $(\hat{T}_{mn})_{\phi, \text{bend}}$ is the

meridional bending control component, and $(\hat{T}_{mn})_{\psi, \text{bend}}$ is the ψ control component. These actuator induced micro-control actions of the toroidal shell modes ($m=1-4, n=1-4$) are analyzed and grouped in **Figures 2-5**: ($m=1-4, n=1$) modes, **Figures 6-9**: ($m=1-4, n=2$) modes, **Figures 10-13**: ($m=1-4, n=3$) modes, and **Figures 14-17**: ($m=1-4, n=4$) modes. To illustrate the spatial distribution and actuation magnitudes in these figures, the toroidal shell is cut open referenced to $\phi = 0^\circ$ and $\psi = 0^\circ$. Also, recall that m denotes the meridional wave number and n denotes the circumferential wave number. Each data point on the graph represents the micro-control action of a segmented actuator patch at the corresponding location of the toroidal shell.

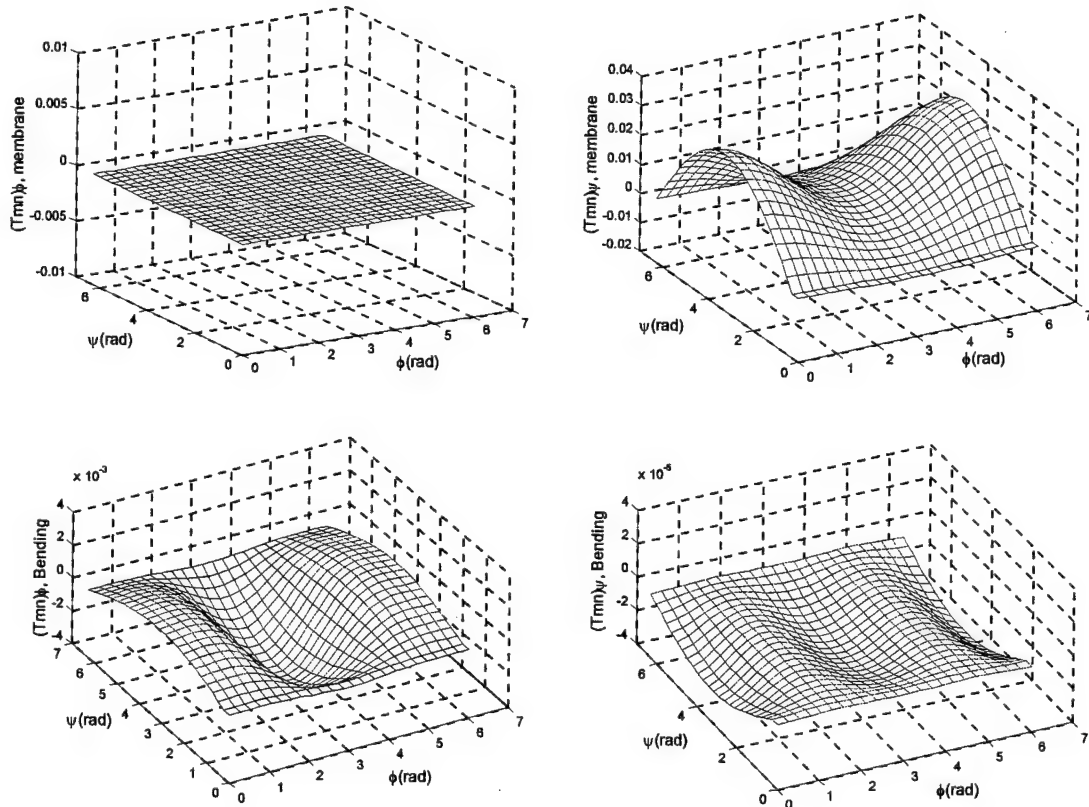


Fig.2 Micro-control actions of the ($m=1, n=1$) toroidal shell mode.

Top-left: $(\hat{T}_{mn})_{\phi, \text{mem}}$; Top-right: $(\hat{T}_{mn})_{\psi, \text{mem}}$; Bottom-left: $(\hat{T}_{mn})_{\phi, \text{bend}}$; Bottom-right: $(\hat{T}_{mn})_{\psi, \text{bend}}$.

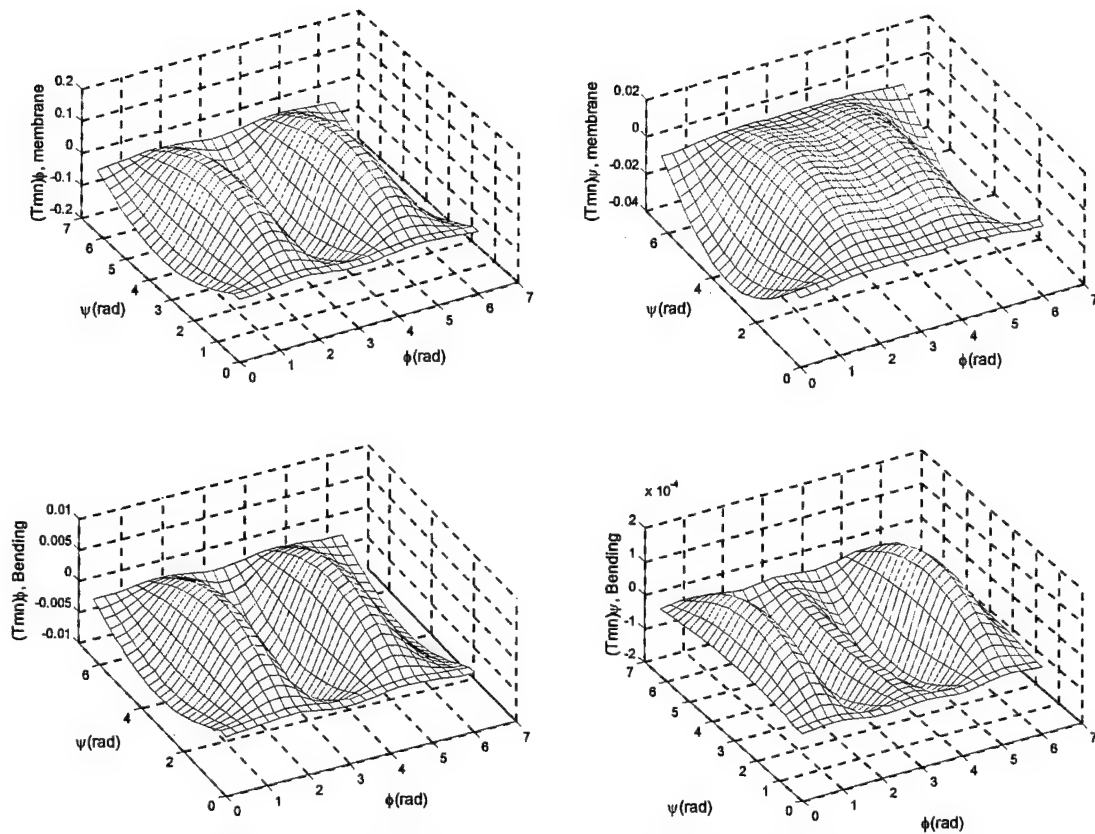
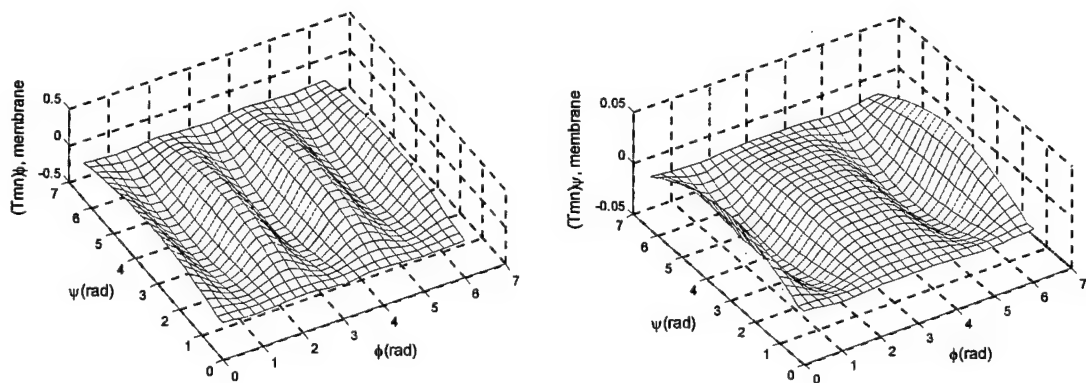


Fig.3 Micro-control actions of the ($m=2, n=1$) toroidal shell mode.



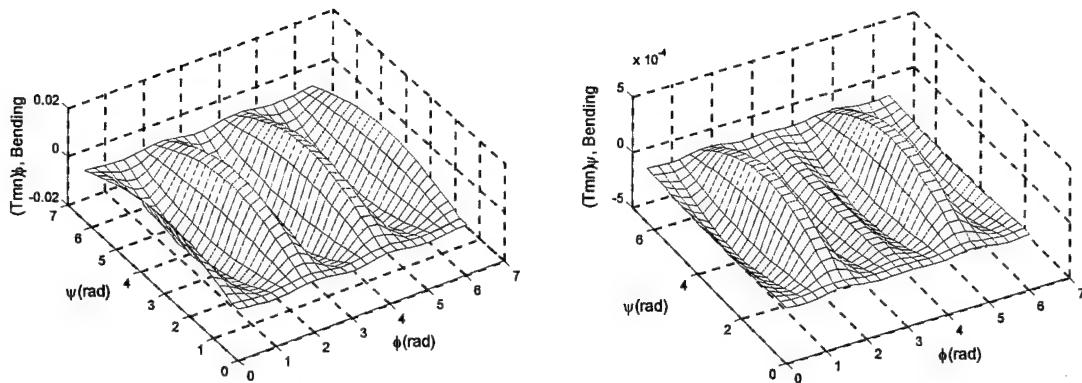


Fig.4 Micro-control actions of the (m=3,n=1) toroidal shell mode.

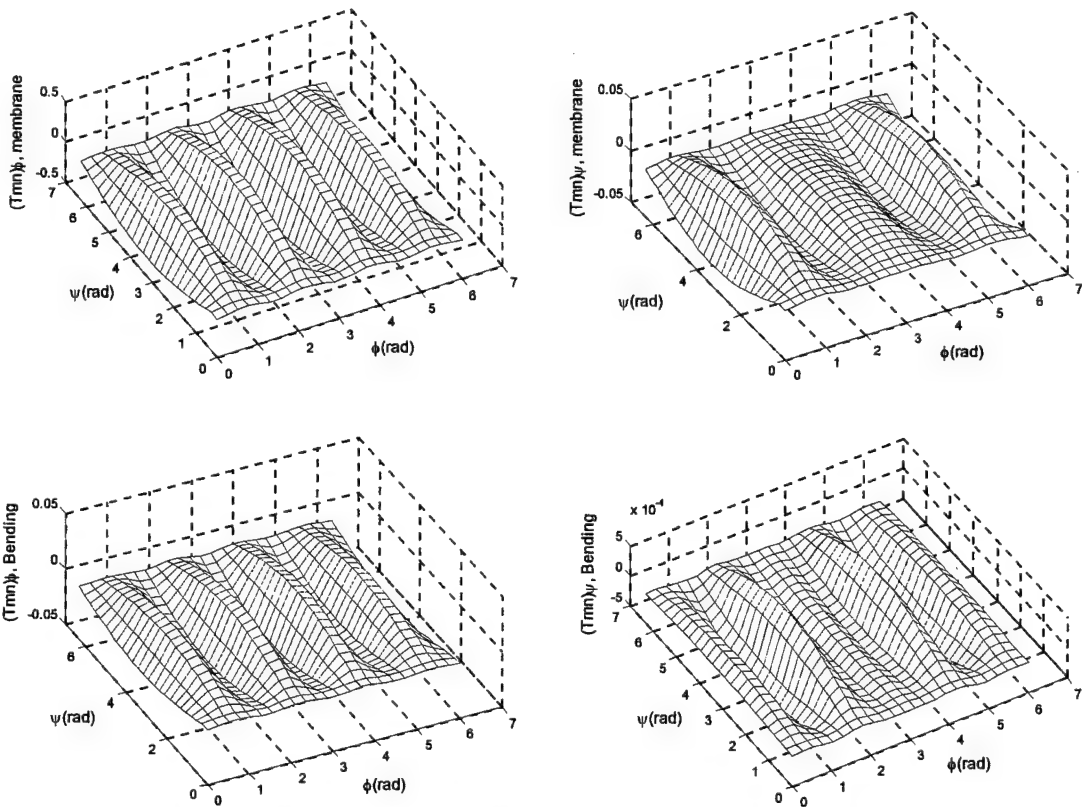


Fig.5 Micro-control actions of the (m=4, n=1) toroidal shell mode.

The micro-control actions of the (m=1-4,n=1) toroidal shell modes reveal that the micro-control actions of the (1,1) mode seem different from the other (m=2-4;n=1) modes, in which $(\hat{T}_{mn})_{\psi,mem} \gg (\hat{T}_{mn})_{\phi,bend} > (\hat{T}_{mn})_{\psi,bend} \gg (\hat{T}_{mn})_{\phi,mem}$. $(\hat{T}_{mn})_{\psi,mem}$ dominates and $(\hat{T}_{mn})_{\phi,mem}$ is negligible (due to the meridional rigid-body mode at m=1) (Gavelya and Kononenko, 1975) in the total control force. The other three higher modes (m=2-4;n=1) show that the meridional membrane control action dominates, i.e., $(\hat{T}_{mn})_{\phi,mem} \gg (\hat{T}_{mn})_{\psi,mem} >$

$(\hat{T}_{mn})_{\phi, \text{bend}} \gg (\hat{T}_{mn})_{\psi, \text{bend}}$, $(\hat{T}_{mn})_{\psi, \text{mem}}$ and $(\hat{T}_{mn})_{\phi, \text{mem}}$ are about the same order of magnitude, $(\hat{T}_{mn})_{\phi, \text{bend}}$ increases at higher circumferential wave numbers, and $(\hat{T}_{mn})_{\psi, \text{bend}}$ is negligible in all four toroidal shell modes. The other three micro-control actions of toroidal shell modes ($m=1-4, n=2-4$) are presented as follows.

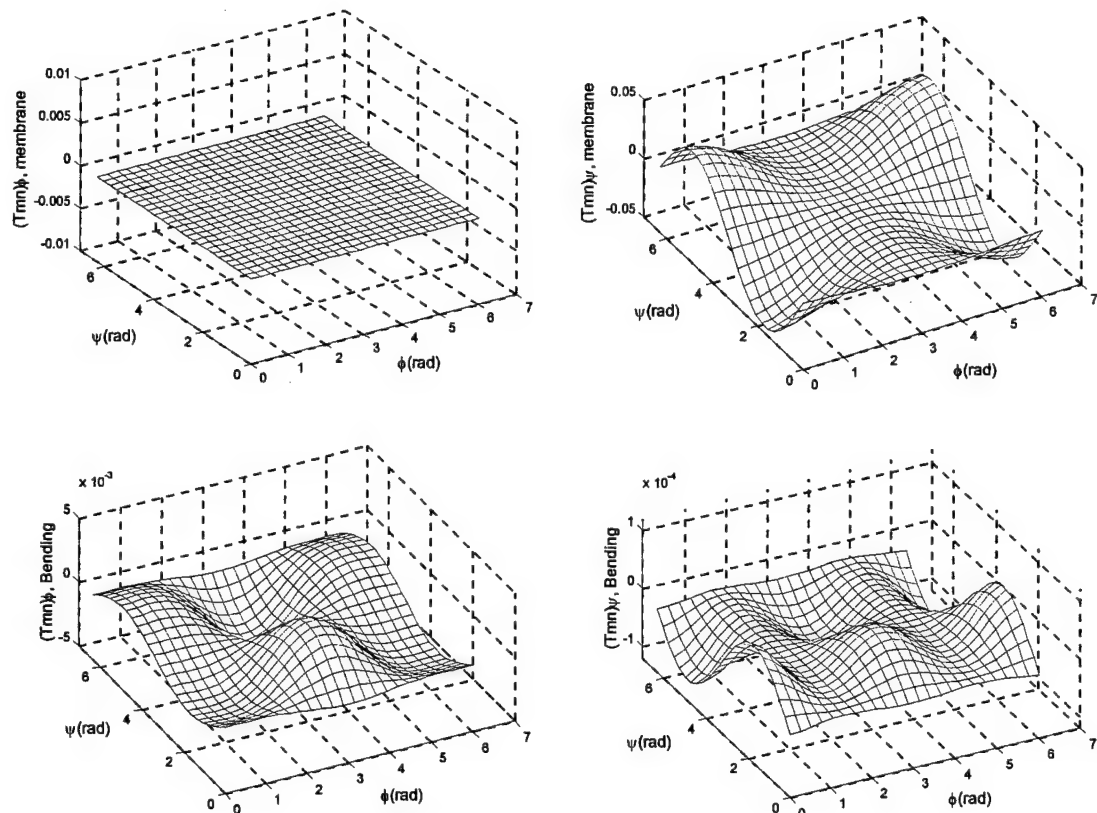


Fig.6 Micro-control actions of the ($m=1, n=2$) toroidal shell mode.

Top-left: $(\hat{T}_{mn})_{\phi, \text{mem}}$; Top-right: $(\hat{T}_{mn})_{\psi, \text{mem}}$; Bottom-left: $(\hat{T}_{mn})_{\phi, \text{bend}}$; Bottom-right: $(\hat{T}_{mn})_{\psi, \text{bend}}$.

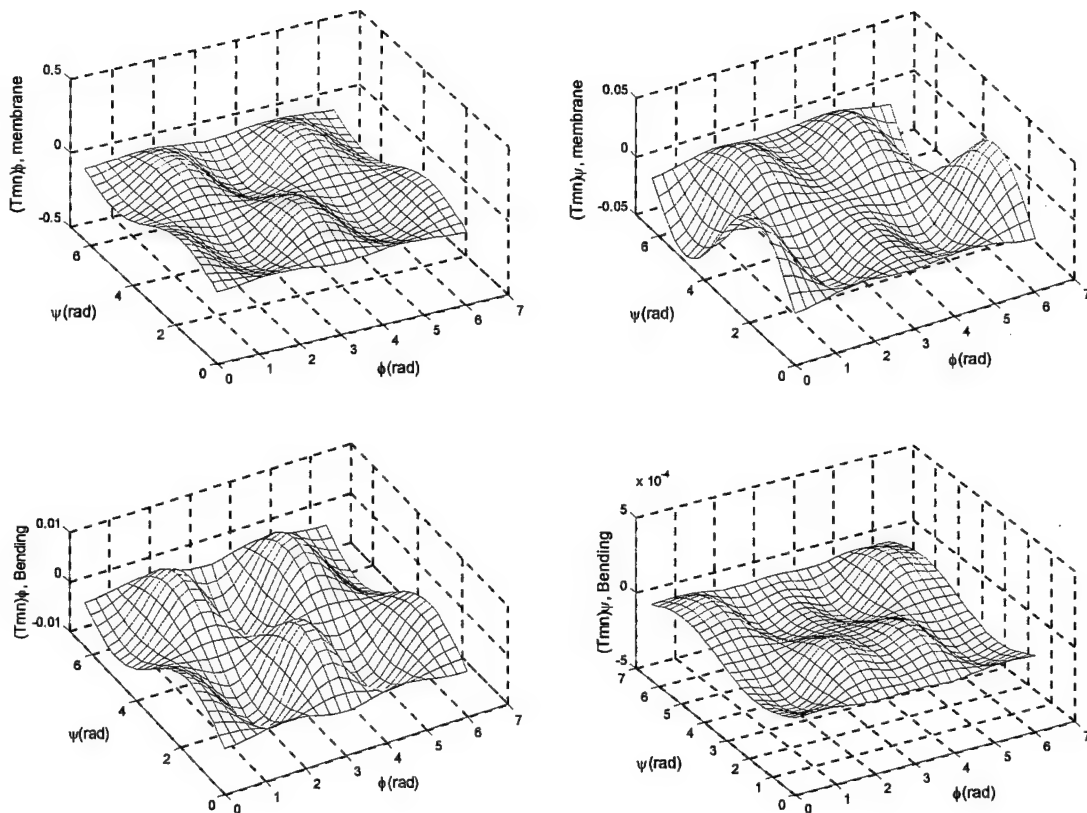
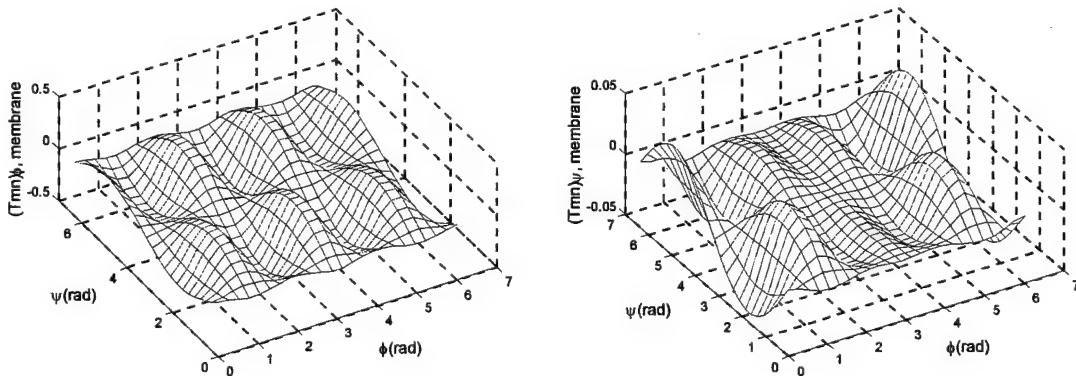


Fig.7 Micro-control actions of the ($m=2, n=2$) toroidal shell mode.



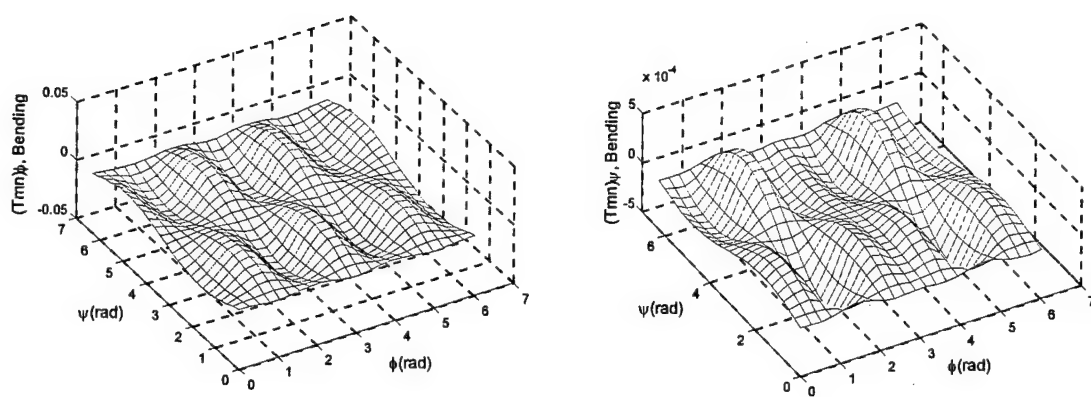


Fig.8 Micro-control actions of the (m=3,n=2) toroidal shell mode.

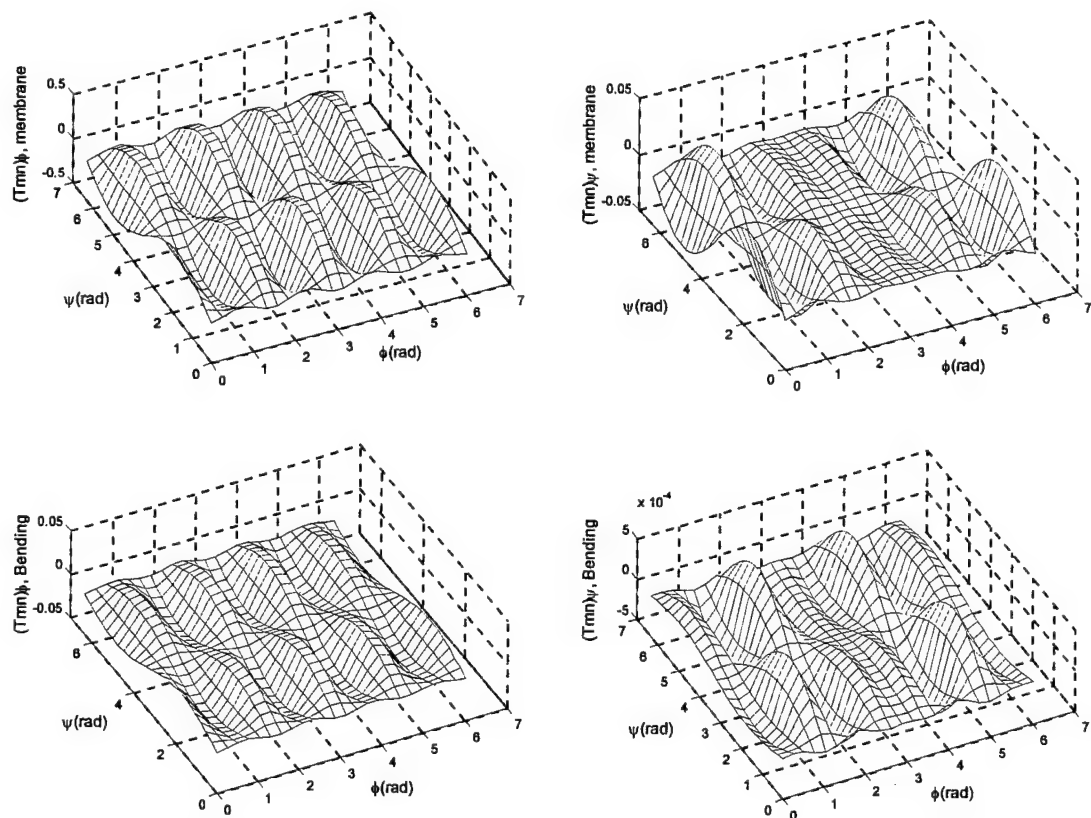


Fig.9 Micro-control actions of the (m=4,n=2) toroidal shell mode.

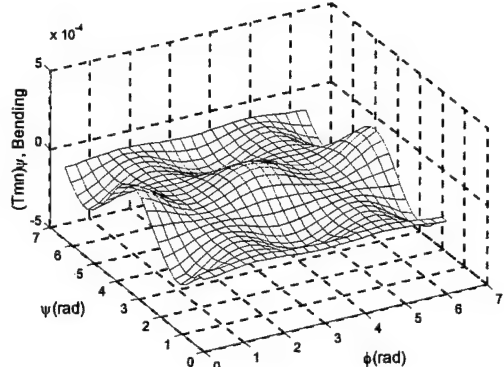
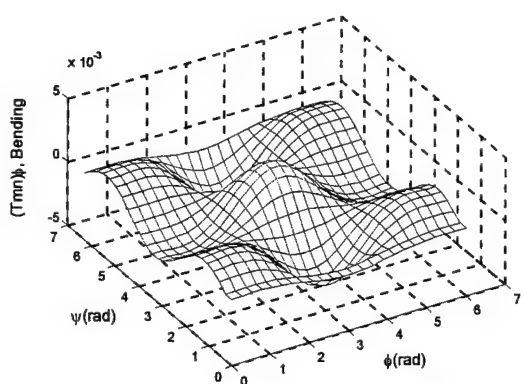
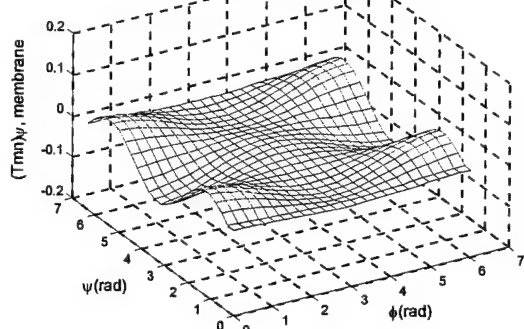
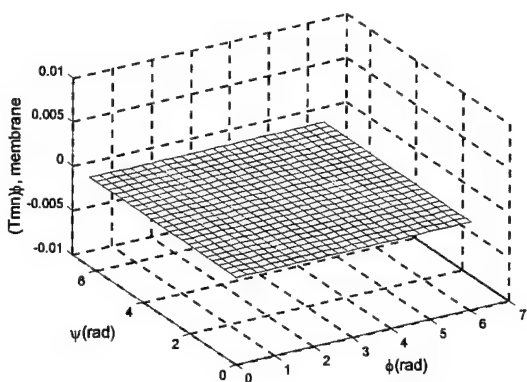
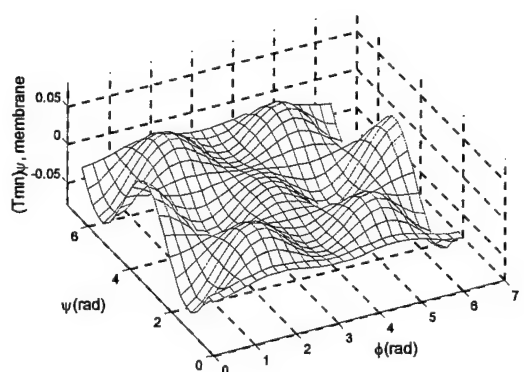
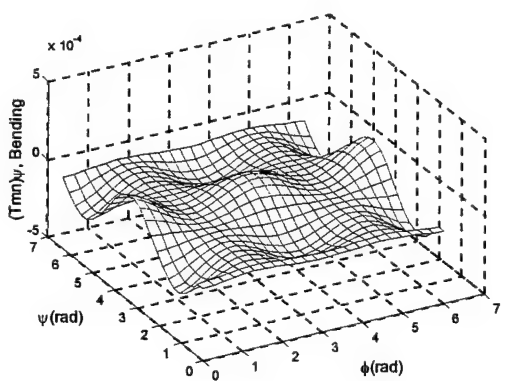


Fig.10 Micro-control actions of the (m=1,n=3) toroidal shell mode.

Top-left: $(\hat{T}_{mn})_{\phi,mem}$; Top-right: $(\hat{T}_{mn})_{\psi,mem}$; Bottom-left: $(\hat{T}_{mn})_{\phi,bend}$; Bottom-right: $(\hat{T}_{mn})_{\psi,bend}$.



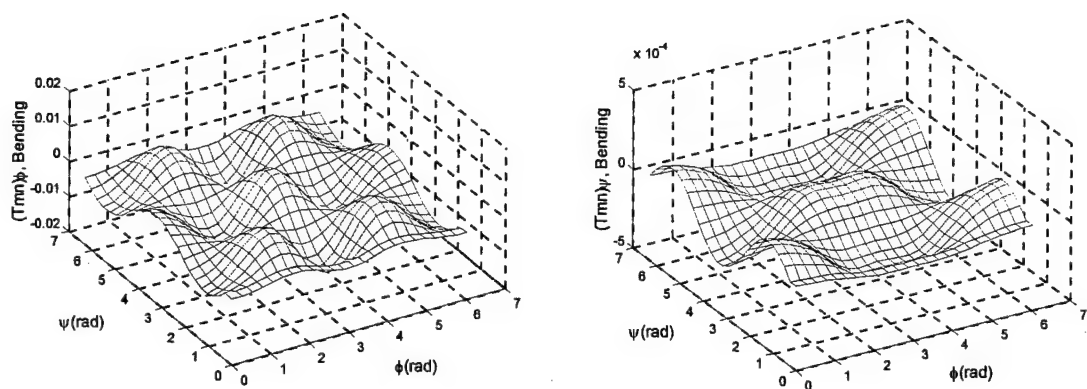


Fig.11 Micro-control actions of the (m=2,n=3) toroidal shell mode.

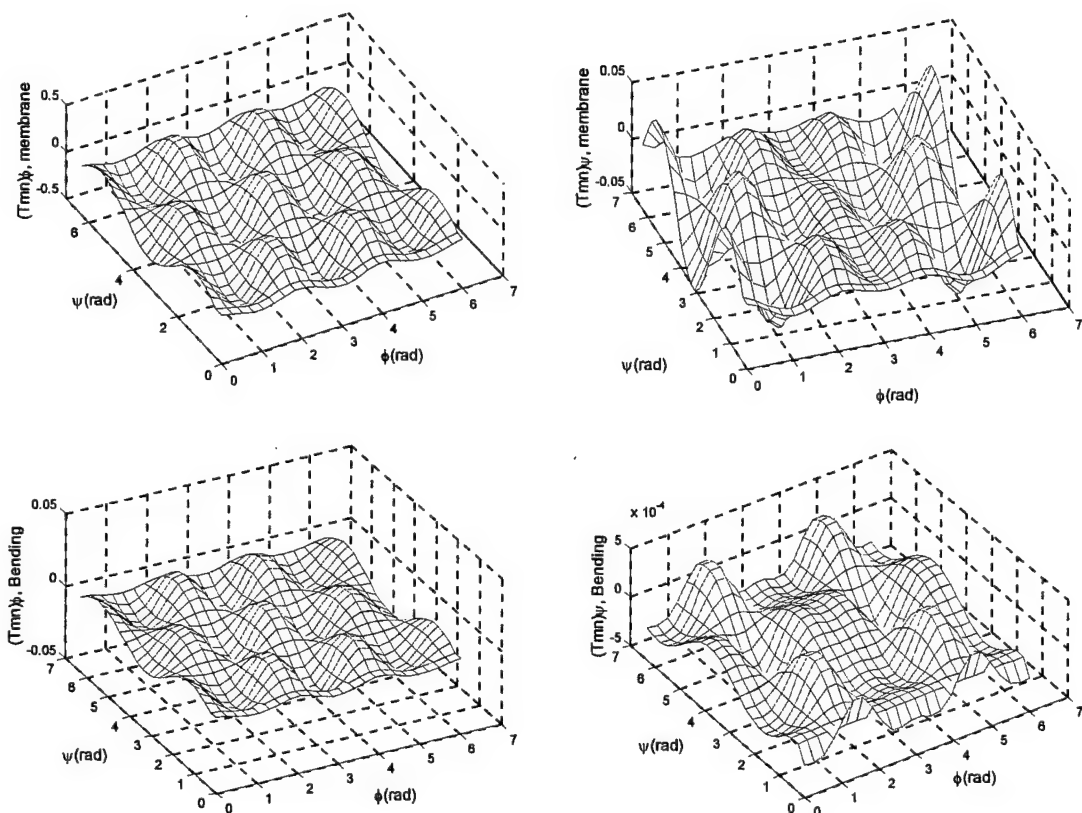


Fig.12 Micro-control actions of the (m=3,n=3) toroidal shell mode.

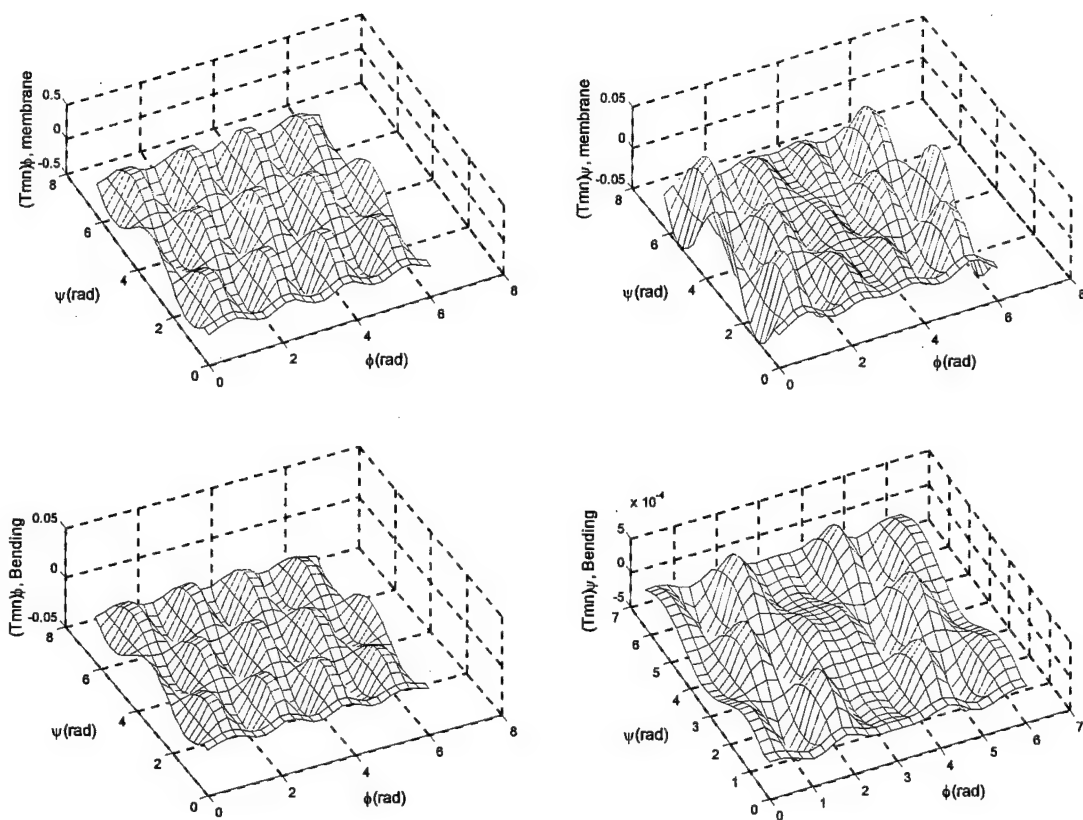
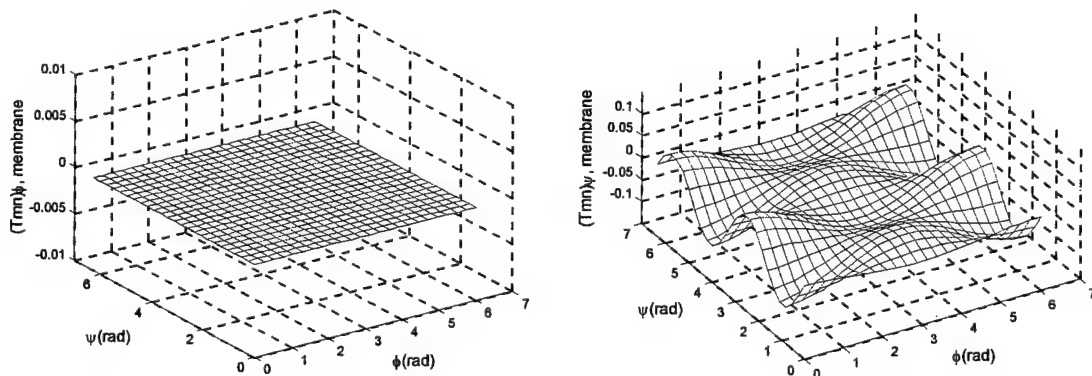


Fig.13 Micro-control actions of the $(m=4, n=3)$ toroidal shell mode.



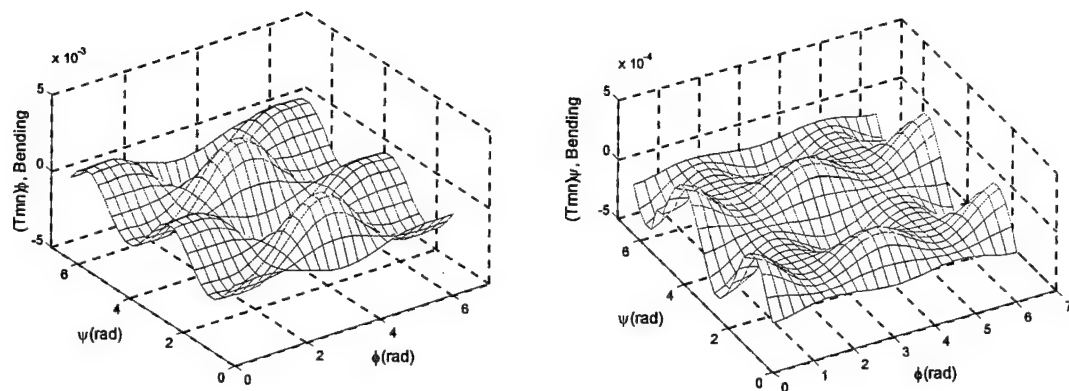


Fig.14 Micro-control actions of the (m=1,n=4) toroidal shell mode.

Top-left: $(\hat{T}_{mn})_{\phi, \text{mem}}$; Top-right: $(\hat{T}_{mn})_{\psi, \text{mem}}$; Bottom-left: $(\hat{T}_{mn})_{\phi, \text{bend}}$; Bottom-right: $(\hat{T}_{mn})_{\psi, \text{bend}}$.

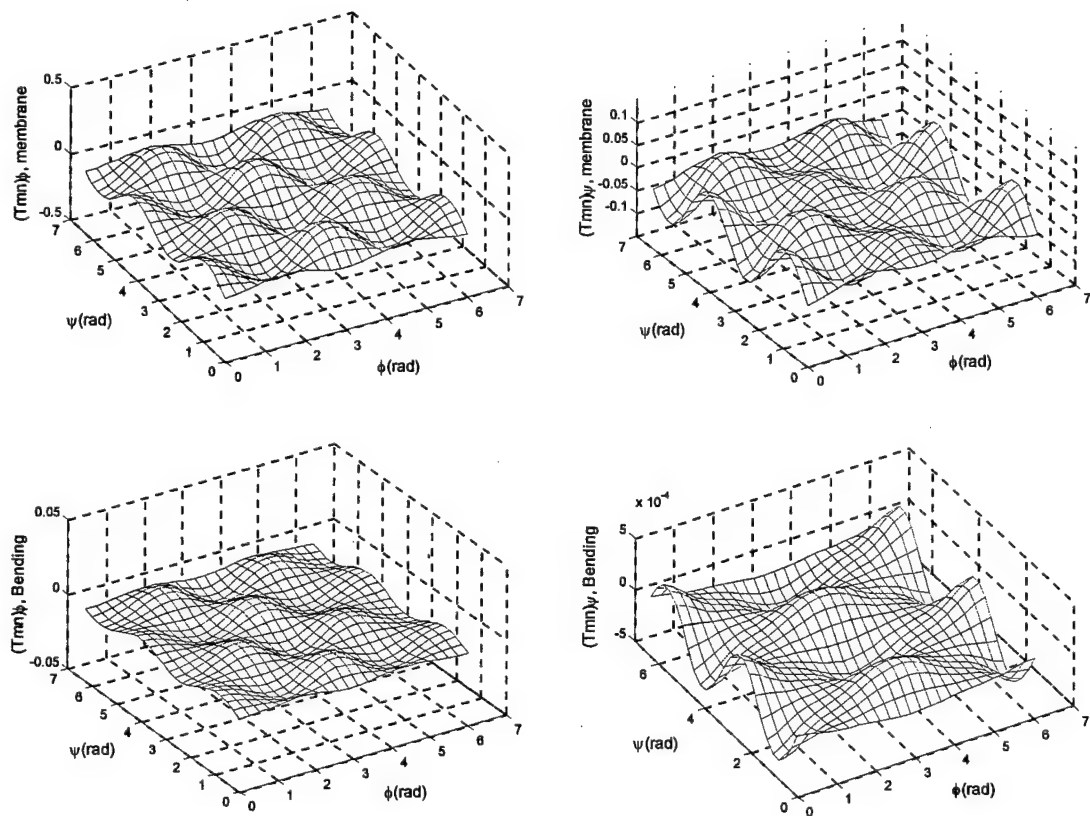


Fig.15 Micro-control actions of the (m=2,n=4) toroidal shell mode.

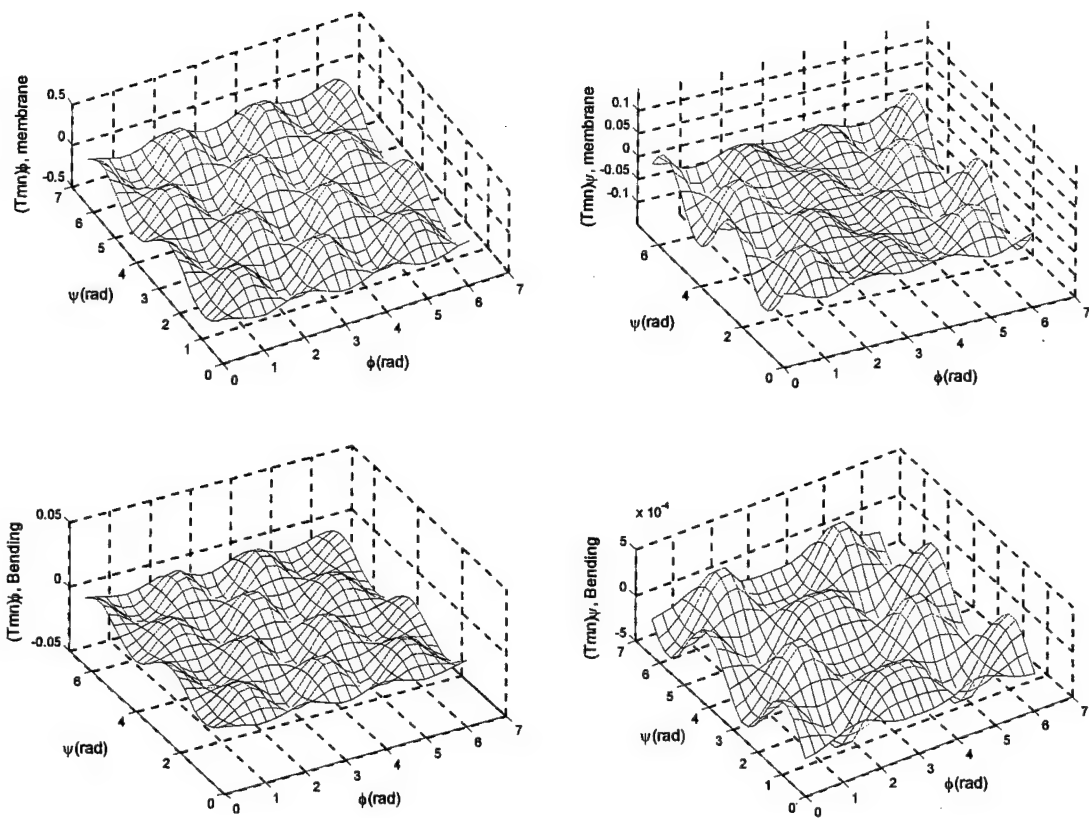
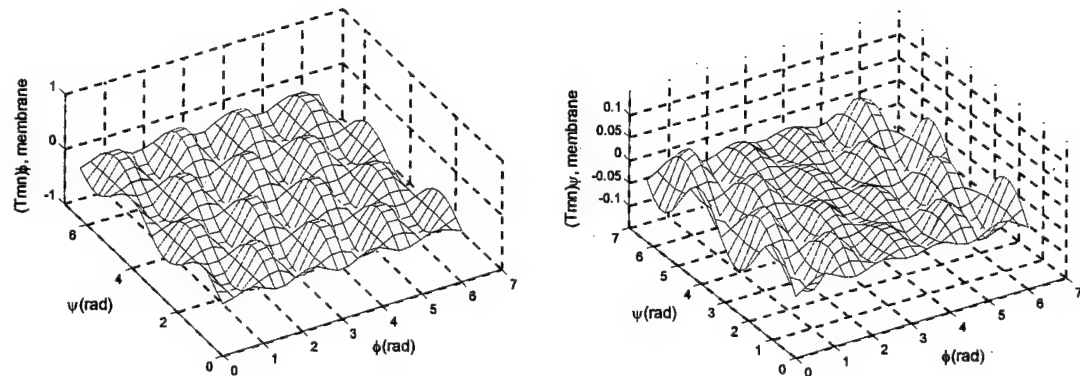


Fig.16 Micro-control actions of the (m=3,n=4) toroidal shell mode.



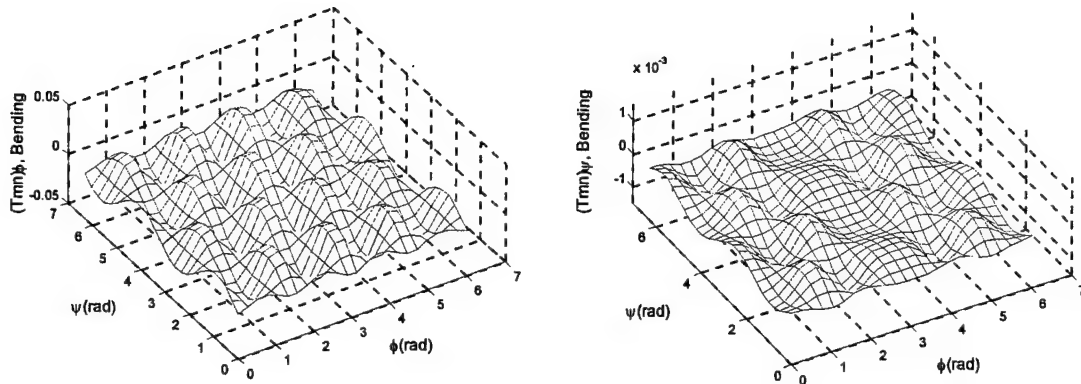


Fig.17 Micro-control actions of the (m=4,n=4) toroidal shell mode.

Analyses of actuator induced micro-control actions of the (m=1-4,n=2-4) toroidal shell modes suggest that micro-control actions $(\hat{T}_{mn})_{\psi,mem} \gg (\hat{T}_{mn})_{\phi,bend} > (\hat{T}_{mn})_{\psi,bend} \gg (\hat{T}_{mn})_{\phi,mem}$ among the (1,2-4) modes. Since the (m=1,n=2-4) modes display the meridional rigid-body-motion modes, the meridional control actions $(\hat{T}_{mn})_{\phi,mem}$ and $(\hat{T}_{mn})_{\phi,bend}$ are negligible and thus the circumferential membrane action $(\hat{T}_{mn})_{\psi,mem}$ dominates the total control force. However, the meridional oscillation behavior appears in the other three mode groups (m=2-4;n=2-4) and therefore the meridional membrane control action becomes dominant, i.e., $(\hat{T}_{mn})_{\phi,mem} \gg (\hat{T}_{mn})_{\psi,mem} > (\hat{T}_{mn})_{\phi,bend} \gg (\hat{T}_{mn})_{\psi,bend}$, provided the control signal remains constant among all shell modes. The micro-control actions among all toroidal shell modes, $(\hat{T}_{mn})_{\psi,mem}$ and $(\hat{T}_{mn})_{\psi,bend}$ stay about the same order of magnitude, $(\hat{T}_{mn})_{\phi,bend}$ increases at higher circumferential wave numbers, and $(\hat{T}_{mn})_{\psi,bend}$ is negligible in all four toroidal shell modes. Also, the magnitudes of micro-control actions depend on locations of the actuator patch, as well as the shell modes. Plots of the spatially distributed micro-control actions clearly reveal the modal dependent behavior and the best actuator locations often change for different shell modes. Influences of the shear-diaphragm boundary conditions at $(\phi = 0^\circ, \psi = 0^\circ)$ and $(\phi = 180^\circ, \psi = 360^\circ)$ to modal control actions also appear in these figures.

CONCLUSIONS

Structures and components of inflatable space structures, space telescopes, tubular cooling systems, etc. often take the shape of toroidal shells. Accordingly, distributed control of toroidal shells becomes a critical issue to precision maneuver and performance of these structures. This study is to evaluate spatially distributed microscopic control actions of segmented actuator patches laminated on flexible toroidal shells. Modal domain governing equations incorporating global actuator induced control forces of toroidal shells laminated with distributed actuator patches were presented first, followed by formulations of distributed control forces and micro-control actions including meridional/circumferential membrane and bending control components. Closed-form analytical mode shape functions are difficult to derive due to the complexity of toroidal shell equations. Thus, based on the Donnell-Mushtari-

Vlasov theory, assumed mode shape functions of a toroidal shell with shear-diaphragm boundary condition were used in the modal control force expressions and the micro-control action analyses. Spatially distributed electromechanical actuation characteristics contributed by various meridional/circumferential membrane and bending control actions were investigated. Distributed control forces and micro-control actions resulting from a constant-size actuator patch at various shell locations were analyzed and their modal-dependent spatial control effectiveness evaluated.

Analysis data suggest that among the four actuator-induced micro-control actions of toroidal shell modes ($m=1-4, n=1-4$), the meridional micro-control action $(\hat{T}_{mn})_{\phi,mem}$, in general, dominates the overall modal control force, followed by $(\hat{T}_{mn})_{\psi,mem}$, $(\hat{T}_{mn})_{\phi,bend}$ and $(\hat{T}_{mn})_{\psi,bend}$. However, since the ($m=1, n=1-4$) toroidal shell modes display meridional rigid-body modal oscillations, $(\hat{T}_{mn})_{\phi,mem}$ is negligible and $(\hat{T}_{mn})_{\psi,mem}$ dominates. Note that a constant control signal is assumed for all cases in this study, so that segmented actuator patches would reveal true inherent spatial micro-control actions. Besides, magnitudes of control forces and micro-control actions are modal dependent. Accordingly, specific layouts and coordinated actuators of various segmented actuator patches can maximize the control effects at the minimal energy or actuator requirement.

ACKNOWLEDGEMENT

This research is supported, in part, by a grant (F49620-98-1-0467) from the Air Force Office of Scientific Research (Project Manager: Brian Sanders). This support is gratefully acknowledged.

REFERENCES

Gabbert, U. and Tzou, H.S., Editors, 2001, *Smart Structures and Structronic Systems*, Kluwer Academic Publishers, Dordrecht/Boston/London.

Galletly, G.D. and Galletly, D.A., 1996, "Buckling of Complex Toroidal Shell Structures," *Thin-Walled Structures*, Vol.26, pp.195-212.

Gavelya, S.P., Kononenko, N.I., 1975, "Characteristic Oscillation and Waves on a Toroidal Shell," *Prikladnaya Mekhanika*, Vol.11, No. 1, pp.41-46.

Huang, D.W., Redekop, D., and Xu, B., 1997, "Natural Frequencies and Mode Shapes of Curved Pipes," *Composite Structures*, Vol.63, pp.465-473.

Leung, A.Y.T. and Kwok, T.C., 1995, "Dynamic Stiffness Analysis of Toroidal Shells," *Thin-Walled Structures*, Vol.21, pp.43-64.

Leung, A.Y.T. and Kwok, T.C., 1994, "Free Vibration Analysis of A Toroidal Shell," *Thin-Walled Structures*, Vol.19, pp.317-332.

Liu, B. and Tzou, H.S., 1998, "Distributed Photostrictive Actuation and Opto-piezothermoelasticity Applied to Vibration Control of Plates," *ASME Transactions, Journal of Vibration & Acoustics*, Vol.120, pp.937-943.

Melo, F.J.M.Q. and de Castro, P.M.S.T., 1997, "Linear Elastic Stress Analysis of Curved Pipes Under Generalized Loads Using A Reduced Integration Finite Ring Element," *Journal of Strain Analysis for Engineering Design*, Vol.32, pp.47-59.

Naboulsi, S.K., Palazotto, A.N., and Greer, J.M. Jr., 2000, "Static-dynamic Analyses of Toroidal Shells," *Journal of Aerospace Engineering*, Vol.13, pp.110-121.

Redekop, D., Xu, B., and Zhang, Y.M., 1999, "Stability of A Toroidal Fluid-Containing Shell," *International Journal of Pressure Vessels and Piping*, Vol.76, pp.575-581.

Tzou, H.S., 1993, *Piezoelectric Shells: Distributed Sensing and Control of Continua*, Kluwer Academic Publishers, Boston /Dordrecht.

Tzou, H.S., Bao Y. and Zhou, Y. 1997, "Nonlinear Piezothermoelasticity and Multi-Field Actuations, Part-1: Nonlinear Anisotropic Piezothermoelastic Shell Laminates; Part-2: Control of Nonlinear Buckling and Dynamics," *ASME Transactions Journal of Vibration & Acoustics*, Vol.119, pp.374-389.

Tzou, H.S., Bao, Y., and Venkayya, V.B., 1996, "Study of Segmented Transducers Laminated on Cylindrical Shells, Part-2: Actuator Patches," *Journal of Sound & Vibration*, Vol.197, No.2, pp.225-249.

Tzou, H.S. and Bergman, L.A., (Ed.), 1998, *Dynamics and Control of Distributed Systems*, Cambridge University Press, New York.

Tzou, H.S., Ding, J.H., and Hagiwara, I., 2002, "Micro-control Actions of Distributed Actuators Laminated on Precision Paraboloidal Structronic Shells," *JSME International Journal*, a special issue on Dynamics and Design of Continuous Systems, Series C, Vol.45, No1, pp.8-15.

Tzou, H.S. and Wang, D.W., 2002, "Micro-sensing Characteristics and Modal Voltages of Linear/nonlinear Toroidal Shells," *Journal of Sound and Vibration*, Vol.254, pp.203-218.

Tzou, H.S., Zhong, J.P., and Hollkamp, J.J., 1994, "Spatially Distributed Orthogonal Piezoelectric Shell Actuators: Theory and Applications," *Journal of Sound & Vibration*, Vol.177, No.3, pp.363-378. (xTordlShlF.TordAct.ShlTodrl)

Zhou, Y.H. and Tzou, H.S., 2000, "Control of Nonlinear Piezoelectric Circular Shallow Spherical Shells," *Journal of Solids and Structures*, Vol.37, pp.1663-1677.

CHAPTER 11

MICRO-ELECTROMECHANICS OF SENSOR PATCHES ON FREE PARABOLOIDAL SHELL STRUCTRONIC SYSTEMS

ABSTRACT

Distributed sensing of structural states is essential to vibration control, health monitoring and shape control of precision strucronic systems. Paraboloidal shells of revolution are widely used in aerospace, telecommunication, etc. structures. However, distributed sensing of paraboloidal shell structures is rarely investigated over the years. Micro-sensing characteristics, sensor segmentation, sensor placements, shell geometric parameters, etc. of deep/shallow paraboloidal shells are evaluated in this study. Signal generation of generic distributed sensors laminated on paraboloidal shells is defined; microscopic signal components of segmented sensor patches laminated on deep/shallow paraboloidal shells with free boundary conditions are analyzed. Parametric studies of microelectromechanics and microscopic signal generations of segmented sensor patches reveal detailed modal sensing signal generation and efficiency of segmented sensor patches laminated at various shell locations of three paraboloidal shells (i.e., a shallow, a standard, and a deep).

INTRODUCTION

Precise measurement of the dynamic state of structure is very important in active vibration control, health monitoring and shape control of strucronic (structure + electronic) systems. Conventional sensing technologies use discrete add-on motion sensors, such as strain gages, eddy current proximeters, linear variable differential transformers (LVDT), accelerometers, potentiometers, etc. However, these devices add additional weights to the structures and change the static and dynamic characteristics of the original structure. Furthermore, the strucronic systems are distributed systems; those discrete sensors are difficult to represent the shell motion precisely. Recent research show that lightweight distributed sensors layered or embedded in the structures can closely monitor local strain variations and dynamic states of flexible structures (Tzou, 1993; Gabbert and Tzou, 2001). Distributed piezoelectric sensors translate mechanical strains into electrical signals averaged over the effective sensor area (Tzou, 1992; Tzou, Zhong and Natori, 1993) and are commonly used in strucronic systems (Giurgiutiu and Zagrai, 2002; Saravanan, Ganesan and Ramamurti, 2000; Chiu, 1997).

Paraboloidal shells of revolution are widely used in aerospace, telecommunication, etc.

systems. Distributed sensing characteristics of different shells, such as cylindrical shells (Tzou, 1993; Birman and Simonyan, 1994; Qiu and Tani, 1995; Tani et al., 1995; Tzou and Bao, 1996; Callahan and Baruh, 1999), conical shells (Tzou, Chai and Wang, 2001), hemi-spherical shells (Tzou and Smithmaitrie, 2001), toroidal shells (Tzou and Wang, 2002), are studied in recent years. However, distributed sensing of paraboloidal shell structures is rarely investigated over the years. Distributed sensing behavior of paraboloidal shells with simply supported boundary is just studied recently (Tzou and Ding, 2002). To further understand the micro-electromechanical sensing behavior of paraboloidal strucronic shells, in this study, formulation of distributed sensing signal equations for paraboloidal shells with free boundary condition and sensing signal equations for segmented sensor patch are presented. Then, micro-sensing signal components of sensor patches at different locations of three paraboloidal shells with different shapes are investigated in case studies.

DISTRIBUTED SENSING SIGNALS OF PARABOLOIDAL SHELLS OF REVOLUTION

The shell strucronic system is formed by laminating a distributed piezoelectric sensor layer (with thickness h^s) on a generic double-curvature elastic shell (with thickness h). The distributed sensing signal is the function of strains. Based on Maxwell's principle and the open-voltage assumption, the sensing signal ϕ^s of a generic shell sensor can be expressed as (Tzou, 1993):

$$\begin{aligned}\phi^s &= \frac{h^s}{S^e} \int_{S^e} (h_{31}S_{11} + h_{32}S_{22} + h_{36}S_{12}) dS^e \\ &= \frac{h^s}{S^e} \int_{S^e} (h_{31}S_{11} + h_{32}S_{22} + h_{36}S_{12}) A_1 A_2 d\alpha_1 d\alpha_2 ,\end{aligned}\quad (1)$$

where S^e is the effective sensor area; h^s is the sensor thickness; S_{11} and S_{22} are the normal strains; S_{12} is the in-plane shear strain; h_{31} , h_{32} and h_{36} are the piezoelectric (displacement) constants; A_1 and A_2 are the shell's Lamé parameters; and α_1 and α_2 are the two curvilinear coordinates. For the shells of revolution defined in the ϕ - ψ coordinate system, Figure 1, the distributed sensing signal is defined as

$$\begin{aligned}\phi^s &= \frac{h^s}{S^e} \int_{S^e} (h_{31}S_{\phi\phi} + h_{32}S_{\psi\psi} + h_{36}S_{\phi\psi}) \cdot A_1 A_2 d\phi d\psi \\ &= \frac{h^s}{S^e} \int_{\phi} \int_{\psi} [h_{31}(s_{\phi\phi}^0 + r_i^s k_{\phi\phi}) + h_{32}(s_{\psi\psi}^0 + r_i^s k_{\psi\psi}) + h_{36}(s_{\phi\psi}^0 + r_i^s k_{\phi\psi})] \\ &\quad \bullet R_{\phi} R_{\psi} \sin \phi \cdot d\phi d\psi ,\end{aligned}\quad (2)$$

where $s_{\phi\phi}^0$, $s_{\psi\psi}^0$ and $s_{\phi\psi}^0$ are the membrane strains; $k_{\phi\phi}$, $k_{\psi\psi}$ and $k_{\phi\psi}$ are the bending strains; r_i^s denotes the sensor placement measured from the neutral surface and $r_i^s = (h + h^s)/2 \approx h/2$, if $h \gg h^s$. Also, $r_1^s = r_2^s$, since both sensor and shell have uniform thickness. The sensing signal equations for paraboloidal shells of revolution can be derived by

substituting the appropriate radii of curvature and Lamé parameters into the generic sensor signal equation for shells of revolution. For paraboloidal shell of revolution, the radii are the meridional radius $R_\phi = [b/\cos^3 \phi]$ and the circumferential radius $R_\psi = [b/\cos \phi]$; the Lamé parameters are $A_1 = [b/\cos^3 \phi]$ and $A_2 = [b \sin \phi / \cos \phi]$, where $b = (a^2/2c)$, “c” denotes the meridian height and “a” denotes the radial distance (Mazurkiewicz and Nagorski, 1991), Figure 1. Note “b” is also twice of the focal length of the parabola.

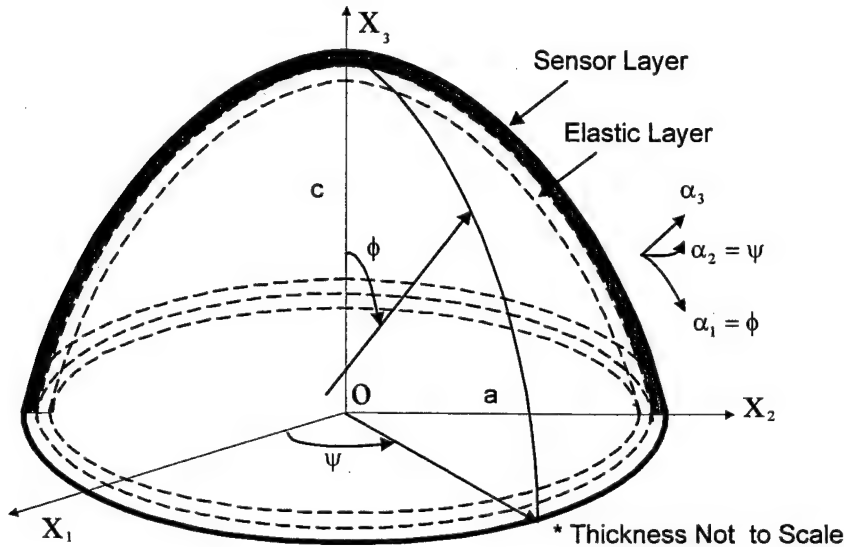


Fig.1 A paraboloidal shell laminated with distributed piezoelectric sensor layer.

The membrane and bending strains of nonlinear paraboloidal shells of revolution, including the von Karman geometric nonlinearity (Tzou and Yang, 2000; Tzou, et al, 1997), are respectively derived as (Tzou and Ding, 2002)

$$s_{\phi\phi}^o = \frac{\cos^3 \phi}{b} \left(\frac{\partial u_\phi}{\partial \phi} + u_3 \right) + \left[\frac{1}{2} \frac{\cos^6 \phi}{b^2} \left(\frac{\partial u_3}{\partial \phi} \right)^2 \right], \quad (3)$$

$$s_{\psi\psi}^o = \frac{\cos \phi}{b \sin \phi} \left(\frac{\partial u_\psi}{\partial \psi} + u_\phi \cos \phi + u_3 \sin \phi \right) + \left[\frac{1}{2} \frac{\cos^2 \phi}{b^2 \sin^2 \phi} \left(\frac{\partial u_3}{\partial \psi} \right)^2 \right], \quad (4)$$

$$s_{\phi\psi}^o = \frac{\cos \phi}{b \sin \phi} \left(\frac{\partial u_\phi}{\partial \psi} + \cos^2 \phi \sin \phi \frac{\partial u_\psi}{\partial \phi} - u_\psi \cos \phi \right) + \left[\frac{\cos^4 \phi}{b^2 \sin \phi} \left(\frac{\partial u_3}{\partial \phi} \frac{\partial u_3}{\partial \psi} \right) \right], \quad (5)$$

$$k_{\phi\phi} = \frac{\cos^6 \phi}{b^2} \left(\frac{\partial u_\phi}{\partial \phi} - \frac{\partial^2 u_3}{\partial \phi^2} \right) - 3 \frac{\cos^5 \phi \sin \phi}{b^2} \left(u_\phi - \frac{\partial u_3}{\partial \phi} \right), \quad (6)$$

$$k_{\psi\psi} = \frac{\cos^2 \phi}{b^2 \sin \phi} \left(\frac{\partial u_\psi}{\partial \psi} - \frac{1}{\sin \phi} \frac{\partial^2 u_3}{\partial \psi^2} + u_\phi \cos^3 \phi - \cos^3 \phi \frac{\partial u_3}{\partial \phi} \right), \quad (7)$$

$$k_{\phi\psi} = -\frac{\cos^5 \phi + 2\cos^3 \phi \sin^2 \phi}{b^2 \sin \phi} u_\psi + \frac{2\cos^3 \phi}{b^2 \sin^2 \phi} \frac{\partial u_3}{\partial \psi} - \frac{2\cos^4 \phi}{b^2 \sin \phi} \frac{\partial^2 u_3}{\partial \psi \partial \phi} + \frac{\cos^4 \phi}{b^2} \frac{\partial u_\psi}{\partial \phi} + \frac{\cos^4 \phi}{b^2 \sin \phi} \frac{\partial u_\phi}{\partial \psi}, \quad (8)$$

where u_ϕ , u_ψ and u_3 represent the displacement in ϕ -direction, ψ -direction and transverse direction, respectively. When the bending approximation (i.e., the inextensional theory) is applied, the membrane strains are zero and only the bending strains given by Eqs.(6)-(8) remain. Based on the bending approximation, the mode shape functions for the free boundary paraboloidal shell of revolution are (Lin and Lee, 1960):

$$U_{\phi m} = -A_m \sin \phi \tan^m \phi \cos m\psi, \quad (9)$$

$$U_{\psi m} = -A_m \tan^{m+1} \phi \sin m\psi, \quad (10)$$

$$U_{3m} = A_m \tan^m \phi (\cos \phi + m \sec \phi) \cos m\psi, \quad (11)$$

where m is the mode number starting from 2, which indicates the number of circumferential waves for the corresponding mode shape; A_m is modal amplitude. Assume the shell oscillation is composed of all participating natural modes – the modal expansion method, i.e., $u_i(\alpha_1, \alpha_2, t) = \sum_{m=1}^{\infty} \eta(t) \cdot U_{im}(\alpha_1, \alpha_2)$ where $\eta(t)$ is the modal participation factor and U_{im} is the m -th mode shape function in the i -th direction. Substituting the mode shape functions into the strain expressions in the distributed sensing signal yields the m -th modal sensing signal ϕ_m^s :

$$\phi_m^s = \frac{h^s}{S^e} \int_s [h_{31} r_\phi^s \frac{A_m \tan^m \phi \cos^3 \phi m(1 - m^2) \cos m\psi}{b^2 \sin^2 \phi} + h_{32} r_\psi^s \frac{A_m \tan^m \phi \cos \phi m(m^2 - 1) \cos m\psi}{b^2 \sin^2 \phi}] \frac{b^2 \sin \phi}{\cos^4 \phi} d\phi d\psi. \quad (12)$$

Note the time-dependent part in sensing signal is the modal participation factor $\eta(t)$, which is not the concern of this study and is not shown in the following equations. The spatially distributed modal signal can be spectrally decomposed from the general sensing signal by certain signal processing technologies, such as using band-pass filters (Ding, 2002).

Distributed Sensing Signal of Segmented Sensor Patch

A generic segmented sensor patch is defined geometrically from ϕ_1 to ϕ_2 and ψ_1 to ψ_2 , shown in Figure 2. The integration in sensing signal expression over the effective sensing area now is from ϕ_1 to ϕ_2 and ψ_1 to ψ_2 along the shell surface.

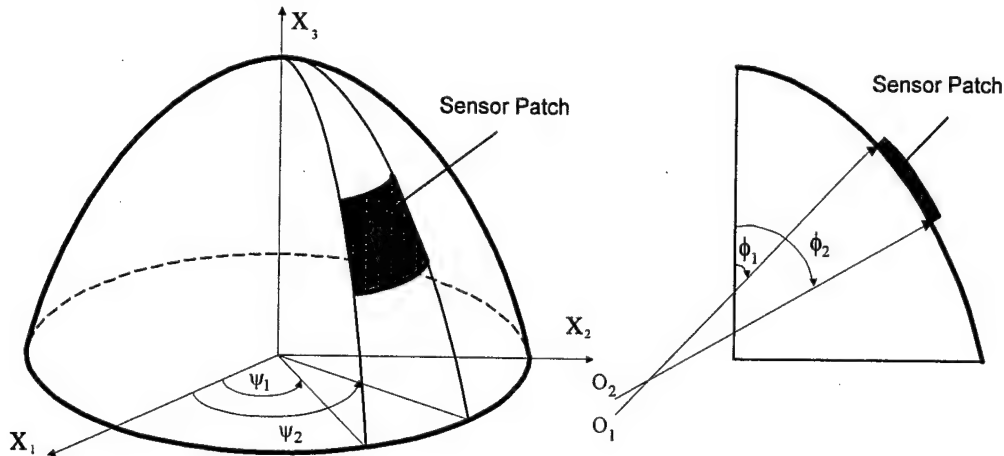


Fig.2 A generic segmented sensor patch on paraboloidal shell.

Thus, the distributed sensing signal of the sensor patch on the paraboloidal shell with free boundary based on the bending approximation is

$$\begin{aligned} \phi_m^s &= \frac{A_m h^s h_{31}}{S^e} \int_{\psi_1}^{\psi_2} \int_{\phi_1}^{\phi_2} \left[\frac{r_\phi^s \tan^m \phi m(1-m^2) \cos m\psi}{\sin \phi \cos \phi} \right. \\ &\quad \left. + \frac{r_\psi^s \tan^m \phi m(m^2-1) \cos m\psi}{\sin \phi \cos^3 \phi} \right] d\phi d\psi \quad (13) \\ &= A_m h^s h_{31}(\Phi) = A_m h^s h_{31}[(\Phi)_{\text{bend}}] = A_m h^s h_{31}[(\Phi_{\phi\phi})_{\text{bend}} + (\Phi_{\psi\psi})_{\text{bend}}], \end{aligned}$$

where $(\Phi) \equiv (\Phi)_{\text{bend}}$ is the sensing signal component defined by excluding the modal amplitude A_m , sensor thickness h^s and piezoelectric constant h_{31} ; $(\Phi_{\phi\phi})_{\text{bend}}$ and $(\Phi_{\psi\psi})_{\text{bend}}$ are the signal components due to the bending strains $k_{\phi\phi}$ and $k_{\psi\psi}$, respectively. Note that $h_{31} = h_{32} = h_{3i}$ in most conventional piezoelectric sensing materials without being mechanically stretched during the manufacturing process.

$$(\Phi_{\phi\phi})_{\text{bend}} = \frac{r_\phi^s}{S^e} \frac{1-m^2}{m} (\sin m\psi_2 - \sin m\psi_1) (\tan^m \phi_2 - \tan^m \phi_1), \quad (14)$$

$$\begin{aligned} (\Phi_{\psi\psi})_{\text{bend}} &= \frac{r_\psi^s}{S^e} \frac{m^2-1}{m+2} (\sin m\psi_2 - \sin m\psi_1) \\ &\quad \cdot (\tan^m \phi_2 \sec^2 \phi_2 + \frac{2}{m} \tan^m \phi_2 - \tan^m \phi_1 \sec^2 \phi_1 - \frac{2}{m} \tan^m \phi_1). \end{aligned} \quad (15)$$

The effective sensing area is calculated by

$$\begin{aligned}
 S^e &= \int_{S^e} A_1 A_2 d\alpha_1 d\alpha_2 = \int_{\psi_1}^{\psi_2} \int_{\phi_1}^{\phi_2} A_1 A_2 d\phi d\psi = \int_{\psi_1}^{\psi_2} \int_{\phi_1}^{\phi_2} \frac{b^2 \sin \phi}{\cos^4 \phi} d\phi d\psi \\
 &= b^2 (\psi_2 - \psi_1) \frac{\cos^3 \phi_1 - \cos^3 \phi_2}{3 \cos^3 \phi_1 \cos^3 \phi_2}.
 \end{aligned} \tag{16}$$

In this study, sensing signal components $(\Phi) = (\Phi)_{bend}$, including their microscopic contributing parts $(\Phi_{\phi\phi})_{bend}$ and $(\Phi_{\psi\psi})_{bend}$ of segmented sensor patches with different location, are evaluated to reveal the microscopic distributed sensing characteristics of strucronic paraboloidal shell systems. Different shell geometric parameters are studied in cases.

CASE STUDIES

Paraboloidal shells with different geometric parameters are studied in cases, Table 1. Case 1 is considered standard, Case 2 is a shallow paraboloidal shell, and Case 3 is a deep paraboloidal shell. Note that the shells are relatively thick in order to satisfy the bending approximation theory.

Table 1 Cases of free boundary paraboloidal shell for micro-sensing signal analysis.

Parameters Cases	Radius (a) (m)	Height (c) (m)	Thickness (h) (m)
1	1	1	0.10
2	2	1	0.10
3	1	2	0.10

Sensing signal components of sensor patches with the location varying from the shell pole to rim (ϕ from 0 to ϕ^* - the meridional boundary angle) along the meridional direction and also along the circumferential direction (ψ from 0 to 2π) are evaluated and plotted. The angular widths of the sensor patches are $\Delta\phi = \phi_2 - \phi_1 = 0.1$ radian and $\Delta\psi = \psi_2 - \psi_1 = 0.2$ radian, which are small enough to guarantee the accurate measurement of the mode up to $m=6$. The micro-signal components $(\Phi_{\phi\phi})_{bend}$, $(\Phi_{\psi\psi})_{bend}$ and $(\Phi)_{bend}$ of the sensor patches are calculated and plotted. In these signal plots, the horizontal plane denotes mesh lines connecting the center points of these sensor patches, i.e., 0.05, 0.15, 0.25, ..., 1.05 radian in the meridional ϕ -coordinate, and 0.1, 0.3, 0.5, 0.7, ..., 6.1 radian in the circumferential ψ -coordinate. The vertical axis denotes the magnitude of the micro-signal components. Or say, every intersection of the mesh line, which is the center point of each sensor patch, stands for the micro-signal component of a specific sensor patch. Since the sensor signal is uniformly distributed on a sensor patch, only one micro-signal magnitude exists for each segmented sensor patch.

The standard paraboloidal shell (Case 1) is defined by a boundary angle $\phi^* = 1.1071$ radian. With sensor widths $\Delta\phi = \phi_2 - \phi_1 = 0.1$ radian and $\Delta\psi = \psi_2 - \psi_1 = 0.2$ radian, there are 11 patches in the ϕ -direction and 31 patches in the ψ -direction on the shell surface, **Figure 3**. Spatially distributed micro-signal components $(\Phi_{\phi\phi})_{\text{bend}}$, $(\Phi_{\psi\psi})_{\text{bend}}$ and the total signal $(\Phi)_{\text{bend}}$ of these sensor patches calculated for the first five natural modes ($m=2$ to 6) are plotted in **Figures 4-8**.

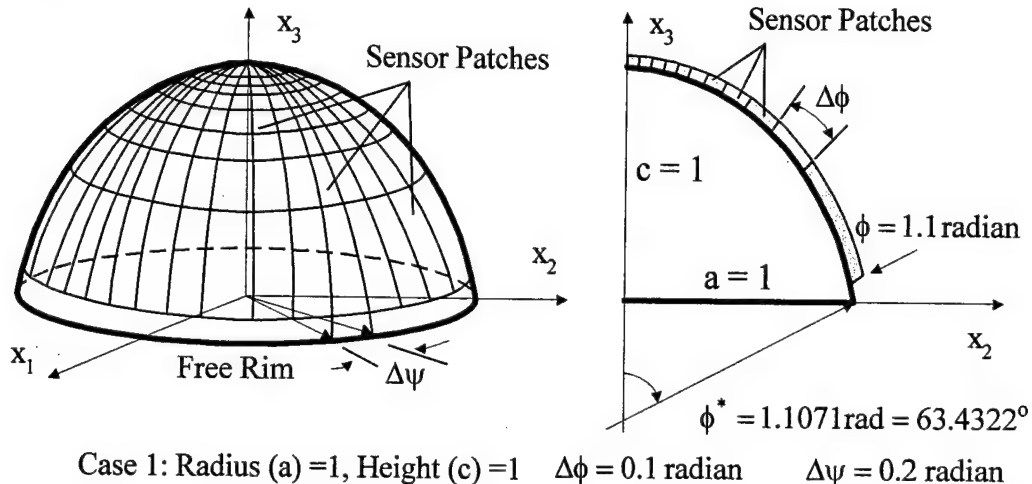


Fig. 3 Sensor patches covering the shell surface, Case 1.

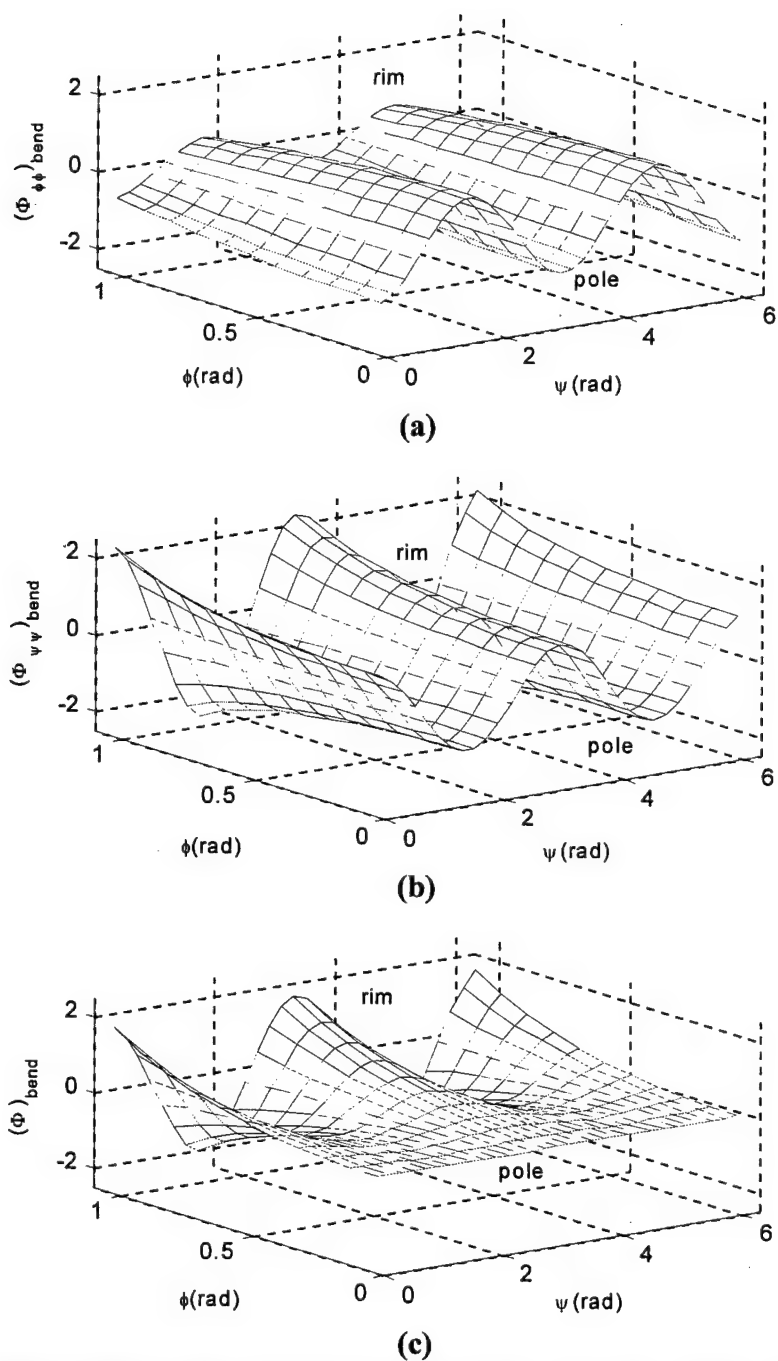


Fig.4 Sensing signal components of sensor patches, $m=2$, Case 1,
(a): $(\Phi_{\phi\phi})_{\text{bend}}$, (b): $(\Phi_{\psi\psi})_{\text{bend}}$, (c): $(\Phi)_{\text{bend}}$.

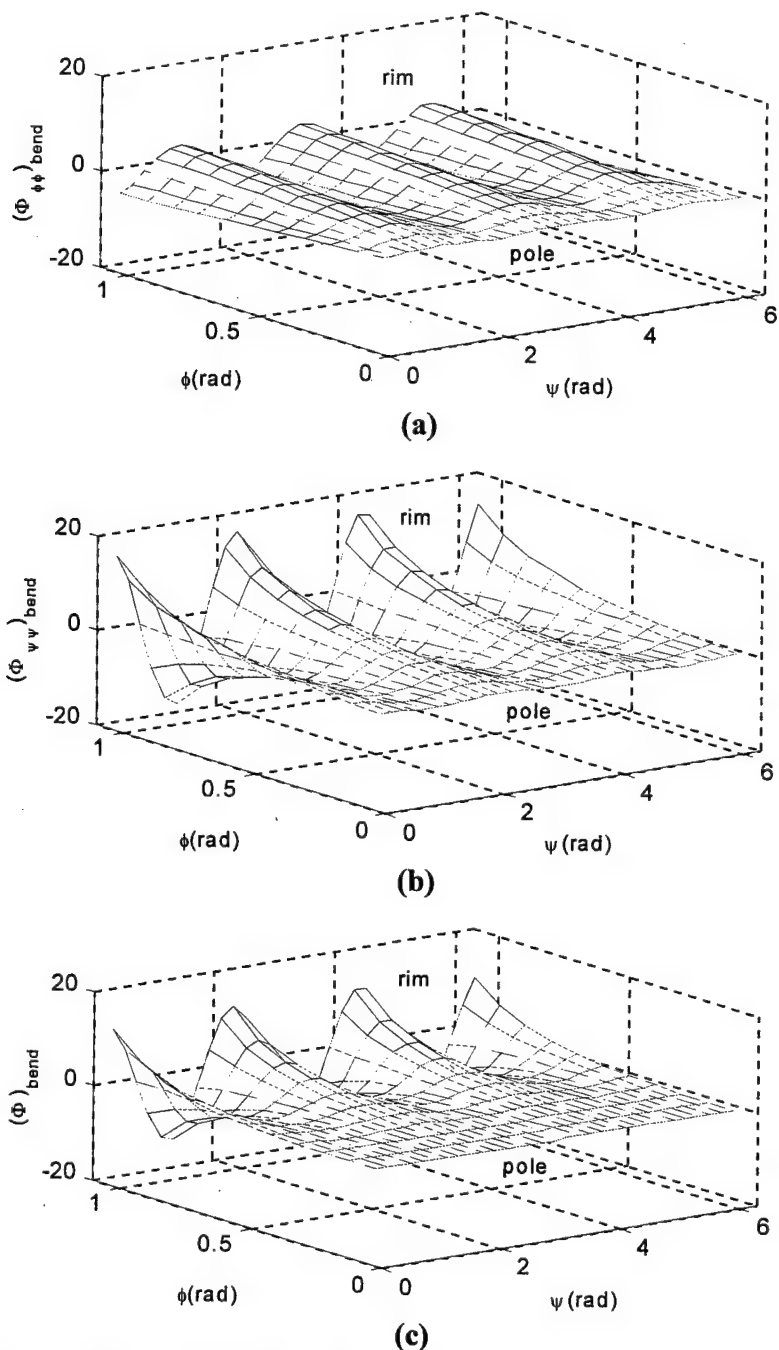


Fig.5 Sensing signal components of sensor patches, $m=3$, Case 1,
(a): $(\Phi_{\phi\phi})_{\text{bend}}$, (b): $(\Phi_{\psi\psi})_{\text{bend}}$, (c): $(\Phi)_{\text{bend}}$.

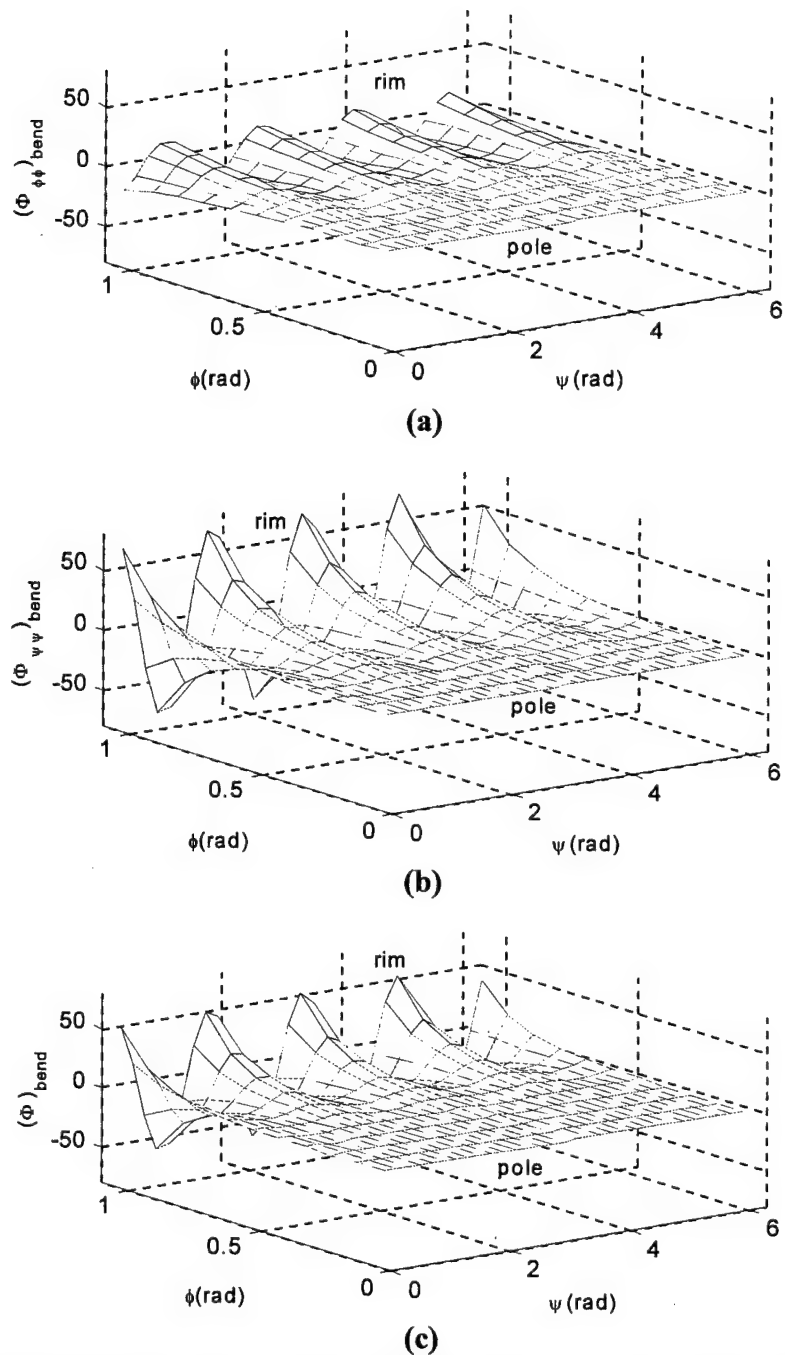


Fig.6 Sensing signal components of sensor patches, $m=4$, Case 1,
 (a): $(\Phi_{\phi\phi})_{\text{bend}}$, (b): $(\Phi_{\psi\psi})_{\text{bend}}$, (c): $(\Phi)_{\text{bend}}$.

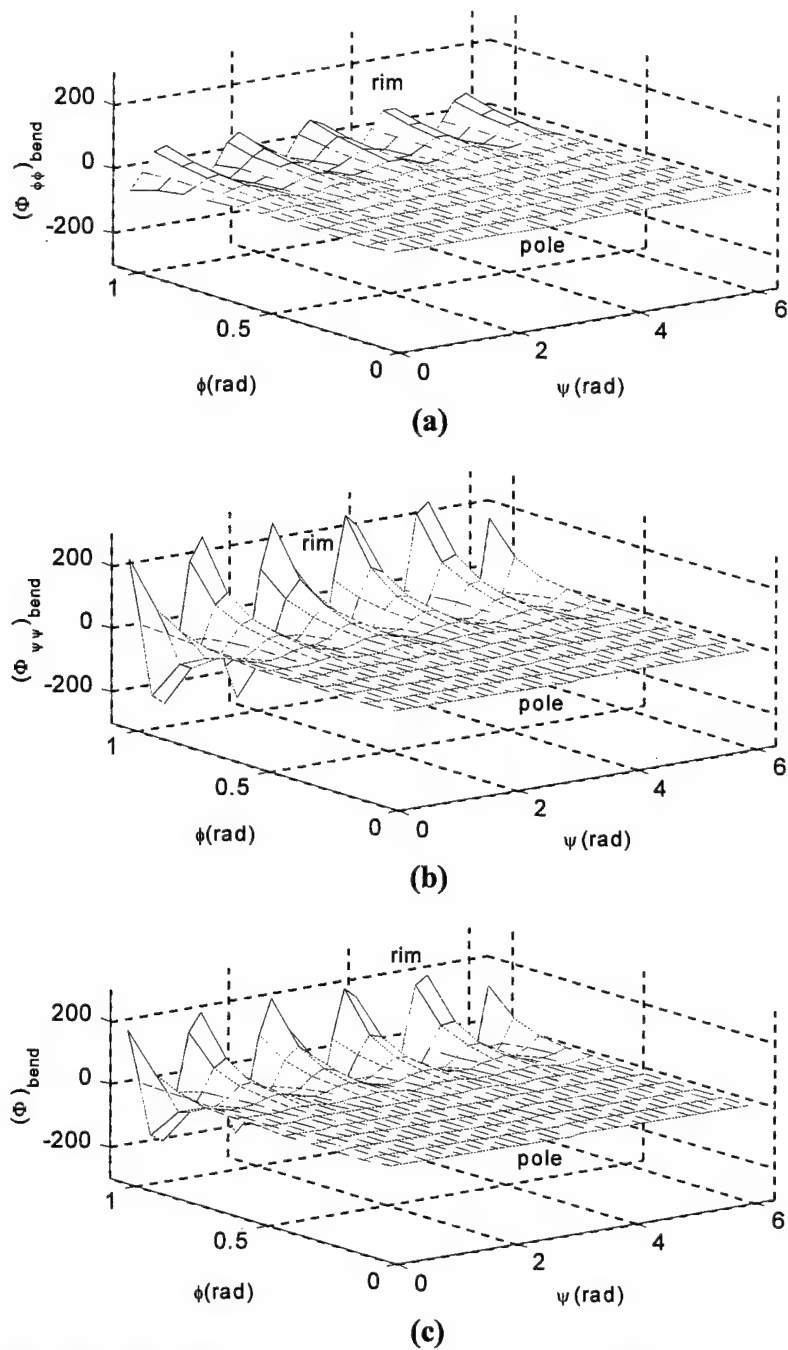


Fig.7 Sensing signal components of sensor patches, $m=5$, Case 1,
(a): $(\Phi_{\phi\phi})_{\text{bend}}$, (b): $(\Phi_{\psi\psi})_{\text{bend}}$, (c): $(\Phi)_{\text{bend}}$.

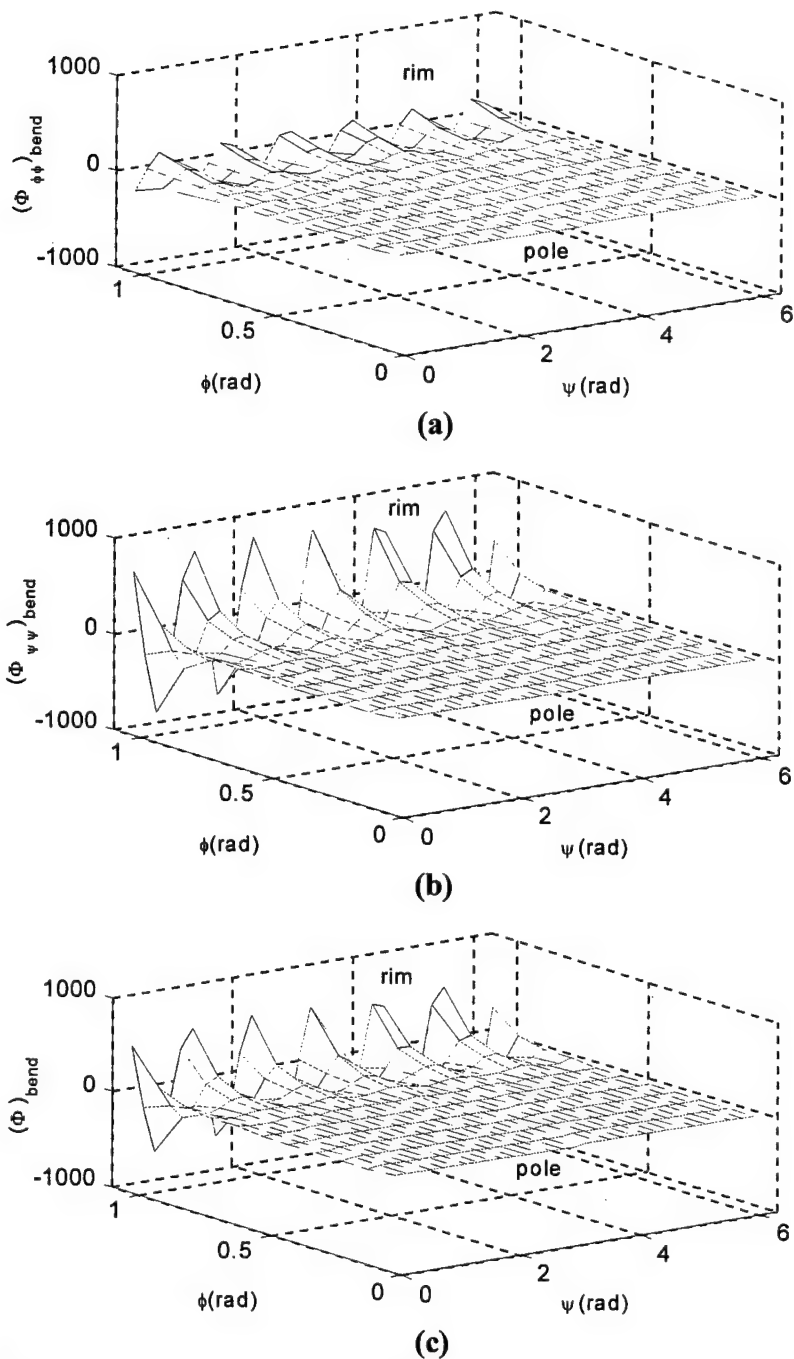


Fig.8 Sensing signal components of sensor patches, $m=6$, Case 1,
(a): $(\Phi_{\phi\phi})_{\text{bend}}$, (b): $(\Phi_{\psi\psi})_{\text{bend}}$, (c): $(\Phi)_{\text{bend}}$.

These spatially distributed signals apparently reveal distinct modal characteristics determined by spatial strain variations. The micro-signal components always peak on the free-boundary and near zero at the pole. Conceptually, the strains are zero at the shell pole ($\phi = 0$). However, the sensor patch closest to the pole is located at meridional $\phi = 0 \sim 0.1$ radains, the resultant strains are not zero at this slightly-offset location, and consequently neither the micro-signal component. For free-boundary paraboloidal shells, the sensor patches near the shell free rim at

modal peaks generate significant sensing signals. As the mode number increases, the signal oscillation pattern increases at the free boundary. These plots also show that the micro-sensing signal magnitude increases as the mode "m" increases, while the influence of modal amplitude A_m is neglected. This tendency can also be predicted from the closed-form sensing signal equation. However, in practice, the modal amplitude A_m usually decreases significantly at higher modes. Thus, the resultant micro-sensing signal magnitude is determined by the combined effect of increasing "m" and decreasing " A_m ". Furthermore, uneven micro-signal amplitudes on the free boundary at high natural modes, (e.g., $m=6$) are induced by non-exact circumferential segmentation of sensor patches. The segmented patches may not exactly cover the maximal or the minimal modal strain regions and any slight offset would induce uneven distribution of micro-signals at modal peaks.

The shallow paraboloidal shell (Case 2) is defined by a boundary angle $\phi^* = 0.7854$ radian. With patch sizes $\Delta\phi = \phi_2 - \phi_1 = 0.1$ radian and $\Delta\psi = \psi_2 - \psi_1 = 0.2$ radian, there can be 7 sensor patches in the ϕ -direction and 31 patches in the ψ -direction on the shell surface, **Figure 9**. A sensor patch located at the meridional angle $0.7 \sim 0.78$ radian ($\Delta\phi = \phi_2 - \phi_1 = 0.08$ radian) is added to cover the shell surface. The spatially distributed micro-signal components $(\Phi_{\phi\phi})_{\text{bend}}$, $(\Phi_{\psi\psi})_{\text{bend}}$ and the total signal $(\Phi)_{\text{bend}}$ for every sensor patch of Case 2 are evaluated. Note that spatial micro-signal distribution patterns of the shallow paraboloidal shell (Case 2) and the deep paraboloidal shell (Case 3) are similar to those of the standard paraboloidal shell. Thus, although they are calculated and analyzed, their individual micro-signal plots are not presented here.

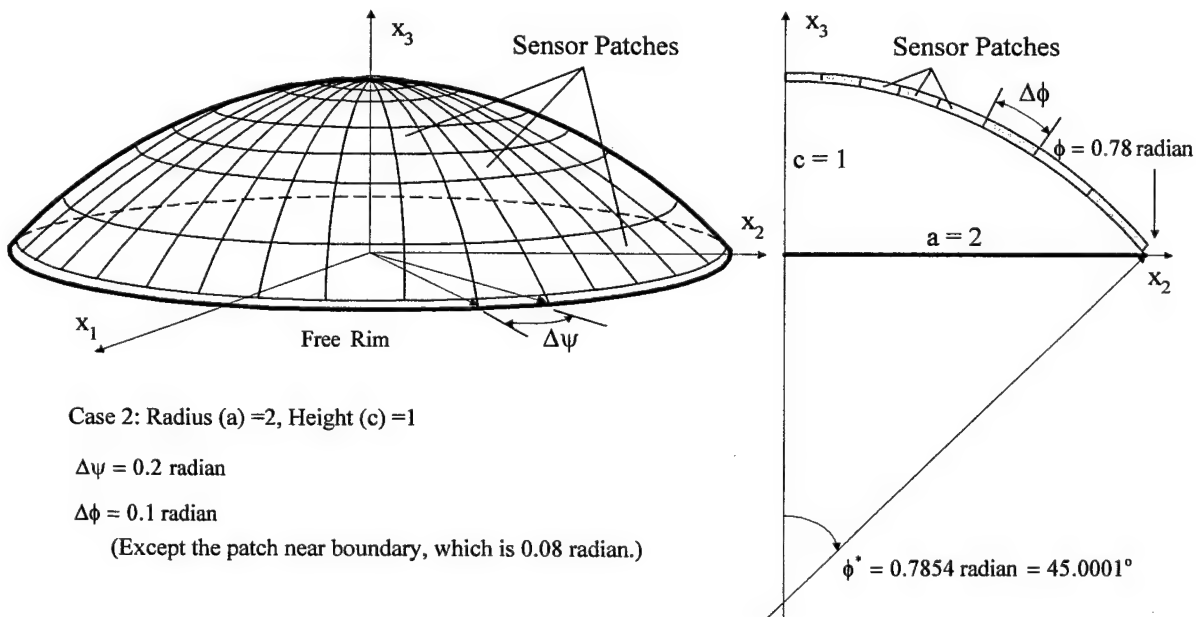
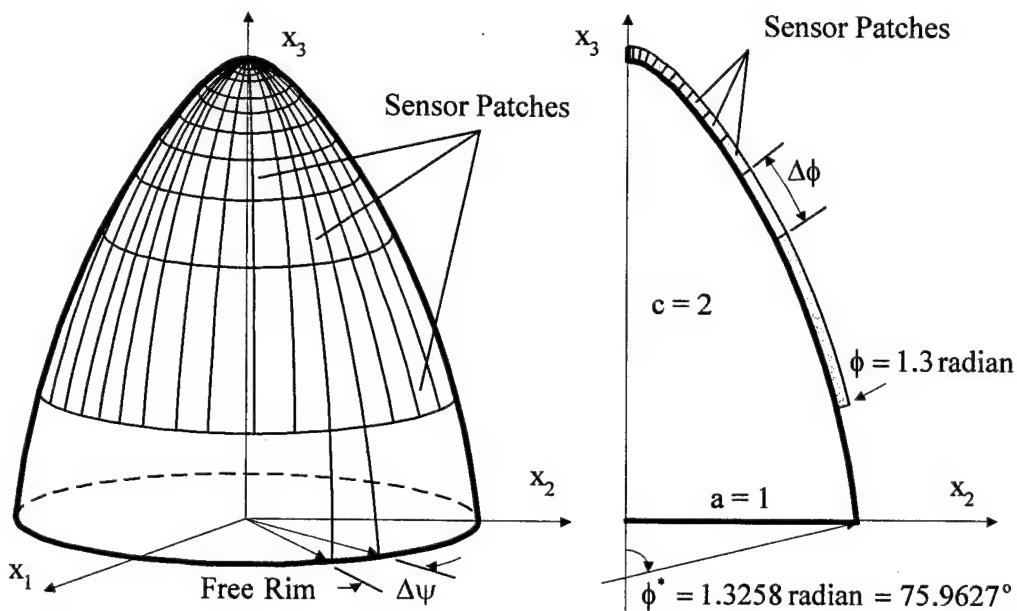


Fig.9 Sensor patches covering the shallow shell surface, Case 2.

The deep paraboloidal shell (Case 3) is defined by a meridional boundary angle

$\phi^* = 1.3258$ radian. With patch sizes $\Delta\phi = \phi_2 - \phi_1 = 0.1$ radian and $\Delta\psi = \psi_2 - \psi_1 = 0.2$ radian, there are 13 sensor patches in the ϕ -direction and 31 patches in the ψ -direction on the shell surface, **Figure 10**. The spatial micro-signal components $(\Phi_{\phi\phi})_{\text{bend}}$, $(\Phi_{\psi\psi})_{\text{bend}}$ and the total signal $(\Phi)_{\text{bend}}$ for every sensor patch of Case 3 are also evaluated. As discussed previously, since the spatial distribution and the micro-signal oscillation patterns of the shallow and deep shells are similar to those of the standard paraboloidal shell, their individual plots are not presented. Based on parametric studies, comparisons and discussions of micro-signal generations among the three shell cases are discussed next.



Case 3: Radius (a) = 1, Height (c) = 2 $\Delta\psi = 0.2$ radian $\Delta\phi = 0.1$ radian

Fig.10 Sensor patches covering the deep shell surface, Case 3.

The radii of curvature of the deep paraboloidal shell (Case 3) are smaller than those of the standard paraboloidal shell (Case 1), and those of the shallow paraboloidal shell (Case 2) are the largest among the three shells. Note that although a constant “angular” size ($\Delta\phi \times \Delta\psi$) is imposed to all sensor patches of three paraboloidal shell cases, i.e., standard, shallow, and deep, the effective patch size actually enlarges as the patch moving from the pole to the shell rim due to an increase of the projected arc length defined by the geometry and curvature of paraboloidal shells. All patches are of equal size located at the same meridional location, due to axisymmetry of shells of revolution. However, since the micro-sensing signal is an average effect over the effective sensor area, the difference in patch sizes doesn’t contribute to the global spatial distribution and these micro-signals are only influenced by their relative shell locations.

The parametric study indicates that the amplitudes of distributed micro-sensing signals of Case 3 are the most significant and those of Case 2 are the least, due to microscopic modal strain distributions on these shells. Also, the effective sensor sizes laminated on shallow shells

are the largest as compared with patches located at similar locations of other two shells, even an identical “angular” size ($\Delta\phi \times \Delta\psi$) is imposed in three shell cases. Since the resultant signal is an averaged effect over the effective sensor area, a larger effective sensor area (or size) would lead to a smaller averaged signal magnitude in shallow shells. The circumferential micro-sensing signal component (i.e., the ψ -coordinate) is larger than the meridional component (i.e., the ϕ -coordinate) and their difference is significant for the deep shell configuration (Case 3). The meridional radius of curvature ($R_\phi = b/\cos^3\phi$) is larger than the circumferential radius of curvature ($R_\psi = b/\cos\phi$), except at the shell pole where both equal to b . And the difference between the two radii increases in deep shells with larger meridional boundary angles. A larger radius of curvature softens the shell and reduces the strain level, so the sensing signals.

CONCLUSIONS

Analysis of the spatially distributed microscopic sensing behavior of paraboloidal shells of revolution reveals detailed sensing signal generation and efficiency of segmented sensor patches laminated at various shell locations with different curvatures. This provides important sensor design guideline applied to distributed active vibration control systems, shape control systems, health monitoring systems, etc. Detailed parametric studies of microelectromechanics and microscopic signal generations of segmented sensor patches laminated on three paraboloidal shells (i.e., a shallow, a standard, and a deep) suggest that

- 1) The distributed sensing signal generated by a segmented sensor patch is contributed by the surface integration of strains divided by the sensor area. Since the distributed sensing signal is an averaged effect over the effective sensor surface, a larger sensor patch doesn't warrant a higher sensing signal magnitude. On the other hand, a smaller sensor patch would provide better measurement resolution at higher natural modes.
- 2) The signal magnitude mostly depends on the sensor placements or locations. Sensor patches on the nodal or modal lines of natural modes generate minimal signals. On the other hand, sensors located at higher modal strain regions generate significant signals. Since the sensor patch is surface laminated and the bending approximation theory was imposed, the resulting sensing signals increases as the shell becomes thicker.
- 3) The placement of sensor patches depends on not only geometries, but also its boundary conditions. For paraboloidal shells with free boundary, the sensors placed near or at the shell free rim contribute excellent sensing efficiency. An earlier study of patch-sensor efficiency of simply-supported paraboloidal shells indicates that the most effective location is near the shell pole (Tzou and Ding, 2002).
- 4) Shell curvature also influences its static and dynamic behavior. Shallow shells with large radii of curvature experiences lower level of strain generation and thus lower signal generations, as compared with that of deep shells, provided the modal oscillation amplitude is constant. Furthermore, internal strain increases as the shell oscillates at higher modes, consequently resulting in higher magnitudes of signal generation.

Note that this parametric study was carried out based on the bending approximation and thus observations and conclusions are preferably applied to sensor patches laminated on relatively thick paraboloidal shell structures with free boundary conditions.

ACKNOWLEDGEMENT

This research is supported, in part, by a grant (F49620-98-1-0467) from the Air Force Office of Scientific Research (Project Manager: Brian Sanders). This support is gratefully acknowledged.

REFERENCES

Birman, V. and Simonyan, A., 1994, "Theory and Applications of Cylindrical Sandwich Shells with Piezoelectric Sensors and Actuators," *Smart Materials and Structures*, Vol.3, No.4, pp.391-396.

Callahan, J. and Baruh, H., 1999, "Modal Sensing of Circular Cylindrical Shells Using Segmented Piezoelectric Elements," *Smart Materials and Structures*, Vol.8, No.1, pp.125-135.

Chiu, W.K., 1997, "Damage Monitoring in Metallic Structures Using Piezoelectric Thin Film Sensors," *Polymers & Polymer Composites*, Vol. 5, No.2, 1997, pp.121-130.

Ding, J.H., 2002, *Micro-piezothermoelastic Behavior and Distributed Sensing/Control of Nonlinear Structronic Beam and Paraboloidal Shell Systems*, Ph.D. Dissertation, University of Kentucky, Lexington, KY.

Gabbert, U. and Tzou, H.S., 2001, *Smart Structures and Structronic Systems*, Kluwer Academic Pub., Dordrecht /Boston /London.

Giurgiutiu, V. and Zagrai, A.N., 2002, "Embedded Self-sensing Piezoelectric Active Sensors for On-line Structural Identification," *Journal of Vibration and Acoustics, Transactions of the ASME*, Vol.124, No.1, Jan., 2002, pp.116-125.

Lin, Y.K. and Lee, F.A., 1960, "Vibrations of Thin Paraboloidal Shells of Revolution," *Journal of Applied Mechanics*, Vol. 27, pp.743-744.

Mazurkiewicz, Z.E., Nagorski, R.T., 1991, *Shells of Revolution*, PWN-Polish Scientific Publishers, Warsaw, pp.7-9, pp.333-341.

Qiu, J. and Tani, J., 1995, "Vibration Control of a Cylindrical Shell Using Distributed Piezoelectric Sensors and Actuators," *Journal of Intelligent Material Systems and Structures*, Vol.6, No.4, pp.474-481.

Saravanan, C., Ganesan, N. and Ramamurti, V., 2000, "Analysis of Active Damping in Composite Laminate Cylindrical Shells of Revolution with Skewed PVDF Sensors/Actuators," *Composite Structures*, Vol.48, No.4, Apr 2000, pp.305-318.

Tzou, H.S., 1992, "Thin-Layer Distributed Piezoelectric Neurons and Muscles: Electromechanics and Applications," *Precision Sensors, Actuators, and Systems*, H.S. Tzou and T. Fukuda, (Editors), Kluwer Academic Publishers, Dordrecht /Boston /London, pp.175-218.

Tzou, H.S., 1993, *Piezoelectric Shells (Distributed Sensing and Control of Continua)*, Kluwer Academic Publishers, Boston /Dordrecht.

Tzou, H. S. and Bao, Y., 1996, "Parametric Study of Segmented Transducers Laminated on Cylindrical Shells, Part 1: Sensor Patches," *Journal of Sound and Vibration*, Vol.197, No.2, pp.207-224.

Tzou, H.S., Bao, Y. and Zhou, Y., 1997, "Nonlinear Piezothermoelasticity and Multi-field Actuations, Part-1: Nonlinear Anisotropic Piezothermoelastic Shell Laminates; Part-2: Control of Nonlinear Buckling and Dynamics," *ASME Transactions, Journal of Vibration & Acoustics*, Vol.119, pp.374-389.

Tzou, H.S., Chai, W.K. and Wang, D.W., 2002, "Modal Voltages and Distributed Signal Analysis of Conical Shells of Revolution," *Journal of Sound and Vibration*. (To appear)

Tzou, H.S. and Ding, J.H., 2002, "Distributed Modal Signals of Nonlinear Paraboloidal Shells with Distributed Neurons," *Journal of Vibration and Acoustics*. (Paper No. JVA 00-161)

Tzou, H. S., Smithmaitrie, P. and Ding, J.H., 2002, "Sensor Electromechanics and Distributed Signal Analysis of Piezo(electric)-Elastic Spherical Shells," *Mechanical Systems and Signal Processing*, Vol.16, No.2/3, March/May 2002, pp.185-199.

Tzou, H.S. and Wang, D.W., 2002, "Distributed Dynamic Signal Analysis of Piezoelectric Laminated Linear and Nonlinear Toroidal Shells," *Journal of Sound and Vibration* (To appear).

Tzou, H.S. and Yang, R.J., 2000, "Nonlinear Piezo-thermoelastic Shell Theory applied to Control of Variable-geometry Shells," *Journal of Theoretical and Applied Mechanics*, No.3, Vol.38, pp.623-644.

Tzou, H.S., Zhong, J.P. and Natori, M.C., 1993, "Sensor Mechanics of Distributed Shell Convolving Sensors Applied to Flexible Rings," *ASME Journal of Vibration & Acoustics*, Vol.115, No.1, pp.40-46. (MicroScrParbFreeMssp.ShlParb3)

CHAPTER 12

DISTRIBUTED MODAL VOLTAGES OF NONLINEAR PARABOLOIDAL SHELLS WITH DISTRIBUTED NEURONS

ABSTRACT

Effective health monitoring and distributed control of advanced structures depends on accurate measurements of dynamic responses of elastic structures. Conventional sensors used for structural measurement are usually add-on “discrete” devices. Lightweight distributed thin-film piezoelectric neurons fully integrated (laminated or embedded) with structural components can serve as in-situ sensors monitoring structure’s dynamic state and health status. This study is to investigate modal voltages and detailed signal contributions of linear or nonlinear paraboloidal shells of revolution laminated with piezoelectric neurons. Signal generation of distributed neuron sensors laminated on paraboloidal shells is defined first, based on the open-voltage assumption and Maxwell’s principle. The neuron signal of a linear paraboloidal shell is composed of a linear membrane component and a linear bending component; the signal of a nonlinear paraboloidal shell is composed of nonlinear and linear membrane components and a linear bending component due to the von Karman geometric nonlinearity. Signal components and distributed modal voltages of linear and nonlinear paraboloidal shells with various curvatures and thickness are investigated.

INTRODUCTION

Effective distributed structural control depends on accurate measurements of structure’s dynamic states. Structural health monitoring, diagnosis, and failure prevention are also essential to structural integrity, reliability, performance, safety, etc. of high-performance structures and machines. Transducers typically convert mechanical energy (input) into electrical energy (output) and present the output quantitatively, usually in voltages. Conventional sensing technologies usually utilize discrete-type sensors, such as strain gages, eddy current proximeters, linear variable differential transformers (LVDT), accelerometers, potentiometers, etc. These sensing systems are, of course, capable of carrying out the sensing functions and fulfilling design and control requirements. However, these transducers are all discrete add-on devices, i.e., devices are installed on the structures using off-the-shelf components. These add-on transducers can add additional weights to the structures, which often is not desirable in many high-precision lightweight structures and machine systems. Recent development of smart structures and strucronic systems (Plubm, et al., 1987; Crawley and de Luis, 1987; Baz and Poh, 1988; Hanagud and Obal, 1988; Tzou, 1987; 1993; Gabbert and Tzou, 2001) has demonstrated that lightweight distributed piezoelectric layers laminated on flexible structures

serve well as in-situ neurons closely monitoring local strain variations and dynamic states of structures and machines.

Distributed piezoelectric sensors translate mechanical strains into electrical signals averaged over the effective sensor area, or electrode area, due to locally generated charges instantly distributed over the sensor surface area (Tzou, 1992; Tzou, Zhong, and Natori, 1993). Accordingly, local dynamic behaviors are usually not observable by large sensor electrodes. However, as the electrodes shrinks to infinitesimally small – “neurons,” all local strain behaviors reveal in their local signal generations (Tzou, 1992). To reflect dynamic signal distributions of natural modes, *modal voltages* are the spatial signal distribution pattern associated with natural mode shapes of distributed elastic structures, such as shells and plates (Tzou, 1993). The modal voltages represent the constituted local sensing signal generation by neurons. Any derivation from the original healthy modal voltages signifies a “hot-spot” or “hot-areas” on the structure. Accordingly, precaution procedures or repairs can be applied to these specific spots or areas to prevent from catastrophic failures. These modal voltages can also be used to design modal orthogonal sensors, such that the designed shaped sensor responds to a specific mode or a group of modes (Tzou, Zhong, and Natori, 1993). Potential applications include many aerospace structures, precision machines, optical reflectors, etc. Note that mode shapes of shells and plates are usually distinctive, and thus, modal voltages are also distinctive and representative. These distributed signals and modal voltages are discussed in this report. Distributed sensing theory is discussed first, followed by case studies of distributed modal voltages. Detailed signal linear and nonlinear components of modal voltages are also evaluated.

DISTRIBUTED SENSING SIGNALS OF SHELLS OF REVOLUTION

It is assumed that a distributed piezoelectric sensor layer (with thickness h^s) is laminated on a generic double-curvature shell (with thickness h) and the sensor layer is much thinner than the shell. Accordingly, the strain variation in the sensor layer can be approximated by the strain variations on the shell’s outer surface, assuming $h \gg h^s$. Since the sensing signal depends on strain variations in the distributed sensor layer, based on Maxwell’s principle and the open-voltage assumption, the sensor signal ϕ^s of a generic shell sensor can be expressed as (Howard, Chai, and Tzou, 2000; Tzou, 1993)

$$\begin{aligned} \phi^s &= \frac{h^s}{S^e} \int_{S^e} (h_{31}S_{11} + h_{32}S_{22} + h_{36}S_{12}) dS^e \\ &= \frac{h^s}{S^e} \int_{S^e} (h_{31}S_{11} + h_{32}S_{22} + h_{36}S_{12}) A_1 A_2 d\alpha_1 d\alpha_2, \end{aligned} \quad (1)$$

where S^e is the effective sensor area; h^s is the sensor thickness; S_{11} and S_{22} are the normal strains; S_{12} is the in-plane shear strain; h_{31} , h_{32} and h_{36} are the piezoelectric (displacement) constants; A_1 and A_2 are the Lamé parameters; and α_1 and α_2 are the two curvilinear coordinates. Since the elastic strains could be either linear (induced by small deformations) or nonlinear (induced by large deformations), accordingly, signal generations from various strain components of linear and nonlinear continua can be evaluated respectively. Distributed sensing

characteristics – the potential distribution and the modal voltage – of the linear and nonlinear paraboloidal shell of revolution are evaluated in this study.

For the shells of revolution defined in the ϕ - ψ coordinate system, Figure 1, the distributed sensing signal is defined as

$$\begin{aligned}\phi^s &= \frac{h^s}{S^e} \int_{S^e} (h_{31} S_{\phi\phi} + h_{32} S_{\psi\psi} + h_{36} S_{\phi\psi}) \cdot A_1 A_2 d\phi d\psi \\ &= \frac{h^s}{S^e} \int_{\phi} \int_{\psi} [h_{31}(s_{\phi\phi}^0 + r_1^s k_{\phi\phi}) + h_{32}(s_{\psi\psi}^0 + r_2^s k_{\psi\psi}) + h_{36}(s_{\phi\psi}^0 + r_{12}^s k_{\phi\psi})] \\ &\quad \bullet R_{\phi} R_{\psi} \sin \phi \cdot d\phi d\psi ,\end{aligned}\quad (2)$$

where $s_{\phi\phi}^0$, $s_{\psi\psi}^0$ and $s_{\phi\psi}^0$ are the membrane strains; $k_{\phi\phi}$, $k_{\psi\psi}$ and $k_{\phi\psi}$ are the bending strains; r_1^s , r_2^s and r_{12}^s denote the sensor placement measured from the neutral surface and $r_1^s = r_2^s = r_{12}^s = (h + h^s)/2 \cong h/2$, if $h \gg h^s$. $r_1^s = r_2^s = r_{12}^s$ since both sensor and shell have uniform thickness. (Note that the sensor layer is assumed very thin and its effect is neglected.) Furthermore, the generic sensor signal equation for shells of revolution can be simplified to account for the distributed sensor laminated on paraboloidal shells when appropriate radii (i.e., the meridional radius $R_{\phi} = [b/\cos^3 \phi]$, the circumferential radius $R_{\psi} = [b/\cos \phi]$), and the Lamé parameters: $A_1 = [b/\cos^3 \phi]$ and $A_2 = [b \sin \phi / \cos \phi]$ are used in the substitution and simplification, where $b = (a^2/2c)$. Note that $b = 2 \times$ (focal length), “c” denotes the meridian height and “a” denotes the radial distance (Mazurkiewicz and Nagorski, 1991), Figure 1.

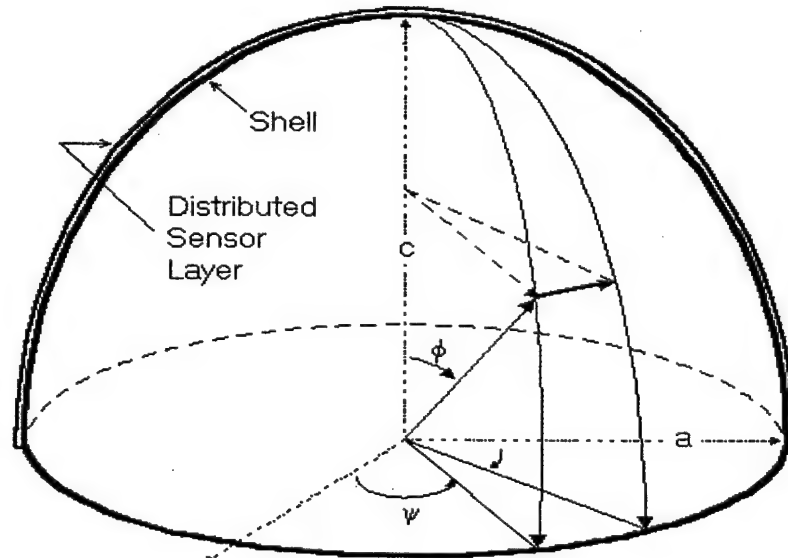


Fig.1 A paraboloidal shell laminated with distributed piezoelectric sensor layer.

Since the shell may experience both small amplitude oscillation and large amplitude oscillation, modal dynamic behaviors of linear and nonlinear shells can be evaluated accordingly. The membrane and bending strains of nonlinear paraboloidal shells of revolution, including the von Karman geometric nonlinearity (Tzou and Yang, 2000; Tzou, et al, 1997), are mathematically defined as

$$s_{\phi\phi}^0 = \frac{\cos^3 \phi}{b} \left(\frac{\partial u_\phi}{\partial \phi} + u_3 \right) + \left[\frac{1}{2} \frac{\cos^6 \phi}{b^2} \left(\frac{\partial u_3}{\partial \phi} \right)^2 \right], \quad (3)$$

$$s_{\psi\psi}^0 = \frac{\cos \phi}{b \sin \phi} \left(\frac{\partial u_\psi}{\partial \psi} + u_\phi \cos \phi + u_3 \sin \phi \right) + \left[\frac{1}{2} \frac{\cos^2 \phi}{b^2 \sin^2 \phi} \left(\frac{\partial u_3}{\partial \psi} \right)^2 \right], \quad (4)$$

$$s_{\phi\psi}^0 = \frac{\cos \phi}{b \sin \phi} \left(\frac{\partial u_\phi}{\partial \psi} + \cos^2 \phi \sin \phi \frac{\partial u_\psi}{\partial \phi} - u_\psi \cos \phi \right) + \left[\frac{\cos^4 \phi}{b^2 \sin \phi} \left(\frac{\partial u_3}{\partial \phi} \frac{\partial u_3}{\partial \psi} \right) \right], \quad (5)$$

$$k_{\phi\phi} = \frac{\cos^6 \phi}{b^2} \left(\frac{\partial u_\phi}{\partial \phi} - \frac{\partial^2 u_3}{\partial \phi^2} \right) - 3 \frac{\cos^5 \phi \sin \phi}{b^2} \left(u_\phi - \frac{\partial u_3}{\partial \phi} \right), \quad (6)$$

$$k_{\psi\psi} = \frac{\cos^2 \phi}{b^2 \sin \phi} \left(\frac{\partial u_\psi}{\partial \psi} - \frac{1}{\sin \phi} \frac{\partial^2 u_3}{\partial \psi^2} + u_\phi \cos^3 \phi - \cos^3 \phi \frac{\partial u_3}{\partial \phi} \right), \quad (7)$$

$$k_{\phi\psi} = - \frac{\cos^5 \phi + 2 \cos^3 \phi \sin^2 \phi}{b^2 \sin \phi} u_\psi + \frac{2 \cos^3 \phi}{b^2 \sin^2 \phi} \frac{\partial u_3}{\partial \psi} - \frac{2 \cos^4 \phi}{b^2 \sin \phi} \frac{\partial^2 u_3}{\partial \psi \partial \phi} \\ + \frac{\cos^4 \phi}{b^2} \frac{\partial u_\psi}{\partial \phi} + \frac{\cos^4 \phi}{b^2 \sin \phi} \frac{\partial u_\phi}{\partial \psi}, \quad (8)$$

where u_ϕ , u_ψ and u_3 represent the displacement in ϕ -direction, ψ -direction and transverse direction, respectively. Based on the von Karman geometrical nonlinearity, only the transverse nonlinear deformation u_3 is included, and this nonlinear effect appears in the membrane strains, i.e., the quadratic term in the bracket, of the first three membrane strain equations. Accordingly, the sensing signal corresponding to nonlinear large deformation paraboloidal shells can be defined. Furthermore, note that the nonlinear strain component is defined with respect to the first derivative of the transverse displacement. Thus, distributed signals resulting from the nonlinear strains of nonlinear paraboloidal shells are functions of "slopes" in the meridional or circumferential directions. The linear part of the strain expressions were compared well with those reported in (Wang and Lin, 1967).

MODAL VOLTAGES OF A PARABOLOIDAL SHELL

It is assumed that the paraboloidal shell only exhibits axisymmetric oscillations, i.e., $\frac{\partial(\bullet)}{\partial \psi} = 0$, and the transverse oscillation dominates, i.e., $u_3 \gg u_\phi$ and u_ψ (or $u_\phi \approx 0$ and $u_\psi \approx 0$). These phenomena were observed in laboratory experiments of free vibration of simply supported paraboloidal shells (Glockner and Tawardros, 1973). Thus, the nonlinear strain-displacement relations are simplified to only functions of the transverse displacement u_3 .

$$S_{\phi\phi} = s_{\phi\phi}^0 + \alpha_3 k_{\phi\phi} \\ = \frac{\cos^3 \phi}{b} u_3 + \left[\frac{1}{2} \frac{\cos^6 \phi}{b^2} \left(\frac{\partial u_3}{\partial \phi} \right)^2 \right] + \alpha_3 \frac{\cos^6 \phi}{b^2} \left(3 \frac{\sin \phi}{\cos \phi} \frac{\partial u_3}{\partial \phi} - \frac{\partial^2 u_3}{\partial \phi^2} \right), \quad (9)$$

$$S_{\psi\psi} = s_{\psi\psi}^0 + \alpha_3 k_{\psi\psi} = \frac{\cos \phi}{b} u_3 - \alpha_3 \frac{\cos^5 \phi}{b^2 \sin \phi} \frac{\partial u_3}{\partial \phi}, \quad (10)$$

$$S_{\phi\psi} = 0, \quad (11)$$

where α_3 is the transverse coordinate defined as the distance from the shell neutral surface. Accordingly, the distributed sensing signal of a paraboloidal shell sensor becomes

$$\phi^s = \frac{h^s}{S^e} \int_{\phi} \int_{\psi} \left\{ h_{31} \left\{ \frac{\cos^3 \phi}{b} u_3 + \left[\frac{1}{2} \frac{\cos^6 \phi}{b^2} \left(\frac{\partial u_3}{\partial \phi} \right)^2 \right] + r_1^s \frac{\cos^6 \phi}{b^2} \left(3 \frac{\sin \phi}{\cos \phi} \frac{\partial u_3}{\partial \phi} - \frac{\partial^2 u_3}{\partial \phi^2} \right) \right\} \right. \\ \left. + h_{32} \left(\frac{\cos \phi}{b} u_3 - r_2^s \frac{\cos^5 \phi}{b^2 \sin \phi} \frac{\partial u_3}{\partial \phi} \right) \right\} \cdot \frac{b}{\cos^3 \phi} \cdot \frac{b \sin \phi}{\cos \phi} d\phi d\psi. \quad (12)$$

Assume the shell oscillation is composed of all participating natural modes – the modal expansion method, i.e., $u_i(\alpha_1, \alpha_2, t) = \sum_{m=1}^{\infty} \eta(t) \cdot U_{im}(\alpha_1, \alpha_2)$ where $\eta(t)$ is the modal participation factor and U_{im} is the m -th mode shape function in the i -th direction. The axisymmetric transverse mode shape function U_{3m} of a simply supported paraboloidal shell of revolution can be approximated by

$$U_{3m} = A_m \cos \frac{(2m-1)\pi}{2\phi^*} \phi = A_m \cos B_m \phi, \quad (13)$$

where A_m is the mode amplitude; $m = 1, 2, 3, \dots$ is the mode (or half-wave) number; ϕ is the angle defining the shell meridional direction and $0 < \phi < \phi^*$. Note that $\phi = \phi^*$ defines the base rim - the simply supported boundary condition; and $B_m = [(2m-1)\pi]/(2\phi^*)$. This mode shape function has been verified by experimental data (Glockner and Tawardros, 1973).

Distributed Sensor Signal

Substituting the mode shape function into the strain expressions in the distributed sensing signal yields the m -th modal voltages ϕ_m^s averaged over the effective sensor area S^e . Note the modal signal can be spectrally decomposed from the general sensing signal by signal processing technologies, such as using band-pass filters.

$$\begin{aligned}
\phi_m^s = & \frac{h^s}{S^e} \int_{\phi} \int_{\psi} \left\{ h_{31} \left[\frac{A_m}{b} \cos^3 \phi \cos B_m \phi + \left[\frac{A_m^2 B_m^2 \cos^6 \phi}{2b^2} \sin^2 B_m \phi \right] \right. \right. \\
& + r_1^s \frac{A_m B_m}{b^2} \cos^5 \phi (B_m \cos \phi \cos B_m \phi - 3 \sin \phi \sin B_m \phi)] \\
& \left. \left. + h_{32} \left[\frac{A_m}{b} \cos \phi \cos B_m \phi + r_2^s \frac{A_m B_m}{b^2} \frac{\cos^5 \phi}{\sin \phi} \sin B_m \phi \right] \right\} \frac{b^2 \sin \phi}{\cos^4 \phi} d\phi d\psi \right. . \\
\end{aligned} \tag{14}$$

Segmented Sensor Patch

For a segmented sensor patch (i.e., the segmented sensor) defined by the boundaries ($\phi_1^* \rightarrow \phi^*$ and $\psi_1^* \rightarrow \psi_2^*$), Figure 2, the modal sensing signal is defined by

$$\begin{aligned}
\phi_m^s = & \frac{h^s}{S^e} \int_{\phi_1^*}^{\phi^*} \int_{\psi_1^*}^{\psi_2^*} \left\{ h_{31} \left[\frac{A_m}{b} \cos^3 \phi \cos B_m \phi + \left[\frac{A_m^2 B_m^2 \cos^6 \phi}{2b^2} \sin^2 B_m \phi \right] \right. \right. \\
& + r_1^s \frac{A_m B_m}{b^2} \cos^5 \phi (B_m \cos \phi \cos B_m \phi - 3 \sin \phi \sin B_m \phi)] \\
& \left. \left. + h_{32} \left[\frac{A_m}{b} \cos \phi \cos B_m \phi + r_2^s \frac{A_m B_m}{b^2} \frac{\cos^5 \phi}{\sin \phi} \sin B_m \phi \right] \right\} \frac{b^2 \sin \phi}{\cos^4 \phi} d\phi d\psi \right. . \\
\end{aligned} \tag{15}$$

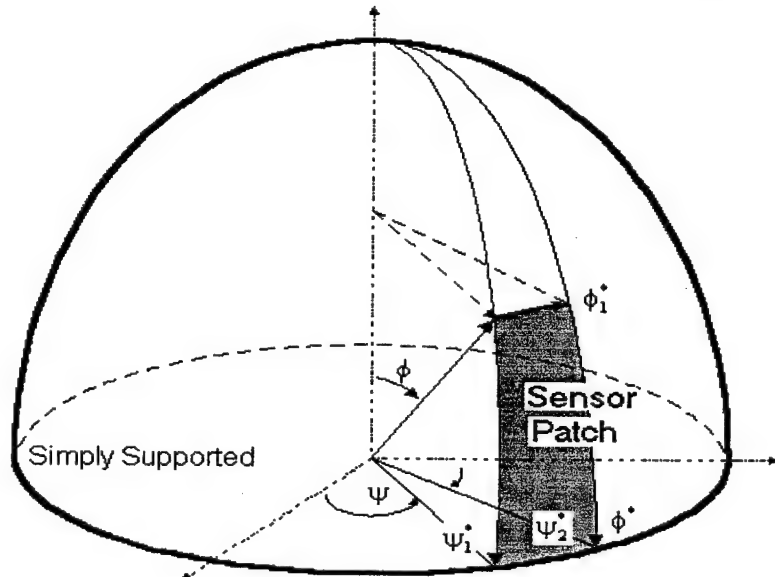


Fig.2 A sensor patch laminated on a paraboloidal shell of revolution.

Local Signals and Modal Voltages by Sensor Neurons

When the local signal behaviors of natural modes are interested, the surface integration and average are neglected and the remaining expression denotes the local signal generation at a specified neuron location $\phi = \phi_k^*$ corresponding the local m-th modal strain behaviors.

$$\begin{aligned}
 \phi_m^s = h^s \{ & h_{31} \left[\frac{A_m}{b} \cos^3 \phi_k^* \cos B_m \phi_k^* + \left[\frac{A_m^2 B_m^2 \cos^6 \phi_k^*}{2b^2} \sin^2 B_m \phi_k^* \right] \right. \\
 & + r_1^s \frac{A_m B_m}{b^2} \cos^5 \phi_k^* (B_m \cos \phi_k^* \cos B_m \phi_k^* - 3 \sin \phi_k^* \sin B_m \phi_k^*)] \\
 & \left. + h_{32} \left[\frac{A_m}{b} \cos \phi_k^* \cos B_m \phi_k^* + r_2^s \frac{A_m B_m}{b^2} \frac{\cos^5 \phi_k^*}{\sin \phi_k^*} \sin B_m \phi_k^* \right] \right\}.
 \end{aligned} \tag{16}$$

Recall that $B_m = [(2m-1)\pi]/(2\phi^*)$, $r_1^s = r_2^s = r_{12}^s = (h + h^s)/2 \cong h/2$, if $h \gg h^s$ and sensor/shell have uniform thickness. Note that infinitesimal electrodes and multiple channel data bus are required to display distributed local signals in practice. Assembling and displaying all local signal distribution patterns on the shell provides a global signal distribution – the spatially ***distributed modal voltages*** – of the paraboloidal shells. Detailed signal components are discussed next and distributed modal voltages of the paraboloidal shell oscillations are presented in case studies.

Components of Distributed Modal Voltages

Recall that the total signal is contributed by two main components: the membrane component and the bending component, i.e., $[\phi_m^s] = [\phi_m^s]_{\text{mem}} + [\phi_m^s]_{\text{bend}}$ where the subscripts "mem" and "bend" denote the membrane part and the bending part respectively. The membrane component can be further divided into the linear part and the nonlinear (quadratic) part. Thus, the signal $[\phi_m^s]_{\text{mem}}^{\ell}$ contributed by the linear membrane component is $h^s \left\{ h_{31} \left\{ \frac{A_m}{b} \cos^3 \phi \cos B_m \phi \right\} + h_{32} \left(\frac{A_m}{b} \cos \phi \cos B_m \phi \right) \right\}$; that $[\phi_m^s]_{\text{bend}}^{\ell}$ contributed by the linear bending component is $h^s \left\{ h_{31} \left\{ r_1^s \frac{A_m B_m}{b^2} \cos^5 \phi (B_m \cos \phi \cos B_m \phi - 3 \sin \phi \sin B_m \phi) \right\} + h_{32} (r_2^s \frac{A_m B_m}{b^2} \frac{\cos^5 \phi}{\sin \phi} \sin B_m \phi) \right\}$; and that $[\phi_m^s]_{\text{mem}}^n \equiv [\phi_m^s]_{\text{mem}}^n$ contributed by the nonlinear membrane component is $[\phi_m^s]^n = h^s h_{31} \left[\frac{A_m^2 B_m^2 \cos^6 \phi}{2b^2} \sin^2 B_m \phi \right]$. Note that $h_{31} = h_{32} = h_{3i}$ in most conventional piezoelectric sensing materials without being mechanical stretched during the manufacturing process. Accordingly, these sensing signal components are specifically divided into their individual components. On the other hand, based on strain magnitudes, the sensing signal can be divided into two parts: the linear strain induced part $[\phi_m^s]^{\ell}$ and the nonlinear strain induced part $[\phi_m^s]^n$ where the nonlinear component is only related to the membrane strains.

$$[\phi_m^s]^\ell = h^s \left\{ h_{31} \left\{ \frac{A_m}{b} \cos^3 \phi \cos B_m \phi \right. \right. \\ \left. \left. + r_i^s \frac{A_m B_m}{b^2} \cos^5 \phi (B_m \cos \phi \cos B_m \phi - 3 \sin \phi \sin B_m \phi) \right\} \right. \\ \left. + h_{32} \left(\frac{A_m}{b} \cos \phi \cos B_m \phi + r_2^s \frac{A_m B_m}{b^2} \frac{\cos^5 \phi}{\sin \phi} \sin B_m \phi \right) \right\} . \quad (17)$$

$$[\phi_m^s]^n = h^s h_{31} \left[\frac{A_m^2 B_m^2 \cos^6 \phi}{2b^2} \sin^2 B_m \phi \right] . \quad (18)$$

Or,

$$[\phi_m^s]^\ell = h^s h_{31} A_m [(\Phi)_{mem}^\ell + (\Phi)_{bend}^\ell] = h^s h_{31} A_m (\Phi)_{Total}^\ell , \quad (19)$$

$$[\phi_m^s]^n = h^s h_{31} A_m^2 (\Phi)_{mem}^n \equiv h^s h_{31} A_m^2 (\Phi)^n . \quad (20)$$

These signal components “ (Φ) ” are plotted and evaluated in case studies. Their electromechanical characteristics with respect to shell geometry variations are investigated.

CASE STUDIES

To examine the distributed modal voltages, a number of (linear and nonlinear) paraboloidal shells with various geometries, e.g., shallow or deep, thin or thick, etc., are investigated in this section. Modal voltage variations of various shell curvatures and thickness are investigated. Table 1 lists these paraboloidal shell cases, in which there are two thickness groups and both shell groups are still considered “thin” and governed by the thin shell theory. Case 1 is only one-fifth the thickness of Cases 4-6 and Case 1 is considered as the standard case. Cases 6 is the deepest; Case 5 is the shallowest; and Cases 1 and 4 are in between. (Note that $b = a^2/2c$ and $b = 2 \times$ focal length, where “ c ” defines the meridian and “ a ” defines the horizontally projected radial distance, see Figure 2.) Three natural modes are considered for each shell case and detailed sensing signal contributions of membrane (linear and nonlinear) components and bending components (including Cases 1,4,5, and 6) are investigated. Note that the case studies presented here are limited to qualitative theoretical analysis, which reveal detailed modal voltage variations and neural signal components with various shell geometry parameters.

Table 1 Paraboloidal shell shapes and their geomtric parameters.

Parameters Cases	Radius (a)	Height (c)	Thickness (h)
1	1	1	0.002
4	1	1	0.010
5	2	1	0.010
6	1	2	0.010

It is assumed that the piezoelectric constants h_{31} and h_{32} are the same, and the modal amplitude A_m is set to unity. Thus, the modal signals are normalized with respect to the modal amplitudes, per se. However, the modal amplitude A_m varies for different modes. In reality, the modal amplitudes of higher modes are usually much smaller than that of the fundamental mode, i.e., $A_1 \gg A_m, m=2,3,4\dots$ Accordingly, the following modal voltage plots only provide qualitative information. Quantitative modal voltages can be inferred only if the "true" modal amplitudes are well defined. This amplitude influence to the nonlinear component is even more significant, since there is a quadratic term involved in the expression, due to the von Karman geometric nonlinearity. The true signals of the nonlinear component are usually very small when the true modal amplitudes are considered.

As demonstrated previously, the modal sensing signals are specifically divided into their individual signal components corresponding to detailed strain distributions. Recall that the total signal of the m -th natural mode is contributed by two main components: the membrane component and the bending component. The membrane component can be further divided into the linear part (i.e., $[\phi_m^s]^\ell = [\phi_m^s]_{\text{mem}}^\ell + [\phi_m^s]_{\text{bend}}^\ell$) and the nonlinear (quadratic) part (i.e., $[\phi_m^s]^n$). For linear paraboloidal shells, the signal resulting from the nonlinear component can be neglected; for nonlinear paraboloidal shells, all signal components need to be considered. Accordingly, detailed signal generations from each component can be evaluated. These signal components: $(\Phi)_{\text{mem}}^\ell$ (denoted by 3), $(\Phi)_{\text{bend}}^\ell$ (denoted by 4), $(\Phi)_{\text{Total}}^\ell$ (denoted by 2), and $(\Phi)_{\text{mem}}^n \equiv (\Phi)^n$ (denoted by 5) are plotted with respect to the original shell surface (denoted by 1) and their individual signal characteristics of the first three natural modes paraboloidal shell cases listed in Table 1 are respectively evaluated in Figures 3-5 (Case 1); 6-8 (Case 4); 9-11 (Case 5), and 12-14 (Case 6).

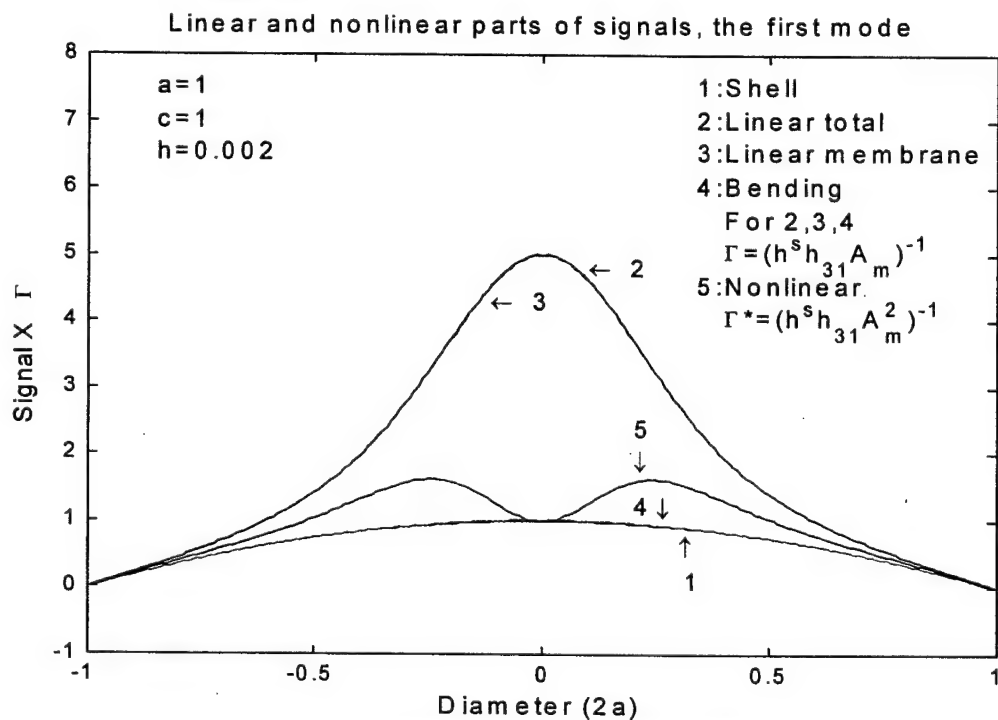


Fig.3 Linear and nonlinear parts of signals (Case 1, the first mode).

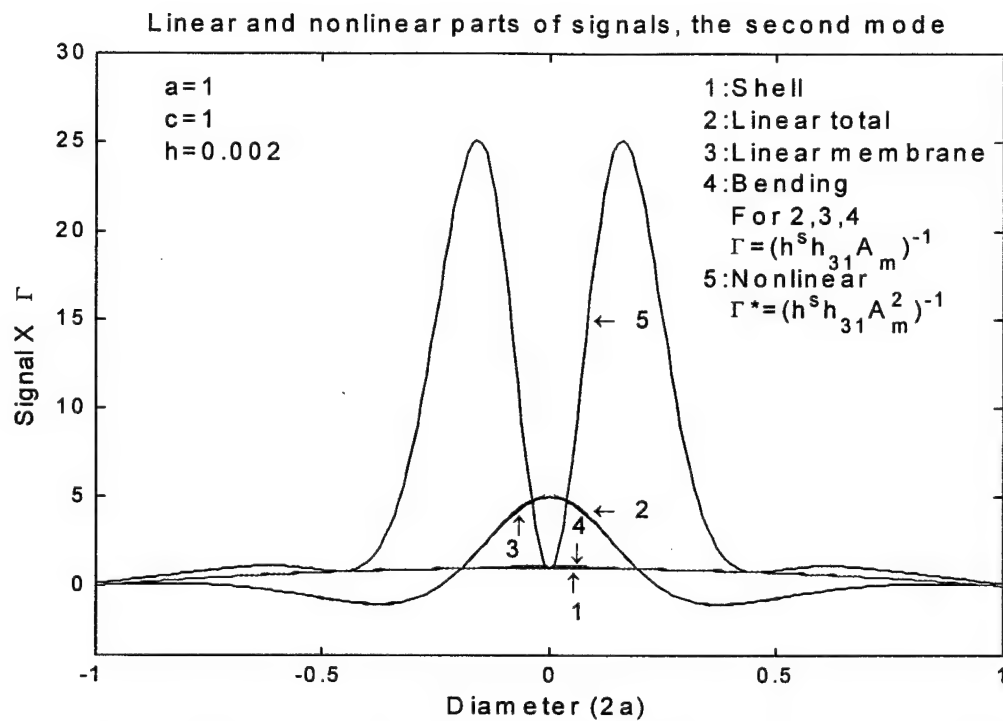


Fig.4 Linear and nonlinear parts of signals (Case 1, the second mode).

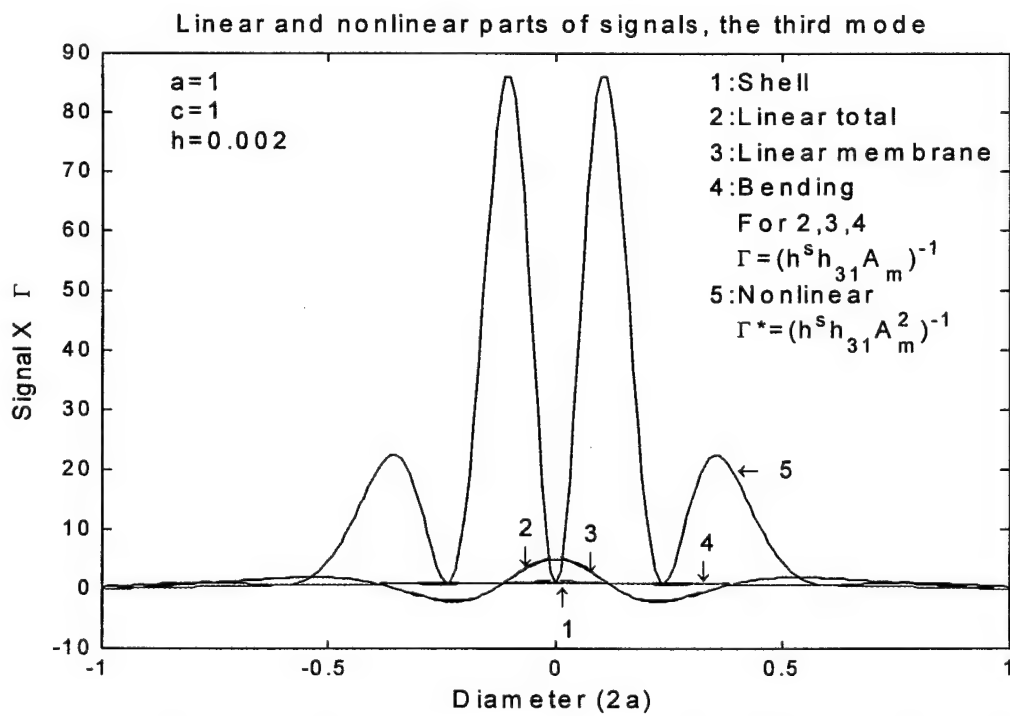


Fig.5 Linear and nonlinear parts of signals (Case 1, the third mode).

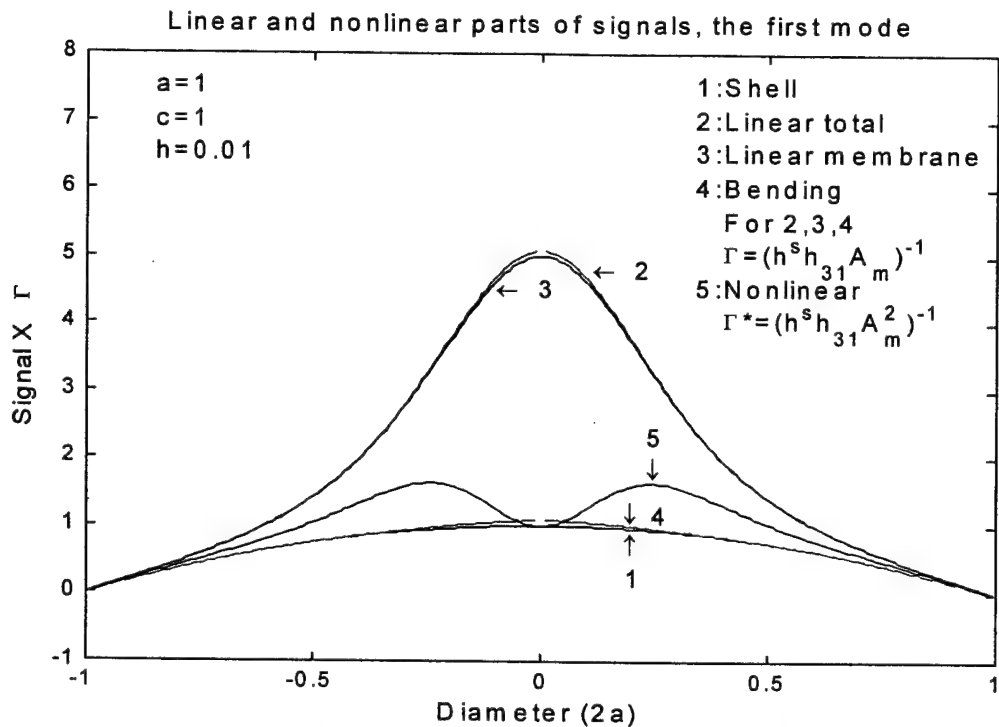


Fig.6 Linear and nonlinear parts of signals (Case 4, the first mode).

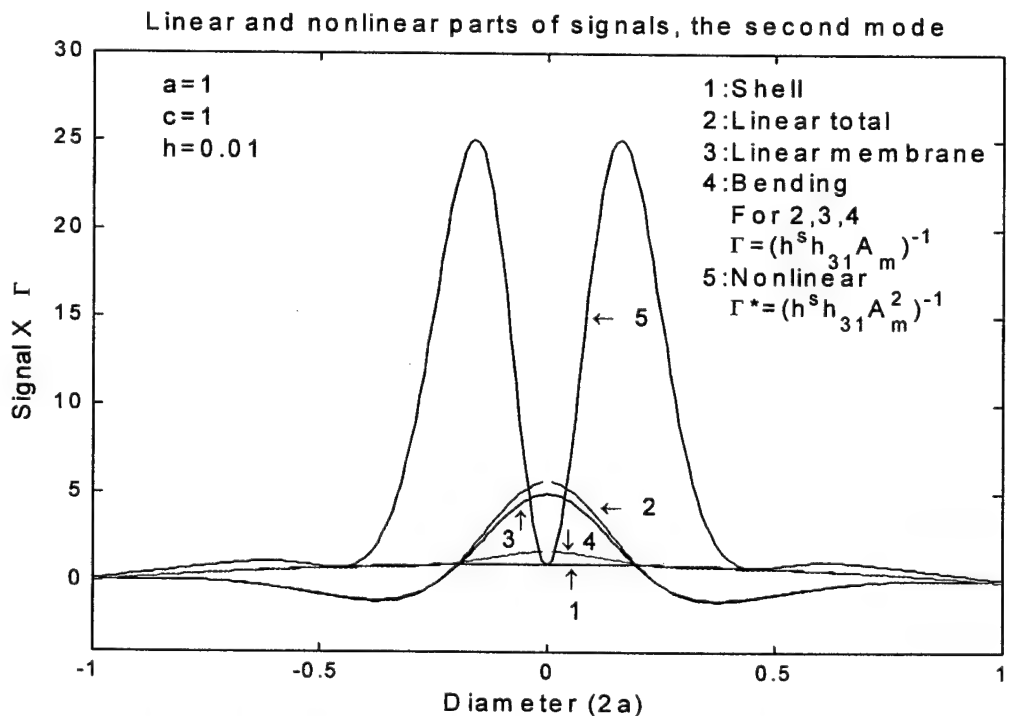


Fig.7 Linear and nonlinear parts of signals (Case 4, the second mode).

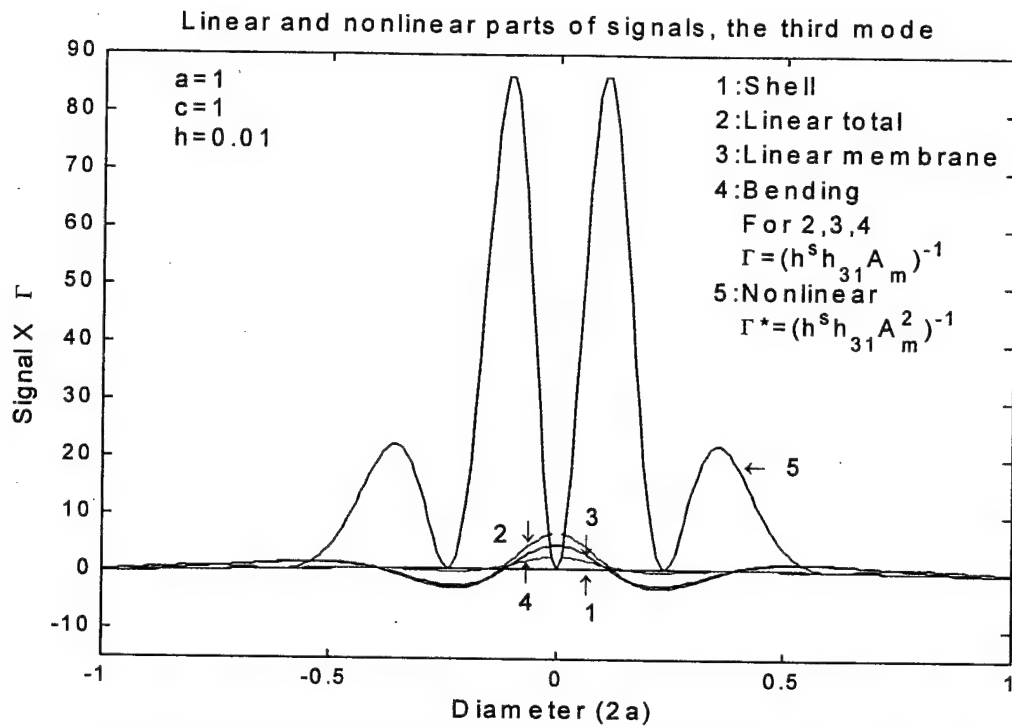


Fig.8 Linear and nonlinear parts of signals (Case 4, the third mode).

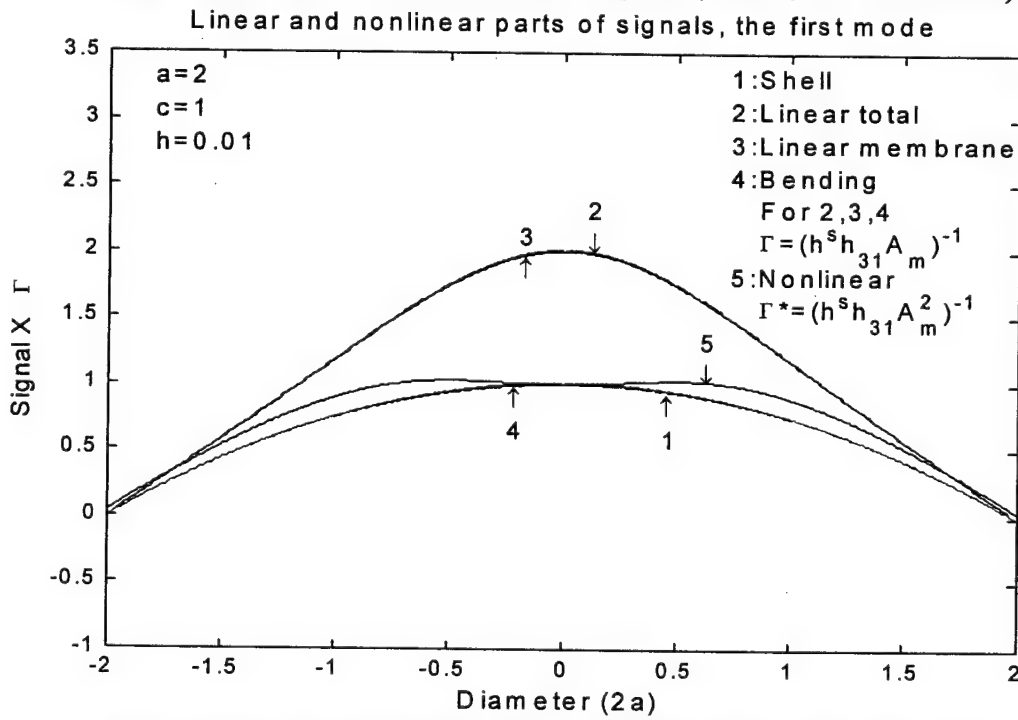


Fig.9 Linear and nonlinear parts of signals (Case 5, the first mode).

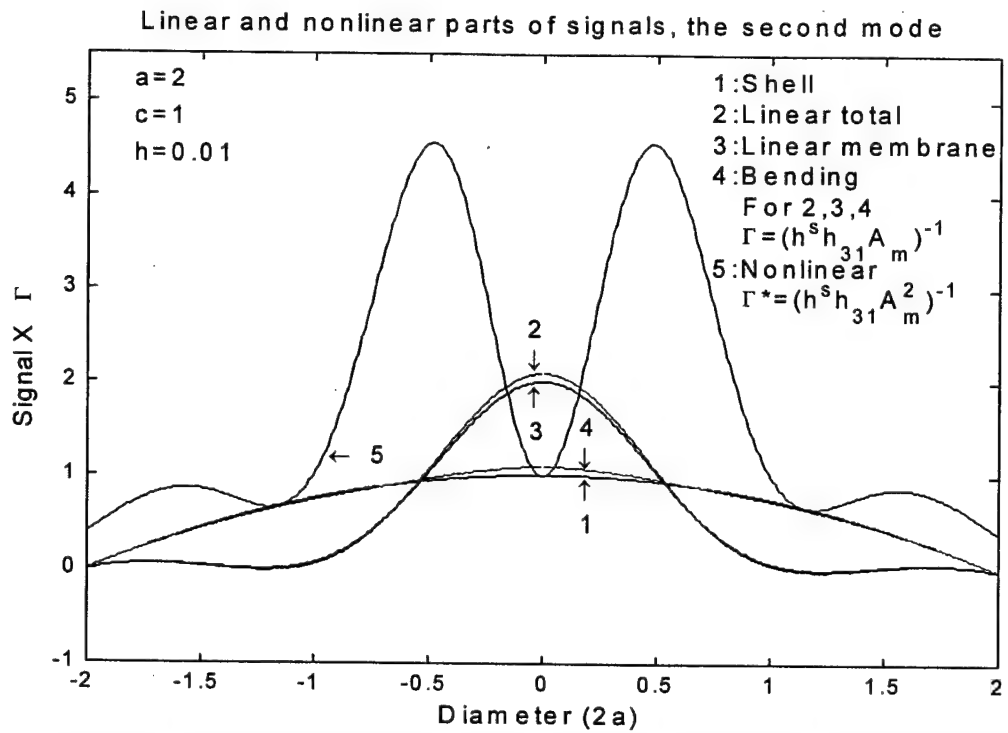


Fig.10 Linear and nonlinear parts of signals (Case 5, the second mode).

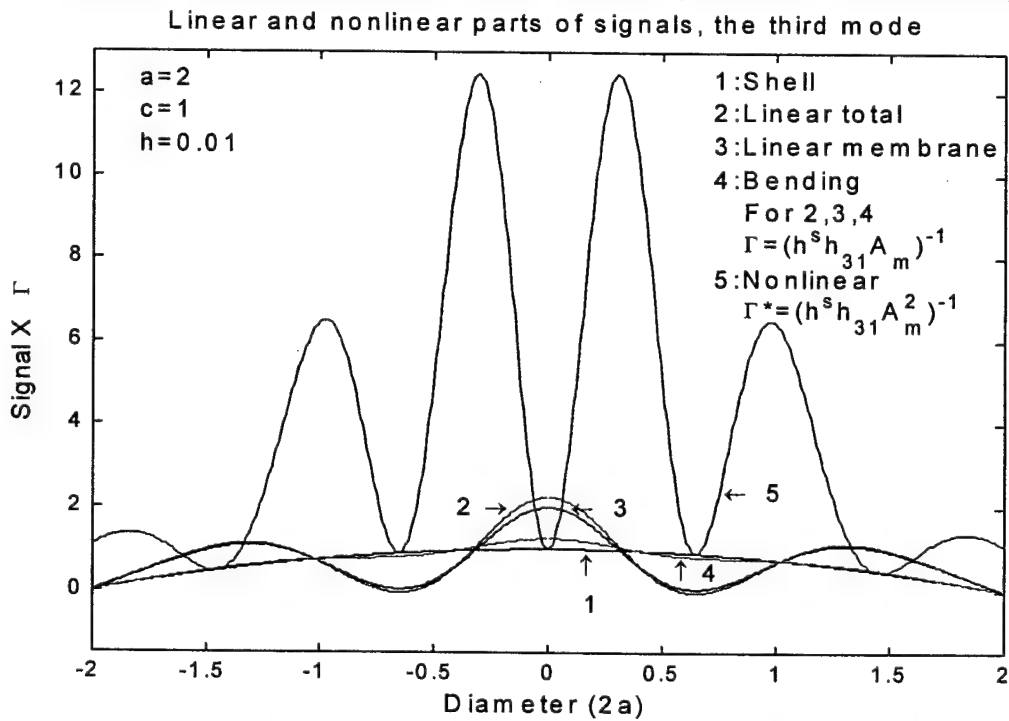


Fig.11 Linear and nonlinear parts of signals (Case 5, the third mode).

Linear and nonlinear parts of signals, the first mode

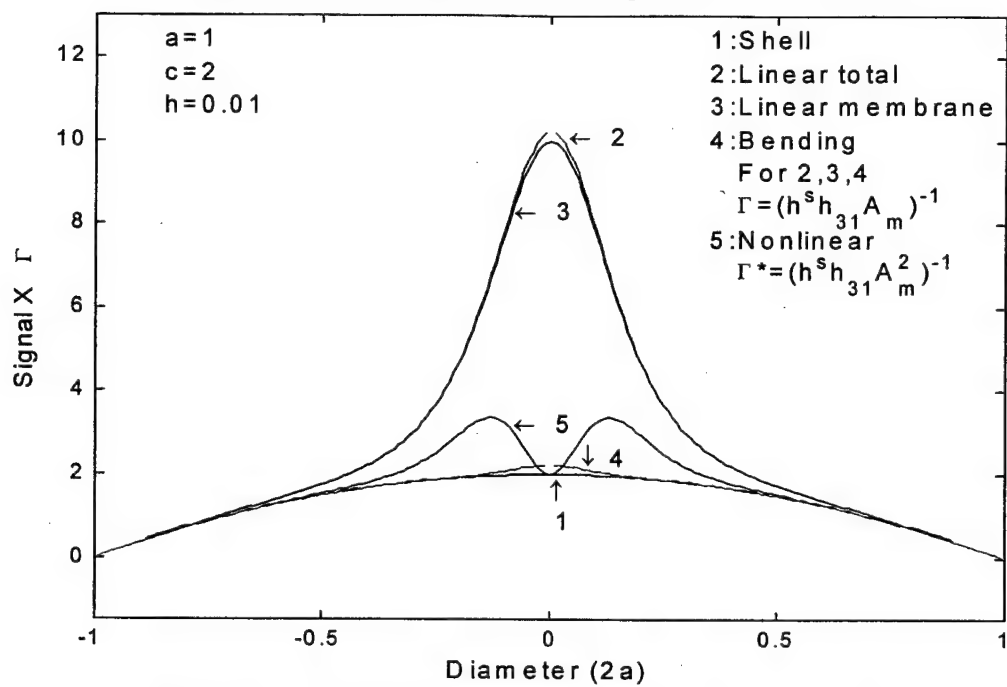


Fig.12 Linear and nonlinear parts of signals (Case 6, the first mode).

Linear and nonlinear parts of signals, the second mode

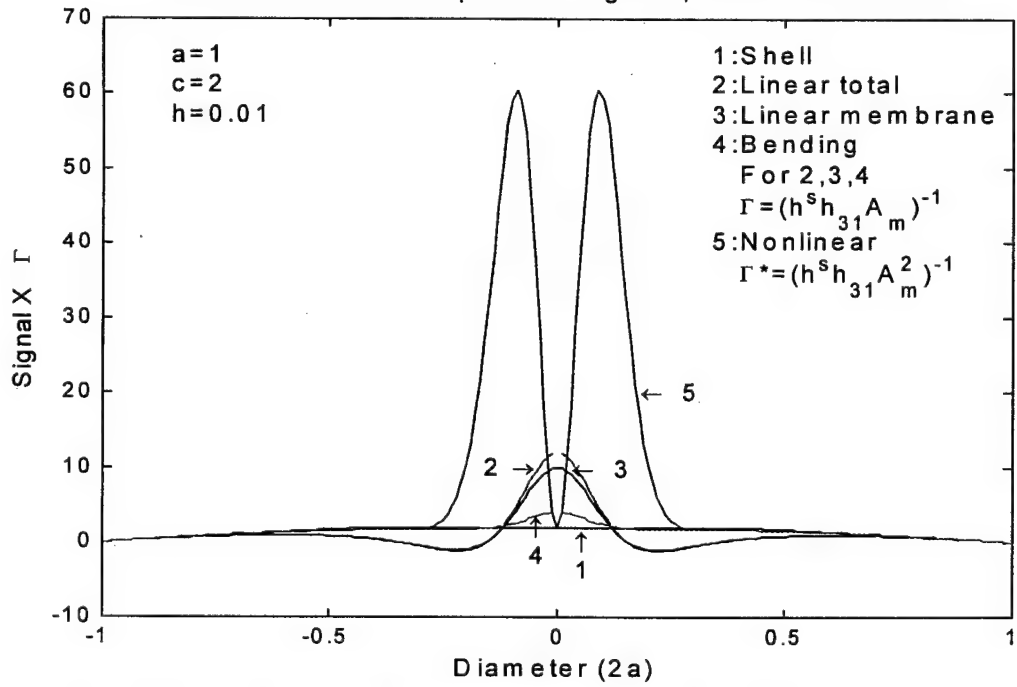


Fig.13 Linear and nonlinear parts of signals (Case 6, the second mode).

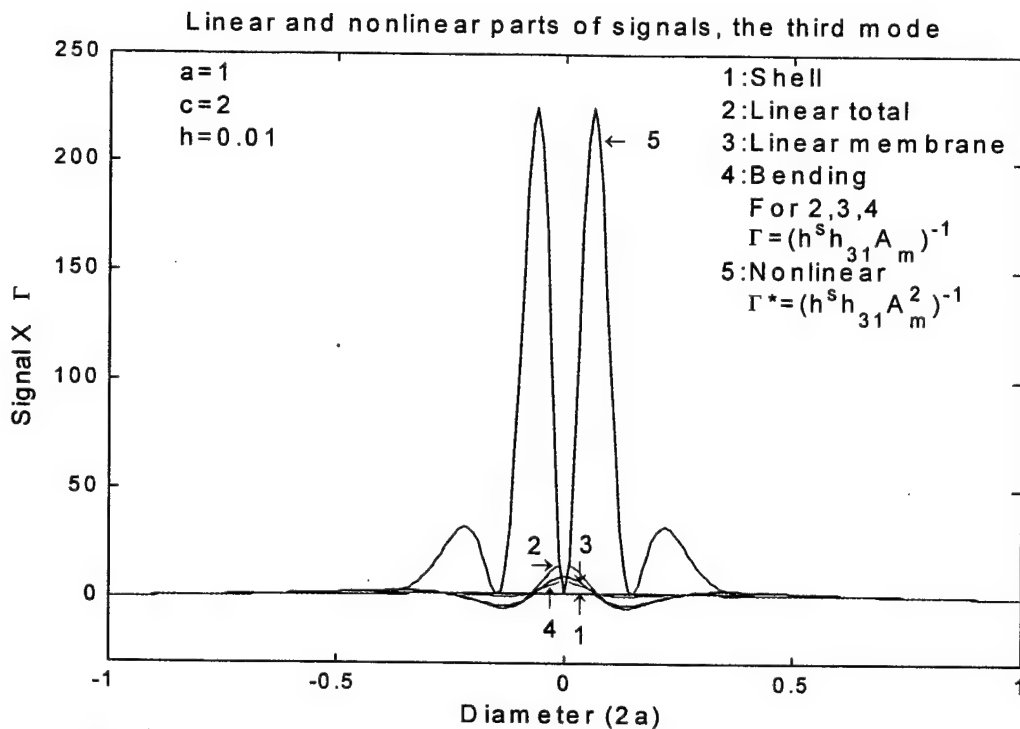


Fig.14 Linear and nonlinear parts of signals (Case 6, the third mode).

Comparing Figures 3 and 6, 4 and 7, and 5 and 8, one can observe that the bending component in thin paraboloidal shell (Case 1) is too insignificant to observe, although this component increases as the mode number increases. The bending component appears, even it is still small, in the thicker paraboloidal shell (Case 4); it becomes relatively significant in the shallower shell (Case 5). (However, it is not so clear in Figure 9, due to the overall signal reduction in shallow shells.) For thin shells, the bending strain is insignificant and the sensing signal component induced by the bending strain, the bending component, is insignificant. Recall that the distributed sensing signal depends on strains, not the motion (displacement). The bend motion (transverse displacement) of thin shell is usually interested, just as discussed before. The signal magnitude is the largest in the deep shell (Case 6), since the signal resulting from the membrane strain dominates the overall output and this membrane component increases as the curvature increases. Also, note that the “ $b = (a^2/2c)$ ” constant appears on the denominator of sensor signals. As “ b ” increases (i.e., shallower), the overall signal magnitudes decreases. Furthermore, the “ b ” influence to the bending signal generation is a quadratic relation. Thus, the bending signal decreases much faster as the shell becomes shallower. On the membrane signal generation, note that the nonlinear component also decreases quadratically faster as the shell becomes shallower. However, in any case, the membrane strain induced signals still dominate the overall signal responses. Note that $h^s h_{31} A_m$ in the linear component and $h^s h_{31} A_m^2$ in the nonlinear component are treated as parameters and the signal plots are normalized with respect to these two constants. (Recall that the modal amplitude is assumed unity in the case studies.) Note that there is a singularity point of the bending signal at the meridian, due to a $\sin \phi$ term on the denominator. However, this singularity is a weak singularity, since $\lim_{\phi \rightarrow 0} (\sin B_m \phi / \sin \phi) \approx B_m$ and $B_m = [(2m-1)\pi]/(2\phi^*)$. Furthermore, there is a

$[B_m]^2 = \{(2m-1)\pi/(2\phi^*)\}^2$ in the nonlinear membrane strain part induced by the von Karman geometric nonlinearity. Thus, the nonlinear signal part increases quadratically with respect to the mode number and it decreases also quadratically with respect to the meridional angle (ϕ^*).

CONCLUSIONS

Effective health monitoring and distributed control depends on accurate measurements of dynamic responses of shells and plates. Distributed modal voltages reveal distributed modal strain responses in distributed elastic shells and plates. This study is to investigate modal voltages and detailed signal contributions of a distributed sensor layer laminated on linear or nonlinear paraboloidal shells of revolution. Definition of sensor signals of distributed sensors laminated on paraboloidal shells of revolution is defined, based on the open-voltage assumption and Maxwell's principle. Signal components and distributed modal voltages of linear and nonlinear paraboloidal shells with various curvatures and thickness are investigated.

The sensor signal of a linear paraboloidal shell is composed of the linear membrane component and the bending component; the signal of a nonlinear paraboloidal shell is composed of the nonlinear and linear membrane components and the bending component. The membrane induced signal component, in general, dominates the overall signal generation, although the bending induced signal component increases as the shell thickness or the mode number increases. The overall signal decreases as the shell curvature decreases, while the bending induced component drops faster than the membrane induced component. It is also observed that the nonlinear induced signal component is related to the membrane strain component, due to the von Karman geometric nonlinearity and it is a quadratic function of slopes. Thus, the signal at the simply-supported boundary exists for nonlinear paraboloidal shells, while the membrane signal component at the boundary vanishes for simply-supported linear paraboloidal shells; however, there is still a very small bending signal component existing at the boundary. Note that this study is primarily a theoretical study and thus various design parameters of shell geometry and nonlinearity can be investigated. Experimental validation of this study would encounter obstacles, since strains would be difficult to separate and thus, individual signal components would be difficult to evaluate.

ACKNOWLEDGEMENT

This research is supported, in part, by a grant (F49620-98-1-0467) from the Air Force Office of Scientific Research (Project Manager: Brian Sanders). This support is gratefully acknowledged.

REFERENCES

Baz A. and Poh S., 1988, "Performance of an Active Control System with Piezoelectric Actuators," *Journal of Sound and Vibration*, Vol.126, No.2, pp.327-343.

Crawley, E.F. and de Luis, J., 1987, "Use of Piezoelectric Actuator as Elements of Intelligent Structures," *AIAA Journal*, 25(10), pp.1373-1385.

Gabbert, U. and Tzou, H.S., 2001, *Smart Structures and Structronic Systems*, Kluwer Academic Pub., Dordrecht /Boston /London.

Glockner, P.G. and Tawardros, K.Z., 1973, "Experiments on Free Vibration of Shells of Revolution," *Experimental Mechanics*, Vol.13, No.10, pp.411-421.

Hanagud S. and Obal, M.W., 1988, "Identification of Dynamic Coupling Coefficients in a Structure with Piezoelectric Sensors and Actuators," AIAA paper No.88-2418.

Howard, R.V., Chai, W.K., and Tzou, H.S., 2001, "Modal Voltages of Linear and Nonlinear Structures using Distributed Artificial Neurons (A Theoretical and Experimental Study)," *Mechanical Systems and Signal Processing (Journal of)*, Vol.15, No.3, pp.629-640.

Mazurkiewicz, Z.E., Nagorski, R.T., 1991, *Shells of Revolution*, PWN-Polish Scientific Publishers, Warsaw, pp.7-9, pp.333-341.

Plumb, J.M., Hubbard, J.E., and Bailey, T., 1987, "Nonlinear Control of a Distributed System: Simulation and Experimental Results," *ASME Journal of Dynamic Systems, Measurements, and Control*, 109(2), pp.133-139.

Tzou, H.S., 1987, "Active Vibration Control of Flexible Structures via Converse Piezoelectricity," *Development in Mechanics*, 14(b), 20th Midwest Mechanical Conference, pp.1201-1206.

Tzou, H.S., 1992, "Thin-Layer Distributed Piezoelectric Neurons and Muscles: Electromechanics and Applications," *Precision Sensors, Actuators, and Systems*, H.S. Tzou and T. Fukuda, (Editors), Kluwer Academic Publishers, Dordrecht /Boston /London, pp.175-218.

Tzou, H.S., 1993, *Piezoelectric Shells (Distributed Sensing and Control of Continua)*, Kluwer Academic Publishers, Boston /Dordrecht.

Tzou, H.S., Bao, Y., and Zhou, Y., 1997, "Nonlinear Piezothermoelasticity and Multi-field Actuations, Part-1: Nonlinear Anisotropic Piezothermoelastic Shell Laminates; Part-2: Control of Nonlinear Buckling and Dynamics," *ASME Transactions, Journal of Vibration & Acoustics*, Vol.119, pp.374-389.

Tzou, H.S. and Yang, R.J., 2000, "Nonlinear Piezo-thermoelastic Shell Theory applied to Control of Variable-geometry Shells," *Journal of Theoretical and Applied Mechanics*, No.3, Vol.38, pp.623-644.

Tzou, H.S., Zhong, J.P., and Natori, M.C., 1993, "Sensor Mechanics of Distributed Shell Convolving Sensors Applied to Flexible Rings," *ASME Journal of Vibration & Acoustics*, Vol.115, No.1, pp.40-46.

Wang, J. T.-S., and Lin, C.-W., 1967, "On the Differential Equations of the Axisymmetric Vibration of Paraboloidal Shells of Revolution," NASA CR-932, Nov 1967.

(ParbSigNon.ParbPr.Shl.Parb)

CHAPTER 13

ACTUATOR PLACEMENT AND MICRO-ACTUATION EFFICIENCY OF ADAPTIVE PARABOLOIDAL SHELLS

ABSTRACT

Paraboloidal shells of revolution are commonly used in communication systems, precision opto-mechanical systems and aerospace structures. This study is to investigate the precision distributed control effectiveness of adaptive paraboloidal shells laminated with segmented actuator patches. Mathematical models of the paraboloidal shells laminated with distributed actuator layers subjected to mechanical, temperature, and control forces are presented first. Then, formulations of distributed actuating forces with their contributing micro-meridional/circumferential membrane and bending components are derived using an assumed mode shape function. Studies of actuator placements, actuator induced control forces, micro-contributing components, and normalized actuation authorities of paraboloidal shells are carried out. These forces and membrane/bending components basically exhibit distinct modal characteristics influenced by shell geometries and other design parameters. Analyses suggest that the membrane-contributed components dominate the overall control effect. Locations with larger normalized forces indicate the areas with high control efficiencies, i.e., larger induced actuation force per unit actuator area. With limited actuators, placing actuators at those locations would lead to the maximal control effects of paraboloidal shells.

INTRODUCTION

Solar reflectors, communication antennas, optical mirrors, etc. usually have the shape of paraboloidal shell of revolution, often due to their focusing and aiming requirement in aerospace and communication structures. This study is to investigate the precision distributed control effectiveness and actuator placement of adaptive paraboloidal shells laminated with segmented actuator patches. Distributed control of shell structures based on the smart structures and strucronics technology has been developing very quickly in recent years. Distributed control of beam and plate structures have been widely studied over the years. Independent modal control of flexible rings using orthogonal convolving piezoelectric sensors and actuators was studied [1]. Distributed excitation and control of cylindrical shells with fully distributed actuator, partially distributed actuators, segmented actuator patches, line actuators, etc. were also investigated [2-4]. Modal control forces of arbitrary located, quarterly segmented piezoelectric actuators laminated on cylindrical shell panels were studied; modal actuation factor, modal feedback factor, and controlled damping ratio were derived and evaluated [5]. Thin cylindrical shells with various piezoelectric actuators were investigated [6,7]; spherical

shells with piezoceramic actuators were also studied [8-10]. Distributed sensing and control of conical shells and shell panels were evaluated [11]. Distributed modal voltages and their spatial strain characteristics of toroidal shells and spherical shells were recently investigated [12,13]. However, distributed sensing and control of other shells of revolution (e.g., paraboloidal, hyperboloidal, logarithmic shells) are scarce in open literatures. This study focuses on distributed control characteristics and design evaluation of distributed actuator patches laminated on of paraboloidal shells commonly used in high-precision aerospace and communication systems.

Distributed modal signals of linear and nonlinear paraboloidal shells were investigated [14]; micro-control characteristics of a deep paraboloidal shell were recently evaluated [15]. In this study, mathematical models of the paraboloidal shells laminated with distributed actuator layers subjected to mechanical, temperature, and control forces are presented first, followed by formulations of distributed actuation forces with their contributing micro-meridional/circumferential membrane and bending components. Studies of actuator induced forces, contributing micro-components, and normalized actuation authorities of a paraboloidal shell with two actuator sizes are carried out. Distributed modal control effects and detailed micro-electromechanics related to various geometric and design parameters are analyzed and general design guidelines are proposed.

MODELING OF PARABOLOIDAL SHELLS WITH DISTRIBUTED ACTUATORS

Assume a paraboloidal shell of revolution with a distributed actuator layer is exposed to mechanical, electric, and temperature excitations, Figure 1. (Note that the electric forces are the control force/moment resultants induced by the spatially distributed actuators.) For a paraboloidal shell of revolution, the radii of curvature are $R_\phi = b/\cos^3\phi$ and $R_\psi = b/\cos\phi$ derived from the fundamental radii of curvature equation of paraboloidal shells [16]. Here $b = a^2/(2c) = 2f$, “a” is the radial distance and “c” is the meridian height at the pole. The Lamé parameters are $A_1 = b/(\cos^3\phi)$ and $A_2 = (b\sin\phi)/(\cos\phi)$. Note that the focal length f of the paraboloidal shell is defined by $f = a^2/(4c)$.

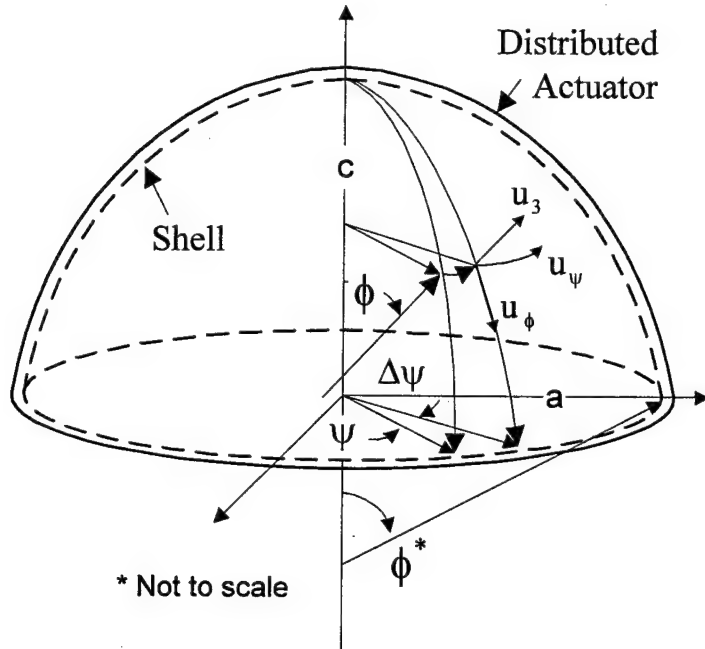


Fig.1 A paraboloidal shell of revolution laminated with distributed actuator.

Mathematical modeling of paraboloidal shells with spatially distributed actuators can be simplified from the system equation of a piezothermoelastic laminated shell system [17]. Note that 1) the shell is usually assumed thin and the in-plane displacements (in α_1 and α_2 direction) vary linearly through the shell thickness while the transverse displacement is independent of α_3 and 2) the transverse shear strains and the influence of rotary inertias are also neglected. Substituting $R_\phi = b/\cos^3 \phi$, $R_\psi = b/\cos \phi$, $A_1 = b/(\cos^3 \phi)$, $A_2 = (b \sin \phi)/(\cos \phi)$ defined for a paraboloidal shell of revolution into the generic composite shell system equations gives the paraboloidal shell system equations.

$$\frac{1}{\cos^3 \phi} \frac{\partial}{\partial \psi} (N_{\psi\phi}^m) + \frac{\partial}{\partial \phi} [(N_{\phi\phi}^m - N_{\phi\phi}^e - N_{\phi\phi}^\theta) \tan \phi] - (N_{\psi\psi}^m - N_{\psi\psi}^e - N_{\psi\psi}^\theta) \frac{1}{\cos^2 \phi} + Q_{\phi 3} \tan \phi + \frac{b \sin \phi}{\cos^4 \phi} q_\phi = \frac{b \sin \phi}{\cos^4 \phi} \rho h \frac{\partial^2 u_\phi}{\partial t^2}, \quad (1)$$

$$\frac{1}{\cos^3 \phi} \frac{\partial}{\partial \psi} (N_{\psi\psi}^m - N_{\psi\psi}^e - N_{\psi\psi}^\theta) + \frac{\partial}{\partial \phi} (N_{\phi\psi}^m \tan \phi) + N_{\psi\phi}^m \frac{1}{\cos^2 \phi} + \frac{\sin \phi}{\cos^3 \phi} Q_{\psi 3} + \frac{b \sin \phi}{\cos^4 \phi} q_\psi = \frac{b \sin \phi}{\cos^4 \phi} \rho h \frac{\partial^2 u_\psi}{\partial t^2}, \quad (2)$$

$$\frac{1}{\cos^3 \phi} \frac{\partial}{\partial \psi} (Q_{\psi 3}) + \frac{\partial}{\partial \phi} (Q_{\phi 3} \tan \phi) - (N_{\phi\phi}^m - N_{\phi\phi}^e - N_{\phi\phi}^\theta) \tan \phi - \frac{(N_{\psi\psi}^m - N_{\psi\psi}^e - N_{\psi\psi}^\theta) \sin \phi}{\cos^3 \phi} + q_3 \frac{b \sin \phi}{\cos^4 \phi} = \frac{b \sin \phi}{\cos^4 \phi} \rho h \frac{\partial^2 u_3}{\partial t^2}. \quad (3)$$

where N_{ij}^m and M_{ij}^m are the elastic forces and moments; N_{ij}^e and N_{ij}^θ are the electric and temperature induced forces; M_{ij}^e and M_{ij}^θ are the electric and temperature induced moments, respectively; $\phi\ddot{u}_i$ denotes the inertia force effect; ρ is the mass density; h is the shell thickness; q_i is the input force; and the superscripts m , e , and θ respectively denote the elastic (or mechanical), electric, and temperature induced components. The electric components are induced by external signals and often are used as control forces/moments in distributed control of shells. Note that actuator control signals resulting in N_{ij}^e are specifically manipulated such that N_{ij}^e counteracts the elastic and temperature forces. The transverse shear effects $Q_{\phi 3}$ and $Q_{\psi 3}$ are defined as

$$Q_{\phi 3} = \frac{\cos^4 \phi}{b \sin \phi} \left\{ \sec^3 \phi \frac{\partial}{\partial \psi} M_{\psi \phi}^m + \frac{\partial}{\partial \phi} [(M_{\phi \phi}^m - M_{\phi \phi}^e - M_{\phi \phi}^\theta) \tan \phi] \right. \\ \left. - (M_{\psi \psi}^m - M_{\psi \psi}^e - M_{\psi \psi}^\theta) \sec^2 \phi \right\}, \quad (4)$$

$$Q_{\psi 3} = \frac{\cos^4 \phi}{b \sin \phi} \left[\sec^3 \phi \frac{\partial}{\partial \psi} (M_{\psi \psi}^m - M_{\psi \psi}^e - M_{\psi \psi}^\theta) + \frac{\partial}{\partial \phi} (M_{\psi \phi}^m \tan \phi) \right. \\ \left. + M_{\psi \phi}^m \sec^2 \phi \right]. \quad (5)$$

The temperature variation is usually much slower as compared with the shell dynamics. Thus, although the temperature effect is included in the governing equations, it is not considered when evaluating resultant micro-control actions contributed by patch actuators. Applying the radii of curvature ($R_\phi = b/\cos^3 \phi$ and $R_\psi = b/\cos \phi$) and Lamé parameters ($A_1 = b/(\cos^3 \phi)$, $A_2 = (b \sin \phi)/(\cos \phi)$) to the basic mechanical (or elastic) force and moment expressions for shells of revolution [2] yields the exact explicit expressions of the elastic force and moment resultants for paraboloidal shells.

$$N_{\phi \phi}^m = \frac{K}{b} \left[\cos^3 \phi \frac{\partial u_\phi}{\partial \phi} + \mu \cot \phi \frac{\partial u_\psi}{\partial \psi} + \mu \frac{\cos^2 \phi}{\sin \phi} u_\phi + (\cos^3 \phi + \mu \cos \phi) u_3 \right], \quad (6)$$

$$N_{\psi \psi}^m = \frac{K}{b} \left[\cot \phi \frac{\partial u_\psi}{\partial \psi} + \frac{\cos^2 \phi}{\sin \phi} u_\phi + \mu \cos^3 \phi \frac{\partial u_\phi}{\partial \phi} + (\cos \phi + \mu \cos^3 \phi) u_3 \right], \quad (7)$$

$$M_{\phi \phi}^m = \frac{D}{b} \left[\cos^3 \phi \frac{\partial \beta_\phi}{\partial \phi} + \mu \cot \phi (\beta_\phi \cos \phi + \frac{\partial \beta_\psi}{\partial \psi}) \right], \quad (8)$$

$$M_{\psi \psi}^m = \frac{D}{b} \left[\cot \phi (\beta_\phi \cos \phi + \frac{\partial \beta_\psi}{\partial \psi}) + \mu \cos^3 \phi \frac{\partial \beta_\phi}{\partial \phi} \right]. \quad (9)$$

The rotation angles β_ϕ and β_ψ are also defined by induced displacements u_i : $\beta_\phi = (u_\phi - \partial u_3 / \partial \phi) / R_\phi$ and $\beta_\psi = (u_\psi \sin \phi - \partial u_3 / \partial \psi) / (R_\psi \sin \phi)$. The membrane stiffness K and the bending stiffness D are respectively defined as $K = Yh/(1-\mu^2)$ and

$D = Yh^3/[12(1-\mu^2)]$ and Y is the modulus of elasticity, μ is Poisson's ratio of the shell continuum. The actuator induced control forces/moment induced by the applied control signal ϕ^a in the spatially distributed actuator layer, Figure 1, are

$$N_{\phi\phi}^e = N_{\phi\phi}^a = d_{31} Y_p \phi^a, \text{ and } N_{\psi\psi}^e = N_{\psi\psi}^a = d_{32} Y_p \phi^a, \quad (10, 11)$$

$$M_{\phi\phi}^e = M_{\phi\phi}^a = r_\phi^a d_{31} Y_p \phi^a, \text{ and } M_{\psi\psi}^e = M_{\psi\psi}^a = r_\psi^a d_{32} Y_p \phi^a, \quad (12, 13)$$

where d_{3i} are the strain constants of the converse piezoelectric effect; Y_p is Young's modulus of the distributed actuator; ϕ^a (in *italic*) is the actuation/control signal; r_i^a are the moment arms measured from the shell neutral surface to the mid-plane of the distributed actuator. For uniform-thickness actuator and shell, $r_\phi^a = r_\psi^a$. The in-plane twisting (shear) effects are usually neglected, i.e., $N_{\phi\psi}^a \approx 0$ and $M_{\phi\psi}^a \approx 0$. The temperature variation is usually much slower as compared with the shell dynamics. Neglecting the temperature effect and considering the resultant elastic and control effect (i.e., $N_{\phi\phi} = K(s_{\phi\phi}^0 + \mu s_{\psi\psi}^0) - N_{\phi\phi}^e$, $N_{\psi\psi} = K(s_{\psi\psi}^0 + \mu s_{\phi\phi}^0) - N_{\psi\psi}^e$, $N_{\phi\psi} = N_{\psi\phi} = [K(1-\mu)/2]s_{\phi\psi}^0 - N_{\phi\psi}^e$, $M_{\phi\phi} = D(k_{\phi\phi} + \mu k_{\psi\psi}) - M_{\phi\phi}^e$, $M_{\psi\psi} = D(k_{\psi\psi} + \mu k_{\phi\phi}) - M_{\psi\psi}^e$, and $M_{\phi\psi} = M_{\psi\phi} = [D(1-\mu)/2]k_{\phi\psi} - M_{\phi\psi}^e$, where s_{ij}^0 and k_{ij} are the membrane strains and bending strains respectively), the total force/moment resultants, including actuator induced forces/moment, become

$$N_{\phi\phi} = N_{\phi\phi}^m - N_{\phi\phi}^e \\ = \frac{K}{b} [\cos^3 \phi \frac{\partial u_\phi}{\partial \phi} + \mu \cot \phi \frac{\partial u_\psi}{\partial \psi} + \mu \frac{\cos^2 \phi}{\sin \phi} u_\phi + (\cos^3 \phi + \mu \cos \phi) u_3] - d_{31} Y_p \phi^a, \quad (14)$$

$$N_{\psi\psi} = N_{\psi\psi}^m - N_{\psi\psi}^e \\ = \frac{K}{b} [\cot \phi \frac{\partial u_\psi}{\partial \psi} + \frac{\cos^2 \phi}{\sin \phi} u_\phi + \mu \cos^3 \phi \frac{\partial u_\phi}{\partial \phi} + (\cos \phi + \mu \cos^3 \phi) u_3] - d_{32} Y_p \phi^a; \quad (15)$$

$$M_{\phi\phi} = M_{\phi\phi}^m - M_{\phi\phi}^e \\ = \frac{D}{b} [\cos^3 \phi \frac{\partial \beta_\phi}{\partial \phi} + \mu \cot \phi (\beta_\phi \cos \phi + \frac{\partial \beta_\psi}{\partial \psi})] - r_\phi^a d_{31} Y_p \phi^a, \quad (16)$$

$$M_{\psi\psi} = M_{\psi\psi}^m - M_{\psi\psi}^e \\ = \frac{D}{b} [\cot \phi (\beta_\phi \cos \phi + \frac{\partial \beta_\psi}{\partial \psi}) + \mu \cos^3 \phi \frac{\partial \beta_\phi}{\partial \phi}] - r_\psi^a d_{32} Y_p \phi^a. \quad (17)$$

Analytical solution procedures of these shells of revolution are usually very complicated. Thus, although the closed-form system equations of paraboloidal shells are defined, evaluation of distributed control effect and micro-control actions is based on an assumed mode shape function [14] presented next. This mode shape function satisfies the shear-diaphragm boundary conditions and is verified by experimental data [15,18]. Furthermore, note that the temperature effect can be important in applications with significant temperature variations, such as space

structures. However, when evaluating resultant control actions solely contributed by patch actuators, the temperature influence is not considered in case studies.

ACTUATOR PLACEMENT AND ACTUATOR INDUCED CONTROL FORCES

Assume there is a segmented distributed actuator patch ranging from ϕ_1 to ϕ_2 and from ψ_1 to ψ_2 laminated on the shell of revolution, Figure 2. Spatial effects of actuator patches, modal characteristics, actuator induced resultant control forces/moments, and their micro-control actions (i.e., contributing meridional/circumferential membrane/bending components) are discussed in this section.

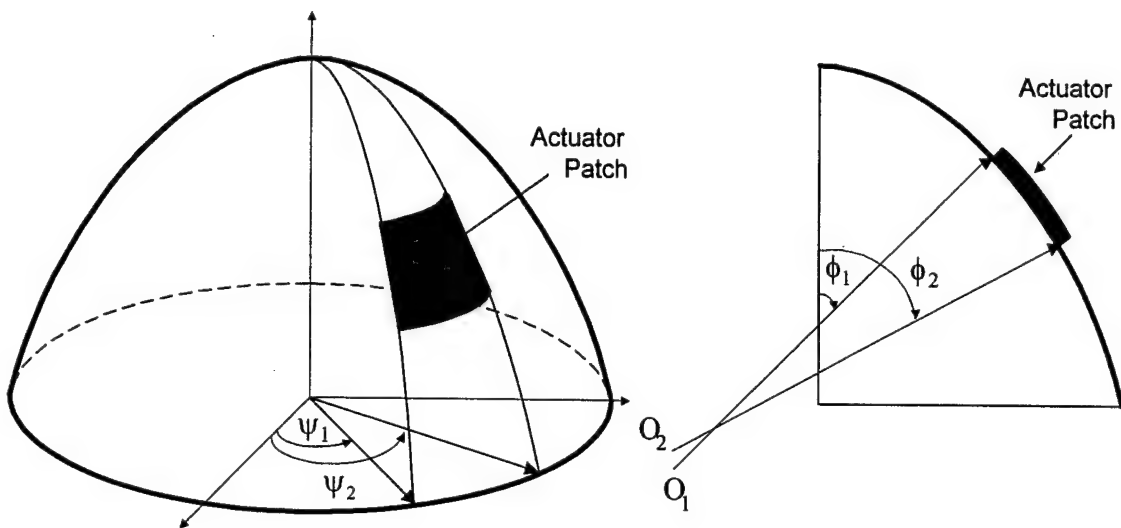


Fig.2 A segmented distributed actuator laminated on the paraboloidal shell.

Since the piezoelectric actuator patch is very thin and lightweight as compared with the elastic shell, material properties of the actuator layers are neglected in the shell system equations. The stiffness coefficients D (bending) and K (membrane) are defined based on the elastic paraboloidal shell only. Also, since the electric resistance on the actuator surface is negligible, the electric potential on the actuator surface is assumed uniformly distributed. Thus, the actuator control signal $\phi^a(\phi, \psi, t)$ is only confined on the actuator patch:

$$\phi^a(\phi, \psi, t) = \phi^a(t)[u_s(\phi - \phi_1) - u_s(\phi - \phi_2)][u_s(\psi - \psi_1) - u_s(\psi - \psi_2)], \quad (18)$$

where $u_s(\cdot)$ is the unit step function: $u_s(\phi - \phi_i) = 1$ when $\phi > \phi_i$, and = 0 when $\phi < \phi_i$, $\phi^a(t)$ is the actuator signal over the actuator patch and it is constant if remains time invariant. Recall that the Lamé parameters $A_1 = b/(\cos^3 \phi)$, $A_2 = (b \sin \phi)/(\cos \phi)$ and the radii of curvature $R_\phi = b/\cos^3 \phi$, $R_\psi = b/\cos \phi$ for paraboloidal shells of revolution. For a simply supported paraboloidal shell with axisymmetric oscillation, the transverse mode shape function can be

approximated by

$$U_{3m} = A_m \cos \frac{(2m-1)\pi}{2\phi^*} \phi = A_m \cos B_m \phi, \quad (19)$$

where A_m is the m -th modal amplitude; $B_m = [(2m-1)\pi]/(2\phi^*)$; ϕ is the meridional angle measure from the pole; ϕ varies from 0 (pole) to ϕ^* (boundary rim) for a shell with a closed apex. ψ defines the circumferential angle and ψ varies from 0 to 2π for a closed paraboloidal shell. Assume the total shell dynamic response is composed of all participating modes, i.e., $u_i(\alpha_1, \alpha_2, t) = \sum_{k=1}^{\infty} \eta_k(t) U_{ik}(\alpha_1, \alpha_2)$, where $\eta_k(t)$ is the k -th modal participating factor or the k -th modal coordinate; $U_{ik}(\alpha_1, \alpha_2)$ is the mode shape function. Also, assume there is no modal coupling and control spillover. Accordingly, the original distributed control equation can be transferred into the modal domain and individual modal control equations can be evaluated based on the mode shape function $U_{3m} = A_m \cos B_m \phi$ and the control actions resulting from distributed actuator patches.

$$\ddot{\eta}_m + \frac{c}{\rho h} \dot{\eta}_m + \omega_m^2 \eta_m = \hat{F}_m. \quad (20)$$

where c is the damping constant; ω_m is the m -th natural frequency. The modal control force \hat{F}_m of an actuator patch defined by ϕ_1 to ϕ_2 and ψ_1 to ψ_2 is given as

$$\begin{aligned} \hat{F}_m &= \frac{1}{\rho h N_m} \iint_{\psi} [L_3^c(\phi_3) U_{3m}] A_1 A_2 d\phi d\psi \\ &= \frac{1}{\rho h N_m} \int_{\phi_1}^{\phi_2} \int_{\psi_1}^{\psi_2} [L_3^c(\phi_3) U_{3m}] \frac{b^2 \sin \phi}{\cos^4 \phi} d\phi d\psi, \end{aligned} \quad (21)$$

where $N_m = \int_{\psi} \int_{\phi} U_{3m}^2 A_1 A_2 d\phi d\psi = \int_{\psi^*}^{\psi^*} \int_{\phi^*}^{\phi^*} (A_m^2 \cos^2 B_m \phi) \cdot \frac{b^2 \sin \phi}{\cos^4 \phi} d\phi d\psi = \psi^* A_m^2 b^2 \int_{\phi^*}^{\phi^*} \cos^2 B_m \phi \frac{\sin \phi}{\cos^4 \phi} d\phi$. ψ^* is the circumferential boundary angle and $\psi^* = 2\pi$ for a closed shell. For a paraboloidal shell of revolution with axisymmetric motion, the Love electric control operator $L_3^c(\phi_3)$ can be simplified and the actuator induced control force can be redefined accordingly.

$$\begin{aligned} L_3^c(\phi_3) &= -\frac{\cos^6 \phi}{b^2} \frac{\partial^2 M_{\phi\phi}^c}{\partial \phi^2} + \frac{\cos^5 \phi (3 \sin^2 \phi - 2)}{b^2 \sin \phi} \frac{\partial M_{\phi\phi}^c}{\partial \phi} + \frac{\cos^5 \phi}{b^2 \sin \phi} \frac{\partial M_{\psi\psi}^c}{\partial \phi} \\ &+ \frac{\cos^4 \phi}{b^2} (M_{\phi\phi}^c - M_{\psi\psi}^c) + \frac{\cos^3 \phi}{b} N_{\phi\phi}^c + \frac{\cos \phi}{b} N_{\psi\psi}^c. \end{aligned} \quad (22)$$

$$\begin{aligned}
\hat{F}_m = & \frac{1}{\rho h N_m} \int_{\phi_1}^{\phi_2} \int_{\psi_1}^{\psi_2} \left[-\frac{\cos^6 \phi}{b^2} \frac{\partial^2 M_{\phi\phi}^c}{\partial \phi^2} + \frac{\cos^5 \phi (3 \sin^2 \phi - 2)}{b^2 \sin \phi} \frac{\partial M_{\phi\phi}^c}{\partial \phi} \right. \\
& + \frac{\cos^5 \phi}{b^2 \sin \phi} \frac{\partial M_{\psi\psi}^c}{\partial \phi} + \frac{\cos^4 \phi}{b^2} (M_{\phi\phi}^c - M_{\psi\psi}^c) - \frac{\cos^2 \phi}{b^2 \sin^2 \phi} \frac{\partial^2 M_{\psi\psi}^c}{\partial \psi^2} \\
& \left. + \frac{\cos^3 \phi}{b} N_{\phi\phi}^c + \frac{\cos \phi}{b} N_{\psi\psi}^c \right] (A_m \cos B_m \phi) \frac{b^2 \sin \phi}{\cos^4 \phi} d\phi d\psi. \tag{23}
\end{aligned}$$

Note that a shape function $W(\phi, \psi)$ can be included in the integration for a generic actuator patch defined by the shaping function $W(\phi, \psi)$ [2]. Imposing the axisymmetric assumption, i.e., $\partial(\bullet)/\partial\psi = 0$, assuming the uniform-thickness actuator and shell, i.e., $r_\phi^a = r_\psi^a = r^a$, the hexagonal piezoelectric materials, i.e., $d_{31} = d_{32}$, substituting the actuator induced forces/momenta, one can write the modal control force for a generic actuator defined by a shape function $W(\phi, \psi)$ as

$$\begin{aligned}
\hat{F}_m = & \frac{Y_p d_{31}}{\rho h N_m} \int_{\phi_1}^{\phi_2} \int_{\psi_1}^{\psi_2} W(\phi, \psi) \left\{ r^a \left[-\frac{\cos^6 \phi}{b^2} \frac{\partial^2 \phi^a}{\partial \phi^2} + \frac{\cos^5 \phi (3 \sin^2 \phi - 2)}{b^2 \sin \phi} \frac{\partial \phi^a}{\partial \phi} + \frac{\cos^5 \phi}{b^2 \sin \phi} \frac{\partial \phi^a}{\partial \phi} \right] \right. \\
& + \frac{\cos^3 \phi}{b} \phi^a + \frac{\cos \phi}{b} \phi^a \} (A_m \cos B_m \phi) \frac{b^2 \sin \phi}{\cos^4 \phi} d\phi d\psi \\
= & \frac{Y_p d_{31} A_m}{\rho h N_m} \int_{\phi_1}^{\phi_2} \int_{\psi_1}^{\psi_2} W(\phi, \psi) \left\{ r^a \left[-\cos^5 \phi \frac{\partial^2 \phi^a}{\partial \phi^2} + \frac{\cos^4 \phi (3 \sin^2 \phi - 2)}{\sin \phi} \frac{\partial \phi^a}{\partial \phi} + \frac{\cos^4 \phi}{\sin \phi} \frac{\partial \phi^a}{\partial \phi} \right] \right. \\
& \left. + b \cos^2 \phi \phi^a + b \phi^a \right\} \frac{\cos B_m \phi \sin \phi}{\cos^3 \phi} d\phi d\psi. \tag{24}
\end{aligned}$$

The effective actuation force induced by the segmented distributed actuator patch defined by ϕ_1 to ϕ_2 and ψ_1 to ψ_2 becomes

$$\begin{aligned}
\hat{F}_m = & \frac{Y_p d_{31} A_m \phi^a(t)}{\rho h N_m} \\
& \cdot \int_{\phi_1}^{\phi_2} \int_{\psi_1}^{\psi_2} \left\{ r^a \left\{ -\cos^5 \phi [u_s(\psi - \psi_1) - u_s(\psi - \psi_2)] \frac{\partial}{\partial \phi} [\delta(\phi - \phi_1) - \delta(\phi - \phi_2)] \right. \right. \\
& + \frac{\cos^4 \phi (3 \sin^2 \phi - 2)}{\sin \phi} [\delta(\phi - \phi_1) - \delta(\phi - \phi_2)] [u_s(\psi - \psi_1) - u_s(\psi - \psi_2)] \\
& \left. \left. + \frac{\cos^4 \phi}{\sin \phi} [\delta(\phi - \phi_1) - \delta(\phi - \phi_2)] [u_s(\psi - \psi_1) - u_s(\psi - \psi_2)] \right\} \right. \\
& + b \cos^2 \phi [u_s(\phi - \phi_1) - u_s(\phi - \phi_2)] [u_s(\psi - \psi_1) - u_s(\psi - \psi_2)] \\
& \left. + b [u_s(\phi - \phi_1) - u_s(\phi - \phi_2)] [u_s(\psi - \psi_1) - u_s(\psi - \psi_2)] \right\} \cdot \frac{\cos B_m \phi \sin \phi}{\cos^3 \phi} d\phi d\psi. \tag{25}
\end{aligned}$$

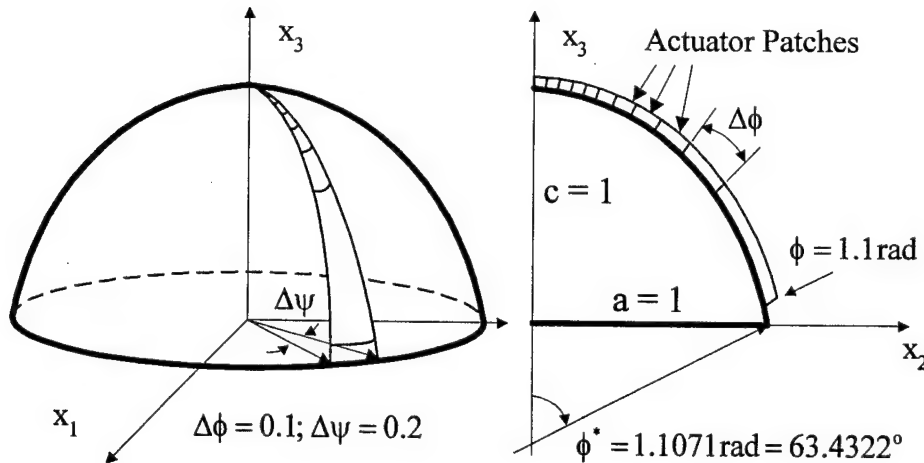
Note that solution of N_m is carried out based on the Taylor series expansion technique and the surface integration defined by the distributed actuator needs to be carried out to evaluate the modal control force. Furthermore, the above expression can be divided into its contributing micro-meridional/circumferential bending and membrane components – the **microscopic control actions**:

$$\begin{aligned}\hat{F}_m &= \frac{Y_p d_{31} A_m \phi^a(t)}{\rho} [(\hat{T}_m)_{\text{Total}}] \\ &= \frac{Y_p d_{31} A_m \phi^a(t)}{\rho} [(\hat{T}_m)_{\phi, \text{bend}} + (\hat{T}_m)_{\psi, \text{bend}} + (\hat{T}_m)_{\phi, \text{mem}} + (\hat{T}_m)_{\psi, \text{mem}}],\end{aligned}\quad (26)$$

where $(\hat{T}_m)_{\text{Total}}$ denotes the overall control effect, excluding the coefficients and modal parameters; $(\hat{T}_m)_{\phi, \text{bend}}$, $(\hat{T}_m)_{\psi, \text{bend}}$, $(\hat{T}_m)_{\phi, \text{mem}}$ and $(\hat{T}_m)_{\psi, \text{mem}}$ respectively denote the micro-control actions resulting from $M_{\phi\phi}^c$ - the actuator induced control moment in the ϕ direction, $M_{\psi\psi}^c$ - the control moment in the ψ direction, $N_{\phi\phi}^c$ - the actuator induced control force in the ϕ direction and $N_{\psi\psi}^c$ - the control force in the ψ direction. These individual contributing micro-control actions are evaluated in case studies. Note that surface integrations in the modal force expression are difficult to carry out exactly. Thus, the Taylor series expansion technique is used in the solution procedures.

EVALUATION OF CONTROL EFFECTIVENESS

Actuator induced modal control forces and microscopic meridional and circumferential contributing membrane/bending components induced by segmented distributed actuator patches laminated on a paraboloidal shell exhibiting axisymmetric oscillations were formulated previously. Modal control forces and contributing components, i.e., $(\hat{T}_m)_{\text{Total}}$, $(\hat{T}_m)_{\phi, \text{bend}}$, $(\hat{T}_m)_{\psi, \text{bend}}$, $(\hat{T}_m)_{\phi, \text{mem}}$, and $(\hat{T}_m)_{\psi, \text{mem}}$, of segmented actuator patches laminated on a thin paraboloidal shell (meridian/radius = $c/a = 1m/1m$, $\phi^* = 1.1071$ radians, and thickness $h = 0.002m$) are evaluated in this section. It is assumed that the actuator patch occupies an area from ϕ_1 to ϕ_2 and ψ_1 to ψ_2 as shown in Figure 3. Two actuator patch sizes: 1) $\Delta\phi = \phi_2 - \phi_1 = 0.1$ radians and 2) $\Delta\phi = \phi_2 - \phi_1 = 0.2$ radians defined in the meridional direction with a standard “angular width” $\Delta\psi = \psi_2 - \psi_1 = 0.2$ radians in the circumferential direction are evaluated. These segmented patches move from the pole ($\phi = 0$) toward the bottom rim ($\phi = \phi^*$) and their reference meridional center points are respectively at $\phi = 0.05$, 0.15 , 0.25 , 0.35 , 0.45 , 0.55 , 0.65 , 0.75 , 0.85 , 0.95 and 1.05 radian for $\Delta\phi = 0.1$ radian and $\phi = 0.1$, 0.3 , 0.5 , 0.7 and 0.9 radian for $\Delta\phi = 0.2$ radian. The actuator control authorities at each location are evaluated.



Radius $a = 1$, Meridian $c = 1$

Fig.3 The standard paraboloidal shell with segmented actuator patches.

Note that these patches do not exhibit uniform sizes because the radii of curvature are not constant. Accordingly, the projected actuator “arc-length” varies as it moves from the pole to the boundary rim, although $\Delta\phi$ is still constant. Modal control forces and contributing components, i.e., $(\hat{T}_m)_{\text{Total}}$, $(\hat{T}_m)_{\phi,\text{bend}}$, $(\hat{T}_m)_{\psi,\text{bend}}$, $(\hat{T}_m)_{\phi,\text{mem}}$, and $(\hat{T}_m)_{\psi,\text{mem}}$ for the first three modes of the two actuator sizes are evaluated, respectively. Again, the case presented in this study has the meridian/radius ratio $c/a=1/1$ with two patch sizes. Due to the axisymmetric property, the actuator location in the circumferential direction doesn't influence the micro-control actions for the same $\Delta\phi$ and $\Delta\psi$.

Patch 1 ($\Delta\phi = 0.1$; $\Delta\psi = 0.2$)

Patch-actuator Induced Control Forces

Modal control forces and their contributing microscopic meridional/circumferential membrane/bending components of Patch 1 are calculated. The first three modal control effects are plotted in Figures 4-6 where “Tm_Total” denotes $(\hat{T}_m)_{\text{Total}}$, “Tm_phi_bend” for $(\hat{T}_m)_{\phi,\text{bend}}$, “Tm_psi_bend” for $(\hat{T}_m)_{\psi,\text{bend}}$, “Tm_phi_mem” for $(\hat{T}_m)_{\phi,\text{mem}}$ and “Tm_psi_mem” for $(\hat{T}_m)_{\psi,\text{mem}}$. The horizontal axis denotes the projected diameter of the paraboloidal shell. Accordingly, these components are plotted with respect to the projected radial distance of the paraboloidal shell. Each data point represents the actuator control effects at a specific location. The horizontal location of the data point is the meridional center of each actuator patch. Thus, actuator induced modal control forces of these standard patches moving from the pole to the rim in the meridional direction can be clearly observed and evaluated in these figures.

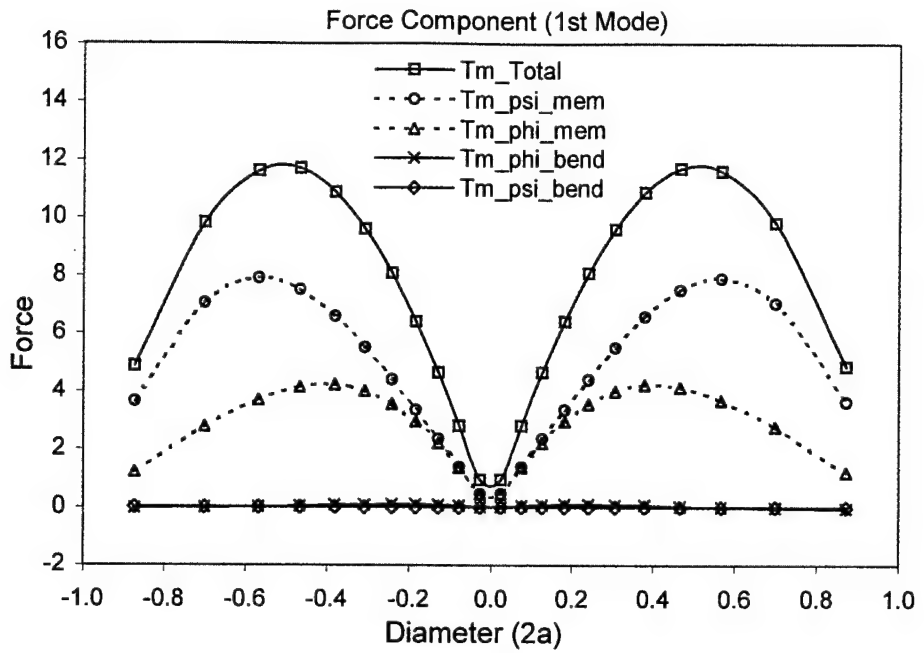


Fig.4 Modal control forces at various actuator locations, 1st mode, $\Delta\phi = 0.1$.
 (□: $(\hat{T}_m)_{Total}$, ○: $(\hat{T}_m)_{\psi,mem}$, Δ: $(\hat{T}_m)_{\phi,mem}$, ×: $(\hat{T}_m)_{\phi,bend}$, ◇: $(\hat{T}_m)_{\psi,bend}$)

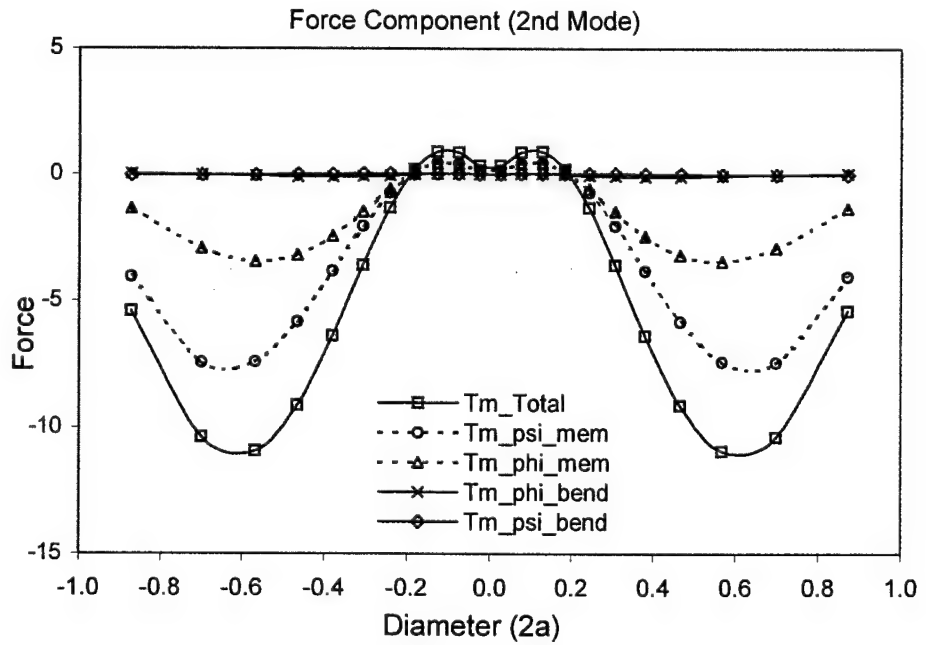


Fig.5 Modal control forces at various actuator locations, 2nd mode, $\Delta\phi = 0.1$.

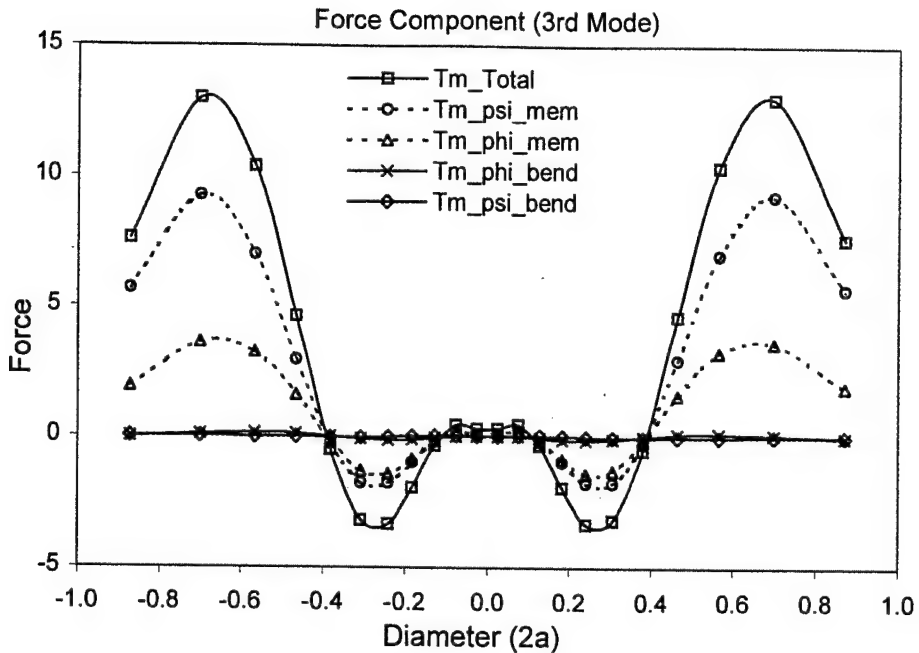


Fig.6 Modal control forces at various actuator locations, 3rd mode, $\Delta\phi = 0.1$.

In general, the actuator induced circumferential and meridional membrane control forces dominate the overall control effects and the bending (both meridional and circumferential) control moments are relatively insignificant. Resultant actuation effects depend on the patch locations and the mode shape variations. Note that there are positive and negative control forces induced by the actuator patch moving in the meridional direction on the shell surface. The positive forces induce positive actuation effects and the negative forces aggravate the shell vibrations when the positive actuation/control signals are used. However, since the sign of control signals can be manipulated in the control circuit, one should look at the “absolute” magnitudes to infer the “net” control effectiveness at these locations. Furthermore, these control effects (i.e., micro-meridional/circumferential membrane and bending effects) are calculated based on the modal force formulation derived in the previous section. These forces are symmetric due to the axisymmetric assumption of the mode shape function. Accordingly, these meridional and circumferential control force/moment effects only represent the global control effect, including the variations of actuator sizes. Modal control effects normalized with respect to the actuator size are evaluated next.

Normalized Actuation Authorities

Note that the projected patch length and width (arc length and width) increase as the standard actuator patch moves from the pole down to the rim, due to variations of shell curvature. Thus, the actuator patch size increases as it moves from the pole down to the boundary rim, although the “meridional angle” $\Delta\phi = 0.1$ radians and the “circumferential angle” $\Delta\psi = 0.2$ are constants. Figure 7 illustrates the “true” patch size variations defined at various shell surface locations. Apparently, the effective actuator size is the smallest at the pole and the largest near the rim, due to variations of projected arc lengths and widths. Accordingly, the actuator induced control forces/moment of the four contributing membrane/bending components need to be normalized (i.e., the total force divided by the actuator area), such that

the true actuation authorities per actuator area can be inferred. These normalized meridional/circumferential membrane and bending components of the first three paraboloidal shell modes are presented in Figures 8-10. Again, these quantities are plotted with respect to the actuator location in the projected radial direction – “radius” or “diameter”.

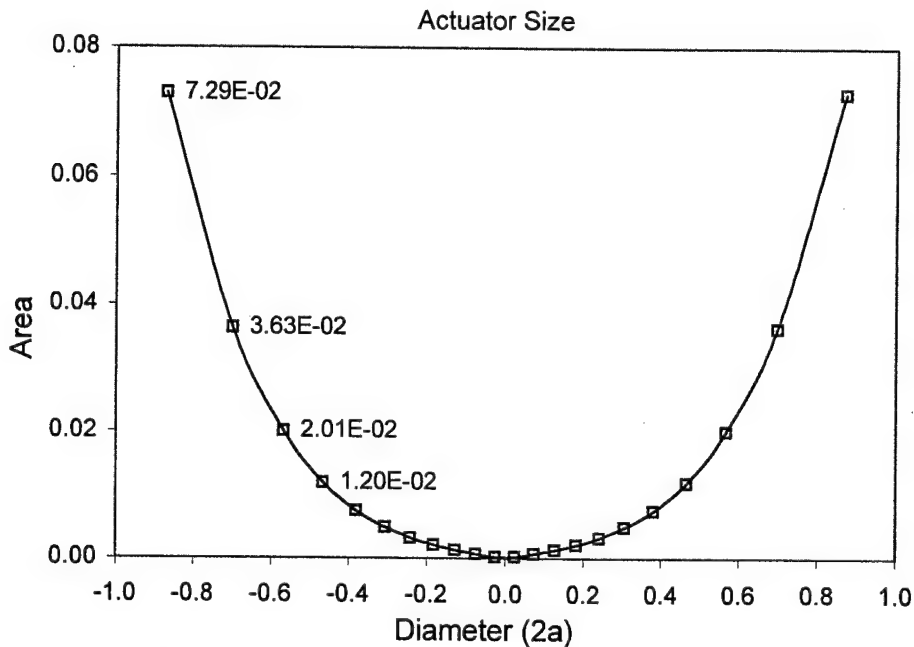


Fig.7 Effective actuator sizes at various patch locations, $\Delta\phi = 0.1$.

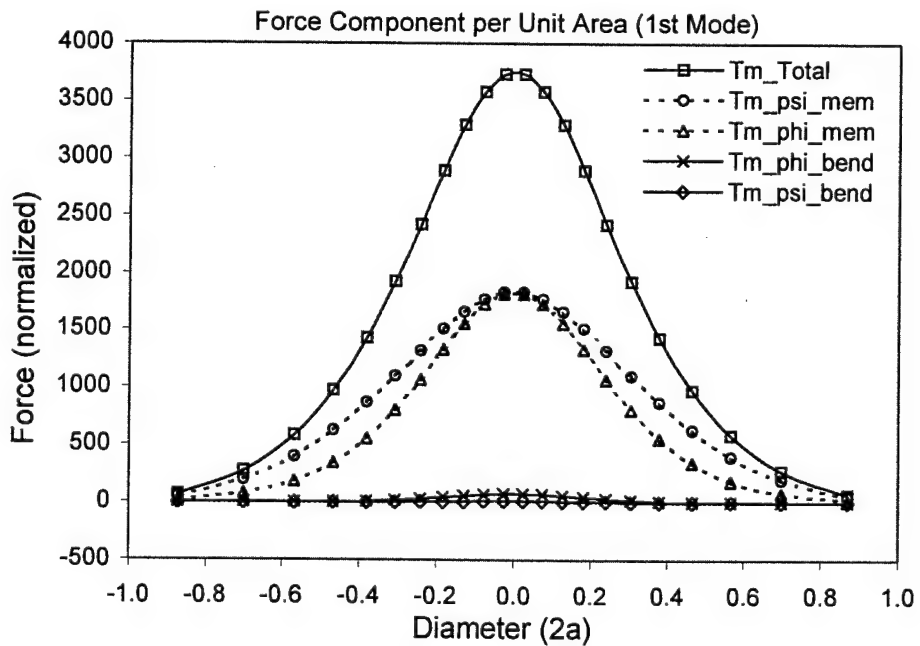


Fig.8 Normalized modal control forces at various locations, 1st mode, $\Delta\phi = 0.1$.

(□: $(\hat{T}_m)_{\text{Total}}$, ○: $(\hat{T}_m)_{\psi,\text{mem}}$, Δ: $(\hat{T}_m)_{\phi,\text{mem}}$, ×: $(\hat{T}_m)_{\phi,\text{bend}}$, ◇: $(\hat{T}_m)_{\psi,\text{bend}}$)

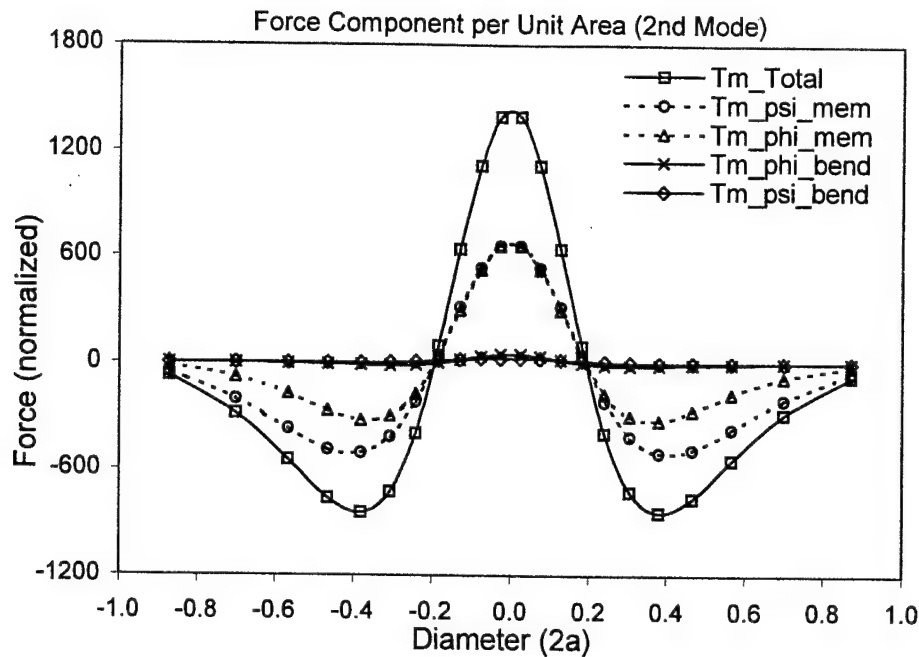


Fig.9 Normalized modal control forces at various locations, 2nd mode, $\Delta\phi = 0.1$.

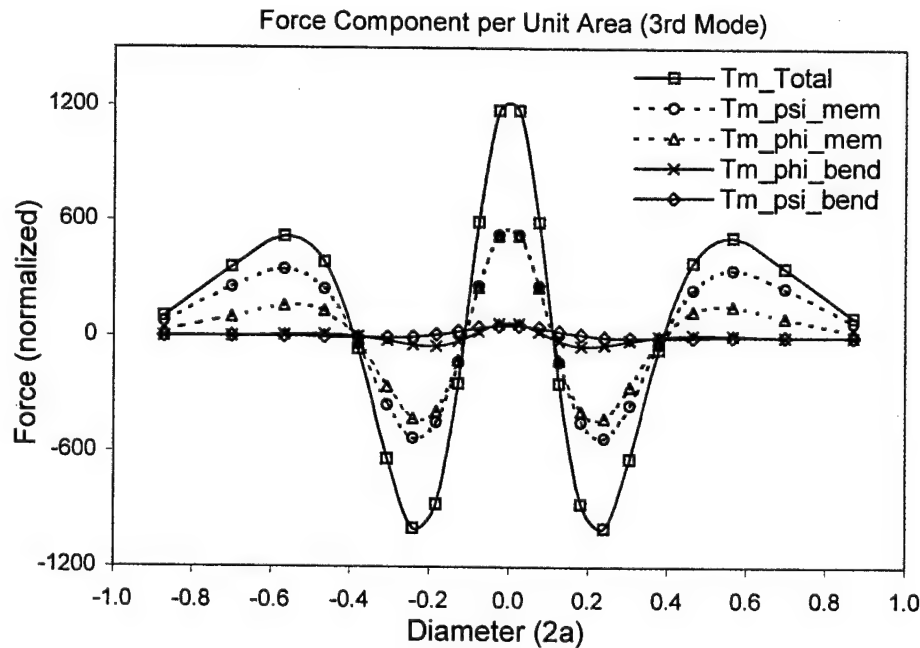


Fig.10 Normalized modal control forces at various locations, 3rd mode, $\Delta\phi = 0.1$.

Observing these plots suggests that the effective (normalized) control effects at various locations exhibit the distinct modal characteristics, although the dominating (membrane)

components still unchanged. The effective control effects are minimal when the actuators are at or near the modal lines and they are maximal at the maximal strain regions of axisymmetric modes. Following the same procedures of Patch 1 on a paraboloidal shell ($c/a=1/1$), patch-actuator induced control forces and normalized actuation authorities of Patch 2 ($\Delta\phi = 0.2$; $\Delta\psi = 0.2$) are studied next.

Patch 2 ($\Delta\phi = 0.2$; $\Delta\psi = 0.2$)

Patch-actuator Induced Control Forces

As discussed above, actuator induced control forces and their microscopic contributing components of Patch 2 ($\Delta\phi = 0.2$; $\Delta\psi = 0.2$) at various locations on the paraboloidal shell are evaluated in Figures 11-13; actuator sizes, the normalized actuation/control authorities and their modal characteristics of the first three natural modes are presented in Figures 14-17, respectively.

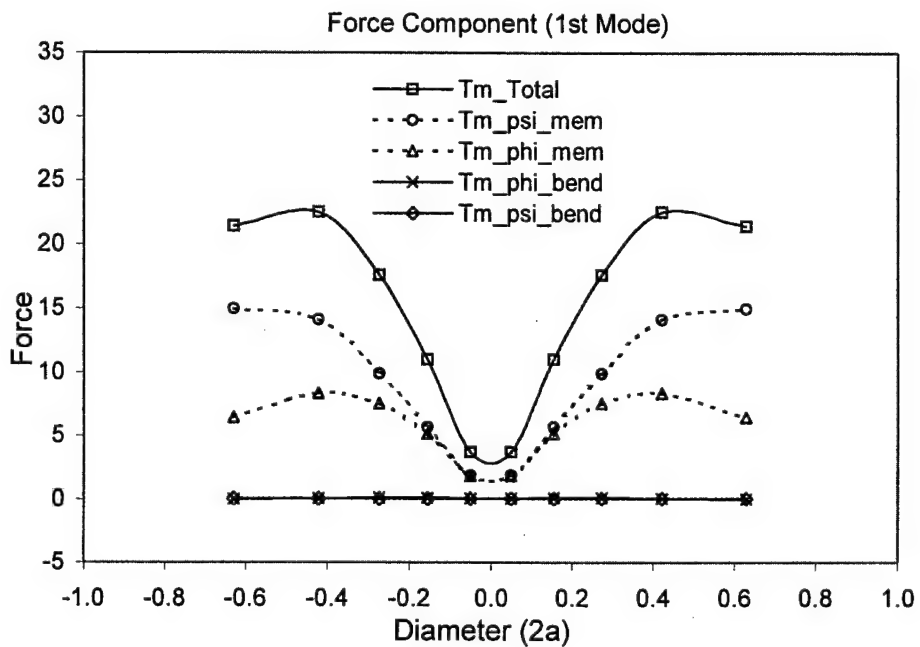


Fig.11 Modal control forces at various actuator locations, 1st mode, $\Delta\phi = 0.2$.

(□: $(\hat{T}_m)_{Total}$, ○: $(\hat{T}_m)_{\psi,mem}$, Δ: $(\hat{T}_m)_{\phi,mem}$, ×: $(\hat{T}_m)_{\phi,bend}$, ◇: $(\hat{T}_m)_{\psi,bend}$)

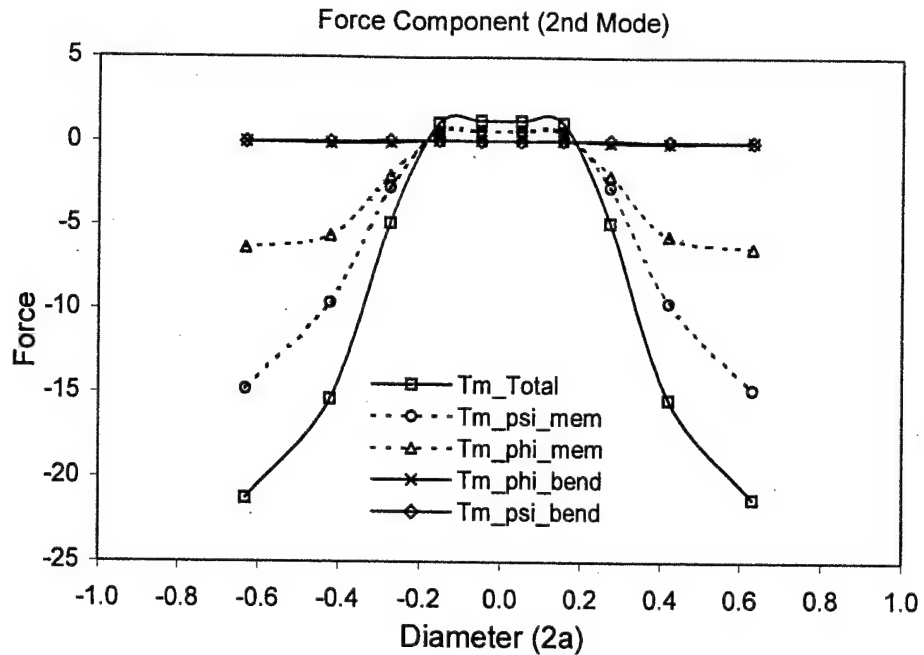


Fig.12 Modal control forces at various actuator locations, 2nd mode, $\Delta\phi = 0.2$.

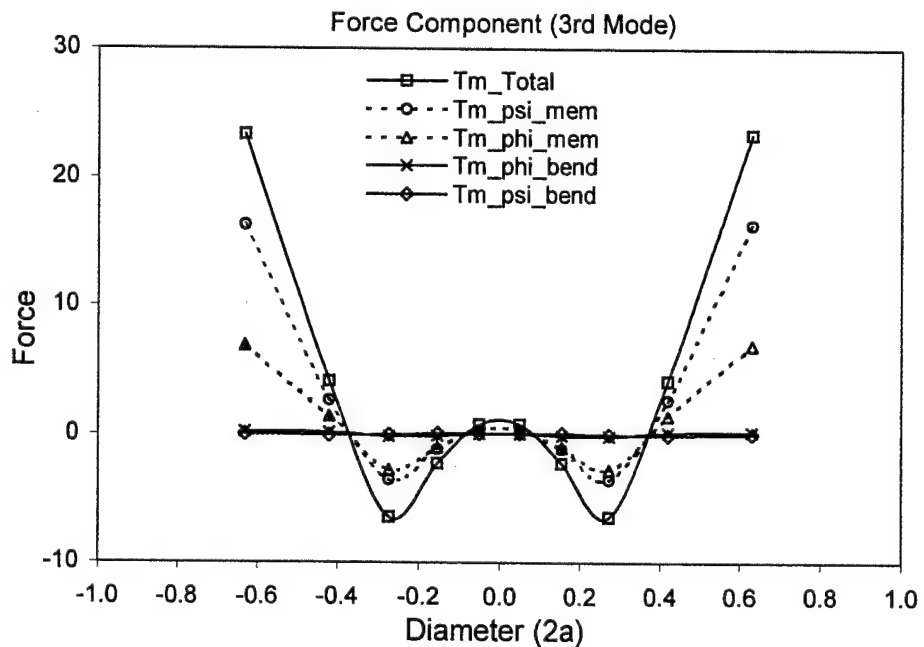


Fig.13 Modal control forces at various actuator locations, 3rd mode, $\Delta\phi = 0.2$.

Normalized Actuation Authorities

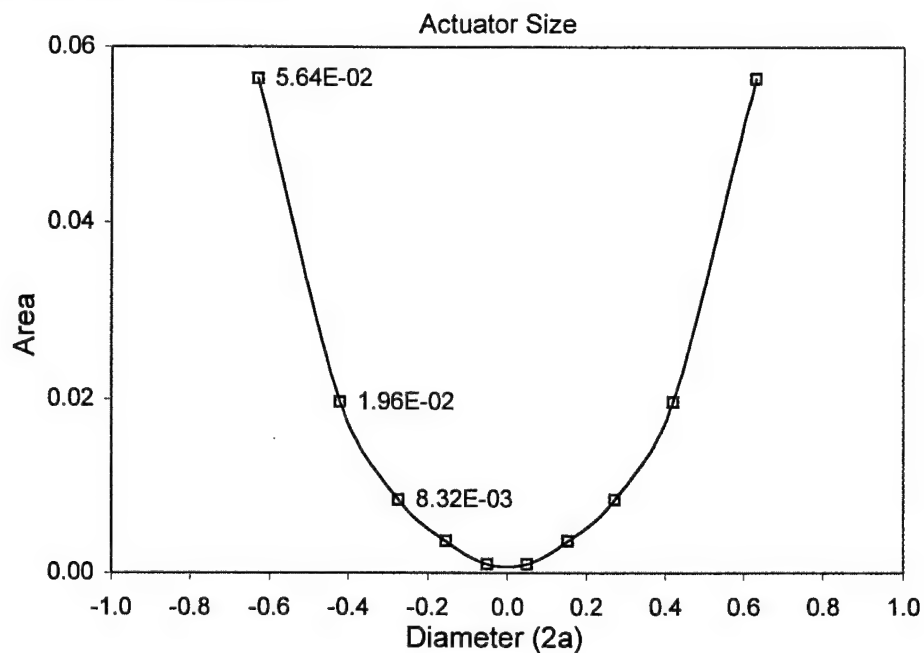


Fig.14 Effective actuator sizes at various patch locations, $\Delta\phi = 0.2$.

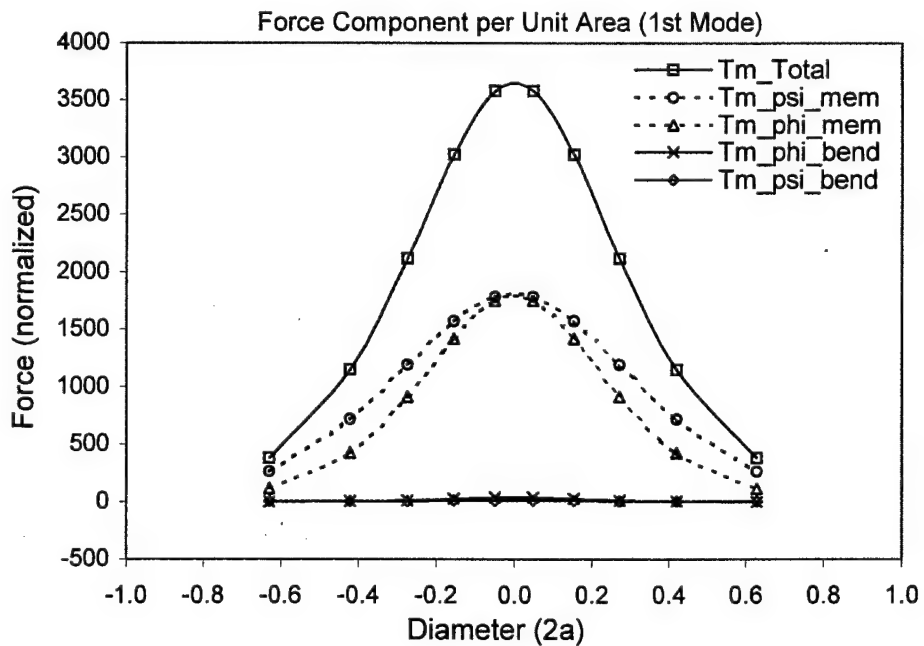


Fig.15 Normalized modal control forces at various locations, 1st mode, $\Delta\phi = 0.2$.

(\square : $(\hat{T}_m)_{\text{Total}}$, \circ : $(\hat{T}_m)_{\psi,\text{mem}}$, Δ : $(\hat{T}_m)_{\phi,\text{mem}}$, \times : $(\hat{T}_m)_{\phi,\text{bend}}$, \diamond : $(\hat{T}_m)_{\psi,\text{bend}}$)

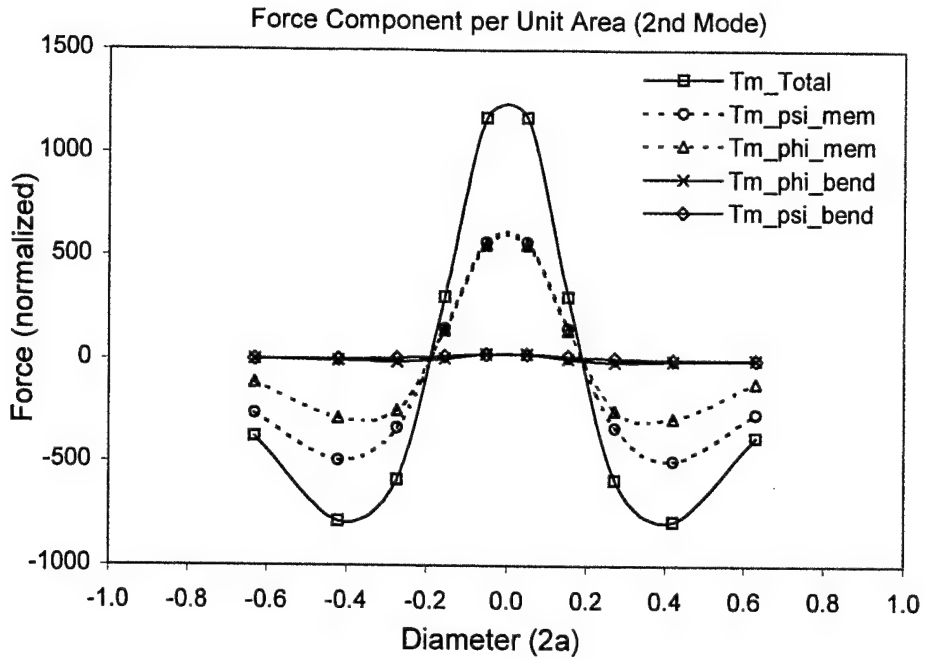


Fig.16 Normalized modal control forces at various locations, 2nd mode, $\Delta\phi = 0.2$.

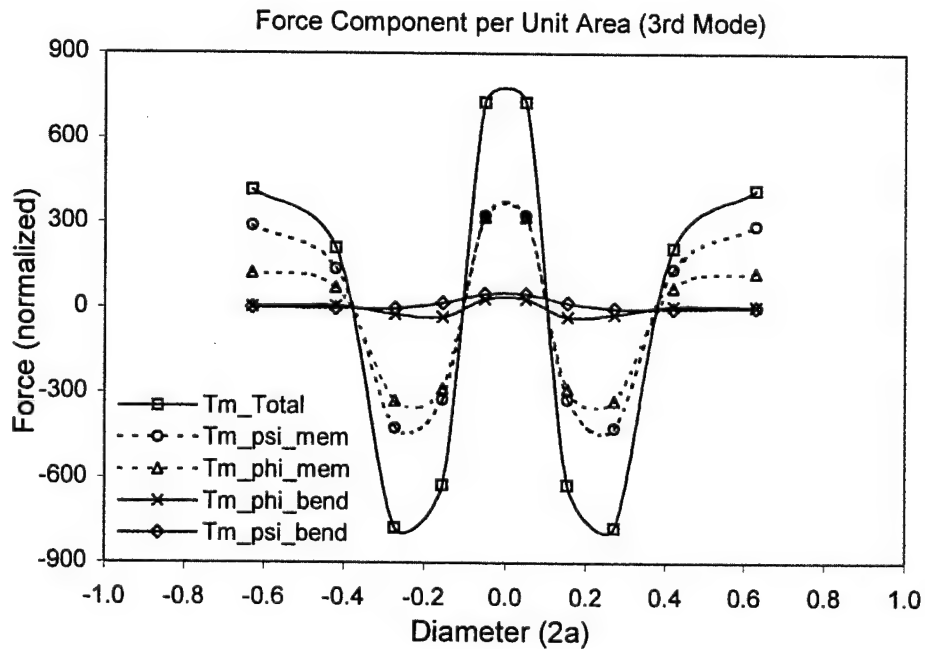


Fig.17 Normalized modal control forces at various locations, 3rd mode, $\Delta\phi = 0.2$.

These data suggest that although larger actuator size leads to larger actuation force, detailed microscopic actuation behavior disappears as the actuator increasing its size. The normalized actuation authority remains about the same as that of the small-patch configuration case.

DISCUSSION AND CONCLUSION

Paraboloidal shells of revolution are commonly used in reflectors, antennas, mirrors, etc. in communication systems, precision opto-mechanical systems, aerospace structures, etc. This study is to investigate the precision distributed control effectiveness of adaptive paraboloidal shells laminated with segmented actuator patches. Mathematical models of the paraboloidal shells laminated with distributed actuator layers subjected to mechanical, temperature, and control forces were presented first, followed by formulations of distributed actuator induced control forces with their micro-control actions (i.e., contributing meridional/circumferential membrane and bending control components). Studies of control forces, contributing components, and normalized control authorities were analyzed and evaluated. Patch-actuator induced distributed modal control forces and their micro-control actions (i.e., meridional/circumferential membrane and bending components) basically exhibit distinct modal characteristics influenced by shell geometries and other design parameters. Usually, these force magnitudes decrease as the mode number increases. Analysis data suggest that the membrane contributed transverse control components (i.e., the meridional and the circumferential membrane components) increase as the shell curvature increases, which are, in fact, the dominating actuation components in control of paraboloidal shells. The two (meridional and circumferential) bending contributed components are small and insignificant at low natural modes; however, they increase their influences as the mode number increases (i.e., high natural modes), the shell thickens, or the radius of curvature increases (i.e., shallow shells). It is also noticed that the patch-actuator induced modal control force is proportional to the width, i.e., the circumferential angle $\Delta\psi$, of the actuator patch, i.e., a wider $\Delta\psi$ leads to larger magnitudes of modal control forces.

Due to increased meridional and circumferential radii of curvature, the effective actuator size enlarges as the actuator patch moves from the pole to the boundary rim when $\Delta\phi$ and $\Delta\psi$ are kept constant. Accordingly, distributed actuator induced control forces and their contributing components were normalized with respect to the actuator size to provide the "true" actuation authorities per unit actuator area. Locations with larger normalized actuator forces indicate the areas with high control efficiencies, i.e., larger induced control force per unit actuator area. With limited actuators, placing actuators at those locations would lead to the maximal control effects; however, placing actuators at "zero" or "near-zero" locations would contribute to zero or the minimal control effects of given paraboloidal shells. The small patch configuration reveals more detailed microscopic local control effects. Thus, small-size actuator patches are recommended, if local microscopic control or control of higher natural modes is required. In summary, this study reveals many detailed patch-actuator induced micro-control actions, distributed control characteristics and control effectiveness of paraboloidal shells laminated with segmented actuator patches. Actuator placement related to targeted controlled vibration modes is a vital design issue for precision strucronic paraboloidal shell systems. These general guidelines can be applied to practical design applications.

ACKNOWLEDGEMENT

This research is supported, in part, by a grant (F49620-98-1-0467) from the Air Force Office of Scientific Research (Project Manager: Brian Sanders). This support is gratefully acknowledged.

REFERENCES

- [1] Tzou, H.S., Zhong, J.P., and Hollkamp, J.J., 1994, "Spatially Distributed Orthogonal Piezoelectric Shell Actuators (Theory and Applications)," *Journal of Sound and Vibration*, Vol.177, No.3, pp.363-378.
- [2] Tzou, H.S., 1993, *Piezoelectric Shells: Distributed Sensing and Control of Continua*, Kluwer Academic Publishers, Boston/Dordrecht.
- [3] Qiu, J. and Tani, J., 1995, "Vibration Control of a Cylindrical Shell Using Distributed Piezoelectric Sensors and Actuators," *Journal of Intelligent Material Systems and Structures*, Vol.6, No.4, July 1995, pp.474-481.
- [4] Faria, A.R., and Almeida, S. F. M., 1998, "Axisymmetric Actuation of Composite Cylindrical Thin Shells with Piezoelectric Rings," *Smart Materials and Structures*, Vol.7, No.6, pp.843-850.
- [5] Tzou, H.S., Bao, Y., and Venkayya, V.B., 1996, "Parametric Study of Segmented Transducers Laminated on Cylindrical Shells, Part 2. Actuator Patches," *Journal of Sound and Vibration*, Vol. 197, No.2, Oct. 1996, pp.225-249.
- [6] Banks, H.T., Smith R.C., and Wang, Y., 1996, *Smart Material Structure, Modeling, Estimation, and Control*, pp.40-44, John Wiley & Sons, Masson, Paris, 1996.
- [7] Saravanan, C., Ganesan, N., and Ramamurti, V., 2000, "Analysis of Active Damping in Composite Laminate Cylindrical Shells of Revolution with Skewed PVDF Sensors/Actuators," *Composite Structures*, Vol.48, No.4, Apr 2000, pp.305-318.
- [8] Jayachandran, V., and Sun, J. Q., 1998, "Modeling Shallow-spherical-shell Piezoceramic Actuators as Acoustic Boundary Control Elements," *Smart Materials and Structures*, Vol.7, No.1, pp.72-84.
- [9] Birman, V., Griffin, S., and Knowles, G., 2000, "Axisymmetric Dynamics of Composite Spherical Shells with Active Piezoelectric/Composite Stiffeners," *Acta Mechanica*, Vol.141, No.1, 2000, pp.71-83.
- [10] Ghaedi, S. K., and Misra, A. K., 1999, "Active Control of Shallow Spherical Shells Using Piezoceramic Sheets," *Proceedings of SPIE – The International Society for Optical Engineering*, v 3668 n II, Mar 1-4, 1999, pp.890-912.
- [11] Tzou, H.S., Wang, D.W., and Chai, W.K., 2002, "Dynamics and Distributed Control of Conical Shells Laminated with Full and Diagonal Actuators," *Journal of Sound and Vibration*. (To appear)
- [12] Tzou, H.S. and Wang, D.W., 2002, "Distributed Dynamic Signal Analysis of Piezoelectric Laminated Linear and Nonlinear Toroidal Shells," *Journal of Sound and Vibration*. (To appear)
- [13] Tzou, H.S., and Smithmaitrie, P., 2002, "Sensor Electromechanics and Distributed Signal Analysis of Piezo(electric)-Elastic Spherical Shells," *Mechanical Systems and Signal Processing*. (To appear)
- [14] Tzou, H.S. and Ding, J.H., 2001, "Distributed Modal Signals of Nonlinear Paraboloidal Shells with Distributed Neurons," Paper No.Vib.21545, 2001 Design Technical Conference, Pittsburgh, PA, Sept.9-12, 2001.
- [15] Tzou, H.S. Ding, J.H., and Hagiwara, I, 2002, "Micro-control Actions of Segmented Actuator Patches Laminated on Deep Paraboloidal Shells," *JSME International Journal*. (To appear)

[16] Mazurkiewicz, Z. E., and Nagorski, R. T., 1991, *Shells of Revolution*, PWN-Polish Scientific Publishers, Warsaw, pp.7-8.

[17] Tzou, H.S., and Bao, Y., 1997, "Nonlinear Piezothermoelasticity and Multi-Field Actuations, Part 1: Nonlinear Anisotropic Piezothermoelastic Shell Laminates," *ASME Transactions Journal of Vibration and Acoustics*, Vol.119, July 1997, pp.374-389.

[18] Glockner, P.G., and Tawardros, K.Z., 1973, "Experiments on Free Vibration of Shells of Revolution," *Experimental Mechanics*, Vol.13, No.10, Oct 1973, pp.411-421.
(ShlParaActPr_JDSMC2F.Ctrl.ShlParb)

CHAPTER 14

MICRO-CONTROL ACTIONS OF SEGMENTED ACTUATOR PATCHES LAMINATED ON DEEP PARABOLOIDAL SHELLS

ABSTRACT

Deep paraboloidal shells of revolution are common components for horns, nozzles, rocket fairings, etc. This study is to investigate the micro-control actions and distributed control effectiveness of precision deep paraboloidal shells laminated with segmented actuator patches. Mathematical models and governing equations of the paraboloidal shells laminated with distributed actuator layers segmented into patches are presented first, followed by formulations of distributed control forces and micro-control actions including meridional/circumferential membrane and bending control components based on an assumed mode shape function and the Taylor series expansion. Distributed control forces, patch sizes, actuator locations, micro-control actions, and normalized control authorities of a deep paraboloidal shell are analyzed in a case study. Analysis indicates that 1) the control forces and membrane/bending components are mode and location dependent, 2) the meridional/circumferential membrane control actions dominate the overall control effect, 3) there are optimal actuator locations resulting in the maximal control effects at the minimal control cost for each natural mode.

INTRODUCTION

There are many advanced paraboloidal shell structures and components used in civil, mechanical, and aerospace structures and systems, ranging from horns, nozzles, rocket fairings, solar collectors, communication antennas, optical mirrors, etc. Static and dynamic characteristics of paraboloidal shell structures have been investigated over the years (1-7). This study is to investigate the distributed control effectiveness and micro-control actions with respect to actuator locations of precision deep paraboloidal shells laminated with segmented actuator patches.

Distributed control of shell structures (or distributed elastic structural systems) based on the “smart structures and structronics” technology has been quickly developing for over a decade. Distributed control of one- and two-dimensional (1D and 2D) flat distributed systems (e.g., beams and plates) has been widely studied, so as rings (8). Distributed control of 2D curved distributed systems – shells – is more challenging, because of the coupled membrane/bending behavior and the in-plane/out-of-plane motions (9). Control of cylindrical shells with fully distributed actuator, partially distributed actuators, segmented actuator patches, line actuators, etc. were investigated (9,10); micro-electromechanics of segmented

actuators was also evaluated (11). Acoustics, vibration and distributed actuation of spherical shells were recently investigated (12-15). Distributed sensing and control of conical shells were evaluated (16), so the micro-sensing characteristics of toroidal shells (17). Distributed modal signals of linear and nonlinear paraboloidal shells were recently investigated (18). In this study, mathematical models of the paraboloidal shells laminated with distributed actuator layers segmented into patches are defined first, followed by formulations of distributed control forces and detailed membrane/bending micro-control actions. Distributed actuator control forces and control authorities at various actuator locations on a deep paraboloidal shell are investigated. Distributed modal control effects and micro- meridional/circumferential membrane/bending control actions are evaluated and general design guidelines are proposed.

SYSTEM MODEL AND DISTRIBUTED ACTUATION

A generic paraboloidal shell of revolution defined in a tri-orthogonal coordinate system is shown in **Figure 1**, where $\alpha_1 = \phi$ and $\alpha_2 = \psi$, a meridional radius of curvature $R_1 = R_\phi = b/\cos^3 \phi$, a circumferential radius of curvature $R_2 = R_\psi = b/\cos \phi$ and the constant $b = a^2/(2c) = 2f$ where “a” is the radial distance, “c” is the meridian height at the pole, and “f” is the focal length. The Lamé parameters are $A_1 = b/(\cos^3 \phi)$ and $A_2 = (b \sin \phi)/(\cos \phi)$. The parabola equation is given as $z = z(r) = c[1 - (\frac{r}{a})^2]$, where “z” is the vertical rise and “r” is the horizontal radius.

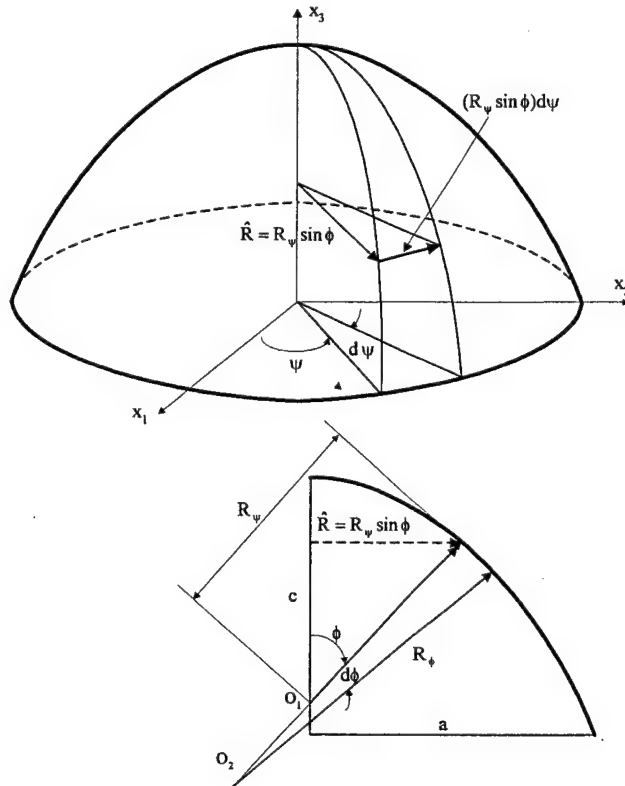


Fig.1 A generic paraboloidal shell of revolution and a part of its cross-section.

Assume a thin distributed actuator layer is laminated on the paraboloidal shell of revolution, which induces control forces/moment leading to precision control of the paraboloidal shell. **Figure 2** illustrates a deep paraboloidal shell laminated with a distributed actuator layer segmented into actuator patches. Since the layer is thin, the mass and stiffness properties can be neglected and only the control actions are considered. Mathematical models are defined first, followed by micro-control actions and their control effectiveness.

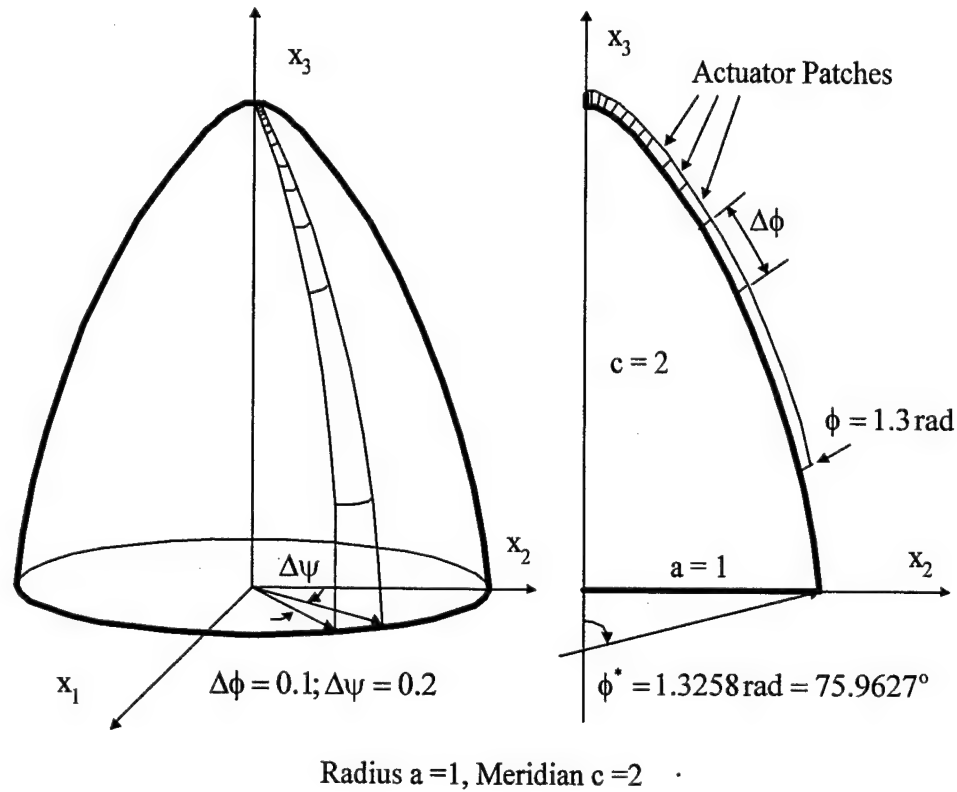


Fig.2 Segmented distributed actuators laminated on a deep paraboloidal shell.

Mathematical model of paraboloidal shells with spatially distributed actuators can be simplified from the system equations of a piezothermoelastic shell laminate system (19) and is derived as follows.

$$\frac{1}{\cos^3 \phi} \frac{\partial}{\partial \psi} (N_{\psi\phi}^m) + \frac{\partial}{\partial \phi} [(N_{\phi\phi}^m - N_{\phi\phi}^e) \tan \phi] \quad (1)$$

$$- (N_{\psi\psi}^m - N_{\psi\psi}^e) \frac{1}{\cos^2 \phi} + Q_{\phi 3} \tan \phi + \frac{b \sin \phi}{\cos^4 \phi} q_\phi = \frac{b \sin \phi}{\cos^4 \phi} \rho h \frac{\partial^2 u_\phi}{\partial t^2},$$

$$\frac{1}{\cos^3 \phi} \frac{\partial}{\partial \psi} (N_{\psi\psi}^m - N_{\psi\psi}^e) + \frac{\partial}{\partial \phi} (N_{\phi\psi}^m \tan \phi) + N_{\psi\phi}^m \frac{1}{\cos^2 \phi} \quad (2)$$

$$+ \frac{\sin \phi}{\cos^3 \phi} Q_{\psi 3} + \frac{b \sin \phi}{\cos^4 \phi} q_\psi = \frac{b \sin \phi}{\cos^4 \phi} \rho h \frac{\partial^2 u_\psi}{\partial t^2},$$

$$\begin{aligned}
& \frac{\cos\phi}{b\sin\phi} \frac{\partial}{\partial\psi} \left[\sec^3\phi \frac{\partial}{\partial\psi} (M_{\psi\psi}^m - M_{\psi\psi}^e) + \frac{\partial}{\partial\phi} (M_{\psi\phi}^m \tan\phi) + M_{\psi\phi}^m \sec^2\phi \right] \\
& + \frac{1}{b} \frac{\partial}{\partial\phi} \left\{ \frac{\partial}{\partial\psi} M_{\psi\phi}^m + \cos^3\phi \frac{\partial}{\partial\phi} \left[(M_{\phi\phi}^m - M_{\phi\phi}^e) \tan\phi \right] - (M_{\psi\psi}^m - M_{\psi\psi}^e) \cos\phi \right\} \\
& - (N_{\phi\phi}^m - N_{\phi\phi}^e) \tan\phi - (N_{\psi\psi}^m - N_{\psi\psi}^e) \frac{\sin\phi}{\cos^3\phi} + q_3 \frac{b\sin\phi}{\cos^4\phi} \rho h \frac{\partial^2 u_3}{\partial t^2},
\end{aligned} \tag{3}$$

where N_{ij}^m and M_{ij}^m are the elastic forces and moments; N_{ij}^e and M_{ij}^e are the electric control forces and moments, respectively; $\rho h \cdot \partial^2 u_i / \partial t^2$ denotes the inertia force effect; ρ is the mass density; h is the shell thickness; q_i is the input force; $Q_{\phi 3}$ and $Q_{\psi 3}$ are the transverse shear effects; and the superscripts "m" and "e" respectively denote the elastic (or mechanical) and electrically induced components. (Note that "e" is changed to "a" when the actuator forces are explicitly defined in later sections.) The elastic force and moment resultants of thin paraboloidal shells following the Love-Kirchoff thin shell assumptions are defined as

$$N_{\phi\phi}^m = \frac{K}{b} \left[\cos^3\phi \frac{\partial u_\phi}{\partial\phi} + \mu \cot\phi \frac{\partial u_\psi}{\partial\psi} + \mu \frac{\cos^2\phi}{\sin\phi} u_\phi + (\cos^3\phi + \mu \cos\phi) u_3 \right], \tag{4}$$

$$N_{\psi\psi}^m = \frac{K}{b} \left[\cot\phi \frac{\partial u_\psi}{\partial\psi} + \frac{\cos^2\phi}{\sin\phi} u_\phi + \mu \cos^3\phi \frac{\partial u_\phi}{\partial\phi} + (\cos\phi + \mu \cos^3\phi) u_3 \right], \tag{5}$$

$$N_{\phi\psi}^m = \frac{K(1-\mu)}{2b} \left[-\frac{\cos^2\phi}{\sin\phi} u_\psi + \cos^3\phi \frac{\partial u_\psi}{\partial\phi} + \frac{\cos\phi}{\sin\phi} \frac{\partial u_\phi}{\partial\psi} \right], \tag{6}$$

$$\begin{aligned}
M_{\phi\phi}^m = & \frac{D}{b^2} \left\{ \cos^6\phi \left(\frac{\partial u_\phi}{\partial\phi} - \frac{\partial^2 u_3}{\partial\phi^2} \right) - 3 \cos^5\phi \sin\phi \left(u_\phi - \frac{\partial u_3}{\partial\phi} \right) \right. \\
& \left. + \mu \frac{\cos^2\phi}{\sin\phi} \left(\frac{\partial u_\psi}{\partial\psi} - \frac{1}{\sin\phi} \frac{\partial^2 u_3}{\partial\psi^2} + u_\phi \cos^3\phi - \cos^3\phi \frac{\partial u_3}{\partial\phi} \right) \right\}, \tag{7}
\end{aligned}$$

$$\begin{aligned}
M_{\psi\psi}^m = & \frac{D}{b^2} \left\{ \frac{\cos^2\phi}{\sin\phi} \left(\frac{\partial u_\psi}{\partial\psi} - \frac{1}{\sin\phi} \frac{\partial^2 u_3}{\partial\psi^2} + u_\phi \cos^3\phi - \cos^3\phi \frac{\partial u_3}{\partial\phi} \right) \right. \\
& \left. + \mu \left[\cos^6\phi \left(\frac{\partial u_\phi}{\partial\phi} - \frac{\partial^2 u_3}{\partial\phi^2} \right) - 3 \cos^5\phi \sin\phi \left(u_\phi - \frac{\partial u_3}{\partial\phi} \right) \right] \right\}, \tag{8}
\end{aligned}$$

$$\begin{aligned}
M_{\phi\psi}^m = & \frac{D(1-\mu)}{2} \left(-\frac{\cos^5\phi + 2 \cos^3\phi \sin^2\phi}{b^2 \sin\phi} u_\psi + \frac{2 \cos^3\phi}{b^2 \sin^2\phi} \frac{\partial u_3}{\partial\psi} \right. \\
& \left. - \frac{2 \cos^4\phi}{b^2 \sin\phi} \frac{\partial^2 u_3}{\partial\psi\partial\phi} + \frac{\cos^4\phi}{b^2} \frac{\partial u_\psi}{\partial\phi} + \frac{\cos^4\phi}{b^2 \sin\phi} \frac{\partial u_\phi}{\partial\psi} \right) \tag{9}
\end{aligned}$$

The membrane stiffness $K = Yh/(1-\mu^2)$ and the bending stiffness $D = Yh^3/[12(1-\mu^2)]$, where Y is the modulus of elasticity and μ is Poisson's ratio of the shell. The control forces/moment induced by the applied control signal ϕ^a in the spatially distributed actuator layer are

$$N_{\phi\phi}^e = N_{\phi\phi}^a = d_{31} Y_p \phi^a, \quad N_{\psi\psi}^e = N_{\psi\psi}^a = d_{32} Y_p \phi^a, \quad (10,11)$$

$$M_{\phi\phi}^e = M_{\phi\phi}^a = r_\phi^a d_{31} Y_p \phi^a, \quad M_{\psi\psi}^e = M_{\psi\psi}^a = r_\psi^a d_{32} Y_p \phi^a, \quad (12,13)$$

where d_{3i} are the strain constants of the converse piezoelectric effect; Y_p is Young's modulus of the distributed actuator; ϕ^a (in *italic*) is the control signal; r_i^a are the moment arms measured from the shell neutral surface to the mid-plane of the distributed actuator. The in-plane twisting (shear) effects are usually neglected, i.e., $N_{\phi\psi}^a \approx 0$ and $M_{\phi\psi}^a \approx 0$, for conventional hexagonal piezoelectric materials. Since the electric resistance on the actuator surface is negligible, the electric potential on the actuator surface is assumed constant and separated by patch divisions. Thus, the transverse control signal $\phi^a(\phi, \psi, t)$ is only confined on the segmented actuator patch electrode ranging from ϕ_1 to ϕ_2 and from ψ_1 to ψ_2 , Figure 2.

$$\phi^a(\phi, \psi, t) = \phi^a(t)[u_s(\phi - \phi_1) - u_s(\phi - \phi_2)][u_s(\psi - \psi_1) - u_s(\psi - \psi_2)], \quad (14)$$

where $u_s(\cdot)$ is the unit step function: $u_s(\phi - \phi_i) = 1$ when $\phi > \phi_i$, and = 0 when $\phi < \phi_i$. For uniform-thickness actuator and shell, $r_\phi^a = r_\psi^a$. Again, the in-plane twisting control effects are usually not considered, i.e., $N_{\phi\psi}^a \approx 0$ and $M_{\phi\psi}^a \approx 0$. Considering the resultant elastic and control effects (i.e., $N_{\phi\phi} = K(s_{\phi\phi}^o + \mu s_{\psi\psi}^o) - N_{\phi\phi}^e$, $N_{\psi\psi} = K(s_{\psi\psi}^o + \mu s_{\phi\phi}^o) - N_{\psi\psi}^e$, $N_{\phi\psi} = N_{\psi\phi} = [K(1-\mu)/2]s_{\phi\psi}^o - N_{\phi\psi}^e$, $M_{\phi\phi} = D(k_{\phi\phi} + \mu k_{\psi\psi}) - M_{\phi\phi}^e$, $M_{\psi\psi} = D(k_{\psi\psi} + \mu k_{\phi\phi}) - M_{\psi\psi}^e$, and $M_{\phi\psi} = M_{\psi\phi} = [D(1-\mu)/2]k_{\phi\psi} - M_{\phi\psi}^e$, where s_{ij}^o and k_{ij} are the membrane strains and bending strains respectively), one can re-define the total force/moment resultants, including control forces/moments and the elastic components. Accordingly, combining the inherent elastic components $N_{\phi\psi}^m$ and $N_{\psi\phi}^m$ and the control components induced by actuator patches ranging from ϕ_1 to ϕ_2 and from ψ_1 to ψ_2 yields

$$N_{\phi\phi} = \frac{K}{b} [\cos^3 \phi \frac{\partial u_\phi}{\partial \phi} + \mu \cot \phi \frac{\partial u_\psi}{\partial \psi} + \mu \frac{\cos^2 \phi}{\sin \phi} u_\phi + (\cos^3 \phi + \mu \cos \phi) u_3] - d_{31} Y_p \phi^a, \quad (15)$$

$$N_{\psi\psi} = \frac{K}{b} [\cot \phi \frac{\partial u_\psi}{\partial \psi} + \frac{\cos^2 \phi}{\sin \phi} u_\phi + \mu \cos^3 \phi \frac{\partial u_\phi}{\partial \phi} + (\cos \phi + \mu \cos^3 \phi) u_3] - d_{32} Y_p \phi^a; \quad (16)$$

$$M_{\phi\phi} = \frac{D}{b^2} \{ \cos^6 \phi \left(\frac{\partial u_\phi}{\partial \phi} - \frac{\partial^2 u_3}{\partial \phi^2} \right) - 3 \cos^5 \phi \sin \phi \left(u_\phi - \frac{\partial u_3}{\partial \phi} \right) + \mu \frac{\cos^2 \phi}{\sin \phi} \left(\frac{\partial u_\psi}{\partial \psi} - \frac{1}{\sin \phi} \frac{\partial^2 u_3}{\partial \psi^2} + u_\phi \cos^3 \phi - \cos^3 \phi \frac{\partial u_3}{\partial \phi} \right) \} - r_\phi^a d_{31} Y_p \phi^a, \quad (17)$$

$$\begin{aligned}
M_{\psi\psi} = & \frac{D}{b^2} \left\{ \frac{\cos^2 \phi}{\sin \phi} \left(\frac{\partial u_\psi}{\partial \psi} - \frac{1}{\sin \phi} \frac{\partial^2 u_3}{\partial \psi^2} + u_\phi \cos^3 \phi - \cos^3 \phi \frac{\partial u_3}{\partial \phi} \right) \right. \\
& \left. + \mu \left[\cos^6 \phi \left(\frac{\partial u_\phi}{\partial \phi} - \frac{\partial^2 u_3}{\partial \phi^2} \right) - 3 \cos^5 \phi \sin \phi \left(u_\phi - \frac{\partial u_3}{\partial \phi} \right) \right] \right\} - r_\psi^a d_{32} Y_p \phi^a
\end{aligned} \tag{18}$$

Note that although the analytical system equations of paraboloidal shells are defined, evaluation of distributed micro-control effects is based on an assumed solution satisfying the given boundary conditions in later analyses, due to complicated analytical solution procedures of the paraboloidal shells of revolution.

DISTRIBUTED MICRO-CONTROL ACTIONS

Assume the shell dynamic response is composed of all participating modes, i.e., the modal expansion method: $u_i(\alpha_1, \alpha_2, t) = \sum_{m=1}^{\infty} \eta_m(t) U_{im}(\alpha_1, \alpha_2)$, where $\eta_m(t)$ is the m-th modal participating factor or the m-th modal coordinate and $U_{im}(\alpha_1, \alpha_2)$ is the mode shape function. Accordingly, the original distributed control equation can be transferred into the modal domain and individual modal control equations can be evaluated based on the mode shape functions and the distributed actuator patch defined from ϕ_1 to ϕ_2 and from ψ_1 to ψ_2 . The displacement and the moment on the boundary perimeter are assumed zero for a simply supported paraboloidal shell structure. Also, since the transverse axisymmetric oscillation dominates, the transverse mode shape function U_{3m} can be approximated by

$$U_{3m} = A_m \cos \frac{(2m-1)\pi}{2\phi^*} \phi = A_m \cos B_m \phi, \quad m = 1, 2, \dots, \infty \tag{19}$$

where A_m is the m-th modal amplitude; $B_m = [(2m-1)\pi]/(2\phi^*)$; ϕ is the meridional angle measured from the pole ($\phi = 0$) to the shell boundary rim at $\phi = \phi^*$. Accordingly, the modal control equation becomes

$$\ddot{\eta}_m + \frac{c}{\rho h} \dot{\eta}_m + \omega_m^2 \eta_m = \hat{F}_m, \tag{20}$$

where c is the damping constant; ω_m is the m-th natural frequency; and \hat{F}_m is the distributed modal control force. Imposing the axisymmetric assumption, i.e., $\partial(\bullet)/\partial\psi = 0$, assuming the uniform-thickness actuator and shell, i.e., $r_\phi^a = r_\psi^a = r^a$, the hexagonal piezoelectric materials, i.e., $d_{31} = d_{32}$, and substituting the control forces/moments, one can define the modal control force induced by the segmented distributed actuator defined by ϕ_1 to ϕ_2 and ψ_1 to ψ_2 .

$$\begin{aligned}
\hat{F}_m = & \frac{Y_p d_{31} A_m \phi^a(t)}{\rho h N_m} \\
& \cdot \int_{\phi_1}^{\phi_2} \int_{\psi_1}^{\psi_2} \left\{ r^a \left\{ -\cos^5 \phi [u_s(\psi - \psi_1) - u_s(\psi - \psi_2)] \frac{\partial}{\partial \phi} [\delta(\phi - \phi_1) - \delta(\phi - \phi_2)] \right. \right. \\
& + \frac{\cos^4 \phi (3 \sin^2 \phi - 2)}{\sin \phi} [\delta(\phi - \phi_1) - \delta(\phi - \phi_2)] [u_s(\psi - \psi_1) - u_s(\psi - \psi_2)] \\
& \left. \left. + \frac{\cos^4 \phi}{\sin \phi} [\delta(\phi - \phi_1) - \delta(\phi - \phi_2)] [u_s(\psi - \psi_1) - u_s(\psi - \psi_2)] \right\} \right. \\
& + b \cos^2 \phi [u_s(\phi - \phi_1) - u_s(\phi - \phi_2)] [u_s(\psi - \psi_1) - u_s(\psi - \psi_2)] \\
& \left. + b [u_s(\phi - \phi_1) - u_s(\phi - \phi_2)] [u_s(\psi - \psi_1) - u_s(\psi - \psi_2)] \right\} \cdot \frac{\cos B_m \phi \sin \phi}{\cos^3 \phi} d\phi d\psi,
\end{aligned} \tag{21}$$

where $N_m = \int_{\psi} \int_{\phi} U_{3m}^2 A_1 A_2 d\phi d\psi = \psi^* A_m^2 b^2 \int_0^* \cos^2 B_m \phi \frac{\sin \phi}{\cos^4 \phi} d\phi$, ψ^* is the circumferential boundary angle, $\psi^* = 2\pi$ for a circumferentially closed shell, $\delta(\cdot)$ is the Dirac delta function, and $u_s(\cdot)$ is the unit step function. Analytical solution of N_m is carried out using the Taylor series expansion and the surface integration defined by the distributed actuator is carried out to evaluate the patch control force. Furthermore, the detailed micro-control action can be divided into its contributing meridional/circumferential bending and membrane control components:

$$\begin{aligned}
\hat{F}_m = & \frac{Y_p d_{31} A_m \phi^a(t)}{\rho} [(\hat{T}_m)_{\text{Total}}] \\
= & \frac{Y_p d_{31} A_m \phi^a(t)}{\rho} [(\hat{T}_m)_{\phi, \text{bend}} + (\hat{T}_m)_{\psi, \text{bend}} + (\hat{T}_m)_{\phi, \text{mem}} + (\hat{T}_m)_{\psi, \text{mem}}],
\end{aligned} \tag{22}$$

where $(\hat{T}_m)_{\text{Total}}$ denotes the overall control effect, excluding the coefficients and modal parameters; $(\hat{T}_m)_{\phi, \text{bend}}$, $(\hat{T}_m)_{\psi, \text{bend}}$, $(\hat{T}_m)_{\phi, \text{mem}}$ and $(\hat{T}_m)_{\psi, \text{mem}}$ respectively denote the control effect resulting from $M_{\phi\phi}^c$ - the control moment in the ϕ direction, $M_{\psi\psi}^c$ - the control moment in the ψ direction, $N_{\phi\phi}^c$ - the control force in the ϕ direction, and $N_{\psi\psi}^c$ - the control force in the ψ direction. These individual contributing control effects are evaluated in case studies. Note that surface integrations in the modal force expression are difficult to carry out exactly. Thus, the Taylor series expansion technique is used in the solution procedures.

CASE STUDY

To validate the assumed mode shape function, mode shapes of the first three natural modes are compared with experimental data first in a case study. Modal control forces and detailed micro-control actions including the meridional and circumferential contributing

membrane/bending components, i.e., $(\hat{T}_m)_{\text{Total}}$, $(\hat{T}_m)_{\phi,\text{bend}}$, $(\hat{T}_m)_{\psi,\text{bend}}$, $(\hat{T}_m)_{\phi,\text{mem}}$, and $(\hat{T}_m)_{\psi,\text{mem}}$, induced by segmented distributed actuator patches at various locations are evaluated next.

Mode Shapes of Paraboloidal Shells

To validate the assumed mode shape functions, analytical solutions are qualitatively compared with experimental data in this section. **Figures 3 to 5** illustrate the first three axisymmetric natural mode shapes (three-dimensional (3D) and profiles) of a paraboloidal shell ($c=0.0330\text{m}$, $a=0.1905\text{m}$, $\phi^*=19.1197^\circ=19^\circ07'$, shell thickness $h=1.2192\text{mm}$), in which analytical solutions and experimental data points are plotted with respect to the original shell profile. The vertical axis denotes the mode amplitude superimposed on the original elastic shell (in dash line) and plotted along the experimental data points by Glockner and Tawardros (2). The experimental modal analysis was based on a simply-supported paraboloidal shell fabricated from polyvinyl-chloride (P.V.C) sheet by a thermo-vacuum process using special molds and templates. Natural frequencies and mode shapes of axisymmetric oscillation were measured and presented (2). These three figures demonstrate that the assumed analytical solutions are compared well with the experimental data for the first three modes. The errors could be introduced by the non-ideal simply supported boundary conditions on the experimental model. The non-ideal boundary condition tends to be relatively rigid at the base boundary and be more flexible at the pole, which can be observed in almost all experiment data. With the understanding of fundamental dynamic characteristics of paraboloidal shells, micro-control actions of distributed segmented actuators are investigated next.

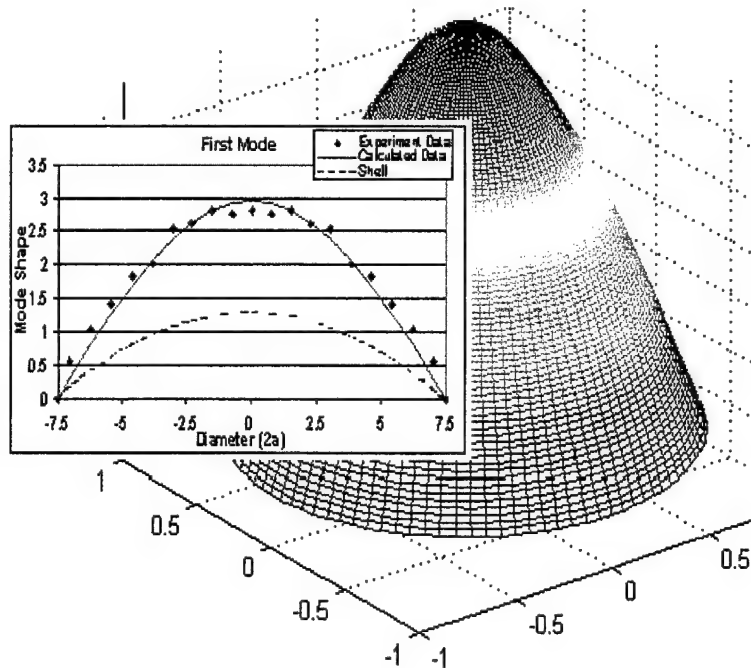


Fig.3 Paraboloidal shell, the first mode.

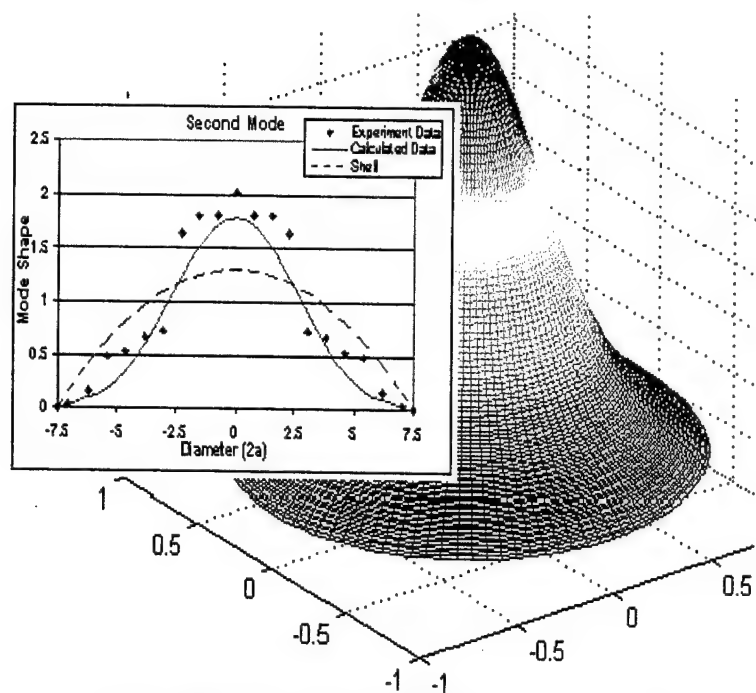


Fig.4 Paraboloidal shell, the second mode.

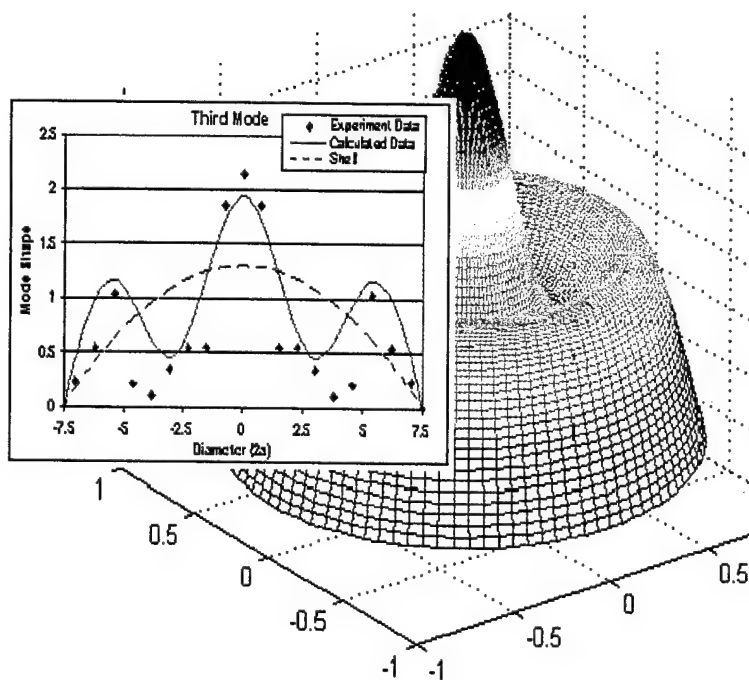


Fig.5 Paraboloidal shell, the third mode.

Micro-control Actions of Distributed Actuator Patches

As discussed previously, a distributed actuator layer laminated on a deep paraboloidal shell is segmented into a number of actuator patches. Micro-control actions and control

authorities of these actuator patches are evaluated. The deep thin paraboloidal shell is defined by meridian/radius = $c/a = 2/1$, $\phi^* = 1.3258$ radians, and thickness $h=0.002$; the actuator patch size is $\Delta\phi = \phi_2 - \phi_1 = 0.1$ radians defined in the meridional direction with a “circumferential width” $\Delta\psi = \psi_2 - \psi_1 = 0.2$ radians. Note that these patch sizes (or the projected meridional and circumferential arc lengths) are not identical as they move from the pole to the rim, because of the curvature effect. Modal control force and micro-control actions, i.e., $(\hat{T}_m)_{\text{Total}}$, $(\hat{T}_m)_{\phi,\text{bend}}$, $(\hat{T}_m)_{\psi,\text{bend}}$, $(\hat{T}_m)_{\phi,\text{mem}}$, and $(\hat{T}_m)_{\psi,\text{mem}}$ for the first three modes are evaluated, respectively. **Figures 6-8** show the first three modal control effects plotted with respect to the horizontal projected diameter of the deep paraboloidal shell. They show the variation of control forces along the shell surface in the meridional direction. (Note that T_m denotes \hat{T}_m in these figures). Accordingly, each data point represents the actuator’s micro-control effects at a specific patch location moving from the top pole to the bottom rim in the meridional direction. The resultant control effects of actuator patches depend on the patch locations and the mode shape variations; these forces are symmetric due to the axisymmetric assumption of the mode shape functions. Note that there are positive and negative control forces induced by the actuator patch moving in the meridional direction on the shell surface. The positive forces induce positive control effects and the negative forces aggravate the vibrations when the positive control signals are used. However, since the sign of control signals can be manipulated in the control circuit, one should look at the “absolute” magnitudes to infer the “absolute” control effectiveness at these locations.

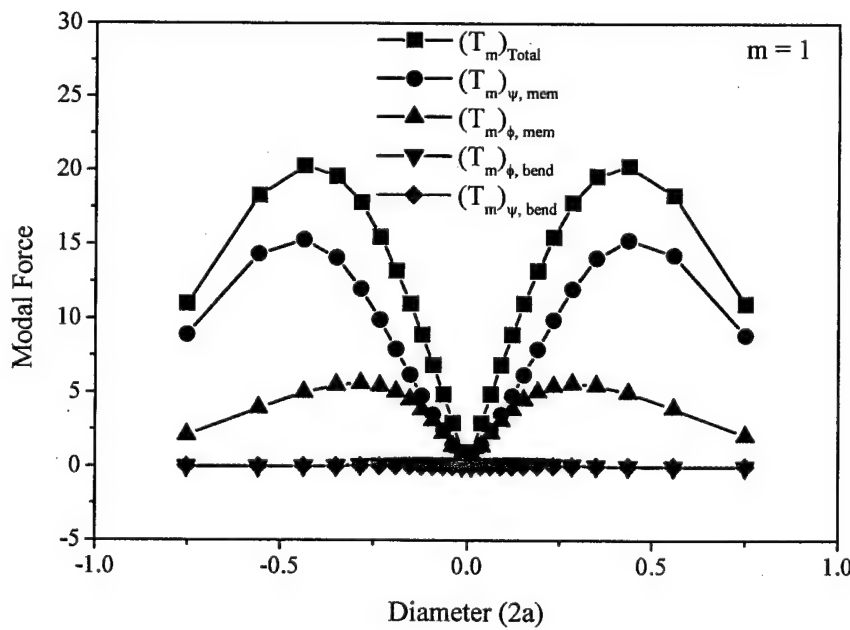


Fig.6 Modal control forces at various actuator locations, 1st mode.

(□: $(\hat{T}_m)_{\text{Total}}$, ○: $(\hat{T}_m)_{\psi,\text{mem}}$, Δ: $(\hat{T}_m)_{\phi,\text{mem}}$, ∇: $(\hat{T}_m)_{\phi,\text{bend}}$, ◇: $(\hat{T}_m)_{\psi,\text{bend}}$)

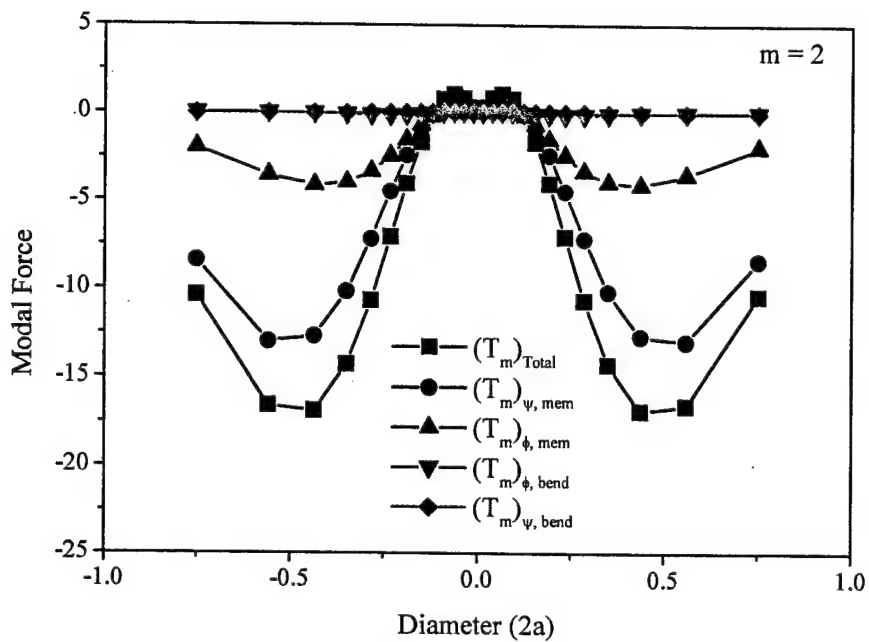


Fig.7 Modal control forces at various actuator locations, 2nd mode.

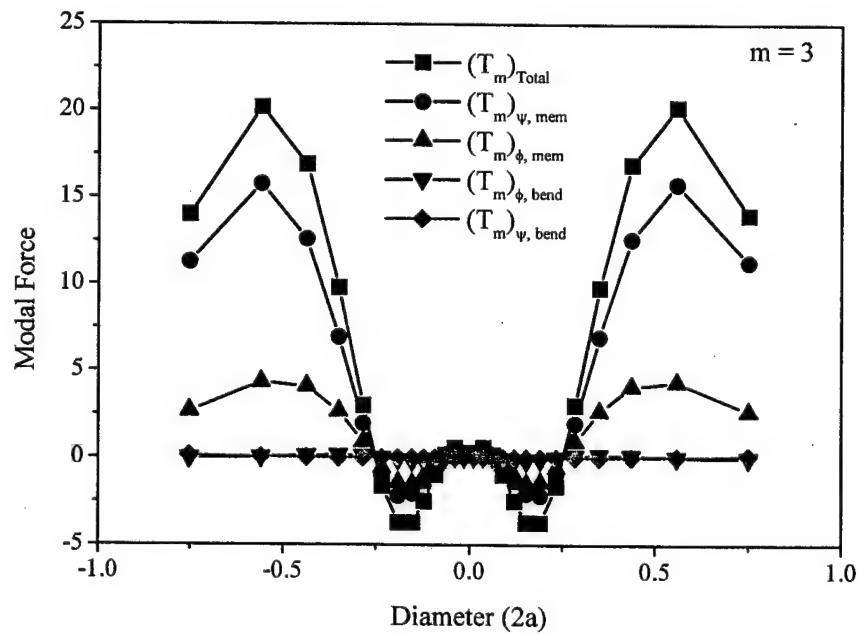


Fig.8 Modal control forces at various actuator locations, 3rd mode.

Detailed micro-control actions reveal that the circumferential and meridional membrane control forces dominate the overall control effects and the bending (both meridional and circumferential) control moments are relatively insignificant. These micro-control effects (meridional/circumferential membrane and bending control effects) are respectively calculated based on the modal force formulation including the effects of actuator sizes. Since these actuator sizes are not constant, these control forces and their micro-control effects need to be normalized in order to evaluate the true control effect per unit actuator area. Considering the curvature variations influencing the projected arc lengths, one can calculate the “true” actuator size at a given location on the deep paraboloidal shell. **Figure 9** indicates that the actuator size changes significantly, depending on the patch location of the deep paraboloidal shell, although they keep identical $\Delta\phi = 0.1$ and $\Delta\psi = 0.2$ radians. Thus, the control forces and the micro-control actions are normalized with respect to the actuator size and these normalized meridional/circumferential membrane and bending components of the first three paraboloidal shell modes are presented in **Figures 10-12**. They show the variation of control forces per unit area along the shell meridional surface and the “size effect” is excluded. Higher nominal values imply that the induced control actions per unit area (or control authorities/actuator size) are higher, i.e., higher control effects at given control cost or power.

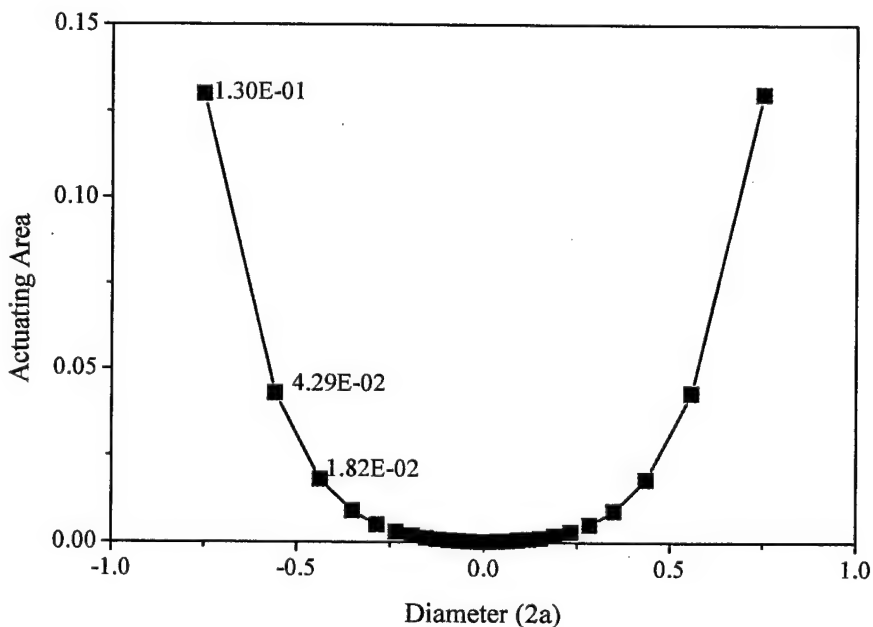


Fig.9 Effective actuator sizes at various patch locations.

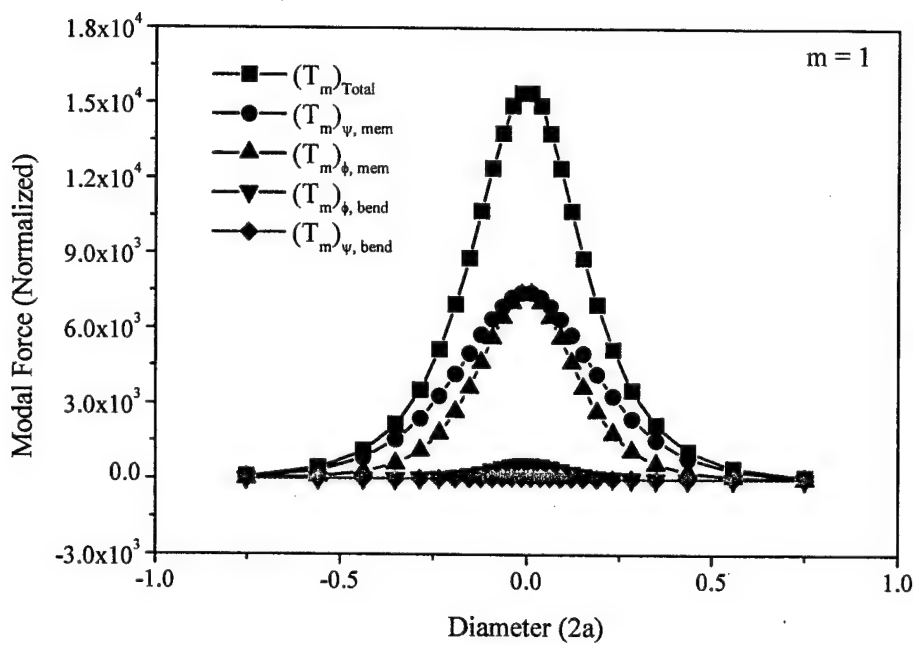


Fig.10 Normalized modal control forces at various locations, 1st mode. (\square : $(\hat{T}_m)_{\text{Total}}$, \circ : $(\hat{T}_m)_{\psi, \text{mem}}$, Δ : $(\hat{T}_m)_{\phi, \text{mem}}$, ∇ : $(\hat{T}_m)_{\phi, \text{bend}}$, \diamond : $(\hat{T}_m)_{\psi, \text{bend}}$)

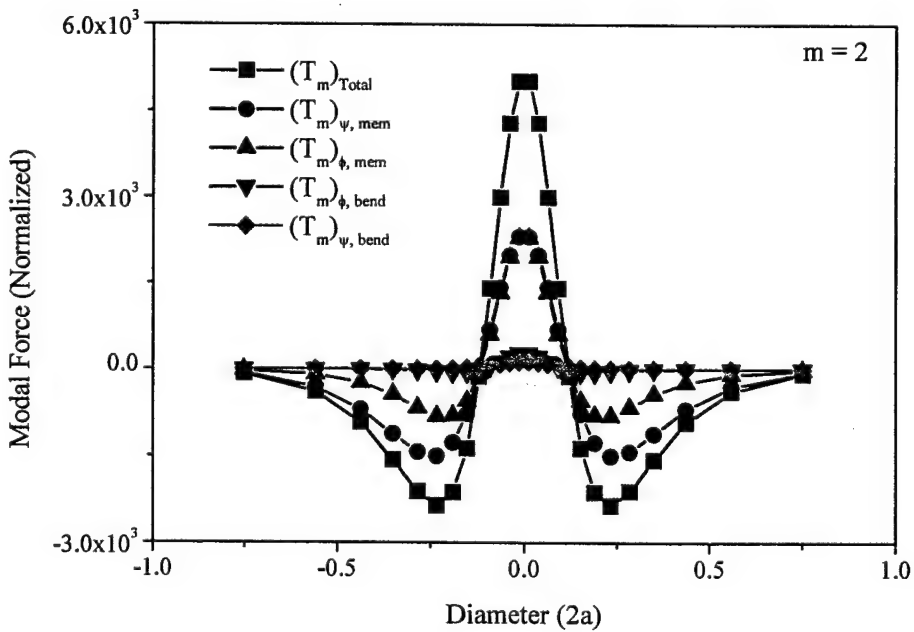


Fig.11 Normalized modal control forces at various locations, 2nd mode.

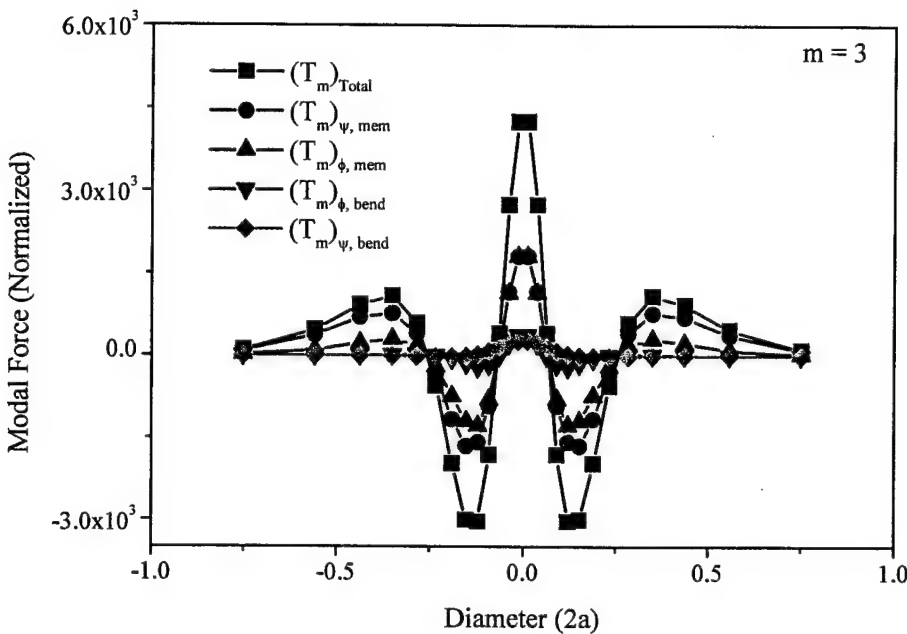


Fig.12 Normalized modal control forces at various locations, 3rd mode.

These data indicate that actuator patches located at the pole provide the best control effects for the first mode. There are three effective locations for the second mode and five locations for the third mode. In any case, centrally located actuator patch yields the most effective control effect for most natural modes of the simply-supported deep paraboloidal shell.

CONCLUSIONS

Deep paraboloidal shells are common components for nozzles, horns, rocket fairings, etc. in high-performance aerospace systems. This study is to evaluate the control effectiveness of distributed segmented actuator patches and to examine their microscopic control actions and authorities of these actuator patches laminated on a deep thin paraboloidal shell. Mathematical models of the paraboloidal shell and the distributed actuator patches were defined first, followed by governing system equations. Theoretical derivations of distributed control forces reveal that the micro-control actions of actuator patches can be divided into 1) the meridional membrane effect, 2) the circumferential membrane effect, 3) the meridional bending effect, and 4) the circumferential bending effect. These micro-control actions were analyzed in a case study. Analytical solutions based on the assumed mode shape function of a simply-supported (or knife-edge) deep paraboloidal shell were derived; these assumed mode shape functions were validated by experimental data.

Analysis of distributed control forces/moment suggests that these control actions are sensitive to actuator locations and natural modes; they generally decrease as the mode number increases. Among the four control actions, the meridional and circumferential membrane

control force components dominate the overall control effect and the meridional control action is slightly higher than the circumferential control action. The bending control actions (both meridional and circumferential) are very small for lower shell modes and they gradually increase as the mode increases when the shell's bending behavior becomes observable. The bending control action is proportional to the shell thickness and it increases as the shell becomes thicker, while the membrane control action remains constant. Furthermore, analysis of micro-control actions, actuator locations, actuator-size variations related to mode shapes reveals a number of ideal patch locations introducing the maximal control effects at the minimal control cost or actuator size. These analysis data provide general design guidelines and optimal actuator locations for precision control of deep paraboloidal shell distributed systems.

ACKNOWLEDGEMENT

This research is supported, in part, by a grant (F49620-98-1-0467) from the Air Force Office of Scientific Research (Project Manager: Brian Sanders). This support is gratefully acknowledged.

REFERENCES

- (1) Hoppmann, W.H.,II, Cohen, M.I., and Kunukkasseril, V.X., 1964, "Elastic Vibrations of Paraboloidal Shells of Revolution," *The Journal of the Acoustic Society of America*, Vol.36, No.2, pp.349-353.
- (2) Glockner, P.G. and Tawardros, K.Z., 1973, "Experiments on Free Vibration of Shells of Revolution," *Experimental Mechanics*, Vol.13, No.10, pp.411-421.
- (3) Beles, A.A., Soare, M.V., 1976, *Elliptic And Hyperbolic Paraboloidal Shells Used In Constructions*, S.P. Christie & Partners, London -Editura Academiei, Bucuresti, pp.144-145.
- (4) Shoemaker, W.L., and Utku, S., 1986, "On the Vibrations of Spinning Paraboloids," *Journal of Sound and Vibration*, Vol.111, No.2, pp.279-296.
- (5) Elliott, G.H., 1988, "The Evaluation of the Modal Density of Paraboloidal and Similar Shells," *Journal of Sound and Vibration*, Vol.126, No.3, pp.477-483.
- (6) Mazurkiewicz, Z.E., Nagorski, R.T., 1991, *Shells of Revolution*, PWN-Polish Scientific Publishers, Warsaw, pp7-9 and pp.333-341.
- (7) Kayran, A., Vinson, J.R., and Ardic, E.S., 1994, "A Method for the Calculation of Natural Frequencies of Orthotropic Axisymmetrically Loaded Shells of Revolution," *ASME Transactions, Journal of Vibration & Acoustics*, Vol.116, pp.16-25.
- (8) Tzou, H.S., Zhong, J.P., and Hollkamp, J.J., 1994, "Spatially Distributed Orthogonal Piezoelectric Shell Actuators (Theory and Applications)," *Journal of Sound and Vibration*, Vol.177, No.3, pp.363-378.
- (9) Tzou, H.S., 1993, *Piezoelectric Shells: Distributed Sensing and Control of Continua*, Kluwer Academic Publishers, Boston/Dordrecht.
- (10) Qiu, J. and Tani, J., 1995, "Vibration Control of a Cylindrical Shell Using Distributed Piezoelectric Sensors and Actuators," *Journal of Intelligent Material Systems and Structures*, Vol.6, No.4, pp.474-481.

- (11) Tzou, H.S., Bao, Y., and Venkayya, V.B., 1996, "Parametric Study of Segmented Transducers Laminated on Cylindrical Shells, Part 2. Actuator Patches," *Journal of Sound and Vibration*, Vol. 197, No.2, pp.225-249.
- (12) Jayachandran, V., and Sun, J. Q., 1998, "Modeling Shallow-spherical-shell Piezoceramic Actuators as Acoustic Boundary Control Elements," *Smart Materials and Structures*, Vol.7, No.1, pp.72-84.
- (13) Birman, V., Griffin, S., and Knowles, G., 2000, "Axisymmetric Dynamics of Composite Spherical Shells with Active Piezoelectric/Composite Stiffeners," *Acta Mechanica*, Vol.141, No.1, pp.71-83.
- (14) Zhou, Y.H. and Tzou, H.S., 2000, "Control of Nonlinear Piezoelectric Circular Shallow Spherical Shells," *Journal of Solids and Structures*, Vol.37, pp.1663-1677.
- (15) Tzou, H.S., and Smithmaitrie, P., 2002, "Electromechanics and Distributed Modal Signal Analysis of Piezo(electric)-Elastic Spherical Shells," *Mechanical Systems and Signal Processing*. (To appear)
- (16) Tzou, H.S., Wang, D.W., and Chai, W.K., 2001, "Dynamics and Distributed Control of Conical Shells Laminated with Full and Diagonal Actuators," No.CIE21272, 2001 Design Technical Conference, Pittsburgh, PA, Sept.9-12, 2001.
- (17) Tzou, H.S. and Wang, D.W., 2002, "Distributed Signals of Piezoelectric Laminated Toroidal Shell Structures," *Journal of Sound and Vibration*. (To appear)
- (18) Tzou, H.S. and Ding, J.H., 2001, "Distributed Modal Signals of Nonlinear Paraboloidal Shells with Distributed Neurons," No.VIB21545, 2001 Design Technical Conference, Pittsburgh, PA, Sept.9-12, 2001.
- (19) Tzou, H.S., and Bao, Y., 1997, "Nonlinear Piezothermoelasticity and Multi-Field Actuations, Part 1: Nonlinear Anisotropic Piezothermoelastic Shell Laminates," *ASME Journal of Vibration and Acoustics*, Vol.119, pp.374-389.

(ParbSigNon.ParbPr.Shl.Parb)

CHAPTER 15

OPTIMAL CONTROL OF PRECISION PARABOLOIDAL SHELL STRUCTRONIC SYSTEMS

ABSTRACT

Paraboloidal shells of revolution are commonly used in advanced aerospace, civil and telecommunication structures, e.g., antennas, reflectors, mirrors, rocket fairings, nozzles, solar collectors, dome structures, etc. A strucronic shell system is defined as an elastic shell embedded, bonded or laminated with distributed piezoelectric sensors and actuators and it is governed by either in-situ or external control electronics. A closed-loop control system of paraboloidal shell strucronic system consists of distributed sensors/actuators and controller coupled with an elastic paraboloidal shell. State equation for the paraboloidal shell strucronic system is derived and optimal linear quadratic (LQ) state feedback control is implemented, such that the "best" shell control performance with the least control cost can be achieved. The gain matrix is estimated based on minimizing a performance criterion function. Optimal control effects are compared with controlled responses with other non-optimal control parameters. Control effects of identical-sized sensor/actuator patches at different locations are studied and compared. Modal control effects for different natural modes are also investigated.

INTRODUCTION

Paraboloidal shells of revolution are commonly used in advanced aerospace, civil and telecommunication structures, e.g., antennas, reflectors, mirrors, rocket fairings, nozzles, solar collectors, dome structures, etc. A shell strucronic system is defined as an elastic shell bonded, embedded or laminated with active-material based sensors and actuators governed by either in-situ or external control electronics. This study is to apply the linear quadratic (LQ) optimal state feedback control to precision paraboloidal shell strucronic systems and to evaluate modal control effects influenced by different sensor/actuator locations. The goal of optimal control is to seek for the best closed-loop control performance at the least control cost. Although the optimal control technique has been introduced to control applications for decades, its application to shell vibration control, especially distributed strucronic shell systems, is still not well explored. Optimal control of distributed parameter systems with spatial and time discretization methods was studied [1], as well as applications to beam and plate structures [2-5]. Dynamic and/or elastic behavior of paraboloidal shells of revolution has been investigated for decades. Lin and Lee [6] derived the mode shape functions and natural frequencies for paraboloidal shells of revolution with free boundary based on the bending approximation. Wang and Lin [7] presented the differential governing equations for the axisymmetric motion of paraboloidal shells of

revolution. However, difficulties for finding analytical solutions to the complicated equations of motion limit the fully development and application of elastic paraboloidal shells of revolution. Distributed sensing and control characteristics of strucronic beam, plate, ring and shells have been investigated over the years [8]-[12]. Distributed sensing behaviors and open-loop actuator characteristics of strucronic paraboloidal shell of revolution systems are recently investigated [12]-[14]. In this study, comprehensive dynamics and closed-loop optimal control performance, with modal-dependent sensor/actuator location sensitivity, of paraboloidal strucronic shells (elastic shell coupled with distributed segmented sensors/actuators) are evaluated. Its advantages are demonstrated by comparing the optimal control with the control based on a non-optimal (i.e., proportional and derivative) gain matrix at the same control gain cost.

A PARABOLOIDAL SHELL STRUCTRONIC SYSTEM

The closed-loop active vibration control of paraboloidal shells of revolution strucronic system is accomplished by distributed sensors, a controller and distributed actuators, as shown in **Figure 1**. The piezoelectric sensor monitors the shell vibration state according to the direct piezoelectric effect. The sensing signal is input to the controller and a control signal is generated based on the sensing signal and the control algorithm. A high-voltage amplifier can be a part of the controller block. The control signal is then transmitted to distributed piezoelectric actuator patches to counteract the shell vibration according to the converse piezoelectric effect.

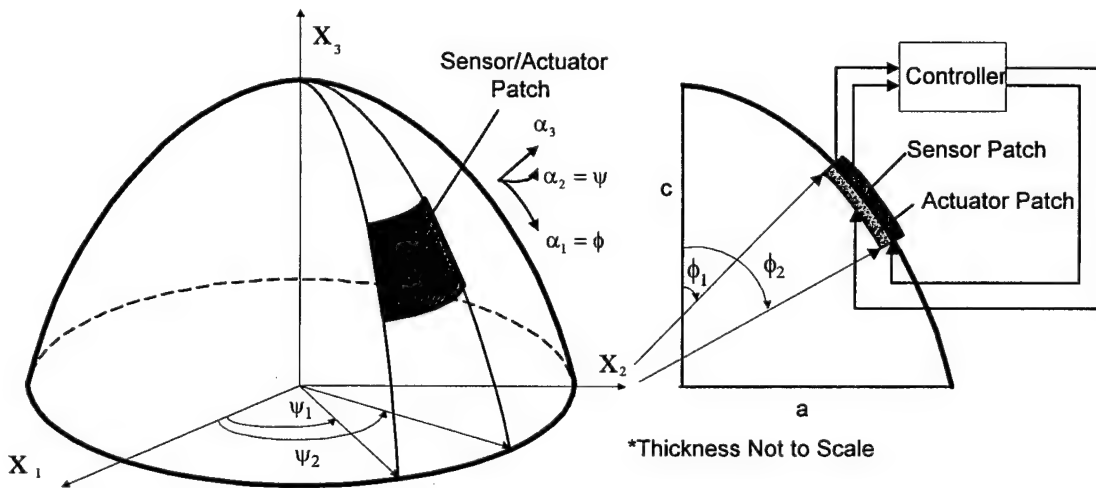


Fig.1 A closed-loop control system for paraboloidal shell strucronic system.

The tri-orthogonal curvilinear coordinates are defined as $\alpha_1 = \phi$ - the meridional direction, $\alpha_2 = \psi$ - the circumferential direction and α_3 - the transverse direction following the right-hand rule, **Figure 1**. $R_1 = R_\phi$ is the radius of meridional curvature, $R_2 = R_\psi$ is the radius of circumferential curvature. The radii of curvature of paraboloidal shells of revolution are $R_\psi = \frac{b}{\cos \phi}$ and $R_\phi = \frac{b}{\cos^3 \phi}$. The Lamé parameters are $A_1 = R_\phi = \frac{b}{\cos^3 \phi}$ and

$A_2 = R_\psi \sin \phi = \frac{b \sin \phi}{\cos \phi}$, where $b = \frac{a^2}{2c}$, a is the maximum circumferential radius and c is the meridian height, **Figure 1** [13]. State-space equations and optimal control are discussed next.

SYSTEM EQUATION IN STATE SPACE

The fundamental equations of motion for a shell of revolution are [8]:

$$R_\phi \frac{\partial}{\partial \psi} (N_{\psi\phi}) + \frac{\partial}{\partial \phi} (N_{\phi\phi} R_\psi \sin \phi) - N_{\psi\psi} R_\phi \cos \phi + R_\phi R_\psi \sin \phi \left(\frac{Q_{\phi^3}}{R_\phi} + q_\phi \right) \\ = R_\phi R_\psi \sin \phi \rho h \frac{\partial^2 u_\phi}{\partial t^2}, \quad (1)$$

$$R_\phi \frac{\partial}{\partial \psi} (N_{\psi\psi}) + \frac{\partial}{\partial \phi} (N_{\phi\psi} R_\psi \sin \phi) + N_{\psi\phi} R_\phi \cos \phi + R_\phi R_\psi \sin \phi \left(\frac{Q_{\psi^3}}{R_\psi} + q_\psi \right) \\ = R_\phi R_\psi \sin \phi \rho h \frac{\partial^2 u_\psi}{\partial t^2}, \quad (2)$$

$$R_\phi \frac{\partial}{\partial \psi} (Q_{\psi^3}) + \frac{\partial}{\partial \phi} (Q_{\phi^3} R_\psi \sin \phi) - \left(\frac{N_{\phi\phi}}{R_\phi} + \frac{N_{\psi\psi}}{R_\psi} \right) R_\phi R_\psi \sin \phi + q_3 R_\phi R_\psi \sin \phi \\ = R_\phi R_\psi \sin \phi \rho h \frac{\partial^2 u_3}{\partial t^2}, \quad (3)$$

where N_{ij} and M_{ij} are the membrane forces and the bending moments; ρ is the shell mass density; h is the thickness; q_i and u_i are respectively the excitation (loading) and displacement in the i -direction ($i=\phi, \psi, 3$); and the transverse shear effects Q_{i3} are

$$Q_{\phi^3} = \frac{1}{R_\phi R_\psi \sin \phi} [R_\phi \frac{\partial}{\partial \psi} M_{\psi\phi} + \frac{\partial}{\partial \phi} (M_{\phi\phi} R_\psi \sin \phi) - M_{\psi\psi} R_\phi \cos \phi], \quad (4)$$

$$Q_{\psi^3} = \frac{1}{R_\phi R_\psi \sin \phi} [R_\phi \frac{\partial}{\partial \psi} M_{\psi\psi} + \frac{\partial}{\partial \phi} (M_{\psi\phi} R_\psi \sin \phi) + M_{\phi\phi} R_\phi \cos \phi]. \quad (5)$$

Substituting the radii of curvature and force/moment expressions into the fundamental equation of motion and imposing the bending approximation yields the transverse oscillation equation of paraboloidal shells.

$$\begin{aligned}
& D \frac{\partial^3 u_\phi}{\partial \phi^3} \left[\frac{\cos^8 \phi \sin^3 \phi}{b^2} \right] + D \frac{\partial^2 u_\phi}{\partial \phi^2} \left[\frac{-16 \cos^7 \phi + 34 \cos^9 \phi - 18 \cos^{11} \phi}{b^2} \right] \\
& + D \frac{\partial u_\phi}{\partial \phi} \left[\frac{(67 \cos^6 \phi - 234 \cos^8 \phi + 266 \cos^{10} \phi - 99 \cos^{12} \phi) - \mu \cos^6 \phi \sin^4 \phi}{b^2 \sin \phi} \right] \\
& + D \frac{\partial^2 u_\phi}{\partial \psi^2} \left[\frac{-2 \cos^3 \phi + 3 \cos^5 \phi}{b^2} \right] + D \frac{\partial^3 u_\phi}{\partial \phi \partial \psi^2} \left[\frac{\cos^4 \phi \sin^2 \phi}{b^2 \sin \phi} \right] \\
& + D u_\phi \left[\frac{(-66 \cos^5 \phi + 295 \cos^7 \phi - 390 \cos^9 \phi + 162 \cos^{11} \phi)}{b^2} \right. \\
& \quad \left. + \frac{\mu(6 \cos^5 \phi - 13 \cos^7 \phi + 7 \cos^9 \phi)}{b^2} \right] \\
& + D \frac{\partial^3 u_\psi}{\partial \psi^3} \left[\frac{1}{b^2} \right] + D \frac{\partial u_\psi}{\partial \psi} \left[\frac{(7 \cos^2 \phi - 10 \cos^4 \phi + 4 \cos^6 \phi) - \mu \cos^2 \phi \sin^2 \phi}{b^2 \sin \phi} \right] \\
& + D \frac{\partial^3 u_\psi}{\partial \psi \partial \phi^2} \left[\frac{\cos^4 \phi \sin^2 \phi}{b^2} \right] + D \frac{\partial^2 u_\psi}{\partial \phi \partial \psi} \left[\frac{-6 \cos^3 \phi + 11 \cos^5 \phi - 5 \cos^7 \phi}{b^2 \sin \phi} \right] \\
& + D \frac{\partial^4 u_3}{\partial \phi^4} \left[\frac{-\cos^8 \phi \sin^4 \phi}{b^2 \sin \phi} \right] + D \frac{\partial^3 u_3}{\partial \phi^3} \left[\frac{16 \cos^7 \phi - 34 \cos^9 \phi + 18 \cos^{11} \phi}{b^2} \right] \\
& + D \frac{\partial^2 u_3}{\partial \phi^2} \left[\frac{(-67 \cos^6 \phi + 234 \cos^8 \phi - 266 \cos^{10} \phi + 99 \cos^{12} \phi) + \mu \cos^6 \phi \sin^4 \phi}{b^2 \sin \phi} \right] \\
& + D \frac{\partial u_3}{\partial \phi} \left[\frac{(66 \cos^5 \phi - 295 \cos^7 \phi + 390 \cos^9 \phi - 162 \cos^{11} \phi)}{b^2} \right. \\
& \quad \left. - \frac{\mu(6 \cos^5 \phi - 13 \cos^7 \phi + 7 \cos^9 \phi)}{b^2} \right] \\
& + D \frac{\partial^4 u_3}{\partial \psi^4} \left[\frac{-1}{b^2 \sin \phi} \right] + D \frac{\partial^2 u_3}{\partial \psi^2} \left[\frac{(-7 \cos^2 \phi + 3 \cos^4 \phi) + \mu \cos^2 \phi \sin^2 \phi}{b^2 \sin \phi} \right] \\
& + D \frac{\partial^4 u_3}{\partial \phi^2 \partial \psi^2} \left[\frac{-2 \cos^4 \phi + 2 \cos^6 \phi}{b^2 \sin \phi} \right] + D \frac{\partial^3 u_3}{\partial \phi \partial \psi^2} \left[\frac{8 \cos^3 \phi - 6 \cos^5 \phi}{b^2} \right] \\
& + q_3 \left[\frac{b^2 \sin^3 \phi}{\cos^4 \phi} \right] = \frac{\partial^2 u_3}{\partial t^2} \left[\frac{b^2 \rho h \sin^3 \phi}{\cos^4 \phi} \right], \tag{6}
\end{aligned}$$

where D is the bending stiffness. Furthermore, the modal expansion method [15] is used in the optimal control and the distributed sensing/control analysis of paraboloidal shells [8]. Thus, the modal expansion equation can be written as

$$u_i(\phi, \psi, t) = \sum_{m=2}^{\infty} \eta_m(t) U_{im}(\phi, \psi), \tag{7}$$

where $i = \phi, \psi, 3$ denote for the three coordinates; $\eta_m(t)$ is the modal participating factor of the

m-th mode; $U_{im}(\phi, \psi)$ is the m-th mode shape function of a free-floating paraboloidal shell [6]:

$$U_{\phi m} = -A_m \sin \phi \tan^m \phi \cos m\psi, \quad (8)$$

$$U_{\psi m} = -A_m \tan^{m+1} \phi \sin m\psi, \quad (9)$$

$$U_{3m} = A_m \tan^m \phi (\cos \phi + m \sec \phi) \cos m\psi, \quad (10)$$

where A_m is the modal amplitude. Note that for paraboloidal shells of revolution with free boundary, the mode number m is the circumferential wave number starting from 2, based on the bending approximation theory [6]. The modal equation can be written as [8]:

$$\ddot{\eta}_m + 2\zeta_m \omega_m \dot{\eta}_m + \omega_m^2 \eta_m = \hat{F}_m(t), \quad (11)$$

where ζ_m is the modal damping ratio, ω_m is the m-th natural frequency, $\hat{F}_m(t)$ is the modal force. In practical implementation, the modal signal can be spectrally decomposed from the sensor signal using band-pass filters or digital filters in conjunction with Fast Fourier Transform (FFT). The total closed-loop control system can be divided into a number of subsystems (modal loops) designed for various natural modes. The final total control signal can be reconstructed by re-composing all actuating signals from the subsystems [16]. Note that the spatial derivatives are respect to the mode shape functions and the temporal derivative is respect to the modal participating factor when both the mode shape functions and the modal expansion equation are substituted into the transverse shell equation, Eq.(6). Accordingly, the shell transverse equation of motion for the m-th mode can be written as

$$\begin{aligned} \eta_m(t) D \left\{ \frac{\partial^3 U_{\phi m}}{\partial \phi^3} \left[\frac{\cos^8 \phi \sin^3 \phi}{b^2} \right] + \frac{\partial^2 U_{\phi m}}{\partial \phi^2} \left[\frac{-16 \cos^7 \phi + 34 \cos^9 \phi - 18 \cos^{11} \phi}{b^2} \right] \right. \\ \left. + \frac{\partial U_{\phi m}}{\partial \phi} \left[\frac{(67 \cos^6 \phi - 234 \cos^8 \phi + 266 \cos^{10} \phi - 99 \cos^{12} \phi) - \mu \cos^6 \phi \sin^4 \phi}{b^2 \sin \phi} \right] \right. \\ \left. + \frac{\partial^2 U_{\phi m}}{\partial \psi^2} \left[\frac{-2 \cos^3 \phi + 3 \cos^5 \phi}{b^2} \right] + \frac{\partial^3 U_{\phi m}}{\partial \phi \partial \psi^2} \left[\frac{\cos^4 \phi \sin^2 \phi}{b^2 \sin \phi} \right] \right. \\ \left. + U_{\phi m} \left[\frac{(-66 \cos^5 \phi + 295 \cos^7 \phi - 390 \cos^9 \phi + 162 \cos^{11} \phi)}{b^2} \right. \right. \\ \left. \left. + \frac{\mu(6 \cos^5 \phi - 13 \cos^7 \phi + 7 \cos^9 \phi)}{b^2} \right] \right\} \end{aligned}$$

$$\begin{aligned}
& + \frac{\partial^3 U_{\psi m}}{\partial \psi^3} \left[\frac{1}{b^2} \right] + \frac{\partial U_{\psi m}}{\partial \psi} \left[\frac{(7 \cos^2 \phi - 10 \cos^4 \phi + 4 \cos^6 \phi) - \mu \cos^2 \phi \sin^2 \phi}{b^2} \right] \\
& + \frac{\partial^3 U_{\psi m}}{\partial \phi^2 \partial \psi} \left[\frac{\cos^4 \phi \sin^2 \phi}{b^2} \right] + \frac{\partial^2 U_{\psi m}}{\partial \phi \partial \psi} \left[\frac{-6 \cos^3 \phi + 11 \cos^5 \phi - 5 \cos^7 \phi}{b^2 \sin \phi} \right] \\
& + \frac{\partial^4 U_{3m}}{\partial \phi^4} \left[\frac{-\cos^8 \phi \sin^3 \phi}{b^2} \right] + \frac{\partial^3 U_{3m}}{\partial \phi^3} \left[\frac{16 \cos^7 \phi - 34 \cos^9 \phi + 18 \cos^{11} \phi}{b^2} \right] \\
& + \frac{\partial^2 U_{3m}}{\partial \phi^2} \left[\frac{(-67 \cos^6 \phi + 234 \cos^8 \phi - 266 \cos^{10} \phi + 99 \cos^{12} \phi) + \mu \cos^6 \phi \sin^4 \phi}{b^2 \sin \phi} \right] \\
& + \frac{\partial U_{3m}}{\partial \phi} \left[\frac{66 \cos^5 \phi - 295 \cos^7 \phi + 390 \cos^9 \phi - 162 \cos^{11} \phi}{b^2} \right. \\
& \quad \left. - \frac{\mu(6 \cos^5 \phi - 13 \cos^7 \phi + 7 \cos^9 \phi)}{b^2} \right] \\
& + \frac{\partial^4 U_{3m}}{\partial \psi^4} \left[\frac{-1}{b^2 \sin \phi} \right] + \frac{\partial^2 U_{3m}}{\partial \psi^2} \left[\frac{(-7 \cos^2 \phi + 3 \cos^4 \phi) + \mu \cos^2 \phi \sin^2 \phi}{b^2 \sin \phi} \right] \\
& + \frac{\partial^4 U_{3m}}{\partial \phi^2 \partial \psi^2} \left[\frac{-2 \cos^4 \phi \sin \phi}{b^2} \right] + \frac{\partial^3 U_{3m}}{\partial \phi \partial \psi^2} \left[\frac{8 \cos^3 \phi - 6 \cos^5 \phi}{b^2} \right] \} \\
& + q_{3m} \left[\frac{b^2 \sin^3 \phi}{\cos^4 \phi} \right] = \frac{d^2 \eta_m(t)}{dt^2} U_{3m} \left[\frac{b^2 \rho h \sin^3 \phi}{\cos^4 \phi} \right], \tag{12}
\end{aligned}$$

where q_{3m} is the modal excitation. This equation is further transferred into the state space, since the state space formulation is the fundamental in modern control techniques. Here, the modal participating factor $\eta_m(t)$ and its time derivative $\dot{\eta}_m(t)$ are chosen to be the system state variables and the equation of motion is rewritten into the state space form as $\dot{x} = Ax + Bu + Ew$ and $y = Cx$, where x is the state-variable vector; u is the control input vector; w is external excitation (disturbance); y is the output vector; A , B , C and E are known coefficient matrices related to the system state, control input, system output and excitation input, respectively. The system state is defined as

$$x = \begin{Bmatrix} x_1 \\ x_2 \end{Bmatrix} = \begin{Bmatrix} \eta_m(t) \\ \dot{\eta}_m(t) \end{Bmatrix}. \tag{13}$$

$\eta_m(t)$ represents the modal displacement of the shell and $\dot{\eta}_m(t)$ represents the modal velocity. The system state equation is

$$\begin{Bmatrix} \dot{\eta}_m(t) \\ \ddot{\eta}_m(t) \end{Bmatrix} = \begin{bmatrix} A_{11} & A_{12} \\ A_{21} & A_{22} \end{bmatrix} \begin{Bmatrix} \eta_m(t) \\ \dot{\eta}_m(t) \end{Bmatrix} + \begin{Bmatrix} B_1 \\ B_2 \end{Bmatrix} \hat{F}_m^c(t) + \begin{Bmatrix} E_1 \\ E_2 \end{Bmatrix} q_{3m}(t). \tag{14}$$

The system output is chosen to be the sensing signal ϕ_m^s , so the output equation is

$$\phi_m^s = [C_1 \quad C_2] \begin{Bmatrix} \eta_m(t) \\ \dot{\eta}_m(t) \end{Bmatrix} = [C_1 \quad 0] \begin{Bmatrix} \eta_m(t) \\ \dot{\eta}_m(t) \end{Bmatrix} = C_1 \eta_m(t). \quad (15)$$

A, **B** and **E** are the coefficient matrices determined by Eqs.(11) and (12); **C** can be determined by the distributed sensing characteristic of free-boundary paraboloidal shell. The modal control force $\hat{F}_m^c(t)$ is the control input and the system state, i.e., the modal displacement and velocity, is the feedback signal in the closed-loop control system. For a linear control law,

$$\hat{F}_m^c(t) = -Gx(t) = -G\{\eta_m(t) \quad \dot{\eta}_m(t)\}^t. \quad (16)$$

In practical applications, the control gain **G** is usually referred to the ratio between the control signal and the sensing signal:

$$\phi_m^a = -G^* \{ \phi_m^s \quad \dot{\phi}_m^s \}^t, \quad (17)$$

where **G*** is the gain that relates the control signal to the sensing signal. The relation between **G*** and the theoretical control gain **G** in Eq.(16) can be estimated based on the system equations and the modal control force analysis. Note that the velocity signal can be measured directly by velocity sensors, or it can be acquired by differentiating the displacement signal. In practice, to avoid the differentiation process amplified noises, appropriate filter selection to keep the signal in a good signal noise ratio (SNR) is required. Furthermore, the closed-loop system equation without external excitation is simplified to $\dot{x} = Ax - BGx = A_c x$, where **A**_c is the closed-loop system state coefficient matrix. When all system matrices are time-invariant, the solution is

$$x(t) = e^{A_c(t-t_0)} x(t_0) \quad (18)$$

where "t" is any time instant after the initial time t_0 , $x(t_0)$ is the system initial state.

OPTIMAL GAIN MATRIX

The criterion function of linear quadratic (LQ) optimal control is the integration of the quadratic form of the state **x** plus a second quadratic form of the control **u** [17]:

$$J = \int_{t_0}^T [x^t(t) Q(t) x(t) + u^t(t) R u(t)] dt, \quad (19)$$

where **x** is the system state; **Q** is the state weighting matrix and **R** is the control weighting matrix (both are positive symmetric matrices); t_0 is the initial time, T is the final time; the superscript "t" denotes the matrix/vector transpose here. Weighting matrices are chosen based on the desired control cost and final control performance. The optimal control gain is searched to minimize this criterion function and is found by $\hat{G} = R^{-1} B^t \hat{M}$, where the matrix \hat{M} is the solution of the matrix Riccati equation in the modern control theory [16]:

$$-\dot{\hat{M}} = \hat{M}A + A^t\hat{M} - \hat{M}BR^{-1}B^t\hat{M} + Q. \quad (20)$$

If the interval time goes to infinite ($T \rightarrow \infty$) and $J_\infty = \int_0^\infty (x^t Q x + u^t R u) dt$ converges, the gain matrix can be a constant and is called the optimal gain in the steady state, noted as

$$\bar{G} = R^{-1} B^t \bar{M}. \quad (21)$$

Then matrix \bar{M} is the solution to

$$0 = \bar{M}A + A^t\bar{M} - \bar{M}BR^{-1}B^t\bar{M} + Q. \quad (22)$$

Note that \bar{M} is related to the optimal gain in the steady state optimal gain \bar{G} and \hat{M} is related to the generic optimal gain \hat{G} . For the paraboloidal shell strucronic system, the coefficient matrices are $A = \begin{bmatrix} 0 & 1 \\ A_{21} & A_{22} \end{bmatrix}$, $B = \begin{bmatrix} 0 \\ 1 \end{bmatrix}$. The state weighting matrix is chosen as $Q = \begin{bmatrix} 1 & 0 \\ 0 & c^2 \end{bmatrix}$, where c is a state weighting coefficient. The control weighting matrix R is now simplified to a single parameter R as the control input is only \hat{F}_m^c , not a vector. \bar{M} is a symmetric matrix due to its definition [16], $\bar{M} = \begin{bmatrix} m_1 & m_2 \\ m_2 & m_3 \end{bmatrix}$, and it is found that

$$m_2 = R(A_{21} \pm \sqrt{A_{21}^2 + 1/R}), \quad (23a)$$

$$m_3 = R[A_{22} \pm \sqrt{A_{22}^2 + (2m_2 + c^2)/R}]. \quad (23b)$$

Since m_1 is not used in the gain calculation, it is not calculated. Thus, the optimal matrix \bar{G} is determined by Eq.(20) as

$$\bar{G} = [A_{21} + \sqrt{A_{21}^2 + 1/R} \quad A_{22} + \sqrt{A_{22}^2 + (2m_2 + c^2)/R}]. \quad (24)$$

These coefficients are defined by $A_{12} = 1$, $A_{22} = -2\zeta_m \sqrt{-A_{21}}$, and

$$\begin{aligned}
A_{21} = & \frac{D \cos^4 \phi}{U_{3m} b^4 \rho h \sin^4 \phi} \left\{ \frac{\partial^3 U_{\phi m}}{\partial \phi^3} [\cos^8 \phi \sin^4 \phi] \right. \\
& + \frac{\partial^2 U_{\phi m}}{\partial \phi^2} [(-16 \cos^7 \phi + 34 \cos^9 \phi - 18 \cos^{11} \phi) \sin \phi] \\
& + \frac{\partial U_{\phi m}}{\partial \phi} [(67 \cos^6 \phi - 234 \cos^8 \phi + 266 \cos^{10} \phi - 99 \cos^{12} \phi) - \mu \cos^6 \phi \sin^4 \phi] \\
& + \frac{\partial^2 U_{\phi m}}{\partial \psi^2} [(-2 \cos^3 \phi + 3 \cos^5 \phi) \sin \phi] + \frac{\partial^3 U_{\phi m}}{\partial \phi \partial \psi^2} [\cos^4 \phi \sin^2 \phi] \\
& + U_{\phi m} [(-66 \cos^5 \phi + 295 \cos^7 \phi - 390 \cos^9 \phi + 162 \cos^{11} \phi) \sin \phi \\
& \quad + \mu (6 \cos^5 \phi - 13 \cos^7 \phi + 7 \cos^9 \phi) \sin \phi] \\
& + \frac{\partial^3 U_{\psi m}}{\partial \psi^3} [\sin \phi] + \frac{\partial U_{\psi m}}{\partial \psi} [(7 \cos^2 \phi - 10 \cos^4 \phi + 4 \cos^6 \phi) \sin \phi - \mu \cos^2 \phi \sin^3 \phi] \\
& + \frac{\partial^3 U_{\psi m}}{\partial \phi^2 \partial \psi} [\cos^4 \phi \sin^3 \phi] + \frac{\partial^2 U_{\psi m}}{\partial \phi \partial \psi} [-6 \cos^3 \phi + 11 \cos^5 \phi - 5 \cos^7 \phi] \\
& + \frac{\partial^4 U_{3m}}{\partial \phi^4} [-\cos^8 \phi \sin^4 \phi] + \frac{\partial^3 U_{3m}}{\partial \phi^3} [(16 \cos^7 \phi - 34 \cos^9 \phi + 18 \cos^{11} \phi) \sin \phi] \\
& + \frac{\partial^2 U_{3m}}{\partial \phi^2} [(-67 \cos^6 \phi + 234 \cos^8 \phi - 266 \cos^{10} \phi + 99 \cos^{12} \phi) + \mu \cos^6 \phi \sin^4 \phi] \\
& + \frac{\partial U_{3m}}{\partial \phi} [(66 \cos^5 \phi - 295 \cos^7 \phi + 390 \cos^9 \phi - 162 \cos^{11} \phi) \sin \phi \\
& \quad - \mu (6 \cos^5 \phi - 13 \cos^7 \phi + 7 \cos^9 \phi) \sin \phi] \\
& - \frac{\partial^4 U_{3m}}{\partial \psi^4} + \frac{\partial^2 U_{3m}}{\partial \psi^2} [(-7 \cos^2 \phi + 3 \cos^4 \phi) + \mu \cos^2 \phi \sin^2 \phi] \\
& \left. + \frac{\partial^4 U_{3m}}{\partial \phi^2 \partial \psi^2} [-2 \cos^4 \phi \sin^2 \phi] + \frac{\partial^3 U_{3m}}{\partial \phi \partial \psi^2} [(8 \cos^3 \phi - 6 \cos^5 \phi) \sin \phi] \right\}. \tag{25}
\end{aligned}$$

Application of the algorithm to the optimal control of paraboloidal shell strucronic system is demonstrated next.

CASE STUDIES

Optimal vibration control of a paraboloidal shell strucronic system with free boundary is studied; control sensitivities at various sensor/actuator locations are evaluated. The maximum circumferential radius of the shell is $a=1m$, height $c=1m$ and thickness $h=0.1m$, shown in **Figure 2**. The shell is made of Plexiglas and the piezoelectric sensor/actuator patches are polyvinylidene-fluoride (PVDF) films. The geometry and material properties are summarized in **Table 1**. Three sensor/actuator locations are studied, i.e., Location 1: $(\phi, \psi) = (0.85, 0.1)$, Location 2: $(\phi, \psi) = (0.95, 0.1)$ and Location 3: $(\phi, \psi) = (1.05, 0.1)$, all in radians. The

circumferential widths of the sensor/actuator patches at the three locations are $\psi=0\sim0.2$ radian to exclude the influence of circumferential wave and these three sensor/actuator patches are of identical sizes, i.e., 0.03628m^2 . The meridional coordinates of the patches at the three locations are Location 1: $\phi=0.76262\sim0.93738$ radian, Location 2: $\phi=0.9\sim1.0$ radian and Location 3: $\phi=1.024565\sim1.075435$ radian. Note that the 1st patch (Location 1) slightly overlaps the 2nd patch (Location 2) in order to keep the same circumferential coordinate and thus, the same size.

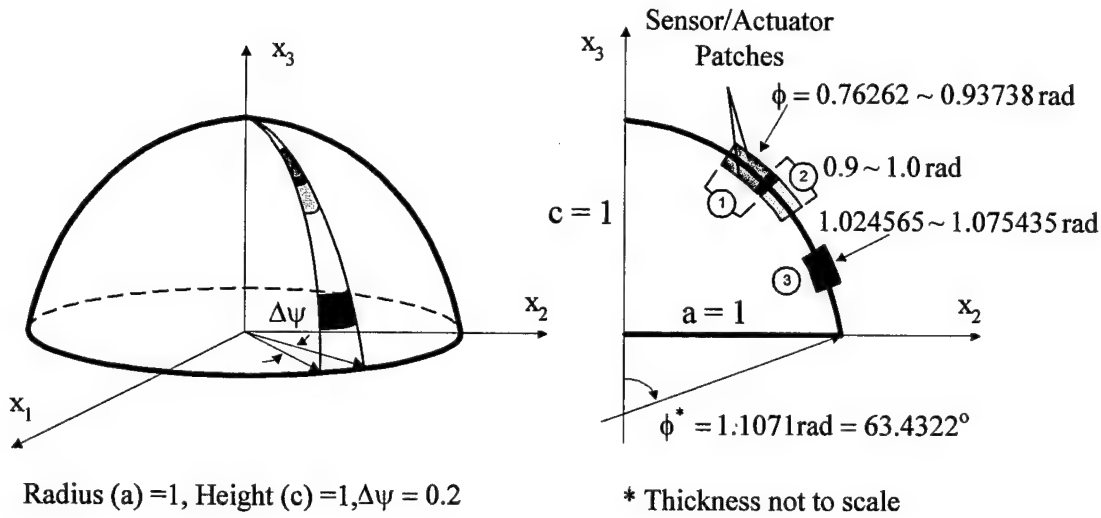


Fig.2 A paraboloidal shell with sensor/actuator patches at three locations.

Table 1 Geometry and material properties of the structronic paraboloidal shell system.

Properties	PVDF Layer	Plexiglas Shell	Units
Circumferential Radius		$a = 1$	m
Meridional Height		$c = 1$	m
Thickness	$h^s = h^a = 5 \times 10^{-4}$	$h = 0.10$	m
Young's Modulus	$Y_p = 2.00 \times 10^9$	$Y = 3.1028 \times 10^9$	N/m ²
Mass Density	$\rho_p = 1800.0$	$\rho = 1190.0$	Kg/m ³
Poisson's Ratio		$\mu = 0.3$	
Bending Stiffness		$D = 2.8414 \times 10^5$	N-m
Membrane Stiffness		$K = 3.4097 \times 10^8$	N/m
Piezoelectric Constants	$h_{31} = 4.32 \times 10^8$		V/m m/m
	$d_{31} = 2.3 \times 10^{-11}$		m/m V/m

Weighting matrices in the optimal control are chosen based on the control performance and the desired control gain cost. (Too large feedback gain is impractical due to physical limitations, although it might provide better control performance.) The total gain cost of G^*

$(G_1^* + G_2^*)$ is assumed to be 300. In order to be compatible with the PD control with $G^* = [200, 100]$, the total gain cost for the optimal control gain \bar{G} is also chosen to be 300. (Note that the exact estimated results from the optimal control algorithm are between 299 and 300 and the gain mentioned here is referred to the ratio between the actuation signal and the sensing signal.) The control input weighting coefficient R is chosen to be 1 for all the optimal control studied here and the state weighting coefficient c is adjusted to achieve the desired gain cost. The optimal gain matrix \bar{G} calculated from the optimal control algorithm indicates that the second entry \bar{G}_2 is dominant, i.e., the gain cost is mostly assigned to the gain related to the second state variable - the derivative component $\dot{\eta}_m$ (i.e., the modal velocity).

Time-history responses of the center of the sensor/actuator patches at three shell locations are investigated, to which an initial displacement 0.001m with zero initial velocity is imposed. Note the initial displacement and velocity need to be converted to the initial system state $x(t_0) = \{\eta(t_0) \ \dot{\eta}(t_0)\}^t$ in the modal domain. Initial modal damping ratio of free vibrations is assumed to be 0.002 and the modal amplitude A_m is set unity. Numerical time steps of the time-history responses are 1000. For comparison, time-histories of the optimal control, free vibration, and the state feedback control using a non-optimal gain, i.e., $G^* = [200, 100]$, of the ($m=2\sim 6$) paraboloidal shell modes at the three sensor/actuator locations are studied and only the ($m=2\sim 4$) responses are presented in **Figures 3-11**. Localized dynamic and control characteristics contribute to the differences among these time histories. Time-histories of the free and control responses are further processed to calculate their inferred equivalent modal damping ratios ($m=2\sim 6$) at these three sensor/actuator locations, resulting from the optimal control (\bar{G}) and the PD control (G^*). **Figure 12** shows the damping ratio variation for the five shell modes ($m=2\sim 6$); **Figure 13** shows the damping ratio variation at three sensor/actuator locations.

These time-history responses clearly reveal that the optimal control is superior to the PD control. However, this control effect reduces at high natural modes, because the oscillation amplitude is usually small, so the sensing and control signals when control gains are fixed. Since the gain estimation involves a specific location and its meridional/circumferential angles of the sensor/actuator patches, the time-history responses at these three locations reveal variations of oscillation frequencies. The coefficients in the system equation and the meridional radii of curvature of paraboloidal shells change with respect to shell locations, and these changes amplify the local characteristics resulting in frequency variations. Natural frequencies of the whole structure are usually the global average effect of all locations on the non-constant radii paraboloidal shell. These local/global phenomena were also observed in lab experiments [18].

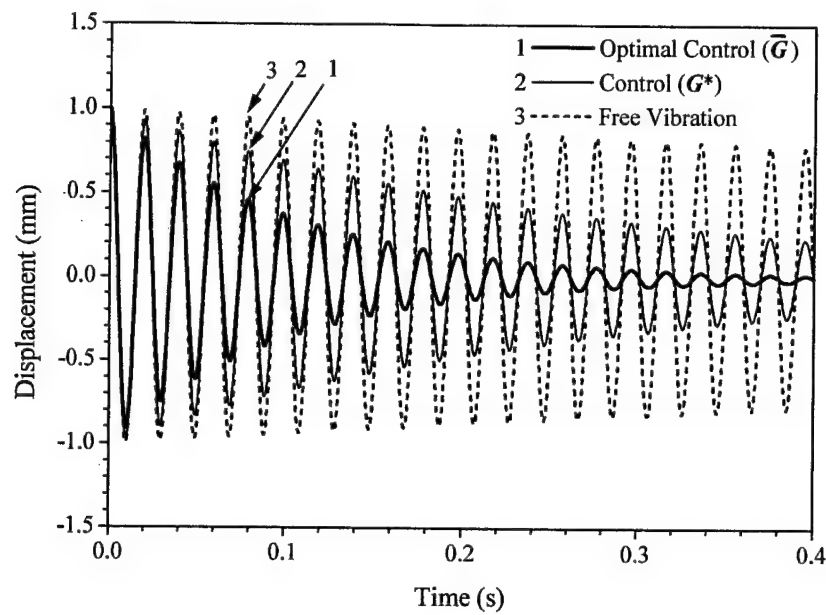


Fig.3 Control with sensor/actuator at Location 1, $m = 2$,
1—Optimal Control (\bar{G}), 2—Control (G^*), 3--- Free Vibration,
 $(G^* = [200, 100], \bar{G} = [8.041272E-05, 299.647600], \text{time step} = 0.4\text{ms})$.

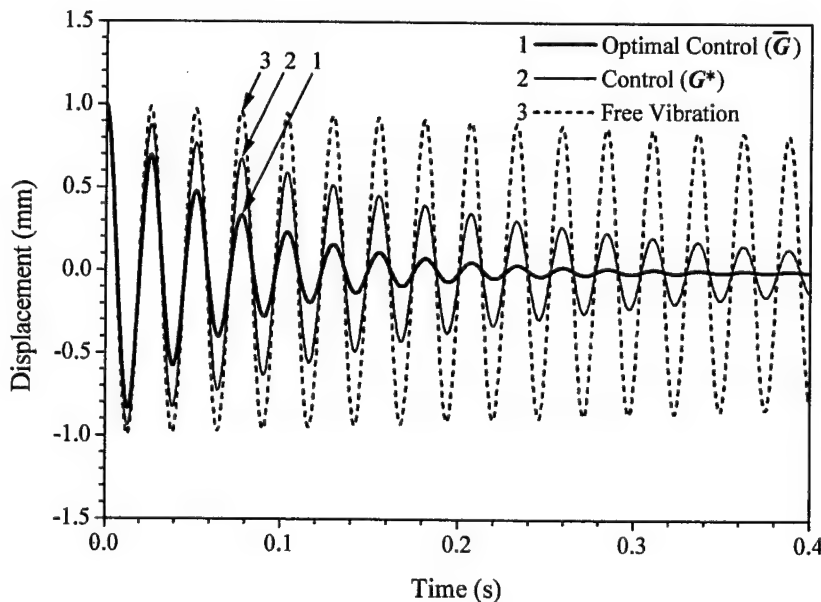


Fig.4 Control with sensor/actuator at Location 2, $m = 2$,
1—Optimal Control (\bar{G}), 2—Control (G^*), 3--- Free Vibration,
 $(G^* = [200, 100], \bar{G} = [9.281180E-05, 299.290900], \text{time step} = 0.4\text{ms})$.

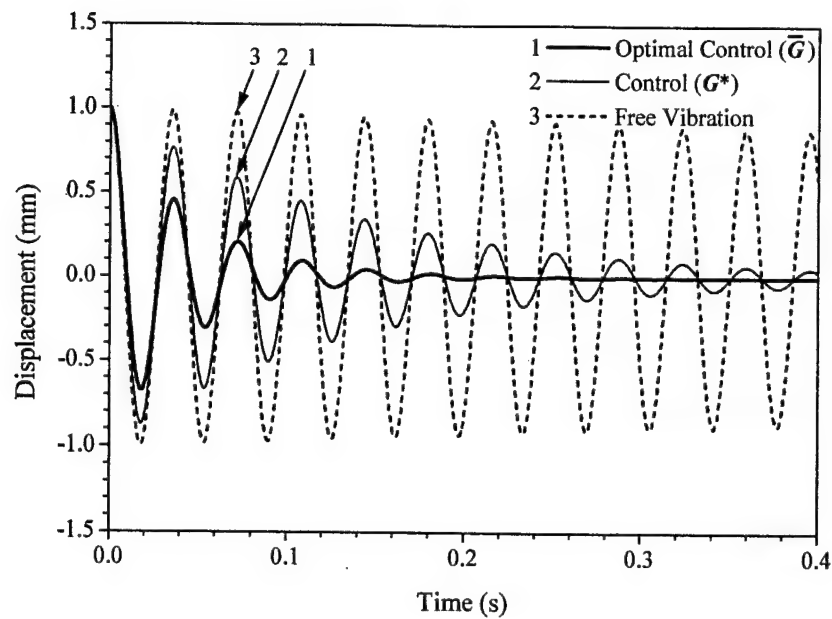


Fig.5 Control with sensor/actuator at Location 3, $m = 2$,
1—Optimal Control (\bar{G}), 2—Control (G^*), 3--- Free Vibration,
 $(G^* = [200, 100], \bar{G} = [1.144451E-04, 299.959400], \text{time step} = 0.4\text{ms})$.

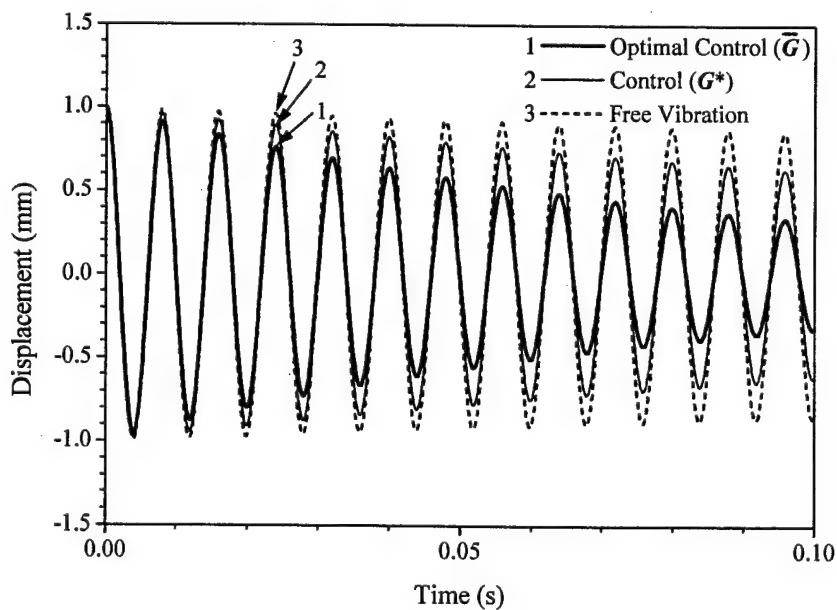


Fig.6 Control with sensor/actuator at Location 1, $m = 3$,
1—Optimal Control (\bar{G}), 2—Control (G^*), 3--- Free Vibration,
 $(G^* = [200, 100], \bar{G} = [1.244259E-05, 299.959700], \text{time step} = 0.1\text{ms})$

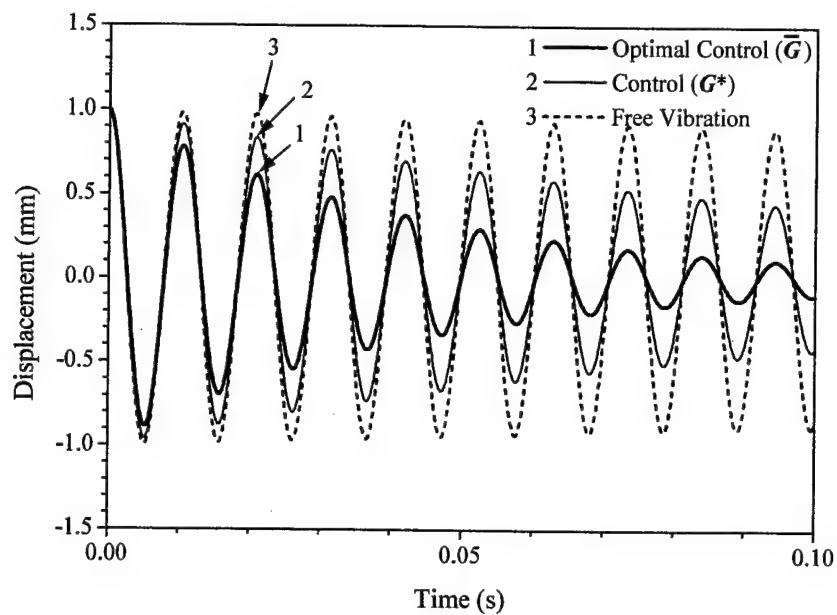


Fig.7 Control with sensor/actuator at Location 2, $m = 3$,
1—Optimal Control (\bar{G}), 2—Control (G^*), 3--- Free Vibration,
 $(G^* = [200, 100], \bar{G} = [9.475585E-06, 299.426500], \text{time step} = 0.1\text{ms})$.

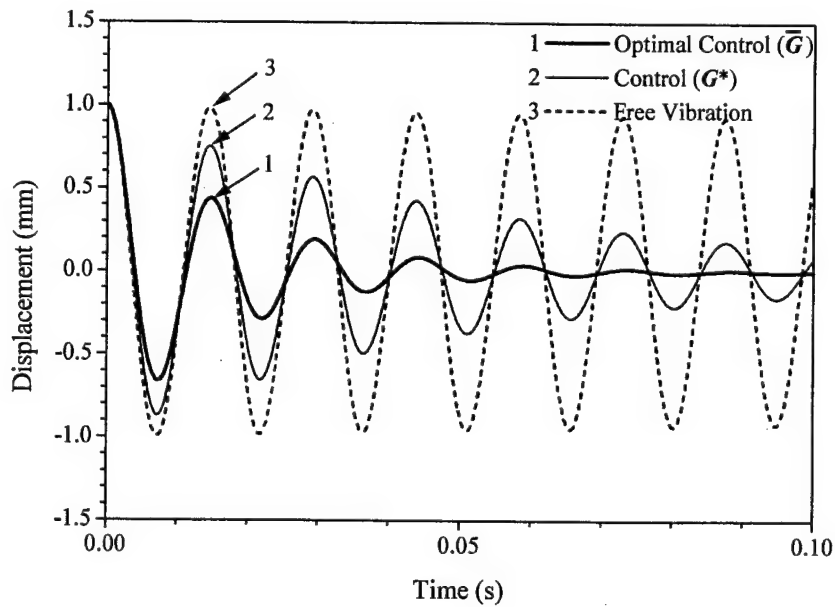


Fig.8 Control with sensor/actuator at Location 3, $m = 3$,
1—Optimal Control (\bar{G}), 2—Control (G^*), 3--- Free Vibration,
 $(G^* = [200, 100], \bar{G} = [7.291031E-06, 299.678100], \text{time step} = 0.1\text{ms})$.

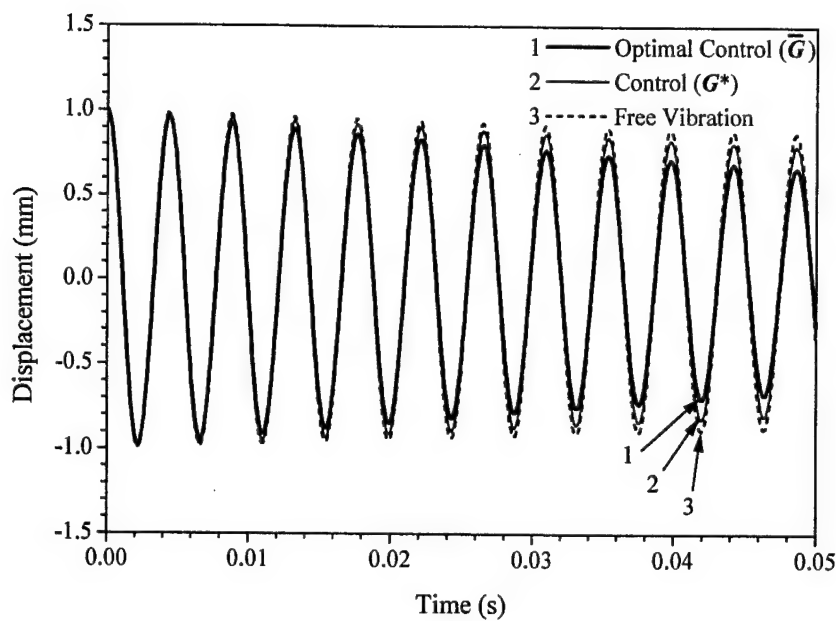


Fig.9 Control with sensor/actuator at Location 1, $m = 4$,
1—Optimal Control (\bar{G}), 2—Control (G^*), 3--- Free Vibration,
 $(G^* = [200, 100], \bar{G} = [6.622339E-06, 299.149400], \text{time step} = 0.05\text{ms})$.

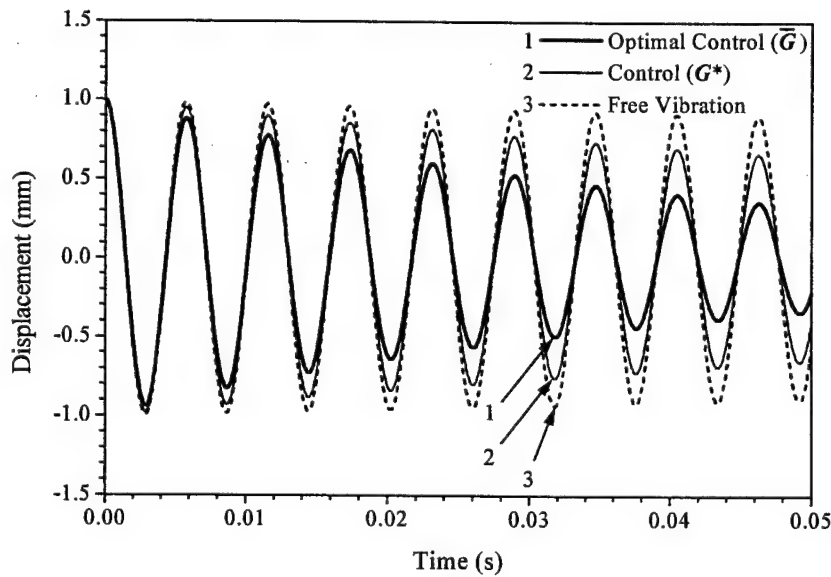


Fig.10 Control with sensor/actuator at Location 2, $m = 4$,
1—Optimal Control (\bar{G}), 2—Control (G^*), 3--- Free Vibration,
 $(G^* = [200, 100], \bar{G} = [3.194133E-06, 299.614500], \text{time step} = 0.05\text{ms})$.

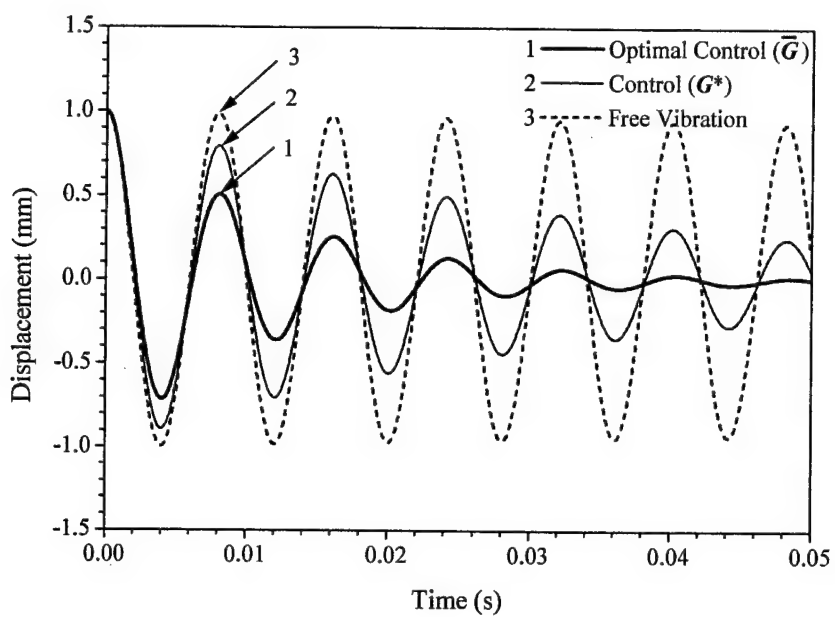
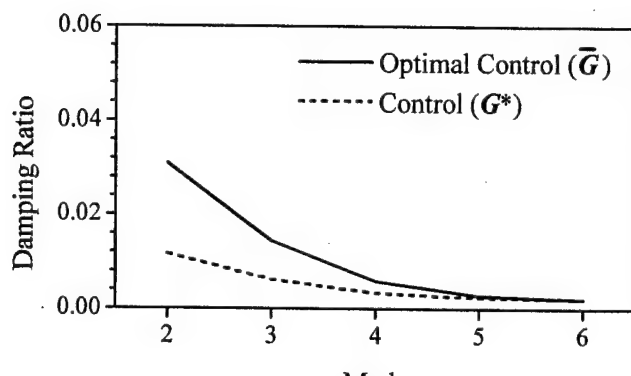
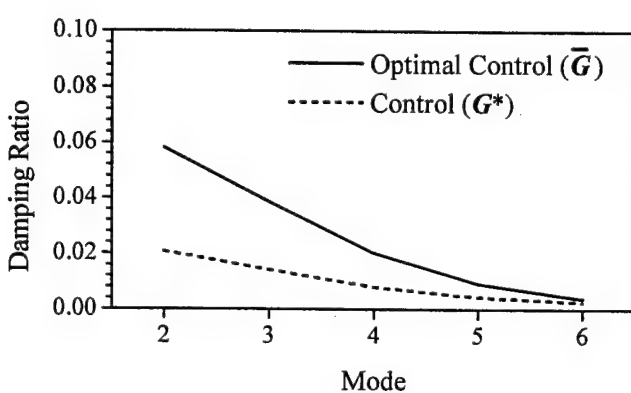


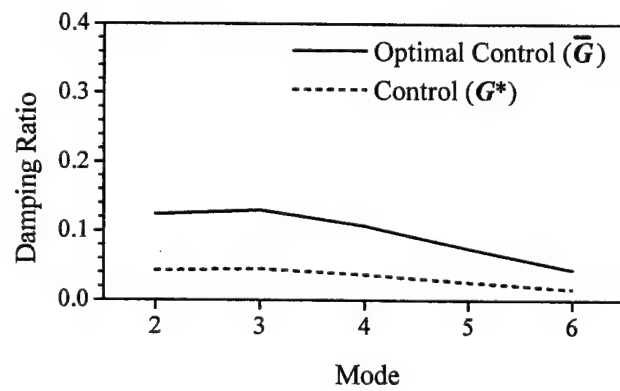
Fig.11 Control with sensor/actuator at Location 3, $m = 4$,
1—Optimal Control (\bar{G}), 2—Control (G^*), 3--- Free Vibration,
 $(G^* = [200, 100], \bar{G} = [1.484552\text{E-}06, 299.465900], \text{time step} = 0.05\text{ms})$.



(a)



(b)

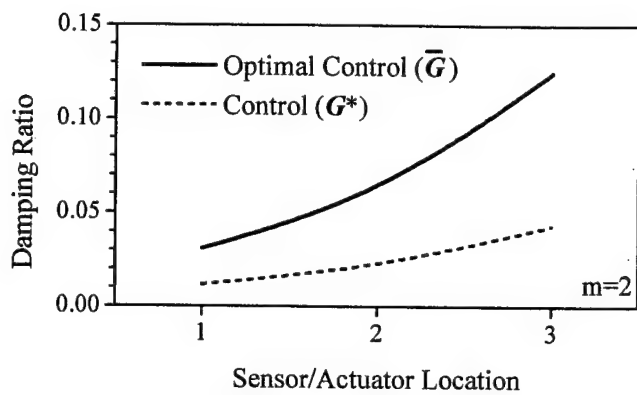


(c)

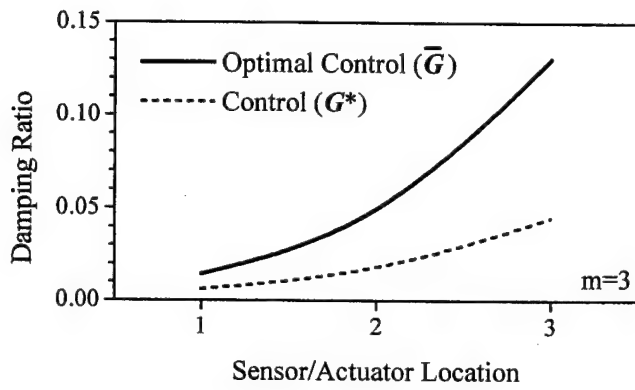
Fig.12 Controlled damping ratio variation with the natural modes,

— Optimal Control (\bar{G}), ---Control (G^*)

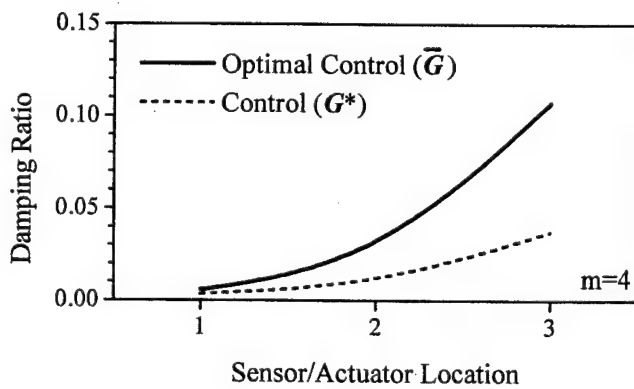
(a): Location 1, (b): Location 2, (c): Location 3.



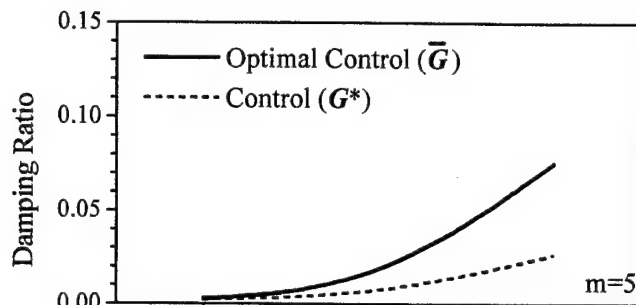
(a)



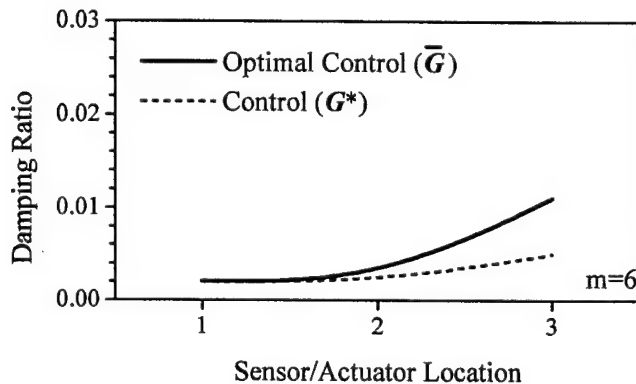
(b)



(c)



(d)



(e)

Fig.13 Controlled damping ratio variation with locations,
— Optimal Control (\bar{G}), ---Control (G^*)
(a): m=2, (b): m=3, (c): m=4, (d): m=5, (e): m= 6.

These data suggest that the sensor/actuator patches near the free shell boundary generate better control results at the same control gain cost. The sensor/actuator patches near the shell boundary have larger sensing/actuating efficiency, besides the shell is also relatively flexible at the free boundary and thus, it is easier to control. The control effects of lower modes are better than those of higher modes at identical feedback gains; the controlled responses are almost unnoticeable at higher modes in some cases, due to low sensing/control signals. It is noted that the controlled damping ratio of the third mode ($m=3$) is slightly larger than that of the second mode ($m=2$) at Location 3 in **Figure 12(c)**. Earlier studies show that there are two modal-influenced contradictory trends in the sensing signal and the open-loop control force characteristics of free-boundary paraboloidal strucronic shells. The sensing efficiency increases with the increase of natural mode, while the control efficiency decreases with the increase of mode. That suggests that the best closed-loop control effect appears at certain medium modes rather than either the lowest or much higher mode. Local frequency variation could also contribute to the modal dependent control effect. To exclude the influence of frequency variation

at different shell locations, the inferred damping ratios are calculated again using the global natural frequencies and the results suggest that 1) the best control effect is now the lowest mode $m=2$; 2) the damping ratio differences among the three locations decrease; and 3) the influence of frequency variation to damping ratio is insignificant at the higher modes [16].

Note that comparing the control effort based on the control energy cost can be an alternative performance evaluation criterion, in which non-constant-cost tuned weightings can be used to achieve specified performances or outcomes (i.e., controlled damping ratios). In this case, the required energy to achieve similar outcomes would be modal dependent, since the in-situ segmented sensor generates less sensing signal at higher natural modes. Accordingly, to achieve a similar outcome, the signal needs a high gain amplification (i.e., more energy) to reach the similar actuator voltage and consequently a similar control effect. In this study, on the other hand, the constant control-cost derived weightings are used and thus the actuator voltage varies, so the controlled modal damping ratios used for comparison among various sensor/actuator locations and natural modes. The former is a goal oriented approach (i.e., comparing cost or energy for a specified performance) and the latter is a **cost** oriented approach (i.e., comparing controlled damping ratios at specified gain costs). Both approaches examine the control effectiveness from two different perspectives.

CONCLUSIONS

A strucronic shell system is defined as an elastic shell bonded, embedded or laminated with active-material based sensors and actuators governed by either in-situ or external control electronics. This study focuses on the optimal vibration control of paraboloidal shell strucronic systems using the linear quadratic (LQ) optimal state feedback. A closed-loop paraboloidal shell strucronic system consisting of distributed sensors/actuators and controller coupled with the elastic paraboloidal shell was defined first, followed by the state-space equation and the optimal control equation based on the LQ state feedback control. Control effects of the same-size sensor/actuator patches at different locations were studied and compared; modal control effects of different shell natural modes were also investigated. The gain matrix was estimated based on minimizing a performance criterion function. Optimal control effects were compared with controlled responses with other non-optimal PD control parameters at the same control energy cost.

Parametric studies demonstrate that the optimal control $\bar{\mathbf{G}}$ of paraboloidal shells with free boundary is, indeed, superior to the PD control \mathbf{G}^* at the same control gain cost. Analysis of sensor/actuator location sensitivity suggests that the sensor/actuator patches placed near the free boundary rim provides the highest control effect of the free-floating paraboloidal shell. Its control effectiveness is obvious for low shell modes and the sensor/actuator located near the free shell rim. This effectiveness becomes insignificant, regardless the control algorithms, for higher shell modes or the sensor/actuator located near the shell pole. This implies that the closed-loop control system for oscillations at higher modes is relatively insensitive to various gain matrices set at identical total gain cost. Accordingly, many system and design parameters, e.g., geometry/material properties, boundary conditions, sensor/actuator placements, feedback control algorithms, dominating vibration modes, frequency performance of control electronics, instruments/devices, etc., influencing the closed-loop control effect need to be considered in

practical implementation of the closed-loop control of precision paraboloidal shell strucronic systems.

ACKNOWLEDGEMENT

This research is supported, in part, by a grant (F49620-98-1-0467) from the Air Force Office of Scientific Research (Project manager: Brian Sanders). This support is gratefully acknowledged.

REFERENCES

- [1] A.P. Sage 1968 *Optimum Systems Control*, Prentice-Hall, Inc, Englewood Cliffs, NJ, 1968, 137-164.
- [2] V. Komkov 1972 *Optimal Control Theory for the Damping of Vibration of Simple Elastic Systems*, Springer-Verlag, Berlin, Heidelberg, New York.
- [3] K. Nonami 1995 *JSME International Journal*, Series C, **38**(3), 367-378. Control performances based on control system design strategies for active structural control.
- [4] M.C. Ray 1998 *AIAA Journal*, **36**(12), Dec. 1998, 2204-2208. Optimal control of laminated plate with piezoelectric sensor and actuator layers.
- [5] B. Fariborzi 2000 *Control of Vibration and Noise: New Millennium, ASME 2000*, AD-Vol.61, 33-145. Design of LQ and LC optimal controllers for plate vibration.
- [6] Y.K. Lin and F.A. Lee 1960 *Journal of Applied Mechanics*, **27**, Dec 1960, 743-744. Vibrations of thin paraboloidal shells of revolution.
- [7] J. T. S. Wang and C. Lin 1967 *NASA CR-932*, Nov 1967. On the differential equations of the axisymmetric vibration of paraboloidal shells of revolution.
- [8] H.S. Tzou 1993 *Piezoelectric Shells (Distributed Sensing and Control of Continua)*, Kluwer Academic Publishers, Boston /Dordrecht.
- [9] J. Qiu and J. Tani 1995 *Journal of Intelligent Material Systems and Structures*, **6**(4), July 1995, 474-481. Vibration control of a cylindrical shell using distributed piezoelectric sensors and actuators.
- [10] H.S. Tzou and Y. Bao 1996 *Journal of Sound and Vibration*, **197**(2), 1996, 207-224. Parametric study of segmented transducers laminated on cylindrical shells, part 1: sensor patches.
- [11] H.S. Tzou and D.W. Wang, 2002 *Journal of Sound & Vibration* **254**(2), 203-218. Distributed dynamic signal analysis of piezoelectric laminated linear and nonlinear toroidal shells.
- [12] J.H. Ding and H.S. Tzou 2003 *Mechanical Systems and Signal Processing (Journal of)*. Micro-electromechanics of sensor patches on free paraboloidal shell strucronic systems. (To appear)
- [13] H.S. Tzou and J.H. Ding 2001 *Proceedings of ASME IMECE 2001, Symposium on Active Control of Noise and Vibration*, New York, NY, Nov 11-16, 2001. *ASME Journal of Dynamics Systems, Measurement, and Control* (Paper No. M01-103) (To appear). Actuator placement and control efficiency of paraboloidal shell structures.
- [14] H.S. Tzou, J.H. Ding and J. Hagiwara 2002 *JSME International Journal*, Series C, **45**(1), 2002. Micro-control actions of segmented actuator patches laminated on deep paraboloidal shells.
- [15] W. Soedel 1981 *Vibrations of Shells and Plates*, Marcel Dekker, Inc., New York and Basel, 47-50, 124-136.

- [16] J.H. Ding 2002 *Micro-piezothermoelastic behavior and distributed sensing/control of nonlinear strucronic beam and paraboloidal shell systems*, Ph.D. Dissertation, University of Kentucky, 394-396.
- [17] B. Friedland 1986 *Control System Design-An Introduction to State-Space Methods*, McGraw-Hill, Inc., New York, 59-63, 337-350.
- [18] P.G. Glockner and K.Z. Tawardros 1973 *Experimental Mechanics*, 13(10), Oct 1973, 411-421. Experiments on free vibration of shells of revolution.

CHAPTER 16

DYNAMICS AND DISTRIBUTED CONTROL OF CONICAL SHELLS LAMINATED WITH FULL AND DIAGONAL ACTUATORS (Finite Element Development and Analysis)

ABSTRACT

Nozzles, rocket fairings and many engineering structures/components are often made of conical shells. This paper focuses on the finite element modeling, analysis, and control of conical shells laminated with distributed actuators. Electromechanical constitutive equations and governing equations of a generic piezo(electric)elastic continuum are defined first, followed by the strain-displacement relations and electric field-potential relations of laminated shell composites. Finite element formulation of a piezoelastic shell element with non-constant Lamé parameters is briefly reviewed; element and system matrix equations of the piezoelastic shell sensor/actuator/structure laminate are derived. The system equation reveals the coupling of mechanical and electric fields, in which the electric force vector is often used in distributed control of shells. Finite element eigenvalue solutions of conical shells are compared with published numerical results first. Distributed control of the conical shell laminated with piezoelectric shell actuators is investigated and control effects of three actuator configurations are evaluated.

INTRODUCTION

Conical shell structures and components are often used as nozzles, injectors, rocket fairings, fan blades, etc. in aerospace structures and turbomachinery. Undesirable dynamic oscillations not only degrade the performance, but also influence structural integrity and reliability. Dynamics and vibrations of conical shells have been widely studied [1,2]; however, distributed vibration control of conical shells has not caught much attention over the years. Recent rapid development of smart structures and structronic systems provides many new design options for the next-generation high-performance mechanical and structural systems [3,4]. Based on the smart structures and structronics technology, this study is to evaluate dynamic characteristics and control effects of conical shells laminated with fully or diagonally distributed piezoelectric sensor/actuator layers.

Piezoelectrics, shape-memory materials, electrostrictive materials, magnetostrictive materials, photostrictive materials, electro- and magneto-rheological materials, etc. are electro-,

magneto-, and/or optoelectro-mechanically controllable materials and thus they are generally accepted as “smart” materials [3,4]. Among these smart materials, piezoelectric materials are probably the most popular smart material applied to both sensor and actuator applications. Distributed sensing and control of shells and plates using piezoelectric materials have been investigated over the years [5]. Distributed control effects of one dimensional and two dimensional planar structures, e.g., beams and plates, are studied and compared [5-11], and also rings and shells [5,12-15]. Piezothermoelastic characteristics and temperature influences on piezoelectric sensors and actuators of beam-type precision devices and cylindrical shell structures have been studied [15-17]. This study is to investigate the modeling, analysis, and distributed vibration control of piezoelectric laminated conical shells. Fundamental piezoelectric constitutive and governing equations are briefly reviewed and formulation of a new piezo(electric)-elastic triangle composite shell finite element with non-constant radii of curvature is presented. Dynamic characteristics and distributed vibration controls of conical shells are investigated. Control effects of three actuator designs are evaluated.

GOVERNING EQUATIONS

Electromechanical constitutive and equilibrium equations of a piezo(electric)elastic continuum are defined first, and followed by generic shell strain-displacement definitions of a double-curvature piezoelectric shell laminate in this section. Finite element formulations are presented in the next section. The linear piezoelectric constitutive equations coupling the electric and elastic fields are [5]

$$T_{ij} = c_{ijkl}^{E,\theta} (S_{kl} - S_{kl}^0) - e_{ijm}^{\theta} E_m \quad \text{and} \quad D_n = e_{nkl}^{\theta} (S_{kl} - S_{kl}^0) + \epsilon_{nm}^{S,\theta} E_m, \quad (1,2)$$

where T_{ij} and D_i denote the stress and electric displacements; $c_{ijkl}^{E,\theta}$, e_{ijm}^{θ} , and $\epsilon_{nm}^{S,\theta}$, respectively denote the elastic moduli, piezoelectric coefficient, dielectric constants; S_{kl} , and S_{kl}^0 are the strain, and initial strains. In addition, the superscripts E, θ , and S denote the coefficients defined at a constant electric field, temperature and strain, respectively. For a piezoelectric shell medium, with a volume V and a limited surface area S , subjected to both electric and mechanical excitations, the linear governing equations, including the coupling among deformation and electric potential, can be defined as follows [16-18].

$$T_{ij,j} + f_{bi} = \rho \ddot{U}_i \quad \text{and} \quad D_{ij} = 0, \quad (3,4)$$

where f_{bi} , ρ , and \ddot{U}_i respectively denote the body force, mass density, and acceleration; and U_i is the displacement. Note that Einstein’s summation convention is used in the expressions.

A piezoelectric laminated shell continuum is composed of N laminae, and each lamina can be either elastic material or piezoelectric material, Figure 1. It is assumed that the piezoelectric shell is exposed to mechanical and electrical inputs. Considering small deformation of the laminated piezoelectric shell, one can derive the strain S_{ij} and electric field E_i equations defined in an orthogonal curvilinear coordinate system $(\alpha_1, \alpha_2, \alpha_3)$. The strain

(S_{ij}) - displacement relations and electric field (E_i) - electric potential (ϕ) relations in a tri-orthogonal shell coordinate system are defined as follows [5,17]

$$S_{11} = \frac{1}{(1 + \frac{\alpha_3}{R_1})A_1} \left[\frac{\partial U_1}{\partial \alpha_1} + \frac{1}{A_2} \frac{\partial A_1}{\partial \alpha_2} U_2 + \frac{A_1}{R_1} U_3 \right], \quad (5)$$

$$S_{22} = \frac{1}{(1 + \frac{\alpha_3}{R_2})A_2} \left[\frac{\partial U_2}{\partial \alpha_2} + \frac{1}{A_1} \frac{\partial A_2}{\partial \alpha_1} U_1 + \frac{A_2}{R_2} U_3 \right], \quad S_{33} = \frac{\partial U_3}{\partial \alpha_3}, \quad (6,7)$$

$$S_{12} = \frac{1}{2(1 + \frac{\alpha_3}{R_1})A_1} \left[\frac{\partial U_2}{\partial \alpha_1} - \frac{1}{A_2} \frac{\partial A_1}{\partial \alpha_2} U_1 \right] + \frac{1}{2(1 + \frac{\alpha_3}{R_2})A_2} \left[\frac{\partial U_1}{\partial \alpha_2} - \frac{1}{A_1} \frac{\partial A_2}{\partial \alpha_1} U_2 \right], \quad (8)$$

$$S_{13} = \frac{1}{2(1 + \frac{\alpha_3}{R_1})A_1} \left[\frac{\partial U_3}{\partial \alpha_1} - \frac{A_1}{R_1} U_1 \right] + \frac{1}{2} \frac{\partial U_1}{\partial \alpha_3}, \quad (9)$$

$$S_{23} = \frac{1}{2(1 + \frac{\alpha_3}{R_2})A_2} \left[\frac{\partial U_3}{\partial \alpha_2} - \frac{A_2}{R_2} U_2 \right] + \frac{1}{2} \frac{\partial U_2}{\partial \alpha_3}, \quad (10)$$

$$E_1 = -\frac{1}{(1 + \frac{\alpha_3}{R_1})A_1} \frac{\partial \phi}{\partial \alpha_1}, \quad E_2 = -\frac{1}{(1 + \frac{\alpha_3}{R_2})A_2} \frac{\partial \phi}{\partial \alpha_2}, \quad E_3 = -\frac{\partial \phi}{\partial \alpha_3}, \quad (11a,b,c)$$

where S_{ij} , ϕ , and E_i denote the strains, electric potential, and electric fields, respectively; R_1 and R_2 are the radii of principal curvature; and A_1 and A_2 are the Lamé parameters.

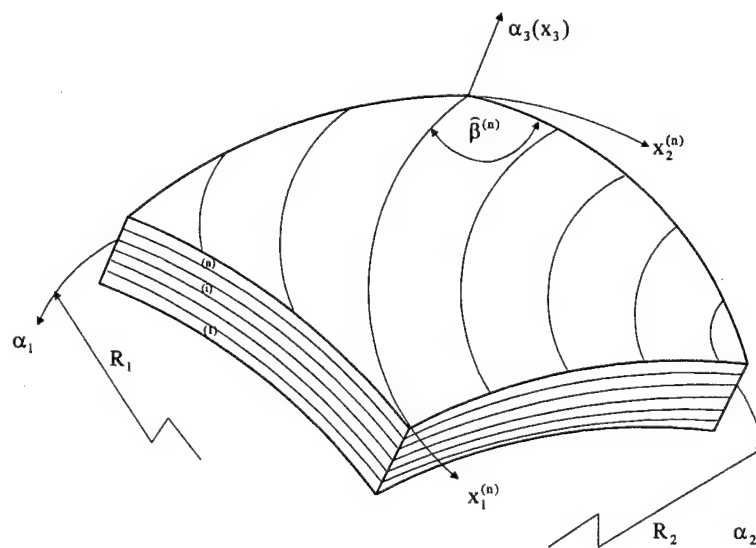


Fig.1 A piezo(electric)elastic laminated shell continuum.

There are mechanical and electric boundary conditions associated with the piezoelastic shell continuum, i.e.,

$$U_i = \bar{U}_i, \quad T_{ij} \ell_j = f_i, \quad (12,13)$$

$$\phi = \bar{\phi}, \quad D_i \ell_i = -Q, \quad (14,15)$$

Where U_i is the displacement; ℓ_i is the direction cosine components; f_i is the surface force; ϕ is the electric potential; Q is the charge; and $(\bar{\cdot})$ denotes a known boundary value. Using the weighted residual method and introducing arbitrary weighting quantities δU_i and $\delta \phi$, one can rewrite the weak form of the equilibrium equations as [17,19]

$$\int \delta U_i (T_{ij,j} + f_{bi} - \rho \ddot{U}_i) dV = 0, \quad (16)$$

$$\int \delta \phi D_{ii} dV = 0, \quad (17)$$

where the quantities δU_i and $\delta \phi$ can be defined as the virtual displacement and electric potential respectively. Integrating each term by parts, taking into account of boundary conditions defined in Eqs.(12)-(15), and noting that $\delta U_i = 0$ on S_u and $\delta \phi = 0$ on S_ϕ , one can simplify Eqs.(16)-(17) to

$$\int T_{ij} \delta S_{ij} dV - \int_{S_T} f_i \delta U_i dS - \int (f_{bi} - \rho \ddot{U}_i) \delta U_i dV = 0, \quad (18)$$

$$\int D_i \delta E_i dV - \int_{S_D} Q \delta \phi dS = 0, \quad (19)$$

Note that Eqs.(18)-(19) are the virtual work expressions of the piezo(electric)-elastic shell continuum.

PIEZOELASTIC FINITE ELEMENT FORMULATION

A new twelve-node, forty-eight degree-of-freedom curved triangular laminated piezoelastic shell element with non-constant radii of curvature (i.e., non-constant Lamé parameters) is developed. Figure 2 illustrates the triangular shell element and all its twelve nodes. Each node allows three displacement variables (i.e., $U_1^{(i)}(\gamma)$, $U_2^{(i)}(\gamma)$, and $U_3^{(i)}(\gamma)$) and one electric potential variable $\phi^{(i)}(\gamma)$ [14,17].

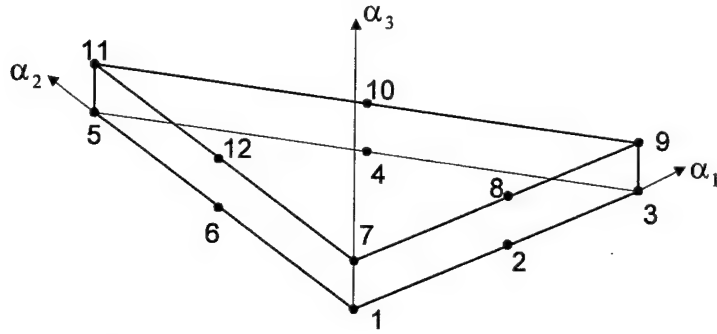


Fig.2 Triangular piezoelastic composite shell finite element.

Assumptions of layerwise constant shear angle and linear variation along thickness of each layer are used in the finite element derivations. Thus, for an arbitrary i -th layer, the displacements $U_1^{(i)}(\gamma)$, $U_2^{(i)}(\gamma)$, and $U_3^{(i)}(\gamma)$ and electric potential $\phi^{(i)}(\gamma)$ can be expressed as

$$U_1^{(i)}(\gamma) = \bar{U}_1^{(i)}(1 - \frac{\gamma}{h_i}) + \bar{U}_1^{(i+1)} \frac{\gamma}{h_i}, \quad U_2^{(i)}(\gamma) = \bar{U}_2^{(i)}(1 - \frac{\gamma}{h_i}) + \bar{U}_2^{(i+1)} \frac{\gamma}{h_i}, \quad (20,21)$$

$$U_3^{(i)}(\gamma) = \bar{U}_3^{(i)}(1 - \frac{\gamma}{h_i}) + \bar{U}_3^{(i+1)} \frac{\gamma}{h_i}, \quad \phi^{(i)}(\gamma) = \bar{\phi}^{(i)}(1 - \frac{\gamma}{h_i}) + \bar{\phi}^{(i+1)} \frac{\gamma}{h_i}, \quad (22,23)$$

where γ is a transverse coordinate defined for the i -th layer; h_i is the thickness of the i -th layer. The displacement and potential expressions can be simply written as functions of shape functions and the i -th layer displacement vector

$$\{U^{(i)}(\gamma)\} = [N_u^{(i)}(\gamma)] \{\bar{U}^{(i)}\}, \quad (24)$$

$$\phi^{(i)}(\gamma) = [N_\phi^{(i)}(\gamma)] \{\bar{\phi}^{(i)}\}, \quad (25)$$

where $\{U^{(i)}(\gamma)\} = \{U_1^{(i)}(\gamma), U_2^{(i)}(\gamma), U_3^{(i)}(\gamma)\}^t$ is a displacement vector of any point on the i -th layer. $\{\bar{U}^{(i)}\} = \{\bar{U}_1^{(i)}, \bar{U}_2^{(i)}, \bar{U}_3^{(i)}, \bar{U}_1^{(i+1)}, \bar{U}_2^{(i+1)}, \bar{U}_3^{(i+1)}\}^t$ and $\{\bar{\phi}^{(i)}\} = \{\bar{\phi}^{(i)}, \bar{\phi}^{(i+1)}\}^t$ are the displacements and electric potential of the i -th and $(i+1)$ -th interfaces along the curvilinear coordinate axes. $[N_u^{(i)}(\gamma)]$ and $[N_\phi^{(i)}(\gamma)]$ are the shape functions in terms of the coordinate γ . The interpolation functions of the surface-parallel displacements and electric potential in each triangular region at the i -th or $(i+1)$ -th interface are chosen to be continuous piecewise quadratic in the form

$$\begin{Bmatrix} \{\bar{U}^{(i)}\} \\ \{\bar{\phi}^{(i)}\} \end{Bmatrix} = a_1 \alpha_1^2 + a_2 \alpha_2^2 + a_3 \alpha_1 \alpha_2 + a_4 \alpha_1 + a_5 \alpha_2 + a_6, \quad (26)$$

where a_i ($i = 1, \dots, 6$) are constants; and α_i ($i = 1, 2, 3$) are the global coordinates. Due to the continuity across the edge between two adjacent triangle elements, Eq.(40) becomes

$$\bar{U}_1^{(i)} = \{N\}^t \{U_1^{(i)}\}, \quad \bar{U}_2^{(i)} = \{N\}^t \{U_2^{(i)}\}, \quad (27,28)$$

$$\bar{U}_3^{(i)} = \{N\}^t \{U_3^{(i)}\}, \quad \bar{\phi}^{(i)} = \{N\}^t \{\phi^{(i)}\}, \quad (29,30)$$

where $\{U_1^{(i)}\} = \{U_{11}^i, \dots, U_{16}^i\}^t$, $\{U_2^{(i)}\} = \{U_{21}^i, \dots, U_{26}^i\}^t$, $\{U_3^{(i)}\} = \{U_{31}^i, \dots, U_{36}^i\}^t$ and $\{\phi^{(i)}\} = \{\phi_1^i, \dots, \phi_6^i\}^t$ are the nodal displacement and electric potential vectors of the element. $\{N\}$ is the quadratic shape function. Substituting Eqs.(27)-(30) into Eqs.(24)-(25) yields to the following displacement $\{\bar{U}^{(i)}\}$ and electric potential $\{\bar{\phi}^{(i)}\}$ expressions

$$\{\bar{U}^{(i)}\} = [N_{u_j}(\alpha_1, \alpha_2)] \{U_j^{(i)}\}, \quad \{\bar{\phi}^{(i)}\} = [N_{\phi_j}(\alpha_1, \alpha_2)] \{\phi_j^{(i)}\}, \quad (31,32)$$

where $\{U_j^{(i)}\} = \{U_{11}^i, U_{21}^i, U_{31}^i, \dots, U_{16}^i, U_{26}^i, U_{36}^i, U_{11}^{i+1}, U_{21}^{i+1}, U_{31}^{i+1}, \dots, U_{16}^{i+1}, U_{26}^{i+1}, U_{36}^{i+1}\}^t$ and $\{\phi_j^{(i)}\} = \{\phi_1^i, \dots, \phi_6^i, \phi_1^{i+1}, \dots, \phi_6^{i+1}\}^t$ are the nodal displacements and the nodal electric potential of the j -th planar layer element located on the i -th layer, respectively. $[N_{u_j}(\alpha_1, \alpha_2)]$ and $[N_{\phi_j}(\alpha_1, \alpha_2)]$ are the shape functions of coordinates α_1 and α_2 . Writing the shell strain-displacement and electric field-potential expressions in terms of nodal variables of the piezoelastic shell finite element gives

$$\begin{aligned} \{S^{(i)}(\gamma)\} &= [L_u^{(i)}] [N_u^{(i)}(\gamma)] [N_{u_j}(\alpha_1, \alpha_2)] \{U_j^{(i)}\} \\ &= [B_u^{(i)}(\gamma)] [B_{u_j}(\alpha_1, \alpha_2)] \{U_j^{(i)}\}, \end{aligned} \quad (33)$$

$$\begin{aligned} \{E^{(i)}(\gamma)\} &= -[L_\phi^{(i)}] [N_\phi^{(i)}(\gamma)] [N_{\phi_j}(\alpha_1, \alpha_2)] \{\phi_j^{(i)}\} \\ &= -[B_\phi^{(i)}(\gamma)] [B_{\phi_j}(\alpha_1, \alpha_2)] \{\phi_j^{(i)}\}, \end{aligned} \quad (34)$$

Substituting the constitutive equations (Eqs.(1)-(2)), displacement-shape function equations (Eqs.(24)-(25) and (31)-(34)) into the equilibrium equations (Eqs.(18)-(19)), one can derive the nodal governing equations of the j -th (planar) element located on the i -th (thickness) layer in a matrix form

$$\begin{bmatrix} [M_{uu_j}^{(i)}] & 0 \\ 0 & 0 \end{bmatrix} \begin{Bmatrix} \{\dot{U}_j^{(i)}\} \\ \{\ddot{\phi}_j^{(i)}\} \end{Bmatrix} + \begin{bmatrix} [C_{uu_j}^{(i)}] & 0 \\ 0 & 0 \end{bmatrix} \begin{Bmatrix} \{\dot{U}_j^{(i)}\} \\ \{\dot{\phi}_j^{(i)}\} \end{Bmatrix} + \begin{bmatrix} [K_{uu_j}^{(i)}] & [K_{u\phi_j}^{(i)}] \\ [K_{\phi u_j}^{(i)}] & [K_{\phi\phi_j}^{(i)}] \end{bmatrix} \begin{Bmatrix} \{U_j^{(i)}\} \\ \{\phi_j^{(i)}\} \end{Bmatrix} = \begin{Bmatrix} \{F_{u_j}^{(i)}\} \\ \{F_{\phi_j}^{(i)}\} \end{Bmatrix}, \quad (35)$$

where $[M_{uu_j}^{(i)}]$ is the mass matrix; $[C_{uu_j}^{(i)}]$ is the damping matrices; $[K_{xy_j}^{(i)}]$ (where $x \& y = u, \phi$), are the stiffness matrices defined for the displacement and electric potential; and $\{F_{u_j}^{(i)}\}$ and $\{F_{\phi_j}^{(i)}\}$ are the mechanical and electric excitations. Detailed element matrices of a laminated piezoelastic shell element are presented in Appendix. The element damping matrix $[C_{uu_j}^{(i)}]$ is

assumed to be proportional to the stiffness and mass matrices: $[C_{uu}^{(i)}] = \alpha [M_{uu}^{(i)}] + \beta [K_{uu}^{(i)}]$ where α and β are Rayleigh's coefficients and are related to $\alpha + \beta \omega_i^2 = 2 \xi_i \omega_i$ and ξ_i and ω_i are the initial damping ratio and natural frequencies [17]. If two damping ratios and two natural frequencies are specified, the damping estimation results in an exact solution for α and β . If more than two damping ratios and frequencies are specified, a least square solution procedure can be used to determine α and β . Assembling all element matrices yields the global system matrix equation

$$\begin{bmatrix} [M_{uu}] & 0 \\ 0 & 0 \end{bmatrix} \begin{Bmatrix} \{\ddot{U}\} \\ \{\ddot{\phi}\} \end{Bmatrix} + \begin{bmatrix} [C_{uu}] & 0 \\ 0 & 0 \end{bmatrix} \begin{Bmatrix} \{\dot{U}\} \\ \{\dot{\phi}\} \end{Bmatrix} + \begin{bmatrix} [K_{uu}] & [K_{u\phi}] \\ [K_{\phi u}] & [K_{\phi\phi}] \end{bmatrix} \begin{Bmatrix} \{U\} \\ \{\phi\} \end{Bmatrix} = \begin{Bmatrix} \{F_u\} \\ \{F_\phi\} \end{Bmatrix}, \quad (36)$$

For static applications, the dynamic system equation is reduced to

$$\begin{bmatrix} [K_{uu}] & [K_{u\phi}] \\ [K_{\phi u}] & [K_{\phi\phi}] \end{bmatrix} \begin{Bmatrix} \{U\} \\ \{\phi\} \end{Bmatrix} = \begin{Bmatrix} \{F_u\} \\ \{F_\phi\} \end{Bmatrix}. \quad (37)$$

In the constant-gain negative velocity feedback control, the feedback control forces $\{F_f^a\}$ are given by [5]

$$\{F_f^a\} = -[K_{u\phi}][K_{\phi\phi}]^{-1}G C_p [K_{\phi\phi}]^{-1}[K_{\phi u}]\{\dot{U}\}, \quad (38)$$

where G is the gain; C_p is the actuator capacitance; $[\cdot]^{-1}$ denotes the matrix inverse, and $\{\dot{U}\}$ is the velocity. Note that, in this case, the feedback gain is constant while the feedback amplitude varies with respect to the negative oscillating velocity (*negative velocity, constant gain proportional feedback control*) [5,16,17]. The developed new piezoelastic shell element with non-constant Lamé parameters and the finite element code are used to investigate dynamics and distributed control of conical shells presented next.

DYNAMICS AND CONTROL OF CONICAL SHELLS

Conical shells are widely used as parts or components of nozzles, rocket fairings, etc. in aerospace structures and turbomachinery. Dynamics and distributed control of conical shells and other shells of revolution with non-constant Lamé parameters can be studied based on the new piezoelastic shell element with non-constant radii of curvature. A conical shell panel laminated with distributed piezoelectric layers is clamped at one end and free on the other three edges (i.e., CFFF). The conical shell is defined in Figure 3 and its dimensions are shown in Figure 4. Geometry and material properties are provided in Table 1. Natural frequencies and modes of a conical shell panel are investigated first and finite element solutions are compared with published numerical results. Distributed vibration control of conical shells with 1) the fully distributed piezoelectric actuator, 2) the partial-diagonally distributed actuator, and 3) the full-diagonally distributed actuator are investigated and their control effects are evaluated in this section.

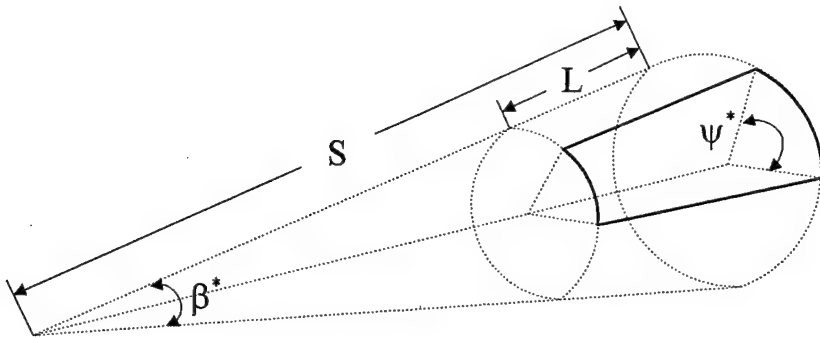


Fig.3 A conical shell panel and its coordinate system.

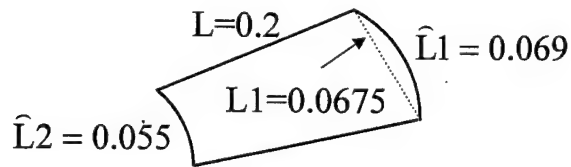


Fig.4 Dimensions of the conical shell panel.

Table 1. Geometry and material properties of the laminated conical shell.

	Aluminum	PVDF
Length, S (m)	1.0	
Length, L (m)	0.2	
Semi-vertex angle, β^* ($^{\circ}$)	15	
Meridional angle, ψ^* ($^{\circ}$)	30.247	
Thickness, h (m)	1×10^{-3}	9×10^{-6}
Density, ρ (Kgm^{-3})	2.6573×10^3	1.8×10^3
Young's modulus, Y (Pa)	6.8947×10^{10}	2.0×10^9
Poisson's constant, μ	0.3	0.29
Piezostain constant, d_{31} (mV^{-1})		2.2×10^{-11}
Electric permittivity, ϵ_{11} (Fm^{-1})		1.062×10^{-10}
Capacitance, C (Fm^{-2})		3.80×10^{-6}

The conical shell panel is divided into (20×10) meshes along the longitudinal and circumferential directions, respectively. Therefore, there are 400 triangular shell elements for each layer and totally 1200 elements are used for the panel, Figure 5.

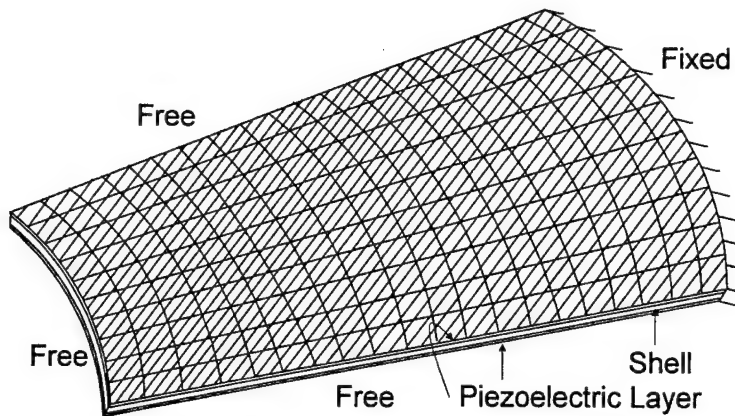


Fig.5 Finite element model of the conical shell panel laminated with fully distributed piezoelectric layers.

Free Vibration Analysis

Natural frequencies and mode shapes of the conical shell panel are studied first. In order to compare with published data, dimensionless frequency parameter $\lambda_n = \omega_n (\beta^*, \psi^*) LL_1 (\rho h / D)^{1/2}$ is used where ω_n is the circular frequency; ρ is the mass density; L is the length of the conical shell panel in the longitudinal direction; L_1 is the projected length of the major edge shown in Figure 4; h is the shell thickness and D is the bending stiffness coefficient $D = (Yh^3) / [12(1 - \mu^2)]$. Finite element solutions (FE) are compared with published numerical results [1,2] in Table 2.

Table 2. Comparison of FE solutions with published data.

Source	λ_1	λ_2	λ_3	λ_4	λ_5	λ_6	λ_7	λ_8
FE	5.3182	8.7357	27.300	28.973	51.111	65.595	72.416	81.477
[1]	5.5130	8.9563	26.989	28.852	50.174	64.497	75.479	79.578
[1]	5.5179	8.9608	27.014	28.909	50.267	64.631	75.541	79.815
[2]	6.1727	9.0708	27.299	29.758	50.669	65.171	74.499	80.201

Note: [1]: Bardell, N. S., 1998; [2]: Lim, C. W. and Liew, K. M., 1995.

These data and comparison suggest that the developed finite element code is capable of analyzing conical shells accurately. The first four mode shapes of the conical shell panel are calculated and they are illustrated in Figure 6.

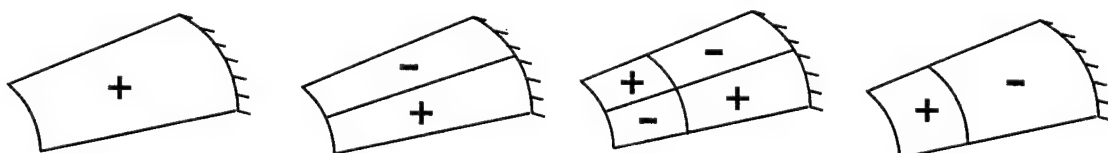


Fig.6 The first four mode shapes of the conical shell panel.

Distributed Vibration Control

The conical shell panel is laminated with two piezoelectric layers on the top and bottom surfaces serving as sensor and actuator, respectively. Three actuator lamination configurations: the full lamination (Figure 5), the partial-diagonal lamination and the full-diagonal lamination (Figure 7) are designed to evaluate their control effectiveness. Two uniform transverse line loadings with a sum of 1 N are applied on the minor-radius free edge. One is applied on the whole free-end edge and the other is applied only on a half of the free end, Figure 8. In general, the initial loading is applied to the free edge first. Then the shell is released and free to oscillate. Free oscillation responses of the conical shells with and without distributed control are evaluated and their inferred damping ratios with different control gains (0,10,20,25) for three lamination configurations are evaluated. Note that control signals generated from the control gains are within the breakdown voltage of the distributed piezoelectric actuators.

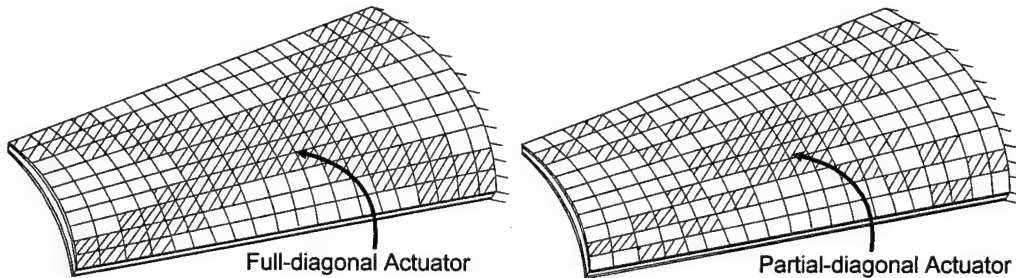


Fig.7 Conical shell panel with full- and partial- diagonally laminated actuators.

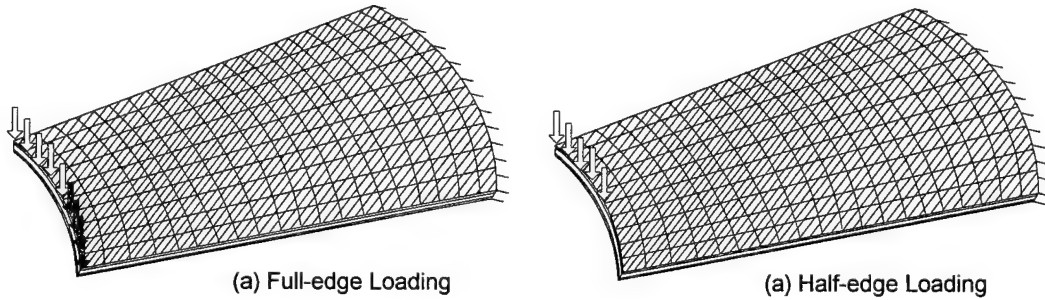


Fig.8 Two loading conditions.

Case 1: Full-edge Loading

Time histories of the free and controlled responses of the conical shell at the full-edge loading are plotted in Figures 9-13 and inferred damping ratios are summarized in Figure 13. Note that Figure 9 is the free response; Figure 10 is the controlled response with the fully distributed actuator; Figure 11 is the controlled response with the partial-diagonal actuator; and Figure 12 is the controlled response with the full-diagonal actuator. In general, the first-mode response dominates both the free and controlled responses. Note that all controlled responses were based on the negative velocity constant-gain feedback control algorithm.

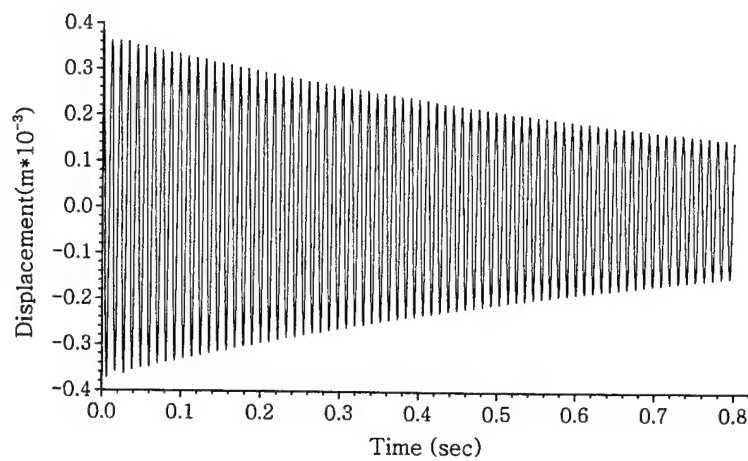


Fig.9 Free displacement response (Full-edge loading).

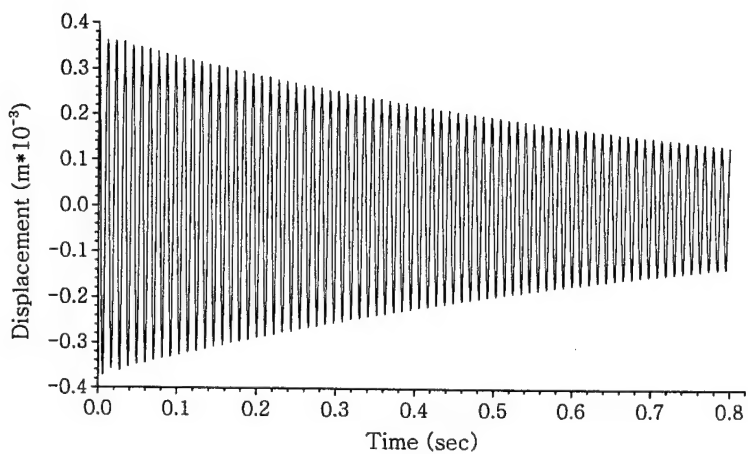


Fig.10 Controlled response (gain = 25)(Fully distributed actuator).

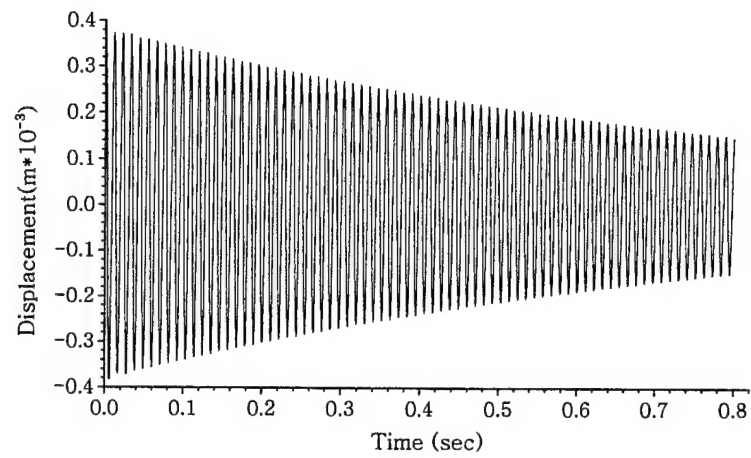


Fig.11 Controlled response (gain = 25)(Partial-diagonal actuator).

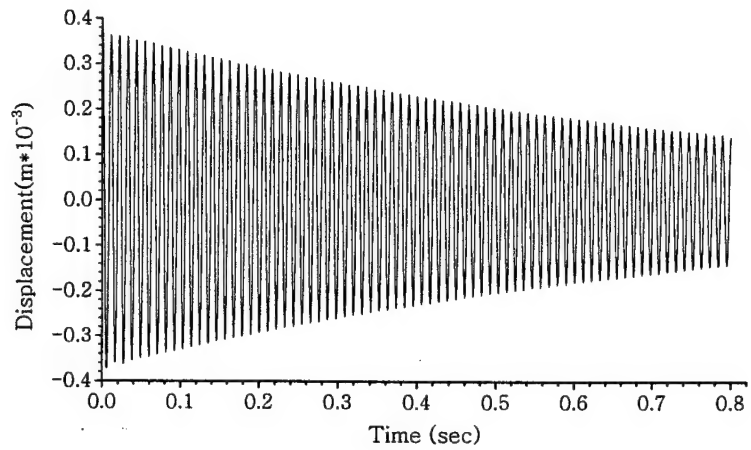


Fig.12 Controlled response (gain = 25)(Full-diagonal actuator).

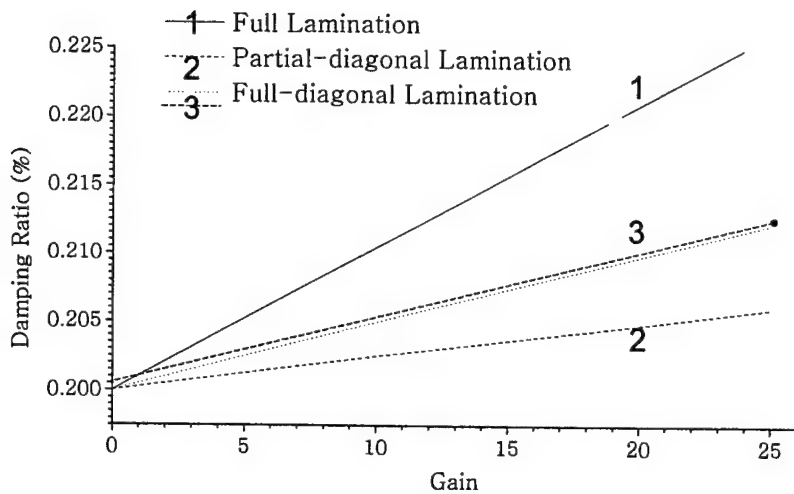


Fig.13 Inferred damping ratios at different gains (Full-edge loading).

Case 2: Half-edge Loading

Again, time histories of the free and controlled responses of the conical shell at the half-edge loading are plotted in Figures 14-17 and inferred damping ratios are summarized in Figure 18. All time-history responses reveal both the first-mode and higher mode frequency components, due to unsymmetrical half-edge loading.

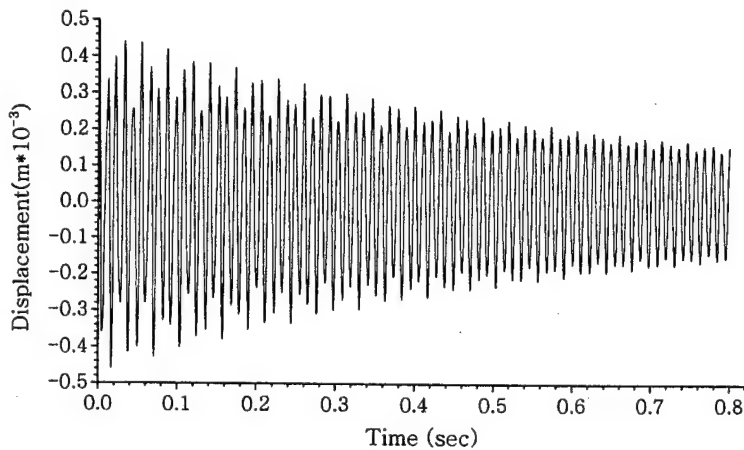


Fig.14 Free displacement response (Half-edge loading).

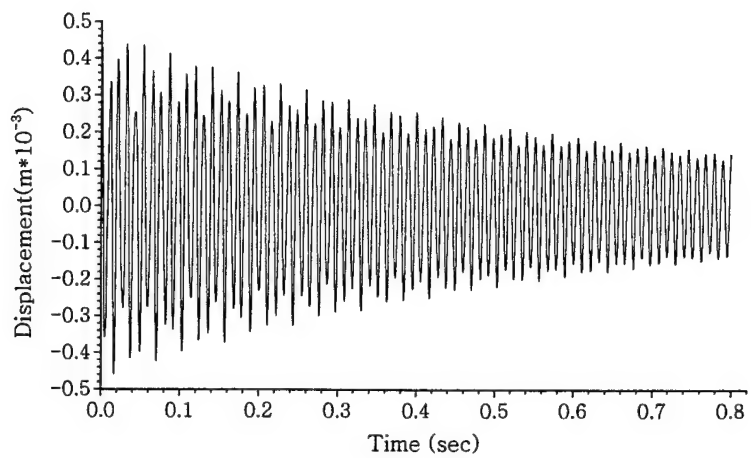


Fig.15 Controlled response (gain = 25)(Fully distributed actuator).

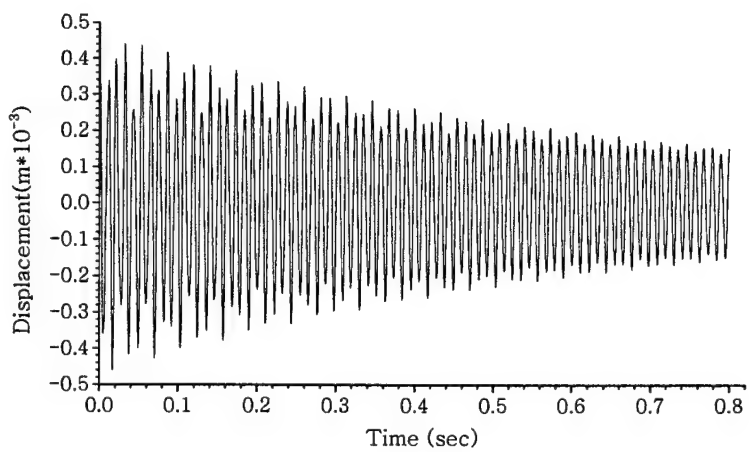


Fig.16 Controlled response (gain = 25)(Partial-diagonal actuator).

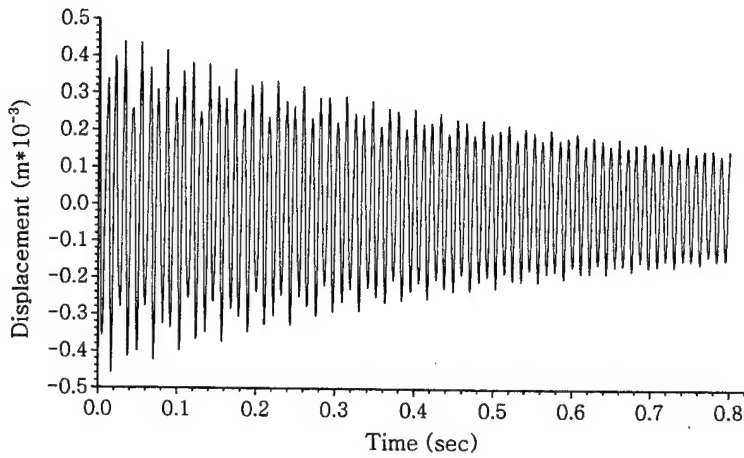


Fig.17 Controlled response (gain = 25)(Full-diagonal actuator).

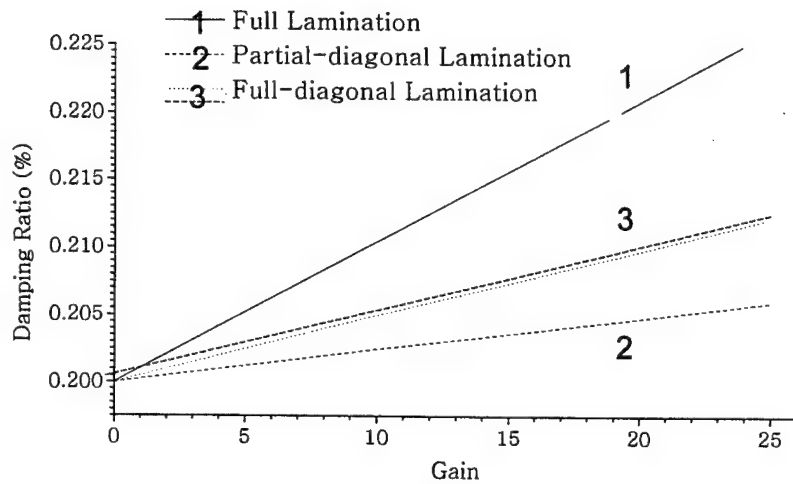


Fig.18 Inferred damping ratios at different gains (Half-edge loading).

These free and controlled time-history responses reveal that the responses are absolutely dominated by the first-mode at the full-edge loading, while higher mode components appear in the responses at the half-edge loading. On the three actuator configurations, the full-lamination configuration has the best control effect and the partial-diagonal lamination configuration has the least control effect for the first-mode oscillation. The fully distributed actuator configuration is effective to the bending dominated natural modes, e.g., the first mode and the fourth mode, Figure 6. The two diagonally laminated actuator configurations would have better control effects in the second-mode and third-mode oscillations, since torsion behaviors appear in these two modes [20].

SUMMARY AND CONCLUSION

Full or partial conical shells often appear as nozzles, injectors, blades, rocket fairings, etc., in aerospace structures and turbomachinery. Undesirable dynamic oscillations not only degrade the performance, but also influence structural integrity and reliability. This report is to evaluate dynamic characteristics and control effectiveness of conical shells laminated with distributed piezoelectric sensor/actuator layers.

Electromechanical constitutive equations, governing equations, strain-displacement-electric field relations, and boundary conditions of a generic piezo(electric)elastic shell continuum were presented first. Finite element formulations of a new triangular piezoelastic shell element with non-constant Lamé parameters were presented, electromechanical element/system/control matrix equations were derived, and then control algorithms defined. Finite element models of a conical shell with three actuator lamination configurations (i.e., the fully distributed, the partial-diagonally distributed, and the full-diagonally distributed) were established and two loading conditions (i.e., the full-edge loading and the half-edge loading) were defined, too.

Natural frequencies and modes of the conical shell finite element models were calculated using the newly developed finite element code. Finite element solutions were compared closely with published numerical results. Thus, the newly developed tool is effective in modeling and analysis of conical shells. Free and controlled time-history responses of the two loading conditions were studied and inferred damping ratios suggest that the fully-distributed configuration is effective to control of bending-dominated natural modes, e.g., 1st and 4th modes; the diagonally laminated configurations are effective to control of torsion-dominated modes, e.g., 2nd and 3rd modes in this case. Accordingly, distributed control of conical shells can be achieved. However, this study suggests that various actuator configurations contribute to different control effectiveness of various natural modes. To maximize the distributed control effects, an in-depth understanding of shell dynamics and dominating modes is a must in effective design and layout of distributed actuators.

ACKNOWLEDGEMENT

This research is supported, in part, by a grant (F49620-98-1-0467) from the Air Force Office of Scientific Research (Project Manager: Brian Sanders). This support is gratefully acknowledged.

REFERENCES

1. N.S. Bardell 1998 *Journal of Sound and Vibration* **217**, 297-320. Free vibration of thin, isotropic, open conical panels.
2. C.W. Lim and K.M. Liew 1995 *Engineering Structures* **17**, 63-70. Vibratory behavior of shallow conical shells by a global Ritz formulation.
3. U. Gabbert and H.S. Tzou 2001 *Smart Structures and Structronic Systems*. Boston/Dordrecht: Kluwer Academic Publishers.
4. H.S. Tzou and G.L. Anderson 1992 *Intelligent Structural Systems*. Boston/Dordrecht: Kluwer Academic Publishers.
5. H.S. Tzou 1993 *Piezoelectric Shells (Distributed Sensing and Control of Continua)*. Boston/Dordrecht: Kluwer Academic Publishers.

6. A. Baz and S. Poh 1988 *Journal of Sound and Vibration* **126**, 327-343. Performance of an Active Control System with Piezoelectric Actuators.
7. E.F. Crawley and K.B. Lazarus 1991 *AIAA Journal* **29**, 944-951. Induced Strain Actuation of Isotropic and Anisotropic Plates.
8. J.E. Hubbard and S.E. Burke 1992 in *Intelligent Structural Systems* (H.S. Tzou and G.L. Anderson, editors), 305-324. Boston/Dordrecht: Kluwer Academic Publishers. Distributed Transducer Design for Intelligent Structural Components.
9. S.K. Ha, C. Keilers and F.K. Chang 1992 *AIAA Journal* **30**, 772-780. Finite Element Analysis of Composite Structures Containing Distributed Piezoceramics Sensors and Actuators.
10. C.K. Lee 1992 in *Intelligent Structural Systems* (H.S. Tzou and G.L. Anderson, editors), 75-167. Boston/Dordrecht: Kluwer Academic Publishers. Piezoelectric Laminates: Theory and Experimentation for Distributed Sensors and Actuators.
11. Y. Gu, R.L. Clark, C.R. Fuller and A.C. Zander 1994 *ASME Journal of Vibration and Acoustics* **116**, 303-308. Experiments on Active Control of Plate Vibration Using Piezoelectric Actuators and Polyvinylidene Fluoride Modal Sensors.
12. H.S. Tzou, Y. Bao, and V.B. Venkayya 1996 *Journal of Sound & Vibration* **197**, 207-249. Study of segmented transducers laminated on cylindrical shells, part-1: sensor patches and part-2: actuator patches.
13. Y.H. Zhou and H.S. Tzou 2000 *Journal of Solids and Structures* **37**, 1663-1677. Control of nonlinear piezoelectric circular shallow spherical shells.
14. H.S. Tzou and R. Ye 1996 *AIAA Journal* **34**, 110-115. Analysis of Piezoelastic Structures with Laminated Piezoelectric Triangle Shell Elements.
15. H.S. Tzou and R.V. Howard 1994 *ASME Journal of Vibration and Acoustics* **116**, 295-302. A Piezothermoelastic Shell Theory Applied to Active Structures.
16. H.S. Tzou and R. Ye 1994 *ASME Journal of Vibration and Acoustics* **114**, 489-495. Piezothermoelasticity and Precision Control of Active Piezoelectric Laminates.
17. H.S. Tzou and R. Ye 2000 *Journal of Sound & Vibration* **231**, 1321-1338. Control of adaptive shells with thermal and mechanical excitations,
18. R.D. Mindlin 1961 in *Problems on Continuum Mechanics* (J. Radok, editor), *Soc. Ind. Appl. Math.*, Philadelphia, 282-290. On the Equations of Motion of Piezoelectric Crystals.
19. O.C. Zienkiewicz and R.L. Taylor 1989 *The Finite Element Method*, 4th Ed., McGraw-Hill, New York. Vol.1, Basic Formulation and Linear Problems.
20. H.S. Tzou, R. Ye, and J.H. Ding 2001 *Journal of Sound & Vibration* **241**, 271-281. A new X-actuator design for controlling wing bending and twisting modes.

APPENDIX: FORMULATION OF ELEMENT MATRICES

Detailed element matrices of a laminated piezoelastic shell element are presented here.

$$[M_{uu_j}^{(i)}] = \int_{S_j} [N_{u_j}(\alpha_1, \alpha_2)]^t \left(\int_{\gamma=0}^{h_i} [N_u^{(i)}(\gamma)]^t \rho^{(i)} [N_u^{(i)}(\gamma)] B_1^i B_2^i d\gamma \right) \\ \cdot [N_{u_j}(\alpha_1, \alpha_2)] A_1 A_2 d\alpha_1 d\alpha_2, \quad (A1)$$

$$[K_{uu_j}^{(i)}] = \int_{S_j} [B_{u_j}(\alpha_1, \alpha_2)]^t \left(\int_{\gamma=0}^{h_i} [B_u^{(i)}(\gamma)]^t [\bar{c}^{(i)}] [B_u^{(i)}(\gamma)] B_1^i B_2^i d\gamma \right) \\ \cdot [B_{u_j}(\alpha_1, \alpha_2)] A_1 A_2 d\alpha_1 d\alpha_2, \quad (A2)$$

$$[K_{u\phi_j}^{(i)}] = \int_{S_j} [B_{u_j}(\alpha_1, \alpha_2)]^t \left(\int_{\gamma=0}^{h_i} [B_u^{(i)}(\gamma)]^t [\bar{e}^{(i)}] [B_\phi^{(i)}(\gamma)] B_1^i B_2^i d\gamma \right) \\ \cdot [B_{\phi_j}(\alpha_1, \alpha_2)] A_1 A_2 d\alpha_1 d\alpha_2, \quad (A3)$$

$$[K_{\phi\phi_j}^{(i)}] = - \int_{S_j} [B_{\phi_j}(\alpha_1, \alpha_2)]^t \left(\int_{\gamma=0}^{h_i} [B_\phi^{(i)}(\gamma)]^t [\bar{\epsilon}^{(i)}] [B_\phi^{(i)}(\gamma)] B_1^i B_2^i d\gamma \right) \\ \cdot [B_{\phi_j}(\alpha_1, \alpha_2)] A_1 A_2 d\alpha_1 d\alpha_2, \quad (A4)$$

$$[K_{\phi u_j}^{(i)}] = [K_{u\phi_j}^{(i)}]^t, \quad (A5)$$

$$\{F_{u_j}^{(i)}\} = \int_{S_j} [N_{u_j}(\alpha_1, \alpha_2)]^t [N_u^{(i)}(\gamma = h_x)]^t \{f^{(i)}\} B_1^i(\gamma = h_x) B_2^i(\gamma = h_x) A_1 A_2 d\alpha_1 d\alpha_2 \\ + \int_{S_j} [N_{u_j}(\alpha_1, \alpha_2)]^t \left(\int_{\gamma=0}^{h_i} [N_u^{(i)}(\gamma)]^t \{f_b^{(i)}\} B_1^i B_2^i d\gamma \right) A_1 A_2 d\alpha_1 d\alpha_2, \quad (A6)$$

$$\{F_{\phi_j}^{(i)}\} = - \int_{S_j} [N_{\phi_j}(\alpha_1, \alpha_2)]^t [N_\phi^{(i)}(\gamma = h_x)]^t Q^i B_1^i(\gamma = h_x) B_2^i(\gamma = h_x) A_1 A_2 d\alpha_1 d\alpha_2. \quad (A7)$$

where $\{f^{(i)}\} = \{f_1^{(i)}, f_2^{(i)}, f_3^{(i)}\}^t$ and $\{f_b^{(i)}\} = \{f_{b1}^{(i)}, f_{b2}^{(i)}, f_{b3}^{(i)}\}^t$ are the surface force and body force along the curvilinear coordinate axes, respectively; Q^i is the electric charge applied on the surfaces of piezoelectric layers; and the thickness $0.0 \leq h_x \leq h_i$.

(FemShlCone.ConeShlWg.ShlCone)

CHAPTER 17

VIBRATION CONTROL OF TOROIDAL SHELLS WITH PARALLEL AND DIAGONAL PIEZOELECTRIC ACTUATORS (Finite Formulation and Analysis)

ABSTRACT

Effective control of toroidal shells, e.g., cooling tubes, space colonies, inflatable space structures, etc., enhances their operational precision, accuracy, and reliability. Dynamics and control effectiveness of toroidal shell panels laminated with distributed piezoelectric sensor/actuator layers are investigated in this study. Mathematical model and finite element formulations of piezo(electric)-elastic shell structures are presented. Element and system matrix equations of the piezoelectric shell strucronic (sensor/actuator/structure/control) system are defined and the system equations reveal the coupling of mechanical and electric (or control) fields. Free vibration analyses of two toroidal shells are investigated and compared favorably with published data. Two sensor/actuator configurations based on identical sensor/actuator sizes, namely the parallel configuration and the diagonal configuration, laminated on the toroidal shell are investigated and analysis data suggest that the diagonal configuration provides better control effects, as compared with the parallel configuration. The parallel configuration is ineffective to anti-symmetrical modes; the diagonal configuration is effective to most natural modes and ineffective to quad-anti-symmetrical modes with respect to the panel center.

INTRODUCTION

Toroidal shell structures are often proposed for components of cooling tubes, space colonies, space telescopes, inflatable space structures, neutron accelerators, etc. over the years. Effective vibration control of these toroidal shell structures or components can enhance operation precision, accuracy, and reliability of these high-performance structural systems. Stress and free-vibration analyses of pipe-type toroidal shells have been investigated recently [1-3]. Static, dynamic, vibration, and buckling characteristics of toroidal shells have also been studied [4-8]. Micro-electromechanics and distributed signal characteristics of toroidal shells have been investigated [9]. This research focuses on studies of dynamics and distributed vibration control of toroidal shells laminated with two piezoelectric actuator configurations using a newly developed shell finite element code encompassing multi-field piezoelectricity/elasticity/control coupling.

Distributed sensing and control of strucronic shells using piezoelectric sensors/actuators have been studied for the last decade [10-13]. Finite element (FE) development, analysis, and control of piezoelectric and piezothermoelastic structures have been

being advanced over the years [14-17]. In this study, mathematical modeling of toroidal shells is discussed first, followed by fundamental constitutive relations of piezoelectricity. Finite element development of a composite piezoelectric-elastic triangular shell finite element is presented next. Dynamic and control analyses of toroidal shells are presented; control effectiveness of two actuator configurations, namely the parallel and the diagonal layouts, is evaluated in case studies.

PIEZOELECTRIC LAMINATED TOROIDAL SHELL PANEL

Theoretical fundamentals, toroidal shell geometry, shell strain/electric field equations, piezoelectric electromechanical constitutive equations are presented in this section.

Shell Geometry

Let $(\alpha_1, \alpha_2, \alpha_3)$ denote a tri-orthogonal curvilinear coordinate system on a toroidal shell with coordinates α_1 and α_2 defining the shell reference surface (or the neutral surface) and α_3 defining the direction normal to the $\alpha_1 - \alpha_2$ surface. In general, a generic infinitesimal distance ds in the shell can be written as

$$(ds)^2 = \sum_{i=1}^3 g_{ii}(\alpha_1, \alpha_2, \alpha_3) (d\alpha_i)^2 , \quad (1)$$

where $g_{ii}(\alpha_1, \alpha_2, \alpha_3) = A_i^2 (1 + \frac{\alpha_3}{R_i})^2$, ($i=1,2$) and $g_{33}(\alpha_1, \alpha_2, \alpha_3) = 1$ are the covariant components of the metric tensor in the $(\alpha_1, \alpha_2, \alpha_3)$ coordinate system; R_1 and R_2 are the principal radii of curvature of the α_1 – and the α_2 – coordinate axes, respectively; and A_1 and A_2 are the Lamé parameters defined by the fundamental form. **Figure 1** shows a toroidal panel and its coordinate system. Note that α_1 denotes the meridional coordinate and α_2 denotes the circumferential coordinate, respectively.

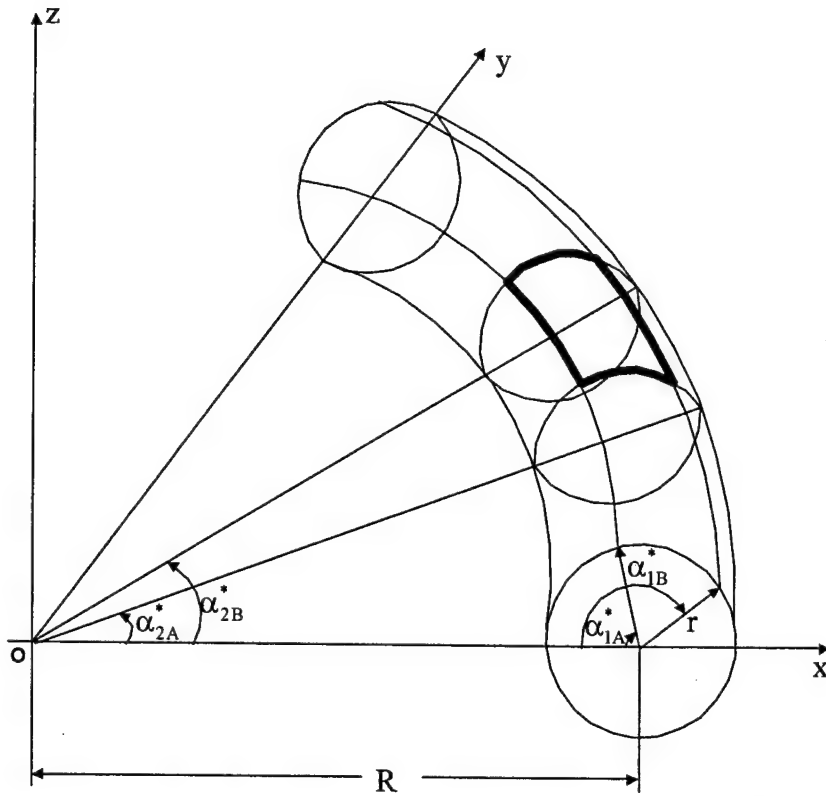


Fig. 1 A toroidal shell panel and its coordinate system.

The Lamé parameters and the curvature radii of toroidal shells of revolution are $A_1 = r$, $A_2 = r\xi$, $R_1 = r$ and $R_2 = r\xi/(\gamma \cos(\pi - \alpha_1))$ where $\xi = 1 + \gamma \cos \alpha_1$ and $\gamma = r/R$.

Stress-Displacement and Electric Field-Electric Potential Relations

The strain-displacement and electric field-potential relations are

$$S_{11} = \frac{1}{(1 + \frac{\alpha_3}{R_1})A_1} \left[\frac{\partial U_1}{\partial \alpha_1} + \frac{1}{A_2} \frac{\partial A_1}{\partial \alpha_2} U_2 + \frac{A_1}{R_1} U_3 \right], \quad (2a)$$

$$S_{22} = \frac{1}{(1 + \frac{\alpha_3}{R_2})A_2} \left[\frac{\partial U_2}{\partial \alpha_2} + \frac{1}{A_1} \frac{\partial A_2}{\partial \alpha_1} U_1 + \frac{A_2}{R_2} U_3 \right], \quad (2b)$$

$$S_{12} = \frac{1}{(1 + \frac{\alpha_3}{R_1})A_1} \left[\frac{\partial U_2}{\partial \alpha_1} - \frac{1}{A_2} \frac{\partial A_1}{\partial \alpha_2} U_1 \right] + \frac{1}{(1 + \frac{\alpha_3}{R_2})A_2} \left[\frac{\partial U_1}{\partial \alpha_2} - \frac{1}{A_1} \frac{\partial A_2}{\partial \alpha_1} U_2 \right], \quad (2c)$$

$$S_{13} = \frac{1}{(1 + \frac{\alpha_3}{R_1})A_1} \left[\frac{\partial U_3}{\partial \alpha_1} - \frac{A_1}{R_1} U_1 \right] + \frac{\partial U_1}{\partial \alpha_3}, \quad (2d)$$

$$S_{23} = \frac{1}{(1 + \frac{\alpha_3}{R_2})A_2} \left[\frac{\partial U_3}{\partial \alpha_2} - \frac{A_2}{R_2} U_2 \right] + \frac{\partial U_2}{\partial \alpha_3}, \quad (2e)$$

$$S_{33} = \frac{\partial U_3}{\partial \alpha_3}; \quad (2f)$$

$$E_1 = -\frac{1}{(1 + \frac{\alpha_3}{R_1})A_1} \frac{\partial \phi}{\partial \alpha_1}, \quad (3a)$$

$$E_2 = -\frac{1}{(1 + \frac{\alpha_3}{R_2})A_2} \frac{\partial \phi}{\partial \alpha_2}, \quad (3b)$$

$$E_3 = -\frac{\partial \phi}{\partial \alpha_3}. \quad (3c)$$

where S_{ij} , U_i , ϕ , and E_i ($i,j = 1,2,3$) respectively denote the strains, displacements, electric potential, and electric fields.

Linear Piezoelastic Constitutive Equations

The linear constitutive equations for the piezoelastic shell structures can be written in the matrix form as [18]

$$T = cS - eE, \quad D = eS + \epsilon E, \quad (4a,b)$$

where T , S , E and D denote the stress, strain, electric field and electric displacement vectors, respectively; c , e and ϵ denote the elastic moduli, piezoelectric coefficient and dielectric permittivity matrices, respectively. For mm2 piezoelastic materials, the constitutive equations can be explicitly written in the component form as

$$\begin{bmatrix} T_{11} \\ T_{22} \\ T_{33} \\ T_{23} \\ T_{13} \\ T_{12} \end{bmatrix} = \begin{bmatrix} c_{11} & c_{12} & c_{13} & c_{14} & 0 & 0 \\ & c_{22} & c_{23} & c_{24} & 0 & 0 \\ & & c_{33} & c_{34} & 0 & 0 \\ & & & c_{44} & 0 & 0 \\ & \text{sym.} & & & c_{55} & c_{56} \\ & & & & & c_{66} \end{bmatrix} \begin{bmatrix} S_{11} \\ S_{22} \\ S_{33} \\ S_{23} \\ S_{13} \\ S_{12} \end{bmatrix} - \begin{bmatrix} 0 & 0 & e_{31} \\ 0 & 0 & e_{32} \\ 0 & 0 & e_{33} \\ 0 & 0 & e_{34} \\ e_{15} & e_{25} & 0 \\ e_{16} & e_{26} & 0 \end{bmatrix} \begin{bmatrix} E_1 \\ E_2 \\ E_3 \end{bmatrix}, \quad (5a)$$

$$\begin{bmatrix} D_1 \\ D_2 \\ D_3 \end{bmatrix} = \begin{bmatrix} 0 & 0 & 0 & 0 & e_{15} & e_{16} \\ 0 & 0 & 0 & 0 & e_{25} & e_{26} \\ e_{31} & e_{32} & e_{33} & e_{34} & 0 & 0 \end{bmatrix} \begin{bmatrix} S_{11} \\ S_{22} \\ S_{33} \\ S_{23} \\ S_{13} \\ S_{12} \end{bmatrix} + \begin{bmatrix} \epsilon_{11} & \epsilon_{12} & 0 \\ \epsilon_{22} & 0 & \\ \text{sym.} & \epsilon_{33} & \end{bmatrix} \begin{bmatrix} E_1 \\ E_2 \\ E_3 \end{bmatrix}, \quad (5b)$$

where T_{ij} , D_i , S_{ij} , E_i ($i, j = 1, 2, 3$) are the stresses, electric displacements, strains, electric fields, respectively; c_{ij} , e_{ij} , ϵ_{ik} ($i, k = 1, 2, 3$; $j = 1, 2, \dots, 6$) are the elastic moduli coefficients, piezoelectric coefficients and dielectric permittivity constants, respectively. The distributed actuators are made of piezoelectric materials laminated on the shell surface. The control actions are introduced based on the converse piezoelectric effect, i.e., Eq.(5a) where E_i denotes the control electric fields [18].

FE FORMULATIONS BY THE VIRTUAL WORK PRINCIPLE

The virtual work principle in the displacement and electric fields can be written as

$$\int T \delta S dV = W_u, \quad \int D \delta E dV = W_\phi. \quad (6a,b)$$

where the integration is carried out over the volume V ; W_u , W_ϕ are the work induced by the mechanical and electric load, respectively, which include terms associated with the inertia forces in dynamic analysis. Substituting Eqs.(4a,b) into Eqs.(6a,b) gives

$$\int (\delta S c S - \delta S e E) dV = W_u, \quad \int (\delta E e S + \delta E \epsilon E) dV = W_\phi. \quad (7a,b)$$

The displacement \mathbf{u} and the electric potential ϕ within each element can be written as

$$\mathbf{u} = \tilde{\mathbf{N}}_u \mathbf{U}, \quad \phi = \tilde{\mathbf{N}}_\phi \Phi, \quad (8a,b)$$

where \mathbf{U} and Φ are the nodal displacement and nodal electric potential, respectively; $\tilde{\mathbf{N}}_u$, $\tilde{\mathbf{N}}_\phi$ are the matrices of displacement and electric potential interpolation functions. (Note that detailed piezoelectric-elastic shell finite element formulation is presented next.) Substituting Eqs.(8a,b) into Eqs.(7a,b) gives

$$\sum_e (\mathbf{K}_{uu}^e + \mathbf{K}_{u\phi}^e) \mathbf{U}^e = \sum_e \mathbf{F}_u^e, \quad (9)$$

$$\sum_e (\mathbf{K}_{\phi\phi}^e - \mathbf{K}_{\phi u}^e) \Phi^e = \sum_e \mathbf{F}_\phi^e, \quad (10)$$

where \mathbf{K}_{uu}^e , $\mathbf{K}_{u\phi}^e$, $\mathbf{K}_{\phi u}^e$, and $\mathbf{K}_{\phi\phi}^e$ are derived from $\int_u \delta \mathbf{S} \mathbf{e} \mathbf{S} dV$, $\int_e \delta \mathbf{S} \mathbf{e} \mathbf{E} dV$, $\int_e \delta \mathbf{E} \mathbf{e} \mathbf{S} dV$, $\int_e \delta \mathbf{E} \mathbf{e} \mathbf{E} dV$ respectively; \mathbf{F}_u^e and \mathbf{F}_ϕ^e are the external nodal forces vector associated with \mathbf{W}_u and \mathbf{W}_ϕ . Assembling all element matrices yields the global system matrix equation

$$\begin{bmatrix} \mathbf{M}_{uu} & 0 \\ 0 & 0 \end{bmatrix} \begin{bmatrix} \ddot{\mathbf{U}} \\ \ddot{\Phi} \end{bmatrix} + \begin{bmatrix} \mathbf{C}_{uu} & 0 \\ 0 & 0 \end{bmatrix} \begin{bmatrix} \dot{\mathbf{U}} \\ \dot{\Phi} \end{bmatrix} + \begin{bmatrix} \mathbf{K}_{uu} & \mathbf{K}_{u\phi} \\ \mathbf{K}_{\phi u} & \mathbf{K}_{\phi\phi} \end{bmatrix} \begin{bmatrix} \mathbf{U} \\ \Phi \end{bmatrix} = \begin{bmatrix} \mathbf{F}_u \\ \mathbf{F}_\phi \end{bmatrix}, \quad (11)$$

where $\ddot{\mathbf{U}}$, $\ddot{\Phi}$, $\dot{\mathbf{U}}$, and $\dot{\Phi}$ are the acceleration and velocity vectors, respectively; \mathbf{M}_{uu} is the mass matrix; \mathbf{C}_{uu} is the damping matrix; \mathbf{K}_{uu} , $\mathbf{K}_{u\phi}$, $\mathbf{K}_{\phi u}$, and $\mathbf{K}_{\phi\phi}$, are the stiffness matrices defined for the displacement and electric field; \mathbf{F}_u and \mathbf{F}_ϕ are the external mechanical and electric forces associated with \mathbf{W}_u and \mathbf{W}_ϕ defined in Eqs.(7a,b). Detailed piezoelectric-elastic shell finite element formulation is presented next.

Laminated Piezoelectric Shell Element

The finite element under consideration is a twelve-node piezoelectric shell element with a triangular geometry shown in **Figure 2**. Six nodes are located on the three edges of the upper surface and the other six nodes are located on the three edges of the lower surface of the triangular element. The shell element is located in a curvilinear coordinate system with the side 1-2-3 coinciding with the α_1 -axis while the side 1-6-5 coinciding with the α_2 -axis. The side 1-7 coincides with the γ -axis perpendicular to the $\alpha_1 - \alpha_2$ surface.

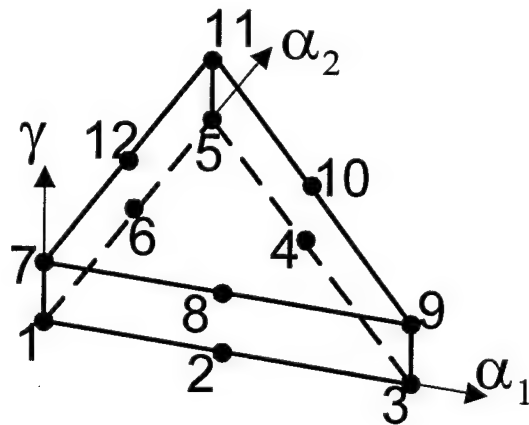


Fig. 2 A laminated piezoelectric shell element.

Each node is associated with four degrees of freedom (DOF) that are u_1 - the displacement component in the α_1 -direction, u_2 - the displacement component in the α_2 -direction, u_3 - the displacement component in the transverse γ -direction, and ϕ - the electric potential. Under the assumption of layerwise constant shear angle theory, for an arbitrary i th layer, the displacement and electric potential can be written as

$$\mathbf{u}^{(i)} = \bar{\mathbf{N}}_u^{(i)}(\gamma) \bar{\mathbf{U}}^{(i)} , \quad \phi^{(i)} = \bar{\mathbf{N}}_\phi^{(i)}(\gamma) \bar{\Phi}^{(i)} , \quad (12a,b)$$

where $\mathbf{u}^{(i)} = \{u_1^{(i)}, u_2^{(i)}, u_3^{(i)}\}^T$, $\bar{\mathbf{U}}^{(i)} = \{\bar{U}_1^{(i)}, \bar{U}_2^{(i)}, \bar{U}_3^{(i)}, \bar{U}_1^{(i+1)}, \bar{U}_2^{(i+1)}, \bar{U}_3^{(i+1)}\}^T$, $\bar{\Phi}^{(i)} = \{\bar{\phi}^{(i)}, \bar{\phi}^{(i+1)}\}^T$; $\{\bullet\}^T$ denotes the transpose and the superscript “i” denotes the ith layer. The surface-parallel displacement and electric potential can be expressed as

$$\bar{\mathbf{U}}^{(i)} = \mathbf{N}_u(\alpha_1, \alpha_2) \mathbf{U}^{(i)} , \quad \bar{\Phi}^{(i)} = \mathbf{N}_\phi(\alpha_1, \alpha_2) \Phi^{(i)} , \quad (13a,b)$$

where $\mathbf{N}(\alpha_1, \alpha_2)$ is the shape function in terms of α_1 and α_2 coordinates;

$$\mathbf{U}^{(i)} = \{U_{11}^{(i)}, U_{21}^{(i)}, U_{31}^{(i)}, \dots, U_{16}^{(i)}, U_{26}^{(i)}, U_{36}^{(i)}, U_{11}^{(i+1)}, U_{21}^{(i+1)}, U_{31}^{(i+1)}, \dots, U_{16}^{(i+1)}, U_{26}^{(i+1)}, U_{36}^{(i+1)}\}^T ;$$

$$\Phi^{(i)} = \{\phi_1^{(i)}, \phi_2^{(i)}, \dots, \phi_6^{(i)}, \phi_1^{(i+1)}, \phi_2^{(i+1)}, \dots, \phi_6^{(i+1)}\}^T .$$

Element Stiffness and Mass Matrices

The strain-displacement and electric field-potential relations can be expressed in terms of nodal variables of the laminated piezoelectric shell finite element

$$\mathbf{S} = \mathbf{L}_u(\alpha_1, \alpha_2) \bar{\mathbf{N}}_u(\gamma) \mathbf{N}_u(\alpha_1, \alpha_2) \mathbf{U} = \bar{\mathbf{B}}_u \mathbf{B}_u \mathbf{U} , \quad (14)$$

$$\mathbf{E} = \mathbf{L}_\phi(\alpha_1, \alpha_2) \bar{\mathbf{N}}_\phi(\gamma) \mathbf{N}_\phi(\alpha_1, \alpha_2) \mathbf{U} = -\bar{\mathbf{B}}_\phi \mathbf{B}_\phi \Phi , \quad (15)$$

where $\mathbf{L}_u(\alpha_1, \alpha_2)$ and $\mathbf{L}_\phi(\alpha_1, \alpha_2)$ are the linear differential operator matrices; $\bar{\mathbf{B}}_u$ and \mathbf{B}_u are the strain shape functions associated with coordinates γ and α_1, α_2 , respectively; $\bar{\mathbf{B}}_\phi$ and \mathbf{B}_ϕ are the electric field shape functions associated with coordinates γ and α_1, α_2 , respectively. Substituting Eqs.(15) and (16) into the integral components of Eqs.(9) and (10), the element stiffness matrices can be written as

$$\mathbf{K}_{uu}^e = \int_e \mathbf{B}_u^T \bar{\mathbf{B}}_u^T \mathbf{c} \bar{\mathbf{B}}_u \mathbf{B}_u |J| \sqrt{g_{11}} \sqrt{g_{22}} d\gamma d\alpha_1 d\alpha_2 , \quad (16)$$

$$\mathbf{K}_{u\phi}^e = \int_e \mathbf{B}_u^T \bar{\mathbf{B}}_u^T \mathbf{e} \bar{\mathbf{B}}_\phi \mathbf{B}_\phi |J| \sqrt{g_{11}} \sqrt{g_{22}} d\gamma d\alpha_1 d\alpha_2 , \quad (17)$$

$$\mathbf{K}_{\phi\phi}^e = \int_e \mathbf{B}_\phi^T \bar{\mathbf{B}}_\phi^T \mathbf{e} \bar{\mathbf{B}}_\phi \mathbf{B}_\phi |J| \sqrt{g_{11}} \sqrt{g_{22}} d\gamma d\alpha_1 d\alpha_2 , \quad (18)$$

$$\mathbf{K}_{\phi u}^e = \mathbf{K}_{u\phi}^e , \quad (19)$$

where \mathbf{J} is the Jacobian transformation matrix; $|\bullet|$ denotes the determinant; and g_{11}, g_{22} are defined in Eq.(1). In dynamic analysis, the inertial forces are included on the right side of Eq.(9). And the element mass matrix can be written in a matrix form as

$$\mathbf{M}^e = \int_e \mathbf{N}_u^T \bar{\mathbf{N}}_u^T \rho \bar{\mathbf{N}}_u \mathbf{N}_u |J| \sqrt{g_{11}} \sqrt{g_{22}} d\gamma d\alpha_1 d\alpha_2 , \quad (20)$$

where ρ is the mass density. The elemental damping matrix \mathbf{C}^e is assumed to be proportional to the stiffness and mass matrices

$$\mathbf{C}_{uu}^e = \alpha \mathbf{M}_{uu}^e + \beta \mathbf{K}_{uu}^e , \quad (21)$$

where α and β are Rayleigh's coefficients and are related to $\alpha + \beta \omega_i^2 = 2 \xi_i \omega_i$; ξ_i and ω_i are the i th-mode initial damping ratio and natural frequency respectively [18]. The external nodal force vectors \mathbf{F}_u^e , \mathbf{F}_ϕ^e in Eqs.(9) and (10) can be written in a matrix form as

$$\mathbf{F}_u^e = \int_e \mathbf{N}_u^T \bar{\mathbf{N}}_u^T \mathbf{f}_b |\mathbf{J}| \sqrt{g_{11}} \sqrt{g_{22}} dy d\alpha_1 d\alpha_2 + \int_e \mathbf{N}_u^T \bar{\mathbf{N}}_u^T \mathbf{f}_s \sqrt{g_{11}} \sqrt{g_{22}} d\alpha_1 d\alpha_2 , \quad (22)$$

$$\mathbf{F}_\phi^e = - \int_e \mathbf{N}_\phi^T \bar{\mathbf{N}}_\phi^T Q \sqrt{g_{11}} \sqrt{g_{22}} d\alpha_1 d\alpha_2 , \quad (23)$$

where \mathbf{f}_b and \mathbf{f}_s denote the body force vector and the surface force vector, respectively; Q is the electric charge; S^e donates surface on which surface force \mathbf{f}_s and electric charge Q are applied. A finite element computer code based on the above procedure is developed and studies of dynamics and control of toroidal shells are carried out next.

DYNAMIC AND CONTROL ANALYSES

A thin toroidal shell panel is defined in **Figure 1**. Its geometry and material properties used in case studies are provided in **Table 1**. Note that the angular arcs of the shell panel are defined by $\alpha_{2B}^* - \alpha_{2A}^* = 2(\alpha_{1B}^* - \alpha_{1A}^*)r/R$. Thus, the toroidal shell panel is nearly square in shape.

Table 1. Geometry and material properties of the toroidal shell panel.

Properties	Symbol	Unit	Steel	PVDF
Meridional angle	$\alpha_{1A}^*, \alpha_{1B}^*$	°	135*, 180*	
Circumferential angle	$\alpha_{2A}^*, \alpha_{2B}^*$	°	0, 7.875	
Meridional radius	r	m	0.56	
Circumferential radius	R	m	3.2	
Thickness	h, h ^s	m	5.6×10^{-3}	9.0×10^{-6}
Mass density	ρ	Kgm^{-3}	7.7×10^3	1.8×10^3
Young's modulus	Y	Pa	2.07×10^{11}	2.0×10^9
Poisson's ratio	μ		0.3	0.29
Piezo-strain constant	d_{31}	mV^{-1}		2.2×10^{-11}
Electric permittivity	ϵ_{11}	Fm^{-1}		1.062×10^{-10}
Capacitance	C	Fm^{-2}		3.80×10^{-6}

Note: 1) Angles with "*" corresponds to Case 3 of Redekop and Xu [7] defined in a different coordinate system;
 2) "PVDF" - Piezoelectric polyvinylidene fluoride.

Dynamics of two toroidal shell cases with distinct boundary conditions are studied in this section. In order to validate the new finite element code, their natural frequencies are compared with published data first. Then, control of a toroidal shell panel laminated with two actuator configurations are investigated next, where detailed element and mesh definitions are presented.

Free Vibration Analysis

Case 1: Shear-Diaphragm and Fixed Boundaries

The two boundaries of the toroidal shell panel on the opposite circumferential edges are assumed to be shear-diaphragms, which are rigid in their own planes, i.e., $N_{\alpha_2} = M_{\alpha_2} = u_1 = u_3 = 0$ at $\alpha = \alpha_{2A}^*, \alpha_{2B}^*$ where $N_{\alpha_2}, M_{\alpha_2}$ are the normal force and moment in the circumferential direction, respectively. The toroidal shell panel is clamped on the two meridional edges, i.e., $u_1 = u_2 = u_3 = 0$ at $\alpha = \alpha_{1A}^*, \alpha_{1B}^*$. Fundamental circular natural frequencies (rad/sec) are calculated and summarized in **Table 2**. The fundamental frequency is compared favorably with published data by Redekop and Xu [7], while higher frequencies are not available for comparison. The first three mode shapes of the toroidal shell panel are calculated and plotted in **Figure 3**.

Table 2 Frequencies of the first toroidal shell panel ($\times 10^4$).

	ω_1	ω_2	ω_3
Present Study (FEM)	0.4636	0.5519	0.6835
Redekop & Xu (FEM)	0.4573	---	---
Redekop & Xu (DQM)	0.4660	---	---

- DQM: Differential Quadrature Method.

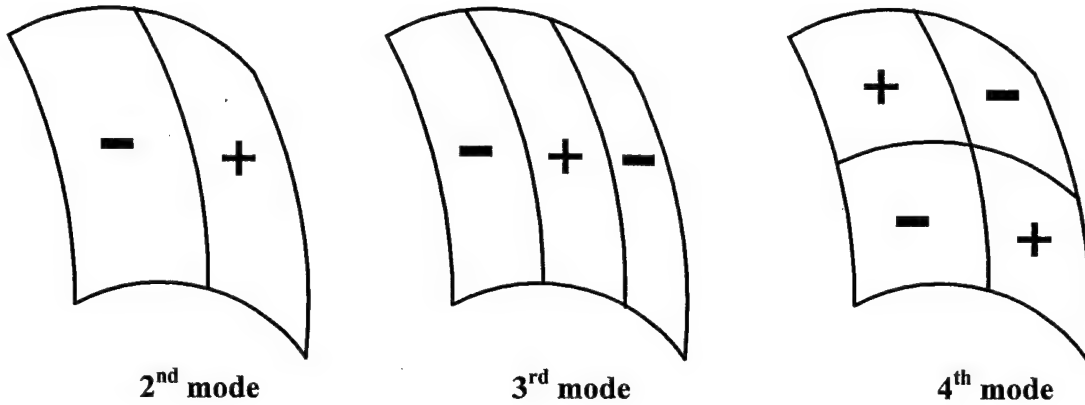


Fig. 3 The first three mode shapes of the toroidal shell panel (Case 1).
(Note: “+” and “-” denote the convex and the concave, respectively.)

Case 2: Shear-Diaphragm and Shear-Diaphragm Boundaries

Boundary supports of the second toroidal shell panel are assumed to be shear-diaphragm on both circumferential and meridional edges, i.e., $N_{\alpha_2} = M_{\alpha_2} = u_1 = u_3 = 0$ at $\alpha_2 = \alpha_{2A}^*, \alpha_{2B}^*$ and $N_{\alpha_1} = M_{\alpha_1} = u_1 = u_3 = 0$ at $\alpha_1 = \alpha_{1A}^*, \alpha_{1B}^*$. Again, natural frequencies (rad/sec) are calculated using the new finite element code and summarized in **Table 3**. The fundamental frequency is compared favorably with the published data by Redekop and Xu [7], while higher frequencies are not available. The first four mode shapes are shown in **Figure 4**.

Table 3 Frequencies of the second toroidal shell panel ($\times 10^{-4}$).

	ω_1	ω_2	ω_3	ω_4
Present Study	0.3463	0.4628	0.5450	0.6783
Redekop & Xu (FEM)	0.3196	----	----	----
Redekop & Xu (DQM [*])	0.3264	----	----	----
Redekop & Xu (FS [*])	0.4727	----	----	----

^{*} DQM: Differential Quadrature Method.

^{*} FS: Fourier series.

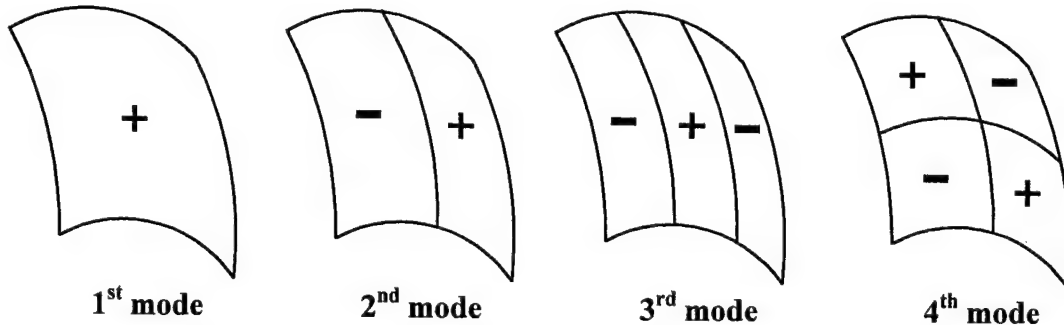


Fig. 4 The first four mode shapes of the toroidal shell panel (Case 2).

(Note: "+" and "-" denote convex and concave, respectively.)

Vibration Control

A toroidal shell panel with shear-diaphragm and clamped boundary conditions of Case 1 is laminated with two layers of piezoelectric polyvinylidene fluoride (PVDF) on the top and bottom surfaces serving as sensor and actuator, respectively – a strucronic toroidal shell system. Two lamination configurations, namely the parallel lamination and the diagonal lamination are designed to test their control effects on toroidal shell panels, shown in **Figures 5 and 6**. Note that these two configurations utilize identical total sensor/actuator lamination sizes, so that the control effect solely depends on the lamination configuration. The toroidal shell panel is divided into 20×10 quadrilateral pattern in the meridional and the circumferential directions, respectively. Therefore, there are 400 triangular elements for each layer and a total of 1200 elements for the toroidal strucronic shell system. The initial damping ratio is assumed to be 0.2%. A uniformly distributed surface load with magnitude of 1 N, denoted by arrows in **Figure 5**, is applied on the left half surface of the panel.

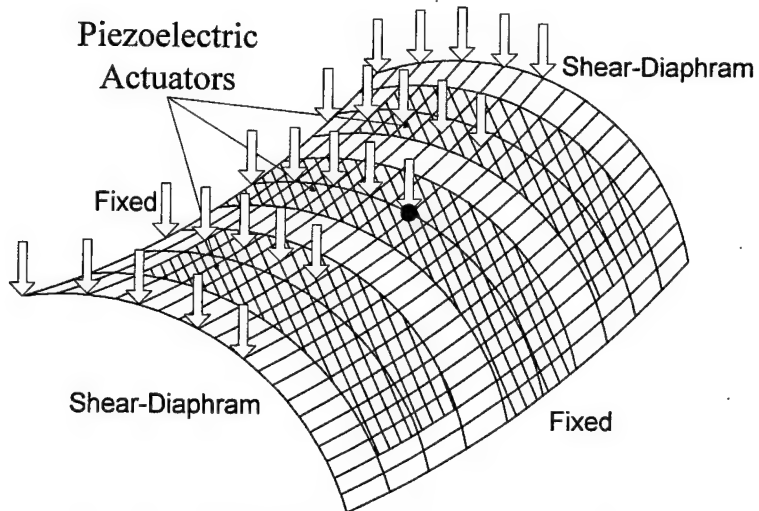


Fig. 5 Toroidal shell panel laminated with three parallel piezoelectric strips.

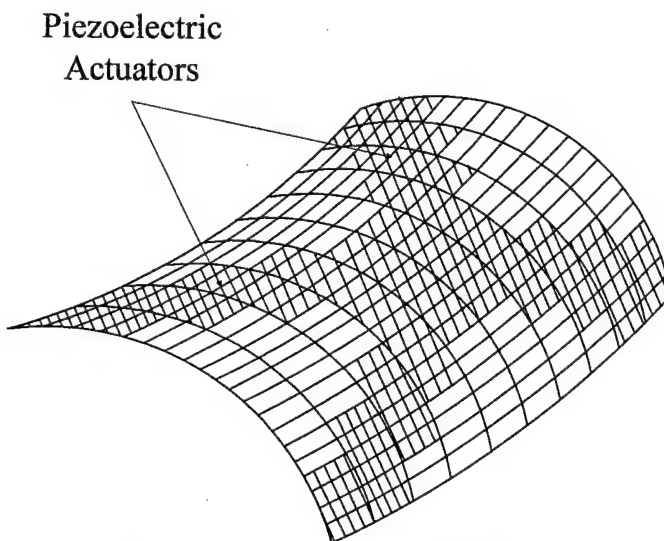


Fig. 6 Toroidal shell panel laminated with diagonal piezoelectric strips.

The converse piezoelectric effect induced control actions governed by the proportional feedback control constrain the shell motion and subsequently control the shell vibration. Note that there is only one continuous sensor electrode and thus the sum of sensing signals resulting from all sensor segments is used as a single reference feedback voltage applied to all actuator strips. Control effects of the two actuator configurations will be evaluated next. Free vibration time history of the toroidal shell panel center (marked with a dot in **Figure 5**) is presented first, followed by controlled time histories at various control gains in each actuator configuration next. **Figure 7** shows the free vibration time history and **Figure 8** shows controlled time history of the parallel actuator configuration. **Figure 9** shows the free vibration time history and **Figure 10** shows controlled time history of the diagonal actuator configuration. Since the first two frequencies are close to each other, beating oscillations appear in all time history responses. Inferred controlled damping ratios at various control gains for each actuator configuration are calculated and summarized in **Figure 11**. It clearly demonstrates the control effectiveness of

the two actuator configurations and the diagonal configuration provides much better control effect, as compares with the parallel configuration.

Parallel Actuator Lamination

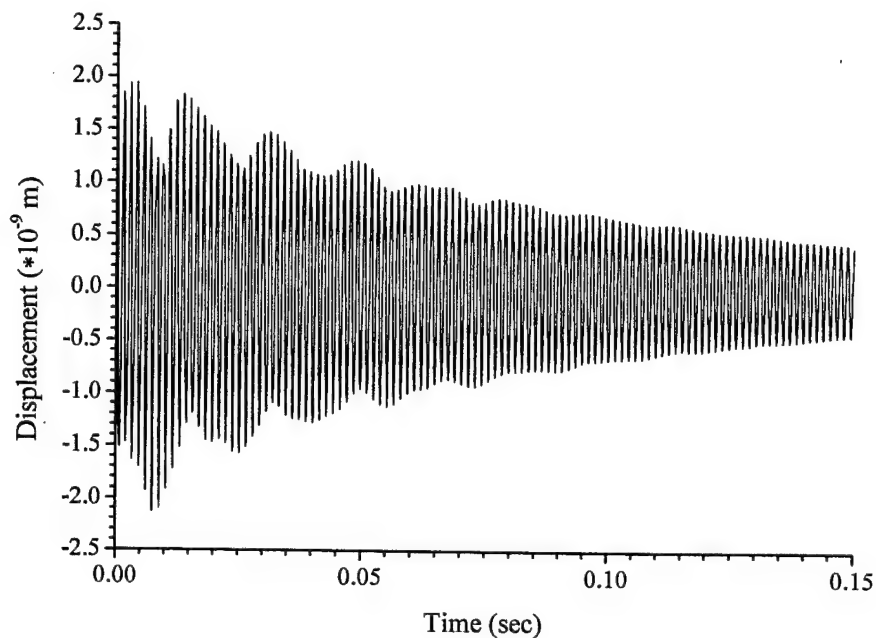


Fig.7 Free displacement response of the toroidal panel.

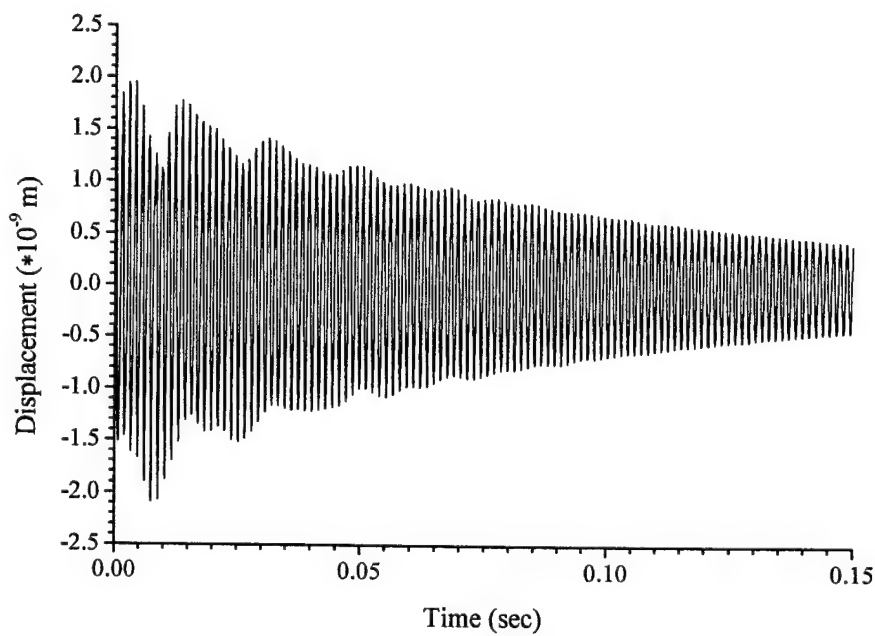


Fig.8 Controlled response of the toroidal panel with parallel actuator (gain=5).

Diagonal Actuator Lamination

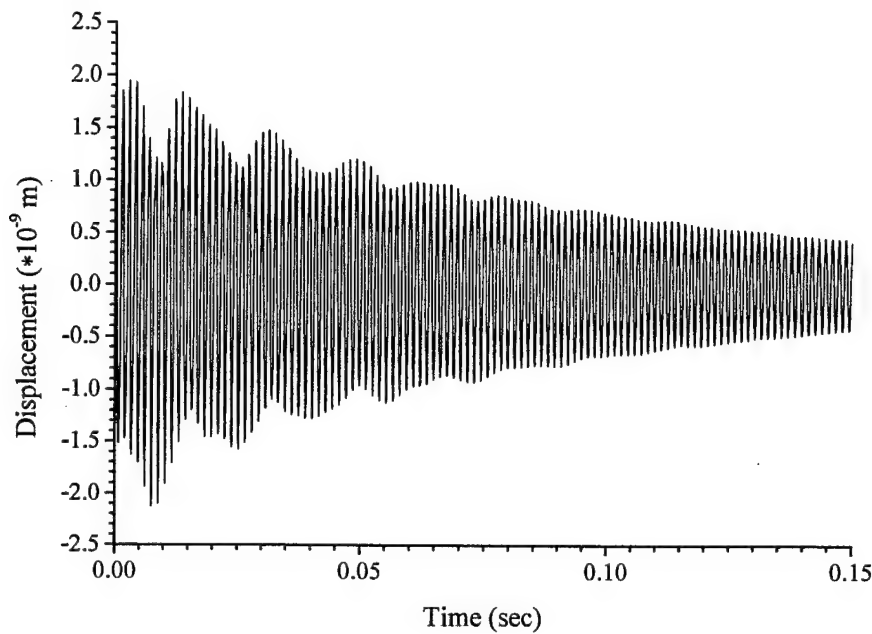


Fig.9 Free displacement response of the toroidal panel.

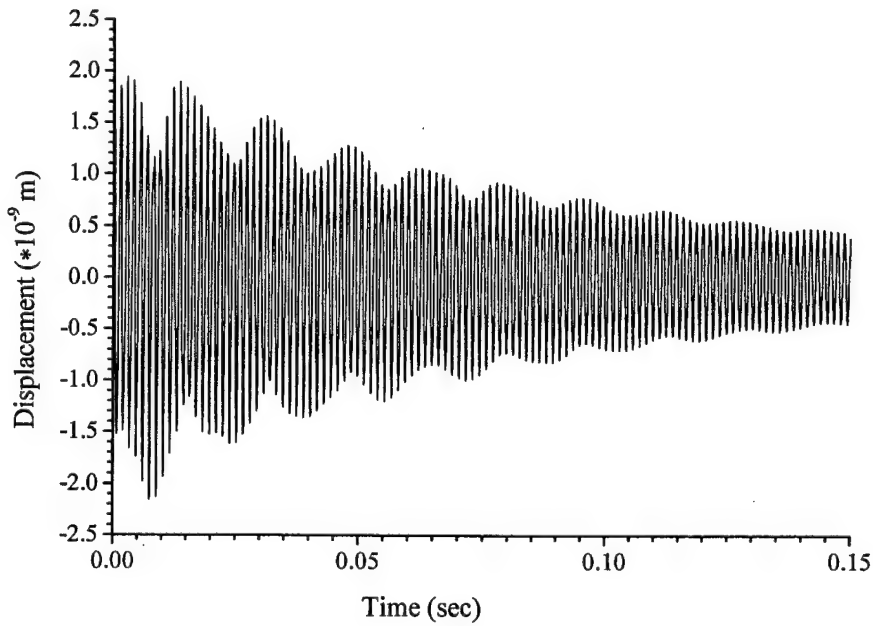


Fig.10 Controlled response of the toroidal panel with diagonal actuator (gain=5).

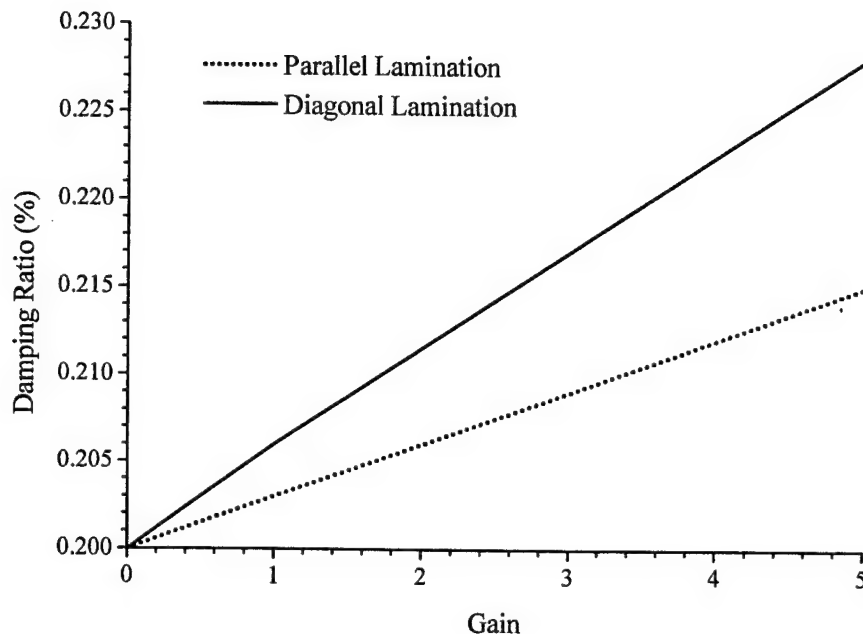


Fig.11 Inferred damping ratios at different gains of the two actuator configurations.

Additional analyses also reveal that the parallel lamination configuration is not effective to the 2nd mode (anti-symmetrical mode), but effective to the 3rd mode. The magnitude of beating decreases with time since only the 2nd mode dominates. Furthermore, the diagonal lamination configuration is effective to both the 2nd and 3rd modes and the beat phenomena become significant, since these two frequencies are close.

SUMMARY AND CONCLUSIONS

Toroidal shell structures and components are widely used in industrial and aerospace applications. Effective distributed control of these toroidal shells can enhance their operation precision, accuracy, and reliability. This study focused on evaluating the dynamic characteristics and control effectiveness of toroidal shell panels laminated with distributed piezoelectric sensor/ actuator layers. Finite element formulations of piezoelastic shell structures were reviewed. Element and system matrix equations of the piezoelastic shell strucronic (sensor/actuator/structure/control) system were derived and the system equations reveal the coupling of mechanical and electric (or control) fields.

Finite element eigen-value solutions of toroidal shell panels were compared favorably with published data in case studies. Vibration control effects of two sensor/actuator configurations, namely the parallel configuration and the diagonal configuration, laminated on toroidal shell panels were investigated. Numerical results suggest that the diagonal configuration provides better control effects, as compared with the parallel configuration, although both configurations utilize identical sensor/actuator sizes. Since the first and second frequencies are close, beat phenomena took place in both the free and controlled dynamic responses. The parallel lamination configuration is not effective to anti-symmetrical modes; the

diagonal lamination configuration is effective to most natural modes, except quad-antisymmetrical modes with respect to the shell center, due to signal cancellations.

ACKNOWLEDGEMENT

This research is supported, in part, by a grant (F49620-98-1-0467) from the Air Force Office of Scientific Research (Project Manager: Brian Sanders). This support is gratefully acknowledged.

REFERENCES

1. Melo, F.J.M.Q. and de Castro, P.M.S.T., 1997, "Linear Elastic Stress Analysis of Curved Pipes Under Generalized Loads Using a Reduced Integration Finite Ring Element," *Journal of Strain Analysis for Engineering Design*, **32**, pp.47-59.
2. Huang, D.W., Redekop, D. and Xu, B., 1997, "Natural Frequencies and Mode Shapes of Curved Pipes," *Composite Structures*, **63**, pp.465-473.
3. Leung, A.Y.T. and Kwok, T.C., 1994, "Free Vibration Analysis of a Toroidal Shell," *Thin-Walled Structures*, **19**, pp.317-332.
4. Zhang, F. and Redekop, D., 1992, "Surface Loading of a Thin-walled Toroidal Shell," *Computers and Structures*, **43**, pp.1019-1028.
5. Yamada, G., Kobayashi, Y., Ohta, Y. and Yokota, S., 1989, "Free Vibration of a Toroidal Shell with Elliptical Cross-section," *Journal of Sound and Vibration*, **135**, pp.411-425.
6. Galletly, G.D. and Galletly, D.A., 1996, "Buckling of Complex Toroidal Shell Structures," *Thin-Walled Structures*, **26**, pp.195-212.
7. Redekop, D. and Xu, B., 1999, "Vibration Analysis of Toroidal Panels Using the Differential Quadrature Method," *Thin-Walled Structures*, **34**, pp.217-231.
8. Naboulsi, S.K., Palazotto, A.N. and Greer, J.M. Jr., 2000, "Static-dynamic Analyses of Toroidal Shells," *Journal of Aerospace Engineering*, **13**, pp.110-121.
9. Tzou, H.S. and Wang, D.W., 2002, "Distributed Signals of Piezoelectric Laminated Toroidal Shell Structures," *Journal of Sound and Vibration*, **254**, pp.203-218.
10. Tzou, H.S., 1992, "Thin-layer Distributed Piezoelectric Neurons and Muscles: Electromechanics and Applications," *Precision Sensors, Actuators, and Systems*, Tzou, H.S. and Fukuda, T., (Editors), Kluwer Academic Publishers, Dordrecht/Boston/London, pp.175-218.
11. Tzou, H.S., Venkayya, V.B. and Hollkamp, J.J., 1998, "Orthogonal Sensing and Control of Continua with Distributed Transducers," *Dynamics and Control of Distributed Systems*, Tzou, H.S. and Bergman, L.A., (Editors), Cambridge University Press, pp.304-370.
12. Tzou, H.S., Bao, Y. and Zhou, Y., 1997, "Nonlinear Piezothermoelasticity and Multi-field Actuations, Part-1: Nonlinear Anisotropic Piezothermoelastic Shell Laminates; Part-2: Control of Nonlinear Buckling and Dynamics," *ASME Transactions, Journal of Vibration and Acoustics*, **119**, pp.374-389.
13. Tzou, H.S. and Yang, R.J., 2000, "Nonlinear Piezothermoelastic Shell Theory Applied to Control of Variable-geometry Shells," *Journal of Theoretical and Applied Mechanics*, **38**, pp.623-644.

14. Tzou, H.S. and Tseng, C.I., 1990, "Distributed Piezoelectric Sensor/Actuator Design for Dynamic Mesaurement/Control of Distributed Parameter Systems: A Finite Element Approach," *Journal of Sound and Vibration*, **138**, pp.17-34.
15. Tzou, H.S. and Ye, R., 1994, "Piezothermoelasticity and Precision Control of Piezoelectric Systems: Theory and Finite Element Analysis," *ASME Transactions, Journal of Vibration and Acoustics*, **116**, pp.489-495.
16. Tzou, H.S. and Ye, R., 1996, "Analysis of Piezoelastic Structures with Laminated Piezoelectric Triangle Shell Element," *AIAA journal*, **34**, pp.110-115.
17. Ye, R. and Tzou, H.S., 2000, "Control of Adaptive Shells with Thermal and Mechanical Excitations," *Journal of Sound and Vibration*, **231**, pp.1321-1338.
18. Tzou, H.S., 1993, *Piezoelectric Shells (Distributed Sensing and Control of Continua)*, Kluwer Academic Publishers, Boston /Dordrecht.

(TordFem_JPVTx.ShlFEM)

CHAPTER 18

CONTROL OF NONLINEAR ELECTRO/ELASTIC BEAM AND PLATE SYSTEMS (Finite Element Formulation and Analysis)

ABSTRACT

Adaptive structures involving large imposed deformation often go beyond the boundary of linear theory and they should be treated as “nonlinear” structures. A generic nonlinear finite element formulation for vibration sensing and control analysis of laminated electro/elastic nonlinear shell structures is derived based on the virtual work principle. A generic curved triangular piezoelectric shell element is proposed based on the layerwise constant shear angle theory. The dynamic system equations, equations of electric potential output and feedback control force defined in a matrix form are derived. The modified Newton-Raphson method is adopted for nonlinear dynamic analysis of large and complex piezoelectric/elastic/control structures. A finite element code for vibration sensing and control analysis of nonlinear active piezoelectric strucronic systems is developed. The developed piezoelectric shell element and finite element code are validated and then applied to control analysis of flexible electro-elastic (piezoelectric/elastic) structural systems. Vibration control of constant-curvature electro/elastic beam and plate systems are studied. Time-history responses of free and controlled nonlinear electro/elastic beam and plate systems are presented and nonlinear effects discussed.

INTRODUCTION

Utilizing active electromechanical materials (e.g., piezoelectrics, electrostrictive materials, electromagnetostrictive materials, shape-memory alloys, electro- and magneto-rheological materials, etc.) in new smart structures and strucronic systems transforms conventional *passive* elastic systems to *active* and adaptive “smart” systems, capable of self-sensing, diagnosis, control, damage compensation/repair, precision actuation, etc. This “strucronics” technology can be applied to small-scale micro-electromechanical systems, as well as to large-scale aircrafts and aerospace systems (Tzou and Fukuda, 1992; Gabbert and Tzou, 2001). Among the electro-active materials, piezoelectric materials are probably the most popular active material used in both sensor and actuator applications. Classical distributed sensing and control characteristics of shells and plates using segmented or spatially shaped sensors/actuators have been investigated (Tzou, 1993). Adaptive structures with controllable shapes or surfaces often involve large deformations and, thus, the geometric nonlinearity should be considered in the design and analysis. A nonlinear theory and governing equations of

piezothermoelastic shells was recently proposed (Tzou and Bao, 1997). Based on analytical procedures and closed-form solutions, static, dynamic, and control analysis of nonlinear plates and shallow spherical shells using piezoelectric actuators were recently investigated (Howard, et al., 2001; Tzou and Zhou, 1997; Zhou and Tzou, 2000; Tzou and Wang, 2002). Finite element (FE) development and analyses of linear piezoelectric and piezoelastic coupled electro/elastic structures have been carried out over the years (Trindade, Benjeddou, and Ohayon, 2001; Sze and Pan, 1999; Tzou and Tseng, 1990; Tzou and Ye, 1994, 1996; Ye and Tzou, 2000; Tzou, et al., 2002). This study focuses on development of a new FE technique and design tool for static, dynamic, and control analyses of nonlinear piezo(electric)/elastic coupled nonlinear electro/elastic structures. FE modeling and active vibration control of nonlinear electro/elastic piezoelectric laminated plates and beams based on a new generic curved triangular piezoelectric shell element are investigated. Dynamic system and control equations are derived and solution procedures discussed. Static, dynamic, and control analyses of electro/elastic (piezoelastic) beams and plates subjected to nonlinear deformation are studied.

TOTAL LAGRANGIAN VIRTUAL WORK EQUATIONS

In this study, it is assumed that the nonlinear piezoelectric/elastic (or piezoelastic) laminates are exposed to a displacement field and an electric field induced control action. To assure high accuracy and stability of FE solutions of geometrically nonlinear structures, the incremental analysis method is adopted in the analysis (Liu and To, 1995), which is to determine the static and kinematic variables, such as stresses, strains, displacement and velocity, in the equilibrium equations in a series of discrete time 0, Δt , $2\Delta t$, ... This method assumes that the solutions in the configurations from the initial configuration 0Z at the initial time to the configuration $'Z$ at time t are known. And the values in an unknown neighboring configuration ${}^{t+\Delta t}Z$ at a later time ($t+\Delta t$) are then determined from these known solutions (Bathe, 1996). For structural problems with both geometric and material nonlinearity, the total Lagrange and the updated Lagrange formulations are used to derive the governing equations. In practice, numerical effectiveness determines the choice of either the total Lagrangian formulation or the updated Lagrangian formulation (Bathe, 1996). For largely deformed structures with small strains, the total Lagrangian formulation is adopted in this study. On the other hand, for structures with both geometric and material nonlinearities, the updated Lagrangian formulation can be utilized (Liu and To, 1995). FE formulations of geometrically nonlinear piezoelastic structures can be derived based on the virtual work principle discussed next.

Let ${}^t u_i$, ${}^t \phi$, ${}^{t+\Delta t} u_i$ and ${}^{t+\Delta t} \phi$ be the displacements and electric potential of any point respectively corresponding to the configurations $'Z$ and ${}^{t+\Delta t}Z$ at time t and $(t+\Delta t)$. Then, the incremental displacement u_i from the previous configuration $'Z$ to the current configuration ${}^{t+\Delta t}Z$ can be written as $u_i = {}^{t+\Delta t} u_i - {}^t u_i$. The virtual work functional in the displacement and electric field can be written as

$$\int_V {}^{t+\Delta t} T_{ij} \delta {}^{t+\Delta t} S_{ij} {}^{t+\Delta t} dV = {}^{t+\Delta t} W_u, \quad (1)$$

$$\int_V {}^{t+\Delta t} D_i \delta {}^{t+\Delta t} E_i {}^{t+\Delta t} dV = {}^{t+\Delta t} W_\phi, \quad (2)$$

where ${}^{t+\Delta t}T_{ij}$, ${}^{t+\Delta t}S_{ij}$, ${}^{t+\Delta t}D_i$ and ${}^{t+\Delta t}E_i$ ($i, j = 1, 2, 3$) are the stress, strain, electric displacement and electric field, respectively; ${}^{t+\Delta t}W_u$ and ${}^{t+\Delta t}W_\phi$ are the virtual work of external mechanical load and electric load, respectively; V is the volume of the piezoelectric continuum. The linear piezoelectricity theory is adopted in this study and the piezoelectric material is assumed class mm2 (Tzou, 1993; Ikeda, 1990). Note that the left superscript denotes in which configuration these variables are. In this case, for example, the variables above are in the current configuration ${}^{t+\Delta t}Z$. The increments in stresses T_{ij} , electric displacements D_i , strains S_{ij} and electric fields E_i from the previous configuration Z to the current configuration ${}^{t+\Delta t}Z$ are defined as

$$T_{ij} = {}^{t+\Delta t}T_{ij} - {}^tT_{ij}, \quad D_i = {}^{t+\Delta t}D_i - {}^tD_i, \quad S_{ij} = {}^{t+\Delta t}S_{ij} - {}^tS_{ij}, \quad E_i = {}^{t+\Delta t}E_i - {}^tE_i. \quad (3a,b,c,d)$$

The incremental strains comprise of linear and nonlinear components S_{ij}^ℓ and S_{ij}^n which can be written in term of the incremental displacements u_i as

$$S_{ij}^\ell = \frac{1}{2}(u_{i,j} + u_{j,i} + {}^tu_{k,i}u_{k,j} + {}^tu_{k,j}u_{k,i}), \quad S_{ij}^n = \frac{1}{2}u_{k,i}u_{k,j}. \quad (4a,b)$$

Note that the right superscript “ ℓ ” and “ n ” denote linear and nonlinear components, respectively. Substituting Eqs.(3a,b,c,d) and (4a,b), one can rewrite Eqs.(1) and (2) as

$$\int_V T_{ij} \delta S_{ij} dV + \int_V {}^tT_{ij} \delta S_{ij}^n dV = {}^{t+\Delta t}W_u - \int_V {}^tT_{ij} \delta S_{ij}^\ell dV, \quad (5)$$

$$\int_V D_i \delta E_i dV = {}^{t+\Delta t}W_\phi - \int_V {}^tD_i \delta E_i dV. \quad (6)$$

Note that the nonlinear equilibrium Eqs.(5) and (6), when employed in dynamic analysis, would be very time consuming, if not computationally infeasible. Using the approximations $T_{ij} = c_{ijkl}S_{kl} - e_{ijm}E_m$, $D_i = e_{ijk}S_{jk} + \epsilon_{ij}E_j$ and $\delta S_{ij} = \delta S_{ij}^\ell$, one can obtain as approximate nonlinear equilibrium Eqs.(5) and (6)

$$\int_V c_{ijkl}S_{kl} \delta S_{ij}^\ell dV - \int_V e_{ijm}E_m \delta S_{ij}^\ell dV + \int_V {}^tT_{ij} \delta S_{ij}^n dV = {}^{t+\Delta t}W_u - \int_V {}^tT_{ij} \delta S_{ij}^\ell dV, \quad (7)$$

$$\int_V \epsilon_{ij}E_j \delta E_i dV + \int_V e_{ijk}S_{jk} \delta E_i dV = {}^{t+\Delta t}W_\phi - \int_V {}^tD_i \delta E_i dV, \quad (8)$$

where c_{ijkl} , e_{ijm} and ϵ_{ij} ($i, j, k, l, m = 1, 2, 3$) are the elastic moduli, piezoelectric coefficients and dielectric coefficients, respectively. The virtual work of the elastic force and electric force can be further expressed as

$${}^{t+\Delta t}W_u = \int_{S_T} {}^{t+\Delta t}f_k \delta u_k ds + \int_V ({}^{t+\Delta t}f_{bk} - \rho {}^{t+\Delta t}\ddot{u}_k) \delta u_k dV, \quad (9)$$

$${}^{t+\Delta t}W_\phi = \int_{S_D} {}^{t+\Delta t}Q \delta \phi ds, \quad (10)$$

where δu_k ($k = 1, 2, 3$) and $\delta \phi$ are the variation of the current displacement component $^{t+\Delta t} u_k$ and electric potential $^{t+\Delta t} \phi$; $^{t+\Delta t} f_k$ and $^{t+\Delta t} f_{bk}$ are the surface force component and the body force component, respectively; $^{t+\Delta t} \ddot{u}_k$ are the components of acceleration, respectively; $^{t+\Delta t} Q$ is the surface charge; ρ is the material mass density; and S_T and S_D are the boundary surfaces specified by the surface force $^{t+\Delta t} f_k$ and charge $^{t+\Delta t} Q$. Note that the subscripts "T" and "D" denote the specified elastic force and charge, respectively. Finite element formulations of nonlinear piezoelectric shell structures and control can be derived based on the virtual work functional in Eqs.(7) and (8), and they are presented in the next section.

PIEZOELECTRIC FINITE ELEMENT FORMULATIONS

The general procedures of the FE method need to divide a continuum into a number of finite elements using imaginary lines or surfaces and to choose a set of functions defining the field variables within each finite element via nodal variables. Assuming that within every element the displacement vector $^t \mathbf{u}$ and the electric potential $^t \phi$ in the configuration $'Z$ can be written as

$$^t \mathbf{u} = \mathbf{N}_u \, ^t \mathbf{U}, \quad \mathbf{u} = \mathbf{N}_u \mathbf{U}, \quad ^t \phi = \mathbf{N}_\phi \, ^t \Phi, \quad \phi = \mathbf{N}_\phi \Phi, \quad (11a, b, c, d)$$

where \mathbf{u} and ϕ are incremental displacement vector and incremental electric potential; $^t \mathbf{U}$ and $^t \Phi$ are nodal displacement vector and nodal electric potential in the configuration $'Z$; \mathbf{U} and Φ are incremental displacement vector and incremental nodal electric potential, respectively; \mathbf{N}_u and \mathbf{N}_ϕ are the matrices of displacement and electric potential interpolation function. Note that the stress, strain, electric displacement and electric field in Eqs.(3a,b,c,d) can be further expressed in terms of the nodal displacement and electric potential in Eqs.(11a,b,c,d). Then the virtual work Eqs.(7) and (8) can be discretized in terms of nodal displacement and electric potential accordingly. If only one element is concerned, for simplification, one can write the element virtual work functional in matrix notation by substituting Eqs.(11a,b,c,d) into Eqs.(7) and (8).

$$\mathbf{M}_{uu} \, ^{t+\Delta t} \ddot{\mathbf{U}} + ({}^t \mathbf{K}_{uu}^\ell + {}^t \mathbf{K}_{uu}^n) \mathbf{U} + {}^t \mathbf{K}_{u\phi}^\ell \Phi = {}^{t+\Delta t} \mathbf{F}_u - {}^t \mathbf{F}_u, \quad (12)$$

$${}^t \mathbf{K}_{\phi u}^\ell \mathbf{U} - {}^t \mathbf{K}_{\phi\phi}^\ell \Phi = {}^{t+\Delta t} \mathbf{F}_\phi - {}^t \mathbf{F}_\phi, \quad (13)$$

where \mathbf{U} and $\ddot{\mathbf{U}}$ are the incremental nodal displacement and acceleration vectors, respectively; Φ is incremental nodal electric potential; ${}^t \mathbf{K}_{xy}^\ell$ (where $x \& y = u, \phi$ and v denotes ℓ or n which represents the linear term and the nonlinear term, respectively) are the stiffness matrices defined for the displacement and electric field; \mathbf{M}_{uu} is the mass matrix; ${}^{t+\Delta t} \mathbf{F}_u$ and ${}^t \mathbf{F}_u$ are the external mechanical excitation vectors; ${}^{t+\Delta t} \mathbf{F}_\phi$ and ${}^t \mathbf{F}_\phi$ are the electric excitation vectors; \mathbf{M}_{uu} , ${}^t \mathbf{K}_{uu}^\ell$, ${}^t \mathbf{K}_{uu}^n$, ${}^t \mathbf{K}_{u\phi}^\ell$, ${}^{t+\Delta t} \mathbf{F}_u$, ${}^t \mathbf{F}_u$ are obtained from $\int_V \rho {}^{t+\Delta t} \ddot{u}_k \delta u_k dV$, $\int_V c_{ijkl} S_{kl}^\ell \delta S_{ij}^\ell dV$,

$\int_V {}^t T_{ij} \delta S''_{ij} dV$, $\int_V e_{ijm} E_m \delta S'_{ij} dV$, $\int_{S_T} {}^{t+\Delta t} f_k \delta u_k ds - \int_V {}^{t+\Delta t} f_{bk} \delta u_k dV$, $\int_V {}^t T_{ij} \delta S'_{ij} dV$, respectively;

And ${}^t K_{\phi u}^\ell$, ${}^t K_{\phi \phi}^\ell$, ${}^{t+\Delta t} F_\phi$, ${}^t F_\phi$ are derived from $\int_V e_{ijk} S'_{jk} \delta E_i dV$, $\int_V \varepsilon_{ij} E_j \delta E_i dV$, $\int_D {}^{t+\Delta t} Q \delta \phi ds$, $\int_V {}^t D_i \delta E_i dV$, respectively. (Detailed definitions of the element matrices are presented in the next section.) If damping is considered, one can write a Rayleigh damping approximation as

$$C_{uu} = \alpha M_{uu} + \beta^0 K_{uu}^\ell, \quad (14)$$

where α and β are the coefficients of proportionality for the mass and elastic stiffness matrices, respectively. Note that the damping ratios can be exactly determined if two modes (e.g., modes m and n) are specified. The damping ratios in the unspecified modes can be calculated based on modes m and n . A least square solution can be used to calculate these two coefficients if damping ratios are specified in more than two modes (Craig, 1981; Cook, et al., 1989). Assembling all the element matrices, one can write the system equations in a compact matrix form

$$\begin{bmatrix} M_{uu} & 0 \\ 0 & 0 \end{bmatrix} \begin{Bmatrix} {}^{t+\Delta t} \ddot{U} \\ {}^{t+\Delta t} \ddot{\Phi} \end{Bmatrix} + \begin{bmatrix} C_{uu} & 0 \\ 0 & 0 \end{bmatrix} \begin{Bmatrix} {}^{t+\Delta t} \dot{U} \\ {}^{t+\Delta t} \dot{\Phi} \end{Bmatrix} + \begin{bmatrix} {}^t K_{uu}^\ell + {}^t K_{uu}^n & {}^t K_{u\phi}^\ell \\ {}^t K_{\phi u}^\ell & -{}^t K_{\phi\phi}^\ell \end{bmatrix} \begin{Bmatrix} U \\ \Phi \end{Bmatrix} = \begin{Bmatrix} {}^{t+\Delta t} F_u - {}^t F_u \\ {}^{t+\Delta t} F_\phi - {}^t F_\phi \end{Bmatrix}. \quad (15)$$

PIEZOELECTRIC SHELL ELEMENT

A general curved triangular laminated nonlinear piezoelastic shell element using the layerwise constant shear angle theory is derived, which is used for modeling and analysis of piezoelastic structures with geometrical nonlinearity. The new finite element is a 12-node piezoelectric shell element with triangular geometry shown in **Figure 1**. Six nodes are located on the three lines of the upper surface and the other six nodes are located on the three lines of the lower surface of the triangular element. Its nodal arrangements are illustrated in **Figure 1**. Each node is associated with four degrees of freedom (DOF). The four DOFs are: u_1 - the displacement component in the α_1 -direction, u_2 - the displacement component in the α_2 -direction, u_3 - the displacement component in the α_3 -direction, and ϕ - the electric potential.

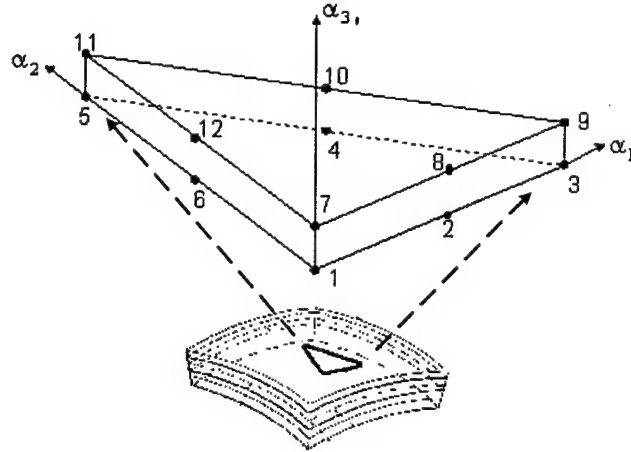


Fig. 1 A laminated piezoelectric shell element.

Contrary to the degenerated shell elements, the general material laws are used; the kinetic and geometric variables are easily interpolated for this shell element; no transition elements are needed when the structure including both solid and thin-walled regions; and the complication on handling finite rotational increments can be avoided (Sze and Yao, 2000). However, it should be pointed out this element suffers from not only shear and membrane locking which bother the degenerated shell elements, but also dilatational, trapezoidal and thickness locking (Stolarski and Belytschko, 1983; Simo and Rifai, 1990). Various compensations were proposed to avoid these locking and systematic development of locking-free shell element formulations for linear and non-linear analyses is well addressed (Bischoff and Ramm, 1997; Hauptmann and Schweizerhof, 1998; Harnau and Schweizerhof, 2002). Also note that without the electric potential degree of freedom, this element is similar to the 12-noded wedge element which has difficulties in modeling rigid body modes (Surana, 1983). Under the assumption of the layerwise constant shear angle theory, for an arbitrary layer i , the displacements and electric potential can be written as

$$\mathbf{U}^{(i)} = \bar{\mathbf{N}}_u^{(i)}(\gamma) \bar{\mathbf{U}}^{(i)}, \quad \phi^{(i)} = \bar{\mathbf{N}}_\phi^{(i)}(\gamma) \bar{\phi}^{(i)}, \quad (16a,b)$$

where $\mathbf{U}^{(i)}$ and $\phi^{(i)}$ are the displacement vector and electric potential of any node on the i -th layer; $\bar{\mathbf{U}}^{(i)}$ and $\bar{\phi}^{(i)}$ are the displacement and electric potential of the i -th and $(i+1)$ -th interfaces along the curvilinear coordinate axes; γ is a transverse coordinate defined for the i -th layer. The surface-parallel displacement and electric potential can be expressed as

$$\bar{\mathbf{U}}^{(i)} = \mathbf{N}_u(\alpha_1, \alpha_2) \mathbf{U}^{(i)}, \quad \bar{\phi}^{(i)} = \mathbf{N}_\phi(\alpha_1, \alpha_2) \Phi^{(i)}, \quad (17a,b)$$

where $\mathbf{U}^{(i)}$ and $\Phi^{(i)}$ are the nodal displacement and nodal electric potential of the element; \mathbf{N}_u and \mathbf{N}_ϕ are the quadratic shape functions defined by coordinates α_1 and α_2 .

Element Stiffness Matrices and Balanced Force Vector

From Eq.(3), the incremental strains and electric field can be written in a vector form as

$$\mathbf{S} = {}^{t+\Delta t} \mathbf{S} - {}^t \mathbf{S}, \quad \mathbf{E} = {}^{t+\Delta t} \mathbf{E} - {}^t \mathbf{E}, \quad (18a,b)$$

where \mathbf{S} , \mathbf{E} are incremental strain and electric field vector, respectively; ${}^t \mathbf{S}$, ${}^{t+\Delta t} \mathbf{S}$, ${}^t \mathbf{E}$ and ${}^{t+\Delta t} \mathbf{E}$ are strain and electric field vectors at time t and $(t + \Delta t)$, respectively. Substituting Eqs.(16a,b) and (17a,b) into Eq.(18a,b), one can write the incremental strains of the i -th layer in terms of nodal variables of the element in a matrix form as

$$\mathbf{S} = \mathbf{B}_u \mathbf{U}, \quad \mathbf{E} = -\mathbf{B}_\phi \Phi \quad (19a,b)$$

where $\mathbf{S} = \{S_{11}, S_{22}, S_{33}, S_{12}, S_{13}, S_{23}\}^T$, $\mathbf{E} = \{E_1, E_2, E_3\}^T$; \mathbf{B}_u and \mathbf{B}_ϕ are the generalized strain shape function; \mathbf{U} , Φ are the same as defined previously. Since the strains have the linear and nonlinear components, correspondingly, \mathbf{B}_u can also be expressed as

$$\mathbf{B}_u = \mathbf{B}_u^{\ell 0} + \mathbf{B}_u^{\ell 1} + \mathbf{B}_u^n, \quad (20)$$

where $\mathbf{B}_u^{\ell 0}$ is the strain shape function of $(u_{i,j} + u_{j,i})/2$ which relates to the linear strain components independent to time; $\mathbf{B}_u^{\ell 1}$ is the strain shape function of $\frac{1}{2}({}^t u_{k,i} u_{k,j} + {}^t u_{k,j} u_{k,i})$ which relates to the linear strain components depending on time; \mathbf{B}_u^n is the strain shape function of S_{ij}^n which relates to the nonlinear strain components. Note that right superscript “0” and “1” denote the usual small strain part and the linear strain part related to the configuration ‘Z’. It is obvious that $\mathbf{B}^{\ell 0}$ is configuration-independent, while $\mathbf{B}^{\ell 1}$ is dependent on the configuration ‘Z’. Thus, ${}^t \mathbf{K}_{uu}^\ell$ can be divided into two parts:

$${}^t \mathbf{K}_{uu}^\ell = {}^t \mathbf{K}_{uu}^{\ell 0} + {}^t \mathbf{K}_{uu}^{\ell 1}, \quad (21)$$

where ${}^t \mathbf{K}_{uu}^{\ell 0} = \int_V {}^t \mathbf{B}_u^{\ell 0 T} \mathbf{c} {}^t \mathbf{B}_u^{\ell 0} dV$, ${}^t \mathbf{K}_{uu}^{\ell 1} = \int_V {}^t \mathbf{B}_u^{\ell 0 T} \mathbf{c} {}^t \mathbf{B}_u^{\ell 1} dV + \int_V {}^t \mathbf{B}_u^{\ell 1 T} \mathbf{c} {}^t \mathbf{B}_u^{\ell 0} dV + \int_V {}^t \mathbf{B}_u^{\ell 1 T} \mathbf{c} {}^t \mathbf{B}_u^{\ell 1} dV$. It is known that ${}^t \mathbf{K}_{uu}^{\ell 0}$ is the usual small displacement (or incremental) stiffness matrix, ${}^t \mathbf{K}_{uu}^{\ell 1}$ is the initial displacement matrix, since it is induced by the initial displacement ${}^t u_i$. The initial stress (or the geometric) stiffness matrix ${}^t \mathbf{K}_{uu}^n$ is

$${}^t \mathbf{K}_{uu}^n = \int_V {}^t \mathbf{B}_u^n T {}^t \mathbf{T} {}^t \mathbf{B}_u^n dV, \quad (22)$$

where ${}^t \mathbf{T}$ is the second Piola-Kirchhoff stress matrix which can be written as

$${}^t\mathbf{T} = \begin{bmatrix} {}^tT_{11} & {}^tT_{12} & 0 \\ {}^tT_{12} & {}^tT_{22} & 0 \\ 0 & 0 & {}^tT_{33} \end{bmatrix} . \quad (23)$$

Other stiffness matrices related to the electric field are ${}^t\mathbf{K}_{u\phi}^t = \int_V {}^t\mathbf{B}_u^t \mathbf{e}^t {}^t\mathbf{B}_\phi^t dV$ and ${}^t\mathbf{K}_{\phi\phi}^t = \int_V {}^t\mathbf{B}_\phi^t \mathbf{e}^t {}^t\mathbf{B}_\phi^t dV$, and ${}^t\mathbf{K}_{\phi u}^t = {}^t\mathbf{K}_{u\phi}^t$. The balanced mechanical force can be expressed as

$${}^t\mathbf{F}_u = \int_V ({}^t\mathbf{B}_u^{t0T} + {}^t\mathbf{B}_u^{t0T}) {}^t\tilde{\mathbf{T}} dV, \quad (24)$$

where ${}^t\tilde{\mathbf{T}}$ is the second Piola-Kirchhoff stress vector defined in configuration $'Z$. Note that the forgoing element matrices are easily calculated provided that the strain shape functions \mathbf{B}_x ($x=u,\phi$) and material coefficient matrices \mathbf{c} , \mathbf{e} and $\mathbf{\epsilon}$ are obtained.

NONLINEAR SOLUTION ALGORITHM

The dynamic equilibrium equation for a piezoelectric system in Eq.(15) can be simplified into a standard form

$$\mathbf{M}^t \ddot{\mathbf{U}} + \mathbf{C}^t \dot{\mathbf{U}} + ({}^t\mathbf{K}^t + {}^t\mathbf{K}^n) \mathbf{U} = {}^{t+\Delta t} \mathbf{P} - {}^t\mathbf{F}, \quad (25)$$

where \mathbf{U} is the incremental displacement vector; ${}^{t+\Delta t}\dot{\mathbf{U}}$ and ${}^{t+\Delta t}\ddot{\mathbf{U}}$ are the velocity and acceleration vectors; ${}^t\mathbf{K}^t$ and ${}^t\mathbf{K}^n$ are the linear and nonlinear stiffness matrices; \mathbf{M} is the mass matrix; \mathbf{C} is the damping matrix; ${}^{t+\Delta t}\mathbf{P}$ and ${}^t\mathbf{F}$ are the external load vector and the balanced force vector, respectively. Accuracy with the incremental solution procedure requires the use of a small time step since the nonlinear stiffness changes over the time increment are ignored. Improved accuracy can be achieved by modifying Eq.(25) to calculate the iterative displacement $\mathbf{U}^{(k)}$. One iterative solution methodology is the modified Newton-Raphson iteration, i.e.,

$$\mathbf{M}^t \ddot{\mathbf{U}}^{(k)} + \mathbf{C}^t \dot{\mathbf{U}}^{(k)} + ({}^t\mathbf{K}^t + {}^t\mathbf{K}^n) \mathbf{U}^{(k)} = {}^{t+\Delta t} \mathbf{P} - {}^{t+\Delta t} \mathbf{F}^{(k)}, \quad (26)$$

where k the is iteration number. Note that ${}^t\mathbf{K}^t$ and ${}^t\mathbf{K}^n$ are constant during the time iteration calculation. The incremental/iterative displacements and balanced force vectors are updated as

$${}^{t+\Delta t} \mathbf{U}^{(k)} = {}^{t+\Delta t} \mathbf{U}^{(k)} + \delta \mathbf{U}^{(k)} = {}^t \mathbf{U} + \mathbf{U}^{(k)}, \quad \mathbf{U}^{(0)} = 0, \quad (27,28)$$

$${}^{t+\Delta t} \mathbf{F}^{(k)} = {}^{t+\Delta t} \mathbf{F}^{(k-1)} + \delta \mathbf{F}^{(k)} = {}^t \mathbf{F} + \mathbf{F}^{(k)}, \quad {}^{t+\Delta t} \mathbf{F}^{(0)} = {}^t \mathbf{F}. \quad (29,30)$$

where δ is iterative change. The acceleration and velocity used in the Newmark's temporal discretization for the modified Newton-Raphson iteration are (Blandford and Glass, 1987)

$$\begin{aligned} {}^{t+\Delta t} \ddot{\mathbf{U}}^{(k)} &= \frac{1}{\alpha \Delta t^2} [{}^{t+\Delta t} \mathbf{U}^{(k)} - {}^t \mathbf{U}] - \frac{1}{\alpha \Delta t} {}^t \dot{\mathbf{U}} + \left(1 - \frac{1}{2\alpha}\right) {}^t \ddot{\mathbf{U}}, \\ {}^{t+\Delta t} \dot{\mathbf{U}}^{(k)} &= \frac{\delta}{\alpha \Delta t} [{}^{t+\Delta t} \mathbf{U}^{(k)} - {}^t \mathbf{U}] + \left(1 - \frac{\delta}{\alpha}\right) {}^t \dot{\mathbf{U}} + \Delta t \left(1 - \frac{\delta}{2\alpha}\right) {}^t \ddot{\mathbf{U}}. \end{aligned} \quad (31a,b)$$

Substituting Eq.(31a,b) into Eq.(26) gives

$${}^t \bar{\mathbf{K}} \mathbf{U}^{(k)} = {}^{t+\Delta t} \mathbf{P} - {}^{t+\Delta t} \mathbf{F}^{(k)}, \quad (32)$$

where ${}^t \bar{\mathbf{K}} = \frac{1}{\alpha \Delta t^2} \mathbf{M} + \frac{\delta}{\alpha \Delta t} \mathbf{C} + {}^t \mathbf{K}^{\ell} + {}^t \mathbf{K}^n$, ${}^{t+\Delta t} \bar{\mathbf{P}} = {}^{t+\Delta t} \mathbf{P} + \mathbf{M} \left\{ \frac{1}{\alpha \Delta t^2} [{}^t \mathbf{U} - {}^{t+\Delta t} \mathbf{U}^{(k)}] \right. \\ \left. + \frac{1}{\alpha \Delta t} {}^t \dot{\mathbf{U}} + \left(\frac{1}{2\alpha} - 1 \right) {}^t \ddot{\mathbf{U}} \right\} + \mathbf{C} \left\{ \frac{\delta}{\alpha \Delta t} [{}^t \mathbf{U} - {}^{t+\Delta t} \mathbf{U}^{(k)}] + \left(\frac{\delta}{\alpha} - 1 \right) {}^t \dot{\mathbf{U}} + \Delta t \left(\frac{\delta}{2\alpha} - 1 \right) {}^t \ddot{\mathbf{U}} \right\}$. The convergence of the iteration scheme of Eq.(26) could follow the out-of-balance load criterion and incremental internal energy criterion (Bathe, 1996). A new FE code incorporating the coupling of electromechanics, piezoelectricity, geometric nonlinearity, control, etc. and the nonlinear solution algorithms is developed and applications are presented in case studies.

CASE STUDIES

To validate the new FE code and its multi-field coupling/control capability, conventional static and dynamic analyses of nonlinear elastic beams and plates are compared with published data, followed by control of nonlinear piezoelastic beams and plates with distributed piezoelectric actuators.

Case 1 – Cantilever Single-layered and Piezoelastic Beam

Two cantilever beams, i.e., a single-layered beam and a laminated piezoelectric beam, as shown in **Figure 2** and **Figure 3**, are studied in this case. Static analysis and comparison are carried out first, followed by dynamic analysis and control of large deflections by piezoelectric actuator layers. Geometry and material properties are outlined in **Table 1**. Note that the polyvinylidene fluoride (PVDF) film is thin and flexible and its effects to static deflections and dynamic/control analyses are considered.

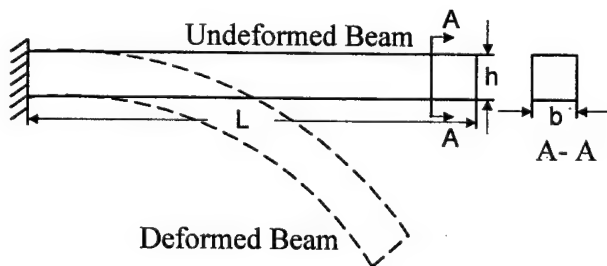


Fig.2 A cantilever single-layered beam.

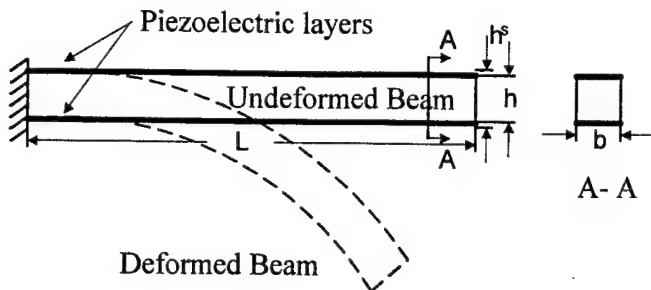


Fig.3 A cantilever laminated piezoelectric beam.

Table 1. Geometry and Material Properties.

Properties	Elastic Material	PVDF
Length L (m)	0.1	0.1
Width b (m)	0.01	0.01
Height h, h ^s (m)	0.01	9.0×10 ⁻⁶
Young's modulus Y (Pa)	1.2×10 ⁸	2.0×10 ⁹
Poisson's ratio μ	0.2	0.29
Piezoelectric constant d_{31} (C/N)		2.2×10 ⁻¹¹
Electric permittivity ϵ (F/m)		1.062×10 ⁻¹⁰

Static Analysis

A uniformly distributed surface load is applied to the top surface of the beam. **Figure 4** shows the tip static deflections of the beam at different load levels. Note that non-dimensional load coefficient $F_0=FL^3/YI$ is used, where I is area moment of inertia of beam cross-section, F is the load, and L and Y are previously defined in **Table 1**. The deflection ratio U_3/L is used and U_3 is the transverse deflection. Present nonlinear FEM solutions are compared with published nonlinear and linear results (Bathe, Ramm and Wilson, 1975) and favorable comparison with the published nonlinear data is observed. The nonlinearity effect stiffens the beam, as also observed. For comparison, the static deflection (with ■ data) of the piezo(electric)elastic beam (**Figure 3**) marked “**” is also provided in **Figure 4**. The reduced deflection of the laminated piezoelectric beam is introduced by a higher stiffness due to the added piezoelectric layers (see **Table 1**).

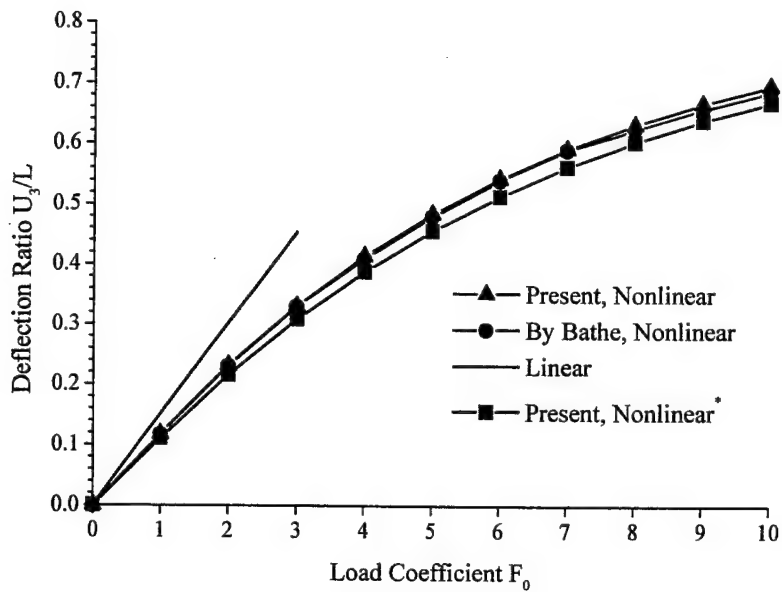


Fig.4 Tip static deflections of single-layerd/laminated piezoelastic beams.

Dynamic and Control Analyses

To better illustrate the control effect, a new cantilever piezoelectric laminated beam is studied to investigate the dynamic and control behaviors. Geometry and material properties are provided in **Table 2**. It is assumed that the structure is undamped. A uniform surface step-load with a magnitude of 45N/m^2 is applied on the top surface of the beam. Time step is set to be 2.0×10^{-3} second. **Figure 5** shows the linear/nonlinear transient responses and the nonlinear effect is to reduce the oscillation magnitude and period, due to the stiffening effect. Vibration control induced by the piezoelectric layer is evaluated next.

Table 2 Geometry and Material Properties.

Properties	Elastic Material	PVDF
Length L (m)	0.2	0.2
Width b (m)	0.02	0.02
Height h, h ^s (m)	2.0×10^{-3}	9.0×10^{-6}
Young's modulus Y (Pa)	2.0955×10^8	2.0×10^9
Poisson's ratio μ	0.25	0.29
Mass density ρ (kg/m ³)	3.21005×10^3	1.8×10^3
Piezoelectric constant d_{31} (C/N)		2.2×10^{-11}
Electric permittivity ϵ (F/m)		1.062×10^{-10}

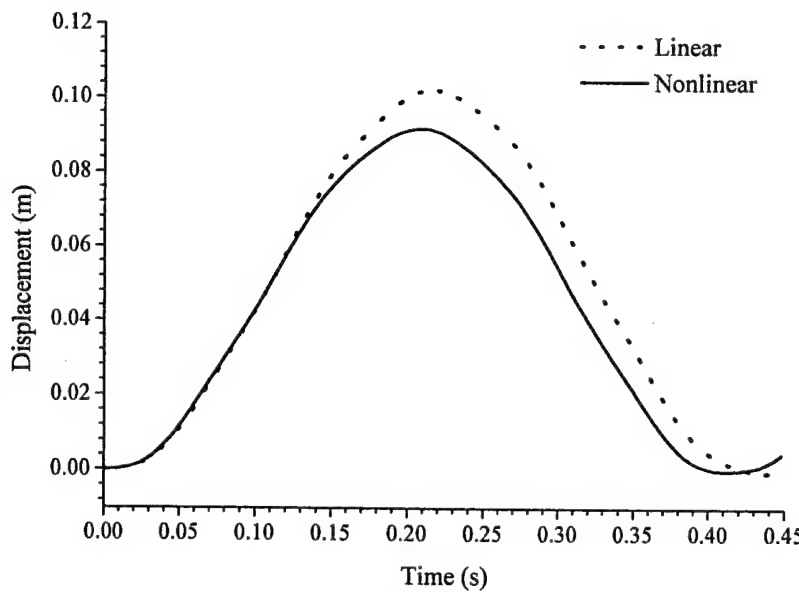


Fig.5 Linear/nonlinear transient responses of the cantilever beam.

Following the procedures, three other surface step-loads with magnitudes 2N/m^2 , 10N/m^2 and 20N/m^2 are applied to generate low, median and high nonlinearities of the piezoelastic beam. The negative velocity proportional control method is used in vibration control and the control gain is set to be 3.0. **Figures 6, 7 and 8** show the controlled transient responses of the three load levels and the control effects are significantly different for these three load cases. Under the same control condition except the load level, the control effect reduces at increased load level, since the beam stiffens due to the increased nonlinearity.

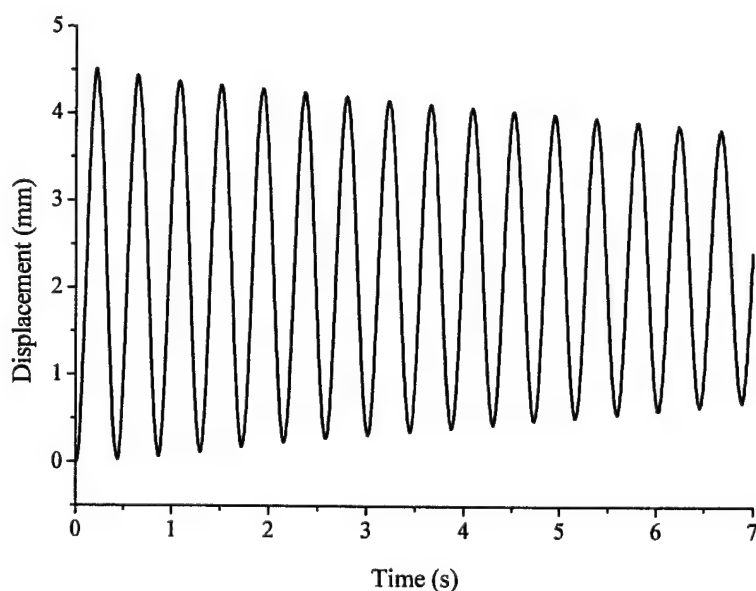


Fig.6 Controlled transient response of the piezoelastic beam (Load= 2N/m^2).

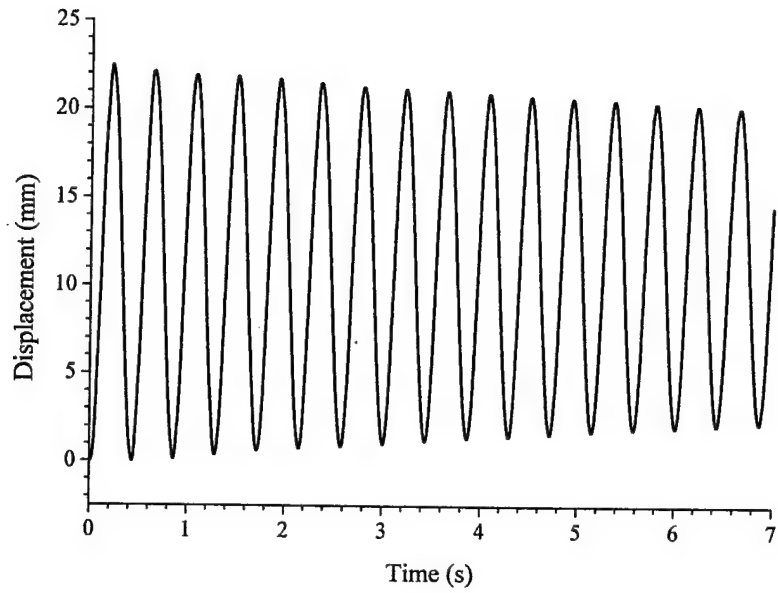


Fig.7 Controlled transient response of the piezoelastic beam (Load=10N/m²).

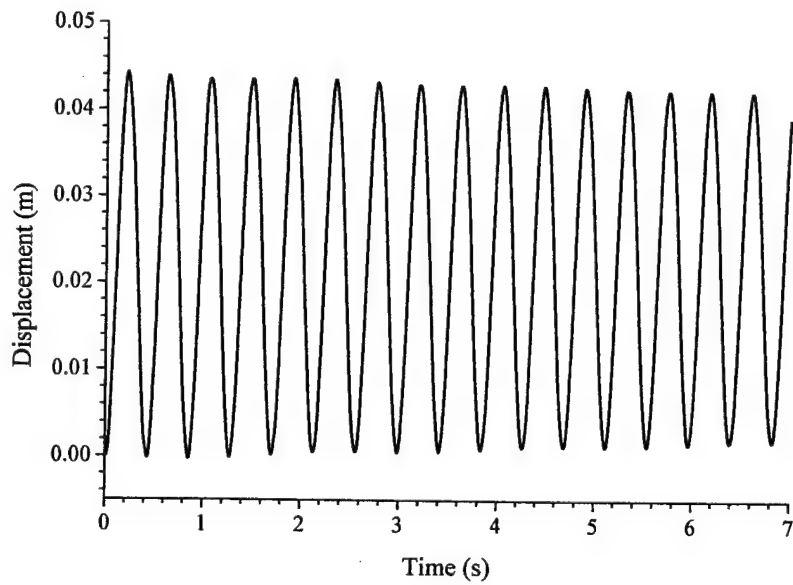


Fig.8 Controlled transient response of the piezoelastic beam (Load=20N/m²).

Case 2 – Simply Supported Laminated Piezoelastic Plate

Linear dynamic response analysis of a simply supported rectangular single-layered elastic plate has been studied (Bathe, Wilson, and Iding, 1974; To and Liu, 1995). **Figure 9** illustrates the simply supported rectangular plate with piezoelectric control layers. (Note that only the elastic plate is analyzed in Dynamic Analysis and the piezoelastic plate in Control Analysis in this section.) Geometry and material properties of this elastic plate are provided in

Table 3 and the structure is assumed undamped. A step-function load with a magnitude of 44.54 N is applied to the plate center and a $\frac{1}{4}$ of the plate is modeled by (6×4) meshes. (Note that each mesh includes two triangular elements and one quarter of the plate is modeled in the FE analysis due to the symmetry of geometry, boundary condition and loading.) For direct time integration, the trapezoidal scheme was employed and the time step size was 0.002 sec in previous beam analyses. In present study, the Newmark method is used and the same time step (0.002 sec) is adopted.

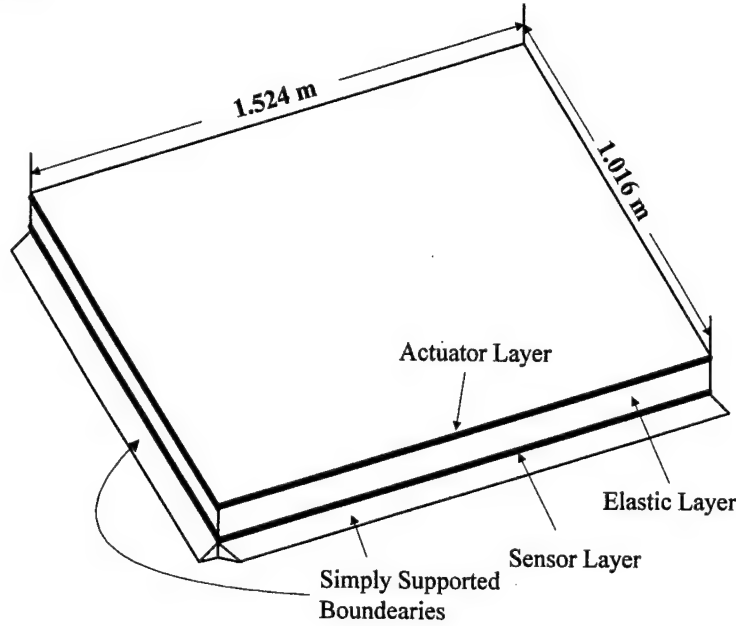


Fig.9 A simply supported rectangular plate with piezoelectric control layers.

Table 3 Geometry and material properties.

Properties:	Elastic Material	PVDF
Length L (m)	1.524	1.524
Width b (m)	1.016	1.016
Height h, h^s (m)	2.54×10^{-2}	2.5×10^{-5}
Young's modulus Y (Pa)	2.0955×10^8	2.0×10^9
Poisson's ratio μ	0.25	0.29
Mass density ρ (kg/m ³)	3.2105×10^3	1.8×10^3
Piezoelectric constant d_{31} (C/N)		2.2×10^{-11}
Electric permittivity ϵ (F/m)		1.062×10^{-10}

Dynamic Analysis

The linear transient center displacement response of the plate, based on the new FE code, is compared with published data as shown in **Figure 10**; the nonlinear transient response is investigated and compared with the linear response as shown in **Figure 11**. The nonlinear effect stiffens the structure and, thus, it reduces the oscillation magnitude and period. Note that

the difference between the linear and nonlinear responses is not significant as compared with the case provided by To and Liu (1995). This may be due to different FE formulations, stress and strain definitions, FE mesh, etc. This case is then extended to control analysis of a multi-layered piezoelectric plate presented next.

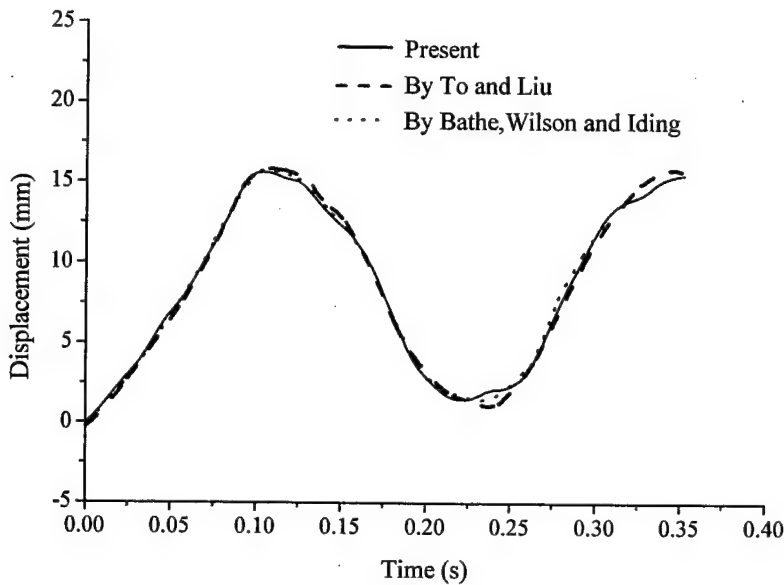


Fig.10 Linear transient center displacement responses of single layer plate.

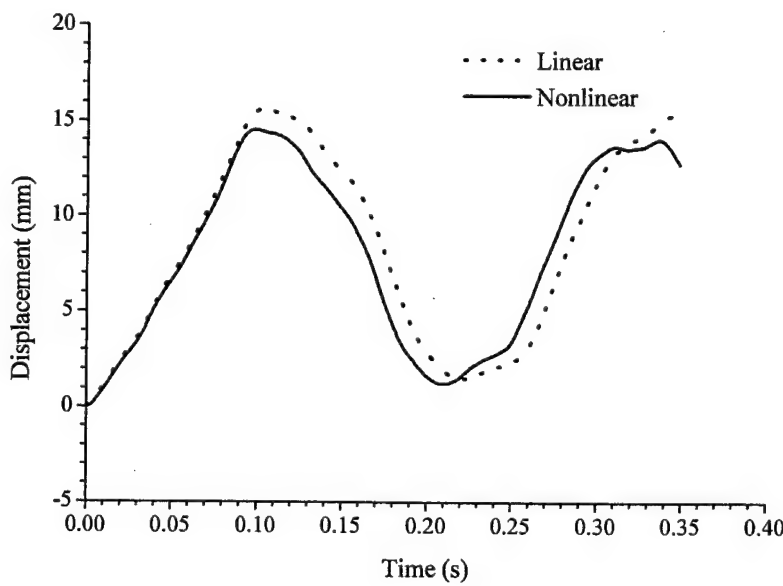


Fig.11 Linear/nonlinear transient responses of the elastic plate.

Control Analysis

Dynamic response and vibration control of the simply supported plate laminated with piezoelectric PVDF sensor and actuator layers are studied. Nonlinear transient response is compared with linear response as shown in **Figure 12**. The nonlinear effect is to decrease the vibration magnitude and period. The magnitudes and periods of linear and nonlinear responses of the piezoelastic plate are smaller than those of the single-layered elastic plate, since PVDF stiffens the structure due to its higher Young's modulus. Next, vibration signals generated on the sensor layer laminated on the bottom surface of the plate is amplified and injected to the actuator layer laminated on the top surface in the proportional feedback vibration control.

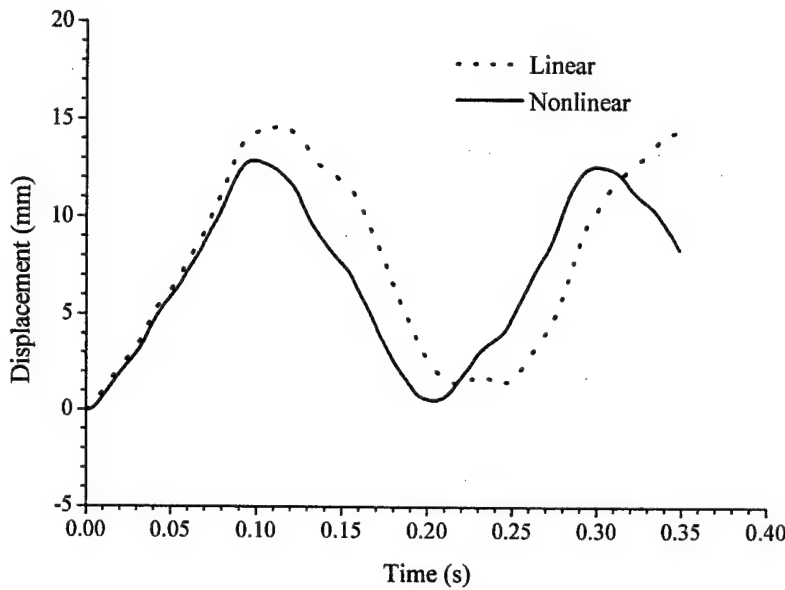


Fig.12 Linear/nonlinear transient responses of the piezoelastic plate.

In control analysis, different load levels are employed in order to investigate the control effects for different levels of geometric nonlinearity. The load levels are chosen to be 10 N, 25N, and 44.54N respectively and the negative velocity control gain is set to be 2.0. The controlled nonlinear transient responses with different loads are plotted in **Figures 13-15**. With higher loads applying on the structure, relatively higher geometric nonlinearity is introduced, and, thus, the structure becomes stiffer. Since the first frequency dominates, it increases as the applied load increased. Furthermore, since the first two frequencies come closer as the load increased, the beat phenomenon appears in the responses, **Figures 14-15**, and the beat phenomenon becomes more significant at a higher load, **Figure 15**, due to increased geometric nonlinearity.

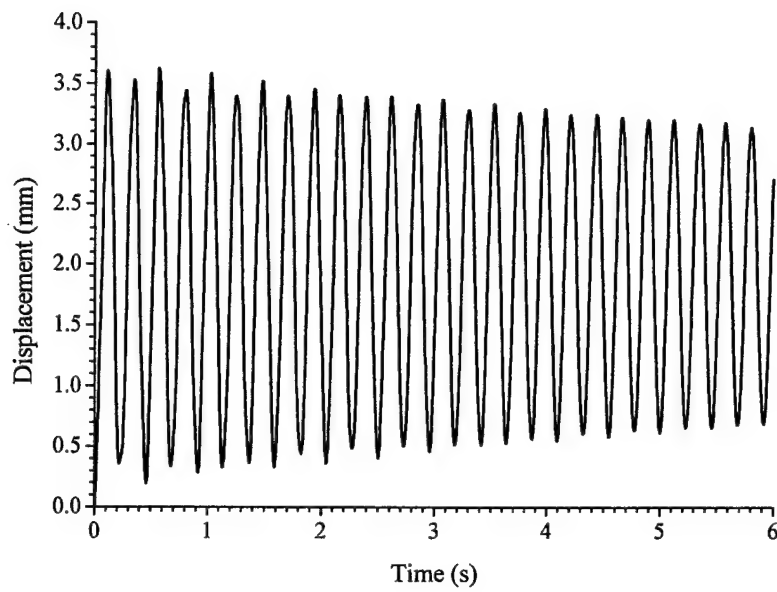


Fig.13 Nonlinear controlled transient response of piezoelastic plate (load = 10 N).

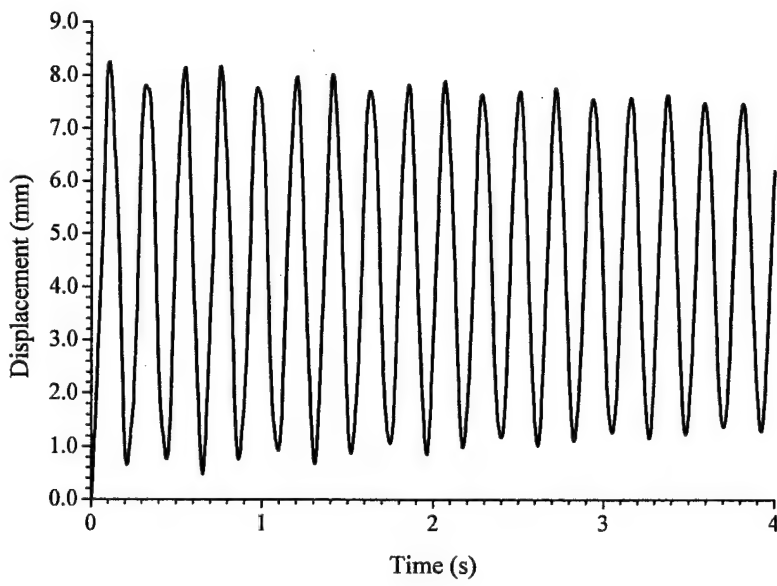


Fig.14 Nonlinear controlled transient response of piezoelastic plate (load = 25 N).

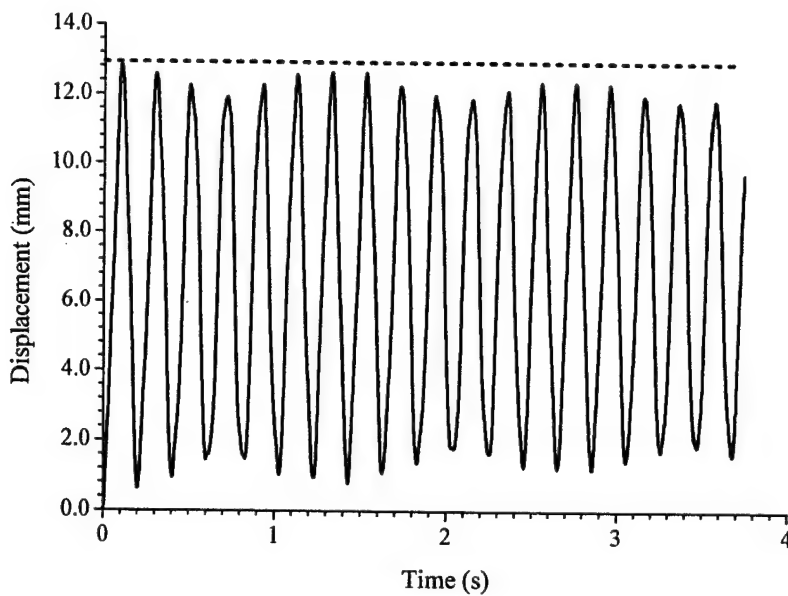


Fig.15 Nonlinear controlled transient response of piezoelastic plate (load = 44.54 N).

SUMMARY AND CONCLUSION

High-performance adaptive structures and strutronic systems capable of shape adaptation often involve large deformations beyond the boundary of linear theory, which should be classified as “geometrically nonlinear” structures. This study is to address 1) development of a new FE design tool, 2) validation of the FE tool, and 3) static, dynamic, and control analyses of nonlinear piezoelectric laminated structures – the electro/elastic strutronic systems. A new generic nonlinear FE formulation for vibration sensing and control analysis of laminated electro/elastic nonlinear shell structures was derived based on the virtual work principle, followed by formulation of a new generic curved triangular piezoelectric shell element and the dynamic system matrix equations encompassing the multi-field coupling of geometric nonlinearity, structural elasticity, mechanical inputs, electric potentials, distributed sensing, feedback control forces, control algorithms, etc. Nonlinear-dynamic analysis and control of large and complex piezoelectric/elastic/control structures was carried out using the modified Newton-Raphson method.

The newly developed piezoelectric shell element and nonlinear FE analysis/design code were validated and compared favorably with available static/dynamic solutions. Then, static and dynamic responses of nonlinear electro/elastic piezoelectric structures were analyzed and compared with the original nonlinear elastic structures. The geometrical nonlinearity induced stiffening effect clearly shows in these static and dynamic responses. Furthermore, control of flexible electro-elastic (piezoelectric/elastic) structural systems (beams and plates) subjected three levels (i.e., low, median, and high) of nonlinearity was evaluated. The control effects are significantly different for these three load cases, due to their respectively induced nonlinearity. Under the same control condition except the load level, the control effect reduces at increased load level, since the beam/plate stiffens due to the increased nonlinearity.

ACKNOWLEDGEMENT

This research is supported, in part, by a grant (F49620-98-1-0467) from the Air Force Office of Scientific Research (Project Manager: Brian Sanders) and, in part, by a NASA fellowship. These supports are gratefully acknowledged.

REFERENCES

Bathe, 1996, *Finite Element Procedures*, Prentic Hall, New Jersey.

Bathe, K.J., Ramm, E. and Wilson, E.L., 1975, "Finite Element Formulations for Large Deformation Dynamic Analysis," *Int. J. Num. Meth. Engng.*, Vol.9, pp.353-386.

Bathe, K.J., Wilson, E.L. and Iding, R.H., 1974, "NONSAP, a structural analysis program for static and dynamic response of nonlinear system", Report No. SESM 74-3, Structural Engineering Laboratory, University of California, Berkeley, CA.

Bischoff, M. and Ramm, E., 1997, "Shear Deformable Shell Elements For Large Strains And Rotations," *Int. J. Numer. Meth. Engng.*, Vol. 40, pp.4427-4449.

Blandford, G.E. and Glass, G., 1987, "Static/Dynamic Analysis of Locally Buckled Frames", *Journal of Structural Engineering*, Vol.113, pp.363-381.

Cook, R.B., Malkus, D.S. and Plesha, M.E., 1989, *Concepts and Applications of Finite Element Analysis*, 3rd Ed., John Wiley & Sons, New York, NY.

Craig, R.R. Jr., 1981, *Structural Dynamics: An Introduction to Computer Methods*, John Wiley & Sons, New York, NY.

Gabbert, U. and Tzou, H.S., Editors, 2001, *Smart Structures and Structronic Systems*, Kluwer Academic Publishers, Dordrecht/Boston/London.

Harnau, M. and Schweizerhof, K., 2002, "About Linear and Quadratic "Solid-Shell" elements at large deformations," *Comput. & Struc.*, Vol.80, pp.805-817.

Hauptmann, R. and Schweizerhof, K., 1998, "A Systematic Development of 'Solid-Shell' Element Formulations for Linear and Nonlinear Analysis Employing Only Displacement Degree of Freedom," *Int. J. Numer. Meth. Engng.*, Vol.42, pp.49-69.

Howard, R.V., Chai, W.K., Tzou, H.S., 2001, "Modal Voltages of Linear and Nonlinear Structures using Distributed Artificial Neurons (A Theoretical and Experimental Study)," *Mechanical Systems and Signal Processing (Journal of)*, Vol.15, No.3, pp.629-640.

Liu, M.L. and To, C.W.S., 1995, "Hybrid Strain Based Three Node Flat Triangular Shell Element – I. Nonlinear Theory and Incremental Formulation", *Computers & Structures*, Vol. 54, pp.1031-1056.

Simo, J. C. and Rifai, S., 1990, "A Class of Mixed Assumed Strain Methods and the Method of Incompatible Modes," *Int. J. Numer. Meth. Engng.*, Vol.29, pp.1595-1638.

Stolarski, H. and Belytschko, T., 1983, "Shear and Membrane Locking in Curved C⁰ Elements," *Computer Methods in Applied Mechanics and Engineering*, Vol.41, pp.279-296.

Surana, K.S., 1983, *FINESSE (Finite Element System for Nonlinear Analysis) Theoretical Manual*, McDonell Douglas Automation Company, St. Louis.

Sze, K.Y., and Pan, Y.S., 1999, "Hybrid Finite Element Models for piezoelectric materials," *Journal of Sound and Vibration*, Vol.226, pp.519-547.

Sze, K.Y., and Yao, L.Q., 2000, "A Hybrid Stress ANS Solid-shell Element and Its Generalization for Smart Structure Modelling. Part I – Solid-shell Element Formulation," *Int. J. Numer. Meth. Engng.*, Vol.48, pp.545-564.

To, C.W.S. and Liu, M.L., 1995, "Hybrid Strain Based Three Node Flat Triangular Shell Element – II. Numerical Investigation of Nonlinear Problems", *Computers & Structures*, Vol. 54, No. 6, pp.1057-1076.

Trindade, M.A., Benjeddou, A. and Ohayon, R., 2001, "Finite element modelling of hybrid active-passive vibration damping of multilayer piezoelectric sandwich beams- Part II: System Analysis," *International Journal for Numerical Methods in Engineering*, Vol.51, No.7, pp.855-864

Tzou, H.S., 1993, *Piezoelectric Shells: Distributed Sensing and Control of Continua*, Kluwer Academic Publishers, Boston /Dordrecht.

Tzou, H.S. and Bao, Y., 1997, "Nonlinear Piezothermoelasticity and Multi-Field Actuations, Part-1: Nonlinear Anisotropic Piezothermoelastic Shell Laminates," *ASME Transactions Journal of Vibration & Acoustics*, Vol.119, pp.374-381.

Tzou, H.S. and Fukuda, T. (Editors), 1992, *Precision Sensors, Actuators, and Systems*, Kluwer Academic Publishers, Dordrecht/Boston/London.

Tzou, H.S. and Tseng, C.I., 1990, "Distributed Piezoelectric Sensor/Actuator Design for Dynamic Measurement/Control of Distributed Parameter Systems: A Piezoelectric Finite Element Approach," *Journal of Sound & Vibration*, Vol.138, No.1, pp.17-34.

Tzou, H.S., Wang, D.W., and Chai, W.K., 2002, "Dynamics and Distributed Control of Conical Shells Laminated with Full and Diagonal Actuators," *Journal of Sound & Vibration*. (To appear)

Tzou, H.S. and Wang, D.W., 2002, "Micro-sensing Characteristics and Modal Voltages of Linear/nonlinear Toroidal Shell," *Journal of Sound and Vibration*, Paper no. NAM/30/10. (To appear).

Tzou, H.S. and Ye, R., 1994, "Piezothermoelasticity and Precision Control of Active Piezoelectric Laminates," *ASME Journal of Vibration and Acoustics*, 114, 489-495.

Tzou, H.S. and Ye, R., 1996, "Analysis of Piezoelastic Structures with Laminated Piezoelectric Triangle Shell Elements," *AIAA Journal*, 34, 110-115.

Tzou, H.S., Ye, R., and Ding, J.H., 2001, "A new X-actuator Design for Controlling Wing Bending and Twisting Modes," *Journal of Sound & Vibration* 241, 271-281.

Tzou, H.S. and Zhou, Y., 1997, "Nonlinear Piezothermoelasticity and Multi-Field Actuations, Part-2: Control of Nonlinear Buckling and Dynamics," *ASME Transactions Journal of Vibration & Acoustics*, Vol.119, pp.382-389.

Ye, R. and Tzou, H.S., 2000, "Control of Adaptive Shells with Thermal and Mechanical Excitations," *Journal of Sound & Vibration*, Vol.231(5), pp.1321-1338.

Zhou, Y.H. and Tzou, H.S., 2000, "Control of Nonlinear Piezoelectric Circular Shallow Spherical Shells," *Journal of Solids and Structures*, Vol.37, pp.1663-1677.

(NonFeDynBmPltF.ShlNon.ShlFem)

CHAPTER 19

DYNAMICS AND CONTROL OF ADAPTIVE NONLINEAR PIEZOTHERMOELASTIC STRUCTURES WITH COUPLED ELECTRIC, THERMAL AND MECHANICAL FIELDS (A Finite Element Approach)

ABSTRACT

Piezoelectric sensors and actuators are widely used in smart structures, mechatronic and strucronic systems, etc. This paper is to investigate the dynamics and control of nonlinear laminated piezothermoelastic shell structures subjected to the combined mechanical, electrical, and thermal excitations by the finite element method. Governing relations of nonlinear strain-displacement, electric field-electric potential, and temperature gradient-temperature field for a piezothermoelastic shell are presented in a curvilinear coordinate system. Based on the layerwise constant shear angle theory, generic curved triangular and hexahedral laminated piezothermoelastic shell elements are developed. Generic nonlinear finite element formulations for vibration sensing and control analysis of laminated piezoelectric shell structures are derived based on the virtual work principle. Dynamic system equations, equations of electric potential output, and feedback control force are derived and discussed. The modified Newton-Raphson method is used for efficient nonlinear dynamic analysis of complex nonlinear piezoelectric/elastic/control structural systems. For vibration sensing and control, various control algorithms are implemented. The developed nonlinear piezothermoelastic shell element and finite element code are validated and applied to analysis of nonlinear flexible strucronic systems. Vibration sensing and control of constant/non-constant curvature piezoelectric shell structures are studied. Thermal effect to static deflection, dynamic response, and control is investigated.

INTRODUCTION

Large deformation and high temperature gradients can introduce geometric nonlinearity in flexible structural systems. Shape change involving geometric nonlinearity could be desirable or unavoidable. However, nonlinearity induced by large temperature gradients can offset shape control and/or vibration control in precision structures and strucronic systems. Accordingly, an in-depth understanding of geometric nonlinearity induced by coupled mechanical and temperature loading and its active control and compensation mechanism is essential to next-generation high-performance adaptive structures and strucronic systems consisting of smart materials, control electronics, etc. A generic mathematical model of nonlinear piezothermoelastic shells was recently proposed (Tzou and Bao, 1997). Based on the

generic nonlinear piezothermoelastic theory, analytical procedures and closed-form solutions, static, dynamic, and control analysis of nonlinear plates and shallow spherical shells using piezoelectric actuators were recently investigated (Howard, et al., 2001; Tzou and Zhou, 1997; Zhou and Tzou, 2000; Tzou and Wang, 2002). Finite element (FE) development and analyses of linear piezoelectric and piezoelastic coupled electro/elastic structures were also investigated over the years (Trindade, Benjeddou, and Ohayon, 2001; Sze and Pan, 1999; Tzou and Tseng, 1990; Tzou and Ye, 1994, 1996; Ye and Tzou, 2000; Tzou, et al., 2002). In general, theoretical solutions of nonlinear piezothermoelastic structures are scarce and experiments are also difficult to conduct. This study is to develop a new design tool based on the finite element method and to evaluate coupled static, dynamic, and control responses of nonlinear piezothermoelastic structures subjected to coupled mechanical, electric, and temperature excitations. Nonlinear static, dynamic, and control responses are investigated in case studies.

PIEZOTHERMOELASTIC CONTINUUM

In this section, fundamental piezothermoelastic shell characteristics, including strain-displacement, electric field- potential and heat flux- temperature relations, are discussed, followed by linear piezothermoelastic constitutive equations.

Strains and Strain-Displacement

Consider a case that a shell configuration with volume V and boundary S changes continuously in a curvilinear coordinate system $(\alpha_1, \alpha_2, \alpha_3)$, due to external forces. The strain tensors can be defined in terms of displacements as

$${}^0S_{ij} = \frac{1}{2}({}^0U_{i,j} + {}^0U_{j,i} + {}^0U_{k,i} {}^0U_{k,j}), \quad {}^tS_{ij} = \frac{1}{2}({}^tU_{i,j} + {}^tU_{j,i} + {}^tU_{k,i} {}^tU_{k,j}), \quad i,j=1,2,3, \quad (1,2)$$

where U_i is the displacement components in α_1 , α_2 and α_3 direction; ${}^0S_{ij}$ is the Green-Lagrange strain tensor (or the Green strain tensor); ${}^tS_{ij}$ is the Almansi strain tensor. Note that the left superscript (t) denotes the body state and the left subscript (0 or t) denotes the reference state. It is noted that the Green strain tensor is objective since their components remain unchanged when the material is subjected to only the rigid body rotation. The Almansi strain tensor, on the other hand, is not objective. The choice of actual form of strain tensor depends on the problems concerned (Bathe, 1996).

Electric Field-Potential and Heat Flux-Temperature Relations

The modified relationship between the electric field and electric potential in a generic curvilinear shell coordinate system can be written as

$$E_i = -1/\sqrt{g_{ii}} \phi_{,i}, \quad (3)$$

where E_i ($i = 1, 2, 3$) and ϕ are the electric field and electric potential, respectively. Heat flux can be expressed in term of temperature rise as follows,

$$h_{di} = -\kappa_{ij}\theta_{,j} , \quad (4)$$

where h_{di} , κ_{ij} and θ denote the heat flux, heat conductivity coefficient and temperature rise from the stress free reference temperature θ_0 , respectively.

Stresses

It is known that the Cauchy stress tensor and the second Piola-Kirchhoff stress tensor are defined on deformed and undeformed configurations, respectively. The Cauchy stress represents the true state of stress, while the second Piola-Kirchhoff stress has little physical meaning. However, the second Piola-Kirchhoff stress tensor is objective since their components are invariant under a rigid body rotation of the material. In addition, it is symmetrical and thus it is suitable to establish stress-strain relations since the strain tensors are always symmetrical (Bathe, 1996).

Linear Piezothermoelastic Constitutive Equations

Several assumptions and rules on the elastic, electric and thermal fields must be followed before establish the constitutive equations for the piezothermoelastic structures. As to the elastic field, the stress and strain should be in accordance with the constitutive law used to model material behaviors. The second Piola-Kirchhoff stress tensor and the Green strain tensor are respectively for elastic and hyperelastic materials whose behaviors are determined from the total current strains, while the Jaumann stress rate tensor and the velocity strain tensor are more effective for analysis of rate form constitutive relations (Bathe, 1996). In linear piezoelectricity theory, the piezoelectric constitutive equation is based on the assumption that the electric displacement is directly proportional to the electric field. This assumption, however, is true only for homogeneous and isotropic dielectric material under a low electric field (Crawley and Lazarus, 1991). It is known that the nonlinear behavior of piezoelectric materials is significant at high electric fields and hence a model incorporating nonlinear behavior is needed to exploit the actuation capacity in the nonlinear range. Unfortunately, the nonlinear piezoelectric constitutive models are not well established (Ajit, Ang and Wang, 2001). Thus, although the temperature and large deformation induced geometric nonlinearity appears in piezothermoelastic structures, the fundamental linear constitutive equations of the piezothermoelastic shell structures are still valid, i.e.,

$$T_{ij} = c_{ijkl}S_{kl} - e_{ijm}E_m - \lambda_{ij}\theta , \quad (5)$$

$$D_n = e_{nkl}S_{kl} + \epsilon_{nm}E_m + p_n\theta , \quad (6)$$

$$\mathcal{E} = \lambda_{kl}S_{kl} + p_mE_m + \alpha_v\theta , \quad (7)$$

where T_{ij} , S_{kl} , D_n , E_m , \mathcal{E} and θ denote the stress, strain, electric displacement, electric field, entropy density and temperature rise from the stress free reference temperature θ_0 ,

respectively; c_{ijkl} , e_{ijm} , λ_{ij} , ε_{nm} , p_n , α_v denote the elastic moduli, piezoelectric coefficients, dielectric permittivity constants, pyroelectric constants, and the material constant related to thermal property, respectively.

VIRTUAL WORK EQUATIONS

It is assumed that the nonlinear piezothermoelastic laminate is exposed to an elastic field, an electric field and a thermal (temperature) field. The incremental formulations can be directly estimated based on the virtual work principle. The total Lagrange formulation is adopted in this study. The virtual work functional for the three-coupled fields in the current state ($t+\Delta t$) can be written as

$$\int_V {}^{t+\Delta t} T_{ij} \delta {}^{t+\Delta t} S_{ij} d^0 V = {}^{t+\Delta t} W_u \quad (8)$$

$$\int_V {}^{t+\Delta t} D_i \delta {}^{t+\Delta t} E_i d^0 V = {}^{t+\Delta t} W_\phi \quad (9)$$

$$\int_V \theta_0 {}^{t+\Delta t} \mathbf{E} \cdot \delta {}^{t+\Delta t} \theta d^0 V = {}^{t+\Delta t} W_\theta \quad (10)$$

where T_{ij} , S_{ij} , D_i , E_i , θ and \mathbf{E} are the same as defined previously. ${}^{t+\Delta t} W_u$, ${}^{t+\Delta t} W_\phi$ and ${}^{t+\Delta t} W_\theta$ are respectively the virtual work of external elastic force, electric force and thermal force at state $t+\Delta t$. Note that the left superscript “ $t+\Delta t$ ” denotes the current state and the left subscript “0” denotes the reference state. Unless stated otherwise, the subscript “0” is ignored in the following derivation. In nonlinear analysis, the above equations governing the current state are solved based on the previous state assumed known. The current variables can be written in incremental forms:

$${}^{t+\Delta t} T_{ij} = {}^t T_{ij} + \dot{T}_{ij}, \quad {}^{t+\Delta t} D_i = {}^t D_i + \dot{D}_i, \quad {}^{t+\Delta t} \mathbf{E} = \mathbf{E}^t + \dot{\mathbf{E}} \quad (11-13)$$

$${}^{t+\Delta t} S_{ij} = {}^t S_{ij} + \dot{S}_{ij}, \quad {}^{t+\Delta t} E_i = {}^t E_i + \dot{E}_i, \quad {}^{t+\Delta t} \theta = {}^t \theta + \dot{\theta} \quad (14-16)$$

where the left superscript “ t ” and “ $t+\Delta t$ ” denote the previous and the current states; the quantities without the left superscript represent an increment from the previous state to the current state. According to Eqs.(1) and (2), the large-deformation strains can be separated into a linear part and a nonlinear part, i.e.,

$$S_{ij} = S_{ij}^\ell + S_{ij}^n, \quad (17)$$

where S_{ij}^ℓ and S_{ij}^n ($i,j = 1,2,3$) are the linear strains and the nonlinear strains, respectively. Note that the right superscript “ ℓ ” and “ n ” denote the linear and nonlinear terms, respectively. Substituting the incremental forms and the linear and nonlinear strains, i.e., Eqs.(11)–(17), into the virtual work functional Eqs.(8)–(10) yields

$$\int_V T_{ij} \delta S_{ij} dV + \int_V {}^t T_{ij} \delta S_{ij}^n dV = {}^{t+\Delta t} W_u - \int_V {}^t T_{ij} \delta S_{ij}^\ell dV \quad (18)$$

$$\int D_i \delta E_i dV = {}^{t+\Delta t} W_\phi - \int {}^t D_i \delta E_i dV \quad (19)$$

$$\begin{aligned} & \int \theta {}^t \mathbf{E} \cdot \delta \theta dV - \int h_{di} \delta \theta_{,i} dV + \int_{S_h} h_v \theta \delta \theta dV \\ & = \int_{S_s} {}^{t+\Delta t} q_s \delta \theta dS - \int_{S_h} h_v ({}^t \theta - \theta_0 + \theta_\infty) \delta \theta dS + \int {}^t h_{di} \delta \theta_{,i} dV - \int \theta_0 {}^t \mathbf{E} \cdot \delta \theta dV \end{aligned} \quad (20)$$

To achieve computational efficiency, linearization of the above nonlinear equations is necessary. Accordingly, the relationship between the incremental stress and strain is assumed linear. In addition, high order terms are disregarded (Liu and To, 1995). Finite element formulations of nonlinear piezothermoelastic shell structures are derived based on the above virtual work functional presented next.

PIEZOTHERMOELASTIC FINITE ELEMENT FORMULATIONS

Assume that a piezothermoelastic continuum with a volume V can be divided into a number of finite elements in the curvilinear coordinate system $\alpha_1, \alpha_2, \alpha_3$. Each element, e , with nodes i, j, m , etc., and line boundary S^e occupies a volume V^e . The element coordinates, displacements, electric potentials and temperature can be written in terms of shape functions as

$${}^0 \alpha_i = \sum_{k=1}^n N_k {}^0 \alpha_i^k, \quad {}^t \alpha_i = \sum_{k=1}^n N_k {}^t \alpha_i^k, \quad {}^{t+\Delta t} \alpha_i = \sum_{k=1}^n N_k {}^{t+\Delta t} \alpha_i^k, \quad (21-23)$$

$${}^t u_i = \sum_{k=1}^n N_k {}^t U_i^k, \quad u_i = \sum_{k=1}^n N_k U_i^k, \quad (24,25)$$

$${}^t \phi = \sum_{k=1}^n N_k {}^t \Phi^k, \quad \phi = \sum_{k=1}^n N_k \Phi^k, \quad (26,27)$$

$${}^t \theta = \sum_{k=1}^n N_k {}^t \Theta^k, \quad \theta = \sum_{k=1}^n N_k \Theta^k, \quad (28,29)$$

where α_i , u_i , ($i=1,2,3$), ϕ , θ denote the curvilinear shell coordinates, displacement, electric potential, and temperature, respectively; the left superscripts “0”, “ t ”, and “ $t+\Delta t$ ” represent the state defining the quantities; U_i^k , Φ^k and Θ^k are the incremental nodal displacement, electric potential and temperature, respectively; N_k is the shape function associated with the node k ; and n is the element node number. Note that the quantities without left superscripts represent incremental quantities. If only one element is concerned, for simplification, one can write the element virtual work functional in a matrix form as

$$({}^t \mathbf{K}_{uu}^\ell + {}^t \mathbf{K}_{uu}^n) \mathbf{U} + {}^t \mathbf{K}_{u\phi}^\ell \Phi - {}^t \mathbf{K}_{u\theta}^\ell \Theta = {}^{t+\Delta t} \mathbf{F}_u - {}^t \mathbf{F}_u, \quad (30)$$

$${}^t \mathbf{K}_{\phi u}^\ell \mathbf{U} - {}^t \mathbf{K}_{\phi\phi}^\ell \Phi + {}^t \mathbf{K}_{\phi\theta}^\ell \Theta = {}^{t+\Delta t} \mathbf{F}_\phi - {}^t \mathbf{F}_\phi, \quad (31)$$

$$\theta_0 {}^t \mathbf{K}_{\theta u}^\ell \dot{\mathbf{U}} - \theta_0 {}^t \mathbf{K}_{\theta\phi}^\ell \dot{\Phi} + {}^t \mathbf{H}_{\theta\theta}^\ell \dot{\Theta} + {}^t \mathbf{K}_{\theta\theta}^\ell \Theta = {}^{t+\Delta t} \mathbf{F}_\theta - {}^t \mathbf{F}_\theta, \quad (32)$$

where \mathbf{U} , $\dot{\mathbf{U}}$ and $\ddot{\mathbf{U}}$ are the incremental nodal displacement, velocity and acceleration vectors, respectively; Φ is the incremental nodal electric potential; Θ is the incremental nodal temperature; ${}^t\mathbf{K}_{xy}^v$ (where $x & y = u, \phi, \theta$ and v denotes ℓ or n which means linear term and nonlinear term, respectively) are the stiffness matrices defined for the displacement and electric field; ${}^{t+\Delta t}\mathbf{F}_u$ is the external mechanical excitation vector; ${}^{t+\Delta t}\mathbf{F}_\phi$ is the electric excitation vector determined by control algorithms in active control applications; ${}^{t+\Delta t}\mathbf{F}_\theta$ is the heat excitation vector; ${}^t\mathbf{F}_u$, ${}^t\mathbf{F}_\phi$, ${}^t\mathbf{F}_\theta$ are the balanced mechanical, electrical and thermal load. The stiffness matrix ${}^t\mathbf{K}_{uu}^\ell$ can be rewritten as

$${}^t\mathbf{K}_{uu}^\ell = {}^t\mathbf{K}_{uu}^{\ell 0} + {}^t\mathbf{K}_{uu}^{\ell 1}, \quad (33)$$

$$\text{where } {}^t\mathbf{K}_{uu}^{\ell 0} = \int_V {}^t\mathbf{B}_u^{\ell 0 T} \mathbf{c} {}^t\mathbf{B}_u^{\ell 0} dV, \quad (34)$$

$${}^t\mathbf{K}_{uu}^{\ell 1} = \int_V {}^t\mathbf{B}_u^{\ell 0 T} \mathbf{c} {}^t\mathbf{B}_u^{\ell 1} dV + \int_V {}^t\mathbf{B}_u^{\ell 1 T} \mathbf{c} {}^t\mathbf{B}_u^{\ell 0} dV + \int_V {}^t\mathbf{B}_u^{\ell 1 T} \mathbf{c} {}^t\mathbf{B}_u^{\ell 1} dV, \quad (35)$$

and $\mathbf{B}_u^{\ell 0}$ and $\mathbf{B}_u^{\ell 1}$ are the strain shape functions associated with the linear time-independent and time-dependent strains defined in Eqs.(1,2); \mathbf{c} is the constitutive coefficient matrix. It is known that ${}^t\mathbf{K}_{uu}^{\ell 0}$ is the usual small displacement (or incremental) stiffness matrix, ${}^t\mathbf{K}_{uu}^{\ell 1}$ is the initial displacement matrix, since it is induced by the initial displacement ${}^t\mathbf{U}$. In dynamic analysis, the element damping matrix \mathbf{C}_{uu} is assumed to be proportional to the elastic stiffness and mass matrices: $\mathbf{C}_{uu} = \alpha \mathbf{M}_{uu} + \beta^0 \mathbf{K}_{uu}^\ell$, where α and β are Rayleigh's coefficients. Assembling all the element matrices, one can write the dynamic system equations in a compact matrix form:

$$\begin{bmatrix} \mathbf{M}_{uu} & 0 & 0 \\ 0 & 0 & 0 \\ 0 & 0 & 0 \end{bmatrix} \begin{Bmatrix} {}^{t+\Delta t} \ddot{\mathbf{U}} \\ {}^{t+\Delta t} \ddot{\Phi} \\ {}^{t+\Delta t} \ddot{\Theta} \end{Bmatrix} + \begin{bmatrix} \mathbf{C}_{uu} & 0 & 0 \\ 0 & 0 & 0 \\ \theta_0 {}^t\mathbf{K}_{\theta u}^\ell & -\theta_0 {}^t\mathbf{K}_{\theta \phi}^\ell & {}^t\mathbf{H}_{\theta \theta}^\ell \end{bmatrix} \begin{Bmatrix} {}^{t+\Delta t} \dot{\mathbf{U}} \\ {}^{t+\Delta t} \dot{\Phi} \\ {}^{t+\Delta t} \dot{\Theta} \end{Bmatrix} \\ + \begin{bmatrix} {}^t\mathbf{K}_{uu}^\ell + {}^t\mathbf{K}_{uu}^n & {}^t\mathbf{K}_{u\phi}^\ell & -{}^t\mathbf{K}_{u\theta}^\ell \\ {}^t\mathbf{K}_{\phi u}^\ell & -{}^t\mathbf{K}_{\phi \phi}^\ell & {}^t\mathbf{K}_{\phi \theta}^\ell \\ 0 & 0 & {}^t\mathbf{K}_{\theta \theta}^\ell \end{bmatrix} \begin{Bmatrix} \mathbf{U} \\ \Phi \\ \Theta \end{Bmatrix} = \begin{Bmatrix} {}^{t+\Delta t} \mathbf{F}_u - {}^t\mathbf{F}_u^\ell \\ {}^{t+\Delta t} \mathbf{F}_\phi - {}^t\mathbf{F}_\phi^\ell \\ {}^{t+\Delta t} \mathbf{F}_\theta - {}^t\mathbf{F}_\theta^\ell \end{Bmatrix}, \quad (36)$$

where \mathbf{M}_{uu} is the mass matrix. In high frequency oscillations, the dynamic couplings of heat transfer with the structural deflection and the electric field are relatively insignificant. Thus, the coupling terms $\theta_0 {}^t\mathbf{K}_{\theta u}^\ell {}^{t+\Delta t} \dot{\mathbf{U}}$ and $-\theta_0 {}^t\mathbf{K}_{\theta \phi}^\ell {}^{t+\Delta t} \dot{\Phi}$ can be neglected from the system equation Eq.(36) in vibration sensing and control applications (Ragulskis, 1988). In fact, these two terms only influence the heat conduction equation, therefore, elimination of these two terms only influences the heat transfer rate in the piezoelectric continuum. In a steady state temperature field, there is no error caused by the elimination. Thus, the heat conduction equation can be simplified to

$${}^t \mathbf{H}_{\theta\theta} \dot{\Theta} + {}^t \mathbf{K}_{\theta\theta} \Theta = {}^{t+\Delta t} \mathbf{F}_\theta - {}^t \mathbf{F}_\theta^\ell . \quad (37)$$

The temperature field can be determined based on to the above heat transfer equation. To solve the nonlinear system equation Eq.(36), the modified Newton-Raphson iteration scheme is adopted and the convergence of the iteration scheme follows the out-of-balance load criterion and the incremental internal energy criterion (Bathe, 1996)

CONTROL STRATEGY

Electromechanical sensing and control characteristics of piezothermoelastic continuum coupled with nonlinear structures are discussed in this section. Dynamic responses and active control of nonlinear structures are also evaluated. Assuming the “weak” coupling between the temperature and the displacement/electric field, one can rewrite the piezothermoelastic system equation Eq.(36) as

$$\begin{aligned} & \mathbf{M}_{uu} {}^{t+\Delta t} \ddot{\mathbf{U}} + \mathbf{C}_{uu} {}^{t+\Delta t} \dot{\mathbf{U}} + {}^t \hat{\mathbf{K}} \mathbf{U} \\ & = ({}^{t+\Delta t} \mathbf{F}_u - {}^t \mathbf{F}_u) + {}^t \mathbf{K}_{u\phi}^\ell {}^t \mathbf{K}_{\phi\phi}^{\ell-1} ({}^{t+\Delta t} \mathbf{F}_\phi - {}^t \mathbf{F}_\phi) + ({}^t \mathbf{K}_{u\theta}^\ell - {}^t \mathbf{K}_{u\phi}^\ell {}^t \mathbf{K}_{\phi\phi}^{\ell-1} {}^t \mathbf{K}_{\phi\theta}^\ell) \Theta , \end{aligned} \quad (38)$$

where ${}^t \hat{\mathbf{K}} = {}^t \mathbf{K}_{uu}^\ell + {}^t \mathbf{K}_{uu}^n + {}^t \mathbf{K}_{u\phi}^\ell {}^t \mathbf{K}_{\phi\phi}^{\ell-1} {}^t \mathbf{K}_{\phi u}^\ell$ and $(\bullet)^{-1}$ denotes the matrix inverse. In distributed sensing and active control, the piezothermoelastic materials embedded in or laminated with a structure can serve as either sensor or actuator. The distributed sensor output signal Φ^s and its derivative with respect to time are determined by

$$\Phi^s = {}^t \mathbf{K}_{\phi\phi}^{\ell-1} ({}^t \mathbf{K}_{\phi u}^\ell \mathbf{U} + {}^t \mathbf{K}_{\phi\theta}^\ell \Theta) , \quad \dot{\Phi}^s = {}^t \mathbf{K}_{\phi\phi}^{\ell-1} ({}^t \mathbf{K}_{\phi u}^\ell \dot{\mathbf{U}} + {}^t \mathbf{K}_{\phi\theta}^\ell \dot{\Theta}) , \quad (39,40)$$

where the superscript “s” denotes the sensing. From Eqs.(39) and (40), it is obvious that the displacement and the velocity information of a nonlinear piezothermoelastic structure are included in the time response of electric potentials. Both the electric potentials and its derivatives with respect to time are regarded as the sensor output signals. The voltage outputs resulting from distributed sensors can be amplified and fed back into the distributed actuators as feedback signals. Based on the sensing output signals in Eqs.(39) and (40), one can write the feedback forces as a function of the displacement and the velocity vectors:

$$\mathbf{F}_f^a = - {}^t \mathbf{K}_{u\phi}^\ell {}^t \mathbf{K}_{\phi\phi}^{\ell-1} \mathbf{G} \mathbf{C}_p {}^t \mathbf{K}_{\phi\phi}^{\ell-1} ({}^t \mathbf{K}_{\phi u}^\ell \mathbf{U} + {}^t \mathbf{K}_{\phi\theta}^\ell \Theta) , \quad (41)$$

$$\mathbf{F}_f^a = - {}^t \mathbf{K}_{u\phi}^\ell {}^t \mathbf{K}_{\phi\phi}^{\ell-1} \mathbf{G} \mathbf{C}_p {}^t \mathbf{K}_{\phi\phi}^{\ell-1} ({}^t \mathbf{K}_{\phi u}^\ell \dot{\mathbf{U}} + {}^t \mathbf{K}_{\phi\theta}^\ell \dot{\Theta}) . \quad (42)$$

where \mathbf{F}_f^a is the feedback force; \mathbf{G} is a gain matrix; and \mathbf{C}_p is a capacitance matrix. Note that the superscript “a” denotes actuation and the subscript “f” denotes the feedback.

It is obvious that the displacement and velocity information are included in the feedback forces in Eqs.(41) and (42), respectively. Various control algorithms based on the proposed

control strategies are implemented in the newly developed FE program. Accordingly, generic curved triangular and hexahedral laminated nonlinear piezothermoelastic shell elements using the layerwise constant shear angle theory are developed (Tzou, etc., 2002; Wang, etc., 2003). And static, dynamic and control characteristics of nonlinear piezothermoelastic shell structures with geometrical nonlinearity and exposed to coupled mechanical, electric and temperature excitations can be investigated.

CASE STUDIES

Two cases, i.e., simply supported piezothermoelastic beam and simply supported piezothermoelastic plate, are analyzed in this section.

Case 1 – Piezothermoelastic Beam

In this section, static, dynamic, and control effects of a piezothermoelastic laminated simply supported (S.S.) beam with large deflection are studied. Von Karman geometric nonlinear assumption in which stiffness in transverse direction is much flexible than the other directions is adopted (Pica, et al., 1980). It is assumed that the piezoelectric layers (PZT) are perfectly bounded on the top and bottom surfaces of the beam. Static deflection of the beam induced by the applied temperature is evaluated first. Then, dynamic and control characteristics of the nonlinear beam subject to steady-state thermal, electric and mechanical fields are investigated.

The beam is 1m long, 0.0508 m wide, and 6.35×10^{-3} m thick as shown in **Figure 1**. The beam is fully laminated with two layers of piezoceramic PZT on the top and bottom surfaces. The thickness of each PZT layer is 2.54×10^{-4} m. The material properties of the steel are: Young's modulus is 68.95 GPa; Poisson's ratio is 0.3; mass density is 7.75×10^{-3} Kg/m³; thermal expansion coefficient is 1.1×10^{-5} m/m°C. The material properties of PZT can be found in literature (Tzou and Ye, 1996). It is assumed that 100V and -100V control voltages are uniformly applied to the top and bottom piezoelectric material layers. The temperature rise is uniform along the longitudinal direction and linear variation through the thickness. Also it is assumed $\theta_b = -\theta_t = \theta$, θ_b and θ_t are the value of θ of the bottom and top of the beam, respectively. The beam is discretized by 120 uniform triangular elements along the longitudinal direction and 40 elements for each layer. Load steps are set to be 60 with uniform increments. Both out-of-balance load criterion and energy convergence tolerances are set to be 1×10^{-6} (Bathe, 1996).

Present FEM nonlinear results are compared with analytical nonlinear solutions and FEM linear solutions of the mid-point of the beam in **Table 1** (Bao, et al., 1998). Good agreement between FEM nonlinear results and the analytical solutions is observed. The difference between nonlinear and linear solutions becomes larger as temperature increases. It can be concluded that the temperature has significant effect on the static deflection of the simply supported piezothermoelastic beam. The applied temperature increases the axial force, while the latter results in the beam stiffness increasing. Therefore, the nonlinearity induced by thermal excitation is to stiffen the structure.

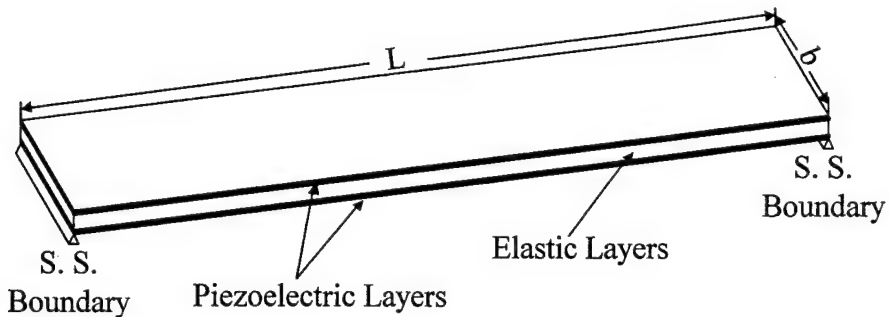


Fig.1 A simply supported beam with piezoelectric layers.

Table 1 Static deflection of the beam under temperature rise ($\phi=100V$)

θ (°C)	Analytical Solutions ^a	FEM (Nonlinear)	FEM (Linear)
10	3.018	3.119	3.363
20	4.110	4.166	6.725
30	4.810	4.781	10.088
40	5.329	5.210	13.451
50	5.743	5.534	16.813
60	6.081	5.800	20.176

^a Bao, et al., 1998.

In the dynamic and control analysis, only thermal loads are considered and the same temperature distribution as that in the static analysis is used. Two cases are studied, i.e., surface temperature $\theta = 10^\circ\text{C}$ and $\theta = 60^\circ\text{C}$ are used to generate minor and significant nonlinearity. The structure is assumed to be undamped. Time step is set to be 5×10^{-3} second. **Figure 2 and 3** show the midpoint linear and nonlinear transient responses of the simply supported piezothermoelastic beam subjected to different temperature distribution ($\theta = 10^\circ\text{C}$ and $\theta = 60^\circ\text{C}$). The linear transient response is verified by the fact that the maximum dynamic displacement (midpoint in this case) is twice the static deflection for a simply supported beam (see **Table 1**) and the frequency is close to the frequency of single-layered steel beam which is 8.593 Hz. The nonlinear effect induced by the imposed temperature field is to decrease the amplitude and period of the center deflection in the transient responses. Further note that the amplitude and period of the nonlinear transient responses in high temperature case ($\theta = 60^\circ\text{C}$) are more significantly decreased than those in low temperature case ($\theta = 10^\circ\text{C}$) since more significant nonlinearity is induced by the higher temperature distribution.

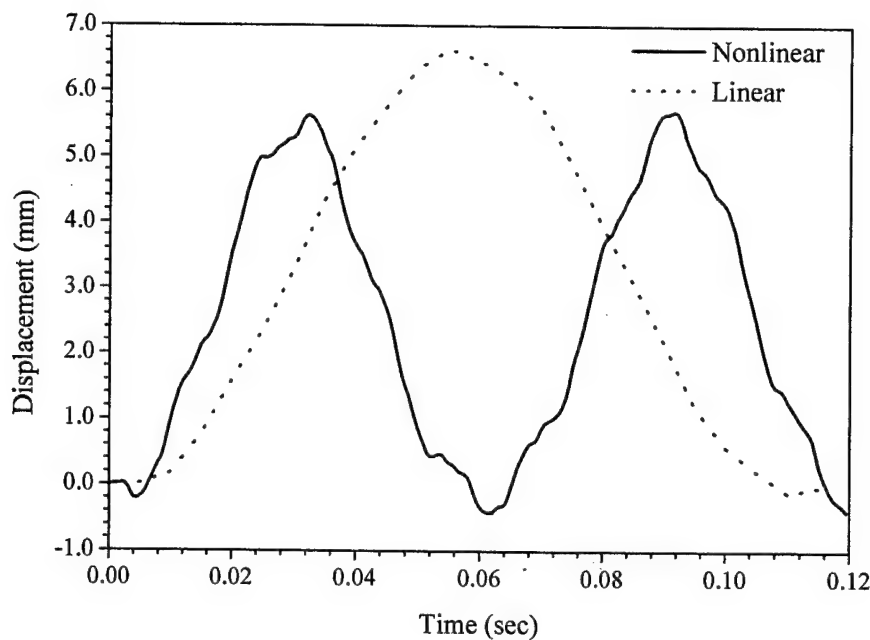


Fig.2 Linear and nonlinear transient responses of midpoint ($\theta = 10^\circ\text{C}$).

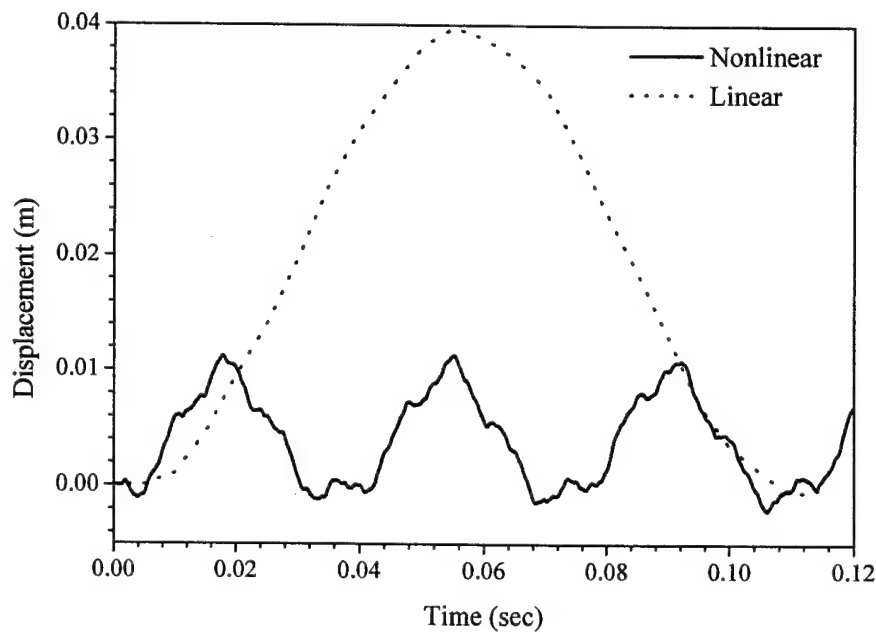


Fig.3 Linear and nonlinear transient responses of midpoint ($\theta = 60^\circ\text{C}$).

Two cases are studied in this section to investigate the control effect to electromechanically induced excitation and thermally induced excitation. In the first case, a uniform surface step load with a magnitude of 300N/m^2 is applied on the top surface of the beam. Meanwhile, a step temperature excitation of 10°C (i.e., $\theta = 10^\circ\text{C}$ and $\theta_b = -\theta_t = \theta$) is imposed on the laminated beam following the same manner as discussed in previous static and dynamic analyses. Again the structure is assumed undamped and a negative velocity proportional control scheme is employed. **Figure 4** illustrates the midpoint nonlinear controlled transient response. Although conventional feedback control schemes are effective to dynamically induced oscillations (Tzou and Ye, 1996), the conventional negative velocity proportional control is not effective to thermal induced oscillation in this case, because there is a steady-state thermal field and the time derivative of the temperature is zero.

The second case involves two loading conditions: A and B. To assure a convergent oscillation within a reasonable time, a 4% initial structural damping is imposed to the nonlinear piezothermoelastic beam in this case. Since the elastic oscillation can converge to its static equilibrium position quickly, temperature, control, and nonlinear behaviors can be better observed. A uniform surface step-load with magnitude of 75N/m^2 is applied to the top surface of the beam. For load condition A, there is only mechanical load employed, i.e., there is no thermal excitation. However, for load condition B, in addition to the mechanical load, a temperature excitation of 10°C (i.e., $\theta = 10^\circ\text{C}$ and $\theta_b = -\theta_t = \theta$) is also applied to the beam simultaneously. Note that the temperature distribution is the same as discussed previously. **Figure 5** shows the midpoint controlled nonlinear responses of the beam, in which the top time history denotes the load condition B (combined mechanical and temperature inputs) and the bottom time-history denotes the load condition A (with mechanical input only). The distributed mechanical loading induces low level of geometric nonlinearity and the beam oscillates at a frequency slightly higher than the linear frequency, as compared with the linear oscillation discussed previously. However, the combined mechanical and temperature loading induces much large nonlinearity and accordingly, the beam oscillates at a high frequency with respect to the steady-state equilibrium position induced by the combined large mechanical and temperature loading. (Note that the temperature difference induces a much higher level of nonlinearity, due to the stiffening effect, and thus the oscillation frequency.) The transient response converges to the equilibrium position, i.e., an offset from the original zero static equilibrium position temperature induced, since the conventional feedback control is not effective to the step-temperature load as previously discussed. The two transient responses converge to the static equilibrium positions respectively induced by the mechanical loading and the combined mechanical and temperature loading. An offset is observed between these two equilibrium positions and it is induced by the temperature loading.

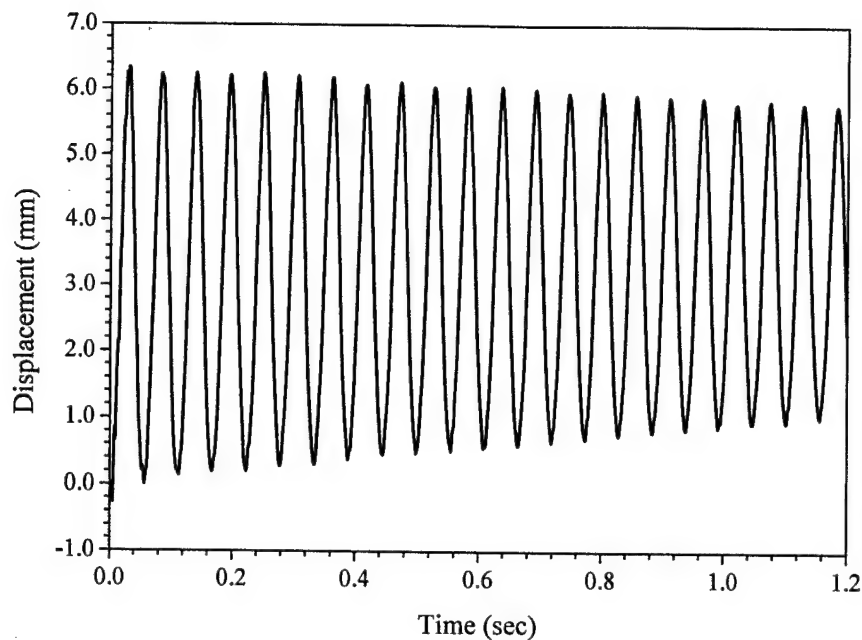


Fig.4 Midpoint nonlinear controlled transient response (gain=30).

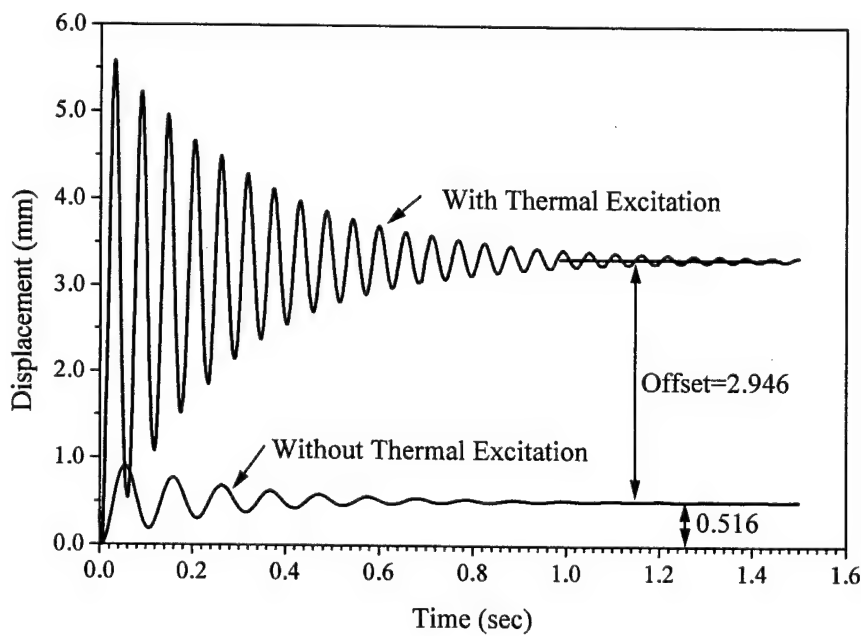


Fig.5 Midpoint nonlinear controlled transient responses (gain=30).

Accordingly, to achieve control of both mechanical and temperature induced excitations, two control voltages are required. One is used to control dynamically induced oscillation and the other is used to control thermally induced static deflection. **Figure 6** illustrates control of the thermally induced static offset at the beam midpoint, via applying static control voltages to distributed piezoelectric control layers. The midpoint deflection is effectively controlled. Note that only one surface laminated PZT actuator on the top surface is used to control the thermally induced deflection.

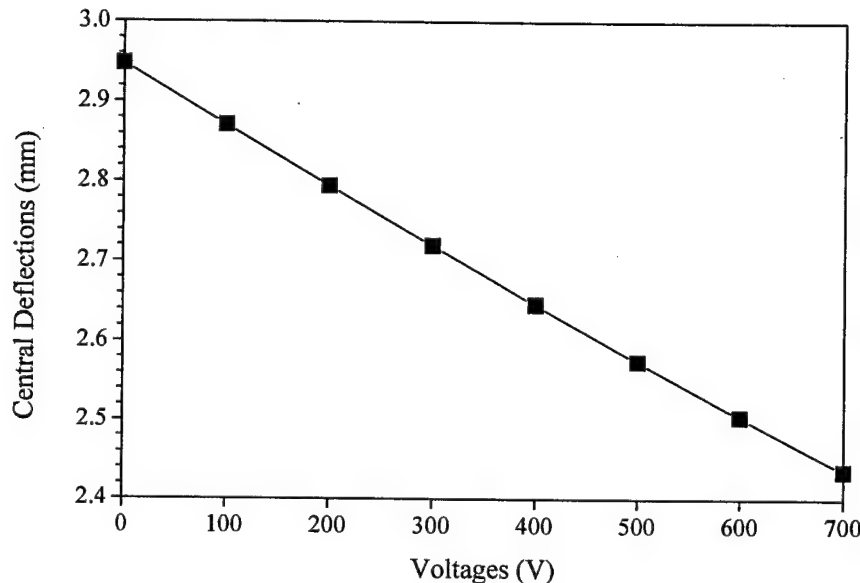


Fig.6 Static control of thermal induced deflections using the PZT actuator on the top surface.

Case 2 – Piezothermoelastic Plate

A simply supported metal matrix based laminated square plate is study in the second case. This case was studied previously by Tenneti and Chandrashekara (1994). The plate is made of two layers of P55/6051 graphite/aluminum [0°/90°]. The geometry and material properties are provided in **Table 2**. Temperature change is assumed to have the following distribution: $\theta = \theta_1 + (\alpha_3/h) \cdot \theta_2$. Note that θ_1 and θ_2 are 250 °C and 500 °C, respectively; α_3 is the transverse coordinate. The plate is fully idealized into 4 by 4 mesh. Note that each mesh contains 2 triangular elements when triangular elements are used. A time step is set to be 4×10^{-5} second for both linear and nonlinear analysis. Note that the computational parameters are kept consistent with those in the previous study. Linear and nonlinear transient responses, which obtained from the triangular (TRI) and hexahedral (HEX) elements, are plotted in **Figure 7** along with the linear response in previous study (Tenneti and Chandrashekara, 1994). The present linear response obtained from the hexahedral elements is compared favorably with the published results using nine node isoparametric elements, while the triangular elements give the linear response with a little bit smaller magnitude. The nonlinear responses have decreased period and magnitude as compared with the linear responses since the geometrical nonlinearity

induced by the temperature excitation stiffens the plate. Further note that the triangular elements smoothen both linear and nonlinear transient responses somehow. One may also note that the magnitude of positive peak of the current nonlinear response is comparable with that provided by Tenneti, however, the magnitude of negative peak is smaller than that obtained by Tenneti. It may due to different elements, stress and strain measurement, etc.

Table 2 Geometry and material properties of the cross-ply plate.^a

Property	Symbol	Unit	Value
Length	L	m	0.254
Thickness	h	m	5.08×10^{-3}
Young's modulus	Y_1	Pa	1.9×10^{11}
Young's modulus	Y_2	Pa	4.83×10^{10}
Shear modulus	G_{12}	Pa	1.73×10^{10}
Shear modulus	G_{13}	Pa	1.73×10^{10}
Shear modulus	G_{23}	Pa	1.65×10^{10}
Mass density	ρ	Kg/m ³	2.4×10^3
Poisson's ratio	μ		0.28
Thermal expansion coefficient	α_{v1}	m/m/°C	3.34×10^{-6}
Thermal expansion coefficient	α_{v2}	m/m/°C	2.61×10^{-5}

^a data from Tenneti and Chandrashekara, 1994.

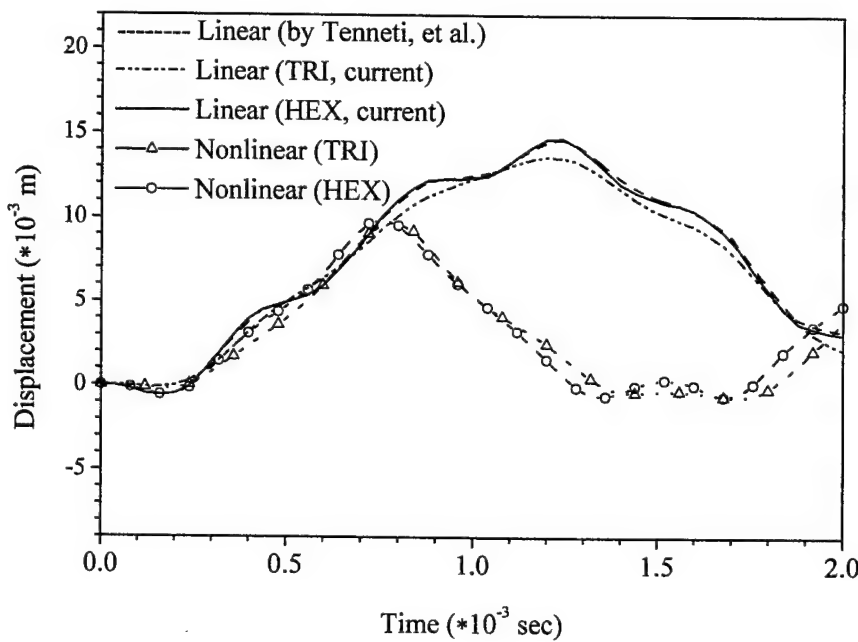


Fig.7 Linear and nonlinear responses of the [0°/90°] cross-ply plate.

The forgoing case is extended to the control analysis of a piezothermoelastic plate then. The aforementioned plate is laminated with two layers of PZT on the top and bottom surfaces

serving respectively as sensor and actuator. The material properties of PZT are the same as in **Case 1**. The thickness of each PZT layer is 2.54×10^{-4} m. The piezothermoelastic plate have the same temperature change distribution as before, i.e., $\theta = \theta_1 + (\alpha_3/h) \cdot \theta_2$. Again, h is the thickness; α_3 is the transverse coordinate; θ_1 and θ_2 are taken as 250 °C and 500 °C, respectively. The negative velocity control is employed in the control analysis. The uncontrolled response of this piezothermoelastic plate is shown in **Figure 8**. The controlled response is plotted in **Figure 9**. It is observed that the controlled response gives the same results as the uncontrolled response as shown in **Figure 8**. The reason is that since the steady-state temperature field is considered, the derivative of voltage induced by temperature with respect to time is zero. Thus the voltage induced by the steady-state temperature field has no effect on the negative velocity control. However, **Figure 9** shows that the temperature gradient offsets the equilibrium position from zero (initial equilibrium position) to around 5 mm (new equilibrium position). Note that this equilibrium position offset is not desired and should be controlled. **Figure 10** shows the central equilibrium position variations induced by the external voltages applied on the PZT actuation layer. It should be pointed out that the deflection variation implies the amount by which the equilibrium position decreases. For example, when the central deflection variation is 0.0, it corresponds to the initial equilibrium position; when the central deflection variation becomes -1.0×10^{-4} m, the equilibrium is decreased by -1.0×10^{-4} m. Also note that only one PZT actuator layer on the bottom surface is used to control the equilibrium position offset.

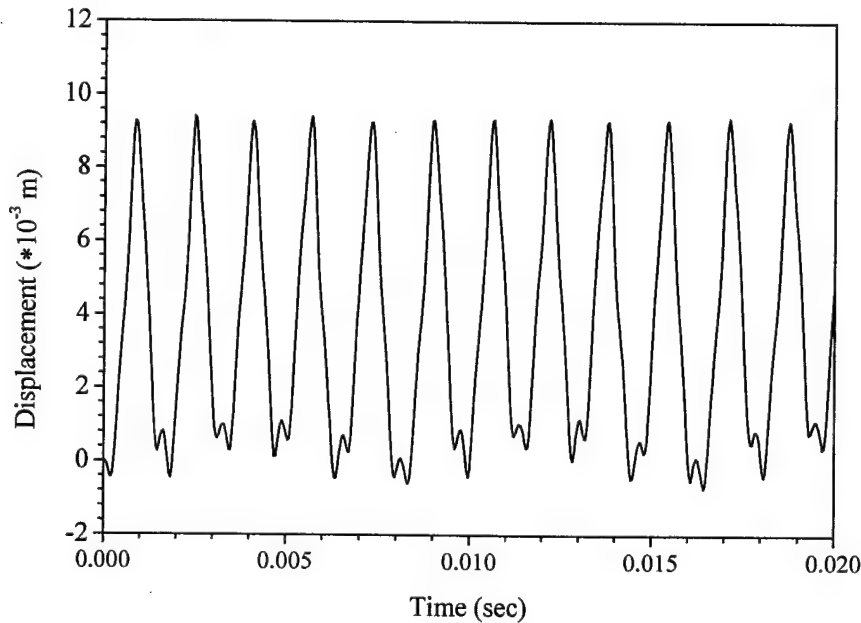


Fig.8 Uncontrolled response of the nonlinear piezothermoelastic plate.

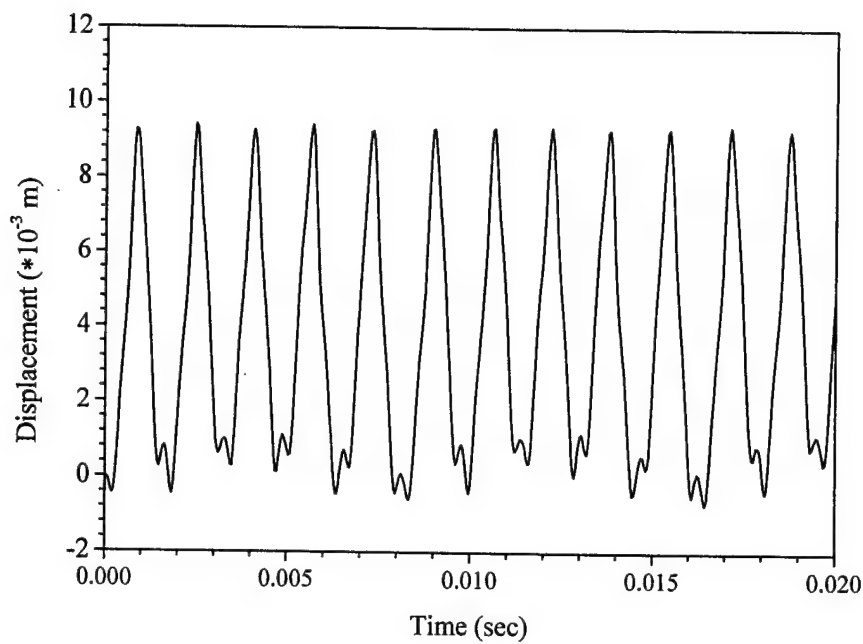


Fig.9 Controlled response of the nonlinear piezothermoelastic plate using negative velocity control scheme.

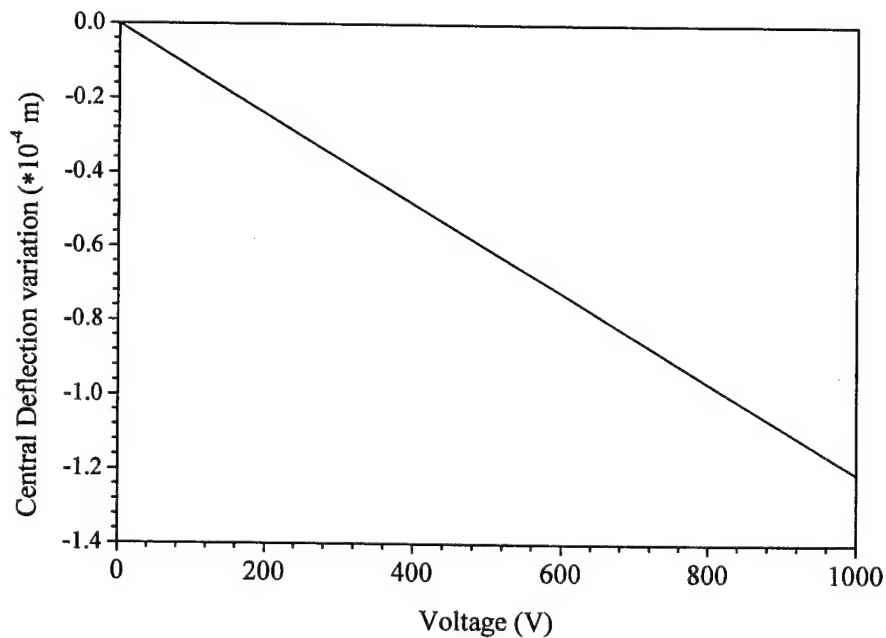


Fig.10 Central deflection variation with respect to the equilibrium position of the piezothermoelastic plate induced by the applied voltages.

The vibration control of the foregoing piezothermoelastic plate subject to another kind of temperature field is investigated in the following section. It is assumed that only the bottom and the top surfaces have the temperature distribution of $-750\text{ }^{\circ}\text{C}$ and $750\text{ }^{\circ}\text{C}$, respectively. The temperature distribution is then suddenly removed from these two surfaces. It is expected that the plate will oscillate with the initial displacements induced by the surface temperature and then converge to the original equilibrium position. Note that the temperature distribution in the earlier study is applied to the whole body of the plate, i.e., $\theta = \theta_1 + (\alpha_3/h) \cdot \theta_2$. All parameters used in the previous study keep valid in the computation in this section. In the control analysis, the negative velocity control is still employed. Note that the sensing signals generated from the sensors are averaged with respect to the sensor area and then feedback to the actuators to conduct the vibration control of the piezothermoelastic plate. The uncontrolled nonlinear response is plotted in **Figure 11**. **Figure 12** and **13** show the controlled nonlinear responses with different gains. Note that the geometric nonlinearity of the piezothermoelastic plate induced by the current temperature field is relatively weak. The control effectiveness is significant as shown in the responses of the piezothermoelastic plate.

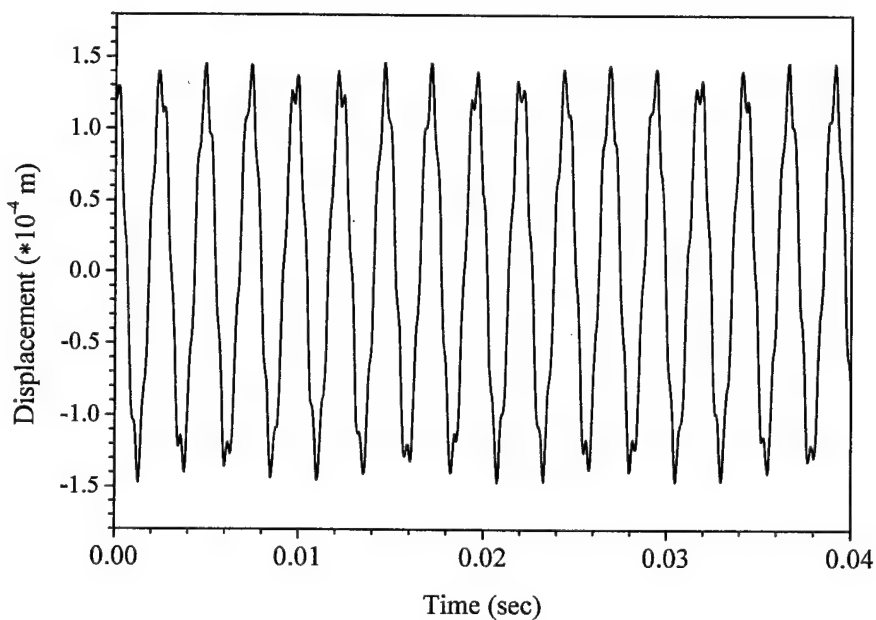


Fig.11 Uncontrolled response of the nonlinear piezothermoelastic plate.

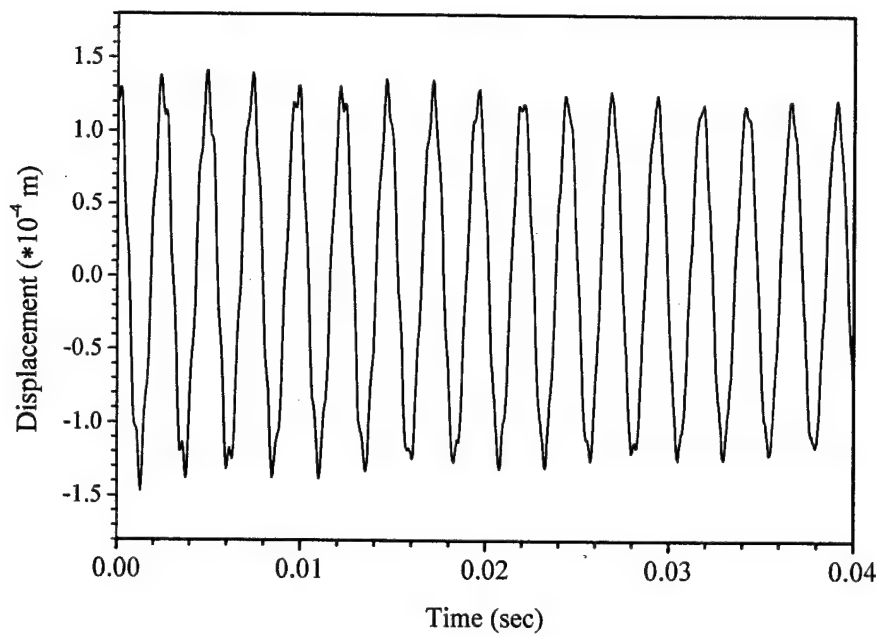


Fig.12 Controlled response of the nonlinear piezothermoelastic plate (gain=5).

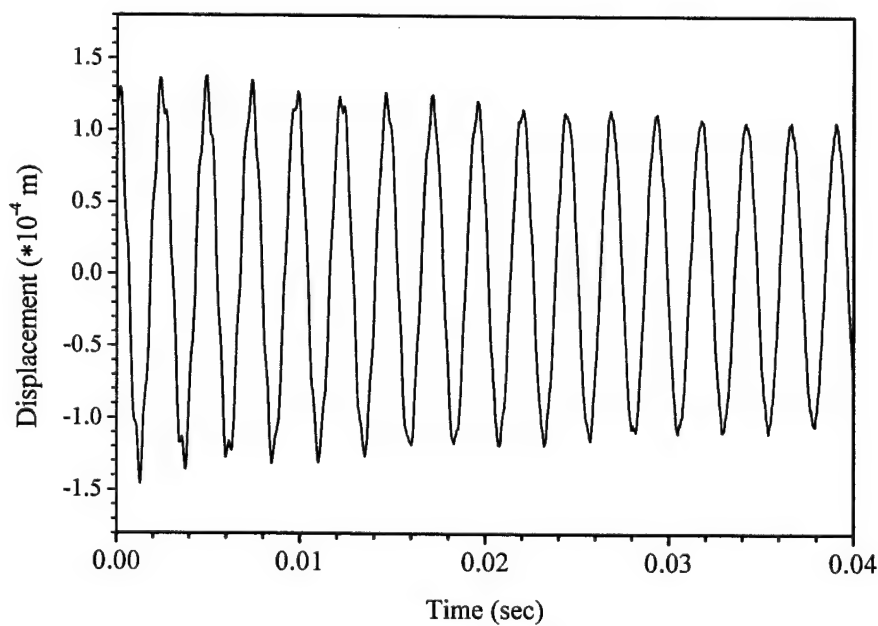


Fig.13 Controlled response of the nonlinear piezothermoelastic plate (gain=10).

SUMMARY AND CONCLUSION

Large deformation and high temperature gradients can introduce geometric nonlinearity in new adaptive structures and strucronic systems. This study is to develop a new design tool based on the finite element method and to evaluate coupled static, dynamic, and control responses of nonlinear piezothermoelastic structures subjected to coupled mechanical, electric, and temperature excitations. Fundamental strain-displacement, electric field relations, as well as piezothermoelastic constitutive equations and virtual work functional were defined. Formulation of a new nonlinear piezothermoelastic shell element was discussed and governing thermoelectromechanical/control system equations derived. Nonlinear dynamic analysis and control of large and complex piezoelectric/elastic/control structures was carried out based on the modified Newton-Raphson iteration scheme. The convergence of the iteration scheme followed the out-of-balance load criterion and the incremental internal energy criterion.

To validate the newly developed nonlinear FE analysis code, case studies were carried out. Nonlinear static deformations of a simply supported beam induced by various temperature gradients were compared very well with the closed-form analytical solutions. Static and dynamic responses of nonlinear piezothermoelastic structures subjected to coupled mechanical, electrical and thermal excitation were also compared with published data. Control of nonlinear beams with various level of geometric nonlinearity induced by mechanical, thermal, and electric (control) loads was investigated. Comparing the nonlinear response with the linear response reveals that the temperature induced geometric nonlinearity stiffens the structure and thus reduces the deflection or increases the oscillation frequency. Conventional negative velocity proportional control scheme is effective to dynamically induced oscillations. However, it is not effective to the steady-state thermal field imposed on the structure, since the thermal load introduced a static offset. Accordingly, an additional static control voltage must be employed in order to control the thermally induced offset.

ACKNOWLEDGEMENT

This research is supported, in part, by a grant (F49620-98-1-0467) from the Air Force Office of Scientific Research (Project Manager: Brian Sanders). This support is gratefully acknowledged.

REFERENCES

Ajit, A., Ang, K.K. and Wang, C.M., 2001, "Shape Control of Coupled Nonlinear Piezoelectric Beams," *Smart Mater. Struct.*, Vol.10, pp.914-924.

Bao, Y., Tzou, H.S. and Venkayya, V.B., 1998, "Analysis of Non-linear Piezothermoelastic Laminated Beams with Electric and Temperature Effects," *Journal of Sound & Vibration*, Vol.209, pp.505-518.

Bathe, 1996, *Finite Element Procedures*, Prentice Hall, New Jersey.

Crawley, E.F. and Lazarus, K.B., 1991, "Induced Strain Actuation of Isotropic and Anisotropic Plates," *AIAA Journal*, Vol.29, pp.944-951.

Howard, R.V., Chai, W.K., Tzou, H.S., 2001, "Modal Voltages of Linear and Nonlinear Structures using Distributed Artificial Neurons (A Theoretical and Experimental Study)," *Mechanical Systems and Signal Processing (Journal of)*, Vol.15, pp.629-640.

Pica, A., Wood, R.D. and Hinton, E., 1980, "Finite Element Analysis of Geometrically Nonlinear Plate Behavior Using a Mindlin Formulation," *Compu. & Struct.*, Vol.11, pp.203-215.

Ragulskis, K., 1988, *Vibration for Precision Microrobots*, Hemisphere Pub. Co., New York.

Sze, K.Y., and Pan, Y.S., 1999, "Hybrid Finite Element Models for piezoelectric materials," *Journal of Sound and Vibration*, Vol.226, pp.519-547.

Tenneti, R. and Chandrashekara, K., 1994, "Nonlinear Thermal Dynamic Analysis of Graphite/Aluminum Composite Plates," *AIAA*, Vol.32, pp.1931-1933.

Trindade, M.A., Benjeddou, A. and Ohayon, R., 2001, "Finite Element Modelling of Hybrid Active-Passive Vibration Damping of Multilayer Piezoelectric Sandwich Beams- Part II: System Analysis," *Int. J. Numer. Meth. Engng*, Vol.51, pp.855-864.

Tzou, H.S. and Bao, Y., 1997, "Nonlinear Piezothermoelasticity and Multi-Field Actuations, Part-1: Nonlinear Anisotropic Piezothermoelastic Shell Laminates," *ASME Transactions, Journal of Vibration and Acoustics*, Vol.119, pp.374-381.

Tzou, H.S. and Tseng, C.I., 1990, "Distributed Piezoelectric Sensor/Actuator Design for Dynamic Measurement/Control of Distributed Parameter Systems: A Piezoelectric Finite Element Approach," *Journal of Sound & Vibration*, Vol.138, pp.17-34.

Tzou, H.S., Wang, D.W., and Chai, W.K., 2002, "Dynamics and Distributed Control of Conical Shells Laminated with Full and Diagonal Actuators," *Journal of Sound & Vibration*. (To appear)

Tzou, H.S. and Ye, R., 1994, "Piezothermoelasticity and Precision Control of Active Piezoelectric Laminates," *ASME Journal of Vibration and Acoustics*, Vol.114, pp.489-495.

Tzou, H.S. and Ye, R., 1996, "Analysis of Piezoelastic Structures with Laminated Piezoelectric Triangle Shell Elements," *AIAA Journal*, Vol.34, pp.110-115.

Tzou, H.S. and Zhou, Y., 1997, "Nonlinear Piezothermoelasticity and Multi-Field Actuations, Part-2: Control of Nonlinear Buckling and Dynamics," *ASME Transactions Journal of Vibration & Acoustics*, Vol.119, pp.382-389.

Wang, D.W., Tzou, H.S., Arnold, S.M. and Lee, H.J., 2003, "Dynamics and Active Control of Largely Deflected Active Structures Using the Finite Element Technique" *2003 ASME International Mechanical Engineering Congress and Exposition*, Paper No. IMECE2003-42390, Washington, D.C., Nov. 16-21.

Ye, R. and Tzou, H.S., 2000, "Control Of Adaptive Shells With Thermal And Mechanical Excitations," *Journal of Sound and Vibration*, Vol.231, pp.1321-1338.

Zhou, Y.H. and Tzou, H.S., 2000, "Control of Nonlinear Piezoelectric Circular Shallow Spherical Shells," *Journal of Solids and Structures*, Vol.37, pp.1663-1677.
(PzTmElsNonFe3.PzThml.ShlFem)

APPENDIX

PERSONNEL INVOLVED

1. Faculty or Research Scientist: H. S. Tzou (Department of Mechanical Engineering); G. E. Blandford (Department of Civil Engineering), and V. B. Venkayya (Flight Dynamics Directorate, Wright Laboratory, WPAFB); Y. Shimamura (Visiting Professor, Department of Mechano-Aerospace Engineering, Tokyo Institute of Technology)
2. Graduate Students: John W. Moore (Ph.D., Civil Engineering); Jiahong Ding (Ph.D., Mechanical Engineering; Dongwei Wang, Ph.D., Mechanical Engineering); Richard M. Howard (M.S., Mechanical Engineering); P. Smithmaitre (Ph.D., Mechanical Engineering)
3. Undergraduate Students: Greg J. DeHaven (Mechanical Engineering) (Continue to Ph.D. in Mechanical Engineering); Jason Cullens; Brandon Crane; Chris Reeves; Shawn Stigall; Bryan Mueller; Scott Munich; Tara Conn; Brandon Delis

KEY PUBLICATIONS

Book

- *Smart Structures and Structronic Systems*, Book, 384 pages, IUTAM Symposium on Smart Structures and Structronic Systems, (ISBN 0-7923-6968-8), U. Gabbert and H.S. Tzou, Editors, Kluwer Academic Publishers, Dordrecht/Boston/London, May 2001.

Edited Volume

- *Control of Vibration and Noise – New Millennium*, Proceedings of the 6th Biennial Symposium on Control of Vibration and Noise, edited by H.S. Tzou, M.F. Golnaraghi, and C.J. Radcliffe, AD-Vol.61, 2000 International Mechanical Engineering Congress and Exposition, Orlando, Florida, November 5-10, 2000. Sponsored by The Aerospace Division, The Applied Mechanics Division, The Design Engineering Division, The Dynamic Systems and Control Division.

Book Chapter

- “Electronic Circuit Modeling and Analysis of Distributed Structronic Systems,” H.S. Tzou and J.H. Ding, *Smart Structures and Structronic Systems*, IUTAM Symposium on Smart Structures and Structronic Systems, (ISBN 0-7923-6968-8), U. Gabbert and H.S.

Tzou, Editors, pp.291-298, Kluwer Academic Publishers, Dordrecht/Boston/London, May 2001.

Journal Publications

1. "Nonlinear Piezo-thermoelastic Shell Theory applied to Control of Variable-geometry Shells," H.S. Tzou and R.J. Yang, *Journal of Theoretical and Applied Mechanics*, No.3, Vol.38, pp.623-644, 2000.
2. "A New X-Actuator Design For Controlling Wing Bending And Twisting Modes," H. S. Tzou, R. Ye, and J. H. Ding, *Journal of Sound & Vibration*, 241(2), pp.271-281, March 2001.
3. "Modal Voltages of Linear and Nonlinear Structures using Distributed Artificial Neurons (A Theoretical and Experimental Study)," R.V. Howard, W.K. Chai, and H. S. Tzou, *Mechanical Systems and Signal Processing (Journal of)*, Vol.15, No.3, pp.629-640, 2001.
4. "Piezoelectric Materials and Continua," H.S. Tzou and M.C. Natori, *Encyclopedia of Vibration*, pp.1011-1018, Academic Press, London, UK, 2001.
5. "Precision Shape Control of Nonlinear Shells and Plates," H.S. Tzou, Y. Bao, and C.S. Chou, *Journal of Wave-Material Interaction*, Vol.14, No.3, pp.103-117, July, 1999.
6. "Sensors and Actuators," H.S. Tzou and C.S. Chou, *Encyclopedia of Vibration*, pp.1134-1144, Academic Press, London, UK, 2001.
7. "Shape Memory Alloys," H.S. Tzou and A. Baz, *Encyclopedia of Vibration*, pp.1144-1152, Academic Press, London, UK, 2001.
8. "Dynamics and Distributed Control of Conical Shells Laminated with Full and Diagonal Actuators," H.S. Tzou, D.W. Wang, and W.K. Chai, *Journal of Sound & Vibration*, Volume 256(1), Sept. 2002, pp.65-79.
9. "Sensor Electromechanics and Distributed Signal Analysis of Piezo(Electric)-Elastic Spherical Shells," H.S. Tzou, P. Smithmaitrie, and Ding, J.H., *Mechanical Systems and Signal Processing (Journal of)*, Vol.16(2-3), pp.185-199, 2002.
10. "Micro-sensing Characteristics and Modal Voltages of Piezoelectric Laminated Linear and Nonlinear Toroidal Shells," H.S. Tzou and D.W. Wang, *Journal of Sound & Vibration* Vol.254(2), pp.203-218, 2002.
11. "Electric Circuit Design and Testing of Integrated Distributed Structronic Systems," H.S. Tzou, J.H. Ding, and P. Smithmaitrie, *Journal of Sound & Vibration*. 257(5), 7, pp.931-943, November 2002.
12. "Micro-control Actions of Distributed Actuators Laminated on Deep Paraboloidal Shells," H.S. Tzou, J.H. Ding, and I. Hagiwara, *JSME International Journal*, a special issue on Dynamics and Design of Continuous Systems, Series C, Vol.45, No1, pp.8-15, 2002.
13. "Distributed Modal Voltages of Paraboloidal Shells," H.S. Tzou and J.H. Ding, *ASME Transactions, Journal of Vibration & Acoustics*. (To appear)
14. "Modal Voltages and Micro-Signal Analysis of Conical Shells of Revolution," H.S. Tzou, W.K. Chai, and D.W. Wang, *Journal of Sound & Vibration*, Vol.260, No.4, pp.589-609, 2003.
15. "Actuator Placement and Control Efficiency of Adaptive Paraboloidal Shells," H.S. Tzou and J.H. Ding, *ASME Transactions, Journal of Dynamic Systems, Measurement, and Control*. (M01-103) (to appear)

16. "Vibration Control of Toroidal Shells with Parallel and Diagonal Piezoelectric Actuators," H.S. Tzou, D.W. Wang, *ASME Transactions, Journal of Pressure Vessel Technology*, Vol.125, pp.171-176, May 2003.
17. "Micro-Electromechanics of Sensor Patches on Free Paraboloidal Shell Structronic Systems," J.H. Ding and H.S. Tzou, *Mechanical Systems and Signal Processing (Journal of)*, Vol.18, pp.367-380, 2004.
18. "Distributed Microscopic Signals and Modal Potentials of Nonlinear Conical Shells," W. K. Chai, P. Smithmaitrie, and H. S. Tzou, Paper submitted *Mechanical Systems and Signal Processing (Journal of)*.
19. "Optimal Feedback Control of Precision Paraboloidal Shell Structronic Systems," H.S. Tzou and J. H. Ding, *Journal of Sound & Vibration*. (To appear)
20. "Micro-control Actions of Actuator Patches Laminated on Hemispheric Shells," P. Smithmaitrie and H.S. Tzou, *Journal of Sound & Vibration*. (To appear)
21. "Control of Nonlinear Electro/Elastic Beam and Plate Systems (Finite Element Formulation and Analysis)," D.W. Wang and H.S. Tzou, Paper submitted to *ASME Transactions, Journal of Vibration & Acoustics*.
22. "Micro-Control Actions and Location Sensitivity of Actuator Patches Laminated on Toroidal Shells," H.S. Tzou, W.K. Chai, and D.W. Wang, *ASME Transactions, Journal of Vibration & Acoustics*. (To appear)

Conference Publications

1. "Simultaneous Bending and Torsion Control of Wing Panels with Diagonal X-Actuators," R. Ye and H. S. Tzou, *Vibration and Noise Control*, DE-Vol.97/DSC-Vol.65, pp.107-112, *Symposium on Active Control of Vibration and Noise*, 1998 ASME International Mechanical Engineering Congress, Anaheim, CA, Nov.15-22, 1998.
2. "Nonlinear Shape Control of Shells and Plates," H.S. Tzou, Y. Bao, and C.S. Chou, *Symposium on Structronics, Mechatronics, and Smart Materials*, Proceedings, Paper No.8387, ASME Design Technical Conferences, Las Vegas, NV, September 12-15, 1999.
3. "Modal Voltages of Linear and Nonlinear Structures using Distributed Artificial Neurons (A Theoretical and Experimental Study)," R.V. Howard, W.K. Chai, and H. S. Tzou, *Adaptive Structures and Material Systems-1999*, AD-Vol.59/MD-Vol.87, pp.219-226, 1999 *Symposium on Adaptive Structures and Material Systems*, Nashville, TN, Nov.14-19, 1999.
4. "A New X-Actuator Design For Controlling Wing Bending And Twisting Modes," R. Ye, J. H. Ding, and H. S. Tzou, *Adaptive Structures and Material Systems-1999*, AD-Vol.59/MD-Vol.87, pp.143-148, 1999 *Symposium on Adaptive Structures and Material Systems*, Nashville, TN, Nov.14-19, 1999.
5. "Nonlinear Axial and Transverse Oscillation and Control of a PZT Laminated Beam System," H.S. Tzou, J.H. Ding, and W.K. Chai, the 6th Biannual Symposium on Active Control of Vibration and Noise (DCSS), AD-Vol.61, pp.125-132, 2000 ASME International Mechanical Engineering Congress, Orlando, FL, Nov.5-10, 2000.
6. "Equivalent Active Circuits of Distributed Control Systems," H.S. Tzou, J.H. Ding, the 6th Biannual Symposium on Active Control of Vibration and Noise (DSC), AD-Vol.61, pp.195-202, 2000 ASME International Mechanical Engineering Congress, Orlando, FL, Nov.5-10, 2000.

7. "Modal Voltages and Distributed Signal Analysis of Conical Shells of Revolution," H.S. Tzou, W.K. Chai, D.W. Wang, Paper No.Vib21544, 2001 Design Technical Conference, Pittsburgh, PA, Spt.9-12, 2001.
8. "Control of Conical Shells Laminated with Full and Diagonal Actuators," H.S. Tzou, D.W. Wang, and W.K. Chai, Paper No.CIE21272, 2001 Design Technical Conference, Pittsburgh, PA, Spt.9-12, 2001.
9. "Spatially Distributed Signals of Nonlinear Paraboloidal Shells with Distributed Neurons," H. S. Tzou and J. H. Ding, Paper No.Vib21545, 2001 Design Technical Conference, Pittsburgh, PA, Spt.9-12, 2001.
10. "Sensor Electromechanics and Distributed Signal Analysis of Piezo(Electptc)-Elastic Spherical Shells Based on the Bending Approximation," H.S. Tzou and P. Smithmaitrie, Paper No.Vib21494, 2001 Design Technical Conference, Pittsburgh, PA, Spt.9-12, 2001.
11. "Distributed Signals of Piezoelectric Laminated Toroidal Shell Structures," H.S. Tzou, D.W. Wang, and I. Hagiwara, Book No.I00521, Paper No.AD23715, CD-Vol.3, 2001 Adaptive Structures and Materials Symposium (Aero), 2001 ASME International Mechanical Engineering Congress, New York, NY, Nov.12-17, 2001.
12. "Precision Actuation Effectiveness of Segmented Actuators Laminated on Paraboloidal Reflectors," H.S. Tzou and J.H. Ding, Book No.I00528, *Symposium on Active Control of Vibration and Noise*, 2001 ASME International Mechanical Engineering Congress, New York, NY, Nov.12-17, 2001.
13. "Dynamics and Control of Adaptive Nonlinear Structures with Coupled Electric, Thermal and Mechanical Fields," H.S. Tzou and D.W. Wang, 2002 *Adaptive Structures and Materials Symposium* (Aero-14), paper no. IMECE2002-33938, 2002 ASME International Mechanical Engineering Congress, New Orleans. LA, Nov.17-22, 2002.
14. Micro-Control Actions of Segmented Actuators on Shallow Paraboloidal Shell Reflectors," S.-S. Lih, G. Hickey, J. H. Ding, and H. S. Tzou, 2002 *Adaptive Structures and Materials Symposium* (Aero-15B), paper no. IMECE2002-33979, 2002 ASME International Mechanical Engineering Congress, New Orleans. LA, Nov.17-22, 2002.
15. "Distributed Microscopic Signals and Modal Potentials of Nonlinear Conical Shells," W. K. Chai, P. Smithmaitrie, and H. S. Tzou, 2002 Adaptive Structures and Materials Symposium (Aero-5), paper no. IMECE2002-33940, 2002 ASME International Mechanical Engineering Congress, New Orleans. LA, Nov.17-22, 2002.
16. "Control of Nonlinear Electro/Elastic Beam and Plate Systems (Finite Element Formulation and Analysis)," D.W. Wang, H.S. Tzou, and H.-J., Lee, *Symposium on Advances of Solids and Structures* (PVP-8), paper no. IMECE2002-32329, 2002 ASME International Mechanical Engineering Congress, New Orleans. LA, Nov.17-22, 2002.
17. "Micro-Electromechanics of Sensor Patches on Free Paraboloidal Shell Structronic Systems," J.H. Ding and H.S. Tzou, *Symposium on Advances of Solids and Structures* (PVP-8), paper no. IMECE2002-32322, 2002 ASME International Mechanical Engineering Congress, New Orleans. LA, Nov.17-22, 2002.
18. "Constitutive Modeling of Controllable Electrostrictive Thin Shell Structures," W.K. Chai and H.S. Tzou, *Symposium on Advances of Solids and Structures* (PVP-8), paper no. IMECE2002-32328, 2002 ASME International Mechanical Engineering Congress, New Orleans. LA, Nov.17-22, 2002.
19. "Optimal Feedback Control of Precision Paraboloidal Shell Structronic Systems,"

H.S. Tzou and J. H. Ding, *Symposium on Active Control of Vibration and Noise* (DSC-8C), paper no. IMECE2002-33550, 2002 ASME International Mechanical Engineering Congress, New Orleans. LA, Nov.17-22, 2002.

20. "Directional Actuation Properties of Patch Actuators on Free Hemispherical Shells," P. Smithmaitrie and H.S. Tzou, *Symposium on Active Control of Vibration and Noise* (DE-3A), paper no. IMECE2002-33570, 2002 ASME International Mechanical Engineering Congress, New Orleans. LA, Nov.17-22, 2002.

21. "Micro-Control Actions and Location Sensitivity of Actuator Patches Laminated on Toroidal Shells," H.S. Tzou, W.K. Chai, and D.W. Wang, *Symposium on Active Control of Vibration and Noise* (DE-3A), paper no. IMECE2002-33580, 2002 ASME International Mechanical Engineering Congress, New Orleans. LA, Nov.17-22, 2002.

22. "Active Control of Largely Deformed Adaptive Structures using the Finite Element Technique," D.W. Wang, H.S. Tzou, S.M. Arnold, H.-J. Lee, IMECE2003-42390, 2003 IMECE Symposium on Active Control of Vibration and Noise, Washington DC on November 16-21, 2003.

23. "Micro-control Characteristics of Conical Shell Sections," W. K. Chai, H. S. Tzou, K. Higuchi, 2003 IMECE Symposium on Active Control of Vibration and Noise, IMECE2003-42387, Washington DC, November 16-21, 2003.

Dissertations

1. Dongwei, Wang, Ph.D., "Finite Element Analysis of Active Nonlinear Piezothermoelastic Structronic Systems applied to Aircraft Structures," Department of Mechanical Engineering, University of Kentucky, Lexington, KY (2003) (Post-doc, UK)
2. Jianghong, Ding, Ph.D., "Micro-Piezothermoelastic Behavior and Distributed Sensing/Control of Nonlinear Structronic Beam and Paraboloidal Shell Systems" Department of Mechanical Engineering, University of Kentucky, Lexington, KY (2002) (Western-digital)

Nonlinear Piezo(electric)thermoelastic/control Interaction Finite Element Code

Available upon request, when appropriate.